G.R.J. Swennen
F. Schutyser
J.-E. Hausamen

Three-Dimensional Cephalometry

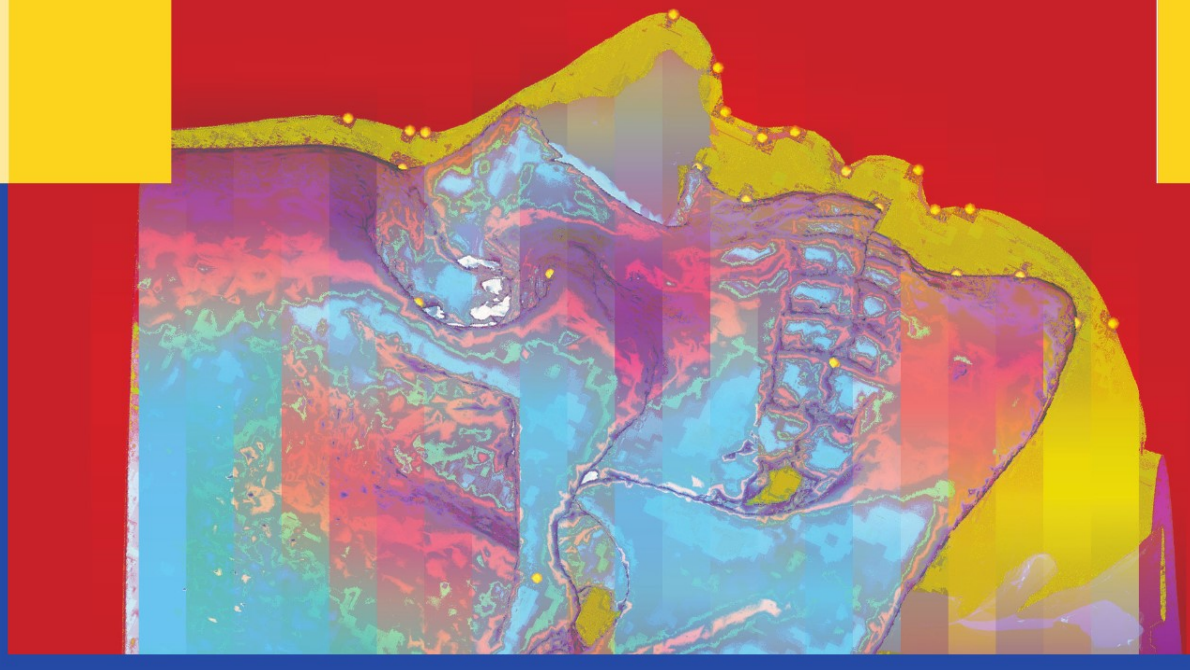

A Color Atlas and Manual

Springer

Gwen R. J. Swennen
Filip Schutyser · Jarg-Erich Hausamen

Three-Dimensional Cephalometry
A Color Atlas and Manual

Gwen R. J. Swennen
Filip Schutyser
Jarg-Erich Hausamen

Three-Dimensional Cephalometry

A Color Atlas and Manual

With 713 Figures, mostly in Colors and 6 Tables

Springer

Gwen R.J. Swennen, MD DMD PhD
Associate Professor
Department of Oral and Maxillofacial Surgery
Medizinische Hochschule Hannover
Hannover, Germany
and
Consultant Surgeon
Department of Plastic Surgery
University Hospital Brugmann
and Queen Fabiola Children's University Hospital
Brussels, Belgium

Filip Schutyser, MSc
Research Coordinator
Medical Image Computing (Radiology – ESAT/PSI)
Faculties of Medicine and Engineering
University Hospital Gasthuisberg
Leuven, Belgium

Jarg-Erich Hausamen, MD DMD PhD
Former Professor and Chairman
Department of Oral and Maxillofacial Surgery
Medizinische Hochschule Hannover
Hannover, Germany

ISBN-10 3-540-25440-4 Springer Verlag Berlin Heidelberg New York

ISBN-13 978-3-540-25440-9 Springer Verlag Berlin Heidelberg New York

Library of Congress Control Number: 2005929880

Springer is a part of Springer Science + Business Media

springeronline.com

Printed in Germany

Editor: Gabriele Schröder, Springer-Verlag, Heidelberg
Desk editor: Martina Himberger, Springer-Verlag, Heidelberg
Production: ProEdit GmbH, Elke Beul-Göhringer, Heidelberg
Cover design: Estudio Calamar, F. Steinen-Broo, Pau/Girona, Spain
Typesetting and reproduction of the figures: AM-productions GmbH, Wiesloch

Printed on acid-free paper
24/3151beu-göh 5 4 3 2 1 0

This book is dedicated to
my wife Valérie and my son Joaquin.

Gwen R. J. Swennen

Foreword

Radiographic cephalometry has been one of the most important diagnostic tools in orthodontics, since its introduction in the early 1930s by Broadbent in the United States and Hofrath in Germany. Generations of orthodontists have relied on the interpretation of these images for their diagnosis and treatment planning as well as for the long-term follow-up of growth and treatment results. Also in the planning for surgical orthodontic corrections of jaw discrepancies, lateral and antero-posterior cephalograms have been valuable tools. For these purposes numerous cephalometric analyses are available. However, a major drawback of the existing technique is that it renders only a two-dimensional representation of a three-dimensional structure.

It was almost 75 years before the next step could be taken in the use of cephalometrics for clinical and research purposes. The development of computed tomography and the dramatic decrease in radiation dose of the newer devices brings three-dimensional analysis of the head and face to the scene. A major step forward is also that 3D hard and soft tissue representations can be combined in the same image, which enables in depth analysis of these tissues in relation to each other possible.

With "Three-Dimensional Cephalometry – A Color Atlas and Manual" by the authors Swennen, Schutyser and Hausamen you have an exciting book in your hands. It shows you how the head can be analysed in three dimensions with the aid of 3D-cephalometry. Of course, at the moment the technique is not available in every orthodontic office around the corner. However, especially for the planning of more complex cases where combined surgical – orthodontic treatment is indicated, it is my sincere conviction that within 10 years time 3D cephalometry will have changed our way of thinking about planning and clinical handling of these patients.

July 2005

Anne Marie Kuijpers-Jagtman,
DDS, PhD, FDSRCS Eng
Professor and Chair
Department of Orthodontics
and Oral Biology
Radboud University Nijmegen
Medical Centre
Nijmegen, The Netherlands

Foreword

Few can fail to feel enlivened by entering a bookshop, and to encounter a new surgical textbook always provokes excitement. I am therefore most honoured to be asked to pen this foreword to what is truly a new book. This is not just a rehashing of old ideas on familiar topics, but a most innovative exploration of an increasingly important diagnostic medium, 3-D imaging.

We have all been assailed by sometimes startling 3-D images, but on cooler reflection have realised these were no more than clever pictures, of little value to patient or clinician. This book, however, provides a logical comprehensive text on the role of 3-D imaging in the surgical management of facial deformity. It skilfully provides a range of knowledge from the basic principles of radiological imaging to its use, giving the patients the best options for a predictable and good outcome. Seeing the list of authors, it should come as no surprise that this is innovative and highly informative. Professor Jarg-Erich Hausamen has established a centre of excellence for maxillofacial surgery. His modest persona, coupled with his great depth of knowledge and teaching skills, has made his unit an international name for innovation, training and, above all, patient care. It is not surprising, therefore, that his co-authors and former colleagues have shown tireless dedication in the production of this book.

It is clear that 3-D imaging has become an essential tool in planning and managing the treatment of facial deformity. The development of spiral CT and cone beam CT has revolutionised this technique, the former providing outstanding resolution and the latter, with its low cost, allowing unique accessibility. Both techniques reduce radiation levels to permit use in non-life-threatening conditions, such as facial deformity. These technological advances would be worthless, however, without this type of comprehensive textbook. This book educates and is a source of reference for all surgeons, regardless of seniority. It will be invaluable to those in other surgical specialities, who are less commonly involved in the management of facial deformity.

This volume is a joy to read and is enhanced by the high quality of the production and technical editing.

July 2005

Peter Ward Booth, FDS, FRCS
Consultant Maxillofacial Surgeon
Queen Victoria Hospital
East Grinstead, United Kingdom

Foreword

Similar to the biological and intellectual environment, craniofacial growth is not a linear phenomenon. It is characterized by periodicity: an initial phase of rapid growth is followed by a slowing of activity until a provision of new resources allows a new period of increased growth.

During the past three decades, craniofacial surgery has witnessed a paradigm shift as a result of the work of Paul Tessier, Fernando Ortiz Monasterio and others. A precise craniofacial imaging system for planning, monitoring and evaluation of results therefore became necessary. During the same three decades, medical imaging has developed in the same way. Since the use of the first cephalometric radiographs in our clinical practice in the 1970s, the development of computer tomography associated with the progress in computer technology gives us today access to unprecedented static and dynamic medical imaging. The need for an atlas that allows appropriate application of advanced three-dimensional craniofacial imaging methods is apparent.

This book is not a "cookbook" for clinical practice but a guide to three-dimensional treatment planning and evaluation of treatment outcome. The step-by-step method that the authors presents in this atlas will allow all professionals, including those who are not experts in imaging but have an interest in virtual computer-aided planning and surgery, to become familiar with three-dimensional cephalometry.

Gwen R. J. Swennen and his co-authors have gained considerable experience in this field. This atlas is the result of a team effort and the reflection of an excellent and safe clinical practice. I have to congratulate Gwen Swennen on his wonderful work, his boundless enthusiasm and his unending dedication to his profession. It is a pleasure and a privilege to work with him in my department as he not only acquires learning but also transmits it.

July 2005

Albert De Mey, MD
Professor and Chairman
Department of Plastic Surgery
University Hospital Brugmann
Brussels, Belgium
Queen Fabiola Children's
University Hospital
Brussels, Belgium

Preface

On the day he won the Nobel Prize in 1979,
Godfrey Hounsfield had some home-spun words
of advice for all would-be Nobel laureates:

Don't worry too much if you don't pass exams,
so long as you feel you have understood the subject.
It's amazing what you can get by the ability
to reason things out by conventional methods,
getting down to the basics of what is happening.

Sir Godfrey N. Hounsfield,
28 August 1919–12 August 2004

„Cephalometric radiography" was introduced in orthodontics in 1931 by B. H. Broadbent and H. Hofrath, who developed simultaneously and independently standardized methods for the production of cephalometric radiographs. It was, however, not until the 1960s that this method gained worldwide acceptance for the evaluation of craniofacial morphology and growth in daily clinical practice. Meanwhile, cephalometric analysis has proven to be a valuable tool for planning, monitoring and evaluation of orthodontic, surgical and combined treatment protocols, especially in regard to stability.

„Computer tomography" (CT), developed by G.N. Hounsfield in 1972 based on the mathematical and pioneer work of A.M. Cormack, represented a major breakthrough in diagnostic radiography. Cormack and Hounsfield's pioneer work was rewarded with the Nobel Prize in Medicine and Physiology, which they shared in 1979. CT is nowadays available practically worldwide, is becoming more and more cost-efficient, and the new generation of spiral multi-slice (MS) CT and cone beam CT causes less irradiation for the patient.

Currently voxel-based craniofacial surgery and virtual assessment of craniofacial morphology and growth are becoming increasingly popular. Recent advances in computer software technology allow the combination of conventional cephalometric radiography and CT methods. It was therefore a fascinating challenge to develop a new method of voxel-based „three-dimensional cephalometry".

Three-dimensional (3-D) cephalometry is a powerful tool for planning, monitoring and evaluation of craniofacial morphology and growth. It allows objective immediate and long-term postoperative assessment of virtual planned or assisted craniofacial surgical procedures. The accuracy and reliability of 3-D cephalometry, however, depends on the correct application of the method. This atlas is a practical straight forward „step-by-step" manual for both orthodontists, maxillofacial, craniofacial and plastic surgeons interested in virtual computer-aided planning and surgery. Because this book is an atlas and manual, the emphasis is on little text and numerous comprehensive color illustrations.

In order to help the reader become familiar with voxel-based 3-D cephalometry, Chap. 1, deals with the principles of 3-D volumetric CT. Chapter 2 focuses on basic craniofacial anatomical knowledge. 3-D cephalometry demands new knowledge from orthodontists regarding interpretation of CT anatomy. On the other hand, maxillofacial and craniofacial plastic surgeons are often not familiar with conventional cephalometry and may need some additional expertise regarding cephalometric radiography. The nomenclature is in English, based on the recommendations found in the 4th edition of *Nomina Anatomica*. Chapter 3 highlights the set-up of a precise and reliable 3-D reference system that allows longitudinal comparison of craniofacial growth patterns and comparison of pre-operative findings, virtual planning and post-operative results. In the following chapters, „step-by-step" virtual definition of 3-D cephalometric hard (Chap. 4) and soft (Chap. 5) tissue landmarks is described concisely. Only landmarks whose accuracy and reliability has been statistically validated are described in detail; additional landmarks are mentioned. To ensure uniformity, internationally accepted landmarks are used and named according to the Greek or Latin anatomical terminology as proposed by L.G. Farkas, who stated „...the use of the internationally accepted anthropometric symbols, without any individual modifications, is a „sine qua non" for easy understanding of papers based on anthropometry...".

The next two chapters deal with 3-D cephalometric planes (Chap. 6) and 3-D cephalometric hard and soft tissue analysis (Chap. 7). A great number of analytical and investigatory cephalometric procedures have been described in the literature. To avoid confusion, meaningful practical cephalometric measurements are described that provide data for clinical decision making. Moreover, additional measurements designed for scientific research and validation purposes are supplied. No descriptive data are given because normative hard and soft tissue data are not yet available. A separate chapter (Chap. 8) deals with the potential of 3-D cephalometry to assess craniofacial growth. Finally, clinical orthodontic and surgical applications of 3-D cephalometry are illustrated in Chap. 9. Since 3-D cephalometry is still very new, the future will certainly bring innovations. The last chapter (Chap. 10) highlights some interesting future perspectives of 3-D cephalometry.

It is our sincere hope that this atlas will prove to be a valuable reference on the basic principles of 3-D cephalometry for different specialities involved in the assessment of the head and the face, such as orthodontics, maxillofacial, craniofacial and plastic surgery, medical anthropology and dysmorphological genetics. We hope that this atlas will stimulate both clinicians and researchers to extend their expertise and to further develop the rapidly expanding and interesting field of virtual craniofacial assessment.

Hannover,
July 2005

Gwen R. J. Swennen, MD DMD PhD
Filip Schutyser, MSc
Jarg-Erich Hausamen,
MD DMD PhD

Acknowlegdements

I especially wish to thank my teacher and mentor Professor Jarg-Erich Hausamen, who encouraged me to write this book. Without his inspiration, guidance and advice the book would never have appeared.

I am also deeply grateful to Johan Van Cleynenbreugel (Medical Image Computing, ESAT/PSI, University of Leuven) for his support. I further wish to thank Professor Albert De Mey (Department of Plastic Surgery, University Hospital Brugmann and Queen Fabiola Children's University Hospital, Brussels) and Professor Chantal Malevez (Department of Maxillofacial Surgery, Queen Fabiola Children's University Hospital, Brussels) for their continuous support. I am very grateful to Professor Henning Schliephake (Department of OMF Surgery, Georg-August University, Göttingen), Dr. Peter Brachvogel (Department of OMF Surgery, Hannover Medical University, Hannover) and Dr. Alex Lemaître (Facial Plastic Surgery, Private Practice, Brussels) for teaching and sharing their clinical and scientific knowledge with me. I also thank Johannes-Ludwig Berten (Department of Orthodontics, Hannover Medical University, Hannover) for the interesting late evening discussions on craniofacial morphology and problems related to orthognathic surgery.

I would like to express my special thanks to Pieter De Groeve (Medicim NV, Sint-Niklaas, Belgium) for his untiring efforts to develop 3-D cephalometry and to my colleagues Dr. Enno-Ludwig Barth and Dr. Christopher Eulzer (Department of OMF Surgery, Hannover Medical University, Hannover) for their invaluable help in validating the 3-D cephalometry method presented here.

I am indebted our photographer Klaus Fröhlich (Department of OMF Surgery, Hannover Medical University, Hannover) for the excellent clinical images and our dental technicians, Mr. Böhrs and Ms Luginbühl (Department of OMF Surgery, Hannover Medical University, Hannover) for their support and help. I wish to thank Professor H. Hecker (Department of Biometry, Hannover Medical University, Hannover) for his assistance in the statistical validation study. I also am very grateful to Professor C. Becker and Ms Utenwold (Neuroradiology Department, Hannover Medical University, Hannover) for their support and help.

Last but not least, I would like to thank Springer for their energy and cooperation in publishing this atlas.

Brussels, July 2005

Gwen R. J. Swennen,
MD DMD PhD

Acknowlegdements

I would like to dedicate this book to the memory of my mentor, Johan Van Cleynenbreugel. He taught me medical image computing and also stimulated my passion for it. I wish to continue working with his scientific spirit and hope to exploit the valuable expertise that he imparted to me „at maximum".

I am grateful to Paul Suetens for his inspiring research environment „ESAT/PSI Medical Image Computing" at the Catholic University of Leuven. I also wish to thank Pieter De Groeve, whose committed efforts were important in realizing the 3-D cephalometric approach as a user-friendly software application.

Leuven, July 2005 Filip Schutyser, MSc

Contents

Contributors

Johan Van Cleynenbreugel, MSc PhD
Professor
Medical Image Computing (Radiology – ESAT/PSI)
Faculties of Medicine and Engineering
University Hospital Gasthuisberg
Leuven, Belgium

Filip Schutyser, MSc
Research Coordinator
Medical Image Computing (Radiology – ESAT/PSI)
Faculties of Medicine and Engineering
University Hospital Gasthuisberg
Leuven, Belgium

Gwen R. J. Swennen, MD DMD PhD
Associate Professor, Department of Oral
and Maxillofacial Surgery
Medizinische Hochschule Hannover
Hannover, Germany
and
Consultant Surgeon, Department of Plastic Surgery
University Hospital Brugmann
and Queen Fabiola Children's University Hospital
Brussels, Belgium

CHAPTER 1 From 3-D Volumetric Computer Tomography to 3-D Cephalometry

Filip Schutyser, Johan Van Cleynenbreugel

With 3-D cephalometry, the head is geometrically analysed in three dimensions. In order to do so, an accurate volumetric measurement of the head is needed, together with the appropriate tools to access this 3-D dataset. This implies a toolset to access the data of importance in a reliable and repeatable way. Moreover, it is important to bridge classical 2-D approaches with new 3-D analysis methods.

To measure the anatomy of the head, CT imaging is the modality of preference because of its high contrast for bony tissues. In Sect. 1 of this chapter the focus is on CT imaging of the head.

After a correct CT acquisition of the head, the 3-D data need to be visualized appropriately. Therefore, a 3-D scene approach is applied. Section 2 of this chapter details this approach.

To bridge this new 3-D technology with the classical clinical daily practice, which consists of the use of 2-D cephalometry, virtual 2-D cephalograms are generated and co-visualized with the 3-D data, taking into account the geometrical relationships. In this way, a combined 2-D and 3-D approach opens the way towards reliable and repeatable 3-D analysis of the head. Section 3 of this chapter explains this technology.

1.1 CT Imaging of the Head

1.1.1 CT Scanner

Computed tomography is an imaging modality that produces cross-sectional images representing the X-ray attenuation properties of the body.

Image formation is based on the following procedure. Using an X-ray beam, a set of acquisitions is made, covering the entire field of view. This process is repeated for a large number of angles, yielding line attenuation measurements for all possible angles and for all possible distances from the centre. Based on all these measurements, the actual attenuation at each point of the scanned volume can be reconstructed.

To acquire a volume of data, two scanning modes are possible: sequential CT or spiral CT. With sequential CT, the table with the patient is positioned, and attenuation data are acquired. Then the table is moved to a next position, and a new acquisition is made. With spiral CT, the table moves from the starting position to the end position while X-ray attenuation data are acquired. From these data, a set of consecutive CT slices is computed.

Three CT technologies can be distinguished (Fig. 1.1):

1. Single-slice CT
   This type of CT scanner is the oldest. From an X-ray source, a fan-beam X-ray is emitted through the imaged object towards a single array of detectors. The tube–detector unit rotates around the patient. Sequential as well as spiral scanning is possible.
2. Multi-slice CT
   The multi-slice CT scanner, introduced in 1998, allows acquisition of multiple slices simultaneously using adjacent detector arrays. In 2004, this number of arrays varies from 2 to 64 slices. This technology implies faster imaging and reduced dose. Sequential as well as spiral scanning is possible.
3. Cone-beam CT
   With cone-beam CT (CBCT) scanners, the detector is extended to a 2-D detector. For the field of dento-

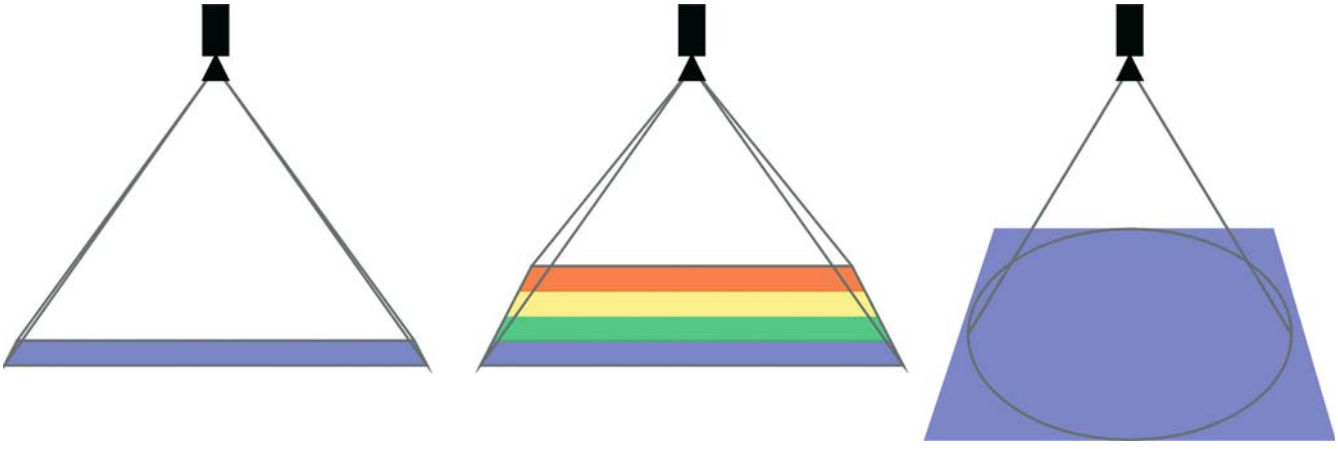

Fig. 1.1. The different types of CT scanners

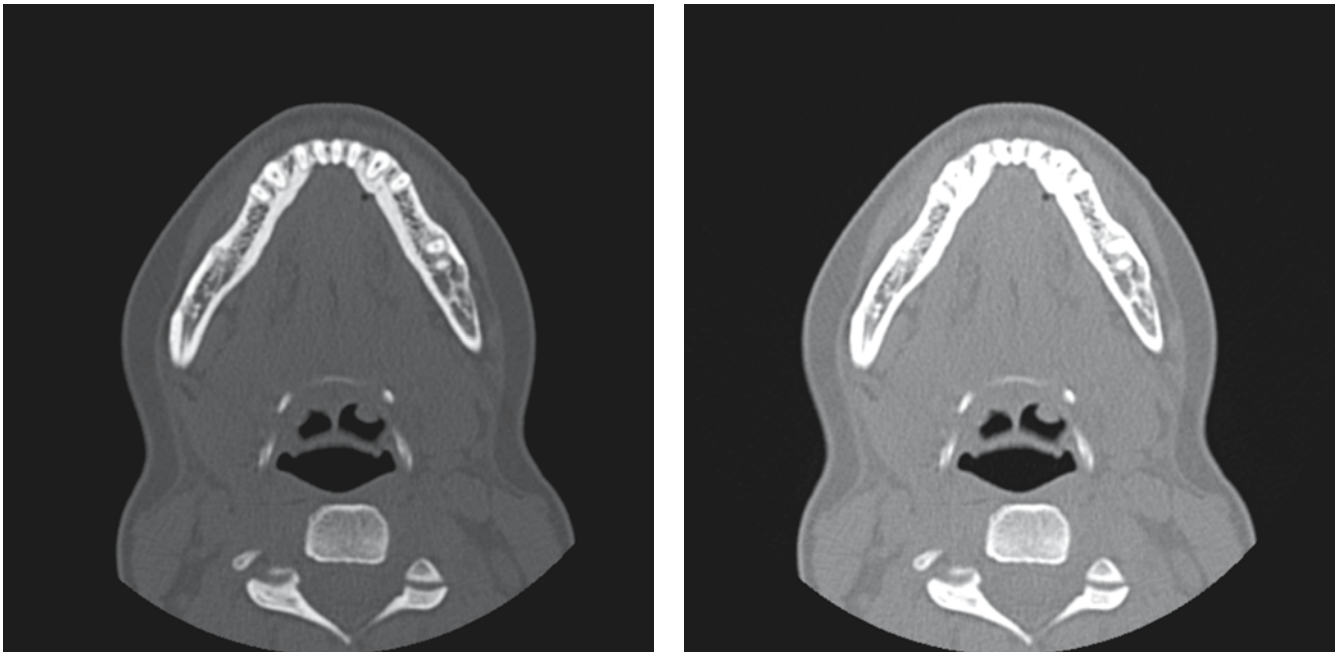

Bone
(window = 3100 HU; level = 700 HU)

Soft tissue
(window = 2200 HU; level = 50 HU)

Fig. 1.2. With appropriate window/level settings, the structures of importance are visualized with the preferred contrast

maxillofacial imaging, dedicated devices are developed. With one rotation of the tube–detector unit, a large part of the skull can be imaged. With dedicated cone-beam reconstruction algorithms, a detailed CT data volume is obtained. Since the focus of CBCT devices is on bone imaging, the dose can be significantly reduced.

1.1.2 Characteristics of a CT Dataset

The attenuated X-rays are captured by the detectors of the CT scanner and digitized. Reconstruction algorithms convert these data into a single CT slice or a set of CT slices. Thus, the slices have a digital nature. They can be printed on film, but, with increasing frequency, they are stored and sent digitally. For digital transmission of CT slices, a dedicated open communication protocol has been established: Digital Imaging and Communications in Medicine (DICOM). DICOM also specifies a file format for storage of CT slices as digital files. Systems to store and retrieve all this image information have been developed. This type of information technology system is called a Picture Archiving and Communication System (PACS).

The CT volume consists of a 3-D array of image elements, called voxels, with a CT number with a range of typically 12 bits, expressed in *Hounsfield units* (HU). By definition, the CT number of water (H_2O) is 0 HU. Air is typically about –1000 HU.

Since the dynamic range is too high to be perceived in a single image, a *window/level* operation – this is a grey level transformation – must be applied. This operation rescales the CT numbers around a defined number, i.e. the level, in a range defined by the window to 256 grey values that are shown on the computer display. With appropriate settings of window/level, soft tissues or bone, for example, are visualized with more contrast (Fig. 1.2).

The spatial *resolution* in a CT image is non-isotropic and non-uniform and depends on a number of factors during acquisition (e.g. focal spot, size detector element and table feed) and reconstruction (reconstruction kernel, interpolation process, voxel size). For dento-maxillofacial CT imaging, a resolution of 0.5 mm in X, Y and Z directions is achievable. When the resolution is reduced, the reduction typically applies to the cranio-caudal (Z) direction.

Image *noise* depends on the total exposure and the reconstruction noise. Increasing the current in the X-ray tube increases the signal-to-noise ratio, and thus reduces the quantum noise of the statistical nature of X-rays, at the expense of patient dose. The applied filters and interpolation methods in the reconstruction algorithm influence image noise.

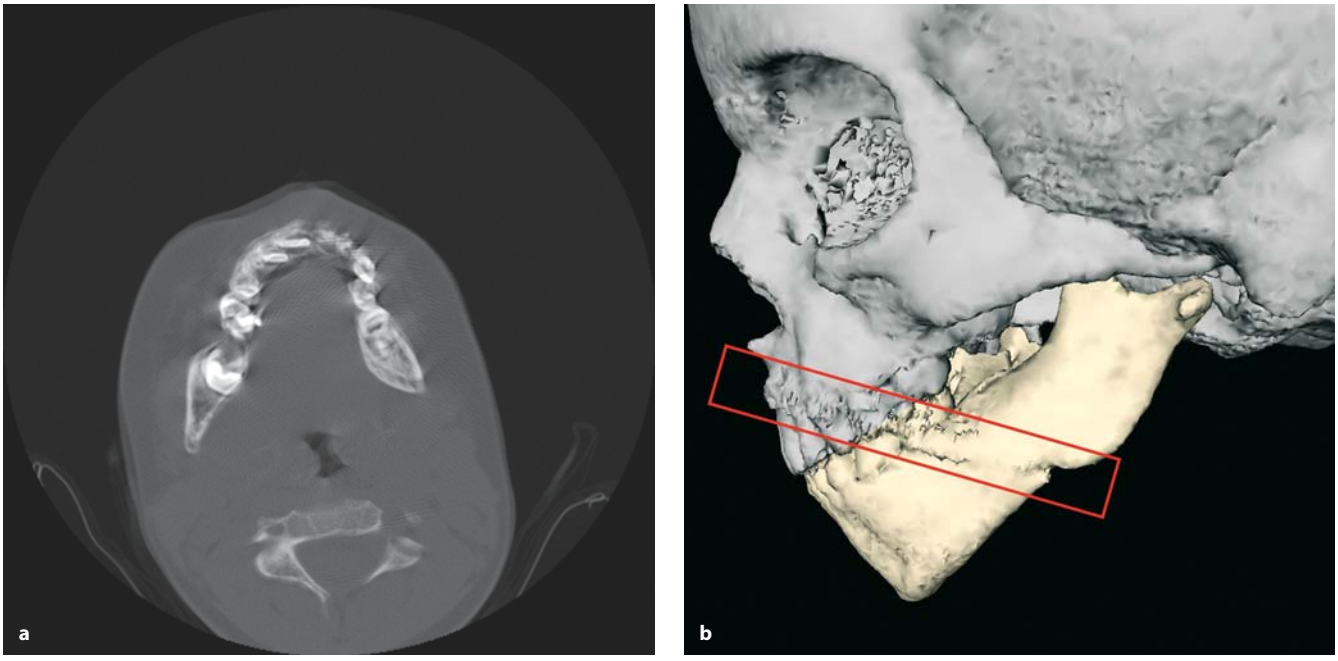

Fig. 1.3. Movements of the patient during CT acquisition results in some blurred CT slices (**a**). As a consequence, the 3-D rendering of the bone is also distorted (**b**) at the position of the blurred CT slices

CT imaging also shows *artefacts*. Several factors influence these artefacts:

- Beam hardening
  Ideally, an X-ray source would emit mono-energetic rays. However, this is not the case. Low-energy photons are preferentially absorbed, i.e. the X-ray beam hardens as it passes through tissue. The harder the beam, the less it is further attenuated. All beams passing through a particular point in the imaged volume follow different paths and therefore experience a different degree of beam hardening. Hence, they attain different attenuation values. This phenomenon causes beam-hardening artefacts such as reduced attenuation towards the centre of an object and streaks that connect objects with strong attenuation.
- Scatter
  Not all photons follow a straight path due to Compton scatter. As a consequence, the measured intensity is always an underestimation of the integrated averaged attenuation. This results in streaks tangent to edges.
- Non-linear partial volume effect
  Because of the finite beam width, every measurement represents an intensity averaged over this beam width. It can be shown that this value corresponds with an underestimation of the integrated averaged attenuation. The larger the attenuation differences along the beam width, the larger this underestimation. This results in streaks tangent to edges.
- Motion
  A short movement of the imaged object results in inconsistent measurements, and thus causes artefacts (Fig. 1.3).
- Stair-step artefact
  The interpolation process inherent to spiral CT involves several types of artefacts. The most common example is the stair-step artefact. This artefact is visible as regular step-like disruptions along edges with an inclination with respect to the longitudinal axis. This artefact can be typically observed in the cranium (Fig. 1.4).
- Other artefacts
  A variety of other artefacts are related to poor calibration or system failure. Also, the number of detectors has to be sufficiently high, or the beam sufficiently wide, to avoid under-sampling artefacts. Moreover, the number of views needs to be sufficiently large to avoid alternating dark and bright streaks in the peripheral image region where the sampling density is smallest.

Artefacts due to amalgam fillings or brackets are typically a combination of beam hardening, scatter and non-linear partial volume effect (Figs. 1.5, 1.6).

Based on these findings, a generic CT protocol is proposed. The patient should be scanned in one con-

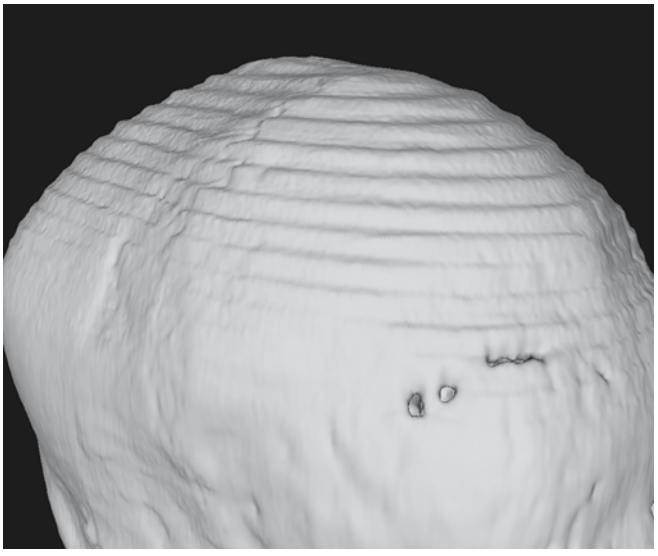

Fig. 1.4. When the slice interval is large, the stair artefact is clearly visible on the cranium

tinuous acquisition, with a tube voltage of 120 kV and current of 80 mAs. In order to reduce the artefacts, the occlusal plane should be parallel to the axial slice plane, and no gantry tilt should be applied. The slice thickness should be equal to the collimation width. The pitch (= table speed / rotation speed) is preferably lower then 1. In order to image the soft tissues correctly, the use of fixation bandages or cushions should be avoided. Although this increases the risk of motion artefacts, only then are the soft tissues correctly imaged. These are the acquisition settings.

For the reconstruction settings, a bone filter is preferred, but very sharp filters should not be used, because this boosts the amount of noise. As a reconstruction interval, half the detector width should be chosen, and this should be in the range of 0.5–1 mm. This typically results in datasets of 150–200 slices, or 75–100 MB.

1.1.3 Radiation Dose

As CT imaging is based on X-rays, radiation dose should be investigated. The *absorbed dose*, i.e. the energy delivered to the traversed material, is expressed in grays (Gy). The absorbed dose is independent of the type of irradiation. For CT, the measurements of absorbed dose are often performed according to IEC 60601–2-44. In a polymethylmethacrylate (PMMA) cylinder with a diameter of 160 mm and a length of 200 mm, dosimeters are inserted in dedicated holes. From these measurements, the CT dose index (CTDI) is defined and expressed in mGy. This dose number gives a good estimate for the average dose applied in the scanned volume as long as the patient is similar in size to the respective dose phantom.

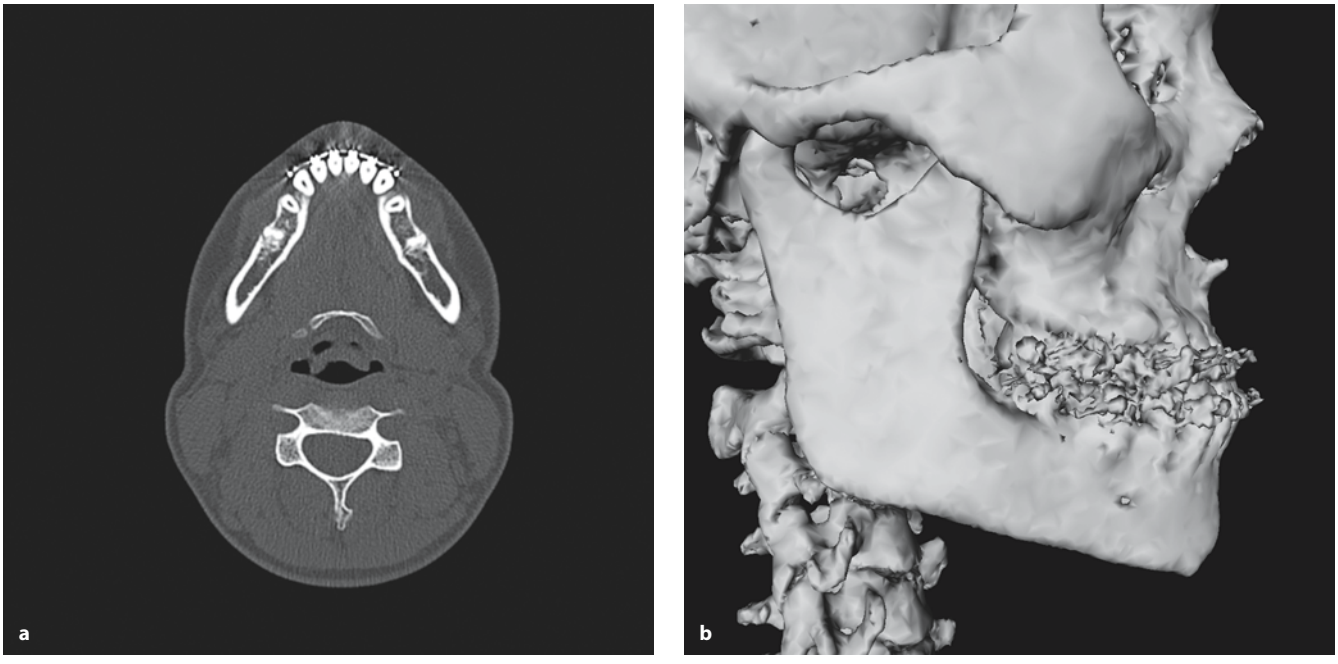

Fig. 1.5 a, b. Metal orthodontic brackets caused some artefacts at the level of the teeth. However, the amount of artefacts is fairly small

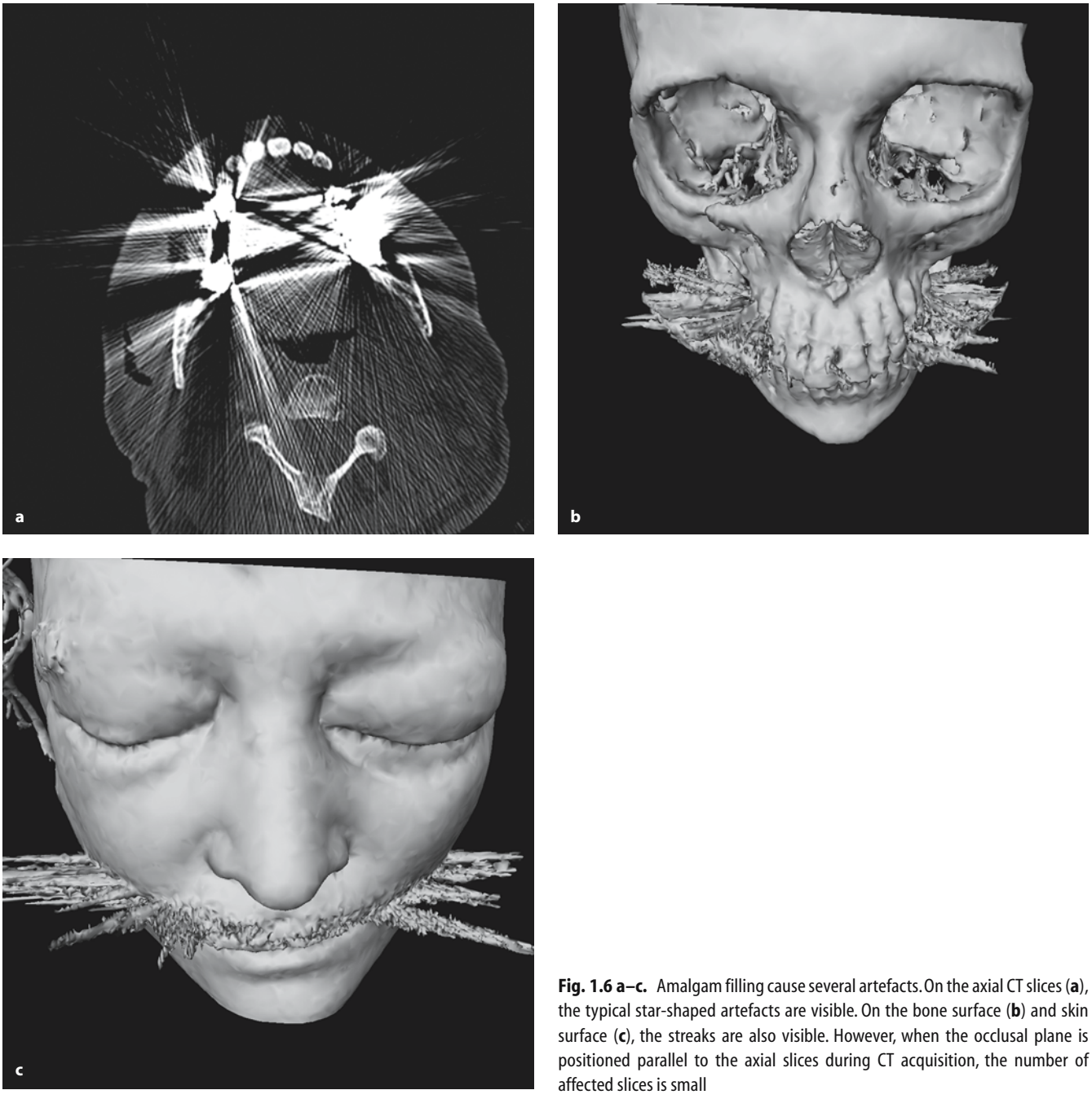

Fig. 1.6 a–c. Amalgam filling cause several artefacts. On the axial CT slices (**a**), the typical star-shaped artefacts are visible. On the bone surface (**b**) and skin surface (**c**), the streaks are also visible. However, when the occlusal plane is positioned parallel to the axial slices during CT acquisition, the number of affected slices is small

However, the biological damage varies not only with the absorbed energy but also depends heavily on the wavelength of the radiation. To take this effect into account, the absorbed dose has to be multiplied by a radiation-weighting factor, yielding the *equivalent dose*.

The harm induced by the radiation also depends on the irradiated organ. The risk for cancer or genetic disorders for the same equivalent dose varies among organs. Therefore, tissue-weighting factors have been developed. Multiplying the equivalent dose of an organ with the corresponding weighting factor gives the *effective dose*, expressed in sieverts (Sv), of that organ. The effective dose for the patient then is the sum of the effective doses for all organs. The sum of all weights equals 1. Well-accepted weighting factors are defined by the International Commission on Radiological Protection (ICRP) in ICRP publication 60. Because of the potential risk of medical irradiation, the ICRP also recommends keeping the magnitude of individual exam-

Table 1.1. The effective doses of different acquisition schemes according to the settings explained in Sect. 1.1.3

Acquisition	Effective dose	Equivalent natural background radiation
CT full skull	0.93 mSv	97 days
CT mandible, maxilla, orbit	0.41 mSv	50 days
CT mandible, maxilla	0.31 mSv	38 days
CT dental mandible	0.27 mSv	33 days
CT dental maxilla	0.21 mSv	26 days
CBCT	0.05 mSv	6 days
Cephalogram	0.1 mSv	12 days
OPG	0.05 mSv	6 days

ination doses *as low as reasonably achievable* (ALARA principle).

The average equivalent dose due to natural sources is estimated at about 3 mSv per year in US.

For a multi-slice scanner (Siemens Sensation 64, tube potential 120 kV, effective tube current 80 mAs, slice thickness 0.75 mm, slice collimation 0.75 mm, table feed 6 mm/s, rotation time 0.75 s, scan length 225 mm, scan time 29.48 s), the effective dose for a complete head scan without thyroid gland is 0.93 mSv. If the effective tube current is reduced, the dose reduces linearly. If the scanning area is reduced to mandible, maxilla and eyes, a effective dose of 0.45 mSv is measured. If the area is further reduced to the mandible and maxilla, the dose reduces to 0.31 mSv.

With CBCT scanners, an important reduction of dose is achieved. For example, the NewTom QR DVT-9000 can, at maximum, scan a height of 70 mm, i. e. a range of mandible and maxilla. The tube potential is 110 kV and the tube current is about 2.5 mA. The resulting effective dose is 0.05 mSv. However, due to this lower dose, the resulting CT images show more noise and artefacts, and detailed information about soft tissues is lost.

These dose values should be compared with the classical cephalogram and orthopantogram (OPG) doses. Table 1.1 gives an overview of the doses, and shows the equivalent time to have the same dose as natural background radiation.

1.1.4 3-D Image Volume

CT imaging of the maxillofacial region results in a stack of 2-D digital images. Each voxel is characterized with a height, width, and depth. A typical voxel size of a CT scan of the maxillofacial complex is $[v_x, v_y, v_z]$ = [0.4 mm 0.4 mm 1 mm]. When all these CT slices are ordered, a block (rectangular prism) of image data is obtained (Fig. 1.7). Thus, CT imaging performs a volumetric measurement of the X-ray attenuation values and therefore images the patient's anatomy in three dimensions with a particularly high contrast for radioopaque structures. These structures are typically bone. Since the voxel sizes are known from the acquisition, correct measurements can be performed.

This understanding of a three dimensional volume of digital data is the key for building 3-D visualization systems. For example, when the CT numbers at the intersection of a rectangle with this volume are computed, a reconstructed slice (reslice) is obtained (Fig. 1.8). Conventional cuts through the volume – axial, coronal and sagittal slices – are straightforward, but also any other reslice is defined in this way.

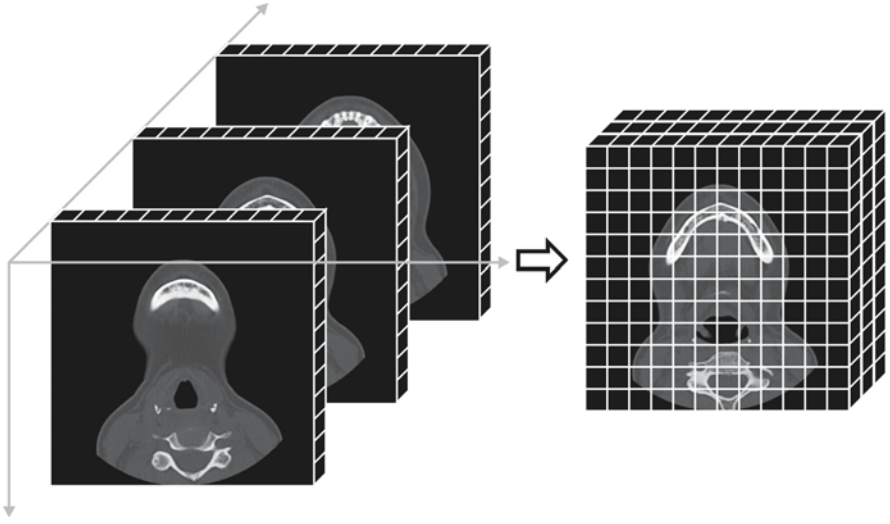

Fig. 1.7. Single CT slices of the imaged object are composed into a block of 3-D image data

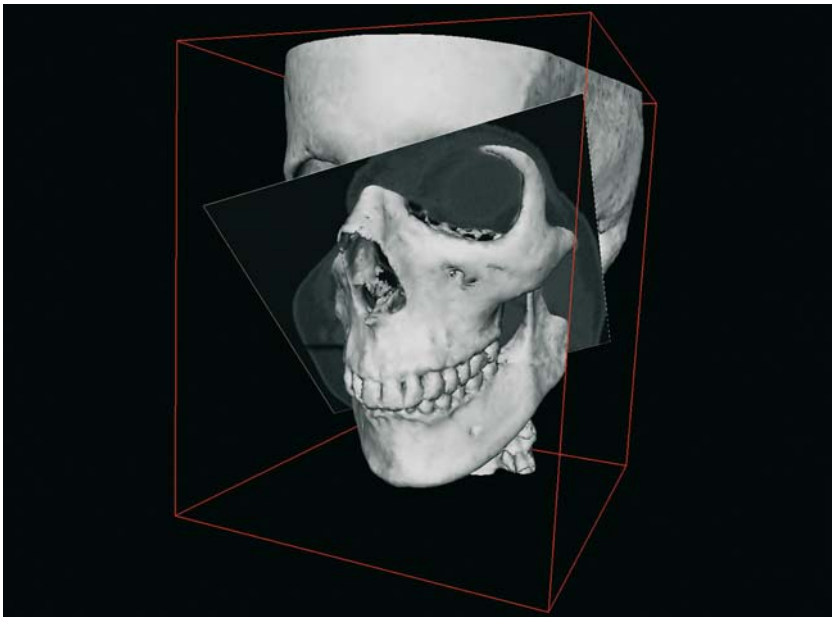

Fig. 1.8. By computing the CT numbers at the intersection of a rectangle with the image volume, any reslice can be defined

1.2 3-D Scene Approach

To effectively depict the volumetric data block of CT numbers, a visualization paradigm is needed. A scene-based approach is adopted. The virtual 3-D space is considered as a 3-D scene with medical image data as actors. This scene is viewed with a virtual camera, and the resulting views are shown on the screen. To inspect the scene from various angles and positions, the camera is moved around.

In this virtual scene, various actors are present. Based on the volumetric CT data, surface models of the bone and skin surface can be computed. These surface representations are computed as isosurfaces. An isosurface is a surface that connects points within the image volume with a specified CT number. These surfaces are added to the scene. Also CT slices are positioned in this scene. Furthermore, related data such as rulers, surgical devices and markers feature in the scene (Fig. 1.9).

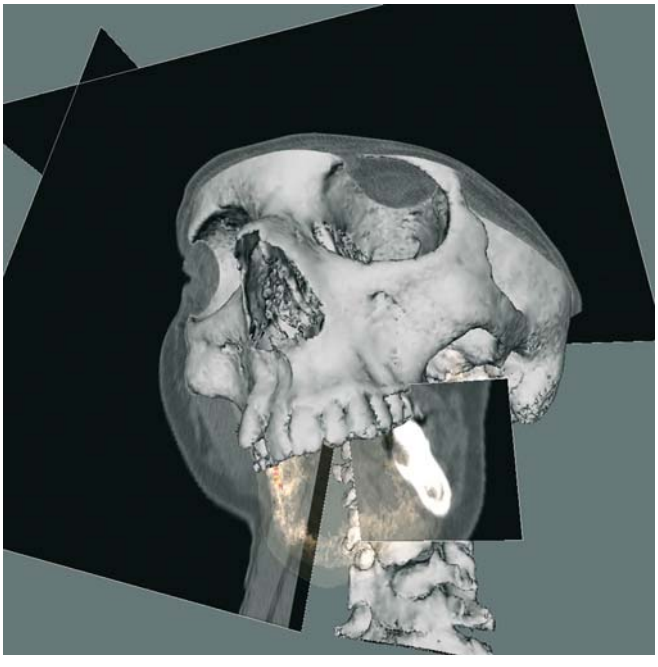

Fig. 1.9. The virtual scene can be composed with the structures of interest

It is important to visualize only the structures of interest during a certain stage of inspecting the patient's anatomy or performing surgical planning. Therefore, all the objects in the scene have a visibility property. Any object hiding the object of interest can be made temporarily invisible.

Besides visualizing the image data, the paradigm also allows for actions in this scene. In addition to the ability to move the virtual camera around, a mode to interact with objects is required. Then actions such as indicating landmarks, performing virtual osteotomies and moving bone fragments become possible (Fig. 1.10).

Today, these visualizations are possible on desktop or laptop computers (e.g. CPU P4 2.0 GHz, RAM 512 MB, graphics card nVidia GeForce Series) with dedicated image-based planning software (e.g. Maxilim, www.medicim.com). The Maxilim data files (.mxm) have an average size of 50 MB.

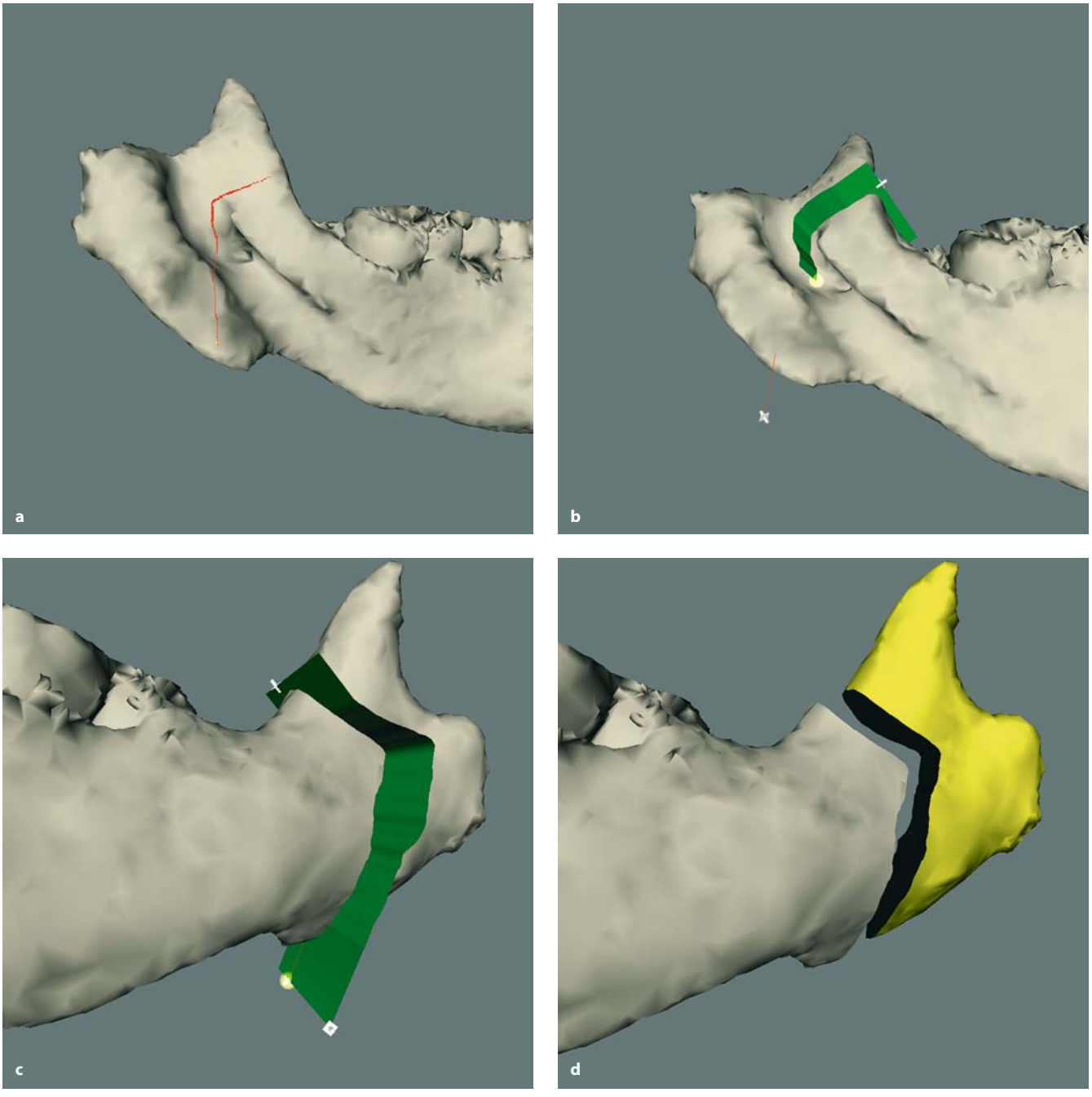

Fig. 1.10 a–d. As an example, virtual osteotomies can be simulated. First a cut surface is designed. A possibility is to draw a line (**a**), and add depth dimension (**b, c**). Finally the bone is cut and split (**d**)

Fig. 1.11. For a lateral cephalogram, the patient is positioned in a standard way in the X-ray machine

1.3 Virtual Cephalograms

1.3.1 Conventional 2-D Cephalograms

Cephalometric X-ray images are widely accepted in daily routine. The patient is installed in a standard way in the X-ray apparatus (Fig. 1.11). Then, the patient's head is exposed to an X-ray beam. The image is captured on film with a screen-film detector, or digitally stored using electronic detectors or computed radiography. The effective dose of an X-ray of the skull is 0.1 mSv.

Ideally, a parallel X-ray beam is generated by the X-ray tube, attenuated by the tissues of the head, and transformed into an image without distortion, with a high dynamic range (good contrast) and with a high signal-to-noise ratio. The resolution, however, is related to the quality of the anode tip, the size of the patient (thicker patients cause more X-ray scattering, deteriorating the image resolution) and the conversion from X-ray to image (either on film or digitally).

1.3.2 Generation of the Virtual Cephalogram

In a 3-D environment, 3-D CT imaging is needed to volumetrically measure the patient's anatomy. However, for a cephalometric analysis, the availability of 2-D lateral and frontal cephalograms is beneficial to indicate landmarks accurately and repeatably in the 3-D scene. Therefore, the geometrical relationship between cephalogram and CT image volume is a prerequisite if one is to benefit from the combination of CT and virtual cephalograms.

To avoid extra radiation dose, and to achieve this geometric relationship, lateral and frontal cephalograms are computed from the CT data. In this way, an unlimited number of virtual X-ray images of the skull can be computed (Chap. 2).

To compute a virtual X-ray image, a bundle of parallel rays is cast through the CT volume (Fig. 1.12). Each CT number is associated with an opacity value. When a ray travels through the CT volume, the CT numbers, modulated with the related opacity value, are accumulated, resulting in a final grey value. The grey values of the bundle of rays compose the virtual X-ray image. Again, the contrast of this projection image can be adjusted by modifying the window/level settings in a similar way as on a native CT slice.

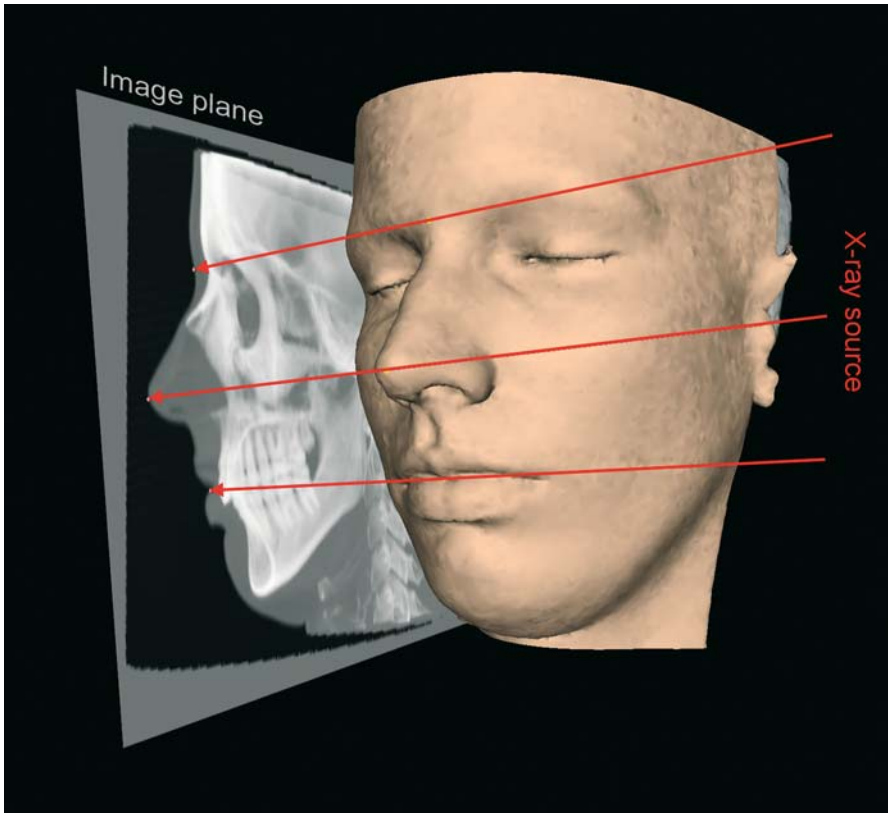

Fig. 1.12. A virtual cephalogram is computed from the CT image volume. A virtual parallel X-ray beam is sent through the patient. Extra radiation dose is avoided, and the geometrical relationship is known

1.3.3 Visualization of Virtual Cephalogram and 3-D Data

The orientation of the virtual X-ray image plane is perpendicular to the bundle of rays. Therefore, this X-ray image can be added to the 3-D scene as a textured rectangle. Since this image is a projection image, its position on the ray is not fixed, but adjacent to the CT image volume.

Since the projection direction is known, for each point of the X-ray image a projection line is defined. All points on this line are projected on a single point in the X-ray image. This line also intersects with the bone or skin surfaces in the 3-D scene. Therefore, when a point is indicated on the cephalogram as a point on the bone surface, the 3-D point should be positioned on this line and on the bone surface. This combination of 2-D and 3-D information is the key to accurate indication of landmarks in a repeatable way.

1.3.4 Benefits of This Environment

The 3-D scene allows combination of 3-D hard and soft tissue representations with lateral and frontal cephalograms. This allows the set-up of a reliable 3-D cephalometric reference system (Chap. 3). Moreover, 3-D cephalometric hard (Chap. 4) and soft (Chap. 5) tissue landmarks can be precisely defined and accurately positioned. Each landmark is visualized on the surface representations together with its projection points on both cephalograms. Depending on the nature of a landmark, it can be easily indicated on the bone surface and adjusted on the cephalograms, or vice versa. This ease of indicating landmarks is an important benefit of this approach.

Once landmarks are defined, they can be combined to define anatomical planes (Chap. 6). Moreover, based on these landmarks and planes, a complete set of hard and soft tissue measurements can be defined: linear measurements (3-D distances, distances with respect to a reference frame) angular and proportional measurements (Chap. 7).

CHAPTER 2 Basic Craniofacial Anatomical Outlines

Gwen R. J. Swennen

2.1 3-D CT Anatomy of the Skull

Skull – Anterior View

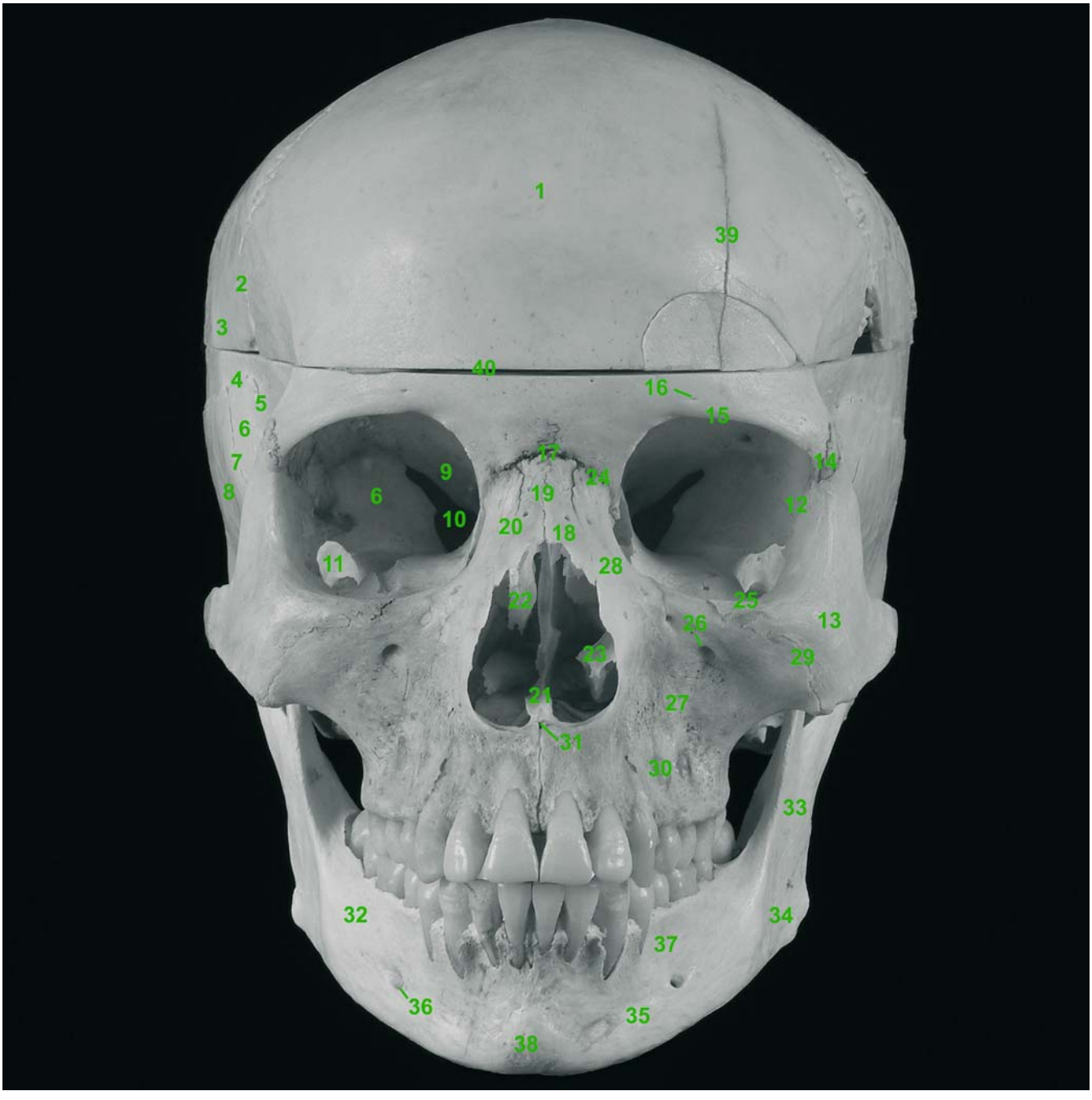

Fig. 2.1. a Anterior view of the skull in centric occlusion (adult cadaver skull). *1* Frontal bone; *2* Coronal suture; *3* Parietal bone; *4* Sphenoparietal suture; *5* Sphenofrontal suture; *6* Greater wing of sphenoid bone; 7 Sphenosquamosal suture; *8* Temporal bone; *9* Lesser wing of sphenoid bone; *10* Superior orbital fissure; *11* Inferior orbital fissure; *12* Sphenozygomatic suture; *13* Zygomatic bone; *14* Zygomaticofrontal suture; *15* Supraorbital margin; *16* Supraorbital foramen; *17* Frontonasal suture; *18* Nasal bone; *19* Internasal suture; *20* Nasomaxillary suture; *21* Vomer; *22* Middle nasal conchae; *23* Inferior nasal conchae; *24* Frontomaxillary suture; *25* Infraorbital margin; *26* Infraorbital foramen; *27* Maxilla; *28* Frontal process of maxilla; *29* Zygomaticomaxillary suture; *30* Alveolar process of maxilla; *31* Anterior nasal spine; *32* Mandible; *33* Vertical ramus of mandible; *34* Mandibular angle; *35* Body (or horizontal ramus) of mandible; *36* Mental foramen; *37* Alveolar process of mandible; *38* Symphysis of mandible; *39* Fracture line; *40* Saw line

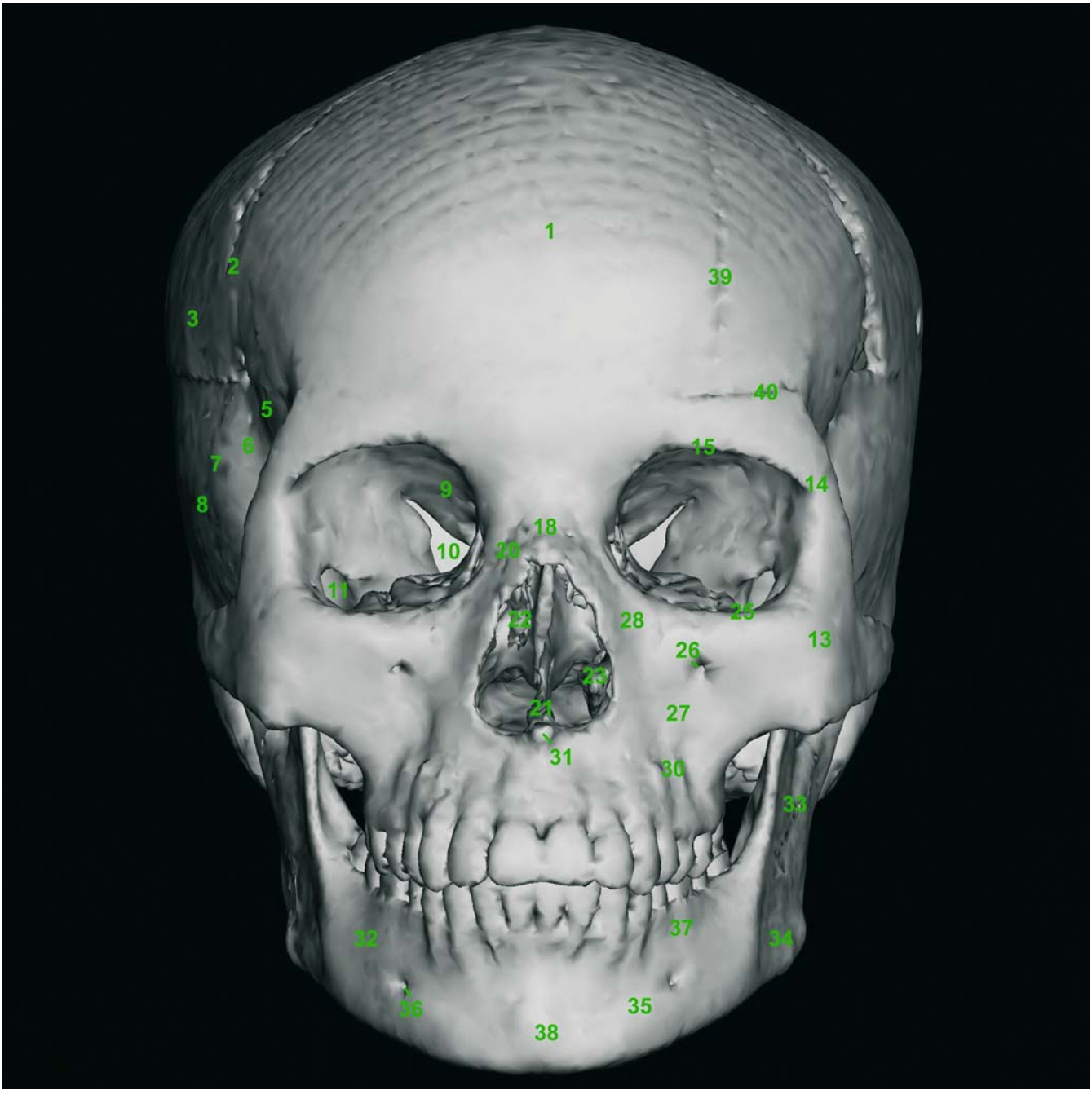

Fig. 2.1. b Anterior view of skull in centric occlusion (3-D CT, adult cadaver skull)

Skull – Lateral View

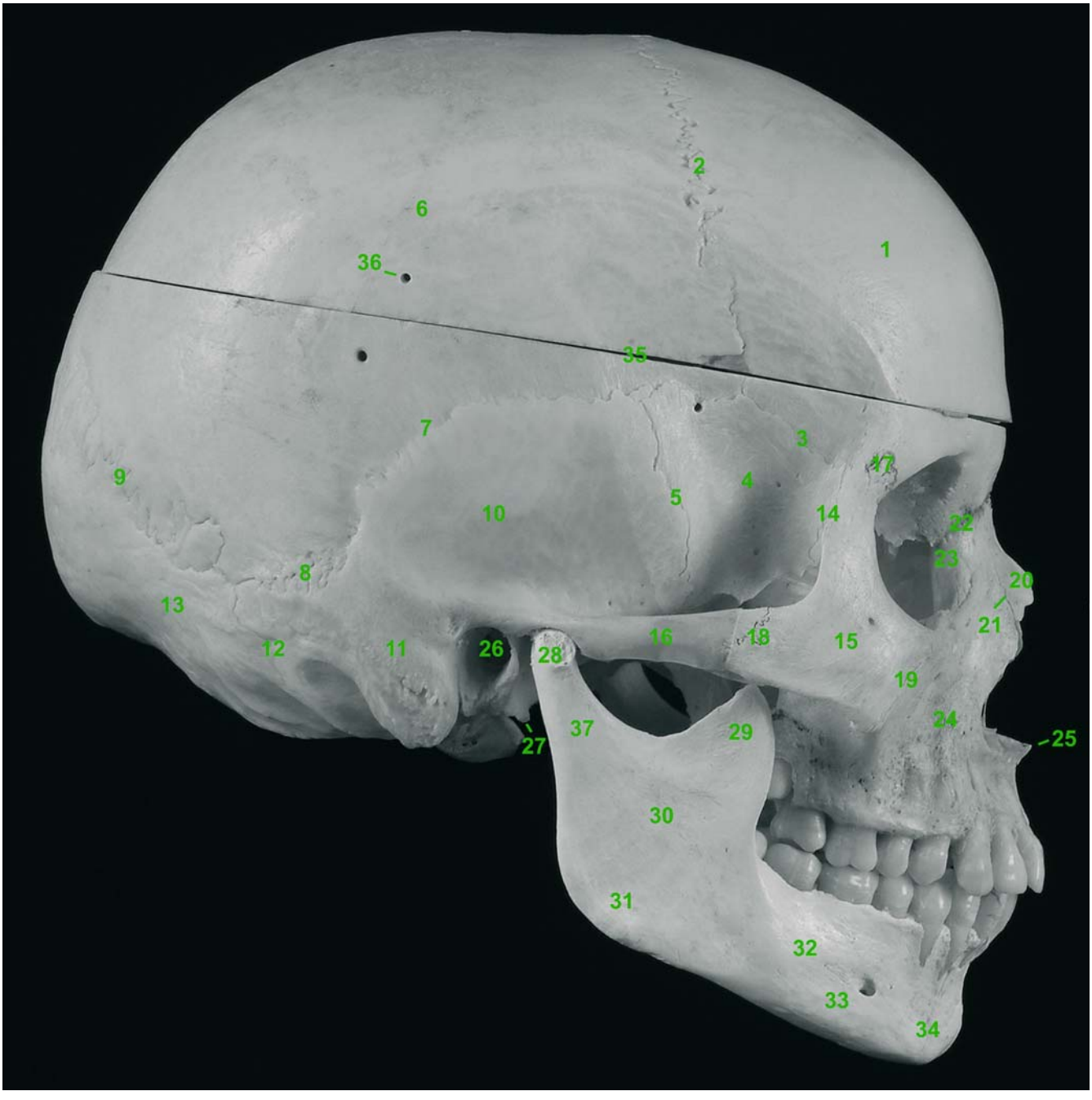

Fig. 2.2. **a** Right lateral view of the skull in centric occlusion (adult cadaver skull). *1* Frontal bone; *2* Coronal suture; *3* Sphenofrontal suture; *4* Greater wing of sphenoid bone; *5* Sphenosquamosal suture; *6* Parietal bone; *7* Squamosal suture; *8* Parietomastoid suture; *9* Lambdoidal suture; *10* Squamous portion of temporal bone; *11* Processus mastoideus of temporal bone; *12* Occipitomastoid suture; *13* Occipital bone; *14* Sphenozygomatic suture; *15* Zygomatic bone; *16* Zygomatic arch; *17* Zygomaticofrontal suture; *18* Zygomaticotemporal suture; *19* Zygomaticomaxillary suture; *20* Nasal bone; *21* Nasomaxillary suture; *22* Frontomaxillary suture; *23* Lacrimal bone; *24* Maxillary bone; *25* Anterior nasal spine; *26* External acousticus meatus; *27* Styloid process (incomplete); *28* Condyle of mandible; *29* Coronoid process of mandible; *30* Vertical ramus of mandible; *31* Mandibular angle; *32* Body of mandible; *33* Mental foramen; *34* Mental protuberance; *35* Saw line; *36* Screwhole; *37* Condylar process of mandible

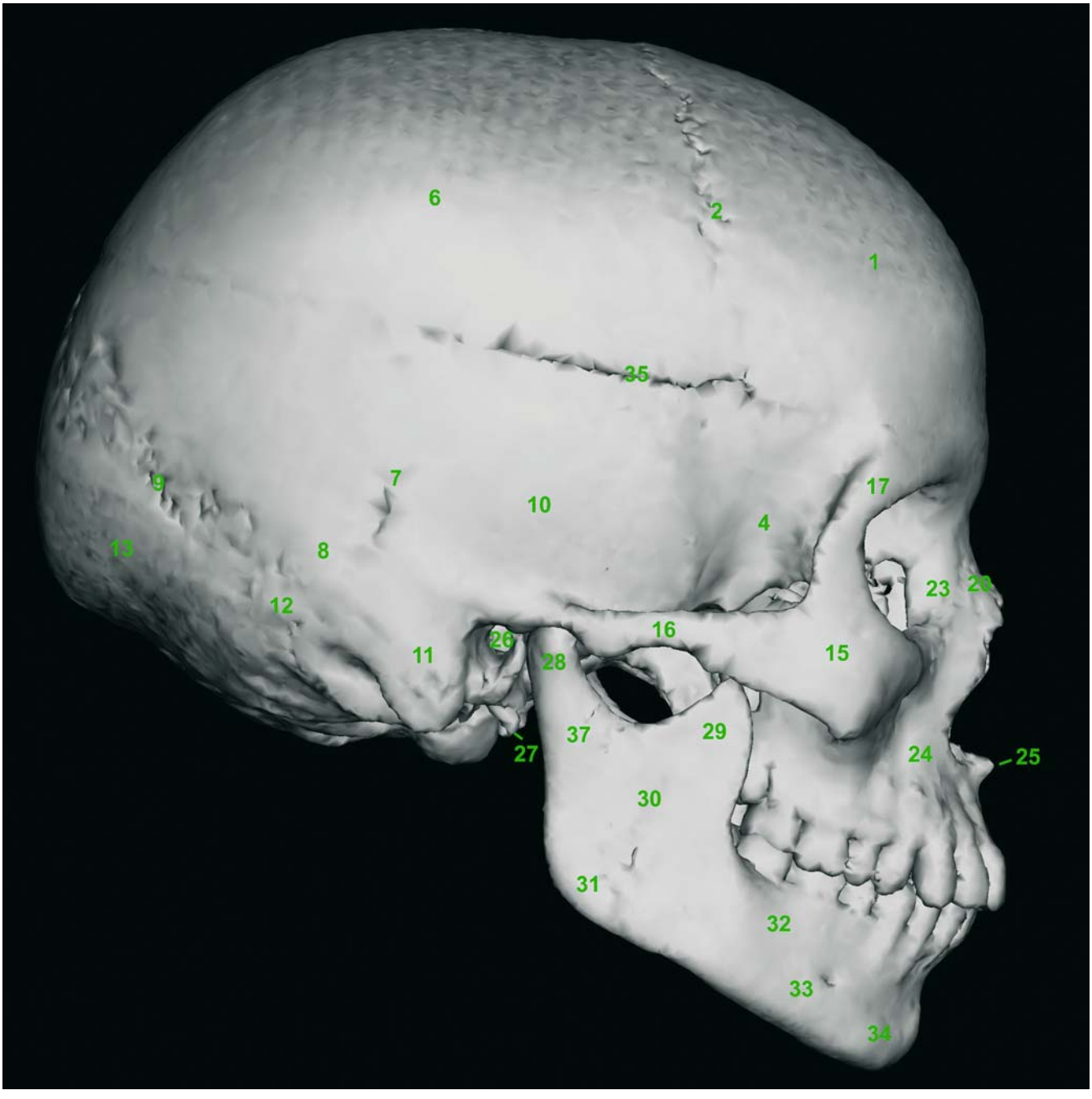

Fig. 2.2. **b** Right lateral view of skull in centric occlusion (3-D CT, adult cadaver skull)

Skull Base – Endocranial View

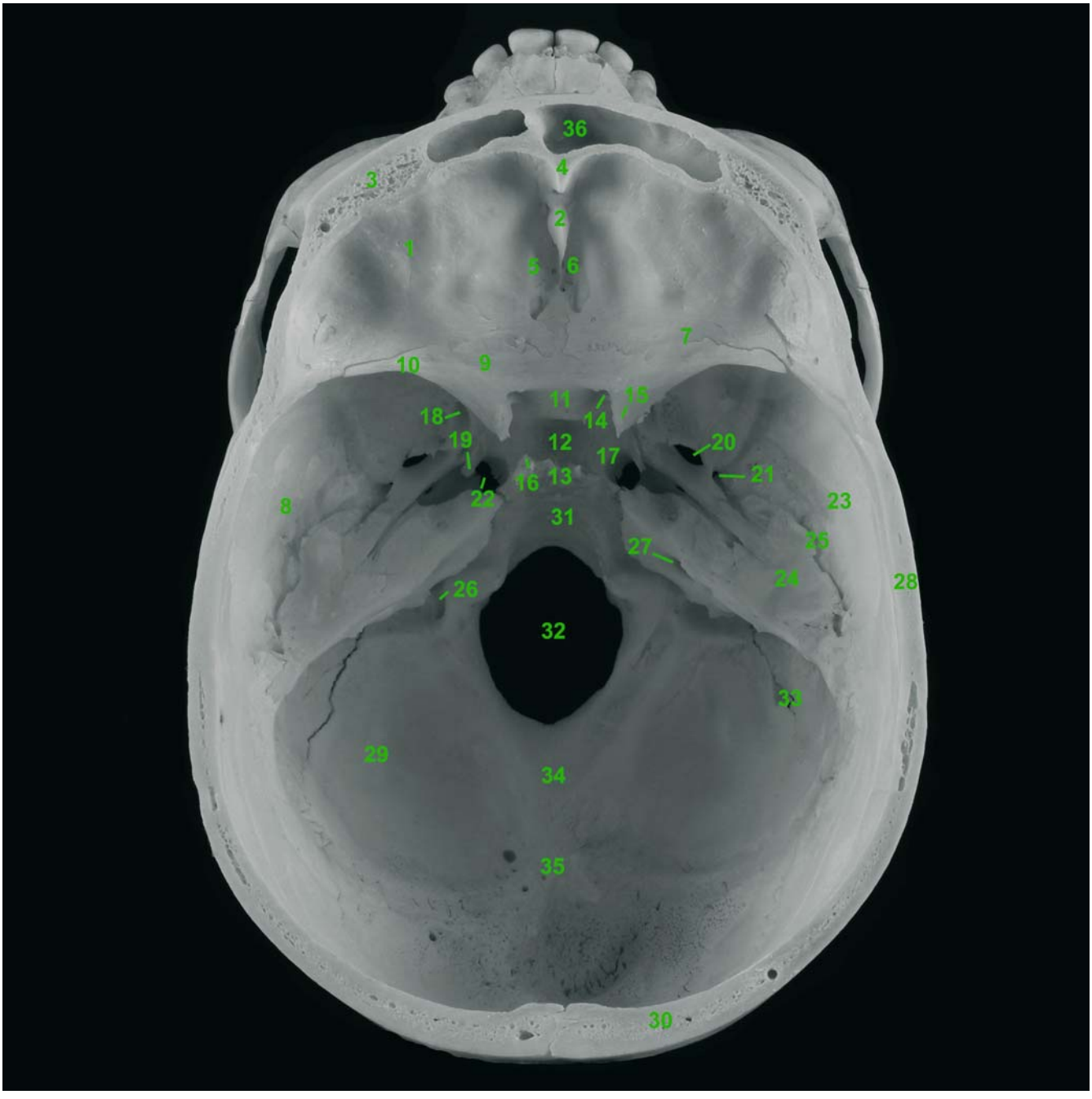

Fig. 2.3. a Endocranial view of the skull base (adult cadaver skull). *1* Anterior cranial fossa; *2* Crista galli; *3* Frontal bone; *4* Frontal crest; *5* Frontoethmoidal suture; *6* Cribriform plate of ethmoid bone; *7* Sphenofrontal suture; *8* Middle cranial fossa; *9* Sphenoid bone; *10* Lesser wing of sphenoid bone; *11* Tuberculum sellae; *12* Hypophyseal fossa (sella turcica); *13* Dorsum sellae; *14* Optic canal; *15* Anterior clinoid process; *16* Posterior clinoid process; *17* Carotid sulcus; *18* Foramen rotundum; *19* Lingula of sphenoid bone; *20* Oval foramen of sphenoid bone (foramen ovale); *21* Spinous foramen (foramen spinosum); *22* Foramen lacerum; *23* Squamous portion of temporal bone; *24* Petrous portion of temporal bone; *25* Petrosquamosal fissure; *26* Jugular foramen (foramen jugulare); *27* Internal acoustic meatus; *28* Parietal bone; *29* Posterior cranial fossa; *30* Occipital bone; *31* Clivus; *32* Great foramen (foramen magnum); *33* Occipitomastoid suture; *34* Internal occipital crest; *35* Internal occipital protuberance; *36* Frontal sinus

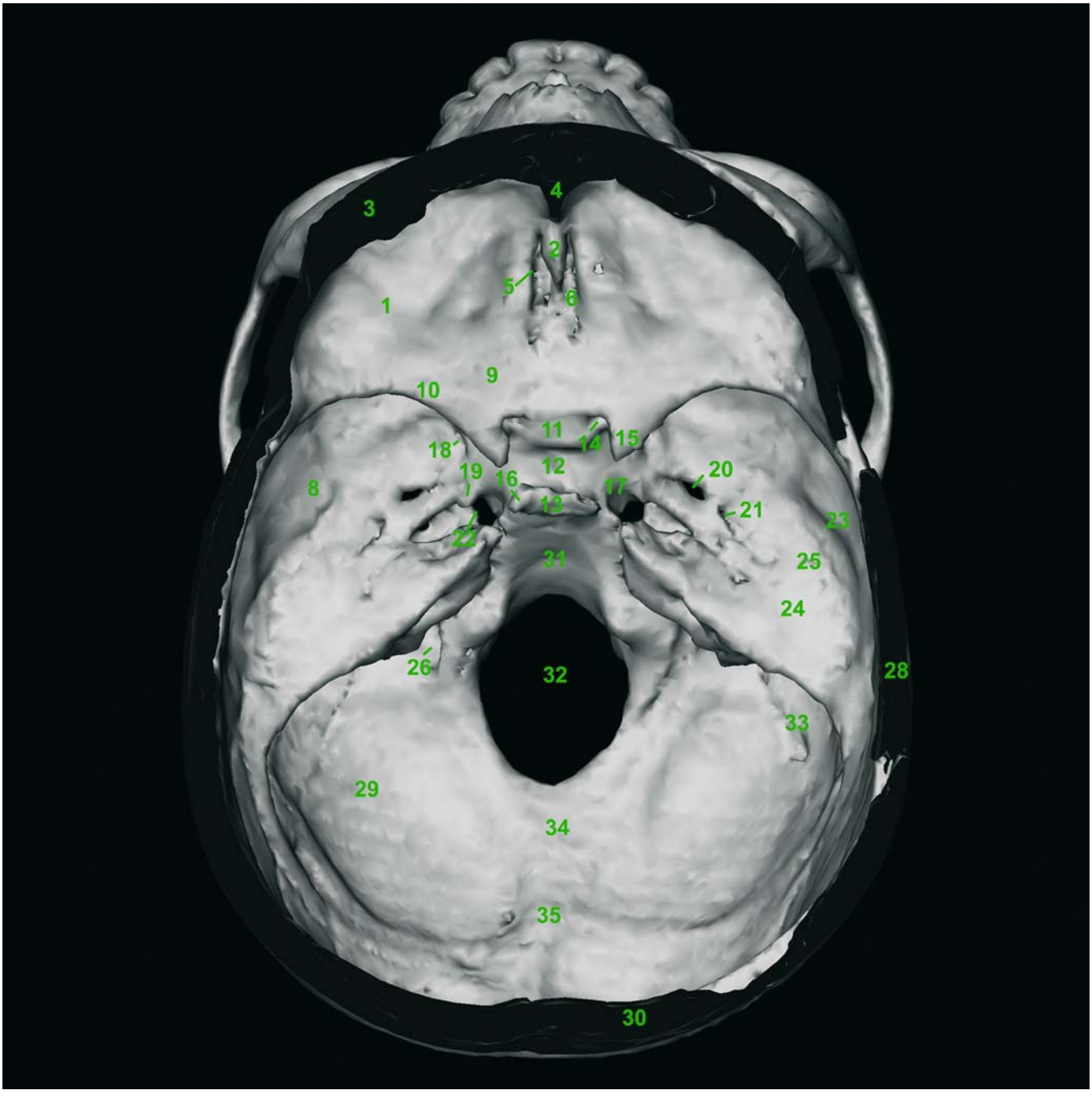

Fig. 2.3. **b** Endocranial view of the skull base (3-D CT, adult cadaver skull)

Skull Base – Exocranial View

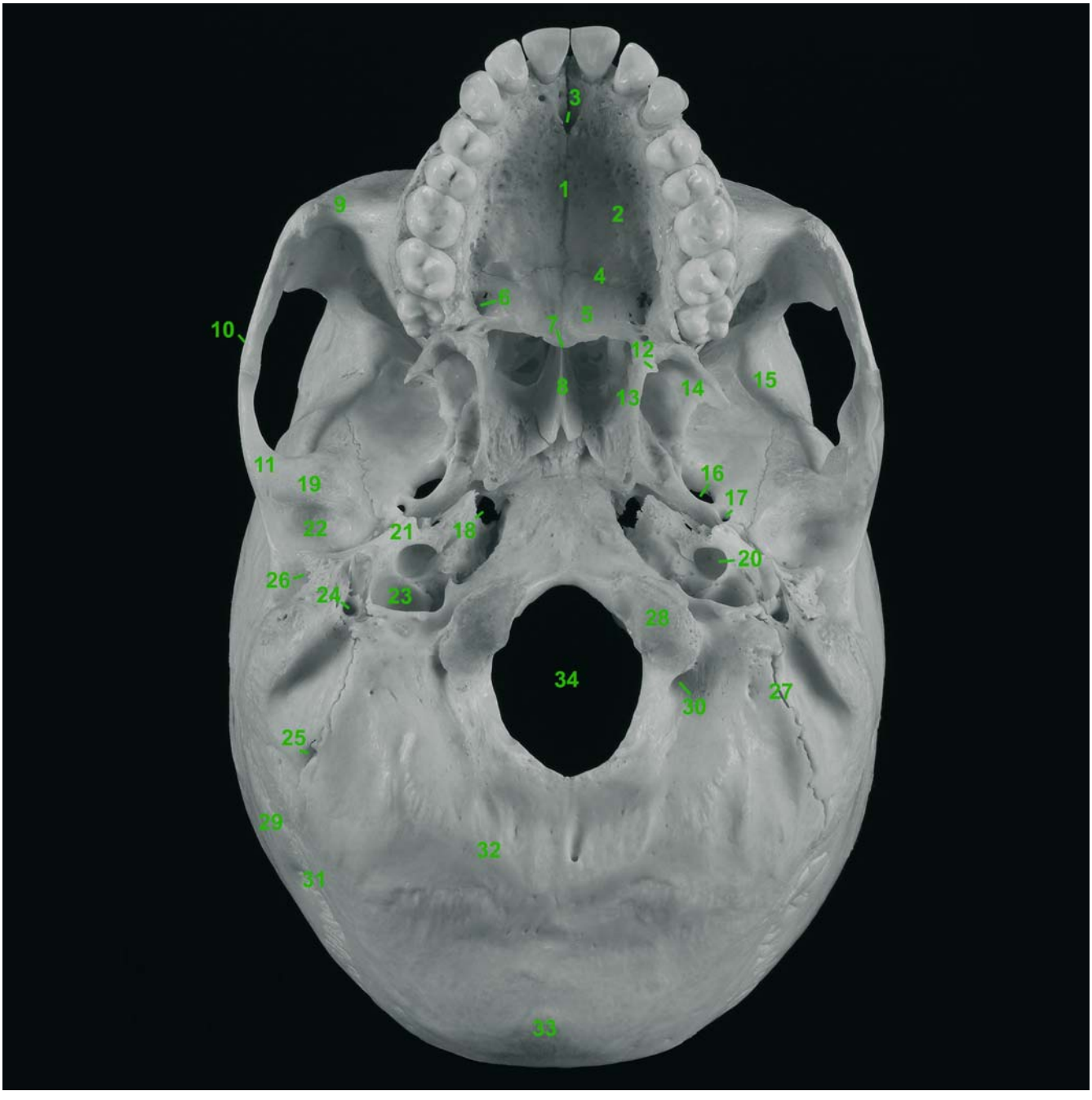

Fig. 2.4. **a** The skull base with the mandible removed: exocranial view (adult cadaver skull). *1* Median palatine suture; *2* Palatine process of maxilla; *3* Incisive foramen (foramen incisivum); *4* Transverse palatine suture; *5* Palatine bone; *6* Greater palatine foramen; *7* Posterior nasal spine; *8* Vomer; *9* Zygomatic process of maxilla; *10* Zygomatic arch; *11* Zygomatic process of temporal bone; *12* Pterygoid hamulus; *13* Medial lamina of pterygoid process; *14* Lateral lamina of pterygoid process; *15* Infratemporal crest, greater wing of sphenoid bone; *16* Oval foramen of sphenoid bone (foramen ovale); *17* Spinous foramen (foramen spinosum); *18* Foramen lacerum; *19* Articular tubercle; *20* Carotid canal; *21* Incomplete styloid process; *22* Mandibular fossa; *23* Jugular foramen (foramen jugulare); *24* Stylomastoid foramen; *25* Mastoid foramen; *26* External acoustic meatus; *27* Occipitomastoid suture; *28* Occipital condyle; *29* Parietal bone; *30* Condylar canal; *31* Lambdoidal suture; *32* Inferior nuchal line; *33* External occipital protuberance; *34* Great foramen (foramen magnum)

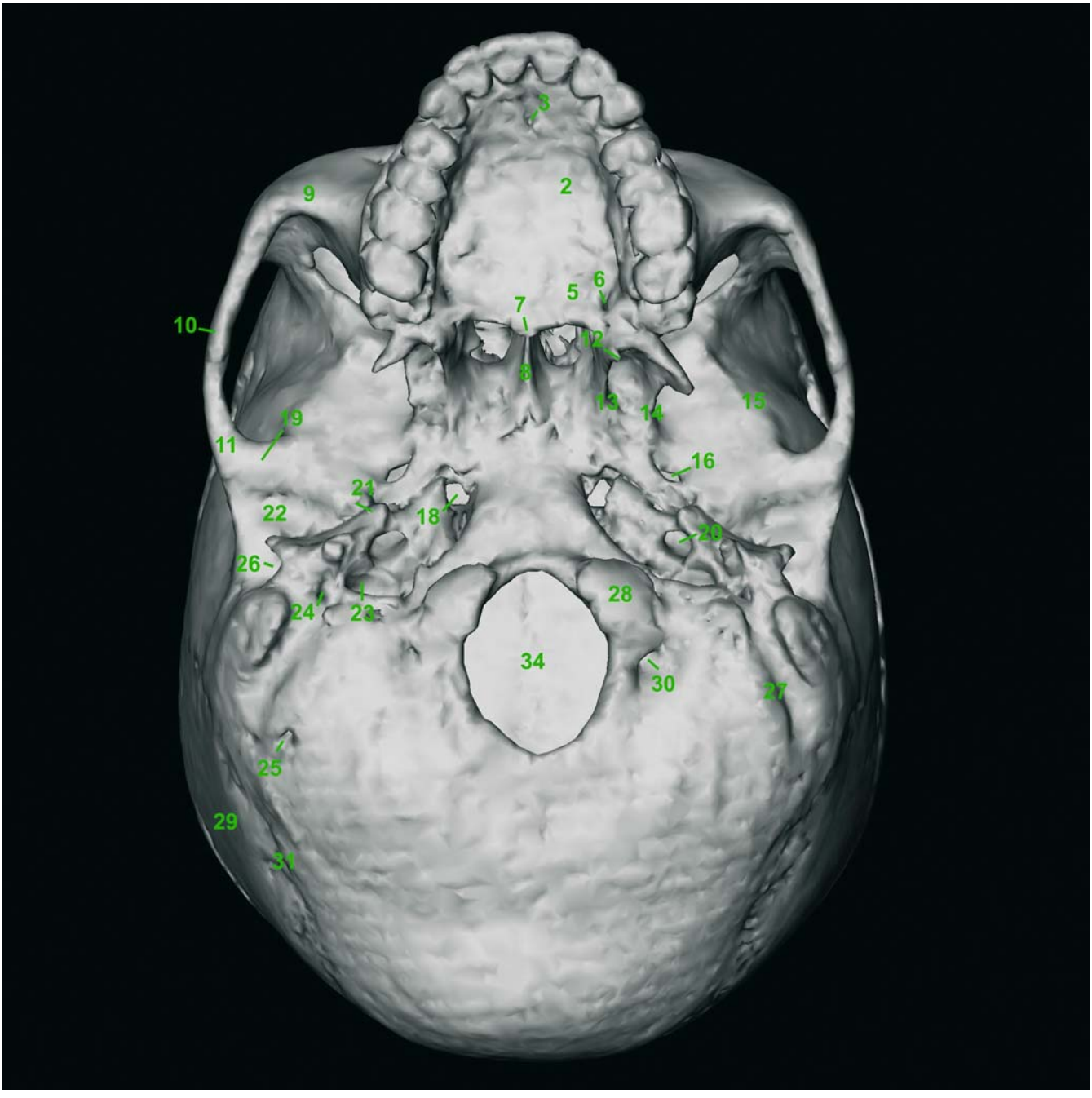

Fig. 2.4. **b** The skull base with the mandible removed: exocranial view (3-D CT, adult cadaver skull)

Skull – Superior View (Calvaria)

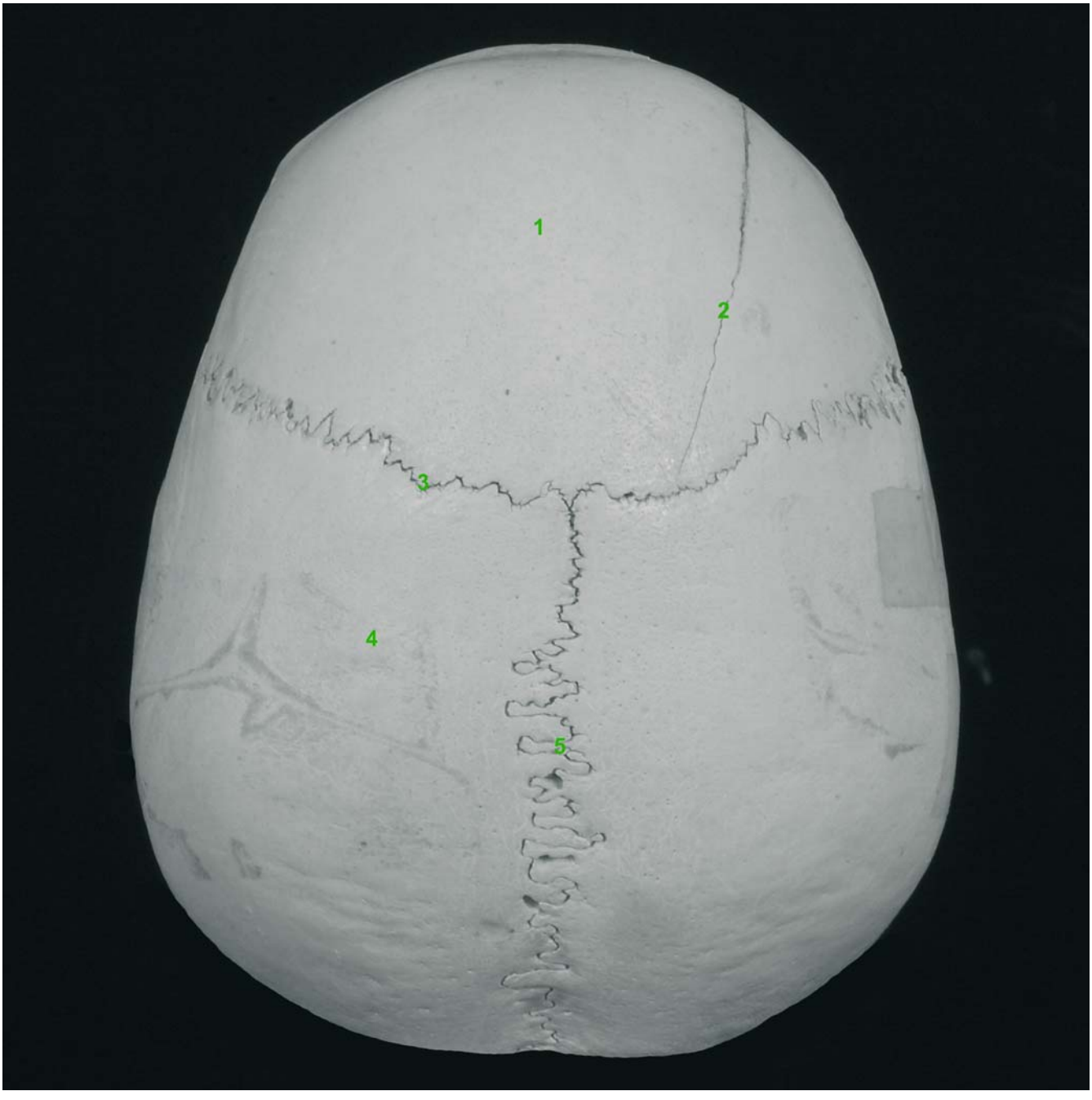

Fig. 2.5. **a** Superior view of the skull (calvaria) (adult cadaver skull). *1* Frontal bone; *2* Fracture line; *3* Coronal suture; *4* Parietal bone; *5* Sagittal suture

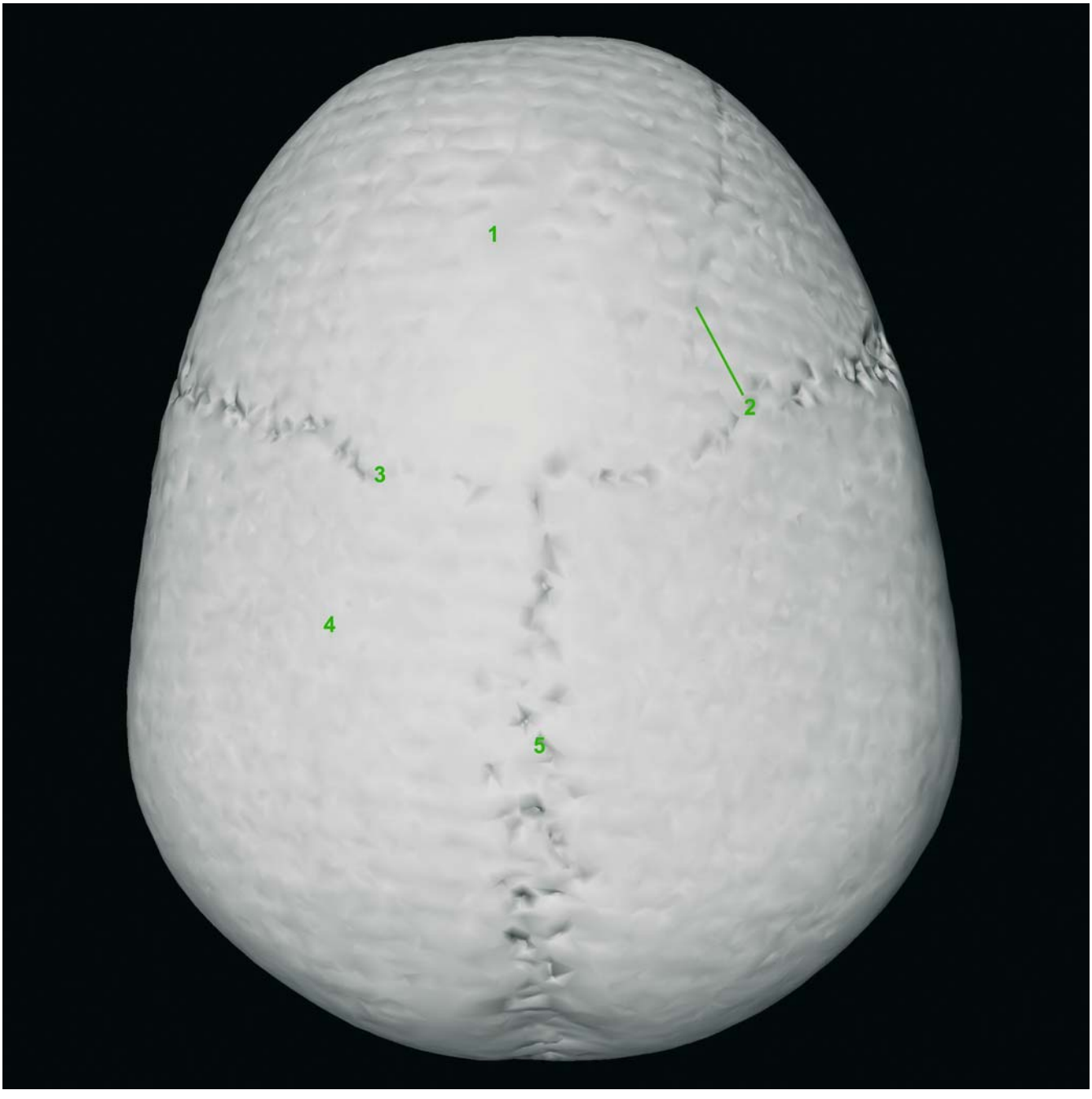

Fig. 2.5. **b** Superior view of the skull (calvaria) (3-D CT, adult cadaver skull)

Calvaria – Interior View

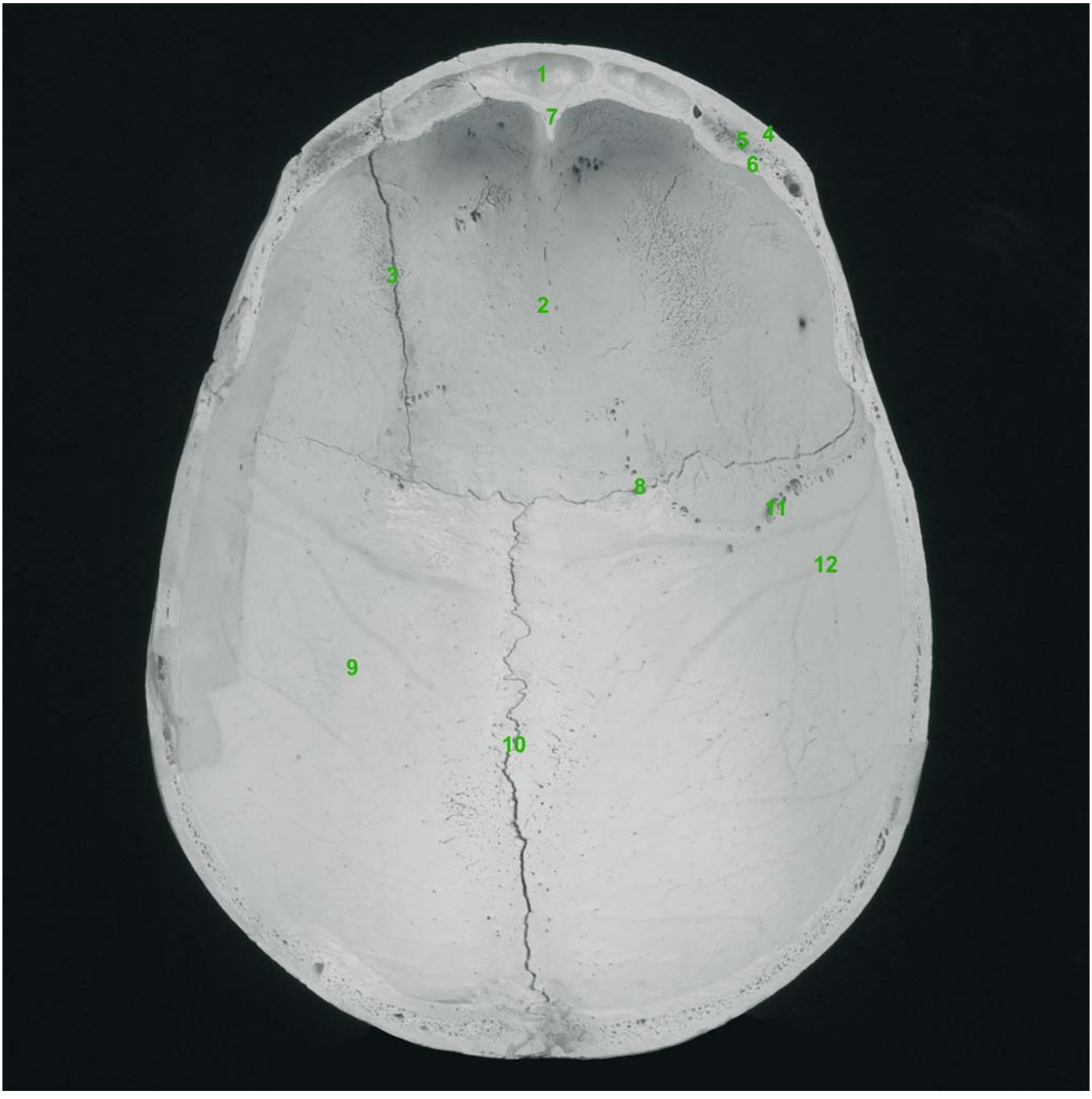

Fig. 2.6. **a** Interior view of the calvaria (adult cadaver skull). *1* Frontal sinus; *2* Frontal bone; *3* Fracture line; *4* Outer table; *5* Diploe; *6* Inner table; *7* Frontal crest; *8* Coronal suture; *9* Parietal bone; *10* Sagittal suture; *11* Foveolae for arachnoid granulations; *12* Meningeal arterial grooves

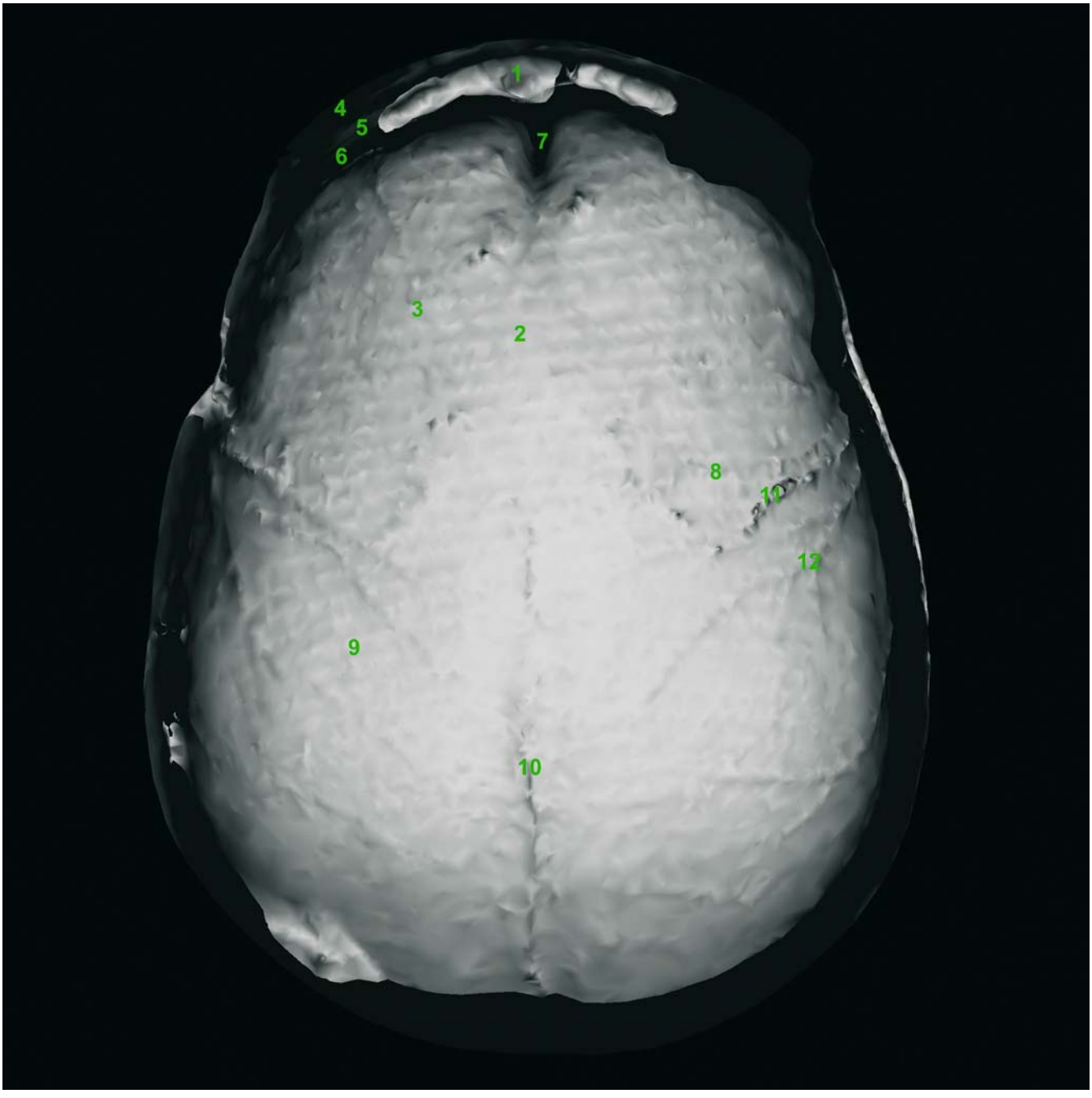

Fig. 2.6. **b** Interior view of the calvaria (3-D CT, adult cadaver skull)

Skull – Dorsal View

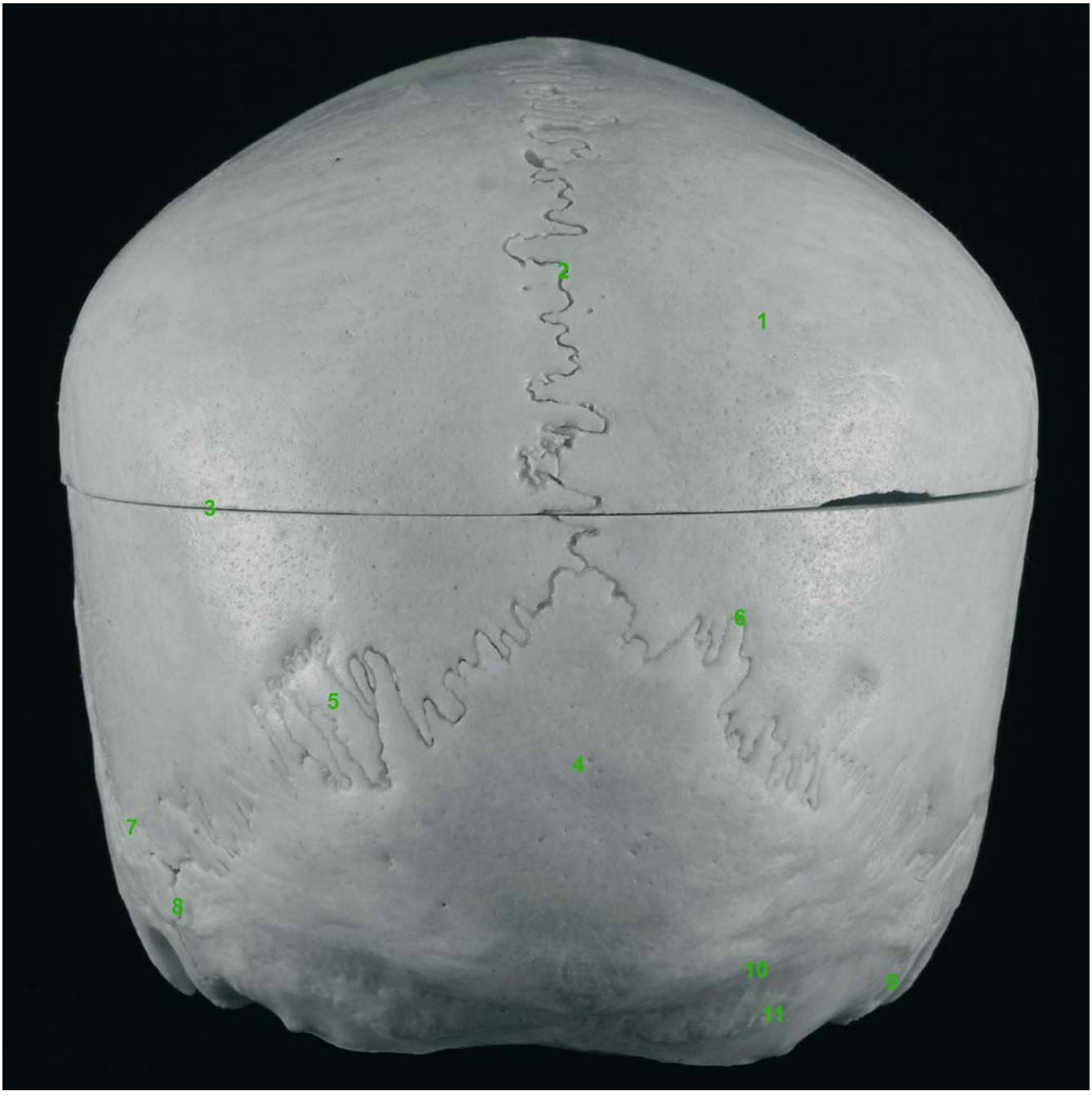

Fig. 2.7. a Dorsal view of the skull (adult cadaver skull). *1* Parietal bone; *2* Sagittal suture; *3* Saw line; *4* Occipital bone; *5* Suture bone; *6* Lambdoidal suture; *7* Parietomastoid suture; *8* Occipitomastoid suture; *9* Mastoid process; *10* Superior nuchal line; *11* Inferior nuchal line

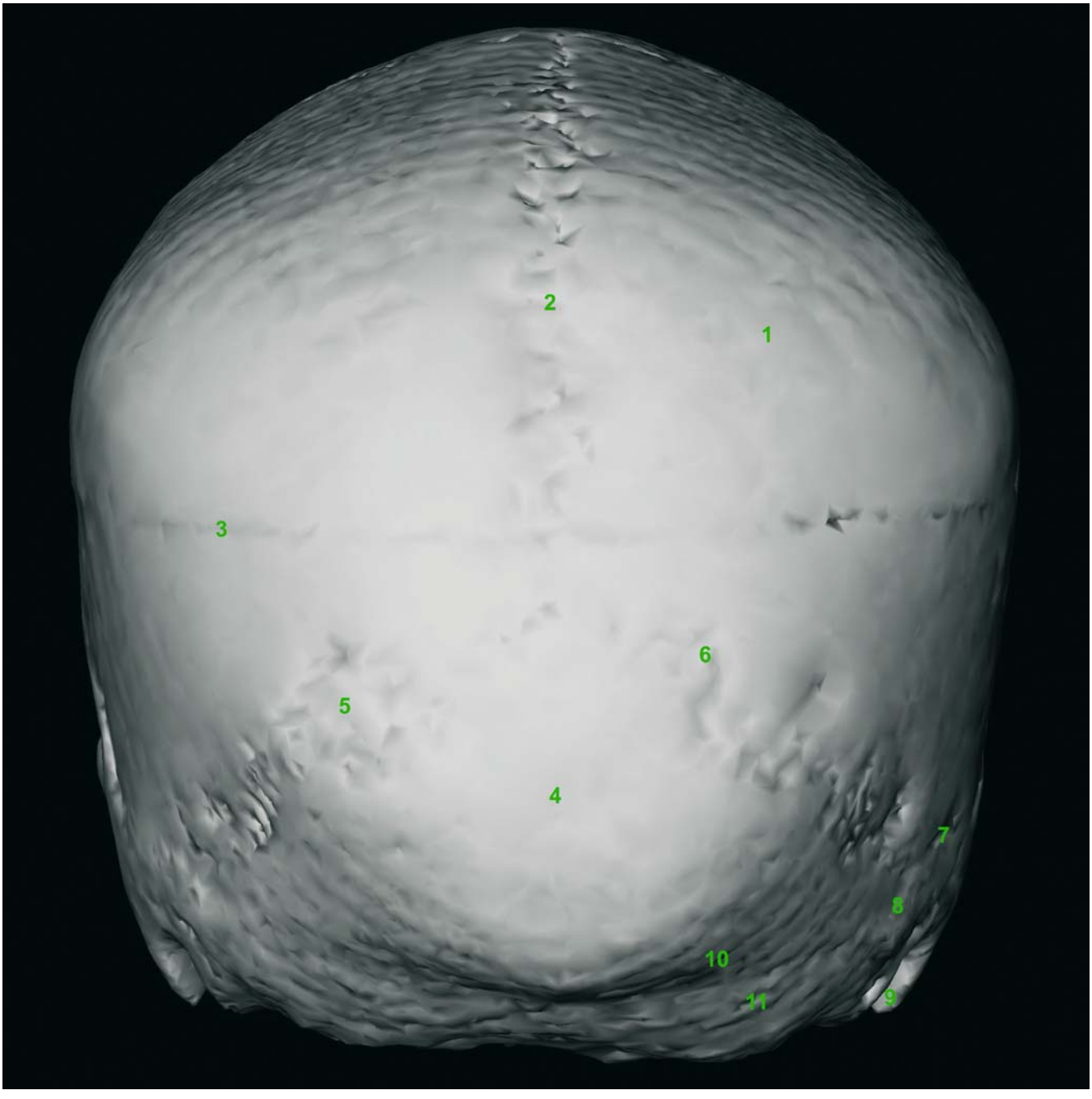

Fig. 2.7. **b** Dorsal view of the skull (3-D CT, adult cadaver skull)

Skull – Paramedian Sagittal View

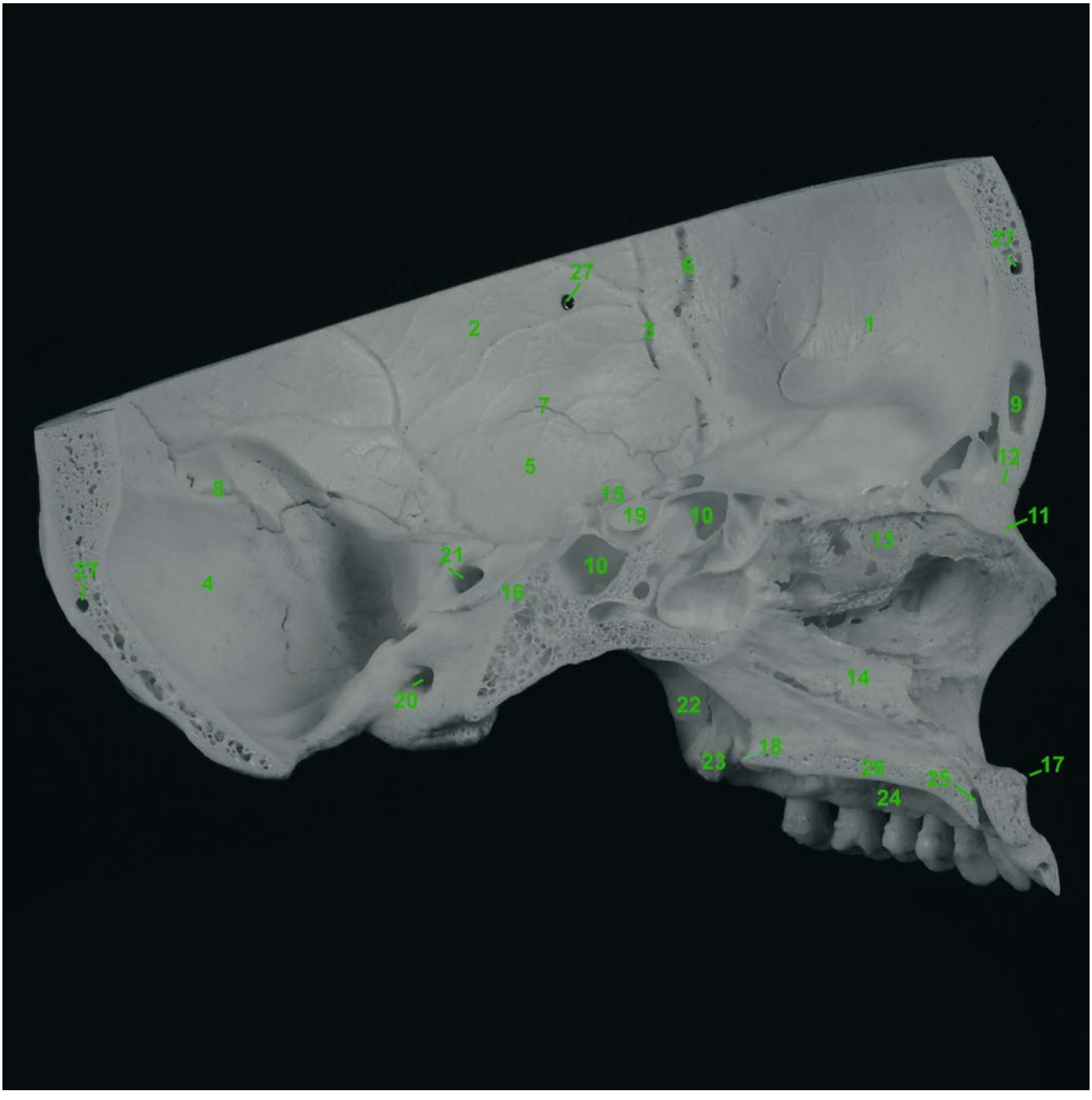

Fig. 2.8. a Paramedian view of the skull with the mandible and calvaria removed (adult cadaver skull). *1* Frontal bone; *2* Parietal bone; *3* Arteria sulci; *4* Occipital bone; *5* Squamosal portion of temporal bone; *6* Coronal suture; *7* Squamosal suture; *8* Lambdoidal suture; *9* Frontal sinus; *10* Sphenoidal sinus; *11* Nasal bone; *12* Frontonasal suture; *13* Perpendicular plate of ethmoid bone; *14* Vomer; *15* Dorsum sellae; *16* Clivus; *17* Spina nasalis anterior; *18* Spina nasalis posterior; *19* Hypophyseal fossa (sella turcica); *20* Hypoglossal canal; *21* Internal acoustic meatus; *22* Pterygoid fossa; *23* Pterygoid hamulus; *24* Alveolar process of maxillary bone; *25* Incisive canal; *26* Palatine process of maxilla; *27* Screwhole

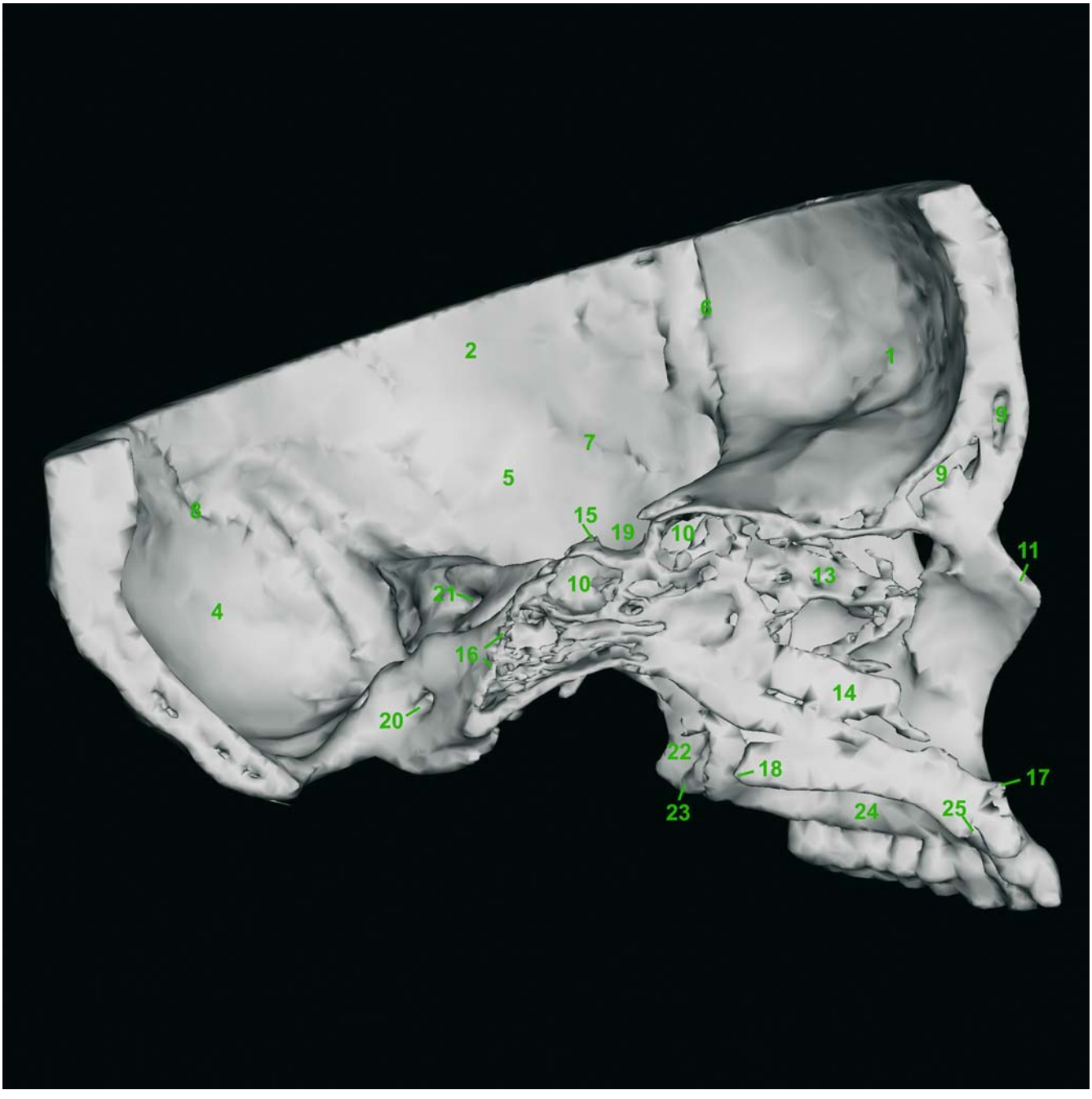

Fig. 2.8. **b** Paramedian view of the skull with mandible and calvaria removed (3-D CT, adult cadaver skull)

Skull of a Newborn

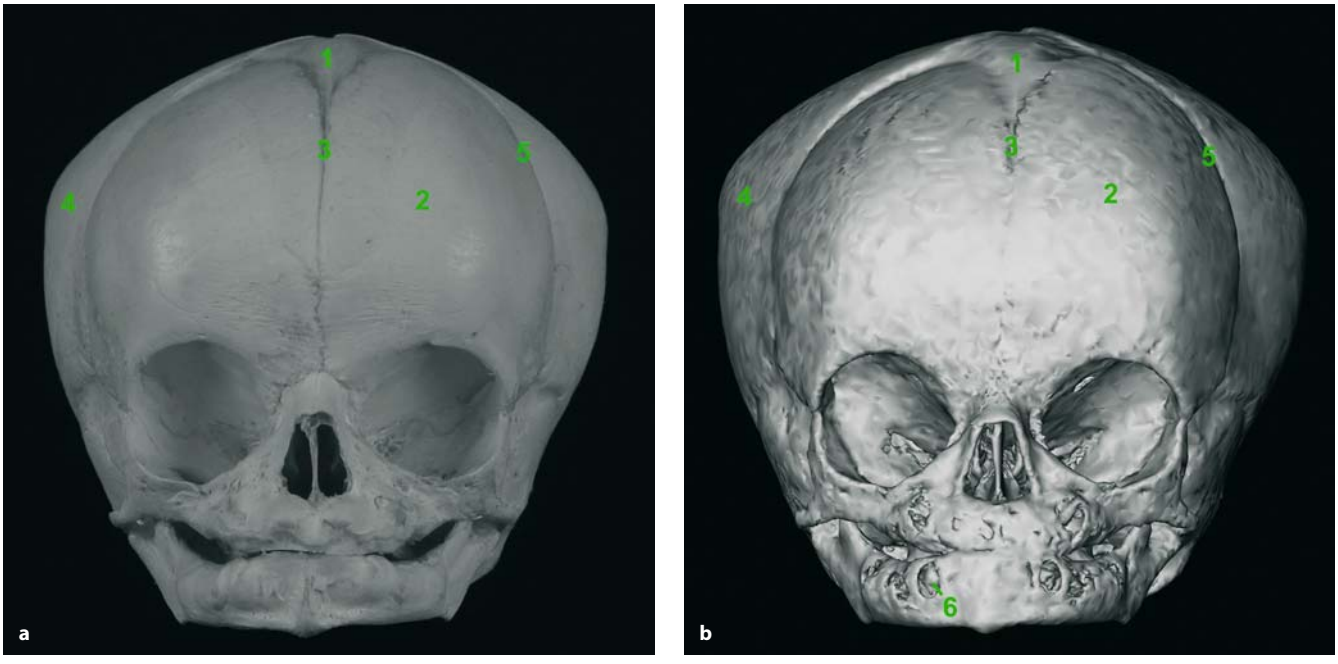

Fig. 2.9. **a** The skull of a new-born: anterior view (cadaver skull). **b** The skull of a new-born: anterior view (3-D CT, cadaver skull). *1* Anterior fontanelle; *2* Frontal eminence; *3* Frontal suture; *4* Parietal eminence; *5* Coronal suture; *6* Deciduous molar

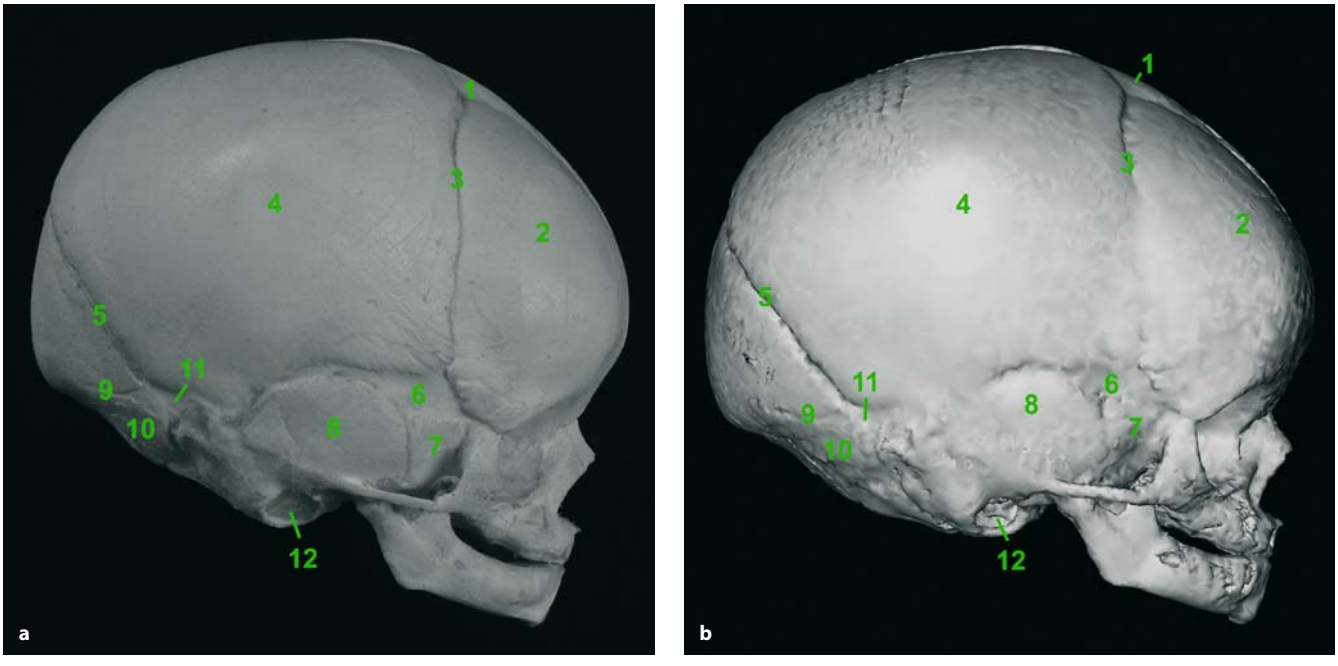

Fig. 2.10. **a** The skull of a new-born: right lateral view (cadaver skull). **b** The skull of a new-born: right lateral view (3-D CT, cadaver skull). *1* Anterior fontanelle; *2* Frontal eminence; *3* Coronal suture; *4* Parietal eminence; *5* Lambdoidal suture; *6* Sphenoidal fontanelle; *7* Greater wing of sphenoid bone; *8* Squamous portion of temporale bone; *9* Transverse occipital suture; *10* Squamous portion of occipital bone; *11* Posterolateral fontanelle; *12* Tympanic ring

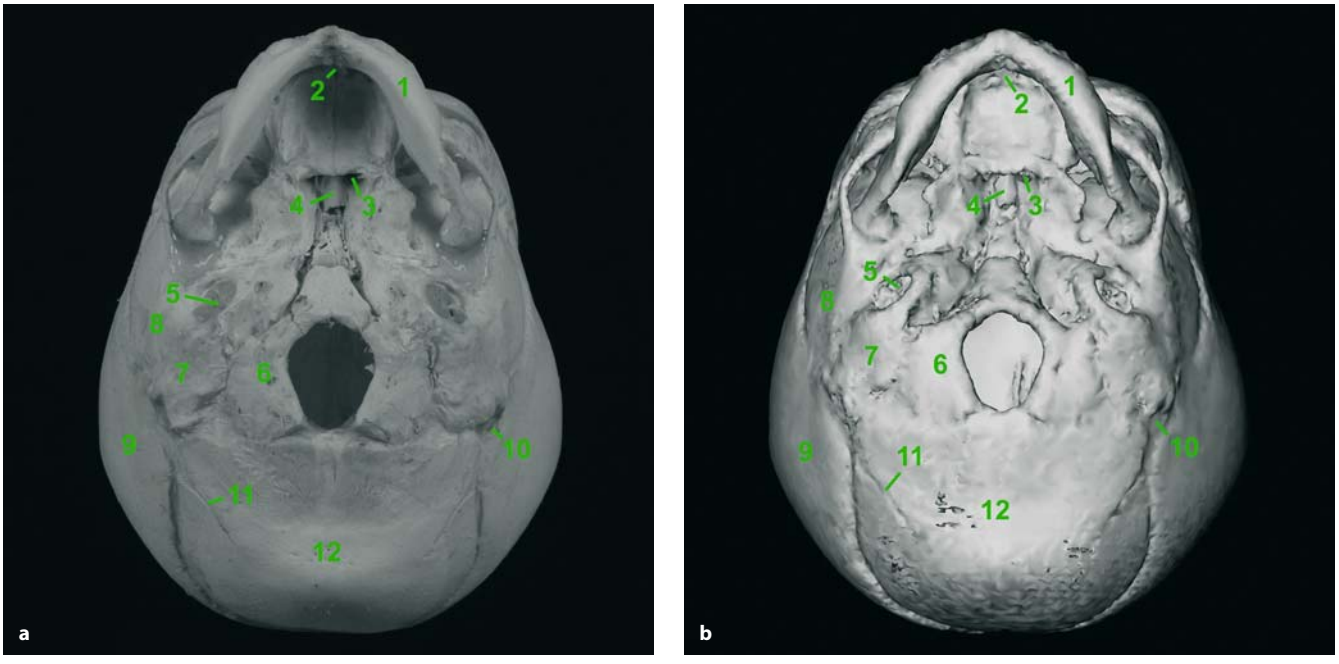

Fig. 2.11. **a** The skull base of a new-born: exocranial view (cadaver skull). **b** The skull base of a new-born: exocranial view (3-D CT, cadaver skull). *1* Mandible; *2* Premaxilla; *3* Choana; *4* Vomer; *5* Tympanic ring; *6* Lateral portion of occipital bone; *7* Petrous portion of temporal bone; *8* Squamous portion of temporal bone; *9* Parietal eminence; *10* Mastoid fontanelle; *11* Transverse occipital suture; *12* Squamous portion of occipital bone

Fig. 2.12. **a** The skull of a new-born: superior view (cadaver skull). **b** The skull of a new-born: superior view (3-D CT, cadaver skull). *1* Frontal eminence; *2* Anterior fontanelle; *3* Coronal suture; *4* Parietal eminence; *5* Sagittal suture; *6* Posterior fontanelle; *7* Squamous portion of occipital bone

Skull of a Newborn

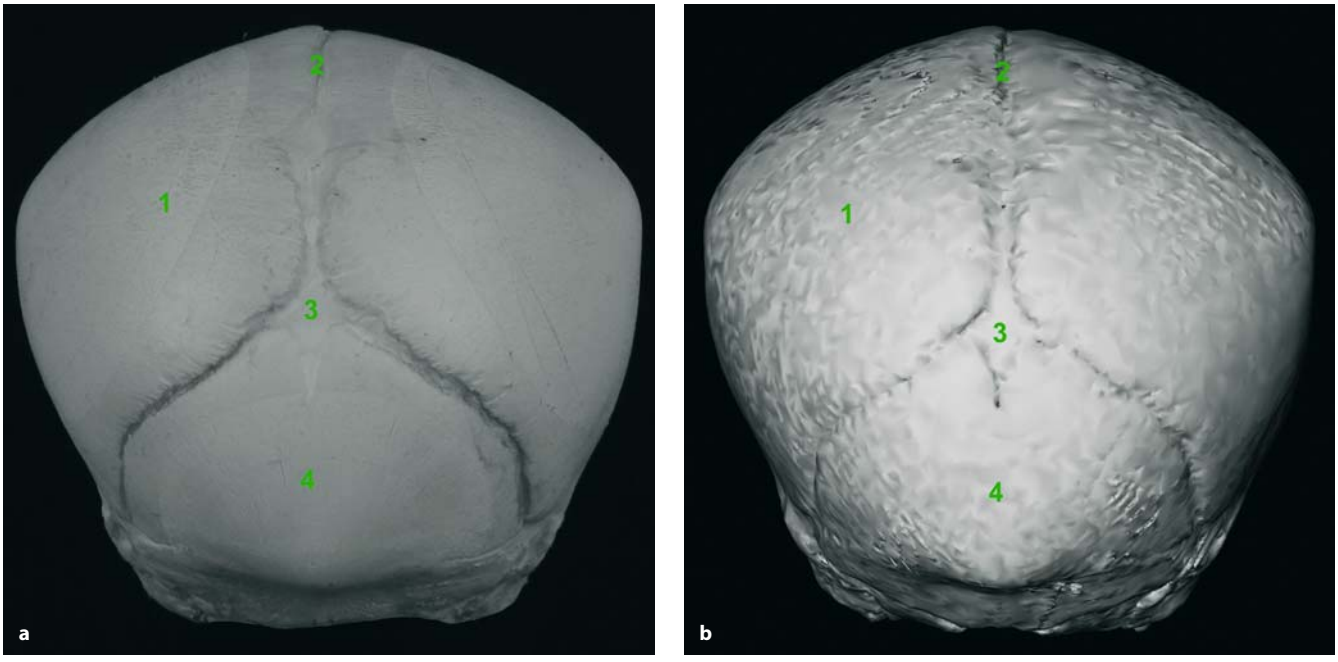

Fig. 2.13. **a** The skull of a new-born: dorsal view (cadaver skull). **b** The skull of a new-born: dorsal view (3-D CT, cadaver skull). *1* Parietal eminence; *2* Sagittal suture; *3* Posterior fontanelle; *4* Squamous portion of occipital bone

Skull of a 6-Year-Old Child

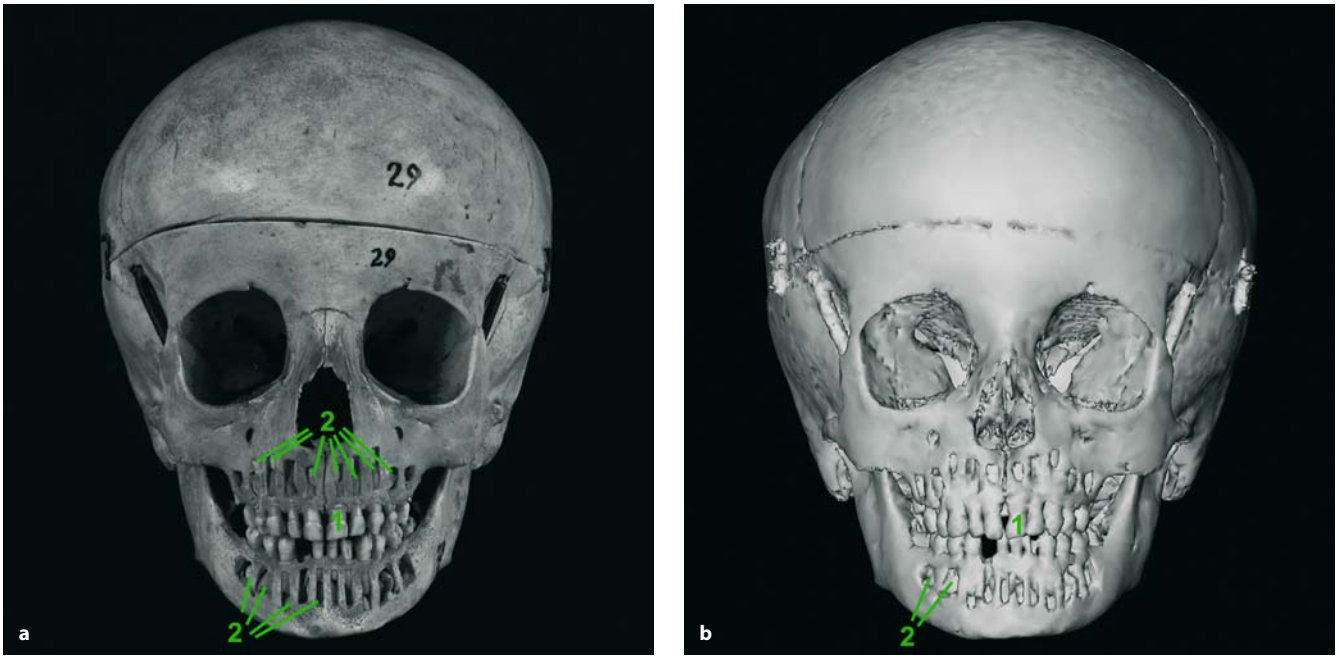

Fig. 2.14. **a** The skull of a 6-year-old child: anterior view (cadaver skull). **b** The skull of a 6-year-old child: anterior view (3-D CT, cadaver skull). *1* Deciduous (milk) teeth; *2* Rudiments of permanent teeth

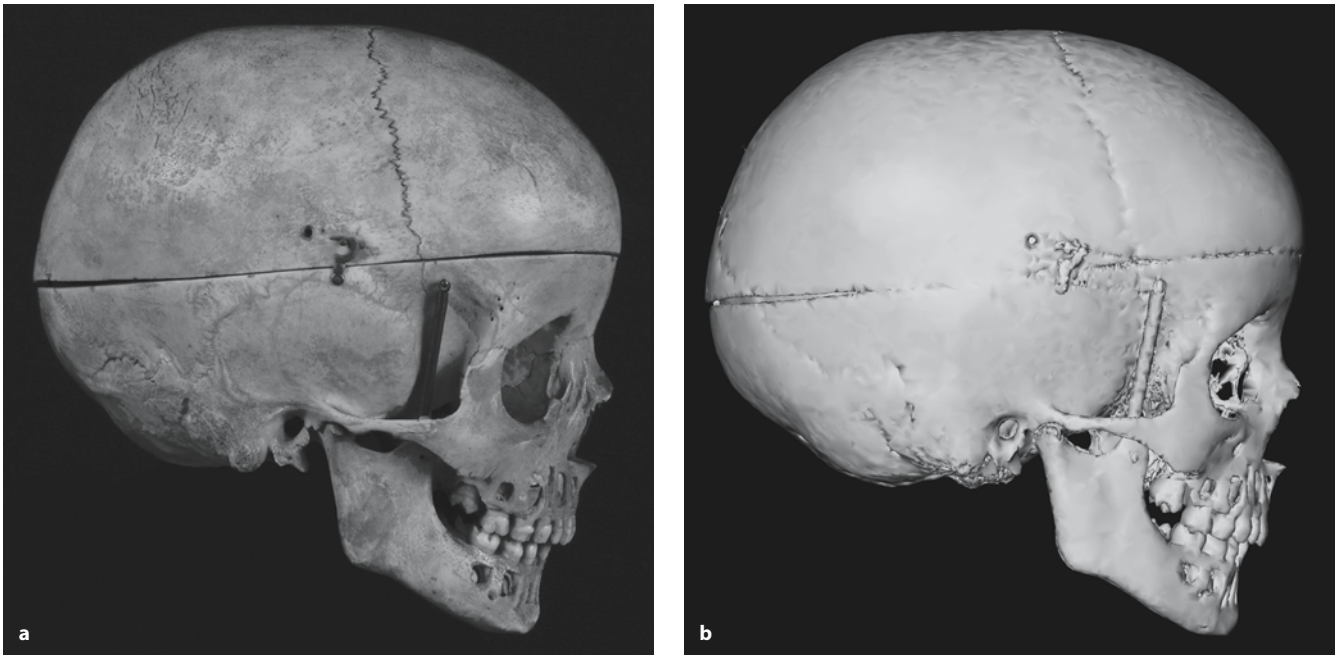

Fig. 2.15. **a** The skull of a 6-year-old child: right lateral view (cadaver skull). **b** The skull of a 6-year-old child: right lateral view (3-D CT, cadaver skull)

Skull of a 6-Year-Old Child

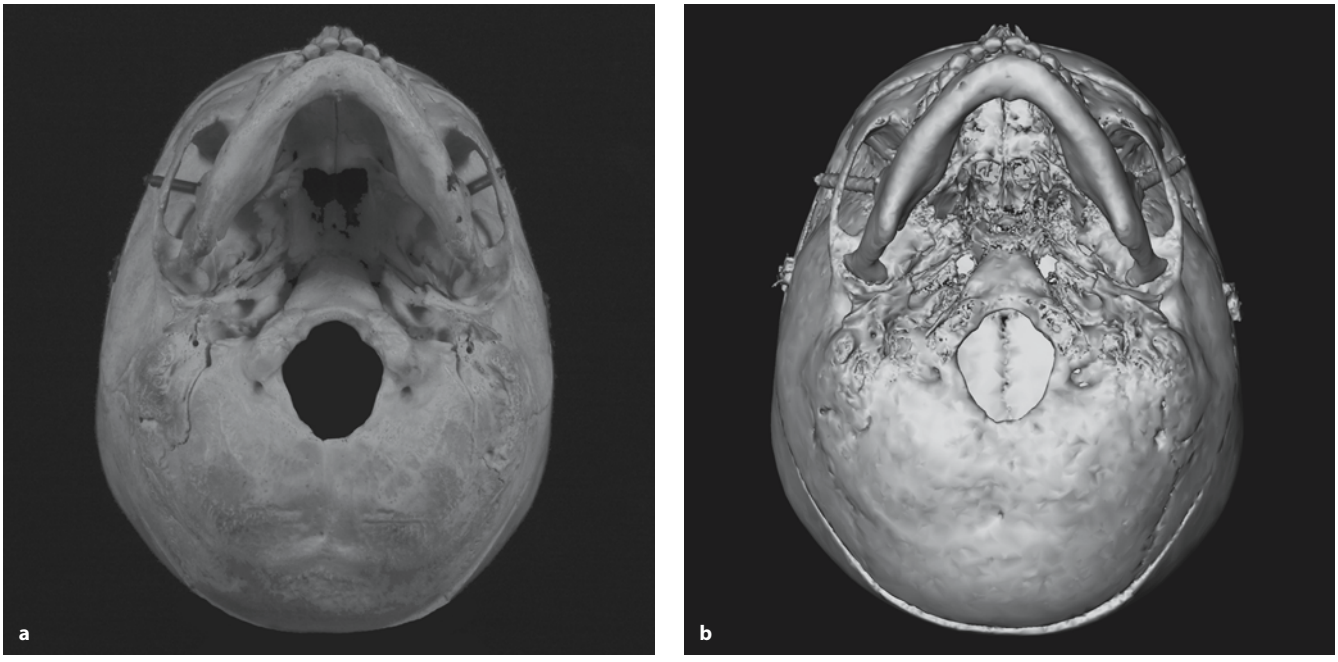

Fig. 2.16. **a** The skull base of a 6-year-old child: exocranial view (cadaver skull). **b** The skull base of a 6-year-old child: exocranial view (3-D CT, cadaver skull)

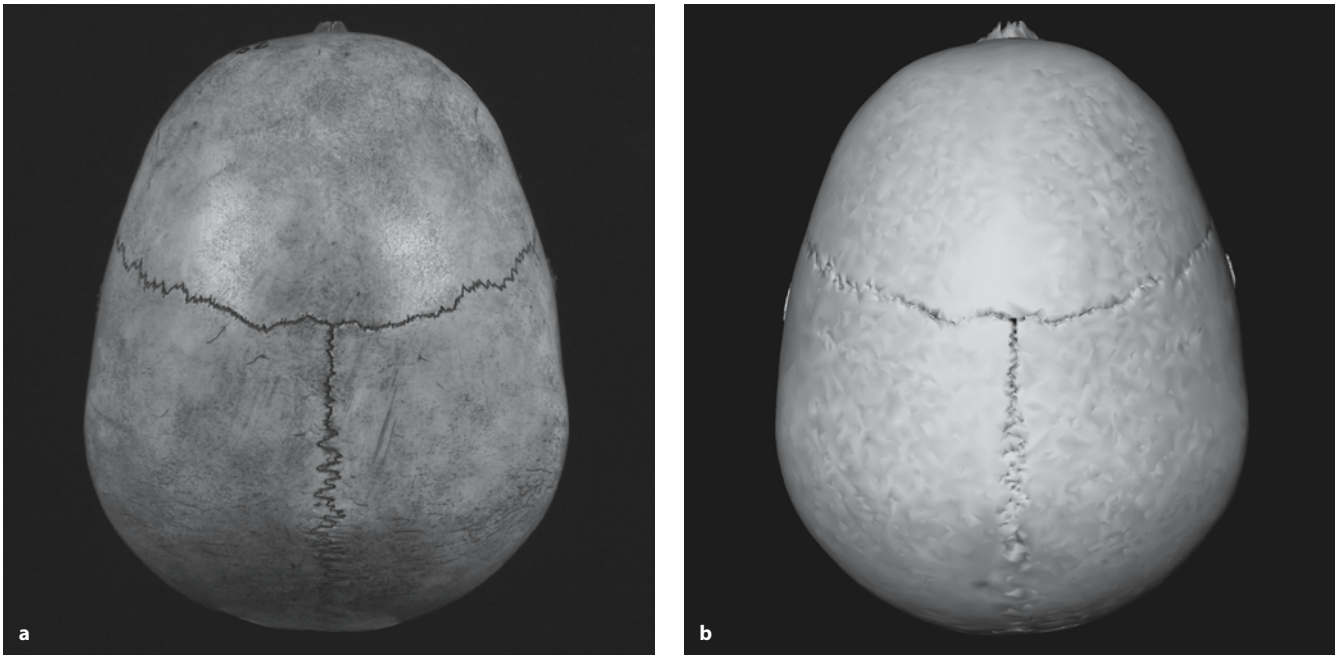

Fig. 2.17. **a** The skull of a 6-year-old child. Superior view (cadaver skull). **b** The skull of a 6-year-old child. Superior view (3-D CT, cadaver skull)

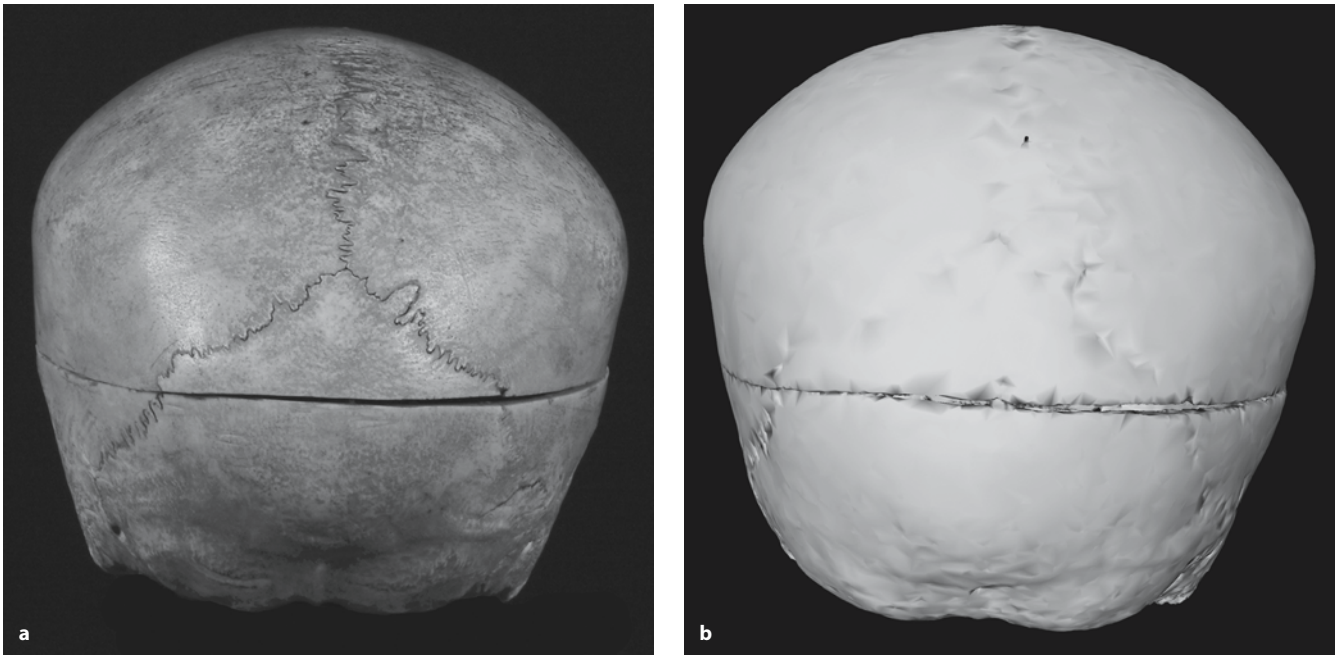

Fig. 2.18. **a** The skull of a 6-year-old child: dorsal view. (cadaver skull). **b** The skull of a 6-year-old child: dorsal view. (3-D CT, cadaver skull)

2.2 Multiplanar CT Anatomy of the Skull

2.2.1 Axial CT Slices

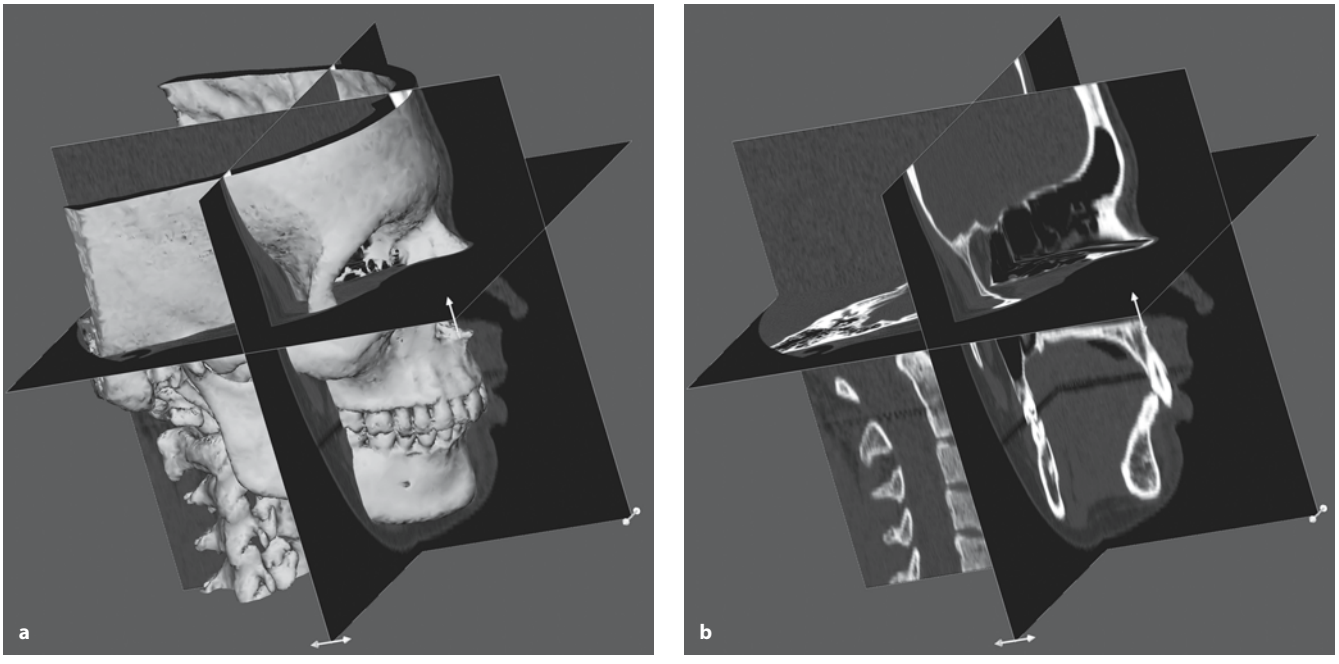

Fig. 2.19. **a** Virtual scene shows 3-D hard-tissue surface representation and orientation of axial, virtually reconstructed coronal and sagittal slices (patient K.C.). **b** Virtual scene shows orientation of axial, virtually reconstructed coronal and sagittal slices (patient K.C.)

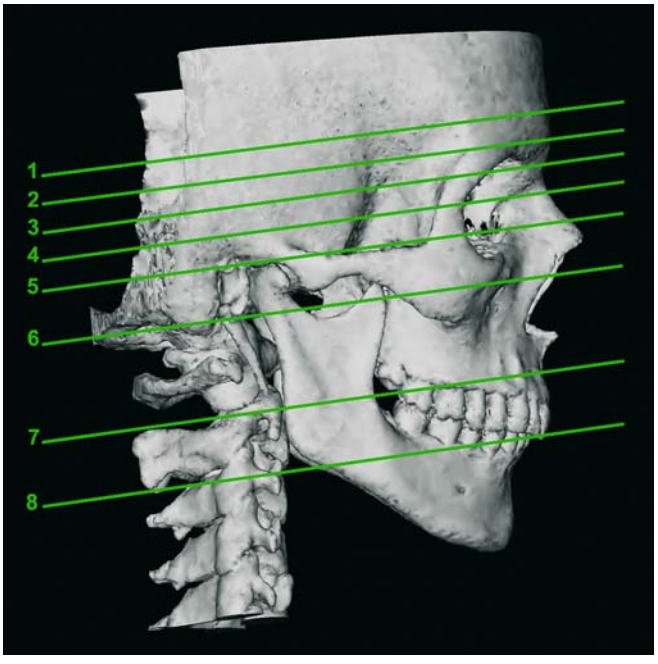

Fig. 2.20. 3-D hard-tissue surface representation shows the position of orbitomeatal orientated axial slices 1–8 (Figs. 2.21–2.28) (patient K.C.)

Axial CT – Slice 1

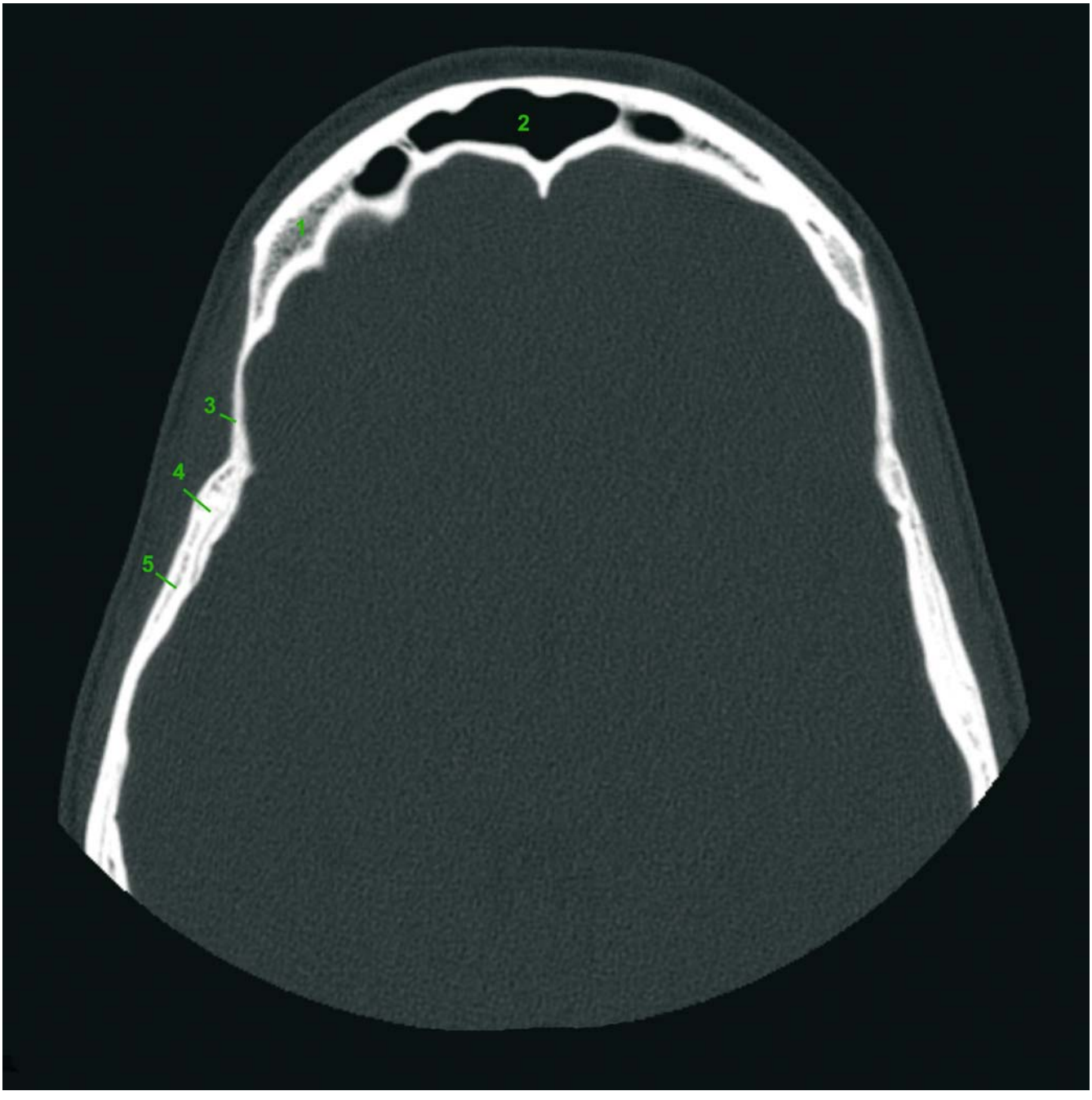

Fig. 2.21. Axial CT slice 1 (patient K.C.). *1* Frontal bone; *2* Frontal sinus; *3* Sphenoid bone; *4* Sphenosquamosal suture; *5* Temporal bone

Axial CT – Slice 2

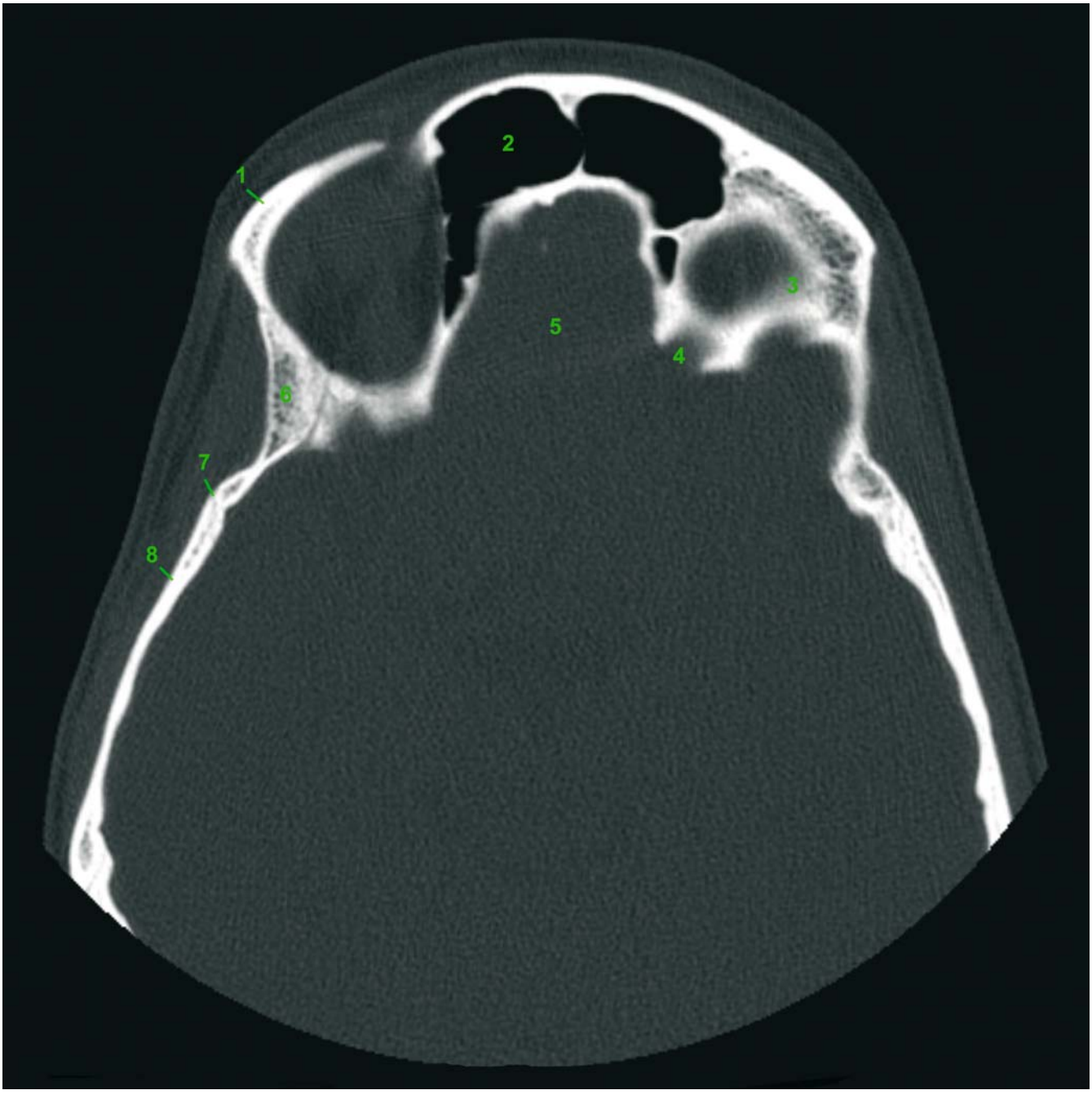

Fig. 2.22. Axial CT slice 2 (patient K.C.). *1* Frontal bone; *2* Frontal sinus; *3* Orbital roof; *4* Optic canal; *5* Anterior cranial fossa; *6* Sphenoid bone; *7* Sphenosquamosal suture; *8* Temporal bone

Axial CT – Slice 3

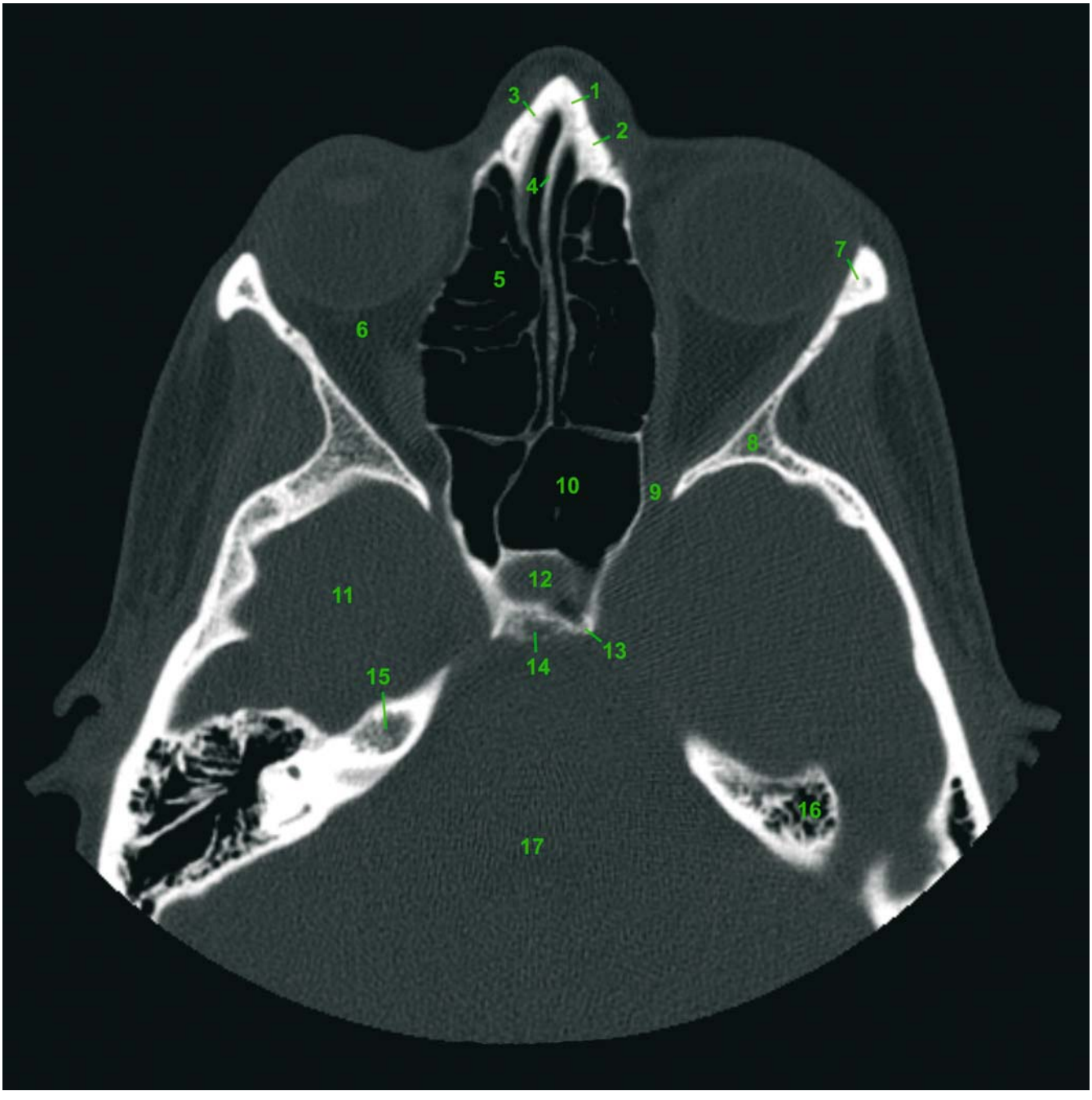

Fig. 2.23. Axial CT slice 3 (patient K.C.). *1* Nasal bone; *2* Maxillary bone; *3* Nasomaxillary suture; *4* Nasal septum; *5* Ethmoid air cells; *6* Orbita; *7* Frontal bone; *8* Sphenoid bone; *9* Superior orbital fissure; *10* Sphenoidal sinus; *11* Medial cranial fossa; *12* Sella turcica; *13* Posterior clinoid process; *14* Dorsum sellae; *15* Internal acoustic meatus; *16* Mastoid air cells; *17* Posterior cranial fossa

Axial CT – Slice 4

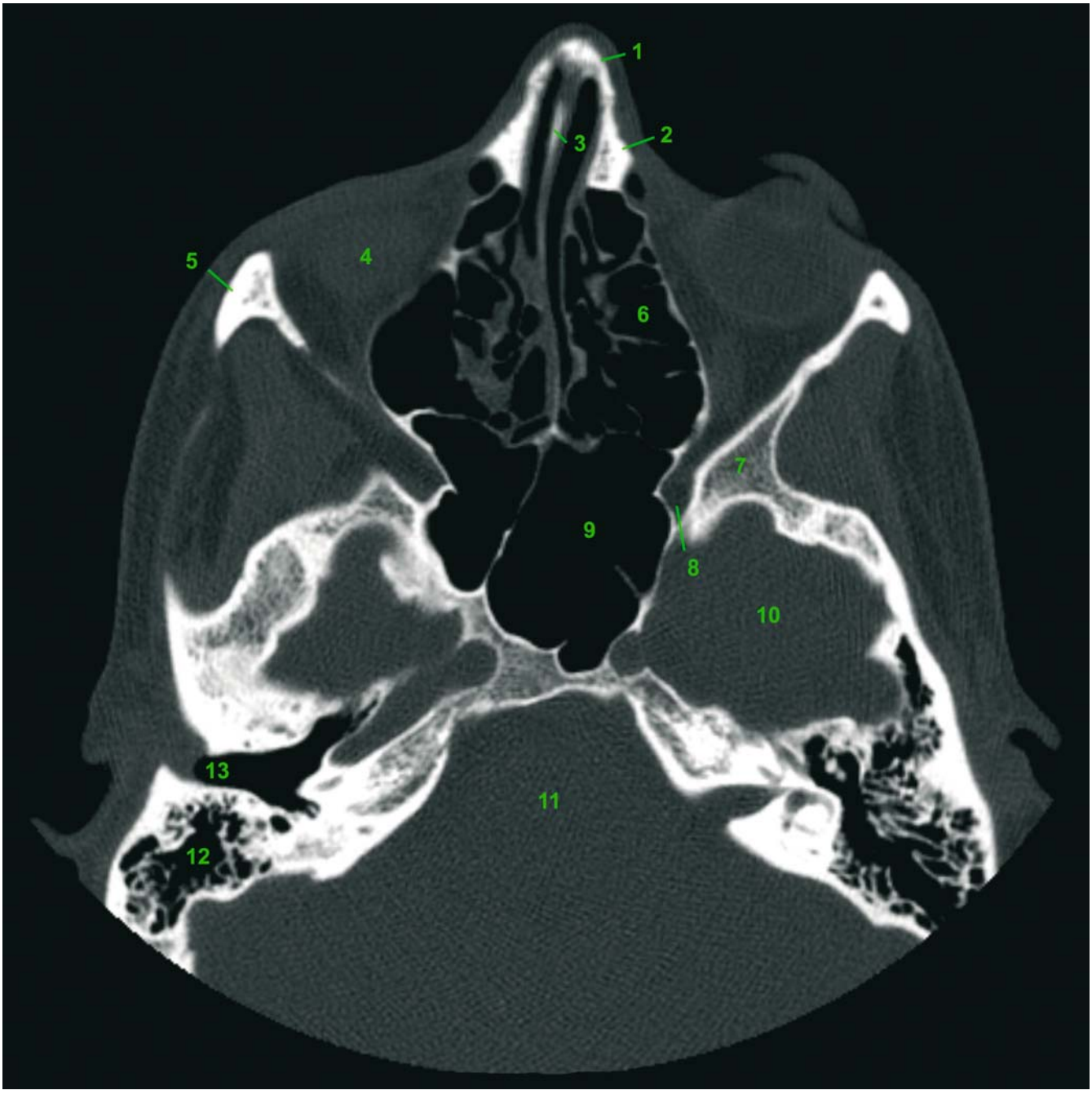

Fig. 2.24. Axial CT slice 4 (patient K.C.). *1* Nasal bone; *2* Maxillary bone; *3* Nasal septum; *4* Orbita; *5* Zygomatic bone; *6* Ethmoidal air cells; *7* Sphenoid bone; *8* Superior orbital fissure; *9* Sphenoidal sinus; *10* Medial cranial fossa; *11* Posterior cranial fossa; *12* Mastoid air cells; *13* External acoustic meatus

Axial CT – Slice 5

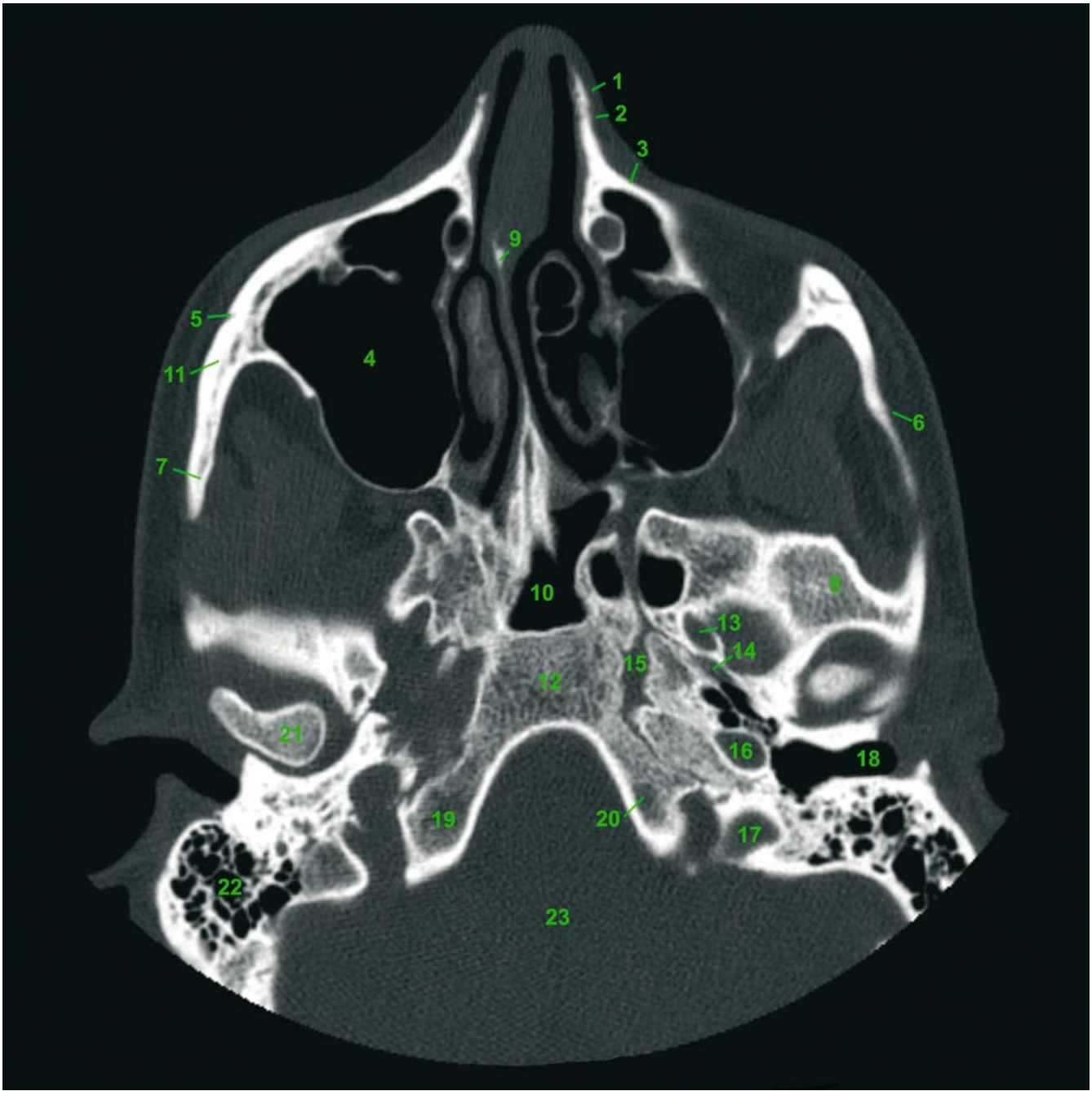

Fig. 2.25. Axial CT slice 5 (patient K.C.). *1* Nasal bone; *2* Nasomaxillary suture; *3* Maxillary bone; *4* Maxillary sinus; *5* Zygomaticomaxillary suture; *6* Zygomaticotemporal suture; *7* Zygomatic arch; *8* Temporal bone; *9* Nasal septum; *10* Sphenoidal sinus; *11* Zygomatic bone; *12* Clivus; *13* Oval foramen of sphenoid bone (foramen ovale); *14* Spinous foramen (foramen spinosum); *15* Foramen lacerum; *16* Carotid canal; *17* Jugular foramen (foramen jugulare); *18* External acoustic meatus; *19* Occipital bone; *20* Hypoglossal nerve canal; *21* Condyle of mandible; *22* Mastoid air cells; *23* Posterior cranial fossa

Axial CT – Slice 6

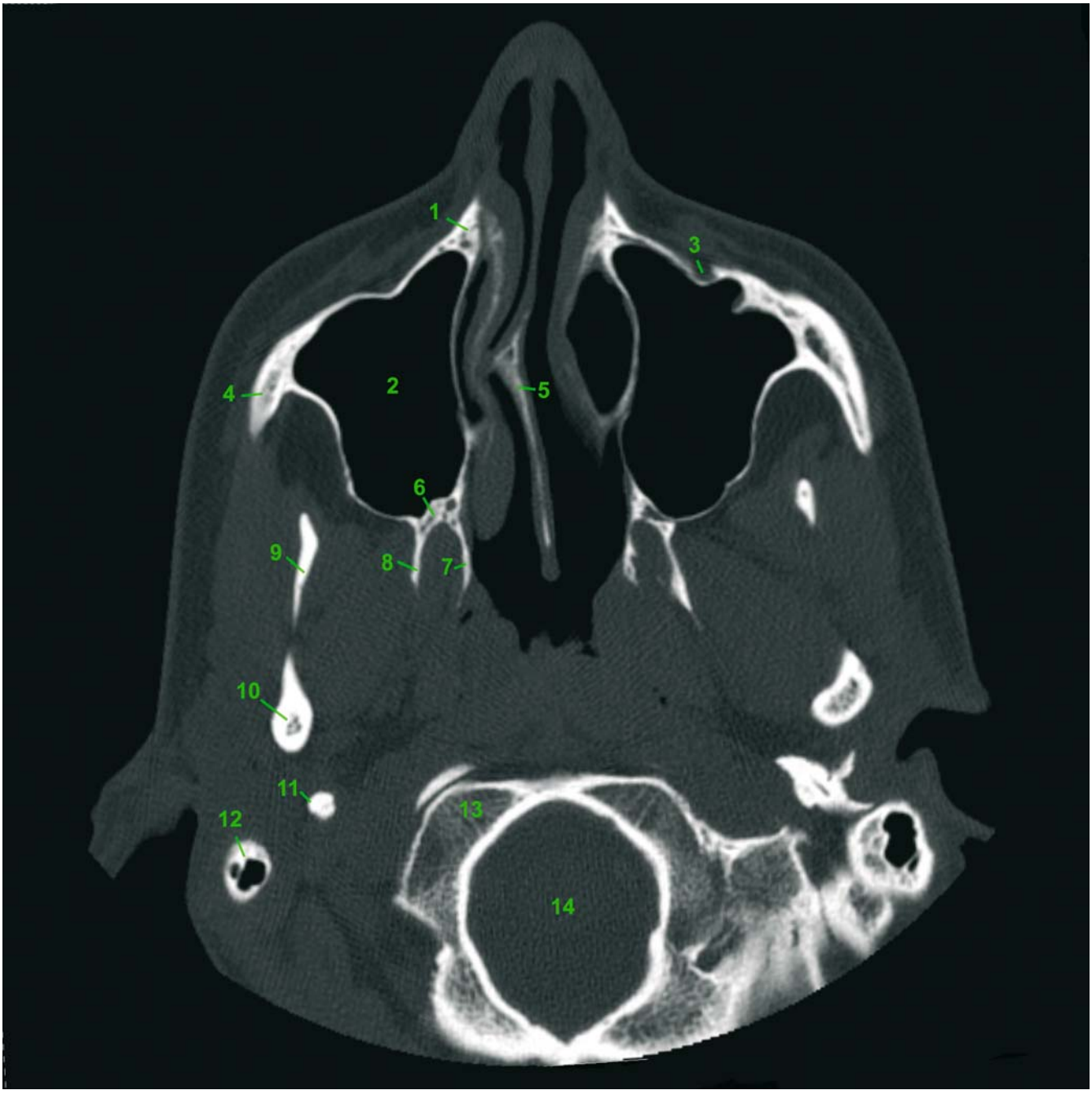

Fig. 2.26. Axial CT slice 6 (patient K.C.). *1* Maxillary bone; *2* Maxillary sinus; *3* Infraorbital canal; *4* Zygomatic bone; *5* Nasal septum; *6* Palatine bone; *7* Medial lamina of pterygoid process; *8* Lateral lamina of pterygoid process; *9* Coronoid process of mandible; *10* Condylar process of mandible; *11* Styloid process; *12* Mastoid process; *13* Occipital condyle; *14* Great foramen (foramen magnum)

Axial CT – Slice 7

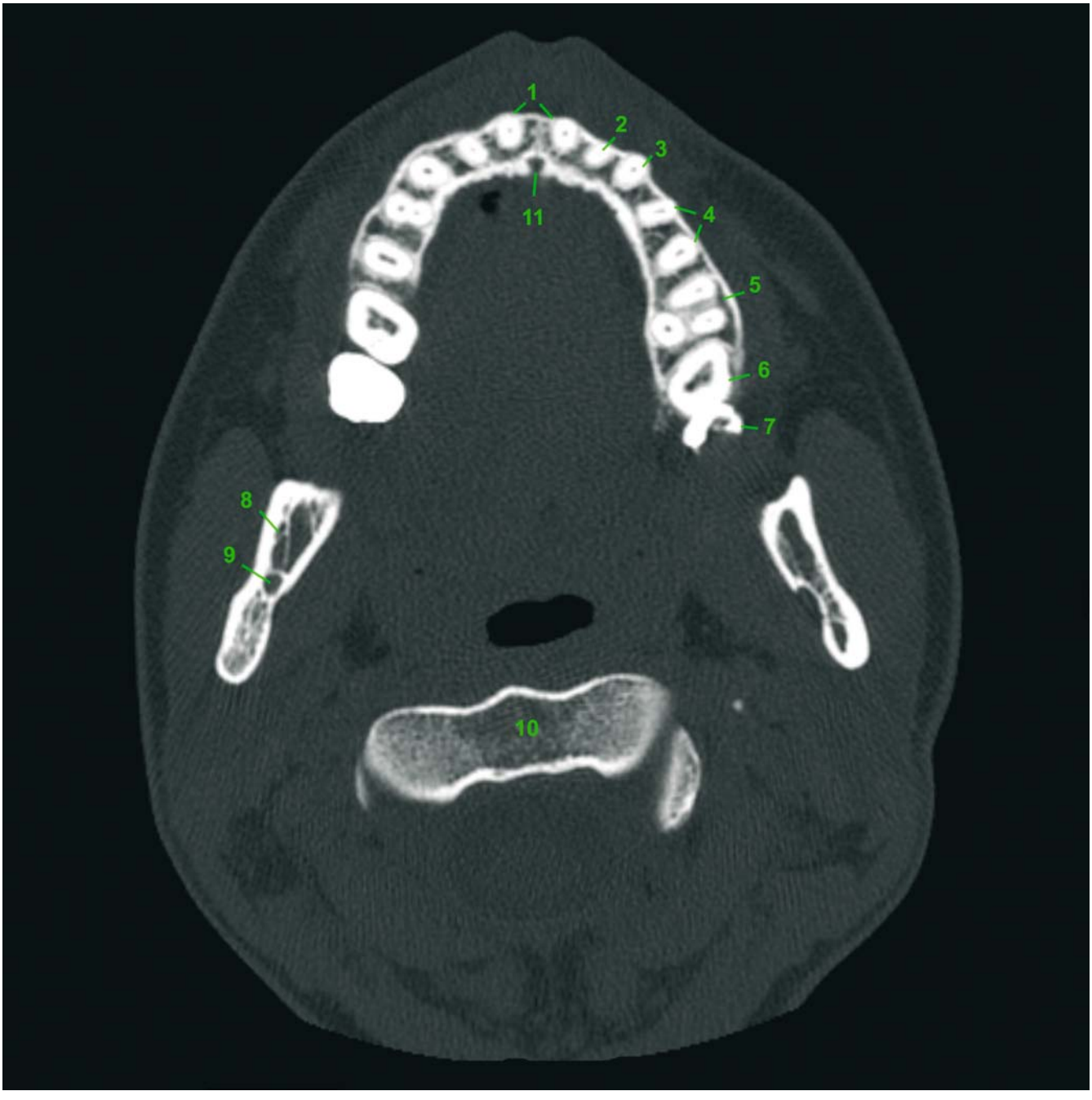

Fig. 2.27. Axial CT slice *7* (patient K.C.). *1* Upper central incisors; *2* Upper left lateral incisor; *3* Upper left canine; *4* Upper left premolars; *5* Upper left first molar; *6* Upper left second molar; *7* Upper left third molar; *8* Vertical ramus of mandible; *9* Mandibular canal; *10* Body of 2nd cervical vertebra (axis); *11* Incisive foramen (foramen incisivum)

Axial CT – Slice 8

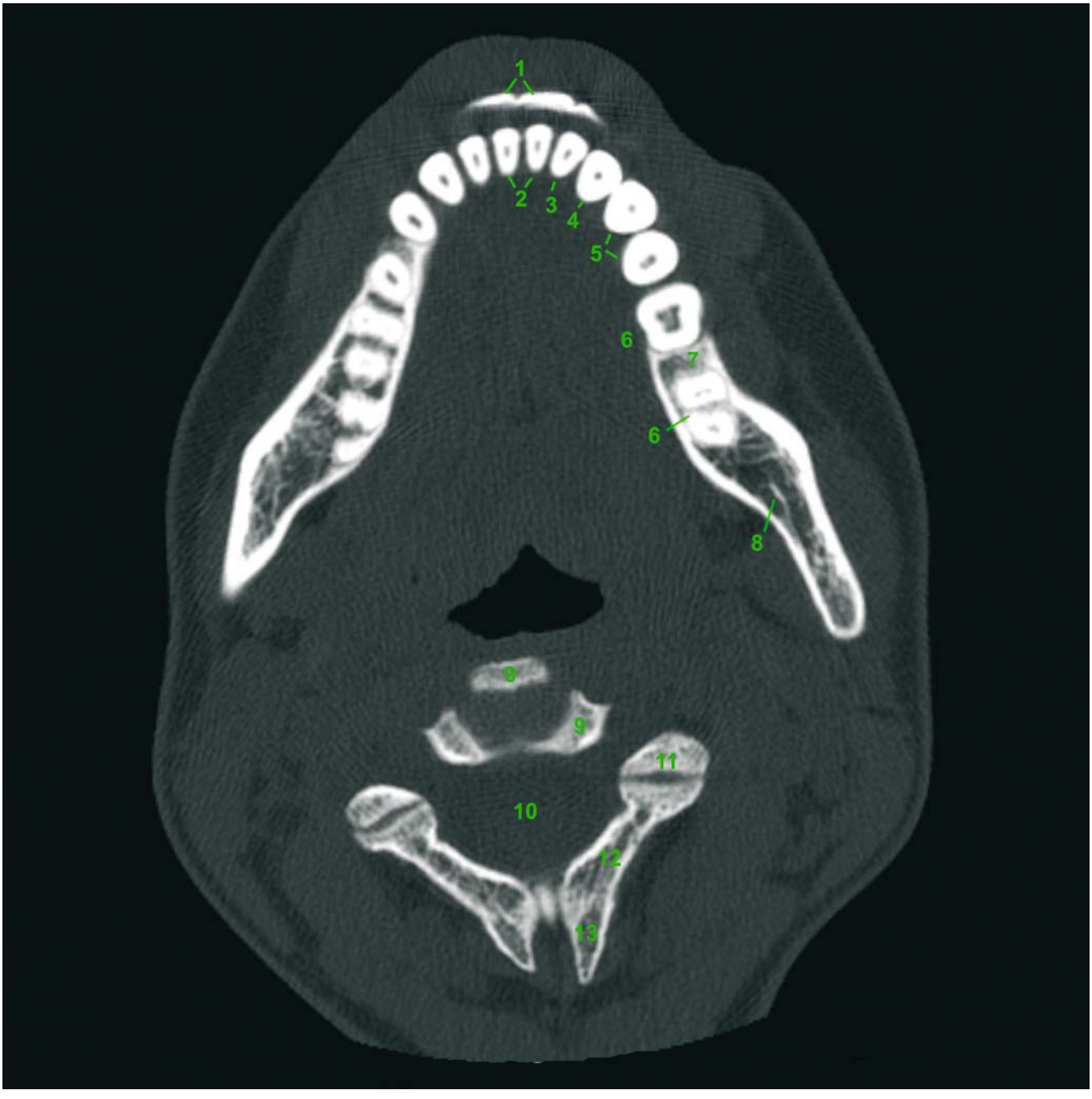

Fig. 2.28. Axial CT slice 8 (patient K.C.). *1* Upper central incisors; *2* Lower central incisors; *3* Lower left lateral incisor; *4* Lower left canine; *5* Lower left premolars; *6* Lower left molars; *7* Mandibular body; *8* Mandibular canal; *9* Body of 3rd cervical vertebra; *10* Vertebral foramen; *11* Articular process of 3rd cervical vertebra; *12* Arch of 3rd cervical vertebra; *13* Spinous process of 3rd cervical vertebra

2.2.2 Virtual Coronal (Frontal) Slice Reconstructions

Coronal Reconstruction – Slice 1

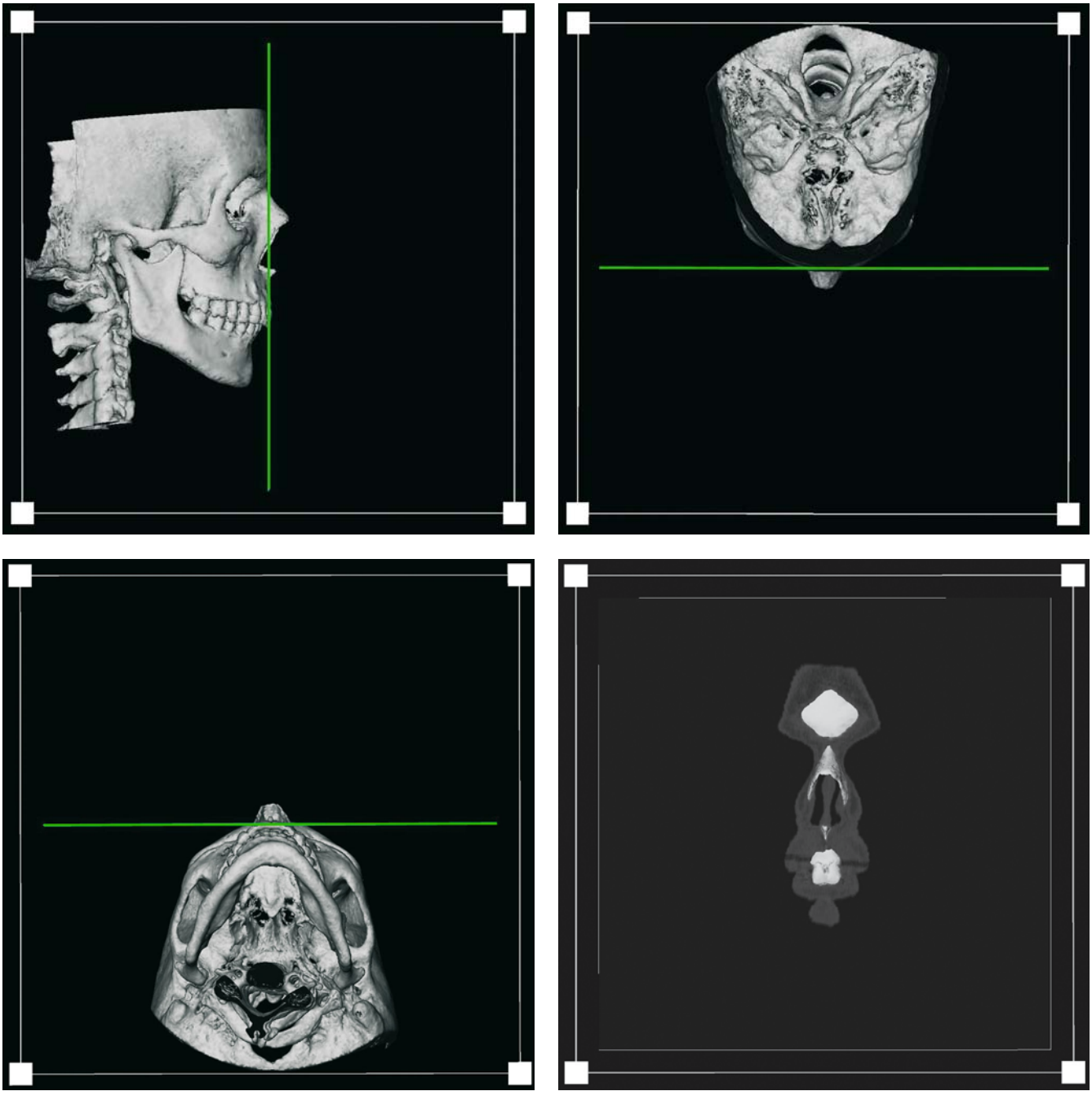

Fig. 2.29. **a** 3-D hard-tissue surface representations show the position of coronal reconstruction slice *1* (patient K.C.)

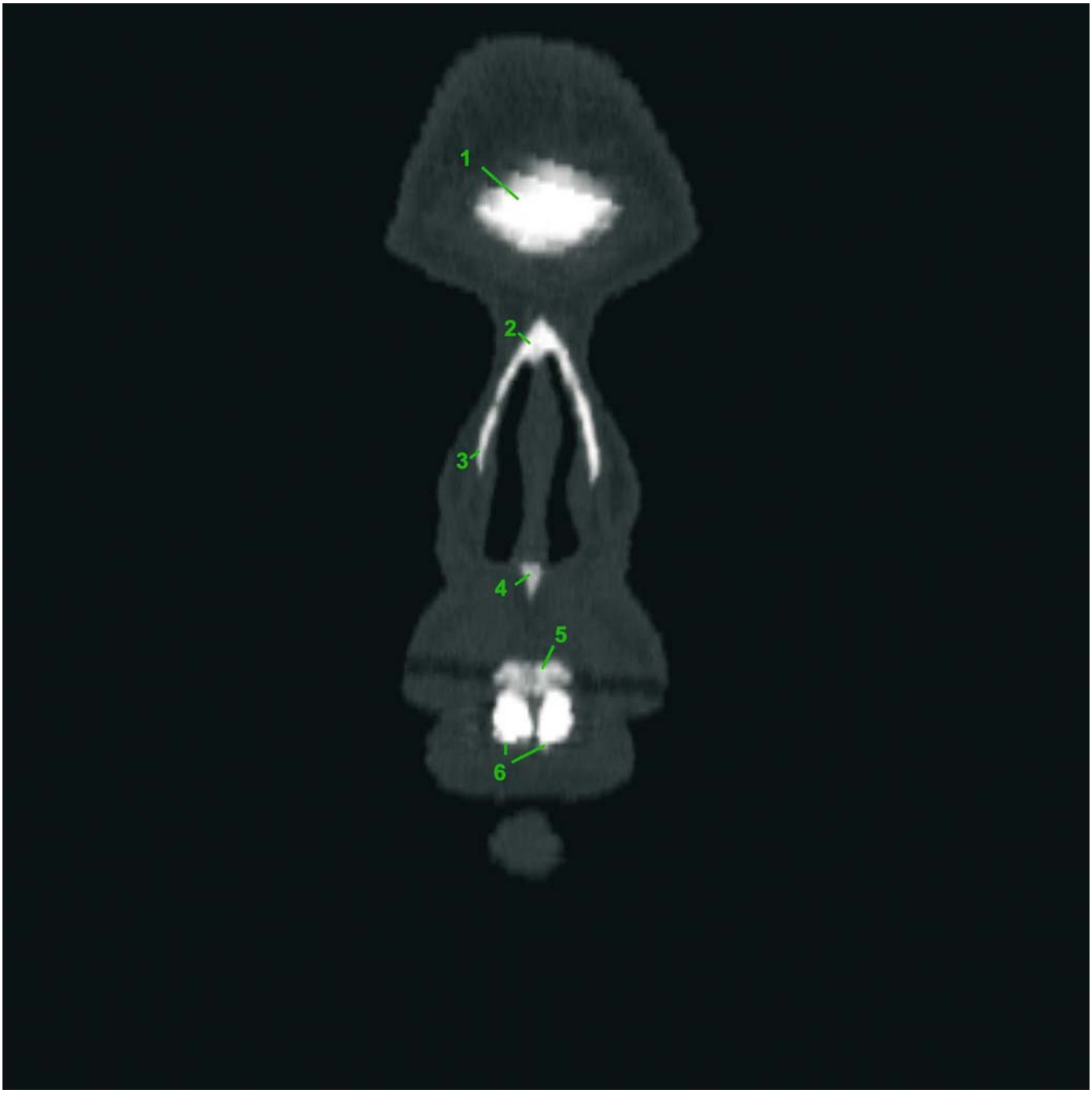

Fig. 2.29. **b** Coronal reconstruction slice *1* (patient K.C.). *1* Frontal bone; *2* Nasal bone; *3* Maxillary bone; *4* Anterior nasal spine; *5* Alveolar process of maxilla; *6* Upper central incisors

Coronal Reconstruction – Slice 2

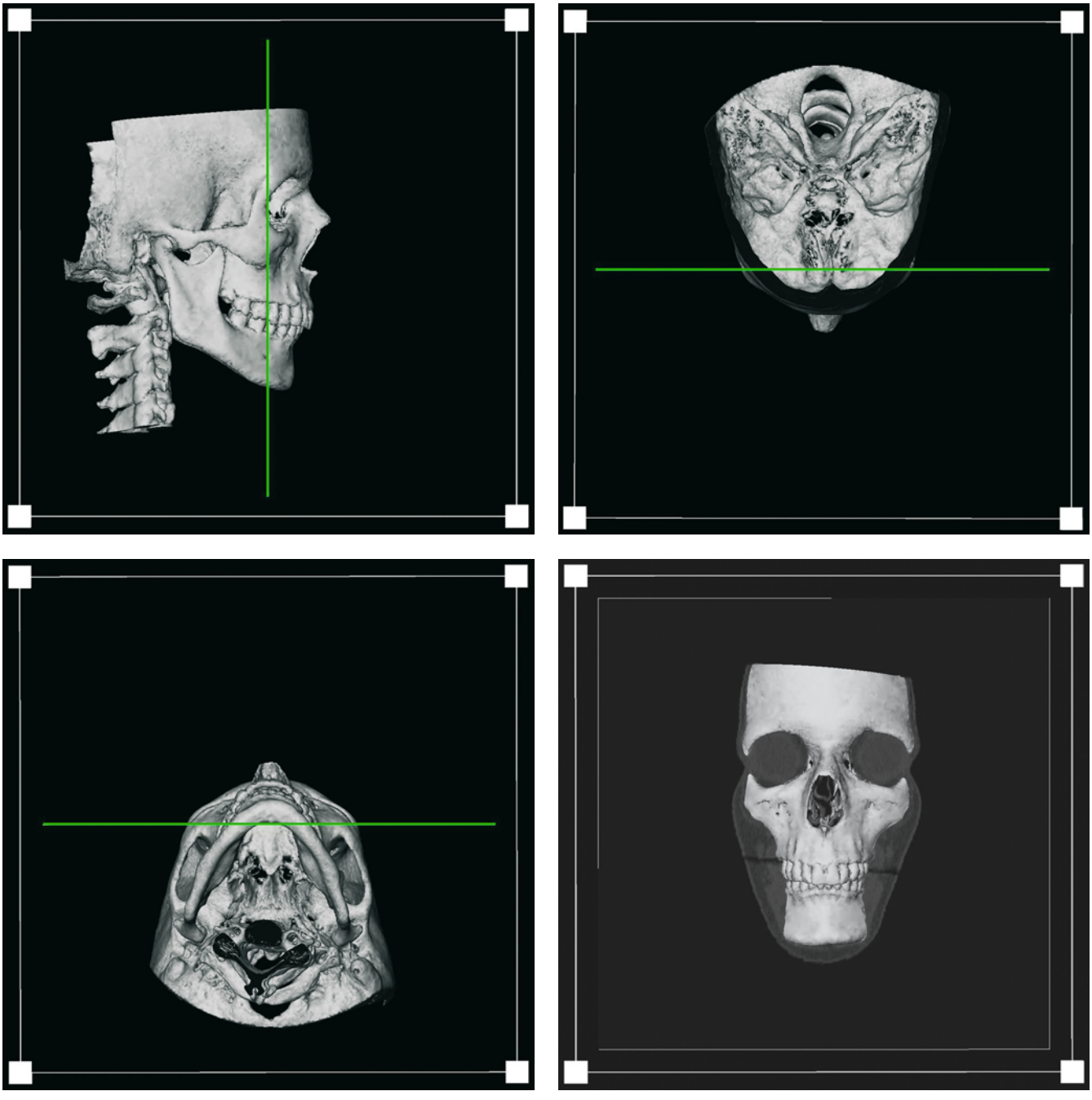

Fig. 2.30. **a**. 3-D hard-tissue surface representations show the position of coronal reconstruction slice 2 (patient K.C.)

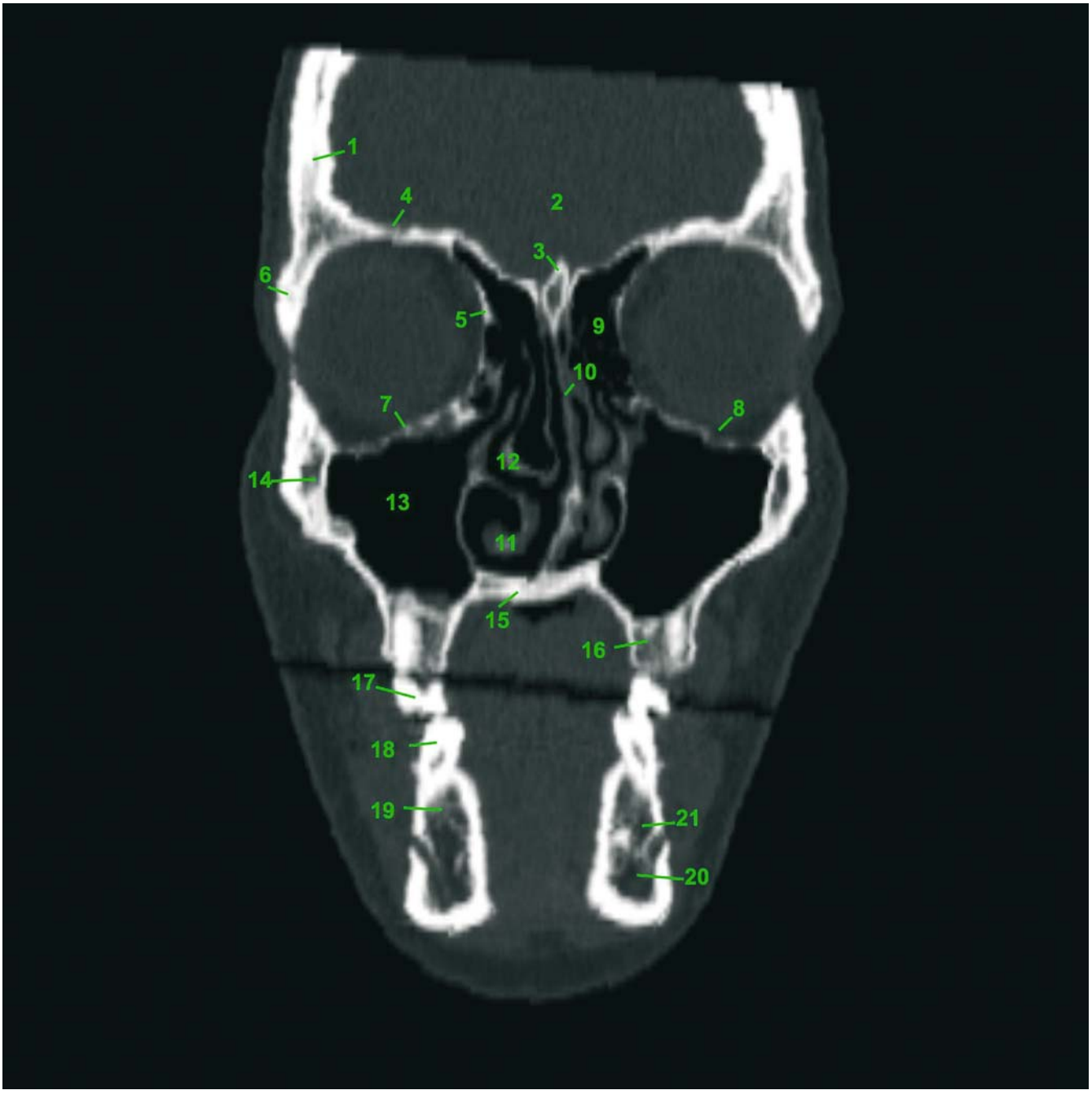

Fig. 2.30. **b** Coronal reconstruction slice 2 (patient K.C.). *1* Frontal bone; *2* Anterior cranial fossa; *3* Crista galli; *4* Orbital roof; *5* Medial wall of orbit; *6* Fronto-zygomatic suture; *7* Orbital floor; *8* Infraorbital canal; *9* Ethmoidal air cells; *10* Nasal septum; *11* Inferior nasal concha; *12* Medial nasal concha; *13* Maxillary sinus; *14* Zygomatic bone; *15* Palatine process of maxilla; *16* Alveolar process of maxilla; *17* First upper right molar; *18* Second lower right premolar; *19* Alveolar process of mandible; *20* Body of mandible; *21* Mandibular canal

Coronal Reconstruction – Slice 3

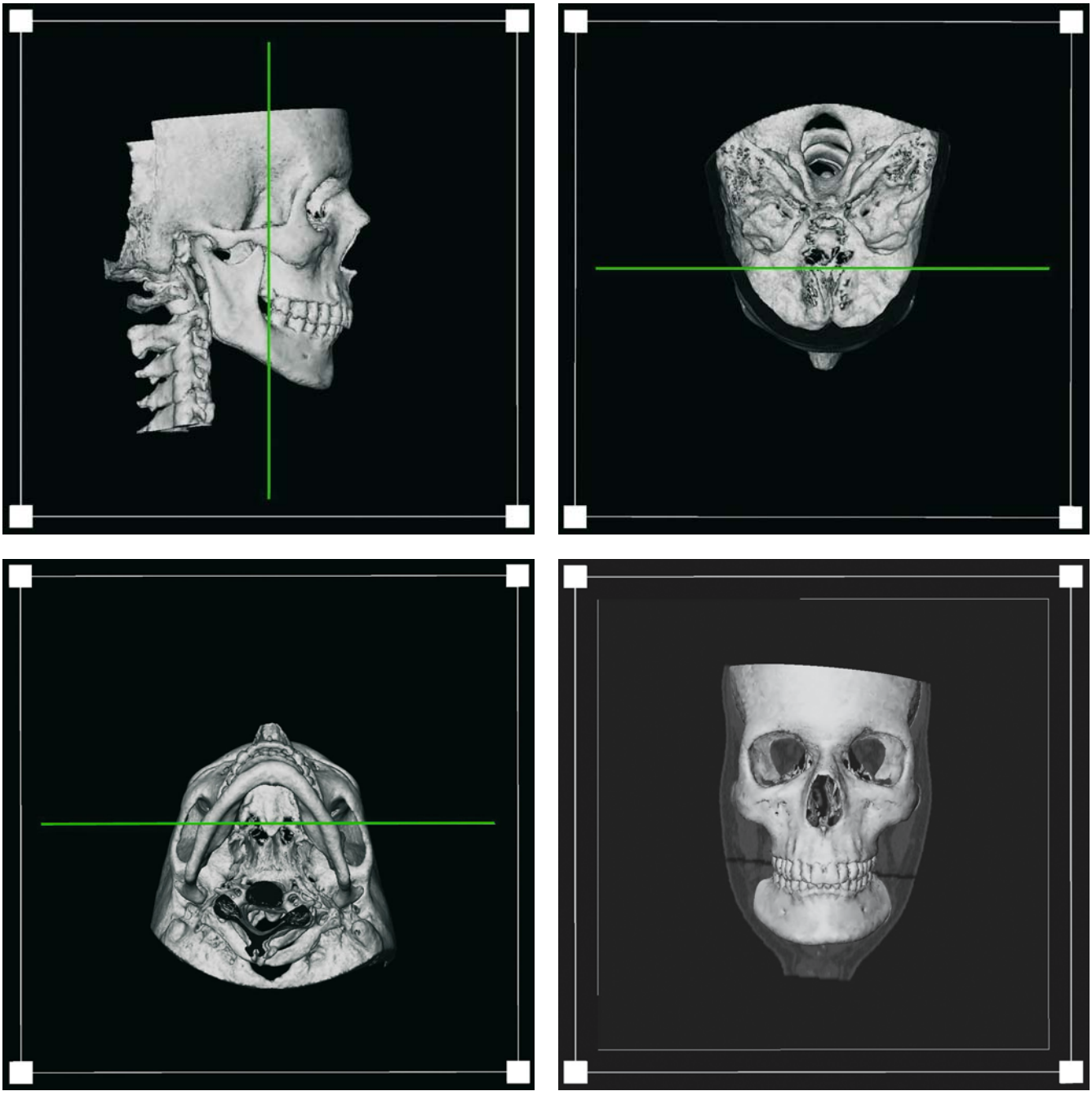

Fig. 2.31. **a** 3-D hard-tissue surface representations show the position of coronal reconstruction slice 3 (patient K.C.)

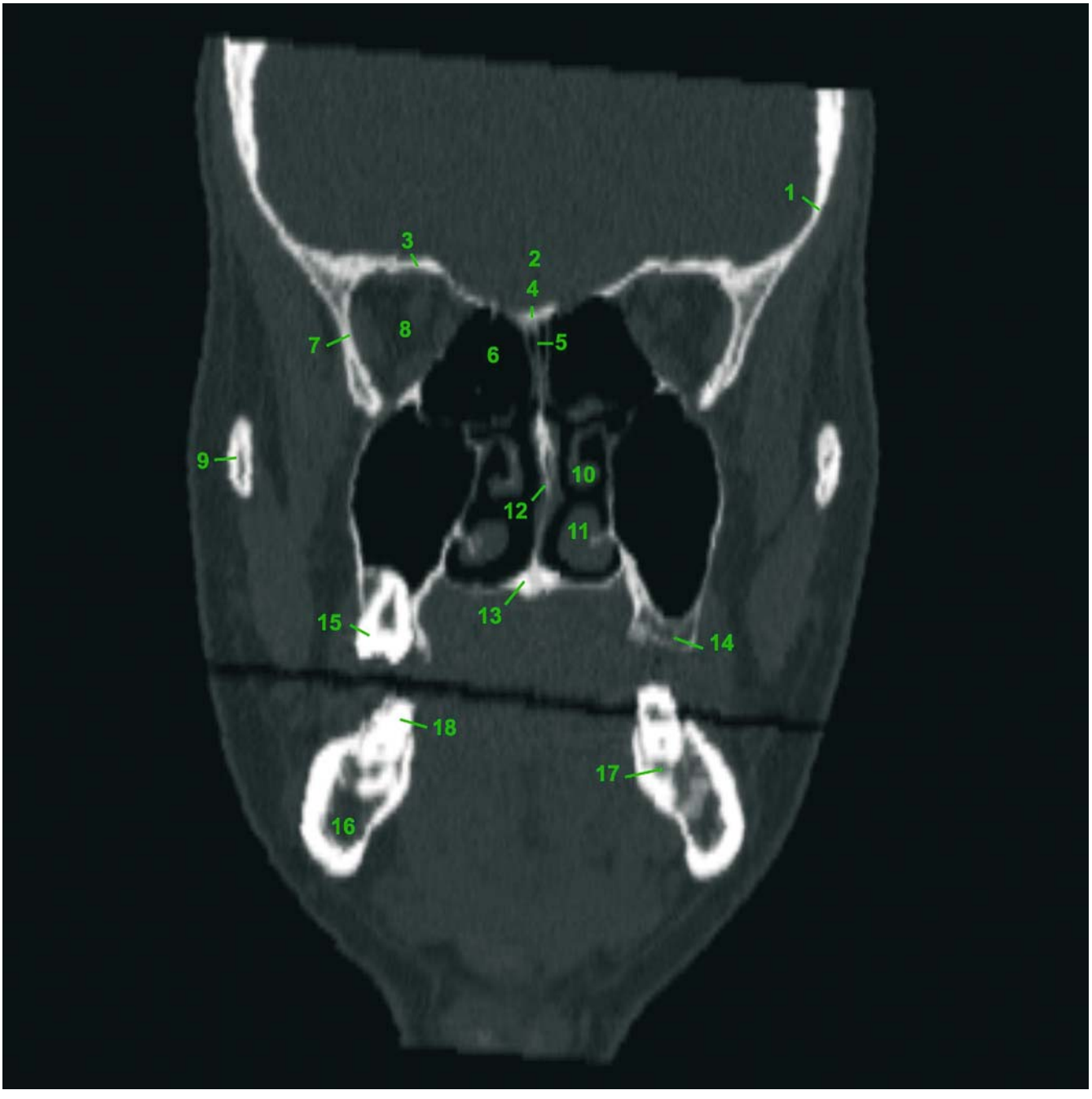

Fig. 2.31. b Coronal reconstruction slice 3 (patient K.C.). *1* Frontal bone; *2* Anterior cranial fossa; *3* Orbital roof; *4* Cribriform plate of ethmoid bone (lamina cribrosa); *5* Perpendicular plate of ethmoid bone; *6* Ethmoidal air cells; *7* Lateral wall of orbit; *8* Orbit; *9* Zygomatic arch; *10* Medial nasal concha; *11* Inferior nasal concha; *12* Nasal septum; *13* Palatine bone; *14* Maxillary tuberosity; *15* Upper right third molar; *16* Body of mandible; *17* Mandibular canal; *18* Lower right third molar

Coronal Reconstruction – Slice 4

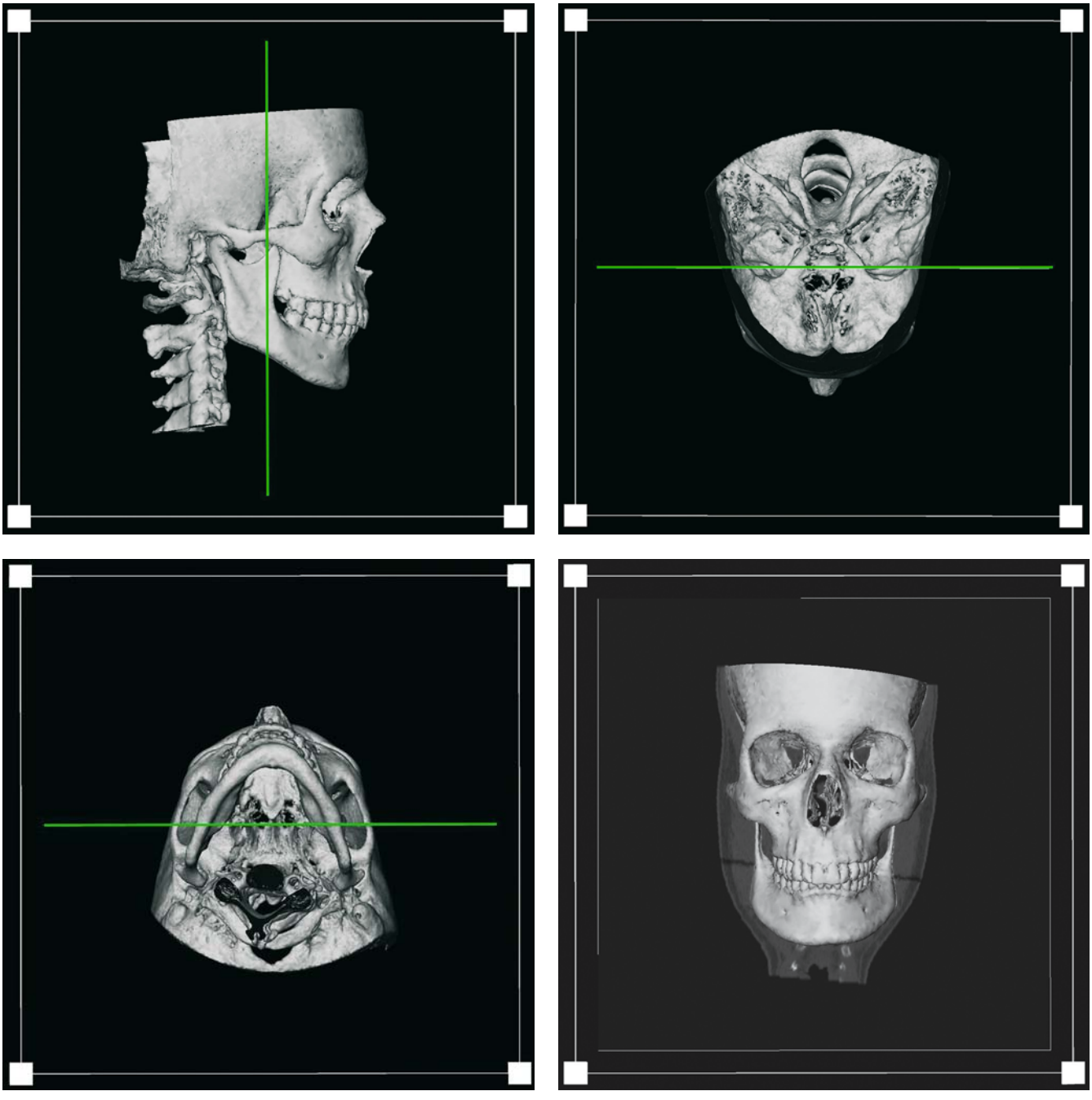

Fig. 2.32. **a** 3-D hard-tissue surface representations show the position of coronal reconstruction slice 4 (patient K.C.)

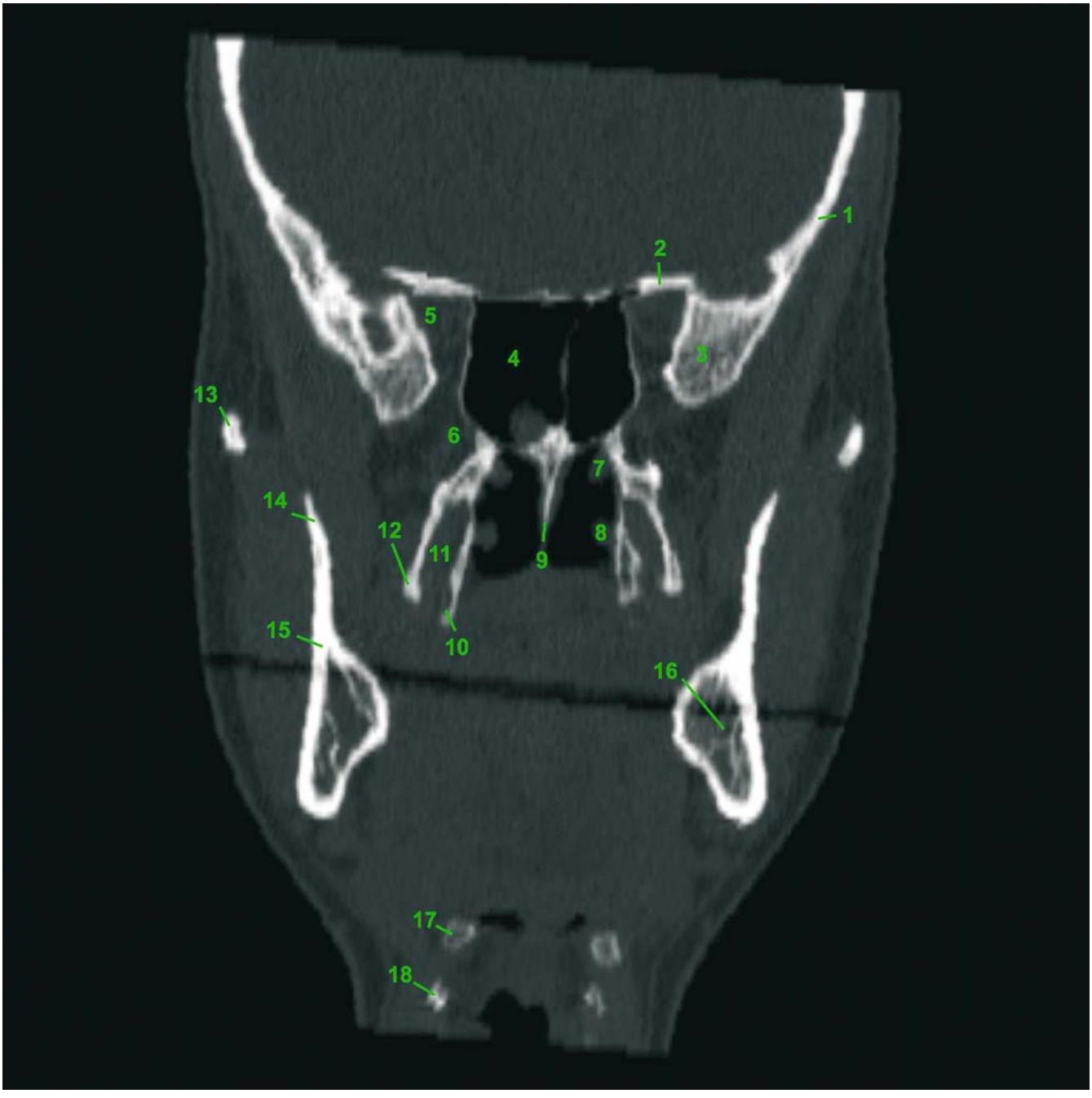

Fig. 2.32. **b** Coronal reconstruction slice 4 (patient K.C.). *1* Frontal bone; *2* Lesser wing (ala minor) of sphenoid bone; *3* Greater wing (ala major) of sphenoid bone; *4* Sphenoidal sinus; *5* Superior orbital fissure; *6* Pterygopalatine fossa; *7* Superior nasal concha; *8* Medial nasal concha; *9* Nasal septum; *10* Medial lamina of pterygoid process; *11* Pterygoid fossa; *12* Lateral lamina of pterygoid process; *13* Zygomatic arch; *14* Coronoid process of mandible; *15* Vertical ramus of mandible; *16* Mandibular canal; *17* Greater cornu of hyoid bone; *18* Superior cornu of thyroid cartilage

Coronal Reconstruction – Slice 5

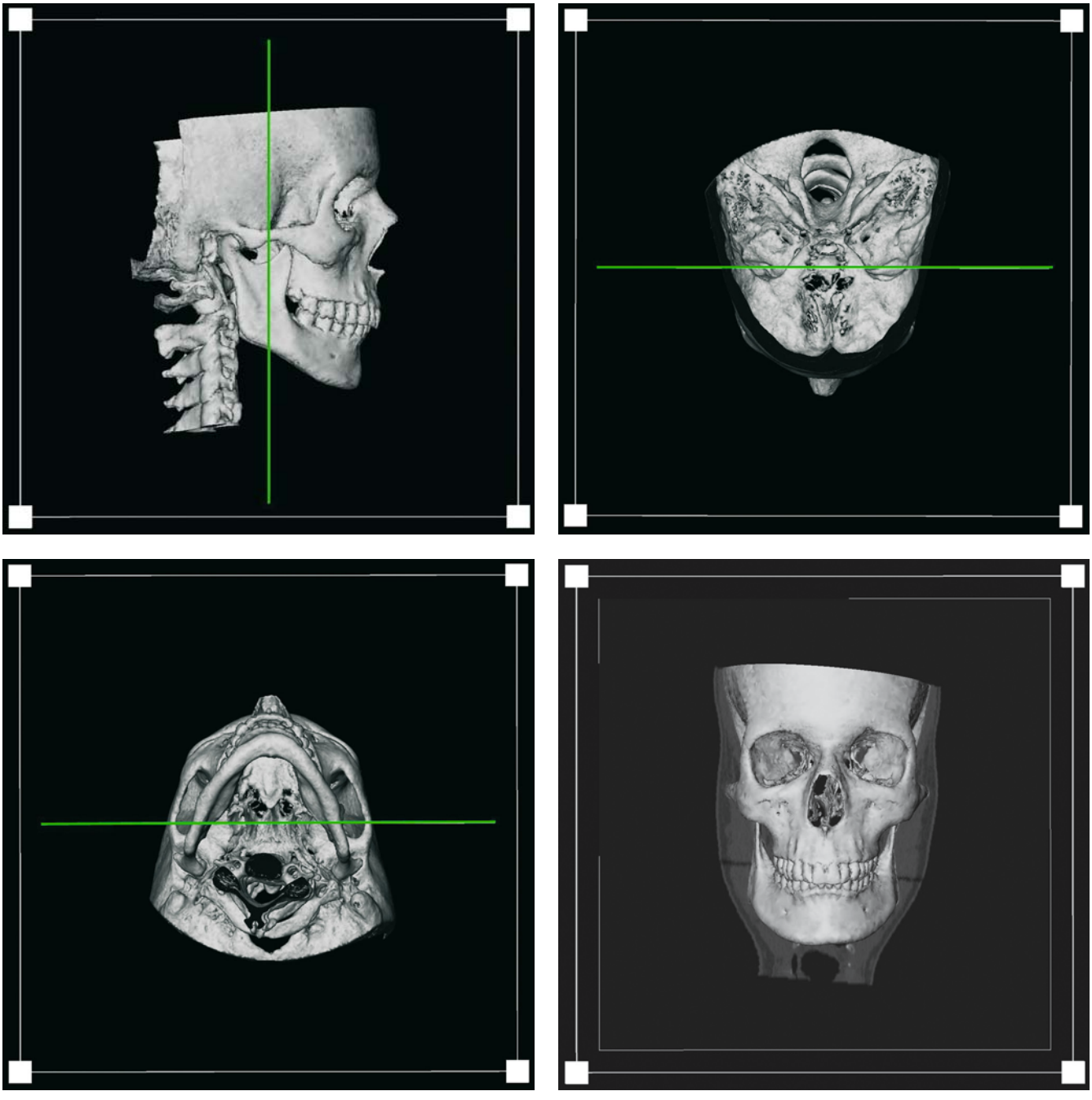

Fig. 2.33. **a** 3-D hard-tissue surface representations show the position of coronal reconstruction slice 5 (patient K.C.)

Fig. 2.33. **b** Coronal reconstruction slice 5 (patient K.C.). *1* Middle cranial fossa; *2* Parietal bone; *3* Squamosal suture; *4* Temporal bone; *5* Lesser wing (ala minor) of sphenoid bone; *6* Optic canal; *7* Superior orbital fissure; *8* Spenoidal sinus; *9* Sphenosquamosal suture; *10* Greater wing (ala major) of sphenoid bone; *11* Pterygoid canal; *12* Nasal septum; *13* Medial lamina of pterygoid process; *14* Pterygoid fossa; *15* Lateral lamina of pterygoid process; *16* Zygomatic arch; *17* Vertical ramus of mandible; *18* Mandibular canal; *19* Greater cornu of hyoid bone

Coronal Reconstruction – Slice 6

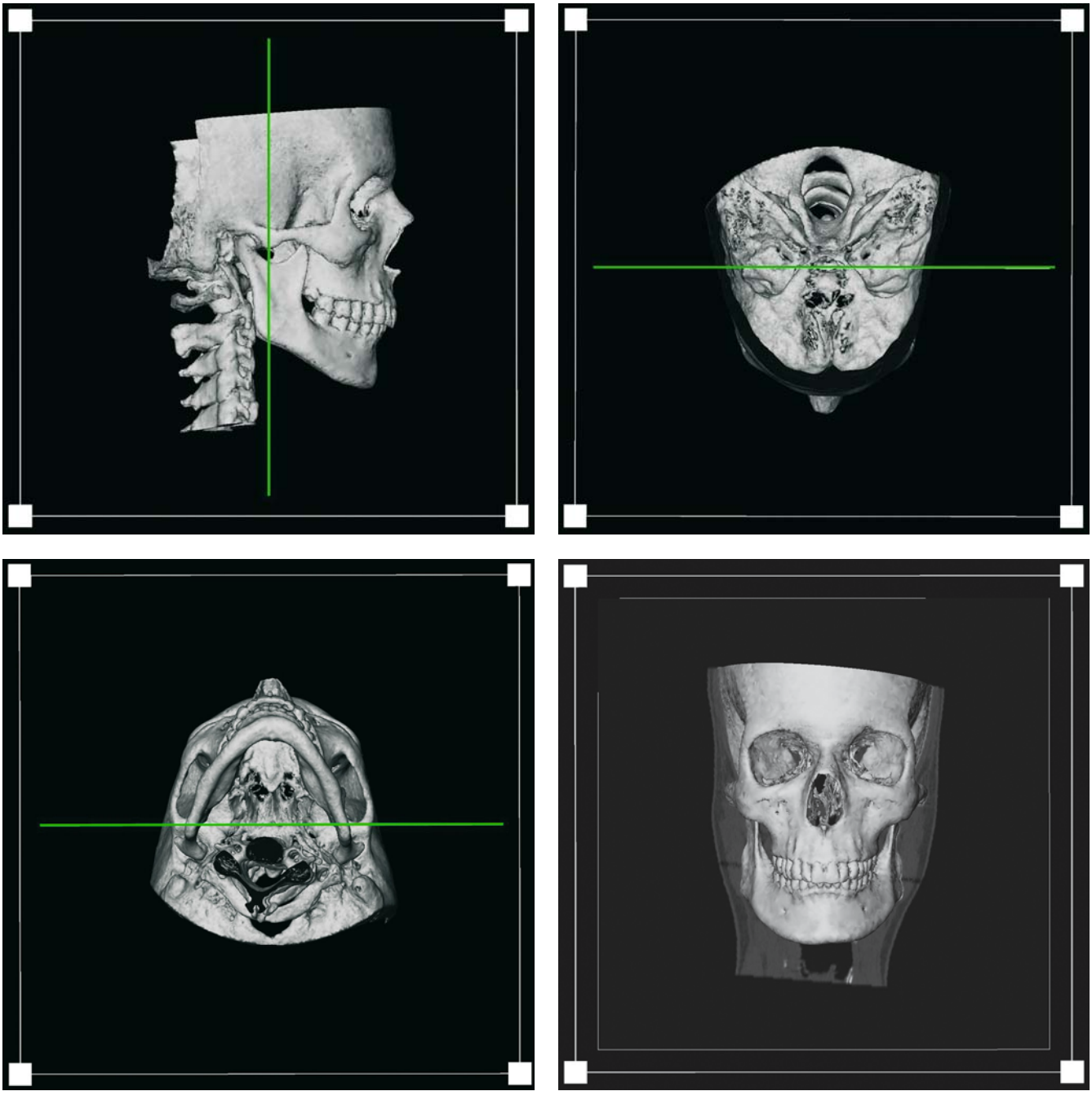

Fig. 2.34. **a** 3-D hard-tissue surface representations show the position of coronal reconstruction slice 6 (patient K.C.)

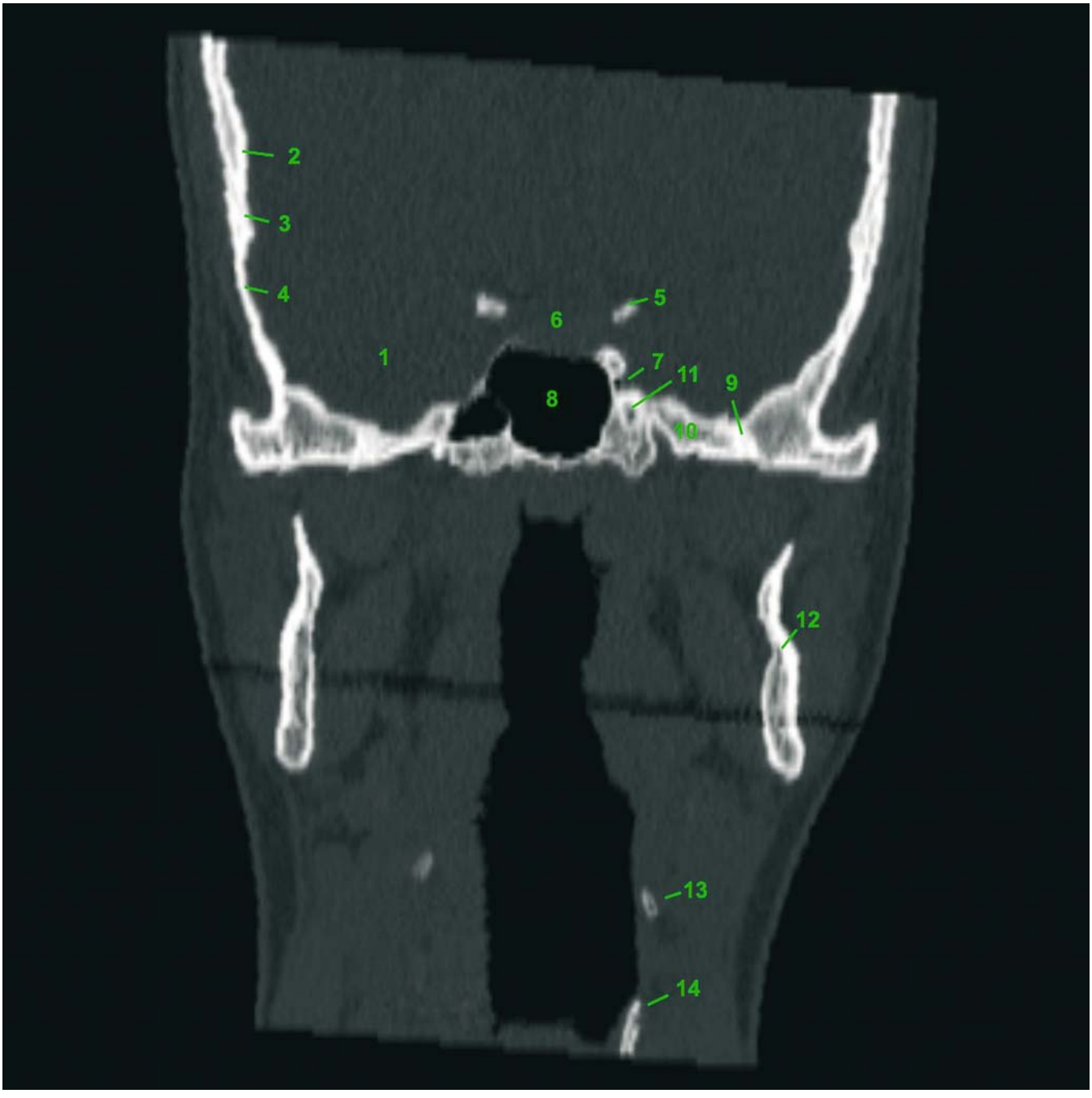

Fig. 2.34. **b** Coronal reconstruction slice 6 (patient K.C.). *1* Middle cranial fossa; *2* Parietal bone; *3* Squamosal suture; *4* Temporal bone; *5* Anterior clinoid process; *6* Hypophyseal fossa (sella turcica); *7* Carotid sulcus; *8* Spenoidal sinus; *9* Sphenosquamosal suture; *10* Greater wing (ala major) of sphenoid bone; *11* Foramen rotundum; *12* Vertical ramus of mandible; *13* Greater cornu of hyoid bone; *14* Thyroid cartilage

Coronal Reconstruction – Slice 7

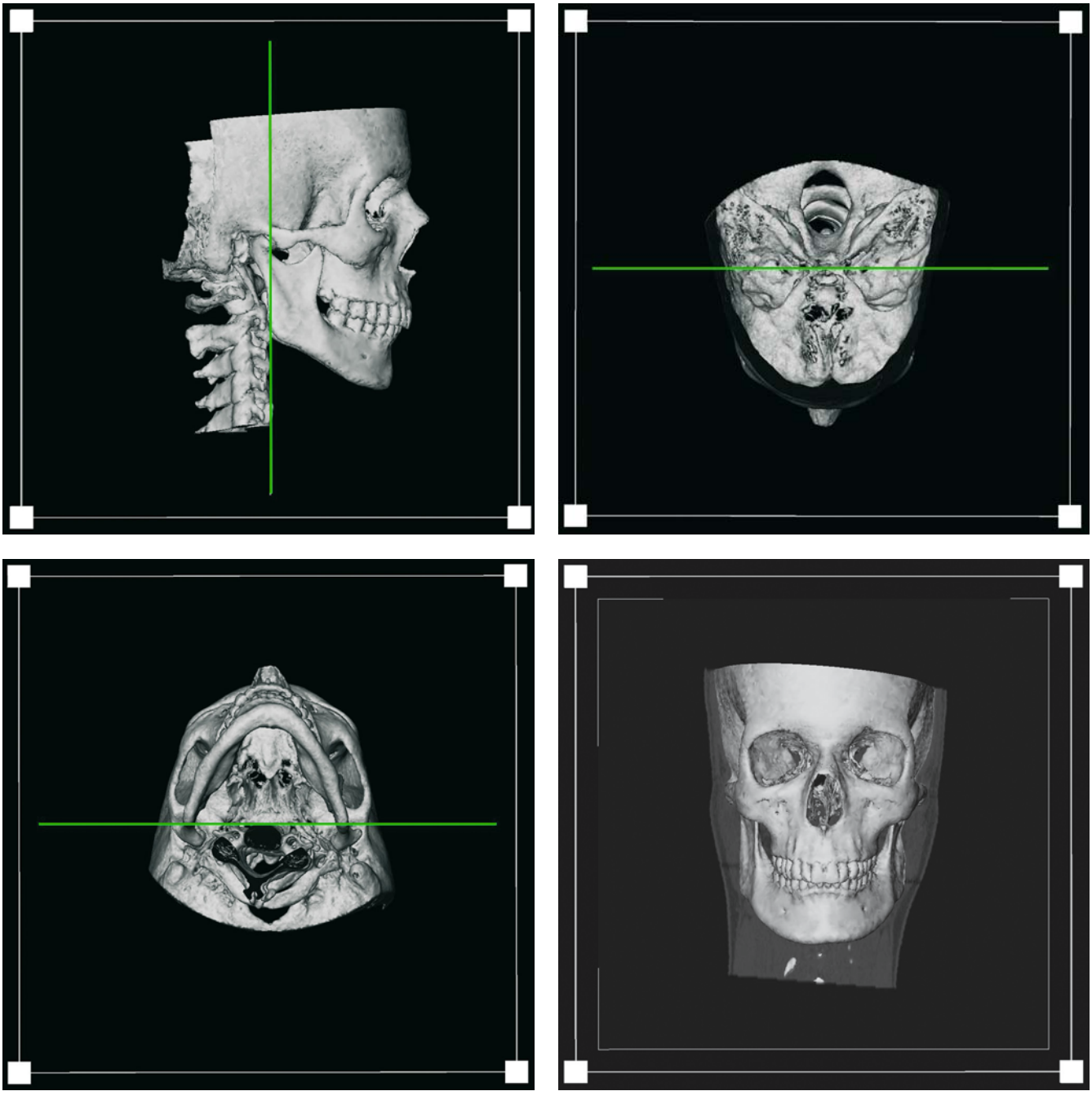

Fig. 2.35. **a** 3-D hard-tissue surface representations show the position of coronal reconstruction slice 7 (patient K.C.)

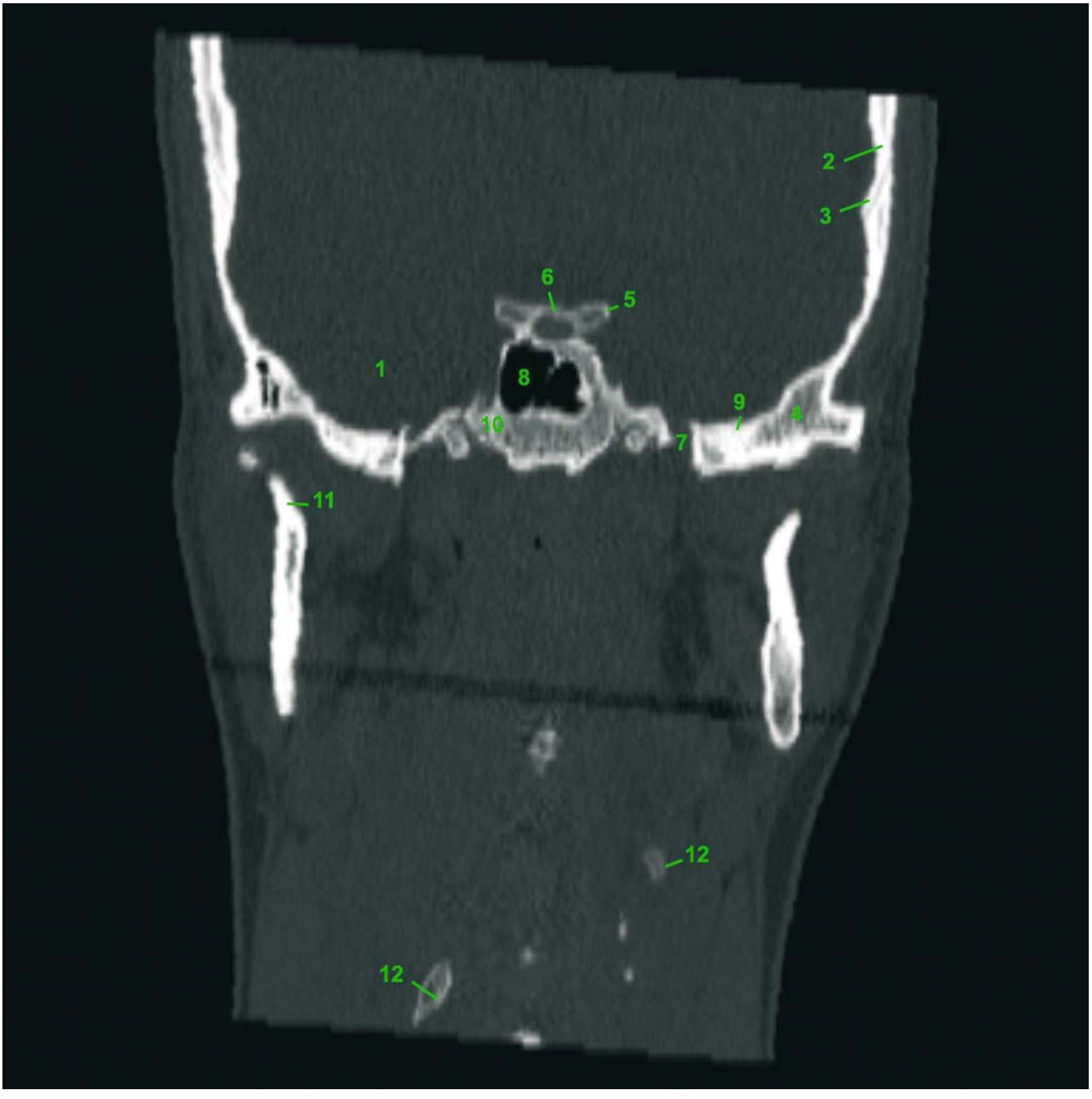

Fig. 2.35. **b** Coronal reconstruction slice 7 (patient K.C.). *1* Middle cranial fossa; *2* Parietal bone; *3* Squamosal suture; *4* Temporal bone; *5* Posterior clinoid process; *6* Clivus; *7* Carotid sulcus; *8* Spenoidal sinus; *9* Sphenosquamosal suture; *10* Sphenoid bone; *11* Condylar process of mandible; *12* Cervical vertebra

Coronal Reconstruction – Slice 8

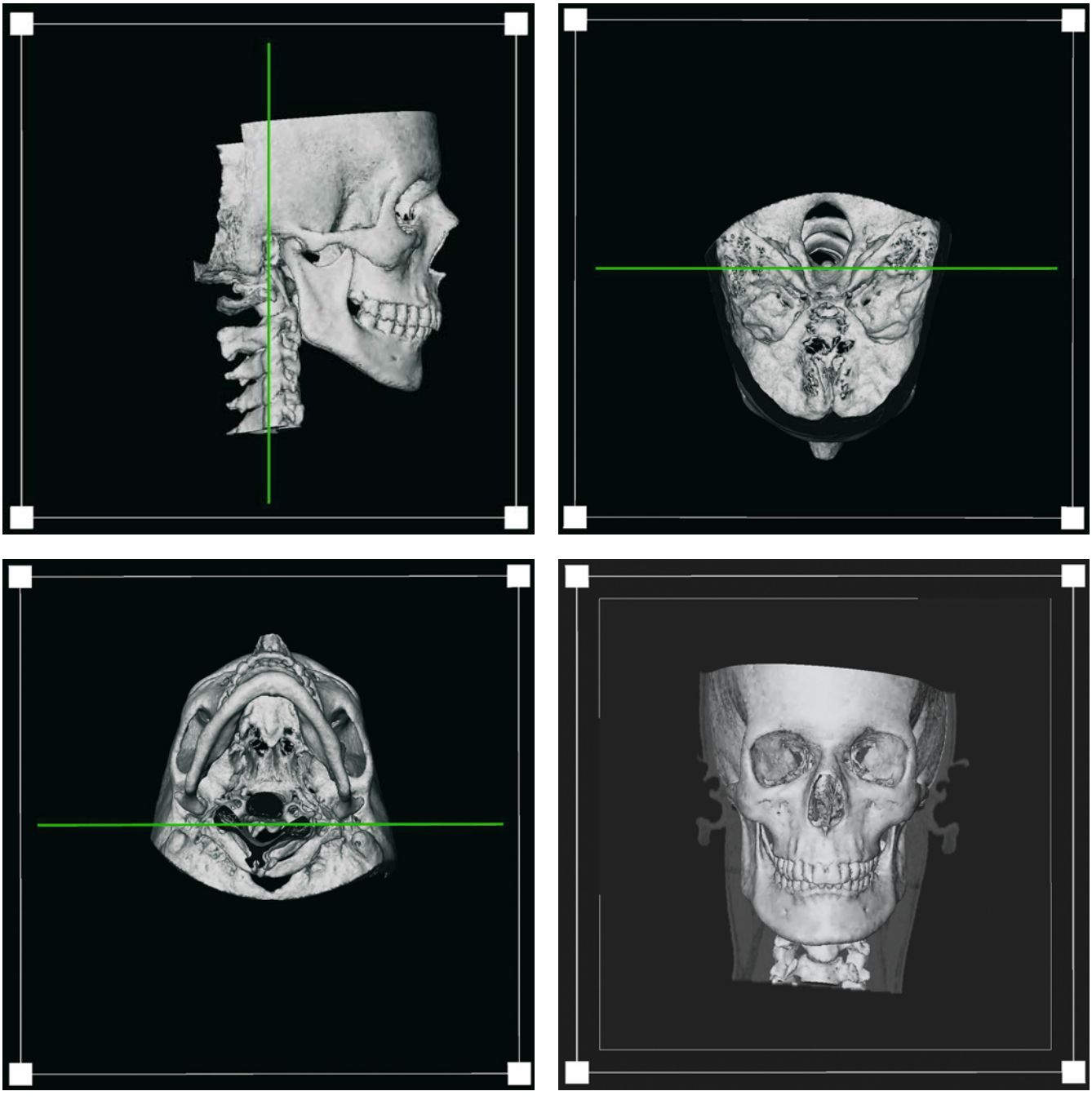

Fig. 2.36. **a** 3-D hard-tissue surface representations show the position of coronal reconstruction slice 8 (patient K.C.)

Fig. 2.36. **b** Coronal reconstruction slice 8 (patient K.C.). *1* Parietal bone; *2* Squamosal suture; *3* Temporal bone; *4* Middle cranial fossa; *5* Posterior cranial fossa; *6* External acoustic meatus; *7* Vestibulum; *8* Arcuate eminence; *9* Foramen stylomastoideum; *10* Facial canal; *11* Styloid process; *12* Petro-occipital fissure (synchondrosis); *13* Occipital bone; *14* Atlanto-occipital articulation; *15* Transverse process of atlas; *16* Lateral mass of atlas; *17* Dens axis (odontoid process); *18* 2nd cervical vertebra; *19* 3rd cervical vertebra; *20* 4th cervical vertebra; *21* 5th cervical vertebra

Coronal Reconstruction – Slice 9

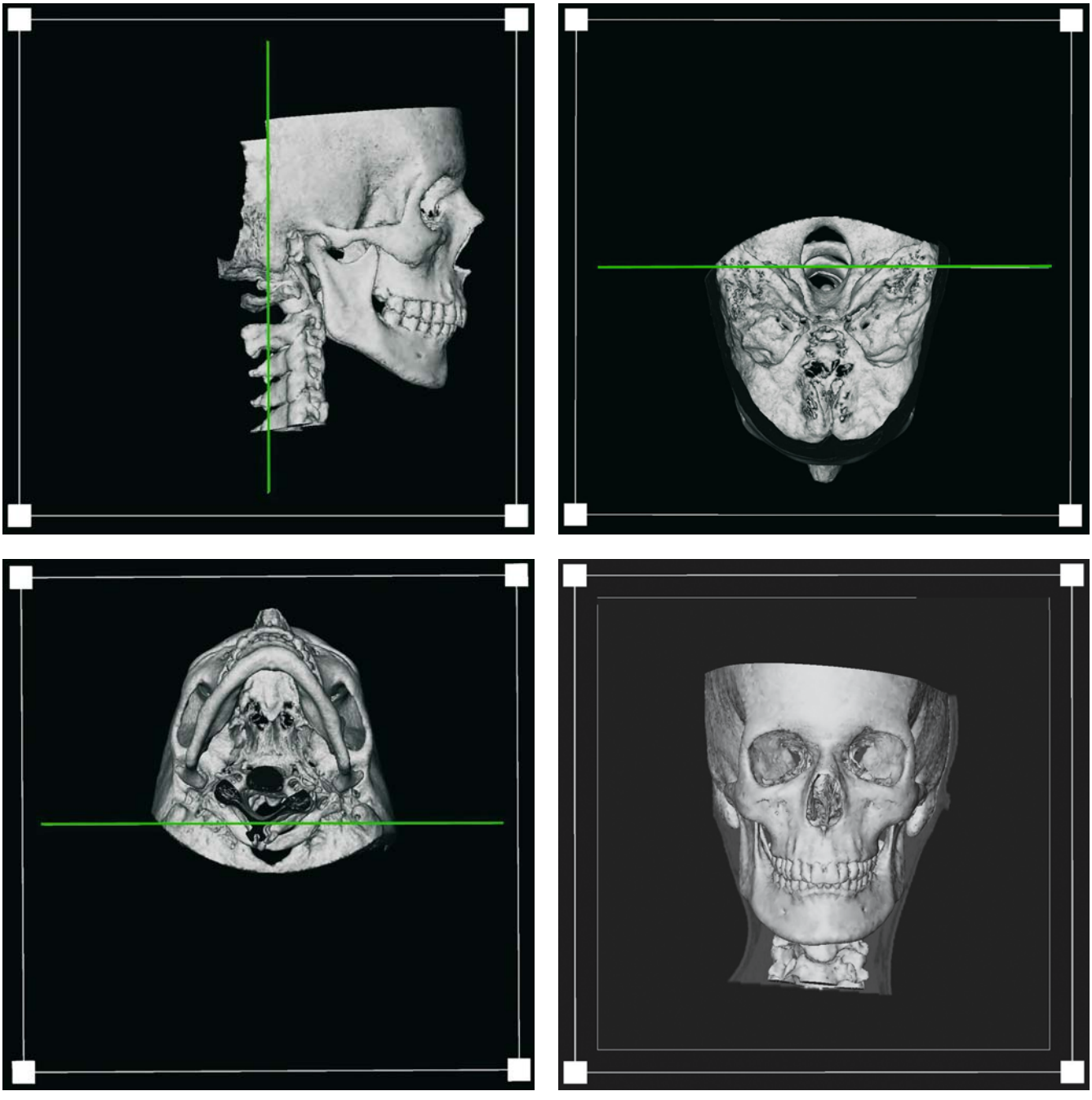

Fig. 2.37. **a** 3-D hard-tissue surface representations show the position of coronal reconstruction slice 9 (patient K.C.)

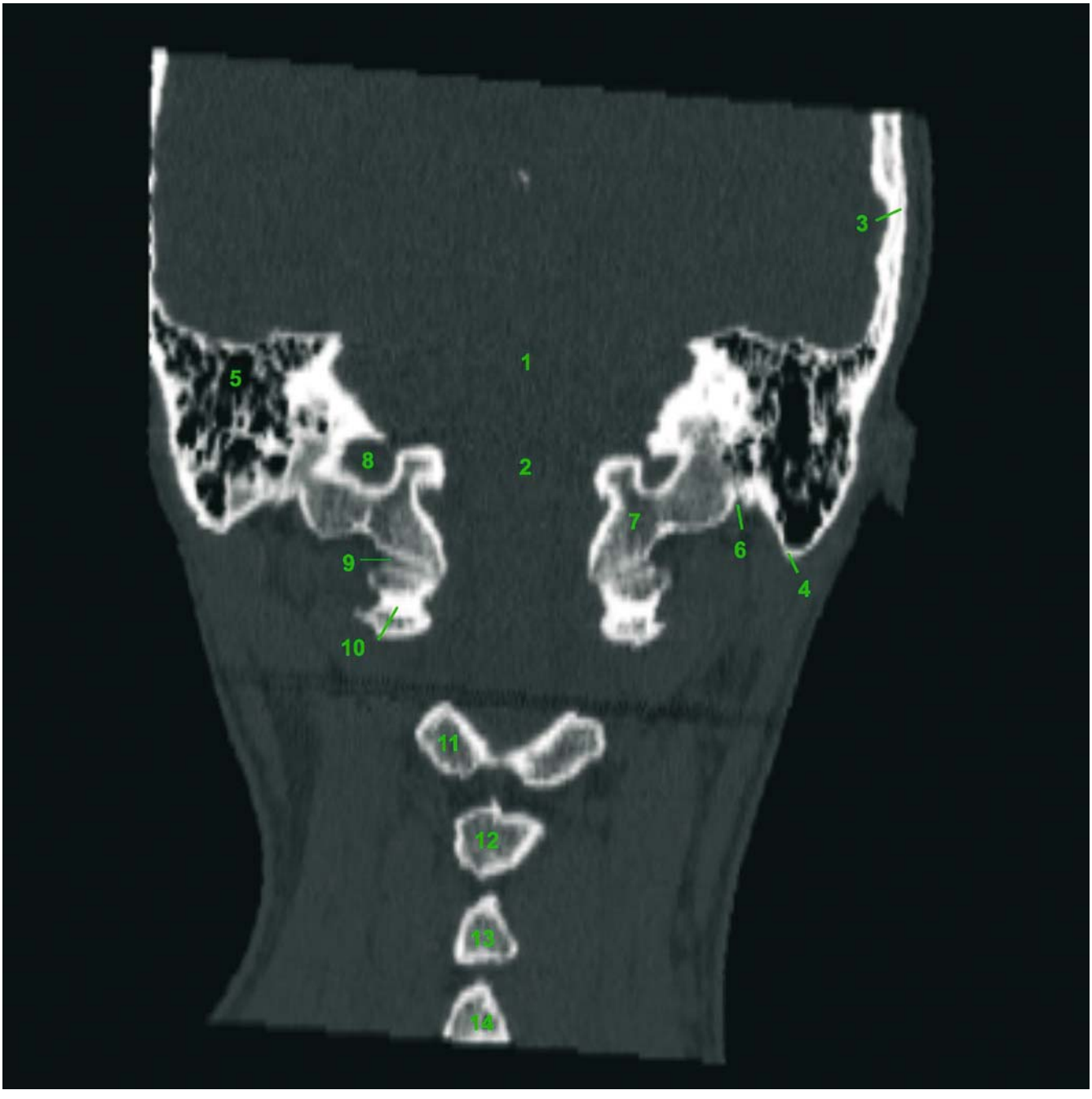

Fig. 2.37. b Coronal reconstruction slice 9 (patient K.C.). *1* Posterior cranial fossa; *2* Foramen magnum; *3* Parietal bone; *4* Mastoid process; *5* Mastoid air cells; *6* Petro-occipital fissure (synchondrosis); *7* Occipital bone; *8* Jugular foramen (foramen jugulare); *9* Atlanto-occipital articulation; *10* Transverse process of atlas; *11* 2nd cervical vertebra; *12* 3rd cervical vertebra; *13* 4th cervical vertebra; *14* 5th cervical vertebra

2.2.3 Virtual Sagittal Slice Reconstructions

Sagittal Reconstruction – Slice 1

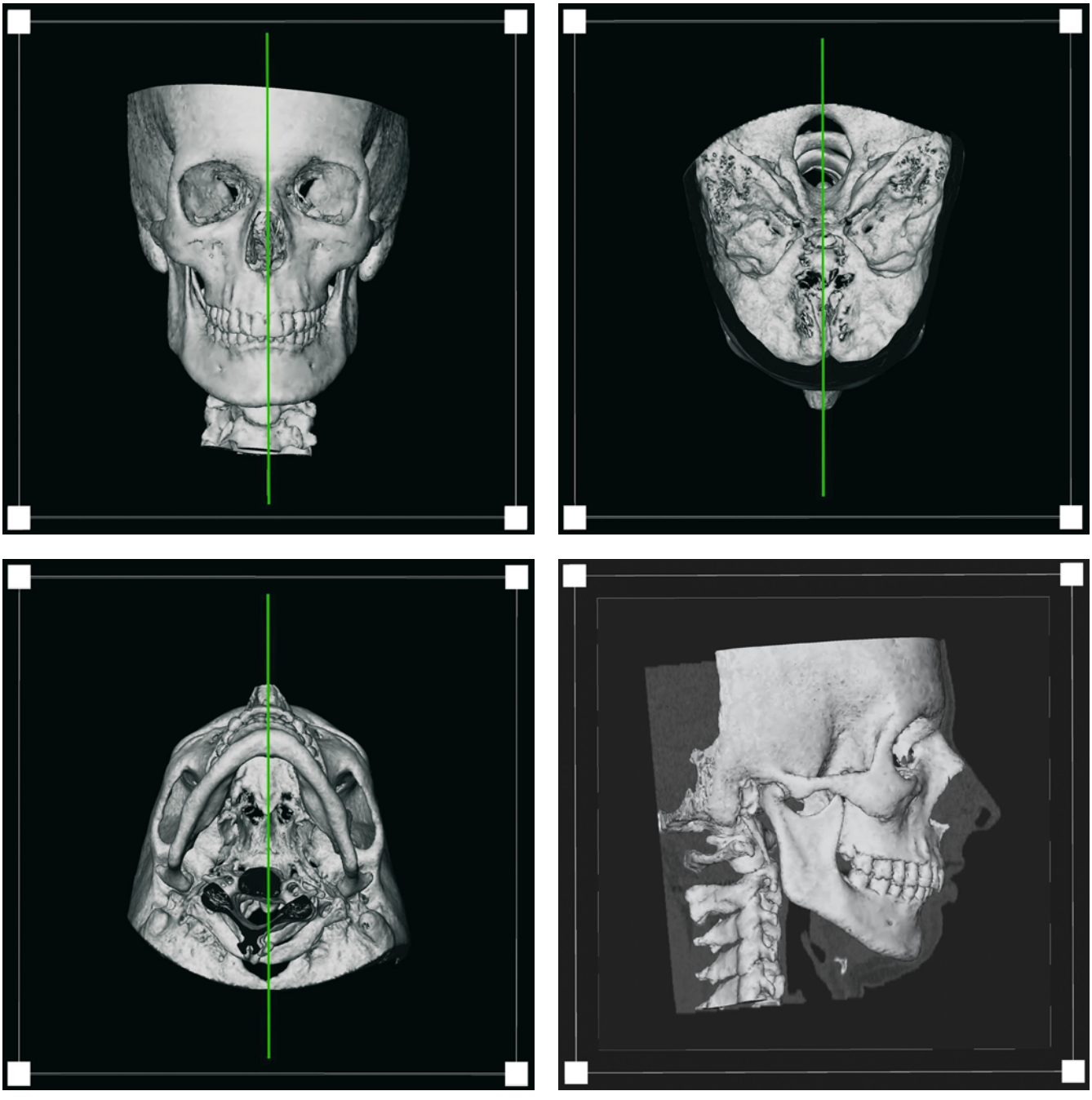

Fig. 2.38. **a** 3-D hard-tissue surface representations show the position of sagittal reconstruction slice *1* (patient K.C.)

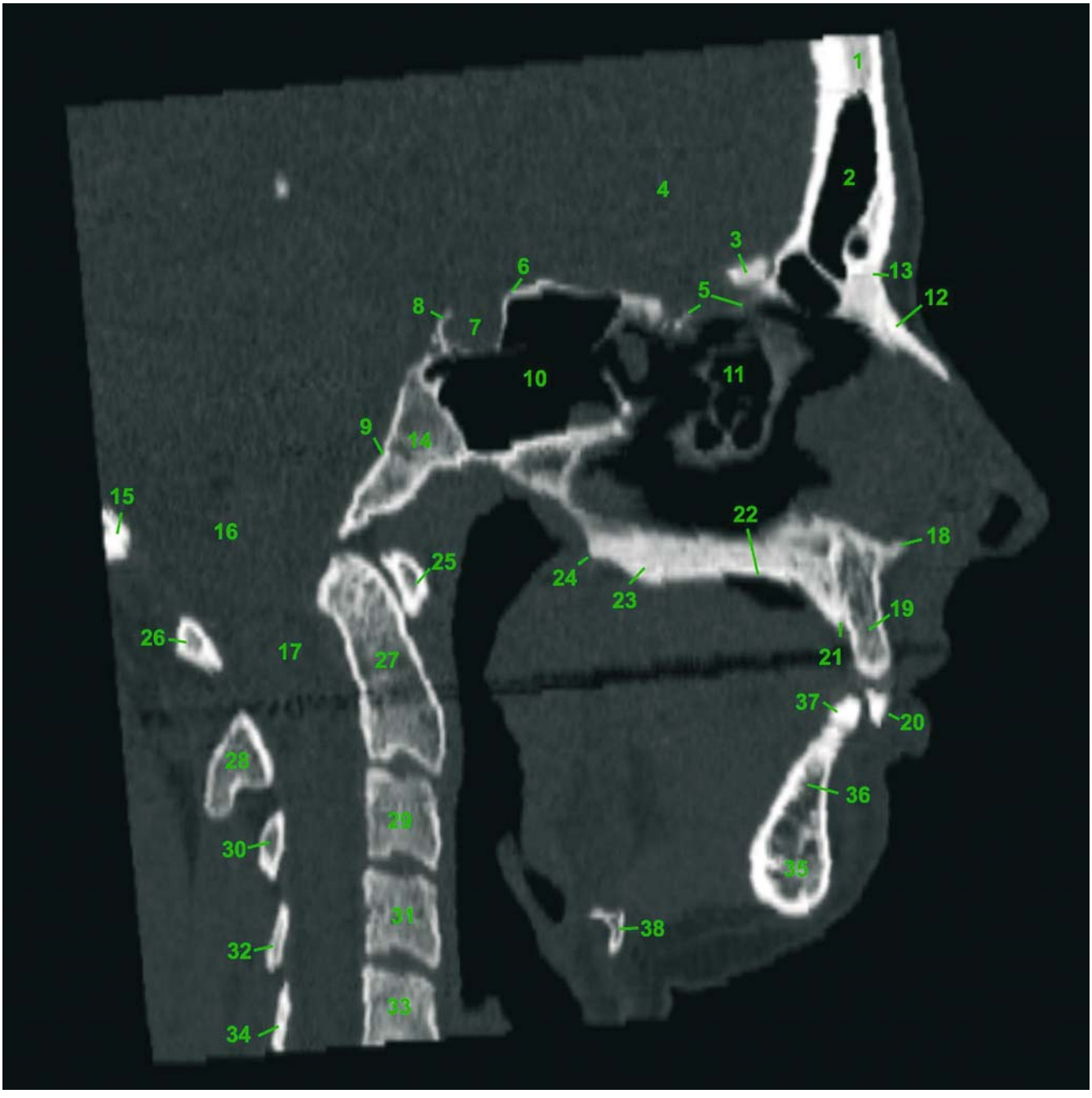

Fig. 2.38. **b** Sagittal reconstruction slice *1* (patient K.C.). *1* Frontal bone; *2* Frontal sinus; *3* Crista galli; *4* Anterior cranial fossa; *5* Cribriform plate of ethmoid bone (lamina cribrosa); *6* Tuberculum sellae; *7* Hypophyseal fossa (sella turcica); *8* Dorsum sellae; *9* Clivus; *10* Sphenoidal sinus; *11* Ethmoidal air cells; *12* Nasal bone; *13* Frontonasal suture; *14* Sphenoid bone; *15* Occipital bone; *16* Great foramen (foramen magnum); *17* Vertebral canal; *18* Anterior nasal spine; *19* Alveolar process of maxilla; *20* Upper central incisor; *21* Incisive canal; *22* Palatine process of maxilla; *23* Palatine bone; *24* Posterior nasal spine; *25* Anterior arch of atlas; *26* Posterior arch of atlas; *27* Dens axis; *28* Spinous process of axis; *29* 3rd cervical vertebra; *30* Spinous process of 3rd cervical vertebra; *31* 4th cervical vertebra; *32* Spinous process of 4th cervical vertebra; *33* 5th cervical vertebra; *34* Spinous process of 5th cervical vertebra; *35* Symphysis of mandible; *36* Alveolar process of mandible; *37* Lower central incisor; *38* Hyoid bone

Sagittal Reconstruction – Slice 2

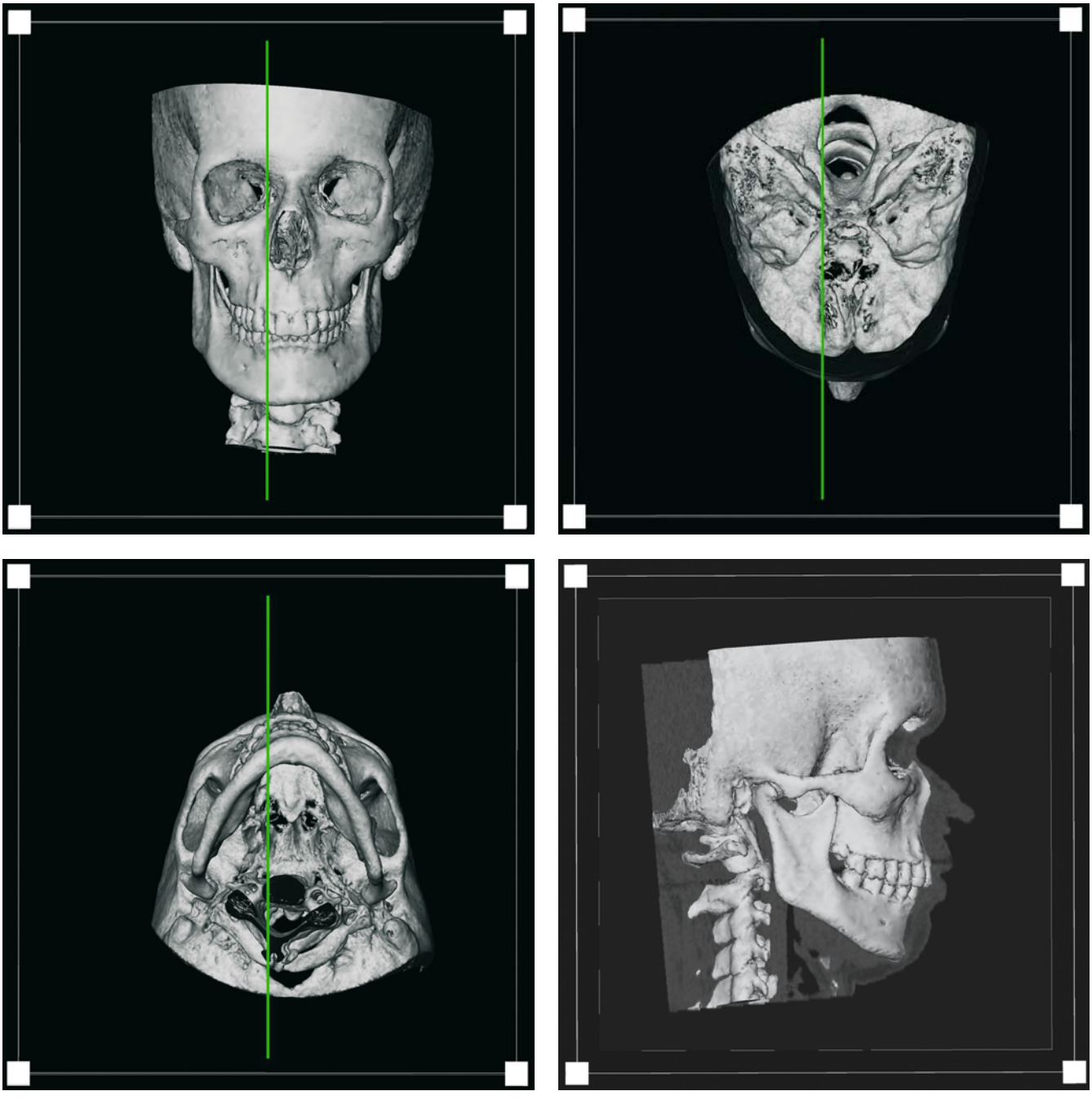

Fig. 2.39. **a** 3-D hard-tissue surface representations show the position of sagittal reconstruction slice 2 (patient K.C.)

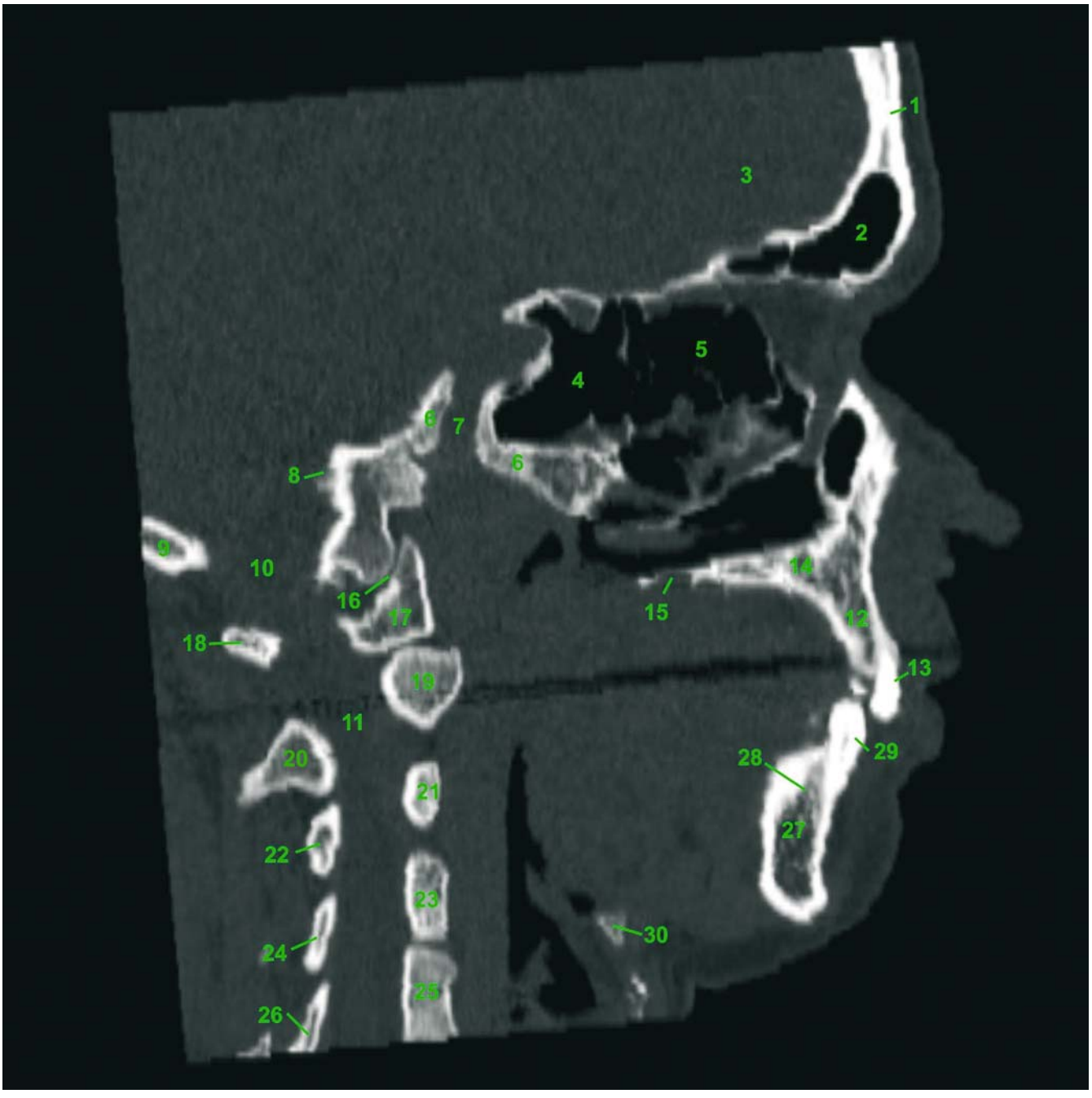

Fig. 2.39. b Sagittal reconstruction slice 2 (patient K.C.). *1* Frontal bone; *2* Frontal sinus; *3* Anterior cranial fossa; *4* Ethmoidal air cells; *5* Sphenoidal sinus; *6* Sphenoid bone; *7* Carotid canal; *8* Hypoglossal nerve canal; *9* Occipital bone; *10* Great foramen (foramen magnum); *11* Vertebral canal; *12* Alveolar process of maxilla; *13* Upper lateral incisor; *14* Palatine process of maxilla; *15* Posterior palatine artery canal; *16* Atlanto-occipital articulation; *17* Anterior arch of atlas; *18* Posterior arch of atlas; *19* 2nd cervical vertebra; *20* Spinous process of axis; *21* 3rd cervical vertebra; *22* Spinous process of 3rd cervical vertebra; *23* 4th cervical vertebra; *24* Spinous process of 4th cervical vertebra; *25* 5th cervical vertebra; *26* Spinous process of 5th cervical vertebra; *27* Body of mandible; *28* Alveolar process of mandible; *29* Lower canine; *30* Hyoid bone

Sagittal Reconstruction – Slice 3

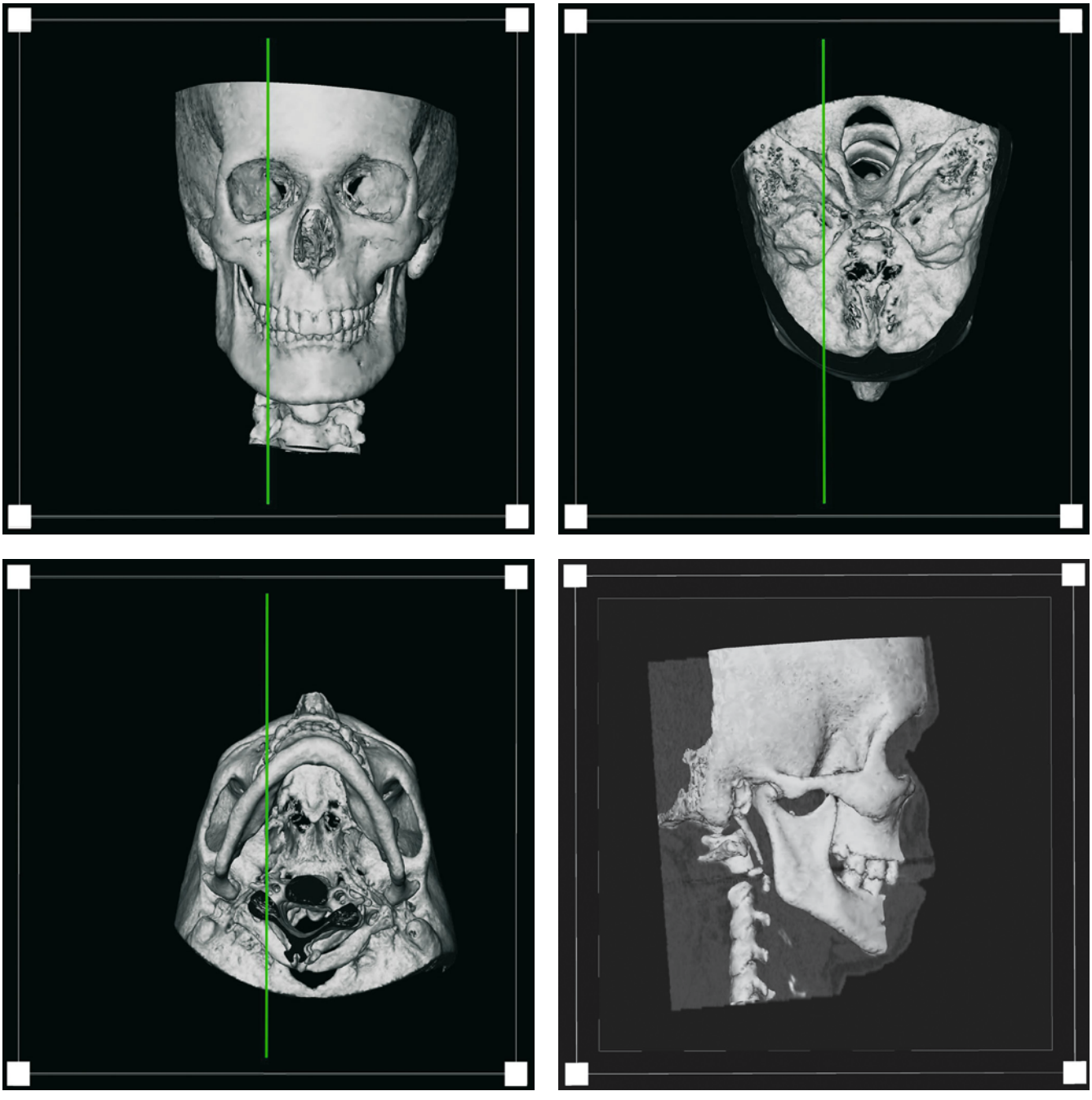

Fig. 2.40. **a** 3-D hard-tissue surface representations show the position of sagittal reconstruction slice 3 (patient K.C.)

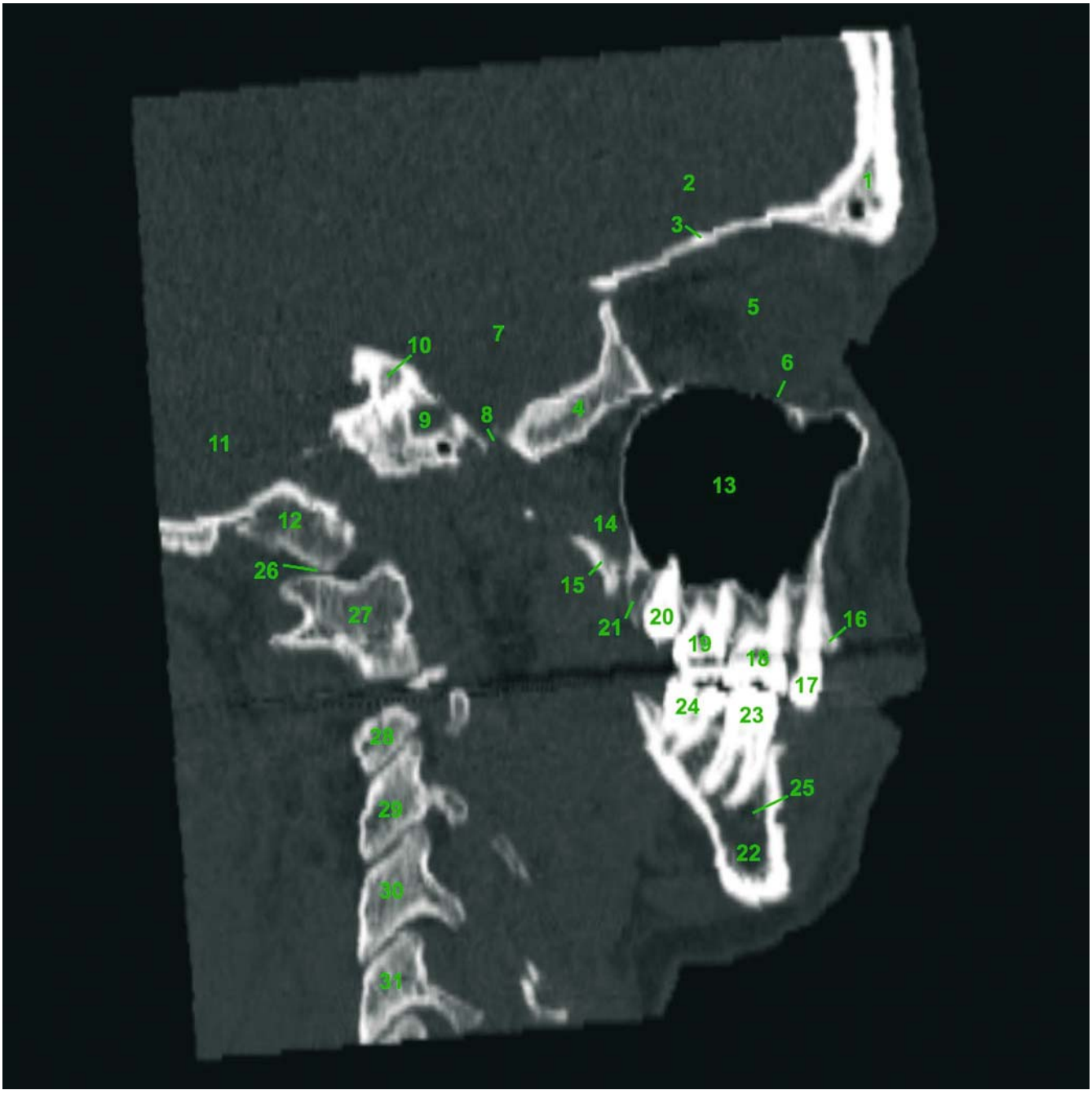

Fig. 2.40. **b** Sagittal reconstruction slice 3 (patient K.C.). *1* Frontal bone; *2* Anterior cranial fossa; *3* Orbital roof; *4* Sphenoid bone; *5* Orbit; *6* Orbital floor; *7* Medial cranial fossa; *8* Oval foramen (foramen ovale); *9* Carotid canal; *10* Internal acoustic meatus; *11* Posterior cranial fossa; *12* Occipital bone; *13* Maxillary sinus; *14* Pterygopalatine fossa; *15* Lateral lamina of pterygoid process; *16* Alveolar process of maxilla; *17* Second upper premolar; *18* First upper molar; *19* Second upper molar; *20* Third molar; *21* Maxillary tuberosity; *22* Body of mandible; *23* First lower molar; *24* Second lower molar; *25* Mandibular canal; *26* Atlanto-occipital articulation; *27* Lateral mass of atlas; *28* 22nd cervical vertebra; *29* 3rd cervical vertebra; *30* 4th cervical vertebra; *31* 5th cervical vertebra

Sagittal Reconstruction – Slice 4

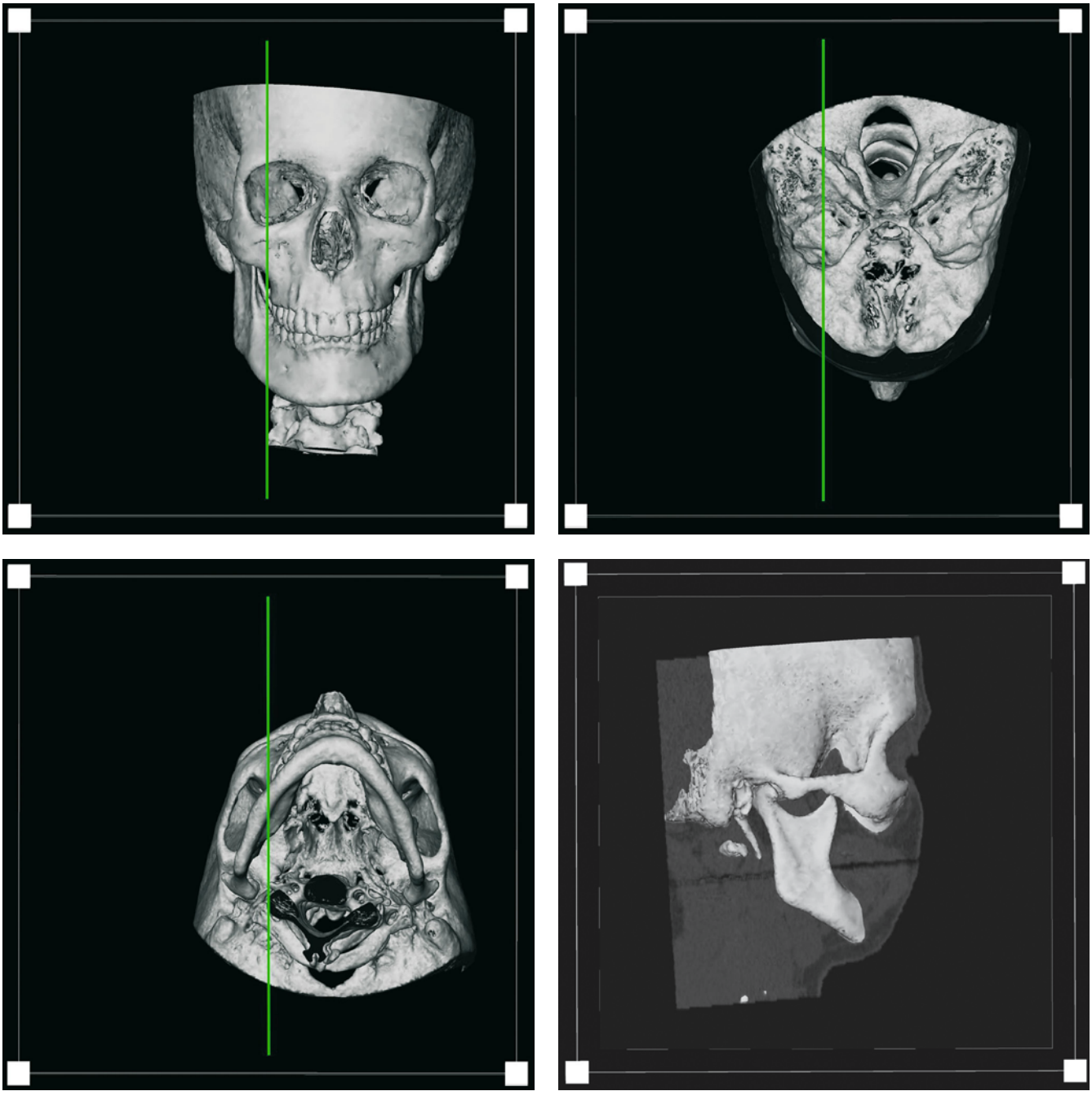

Fig. 2.41. **a** 3-D hard-tissue surface representations show the position of sagittal reconstruction slice 4 (patient K.C.)

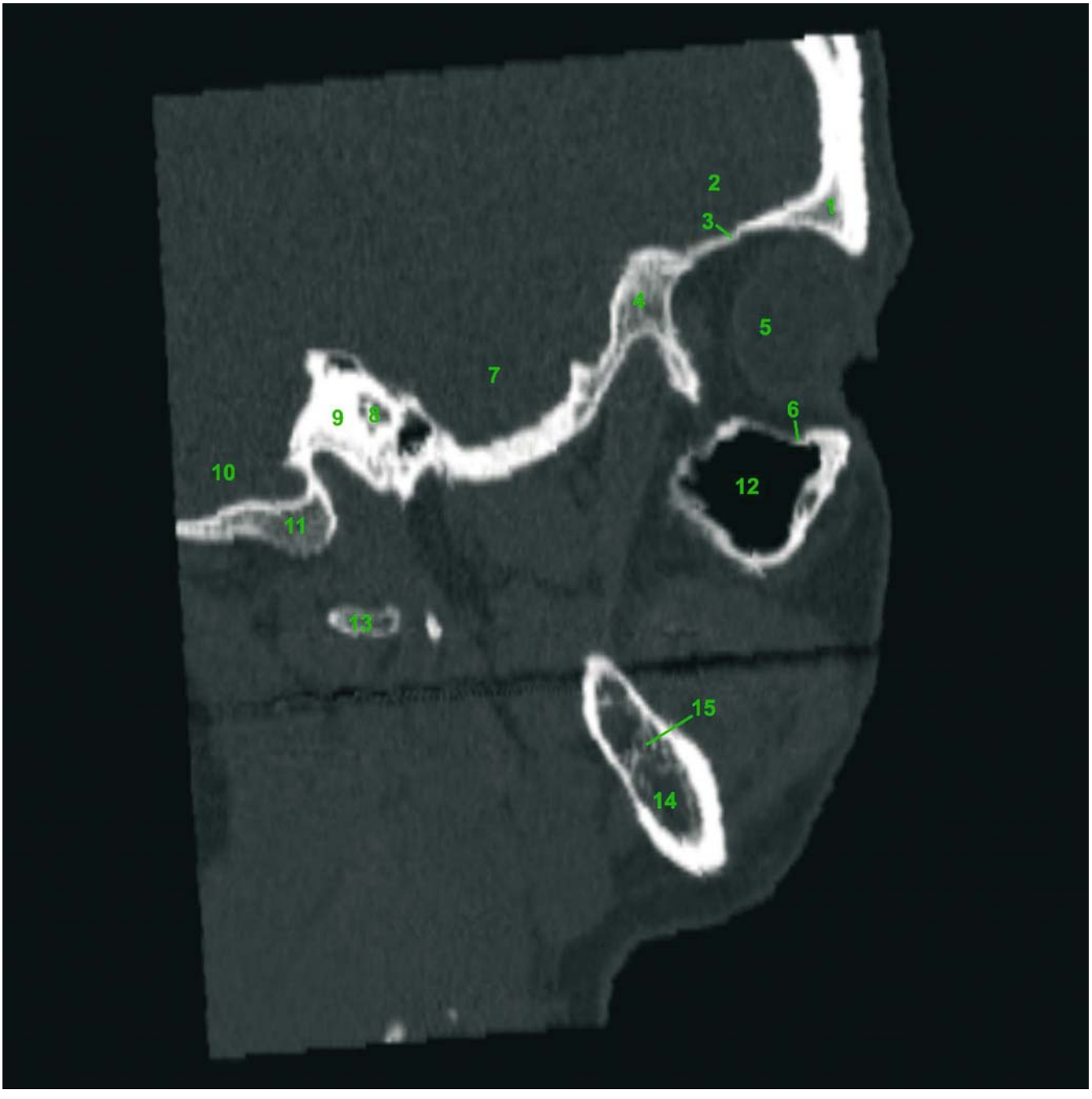

Fig. 2.41. **b** Sagittal reconstruction slice 4 (patient K.C.). *1* Frontal bone; *2* Anterior cranial fossa; *3* Orbital roof; *4* Sphenoid bone; *5* Orbit; *6* Orbital floor; *7* Medial cranial fossa; *8* Internal acoustic meatus; *9* Temporal bone; *10* Posterior cranial fossa; *11* Occipital bone; *12* Maxillary sinus; *13* Transverse process of atlas; *14* Body of mandible; *15* Mandibular canal

Sagittal Reconstruction – Slice 5

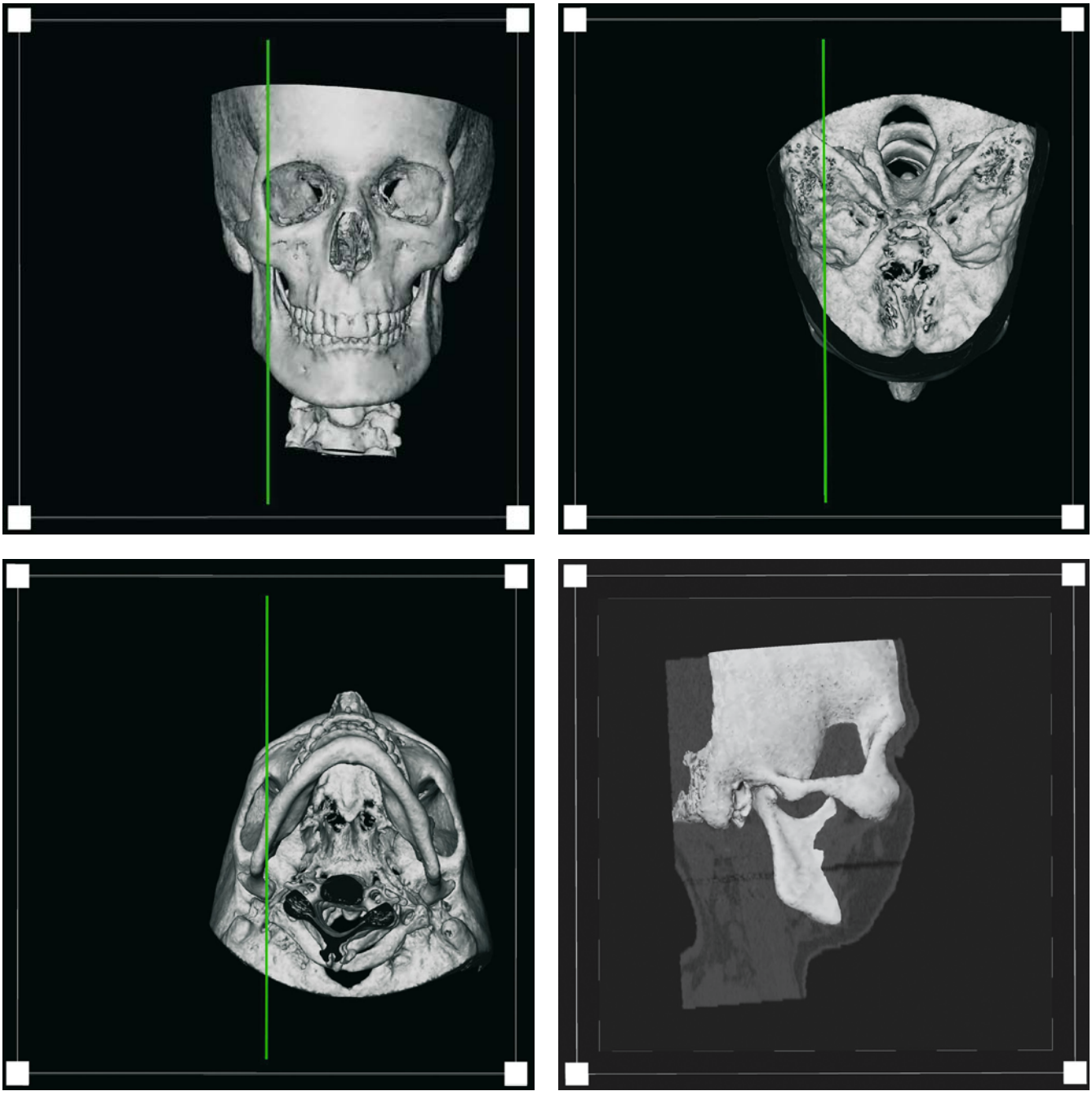

Fig. 2.42. **a** 3-D hard-tissue surface representations show the position of sagittal reconstruction slice 5 (patient K.C.)

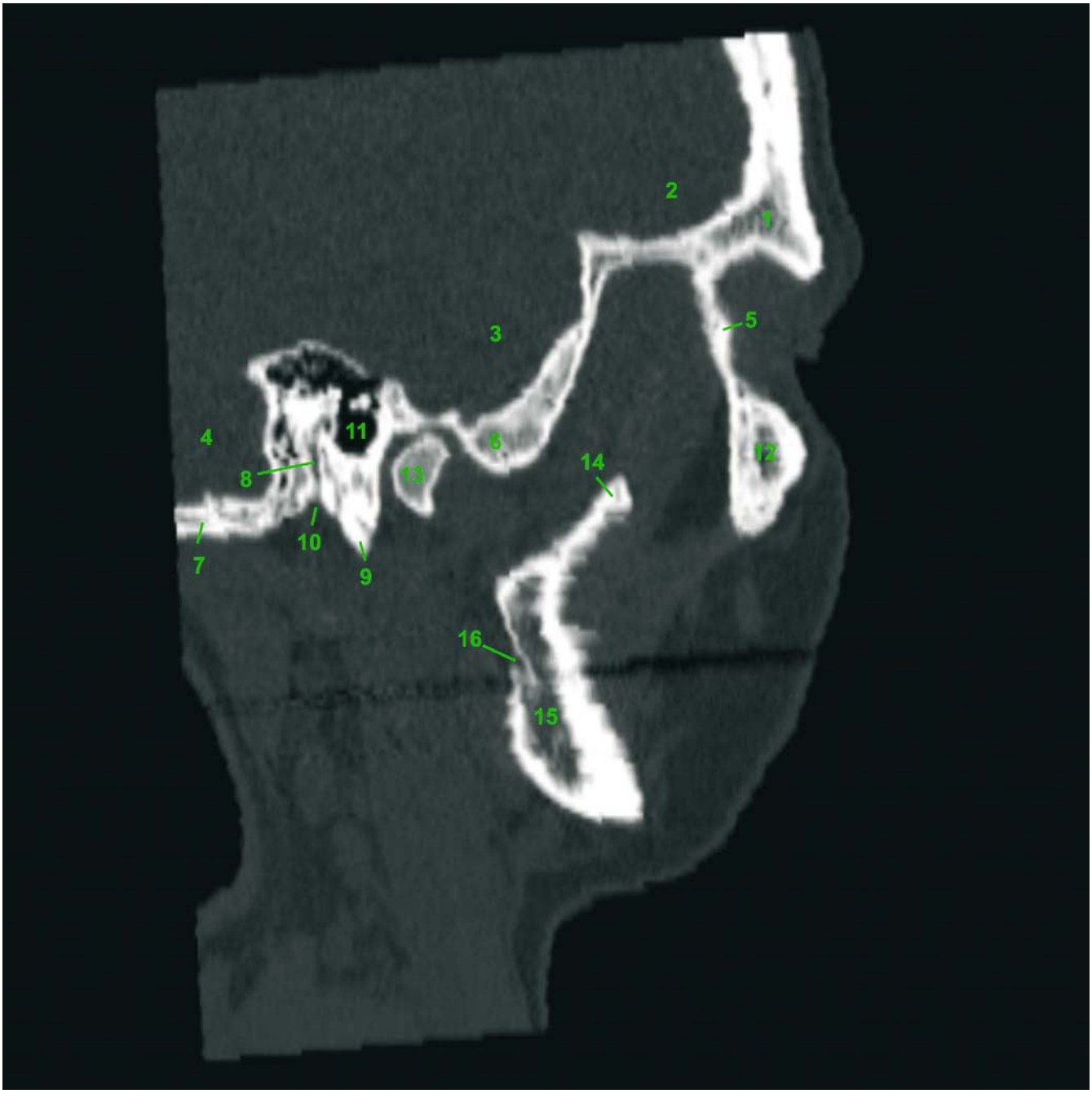

Fig. 2.42. **b** Sagittal reconstruction slice 5 (patient K.C.). *1* Frontal bone; *2* Anterior cranial fossa; *3* Medial cranial fossa; *4* Posterior cranial fossa; *5* Lateral orbital wall; *6* Temporal bone; *7* Occipital bone; *8* Facial canal; *9* Styloid process; *10* Stylomastoid foramen (foramen stylomastoideum); *11* Tympanic cavity; *12* Zygomatic bone; *13* Condyle of mandible; *14* Coronoid process of mandible; *15* Vertical ramus of mandible; *16* Mandibular canal

Sagittal Reconstruction – Slice 6

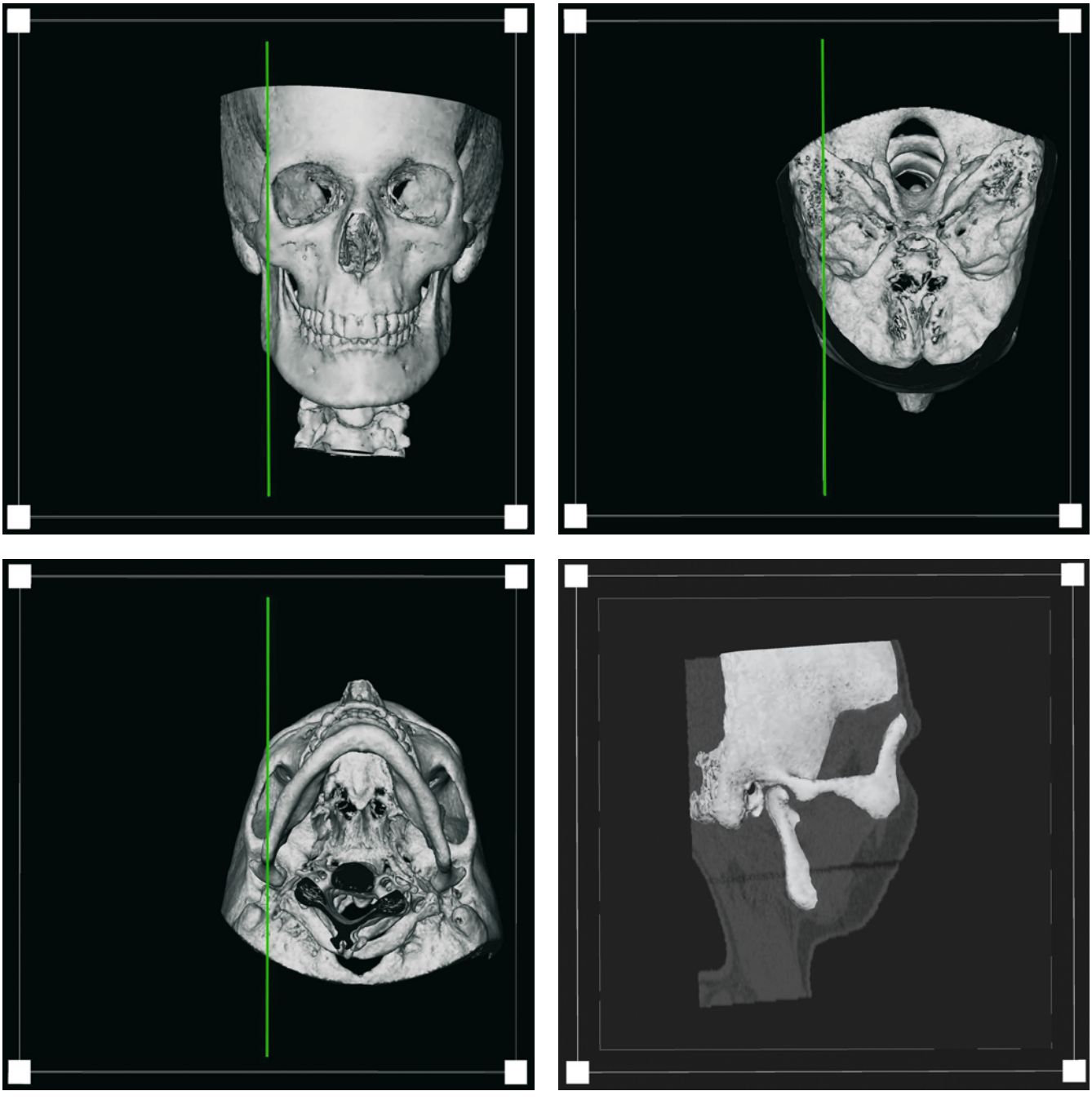

Fig. 2.43. **a** 3-D hard-tissue surface representations show the position of sagittal reconstruction slice 6 (patient K.C.)

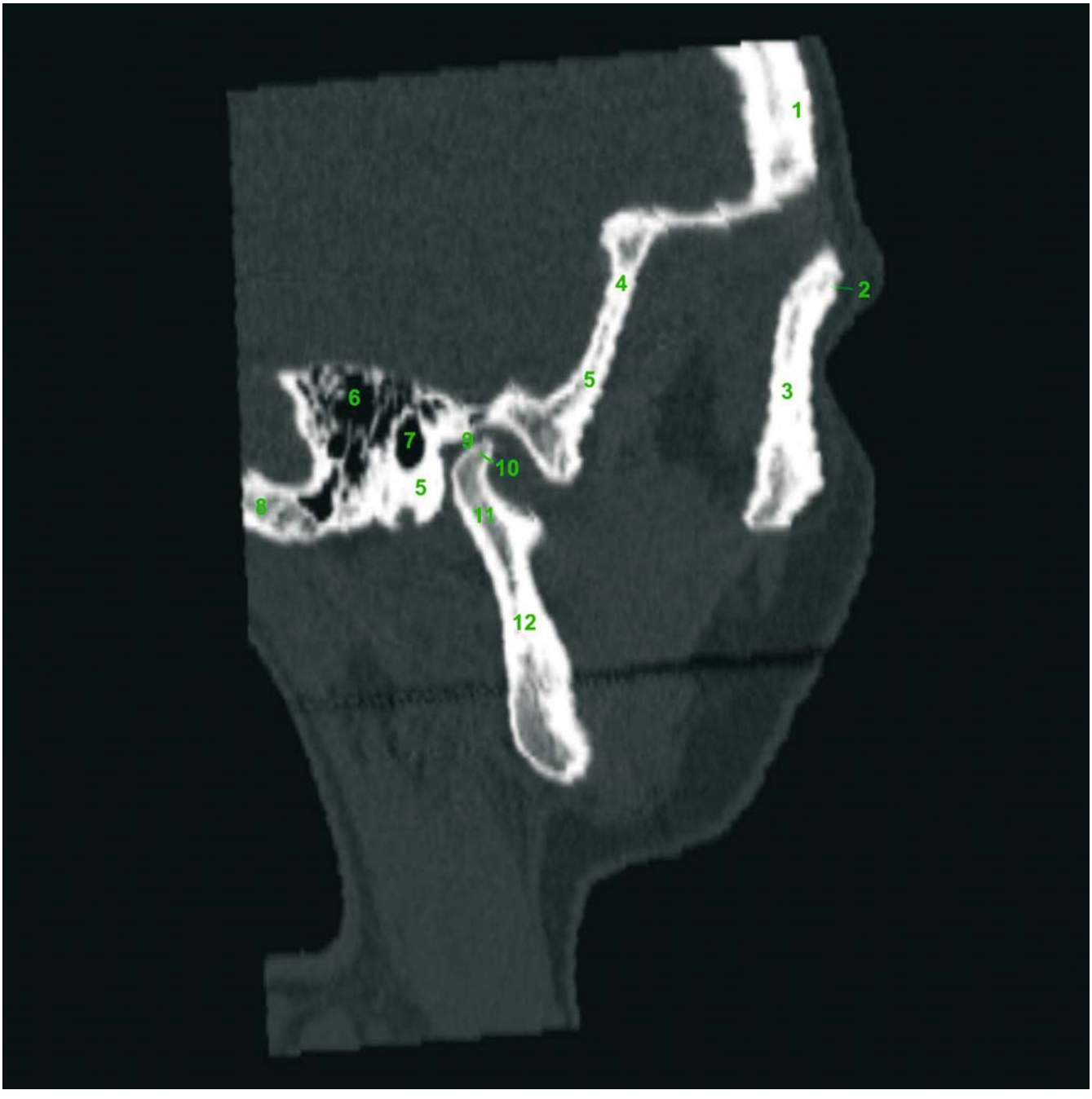

Fig. 2.43. b Sagittal reconstruction slice 6 (patient K.C.). *1* Frontal bone; *2* Frontozygomatic suture; *3* Zygomatic bone; *4* Sphenoid bone; *5* Temporal bone; *6* Mastoid air cells; *7* External acoustic meatus; *8* Occipital bone; *9* Mandibular fossa; *10* Condyle of mandible; *11* Condylar process of mandible; *12* Vertical ramus of mandible

2.3 Virtual X-Rays of the Skull

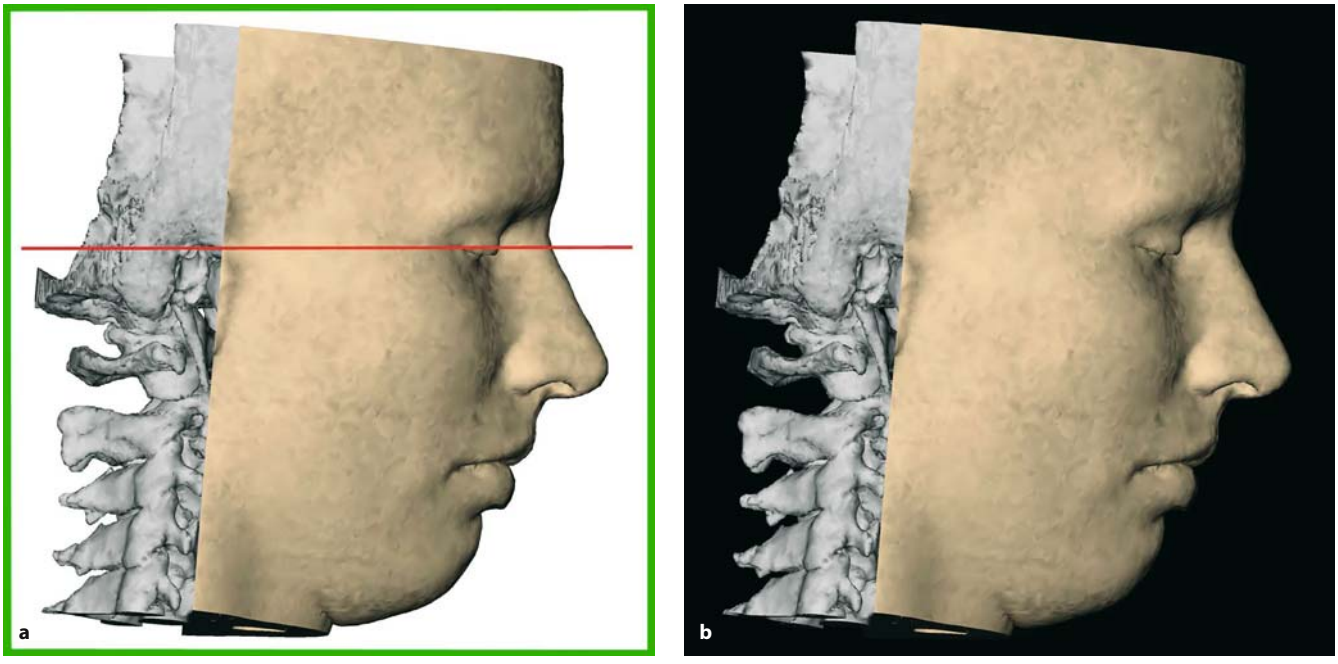

Fig. 2.44 a,b. Lateral view (patient K.C.). In order to compute the virtual lateral X-ray, the skull is virtually positioned in the right profile view with the cantho-meatal or trago-canthal line (the line that extends from the external acoustic meatus or tragus to the lateral junction of the eyelids) parallel to the horizontal plane

Fig. 2.45. Virtual X-ray film of the skull, lateral view (patient K.C.)

Virtual X-Ray – Frontal View

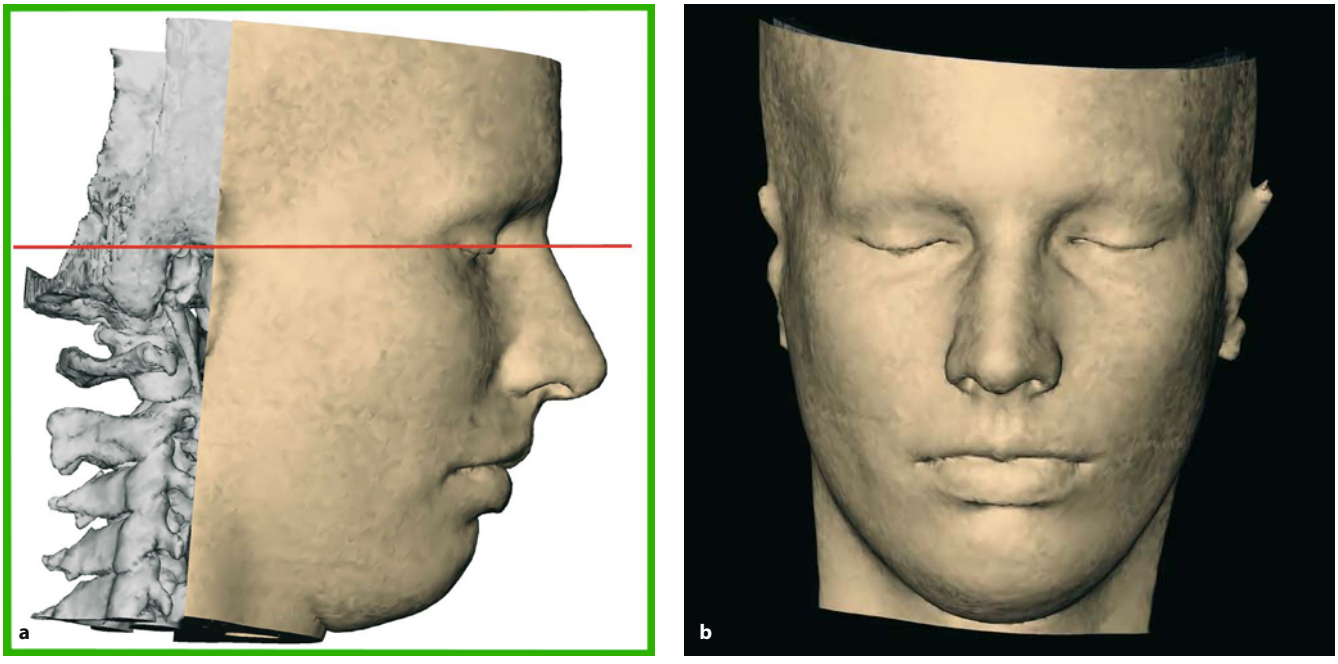

Fig. 2.46 a,b. Frontal view (patient K.C.). In order to compute the virtual frontal X-ray, the skull is virtually positioned in the frontal view with the cantho-meatal or trago-canthal line parallel to the horizontal plane

Fig. 2.47. Virtual X-ray film of the skull, frontal view (patient K.C.)

Virtual X-Ray – Modified Waters View

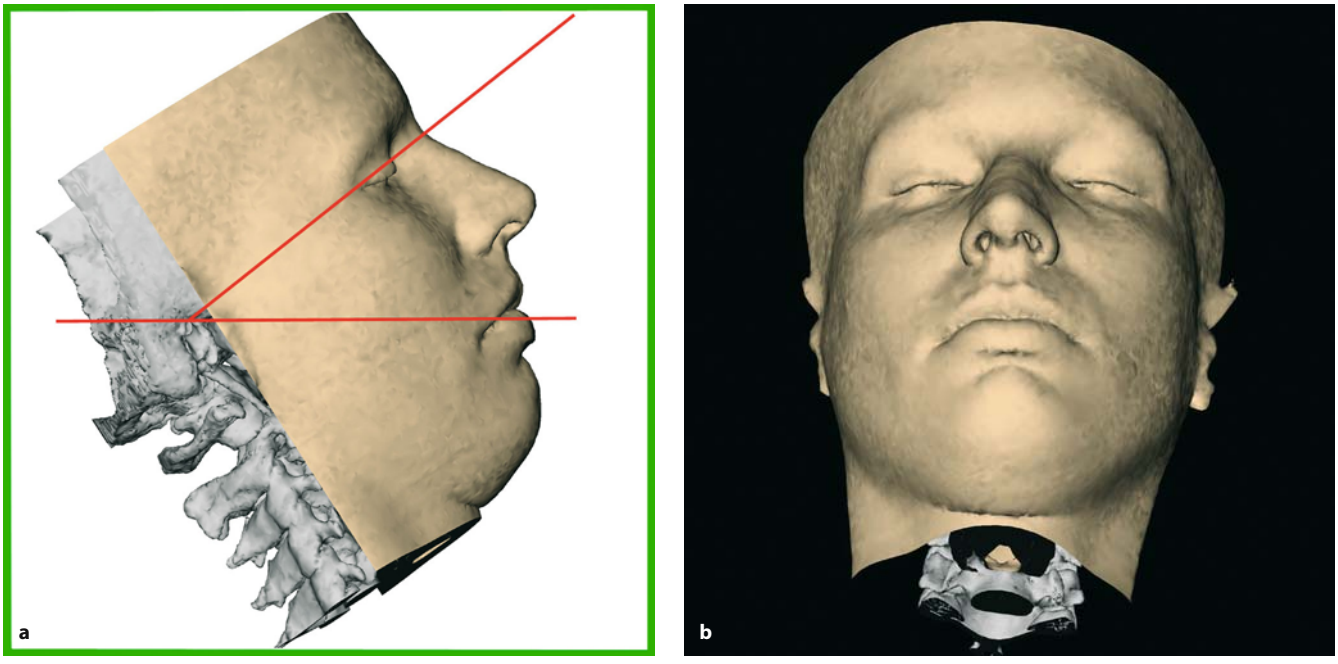

Fig. 2.48 a,b. Modified Waters view (patient K.C.). In order to compute the virtual modified Waters X-ray, the skull is virtually positioned in the frontal view and posteriorly inclined until the cantho-meatal or trago-canthal line is 37° to the horizontal plane

Fig. 2.49. Virtual X-ray film of the skull, modified Waters view (patient K.C.)

Virtual X-Ray – Modified Caldwell View

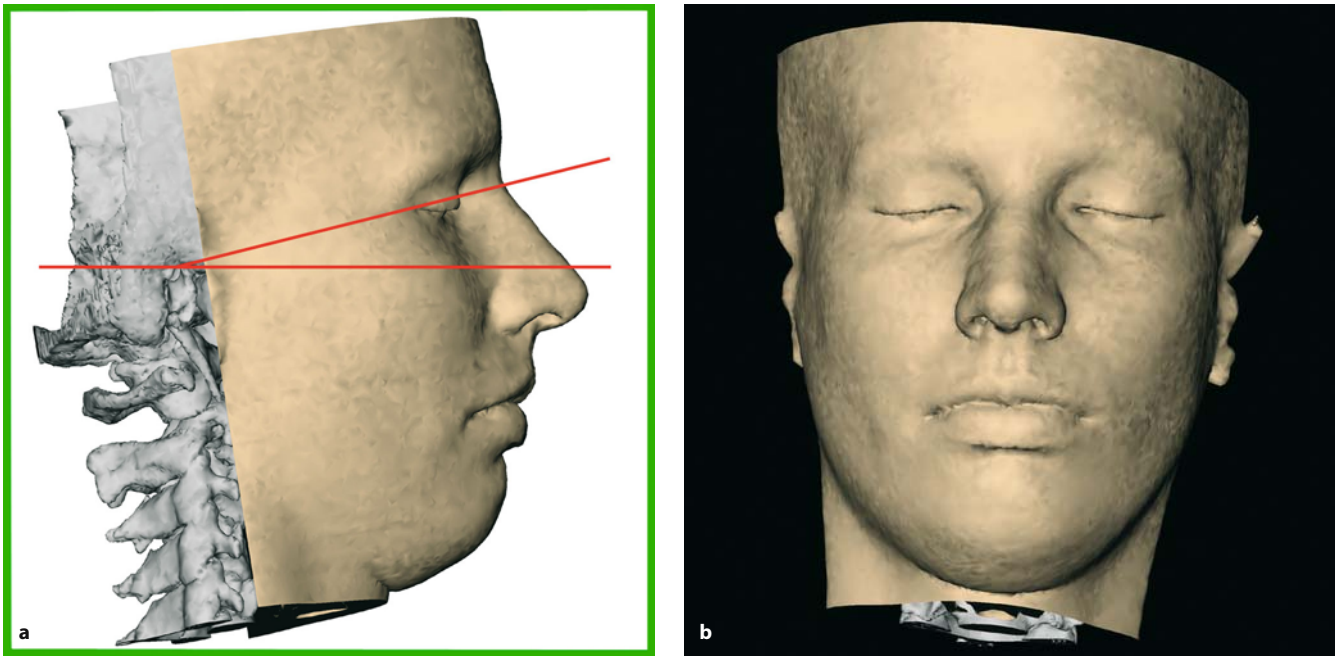

Fig. 2.50 a,b. Modified Caldwell view (patient K.C.). In order to compute the virtual modified Caldwell X-ray, the skull is virtually positioned in the frontal view and posteriorly inclined until the cantho-meatal or trago-canthal line is approximately 23° (15° for children) to the horizontal plane

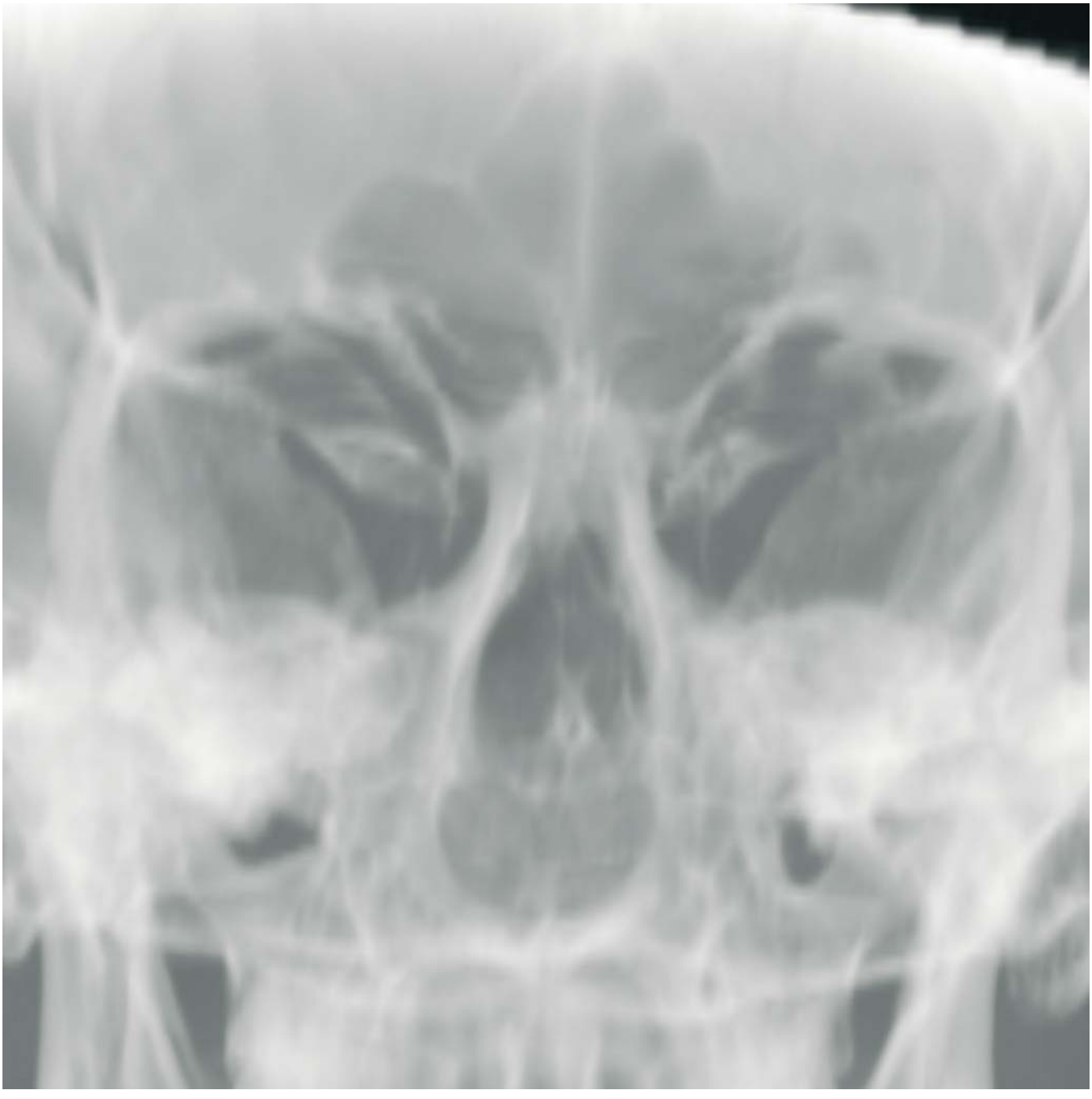

Fig. 2.51. Virtual X-ray film of the skull, modified Caldwell view (patient K.C.)

Virtual X-Ray – Base View

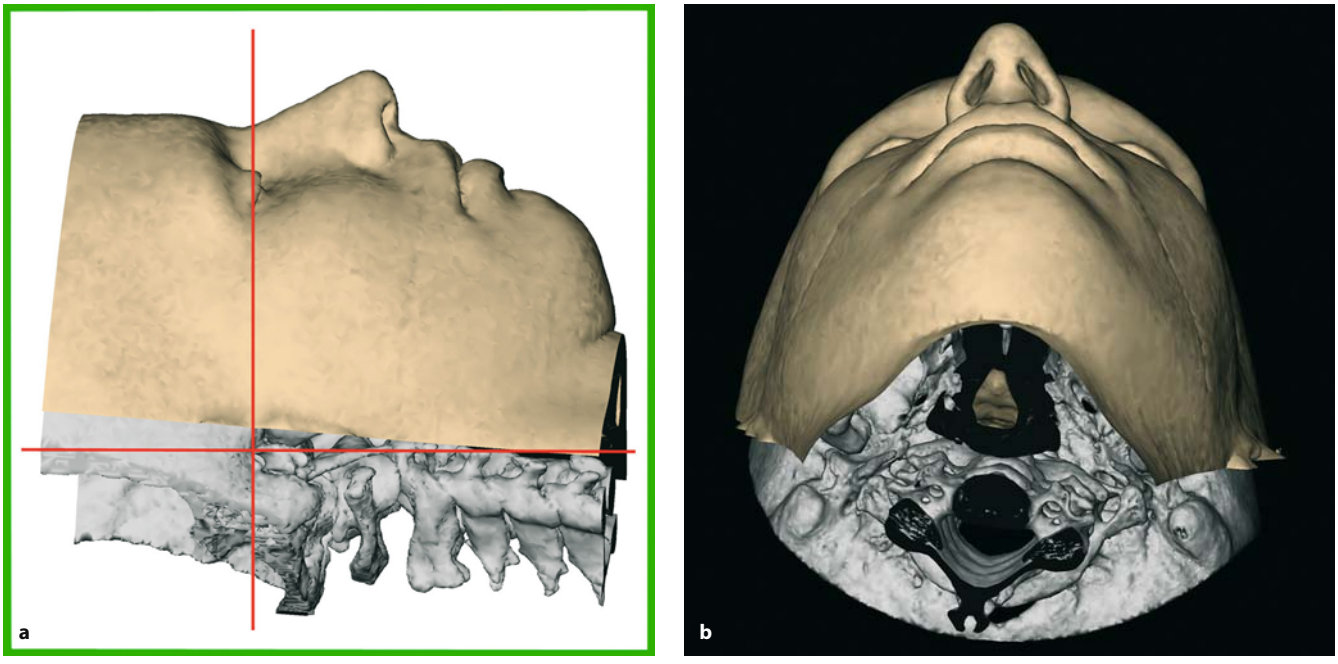

Fig. 2.52 a,b. Base view (patient K.C.). In order to compute the virtual base view X-ray, the skull is virtually positioned in the frontal view and posteriorly inclined until the cantho-meatal or trago-canthal line is perpendicular to the vertical plane

Fig. 2.53. Virtual X-ray film of the skull, base view (patient K.C.)

Virtual Lateral Cephalogram

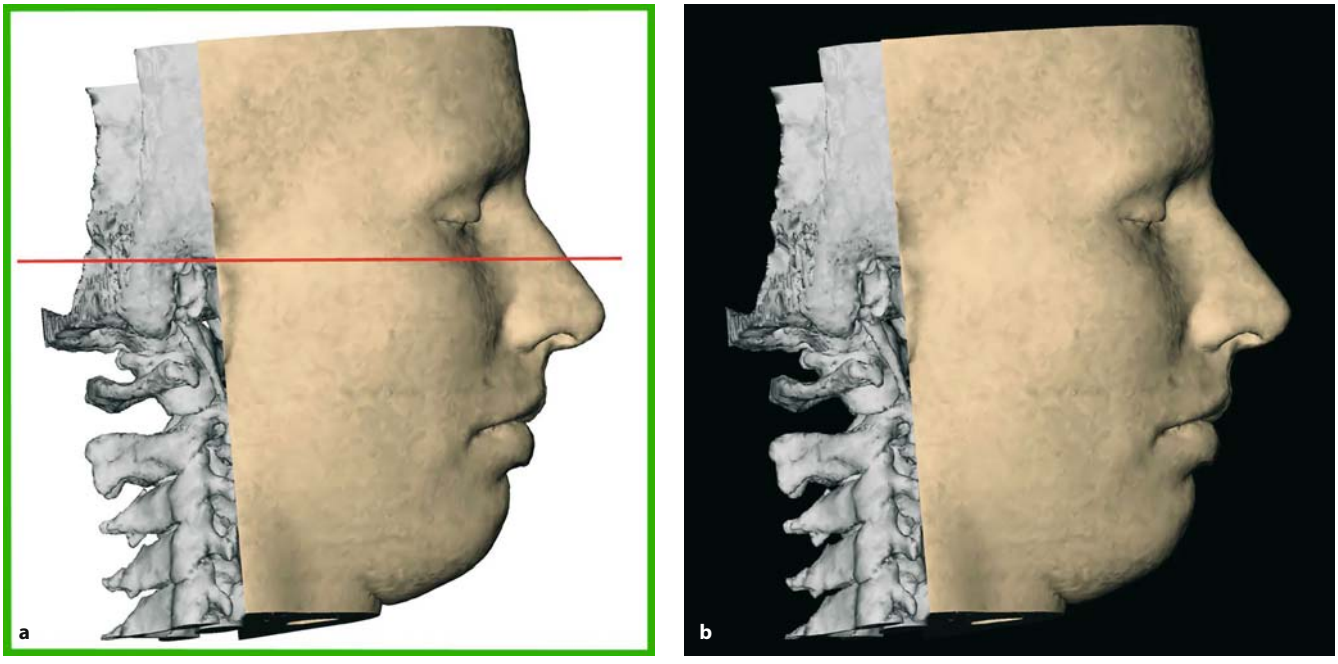

Fig. 2.54 a,b. Virtual lateral cephalogram (patient K.C.). In order to compute the virtual lateral cephalogram, the skull is virtually positioned in the right profile view with Frankfort horizontal (FH) parallel to the horizontal plane

Fig. 2.55. Virtual lateral cephalogram (patient K.C.)

Virtual Frontal Cephalogram

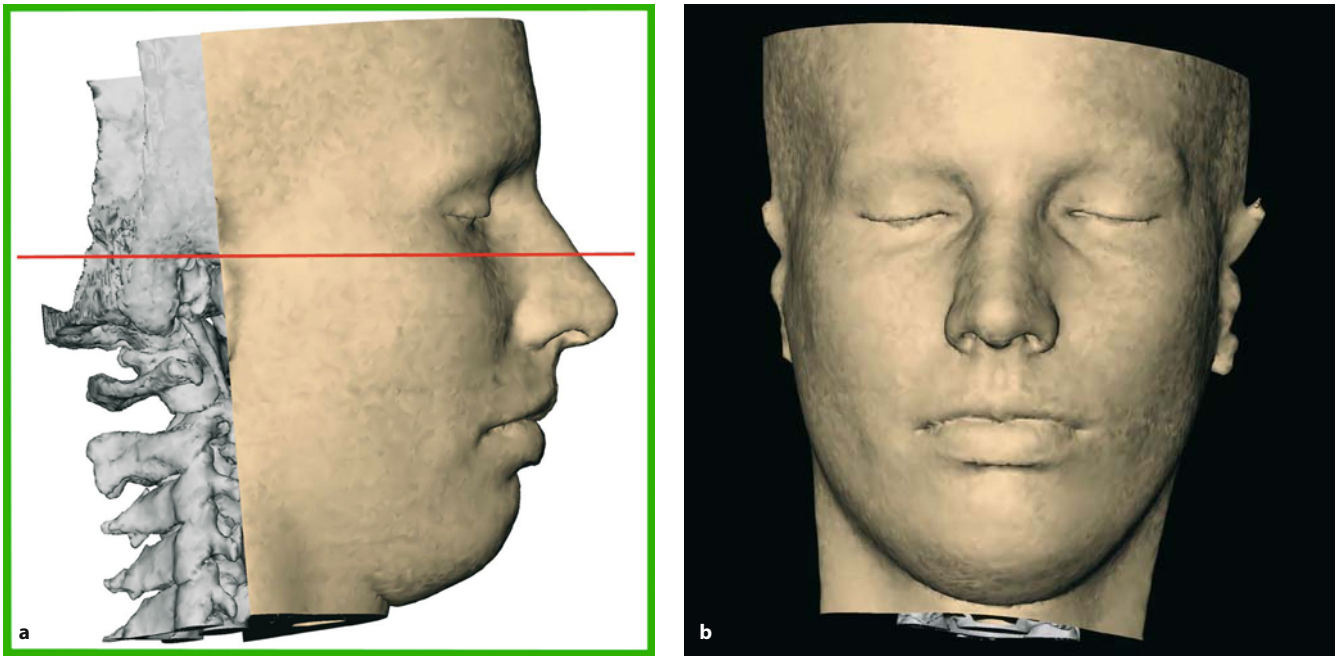

Fig. 2.56 a,b. Virtual frontal cephalogram (patient K.C.). In order to compute the virtual frontal cephalogram, the skull is virtually positioned in the frontal view with Frankfort horizontal (FH) parallel to the horizontal plane

Fig. 2.57. Virtual frontal cephalogram (patient K.C.)

CHAPTER 3 3-D Cephalometric Reference System

Gwen R.J. Swennen

Assessment of craniofacial morphology is inherently influenced by the experience and subjective perception of the examiner. Hence, standardized positioning of the patient and standardized measurement acquisition systems are crucial for objective assessment. Standardized methods for the production of cephalometric radiographs were introduced and developed by Broadbent and Hofrath in 1931. In cephalometric radiography special holders known as cephalostats (Chap. 1, Fig. 1.11), are used to keep the patient's head in a standardized position to the Frankfort horizontal (FH). Cross-sectional and longitudinal multicentre studies on craniofacial morphology, however, often have to deal with different enlargement factors used in cephalometric radiography. To minimize analysis bias, scaling procedures (e.g. to the anterior cranial base) are frequently used or linear measurements are excluded and only angular and proportional measurements are employed.

Spiral CT-based 3-D cephalometry using standardized CT scanning protocols (Chap. 1) has the great advantage that all measurements are real size (1:1) which allows both cross-sectional and longitudinal comparison of 3-D distances, linear projective and orthogonal measurements. Contrary to cephalometric radiography, spiral CT-based 3-D cephalometry does not necessitate standardized fixation of the skull during record taking, because the 3-D virtual scene approach allows standardized virtual positioning of the skull to the FH.

Once standardized data are available, an accurate 3-D coordinate system is required that can be reliably transferred to allow cross-sectional and longitudinal comparison of craniofacial morphology and pre-operative status, virtual planning and post-operative surgical treatment outcome. In conventional radiographic cephalometry, different anatomic reference systems have been proposed. The best-known of these are based on the FH or the anterior cranial base (S-N). Proffit and co-workers advocate a reference system with the horizontal plane six degrees below the Sella–Nasion (S-N) line.

This chapter describes, step by step, the set-up of a Cartesian anatomical 3-D cephalometric reference system. The 3-D virtual scene approach allows standardized virtual positioning of the patient, generation of virtual cephalograms, easy and accurate location of the Sella and Nasion landmarks, subsequently automatic definition of a horizontal plane according to Proffit and co-workers and finally the set-up of the 3-D cephalometric reference system. The presented 3-D cephalometric system can be used as a registration system for evaluation of craniofacial growth and development (Chap. 8); however, it is important to take into account that the cranial base undergoes remodelling changes during childhood and that cranial base-related landmarks such as Sella and Nasion can change during growth.

The potential of the presented 3-D cephalometric reference system lies in the fact that both hard and soft tissue CT surface representations are linked to the same Cartesian anatomic coordinate system, which allows cross-sectional and longitudinal quantitative comparison of craniofacial morphology and growth patterns. Moreover, the 3-D cephalometric reference system presents an alternative and is complementary to rigid registration (point-, surface- or voxel-based) techniques to compare pre-operative status, virtual planning and post-operative outcome of voxel-based surgery. The orthogonal coordinate data of the 3-D cephalometric landmarks have been used for validation of the 3-D cephalometric reference system and have shown a high intra-observer and inter-observer accuracy and reliability (Chap. 7).

3.1 Standardized Virtual Positioning of the Skull

Once the 3-D CT hard and soft tissue representations of the patient's skull are rendered in the virtual scene, the skull has to be positioned virtually in a standardized manner.

Standardized Virtual Positioning of the Skull

Step 1: Position the skull oriented to the median plane using paired midfacial anatomic structures (e.g. the orbits, frontal process of the maxilla, frontozygomatic suture) in the frontal view of the 3-D hard tissue surface representation (Fig. 3.1).

Step 2: Position the skull parallel to the FH in the right profile view of the 3-D hard tissue surface representation (Fig. 3.2). The FH connects the most superior point of the external acoustic meatus (Porion) with the most inferior point of the infraorbital rim (Orbitale) (Chap. 4).

Step 3: Verify the position of the skull with regard to the FH in the left profile view of the 3-D hard tissue surface representation (Fig. 3.3). If a discrepancy between the right and left FH is present (Fig. 3.3), always orient the skull parallel to the right FH. In unilateral congenital malformations (e.g. Goldenhar syndrome, hemifacial microsomia) or acquired malformations (e.g. fracture of the infraorbital rim) the non-affected FH should be used to position the skull, while in bilateral malformations, an effort should be made to orient the skull parallel to the FH using other landmarks.

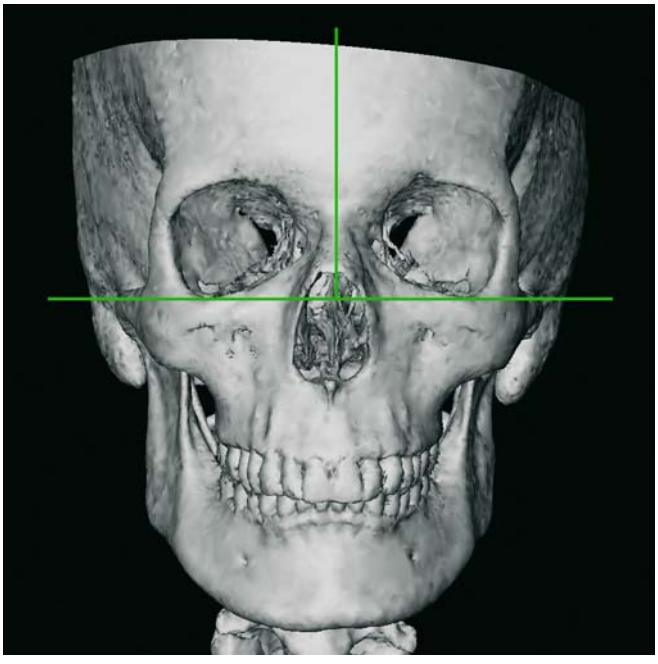

Fig. 3.1. Virtual positioning of the skull in the frontal view of the 3-D hard tissue surface representation (3-D CT, patient K.C.)

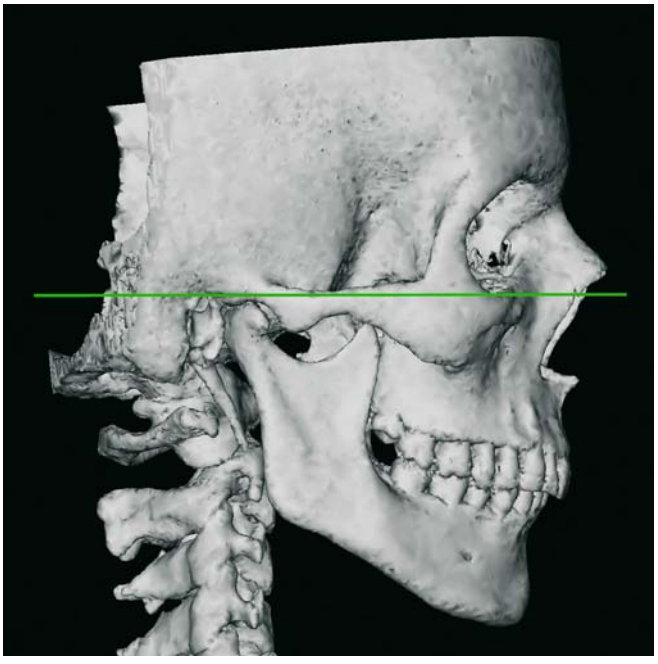

Fig. 3.2. Virtual positioning of the skull parallel to the right Frankfort horizontal (FH) (3-D CT, patient K.C.)

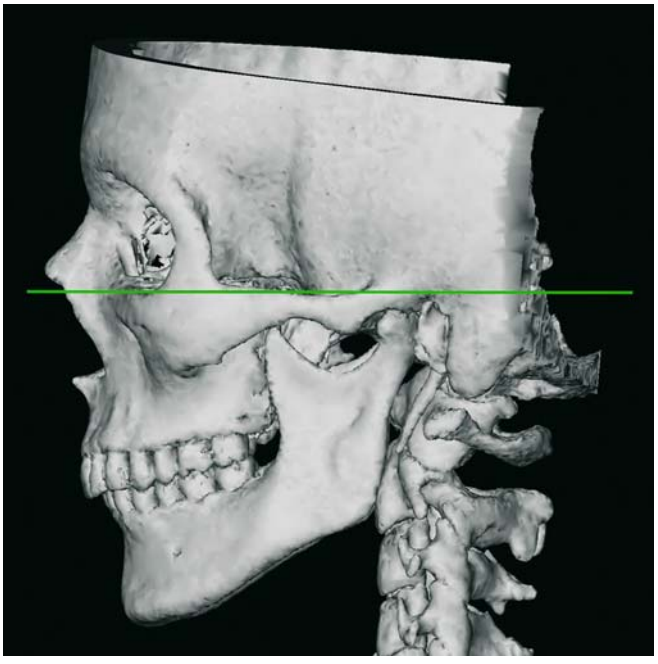

Fig. 3.3. The left profile view of the 3-D hard tissue surface representation illustrates a discrepancy between the right and the left FH, due to an uneven vertical level of the Porion 3-D cephalometric landmarks. The left Porion is more inferiorly localized than the right Porion. In case of uneven FHs, it is proposed to orient the skull on the right FH for standardization. (3-D CT, patient K.C.)

3.2 Computing of Virtual Lateral and Frontal Cephalograms

Once the patient's skull is virtually placed in the standardized position, virtual lateral (Fig. 3.4, Fig. 2.55) and frontal (Fig. 3.5, Fig. 2.57) cephalograms are generated from the CT data set (Chaps. 1 and 2) and linked to the 3-D hard tissue surface representation.

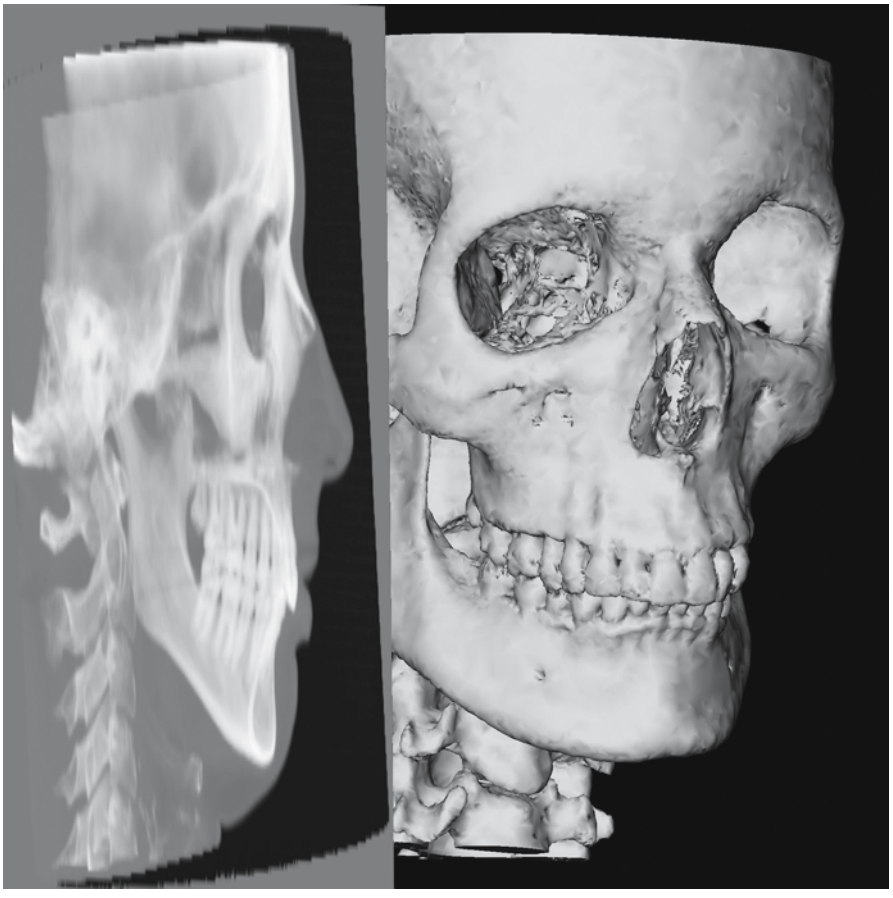

Fig. 3.4. Virtual lateral cephalogram linked to the 3-D hard tissue surface representation (patient K.C.)

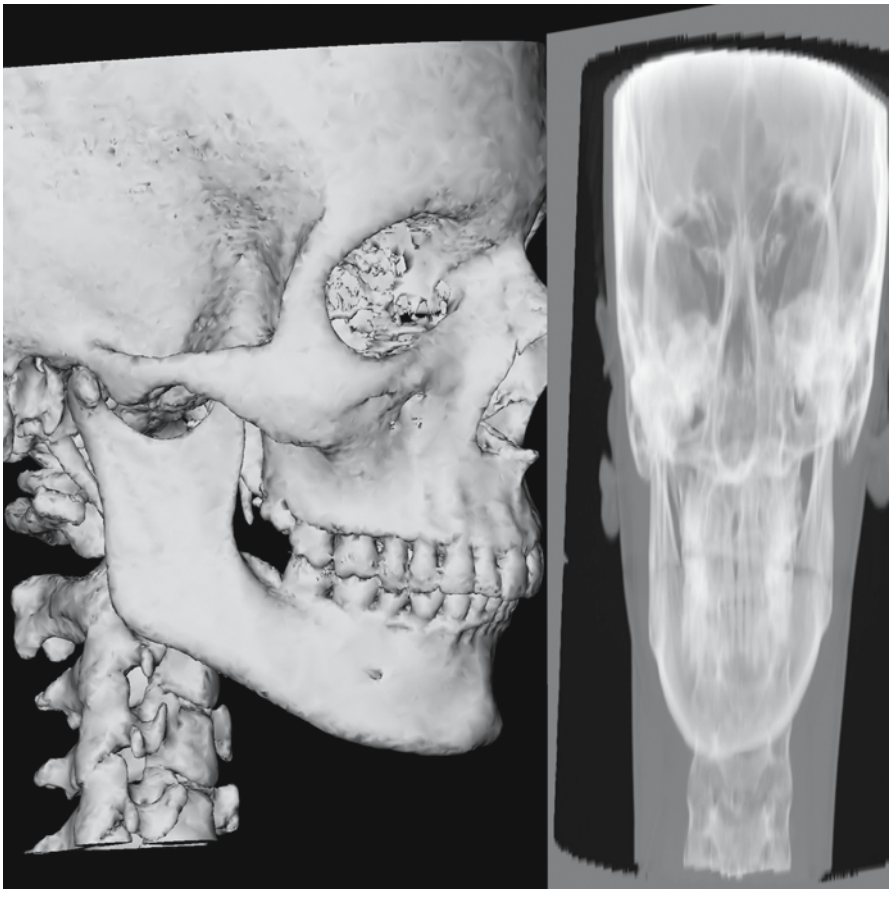

Fig. 3.5. Virtual frontal cephalogram linked to the 3-D hard tissue surface representation (patient K.C.)

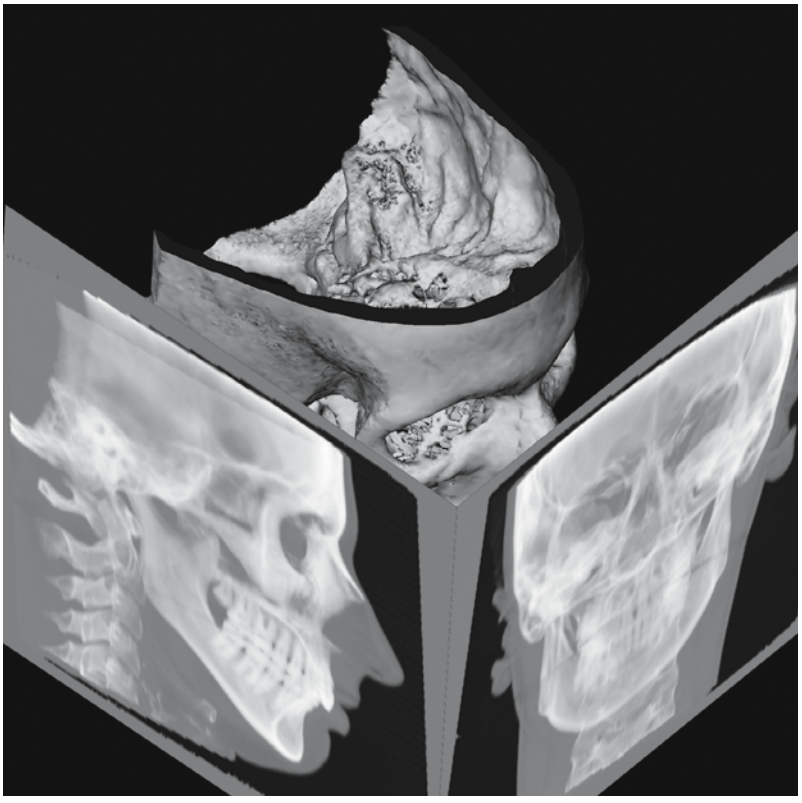

Fig. 3.6. Virtual lateral and frontal cephalograms linked to the 3-D hard tissue surface representation (patient K.C.)

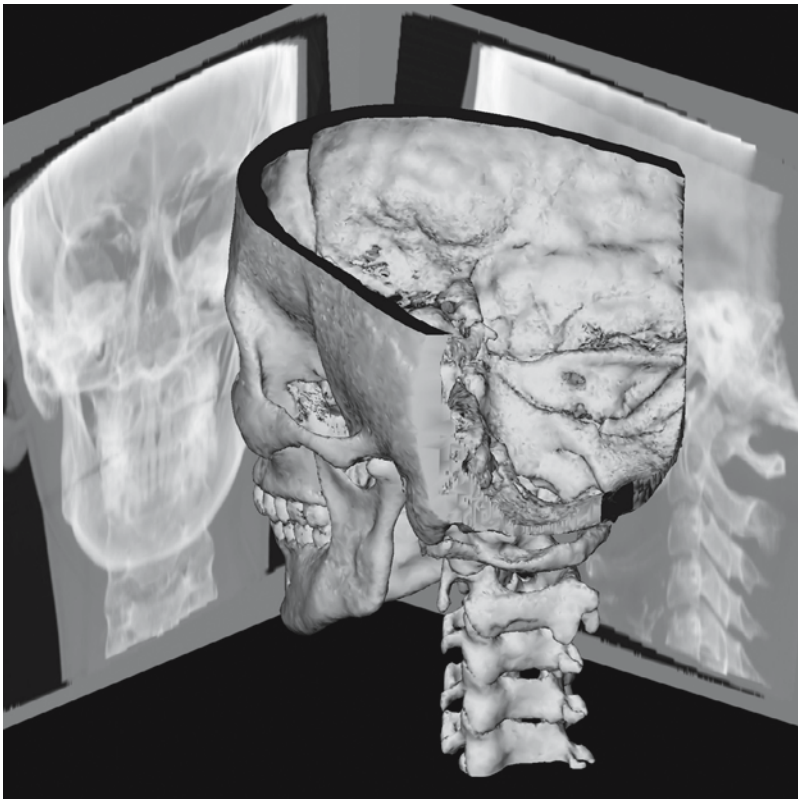

Fig. 3.7. Virtual lateral and frontal cephalograms linked to the 3-D hard tissue surface representation (patient K.C.)

3.3 Definition of the Nasion and Sella 3-D Cephalometric Landmarks

Nasion: N

Definition of the Nasion Landmark

Nasion is the midpoint of the frontonasal suture.

Fig. 3.8. Nasion. Frontal view (cadaver skull)

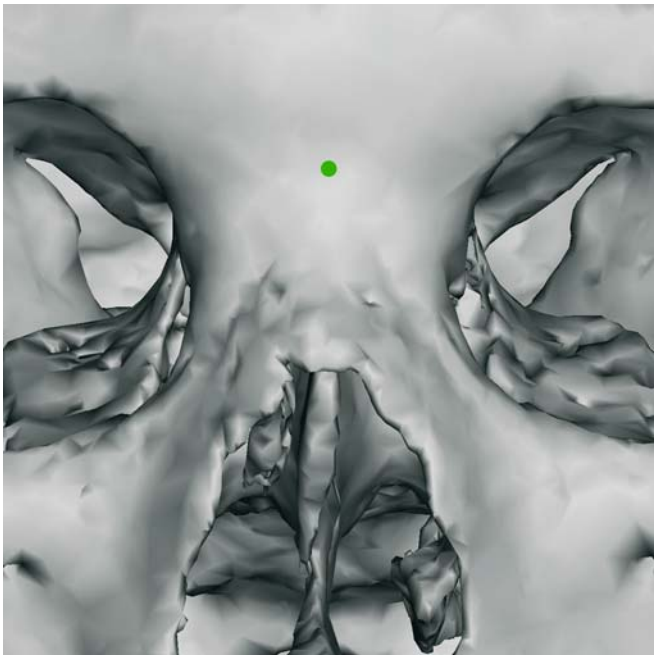

Fig. 3.9. Nasion. Frontal view (3-D CT, cadaver skull). Note that it is not possible to precisely define the Nasion landmark on the 3-D hard tissue representation because the frontonasal suture is not clearly visible

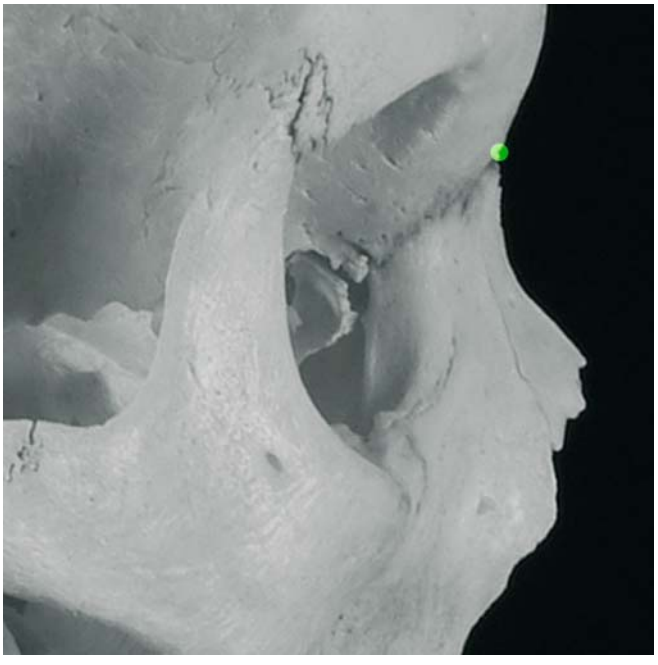

Fig. 3.10. Nasion. Profile view right (cadaver skull)

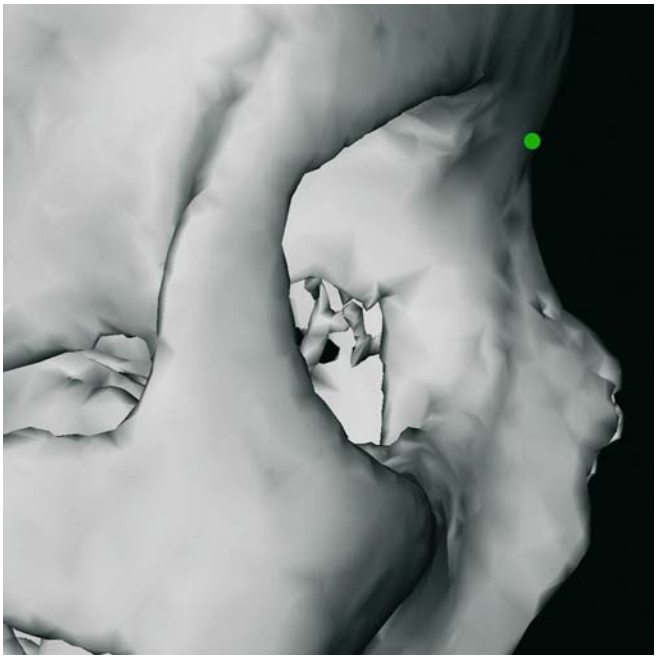

Fig. 3.11. Nasion. Profile view right (3-D CT, cadaver skull)

Virtual Definition of the Nasion Landmark

Step 1: Define Nasion on the virtual lateral cephalogram (Figs. 3.12, 3.13).
Step 2: Verify and correct the median position of the Nasion landmark on the frontal view of the 3-D hard tissue surface representation (Fig. 3.14).
Step 3: The position of the Nasion landmark is verified on the left and right 3-D profile views of the 3-D hard tissue surface representations (Figs. 3.15, 3.16).

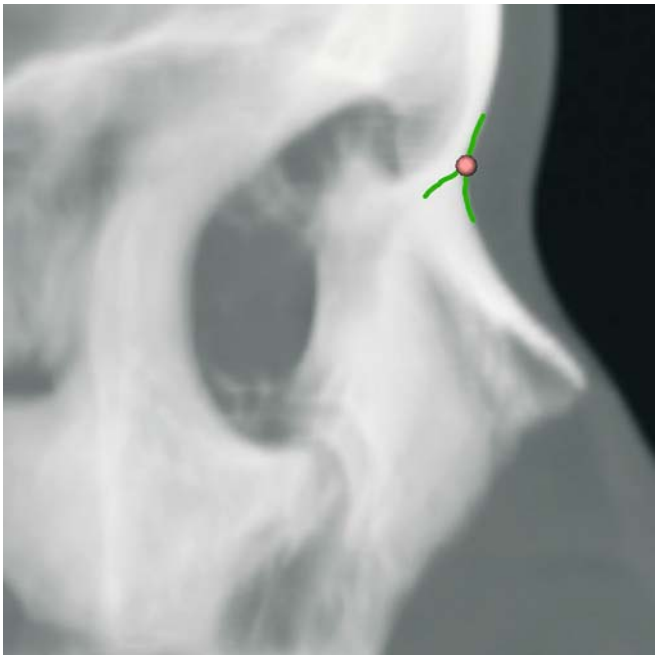

Fig. 3.12. Nasion. Virtual lateral cephalogram (patient K.C.)

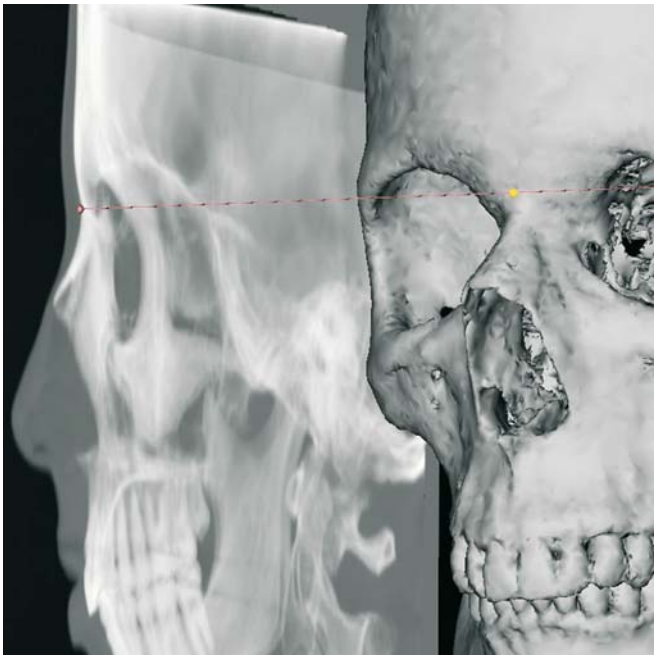

Fig. 3.13. Nasion. Virtual lateral cephalogram linked to the 3-D hard tissue surface representation (patient K.C.)

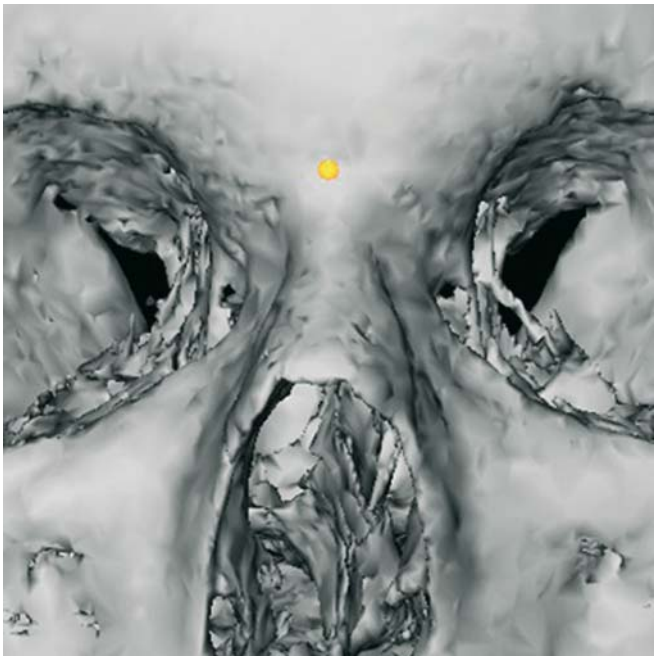

Fig. 3.14. Nasion. Frontal view (3-D CT, patient K.C.)

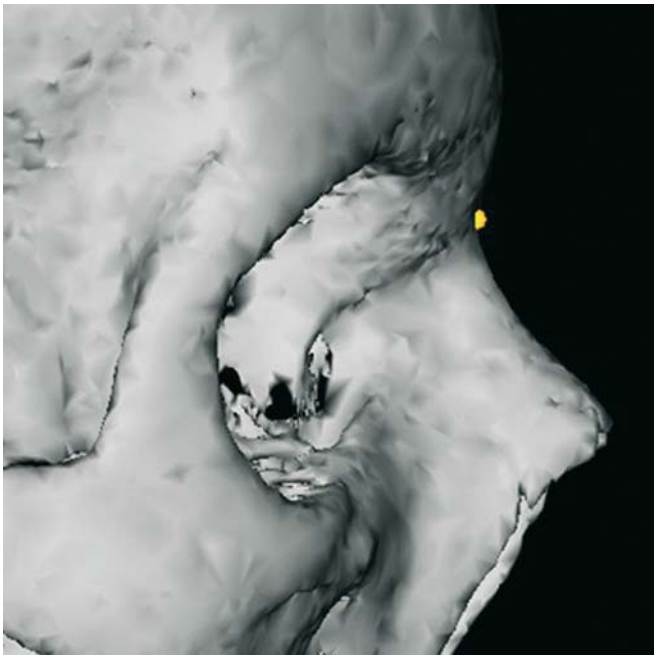

Fig. 3.15. Nasion. Profile view right (3-D CT, patient K.C.)

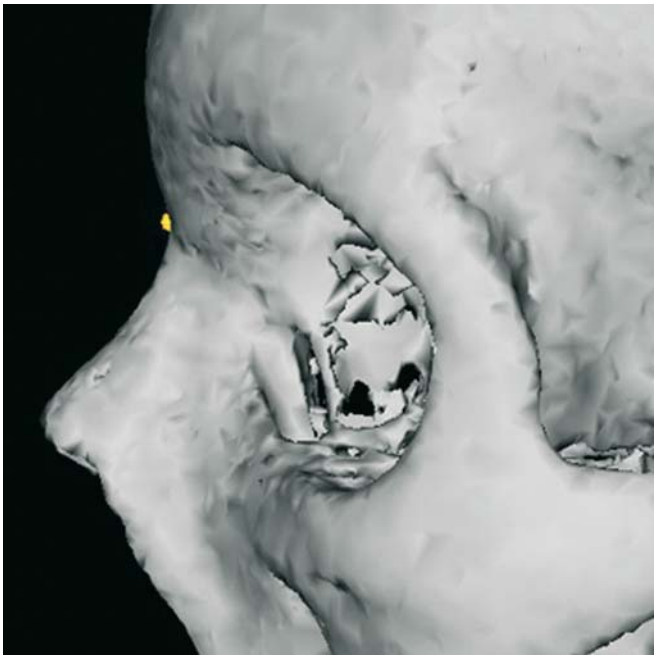

Fig. 3.16. Nasion. Profile view left (3-D CT, patient K.C.)

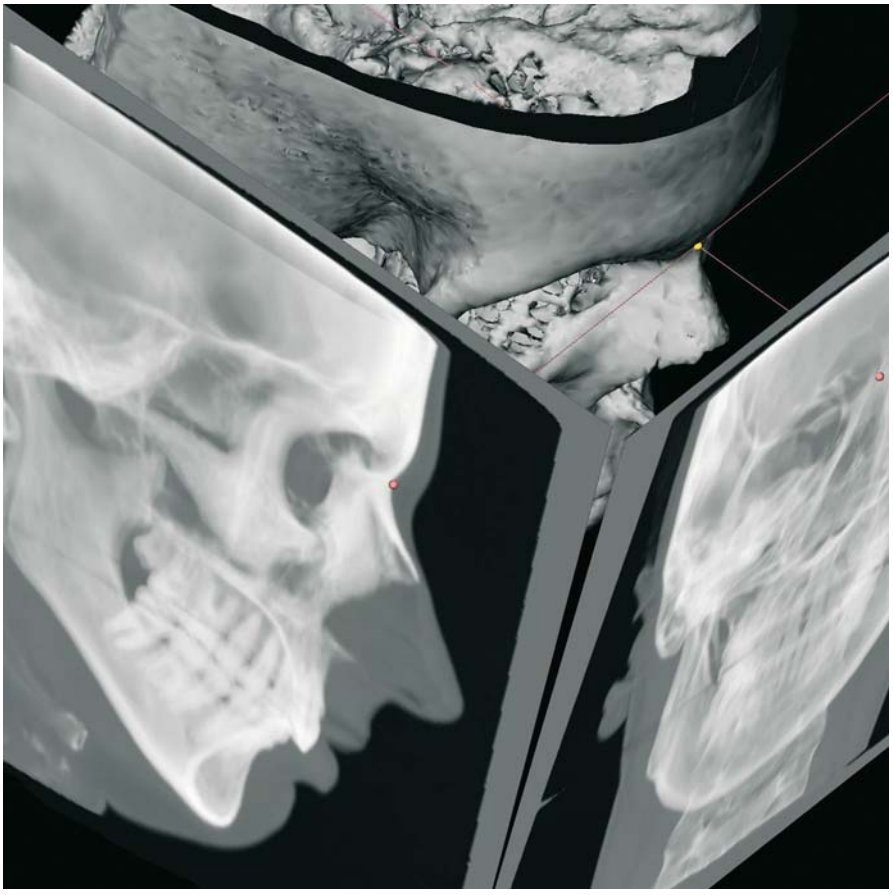

Fig. 3.17. Nasion. Virtual lateral and frontal cephalograms linked to the 3-D hard tissue surface representation (patient K.C.)

Sella: S

Definition of the Sella Landmark

Sella is the centre of the hypophyseal fossa (sella turcica).

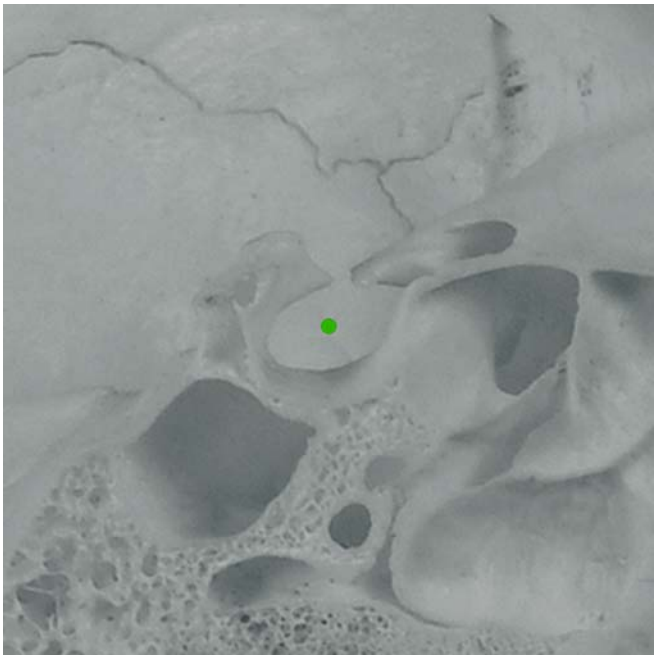

Fig. 3.18. Sella. Paramedian view right (cadaver skull)

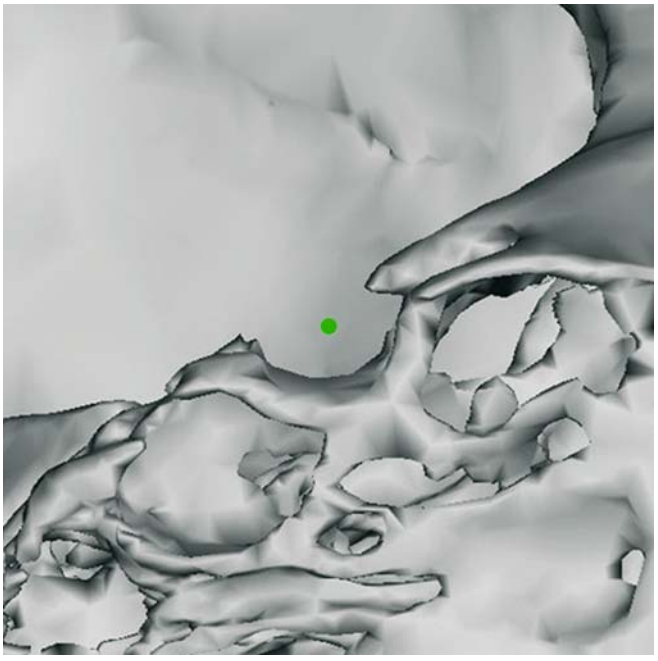

Fig. 3.19. Sella. Paramedian view right (3-D CT, cadaver skull)

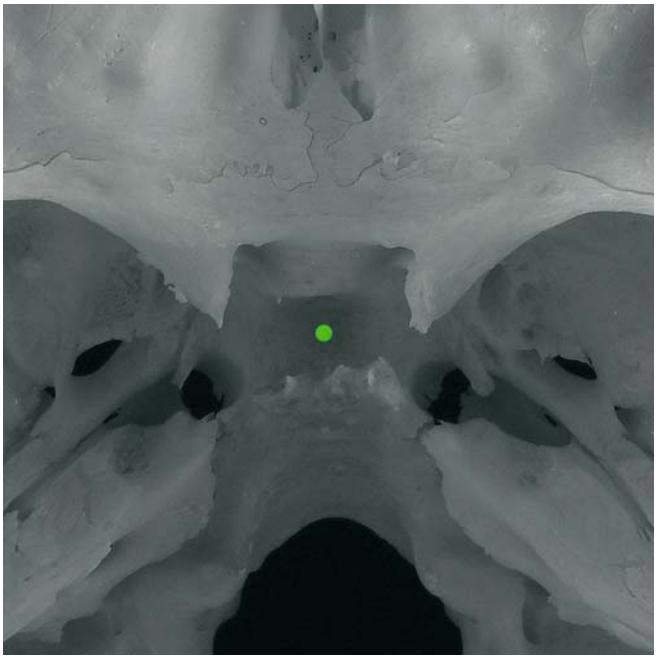

Fig. 3.20. Sella. Endocranial skull base view (cadaver skull)

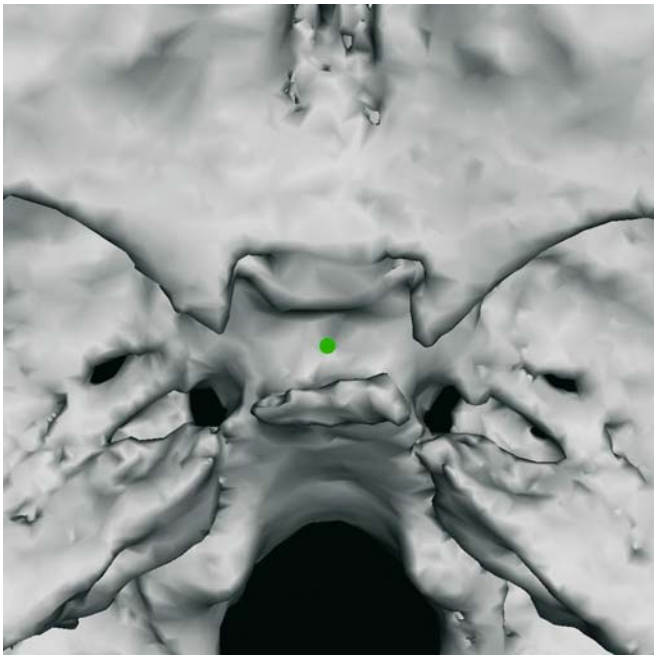

Fig. 3.21. Sella. Endocranial skull base view (3-D CT, cadaver skull)

Virtual Definition of the Sella Landmark

Step 1: Define Sella on the virtual lateral cephalogram (Figs. 3.22, 3.23).
Step 2: Verify the position of the Sella landmark on the left and right paramedian views of the 3-D hard tissue surface representation (Figs. 3.24, 3.25).
Step 3: Verify the midline position of the Sella landmark on the endocranial skull base view (Fig. 3.26).

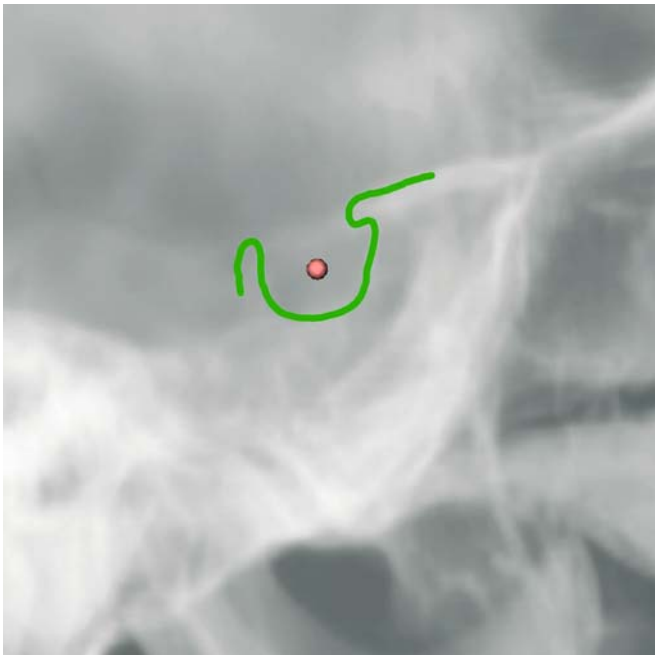

Fig. 3.22. Sella. Virtual lateral cephalogram (patient K.C.)

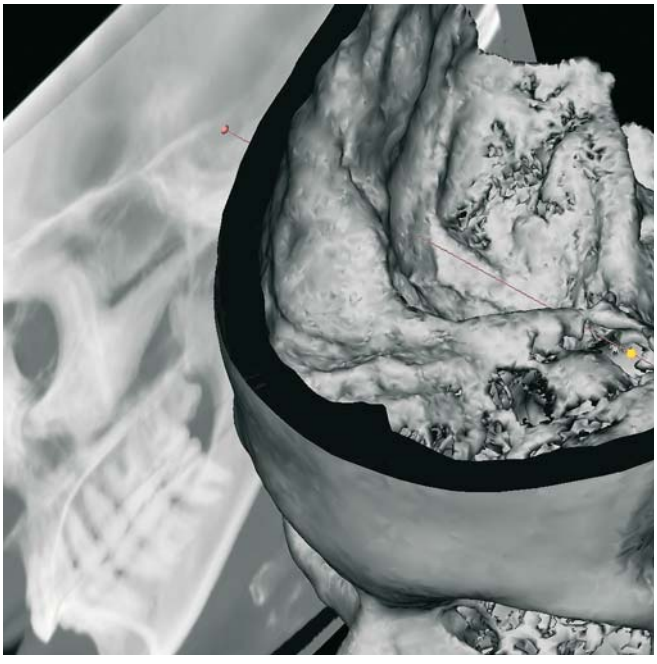

Fig. 3.23. Sella. Virtual lateral cephalogram linked to the 3-D hard tissue representation

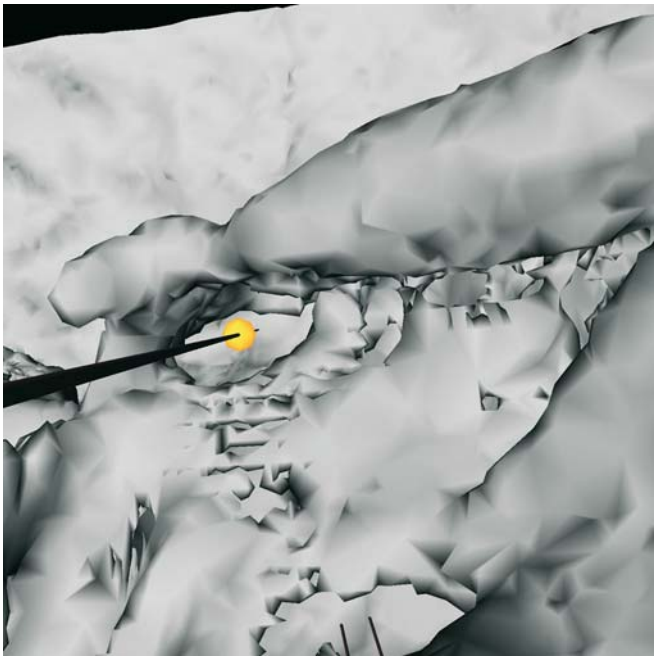

Fig. 3.24. Sella. Paramedian view right (3-D CT, patient K.C.)

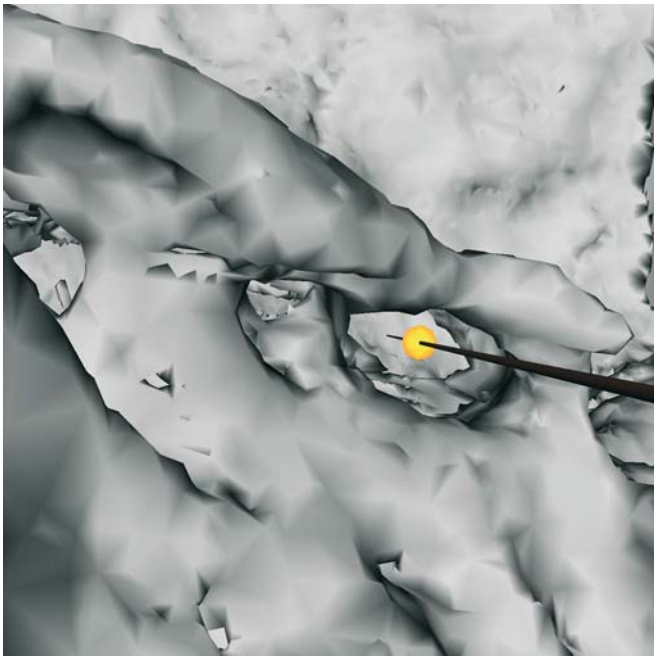

Fig. 3.25. Nasion. Paramedian view left (3-D CT, patient K.C.)

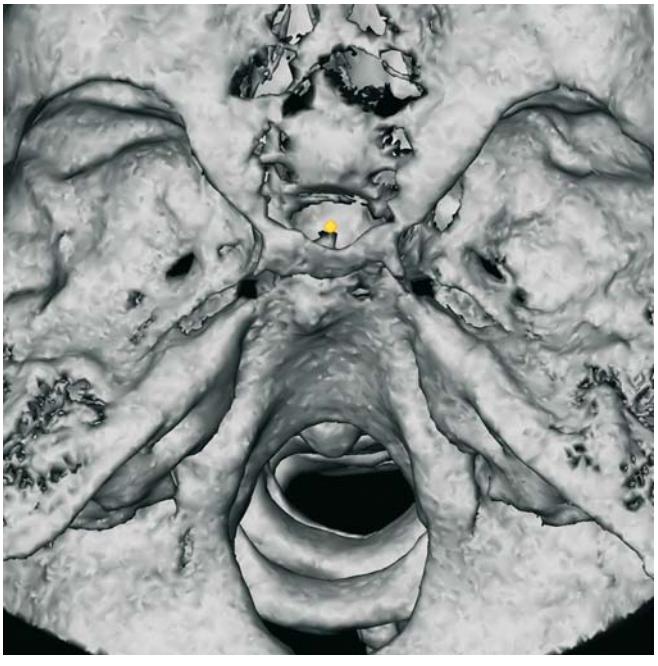

Fig. 3.26. Sella. Endocranial skull base view (3-D CT, patient K.C.)

3.4 Set-up of the Anterior Cranial Base (S-N) Plane

Once virtual definition of the Nasion and Sella 3-D cephalometric landmarks is accomplished, the anterior cranial base (S-N) plane is automatically computed.

Virtual Definition of the Anterior Cranial Base (S-N) Plane

The anterior cranial base (S-N) plane is a plane that passes the Nasion and Sella landmarks and is perpendicular to the virtual lateral cephalogram (Fig. 3.27).

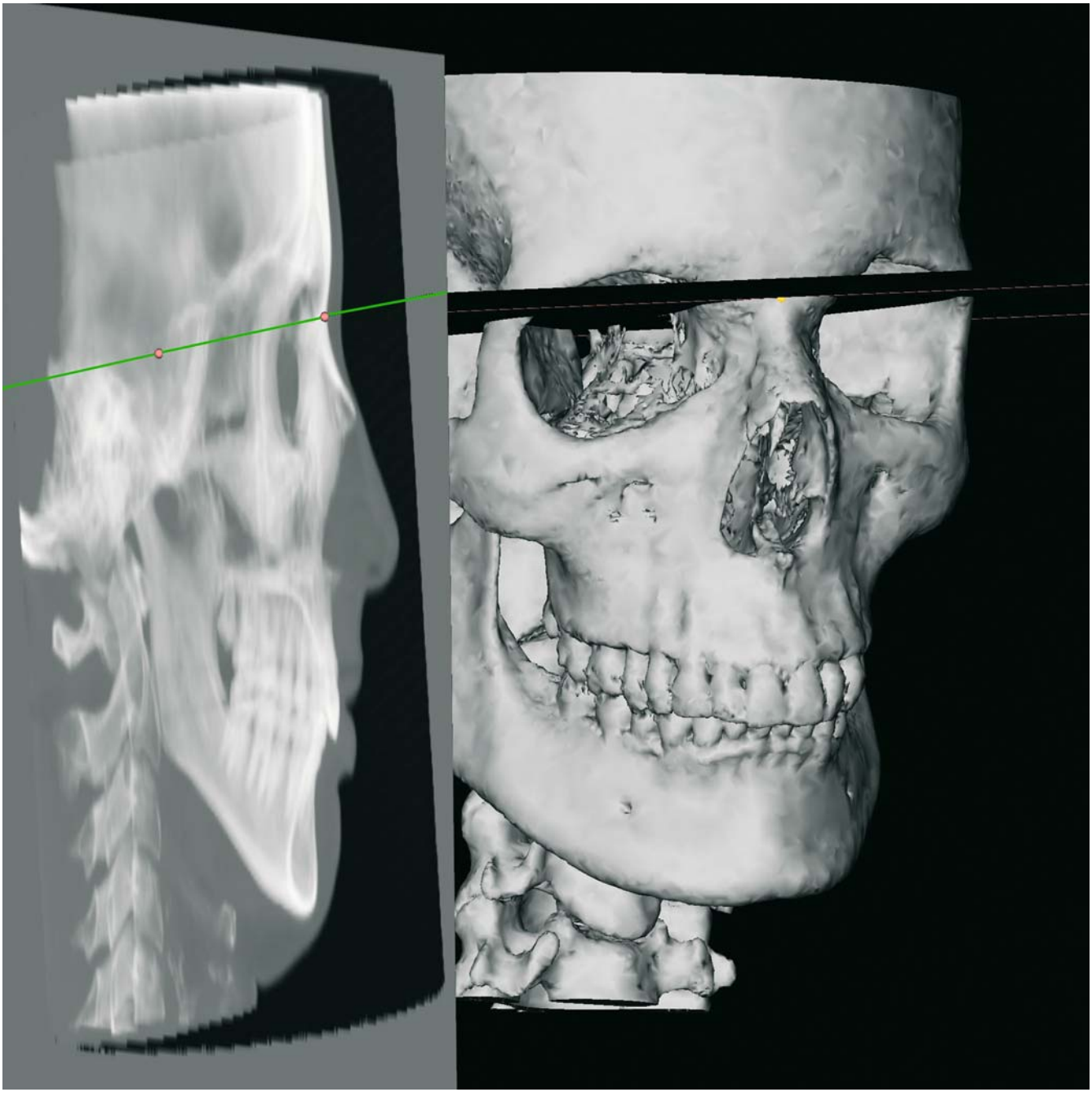

Fig. 3.27. Anterior cranial base (S-N) plane. Virtual lateral cephalogram linked to the 3-D hard tissue surface representation (3-D CT, patient K.C.)

3.5 Set-up of the 3-D Cephalometric Reference System

With the geometric information that is now available, the 3-D virtual scene approach allows the automatic generation of a 3-D cephalometric reference system as an anatomic Cartesian coordinate system.

Virtual Definition of the 3-D Cephalometric Reference System

The horizontal (x) 3-D cephalometric reference plane is automatically computed as a plane 6 degrees below the anterior cranial base (S-N) plane, with the origin in Sella perpendicular to the virtual lateral cephalogram (Fig. 3.28). The vertical (y) 3-D cephalometric reference plane is computed as a plane with the origin in Sella and perpendicular to the horizontal (x) 3-D cephalometric reference plane. The median (z) 3-D cephalometric reference plane is computed as a plane with the origin in Sella and perpendicular to both the horizontal (x) and the vertical (y) 3-D cephalometric reference plane (Fig. 3.29).

3-D Cephalometric Reference System

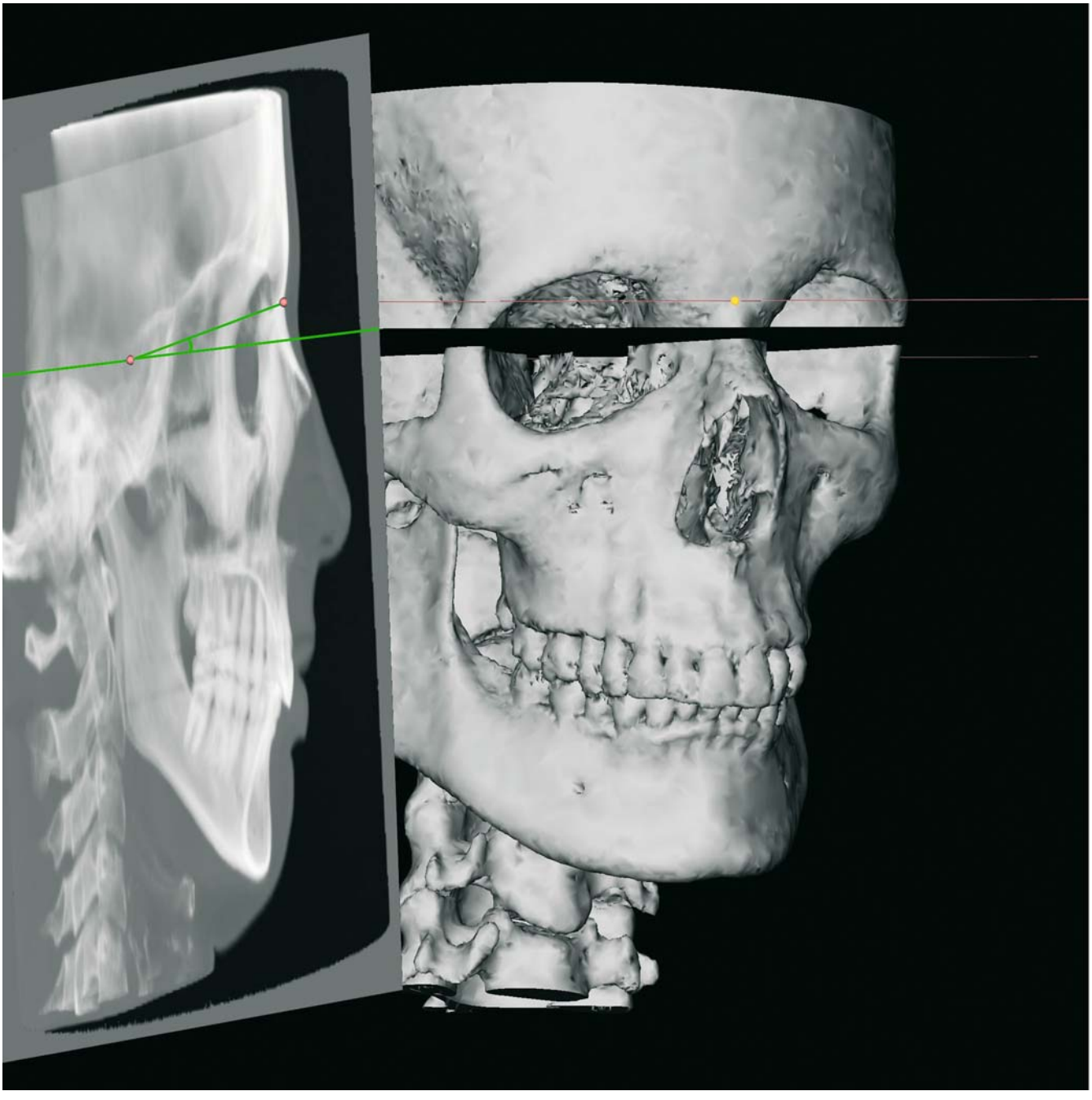

Fig. 3.28. Horizontal (*x*) 3-D cephalometric reference plane. Virtual lateral cephalogram linked to the 3-D hard tissue surface representation (3-D CT, patient K.C.)

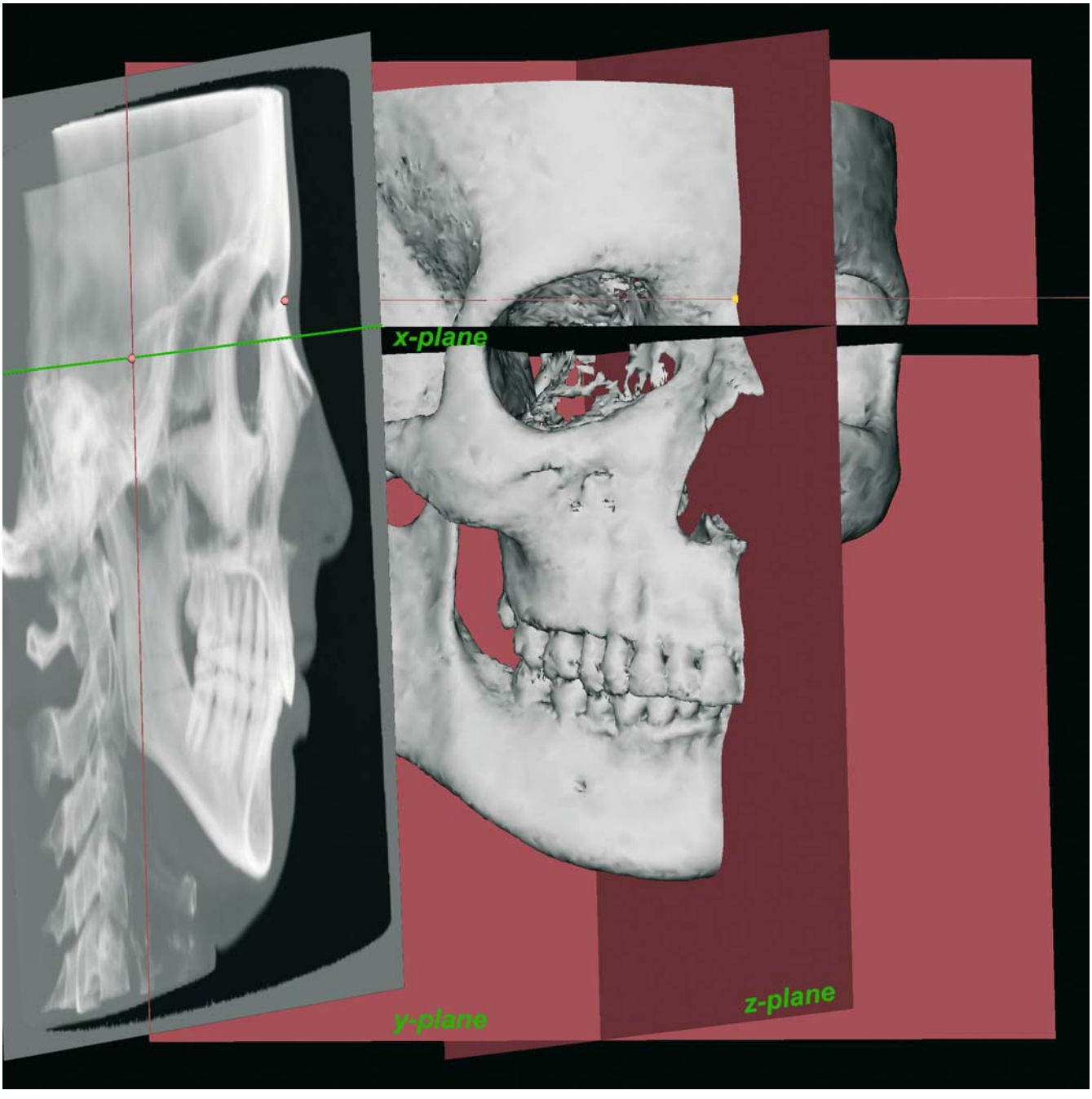

Fig. 3.29. 3-D cephalometric reference system. Virtual lateral cephalogram linked to the 3-D hard tissue surface representation (3-D CT, patient K.C.)

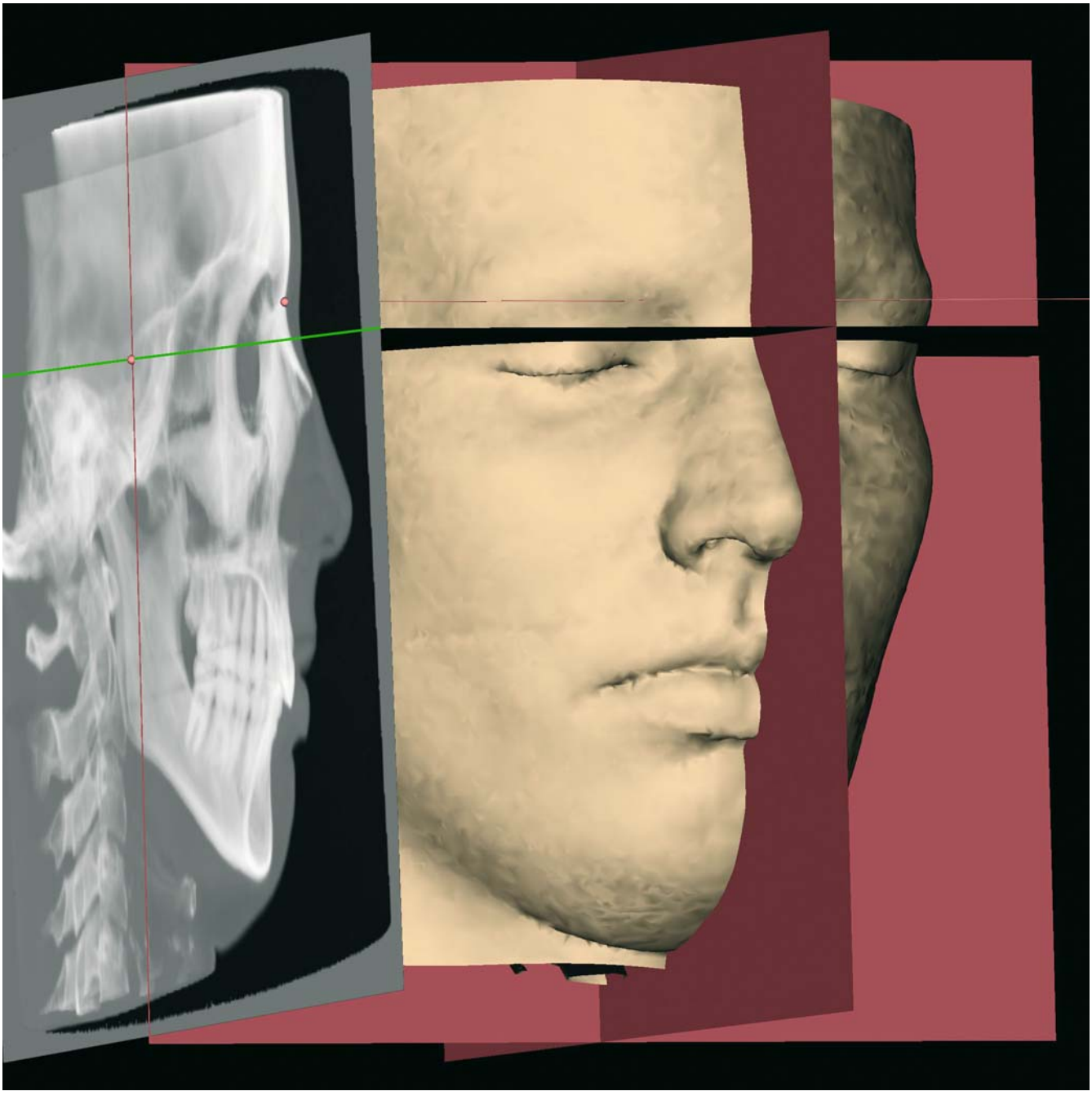

Fig. 3.30. 3-D cephalometric reference system. Virtual lateral cephalogram linked to the 3-D soft tissue surface representation (3-D CT, patient K.C.)

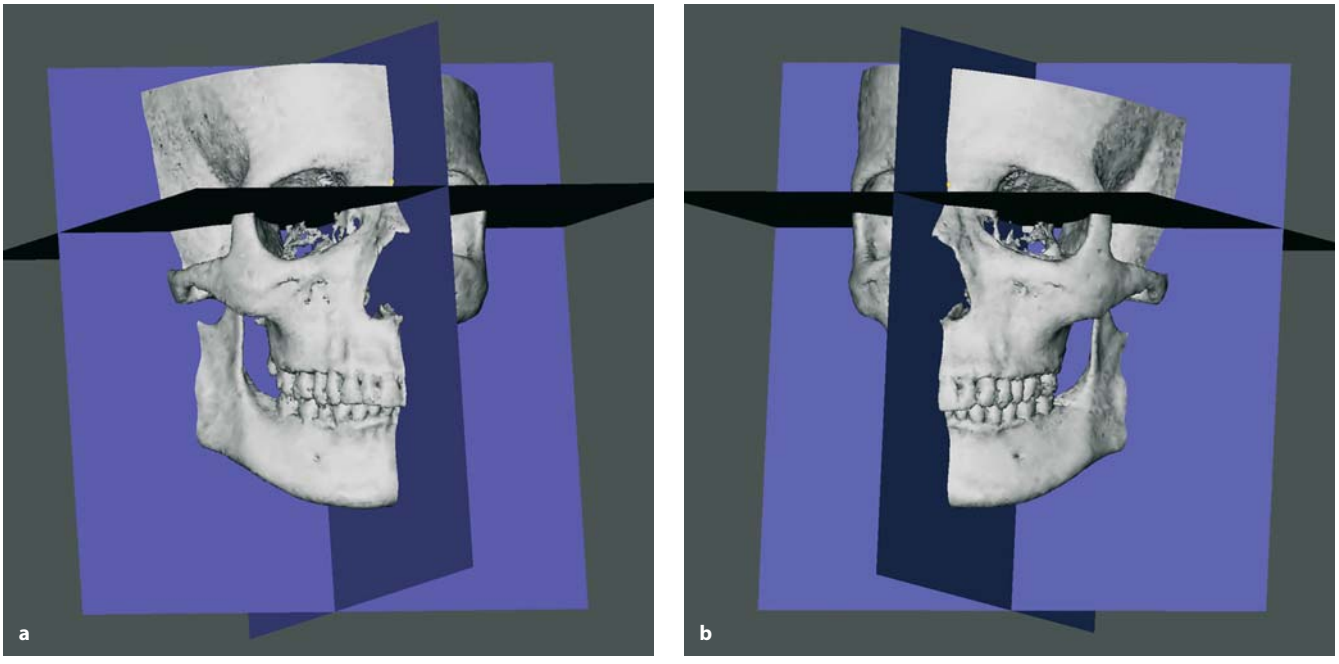

Fig. 3.31 a, b. 3-D cephalometric reference system superimposed on the hard tissue surface representations (3-D CT, patient K.C.)

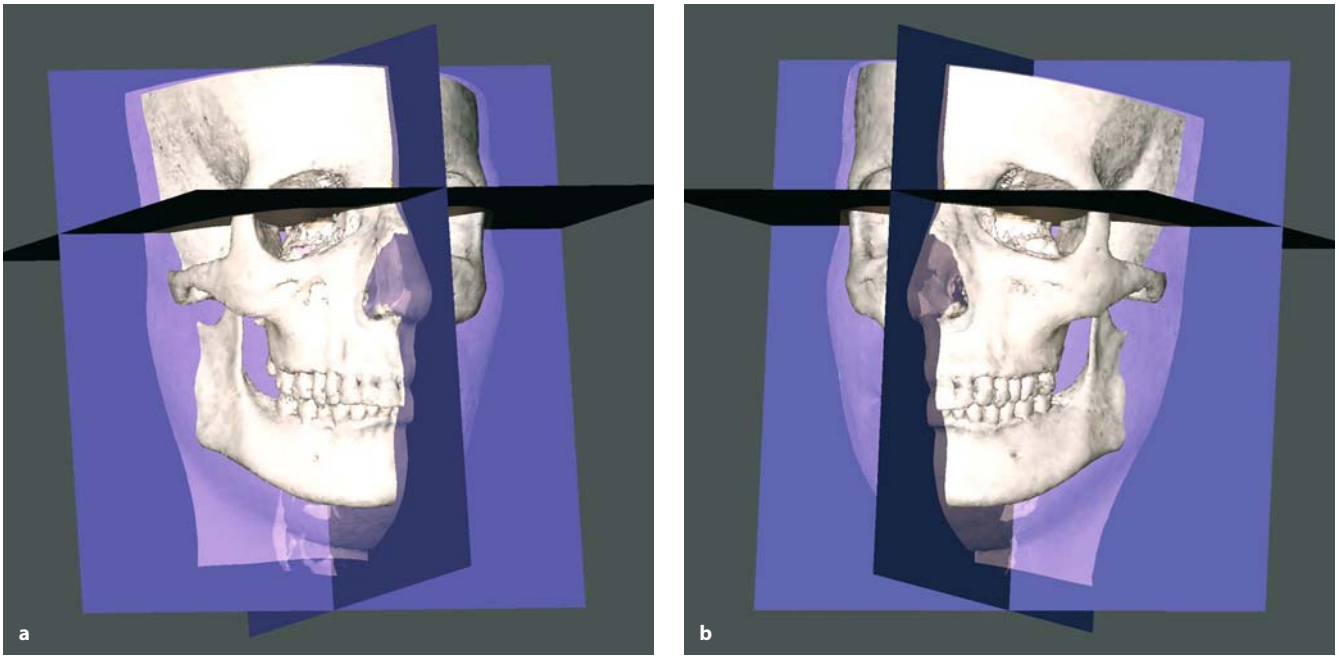

Fig. 3.32 a, b. 3-D cephalometric reference system superimposed on the hard and transparent soft tissue surface representations (3-D CT, patient K.C.)

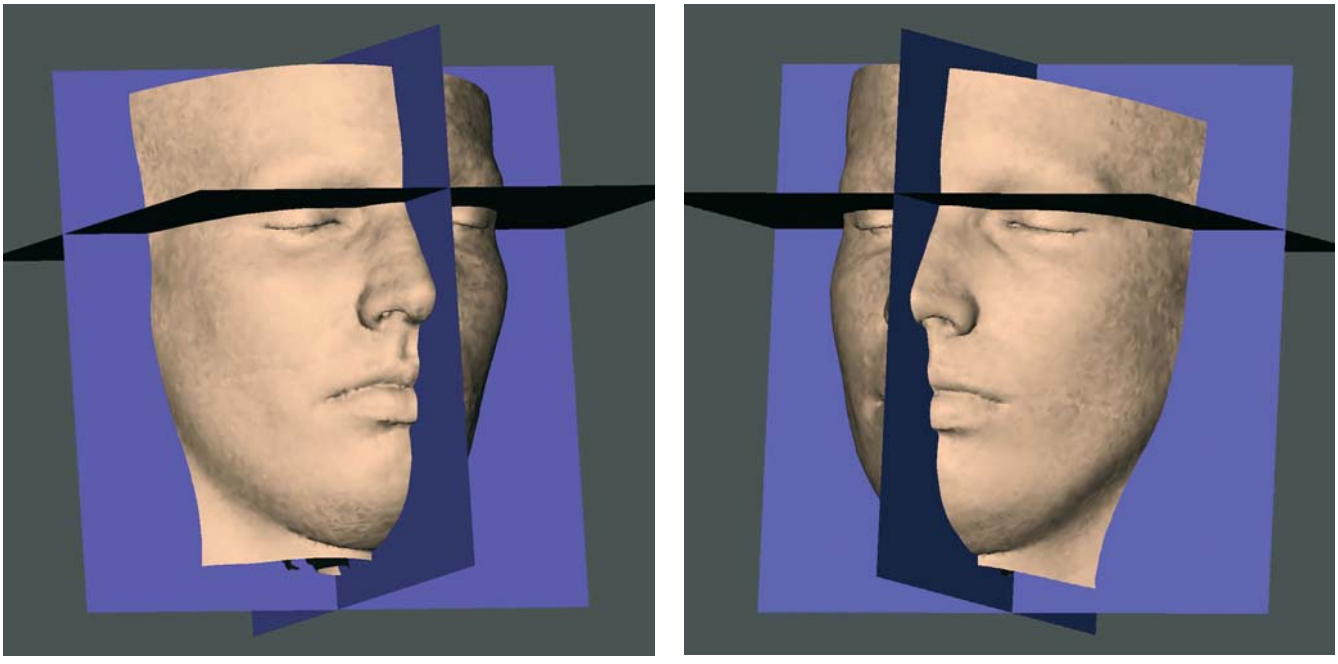

Fig. 3.33 a, b. 3-D cephalometric reference system superimposed on the soft tissue surface representations (3-D CT, patient K.C.)

CHAPTER 4 3-D Cephalometric Hard Tissue Landmarks

Gwen R. J. Swennen

Cephalometric radiography, introduced by Broadbent and Hofrath in 1931, allows orthodontists, maxillofacial, craniofacial and plastic surgeons to diagnose the patient's craniofacial morphology and growth and enables them to plan, monitor and evaluate the appropriate treatment. The most important shortcoming of cephalometric radiography is its two-dimensional character. Lateral cephalometric radiographs are most commonly used and allow 2-D evaluation of craniofacial morphology and growth but ignore the mediolateral axis. Frontal cephalometric radiographs are useful for facial asymmetry assessment but neglect the postero-anterior dimension. Multi-planar cephalometric radiography was developed by Grayson and co-workers. By tracing cephalometric landmarks localized on the midsagittal plane (Sella, Nasion, Anterior Nasal Spine, incisal tip of maxillary central incisor, incisal tip of mandibular central incisor, Menton and Pogonion) on both lateral and postero-anterior cephalometric radiographs, 3-D cephalograms could be generated after combining and integrating the data of both 2-D projecting cephalograms. The major shortcoming of this method is that the 3-D cephalogram does not present a truly 3-D depiction; they are generated from 2-D cephalometric radiographs, which involves an inherent analysis bias.

Recent innovations in computer software technology enabled the development of a new virtual voxel-based 3-D cephalometric method by our research group. This approach of 3-D cephalometry is based on a single dataset in which virtual lateral and frontal cephalograms are linked to the 3-D hard and soft tissue surface representations. It is therefore less sensitive to analysis bias than multi-planar cephalometric radiography. Moreover, it offers real three-dimensional landmark definition and cephalometric analysis.

Precise definition of cephalometric landmarks is essential for the accuracy and reliability of the cephalometric analysis. In this atlas we decided to define landmarks that are situated on the bone (also referred as "osseous", "bony") as "3-D cephalometric hard tissue landmarks", whereas landmarks situated on the skin are termed "3-D cephalometric soft tissue landmarks". Abbreviations (symbols) for hard tissue landmarks are in capitals as in conventional cephalometry, whereas soft tissue landmarks are styled in lower-case letters as in anthropometry and conventional soft tissue cephalometric analysis.

This chapter deals with the definition and identification of 3-D cephalometric hard tissue landmarks. Accurate identification of landmarks requires anatomic knowledge and experience in landmark definition. Compared to conventional cephalometric radiography, some landmarks (e.g. Anterior Nasal Spine) are easier, others (e.g. Sella) more difficult to define in 3-D cephalometry. Moreover, sometimes the definition of conventional 2-D cephalometric landmarks has to be modified because of the third dimension, or new 3-D cephalometric landmarks (e.g. Posterior Maxillary Point) have to be defined for computing 3-D cephalometric planes. This chapter offers "step-by-step" guidelines for precise definition of 3-D cephalometric hard tissue landmarks. A total of 18 landmarks in regard to the facial skeletal units (forehead, nasal, periorbital, midface and mandible) are described in detail. Two other 3-D cephalometric hard tissue landmarks (Nasion and Sella) have already been described in Chap. 3. Some more facial skeletal and skull cephalometric landmarks are merely listed at the end of this chapter because they have not yet been validated.

4.1 Definition of 3-D Cephalometric Hard Tissue Landmarks

Porion: Po_r – Po_l

Definition of the Porion Landmarks

Porion (Po) is the most superior point of each external acoustic meatus.

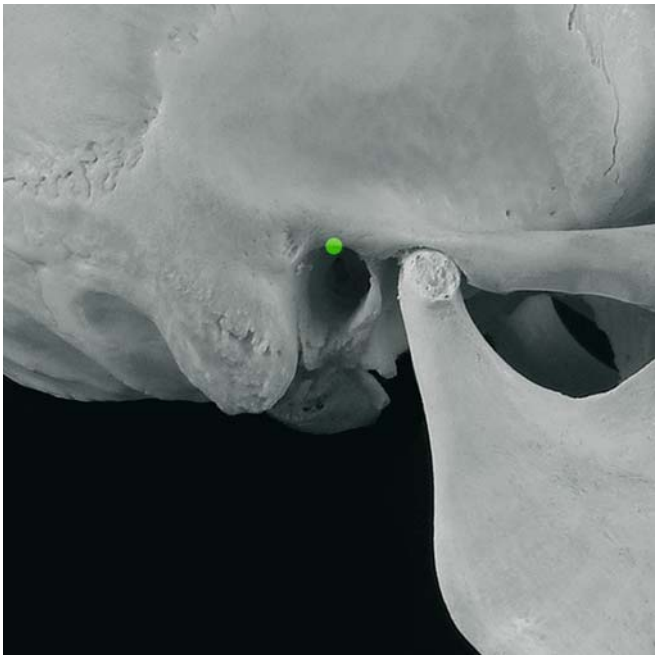

Fig. 4.1. $Porion_r$. Profile view right (cadaver skull)

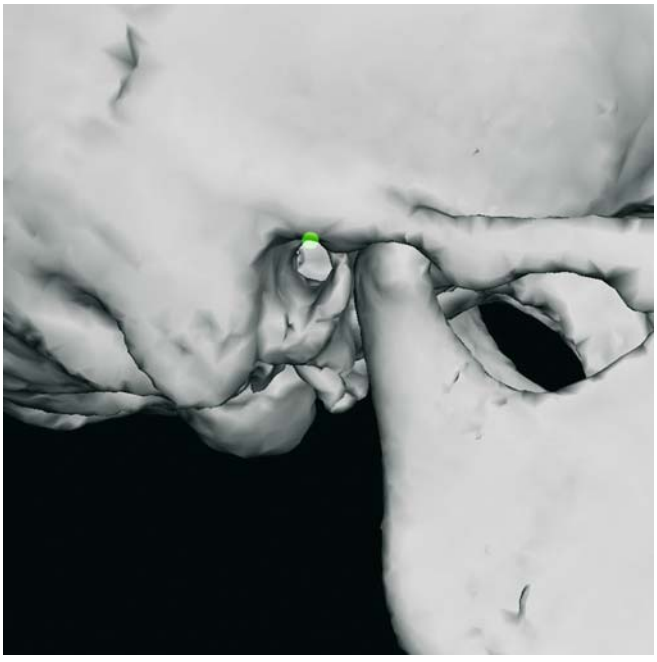

Fig. 4.2. $Porion_r$. Profile view right (3-D CT, cadaver skull)

Virtual Definition of the Porion Landmarks

Step 1: Define $Porion_r$ and $Porion_l$ on the right (Fig. 4.3) and left (Fig. 4.4) profile views of the 3-D hard tissue surface representations.

Step 2: Verify the transversal position of $Porion_r$ and $Porion_l$ on the linked virtual frontal cephalogram (Fig. 4.5).

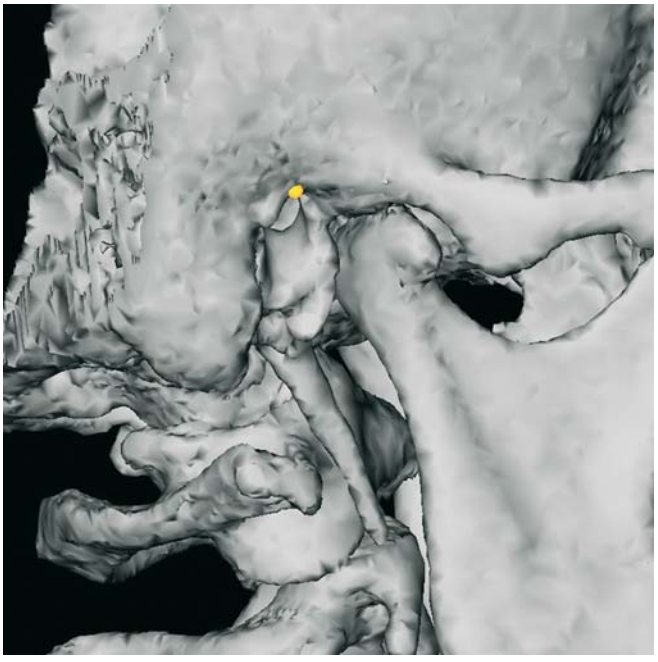

Fig. 4.3. $Porion_r$. Profile view right (3-D CT, patient K.C.)

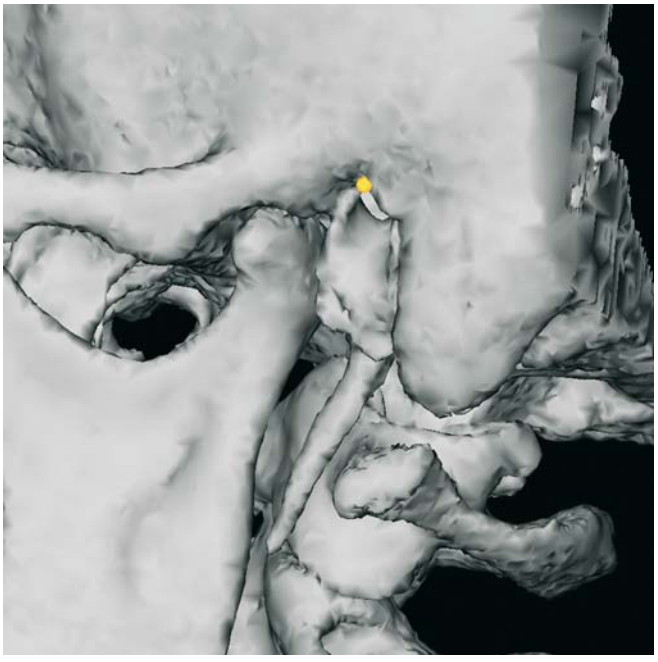

Fig. 4.4. $Porion_l$. Profile view left (3-D CT, patient K.C.)

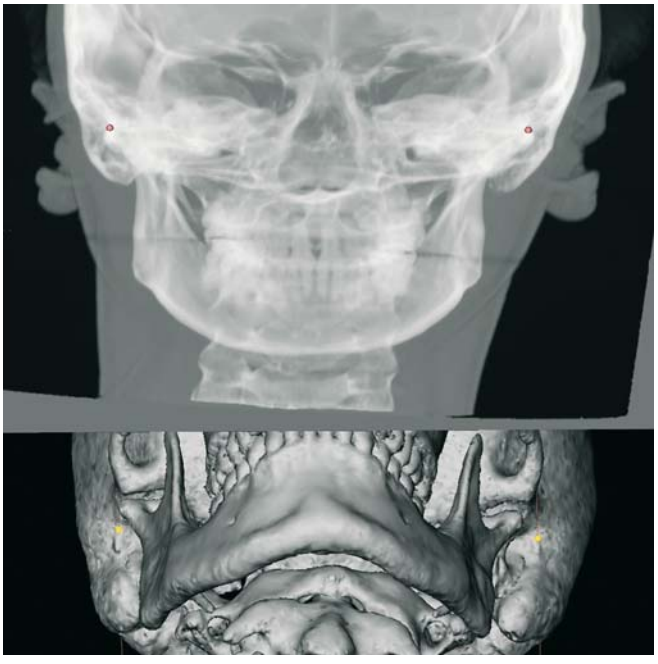

Fig. 4.5. Porion. Virtual frontal cephalogram linked to the 3-D hard tissue surface representation (3-D CT, patient K.C.) allows verification of the transversal position of the Porion landmarks

Orbitale: Or_r – Or_l

Definition of the Orbitale Landmarks

Orbitale (Or) is the most inferior point of each infraorbital rim.

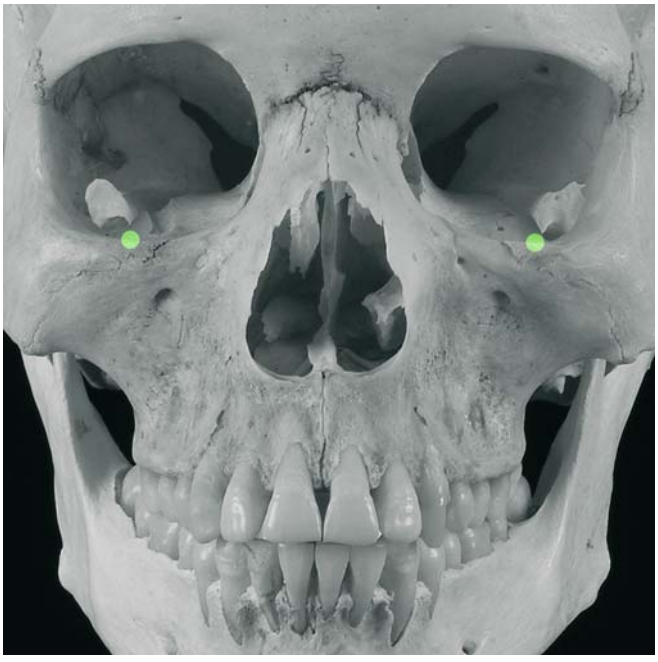

Fig. 4.6. $Orbita_r$ and $Orbita_l$. Frontal view (cadaver skull)

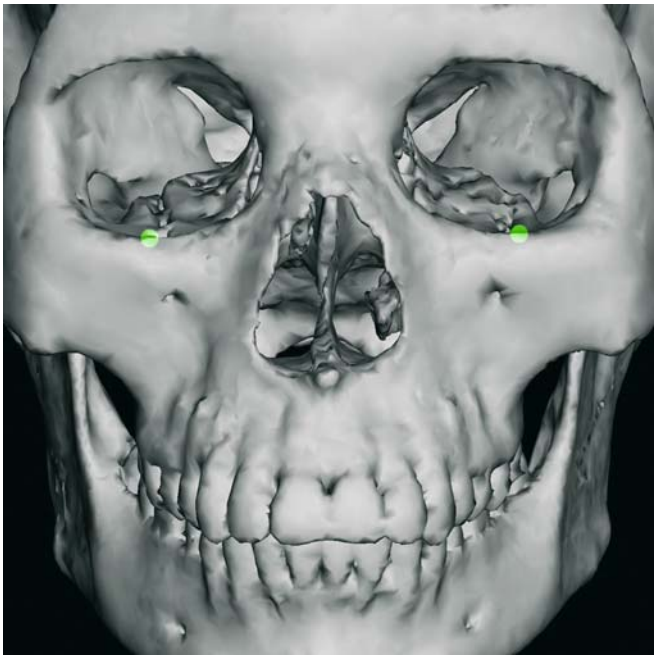

Fig. 4.7. $Orbita_r$ and $Orbita_l$. Frontal view (3-D CT, cadaver skull)

Virtual Definition of the Orbitale Landmarks

Step 1: Define $Orbita_r$ and $Orbita_l$ on the frontal view of the 3-D hard tissue surface representation (Fig. 4.8).

Step 2: Verify the position of $Orbita_r$ and $Orbita_l$ on the linked virtual frontal cephalogram (Fig. 4.9).

Fig. 4.8. $Orbita_r$ and $Orbita_l$. Frontal view (3-D CT, patient K.C.)

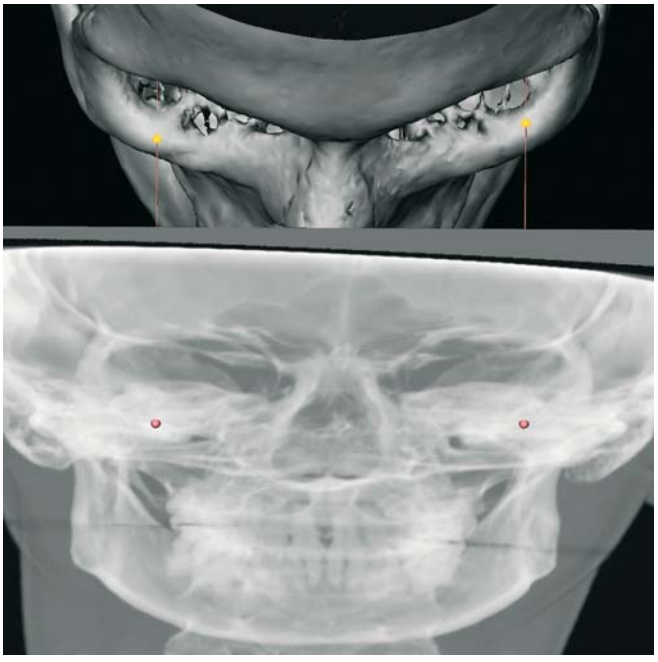

Fig. 4.9. $Orbita_r$ and $Orbita_l$. Virtual frontal cephalogram linked to the 3-D hard tissue surface representation (3-D CT, patient K.C.) allows verification of the position of the $Orbita_r$ and $Orbita_l$ landmarks

Anterior Nasal Spine: ANS

Definition of the Anterior Nasal Spine Landmark

Anterior Nasal Spine is the most anterior midpoint of the anterior nasal spine of the maxilla.

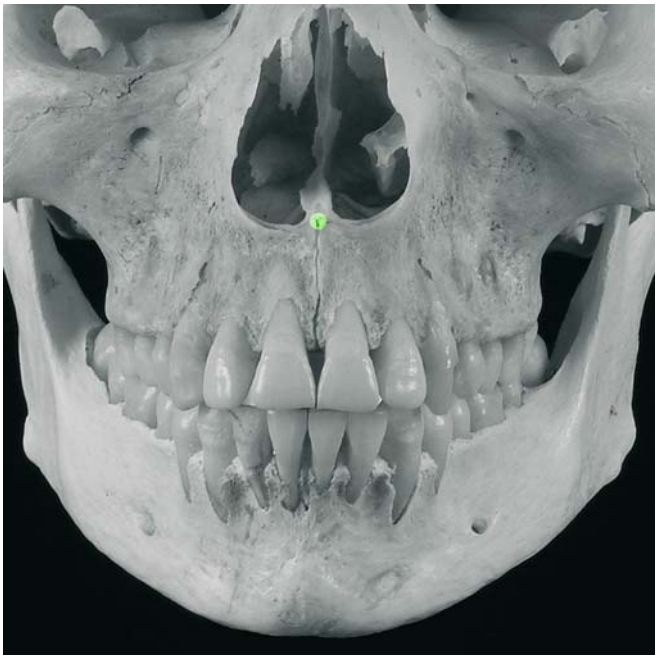

Fig. 4.10. Anterior nasal spine. Frontal view (cadaver skull)

Fig. 4.11. Anterior nasal spine. Frontal view (3-D CT, cadaver skull)

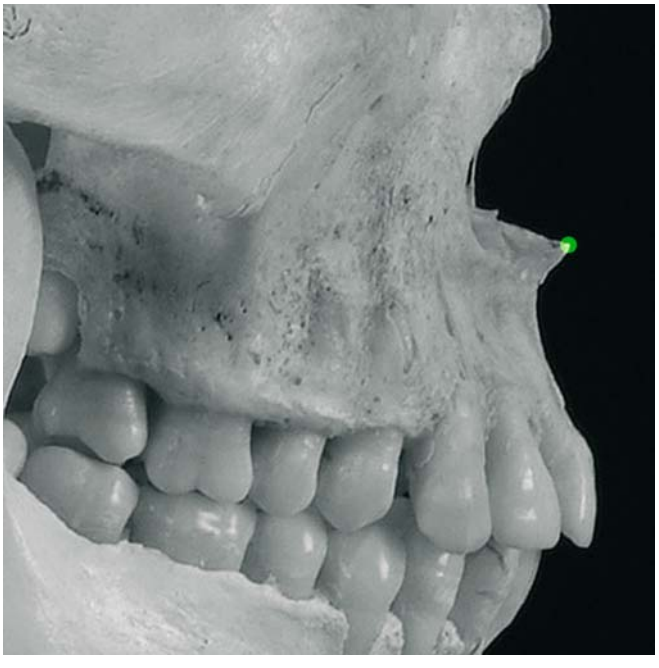

Fig. 4.12. Anterior nasal spine. Profile view right (cadaver skull)

Fig. 4.13. Anterior nasal spine. Profile view right (3-D CT, cadaver skull)

Virtual Definition of the Anterior Nasal Spine Landmark

Step 1: Define Anterior Nasal Spine on the virtual lateral cephalogram (Figs. 4.14, 4.15).

Step 2: Verify and correct the median position of Anterior Nasal Spine on the frontal view of the 3-D hard tissue surface representation (Fig. 4.16).

Step 3: The position of Anterior Nasal Spine is verified on the left and right 3-D profile views of the 3-D hard tissue surface representations (Figs. 4.17, 4.18.). Additionally Anterior Nasal Spine can be verified on the virtual frontal cephalogram linked to the 3-D hard tissue surface representation (Fig. 4.19).

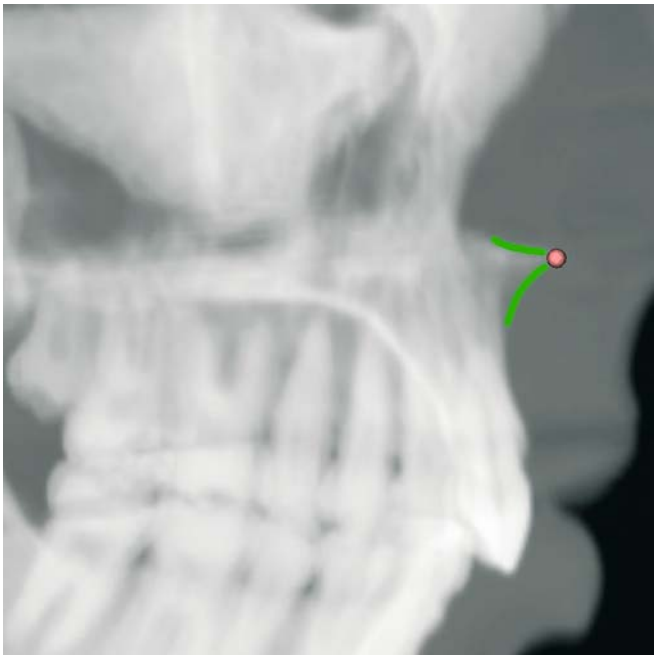

Fig. 4.14. Anterior Nasal Spine. Virtual lateral cephalogram (patient K.C.)

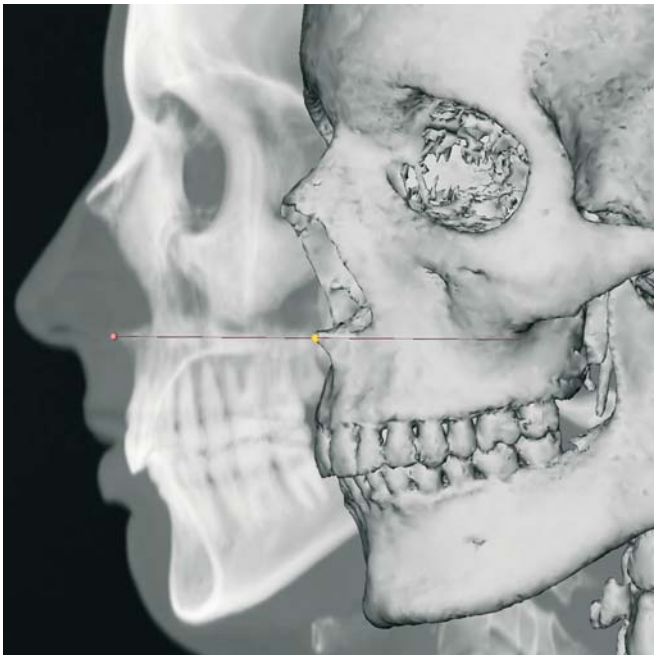

Fig. 4.15. Anterior Nasal Spine. Virtual lateral cephalogram linked to the 3-D hard tissue surface representation (patient K.C.)

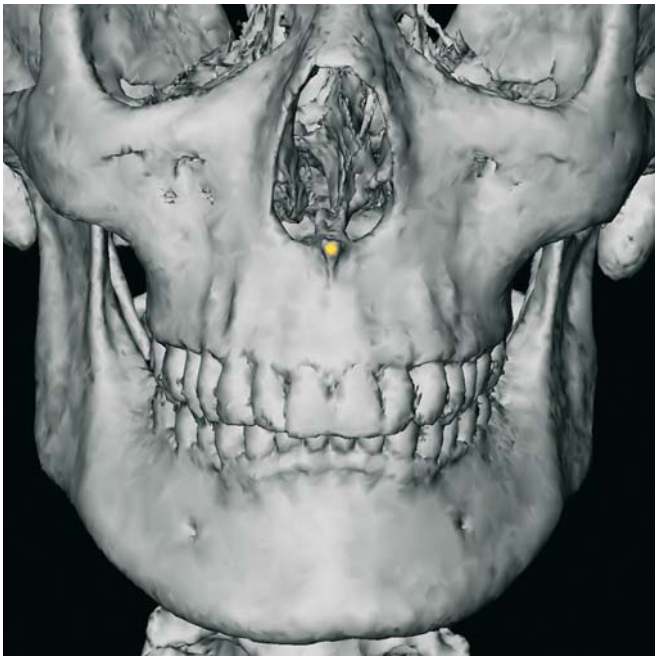

Fig. 4.16. Anterior Nasal Spine. Frontal view (3-D CT, patient K.C.)

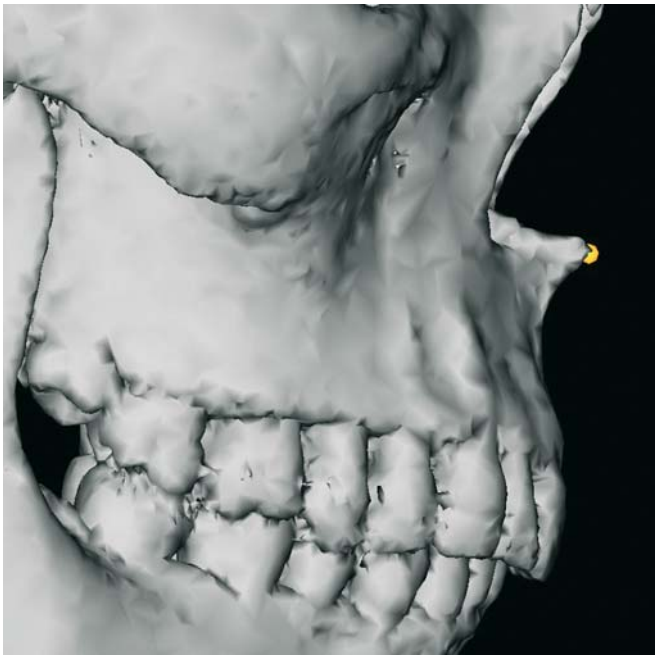

Fig. 4.17. Anterior Nasal Spine. Profile view right (3-D CT, patient K.C.)

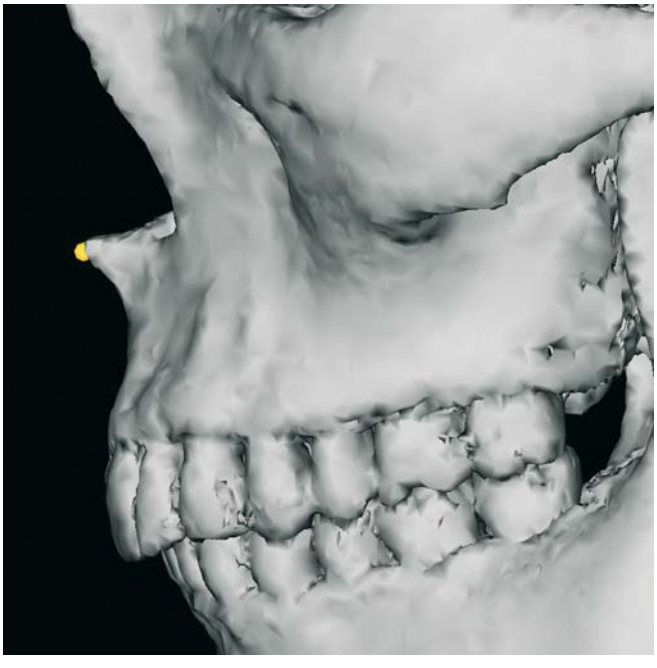

Fig. 4.18. Anterior Nasal Spine. Profile view left (3-D CT, patient K.C.)

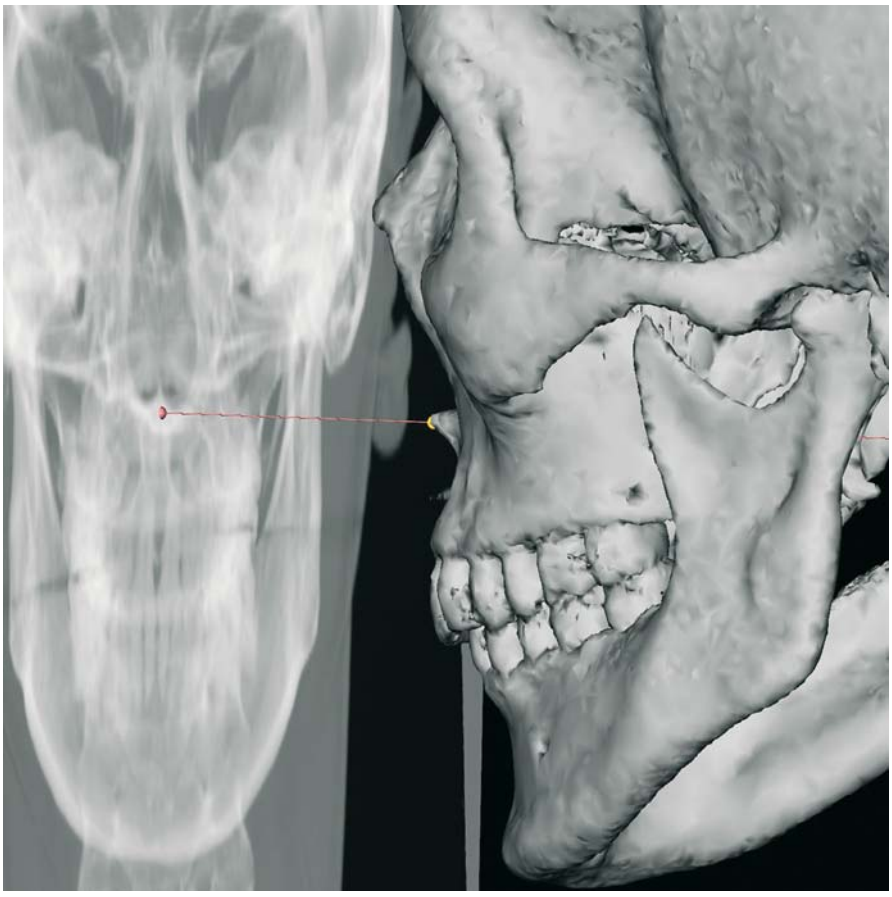

Fig. 4.19. Anterior Nasal Spine. Virtual frontal cephalogram linked to the 3-D hard tissue surface representation (3-D CT, patient K.C.)

Posterior Nasal Spine: PNS

Definition of the Posterior Nasal Spine Landmark

Posterior Nasal Spine is the most posterior midpoint of the posterior nasal spine of the palatine bone.

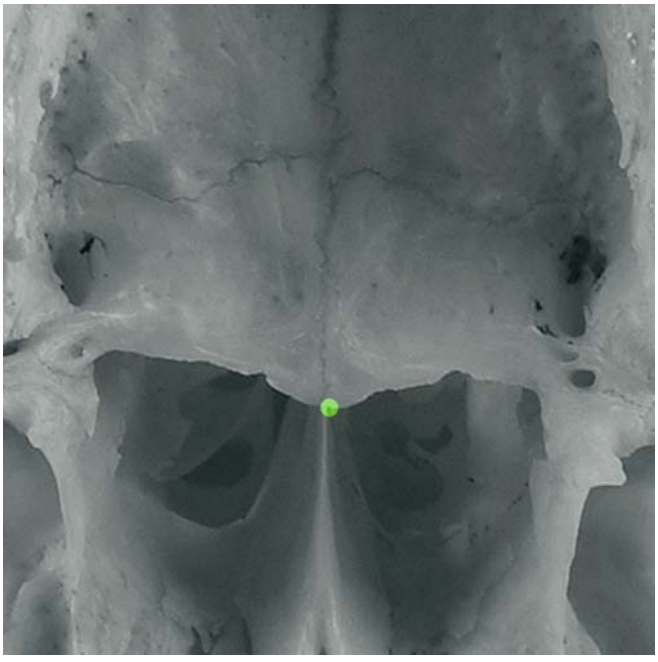

Fig. 4.20. Posterior nasal spine. Exocranial skull base view (cadaver skull)

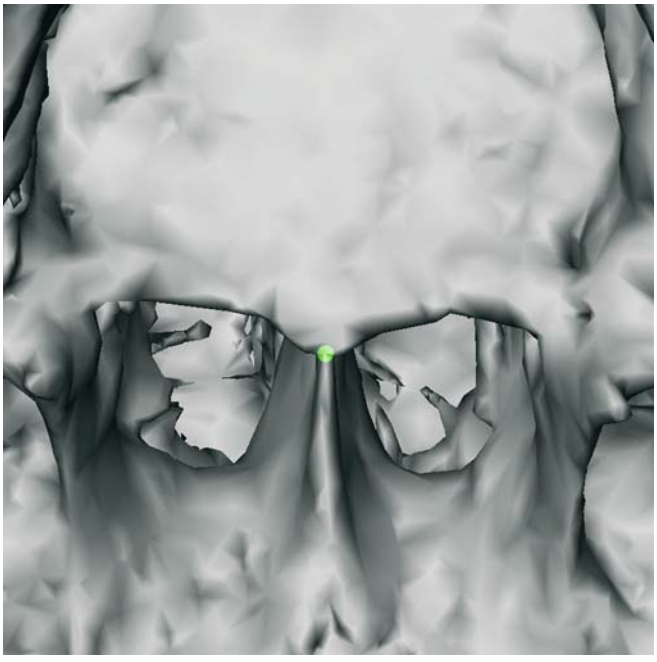

Fig. 4.21. Posterior nasal spine. Exocranial skull base view (3-D CT, cadaver skull)

Virtual Definition of the Posterior Nasal Spine Landmark

Step 1: Define Posterior Nasal Spine on the exocranial skull base view of the 3-D hard tissue surface representation (Fig. 4.22).

Step 2: Verify and correct the vertical position of Posterior Nasal Spine on the virtual lateral cephalogram (Fig. 4.23) which is linked to the 3-D hard tissue surface representation (Fig. 4.24).

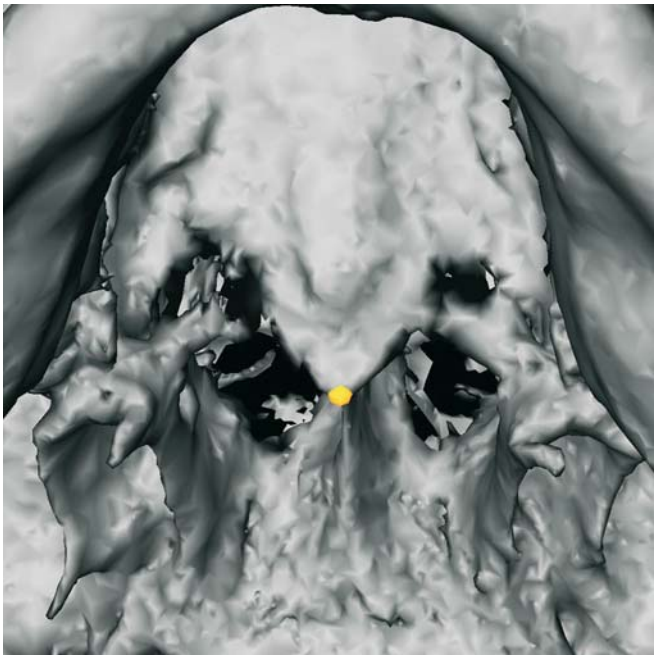

Fig. 4.22. Posterior nasal spine. Exocranial skull base view (3-D CT, patient K.C.)

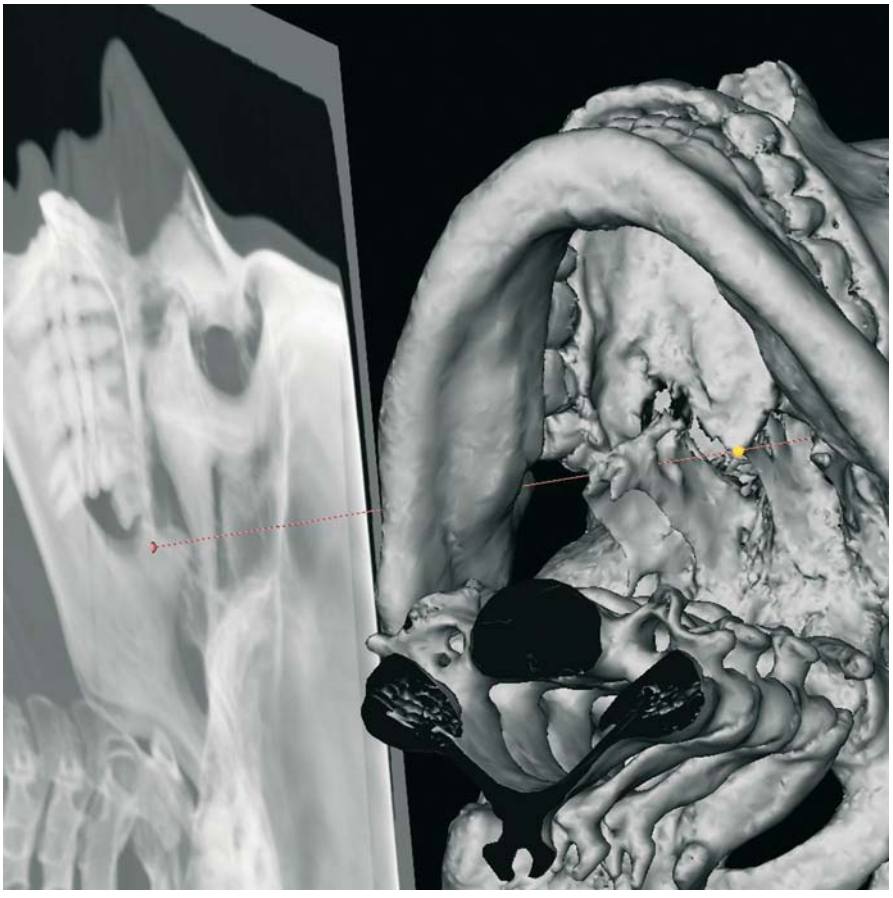

Fig. 4.23. Posterior Nasal Spine. Virtual lateral cephalogram linked to the 3-D hard tissue surface representation (3-D CT, patient K.C.)

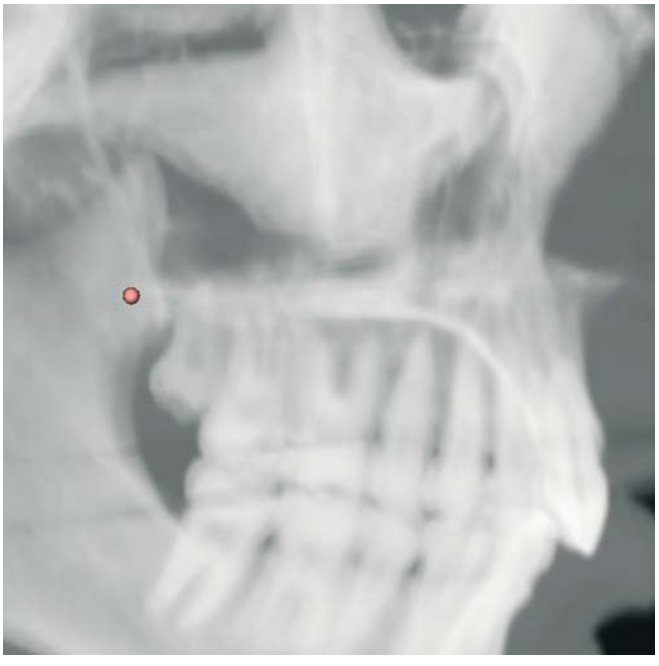

Fig. 4.24. Posterior Nasal Spine. Virtual lateral cephalogram (3-D CT, patient K.C.)

Posterior Maxillary Point: PMP_r – PMP_l

Definition of the Posterior Maxillary Point Landmarks

Posterior Maxillary Point is the point of maximum concavity of the posterior border of the palatine bone in the horizontal plane at both sides.

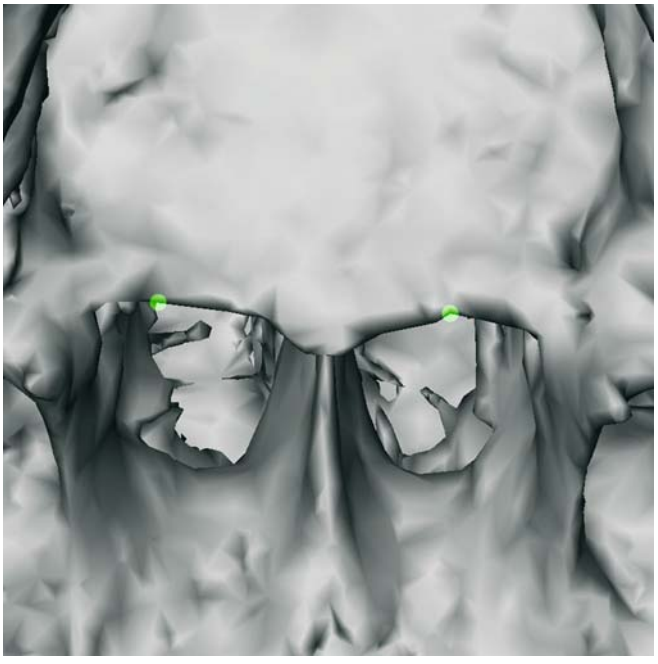

Fig. 4.25. Posterior Maxillary Point (PMP_r-PMP_l) landmarks. Exocranial skull base view (cadaver skull)

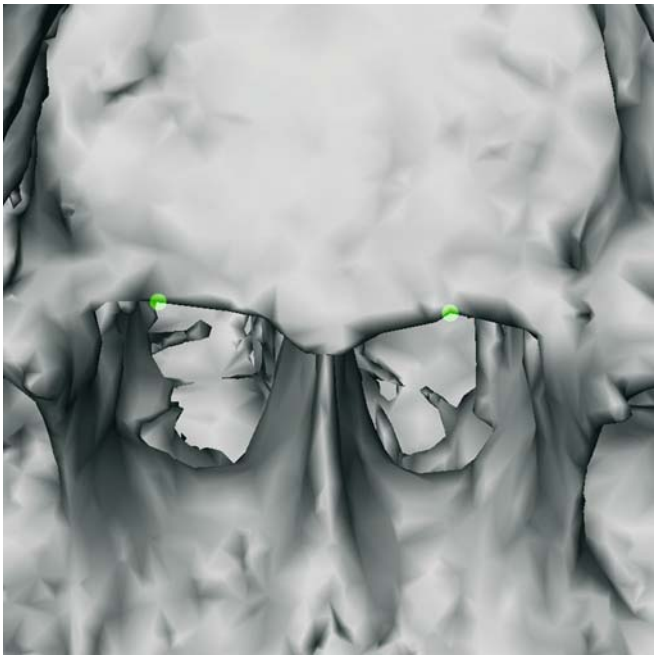

Fig. 4.26. Posterior Maxillary Point (PMP_r – PMP_l) landmarks. Exocranial skull base view (3-D CT, cadaver skull)

Virtual Definition of the Posterior Maxillary Point Landmarks

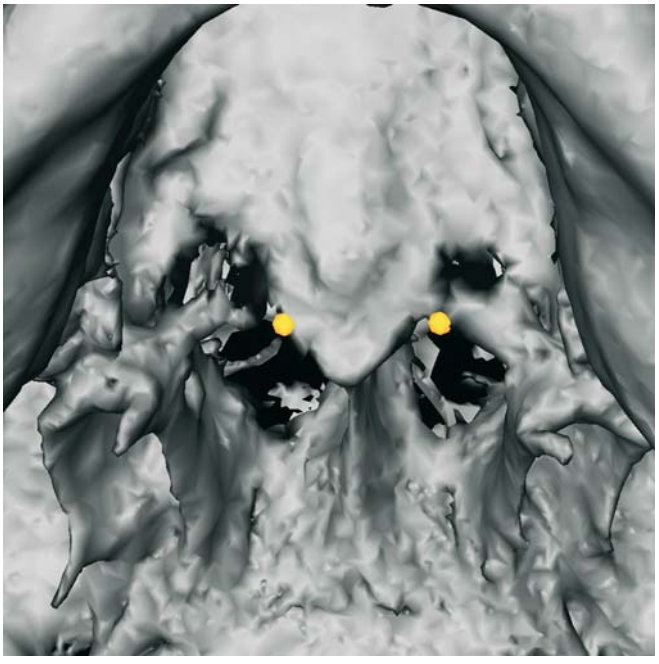

Fig. 4.27. Posterior Maxillary Point (PMP_r – PMP_l) landmarks. Exocranial skull base view (3-D CT, patient K.C.)

Step 1: Define Posterior Maxillary $Point_r$ and Posterior Maxillary $Point_l$ on the exocranial skull base view of the 3-D hard tissue surface representation (Fig. 4.27).

Step 2: Verify the vertical position of Posterior Maxillary $Point_r$ and Posterior Maxillary $Point_l$ on the virtual frontal cephalogram which is linked to the 3-D hard tissue surface representation (Figs. 4.28, 4.29).

Fig. 4.28. Posterior Maxillary Point (PMP_r – PMP_l) landmarks. Virtual frontal cephalogram linked to the 3-D hard tissue surface representation (3-D CT, patient K.C.)

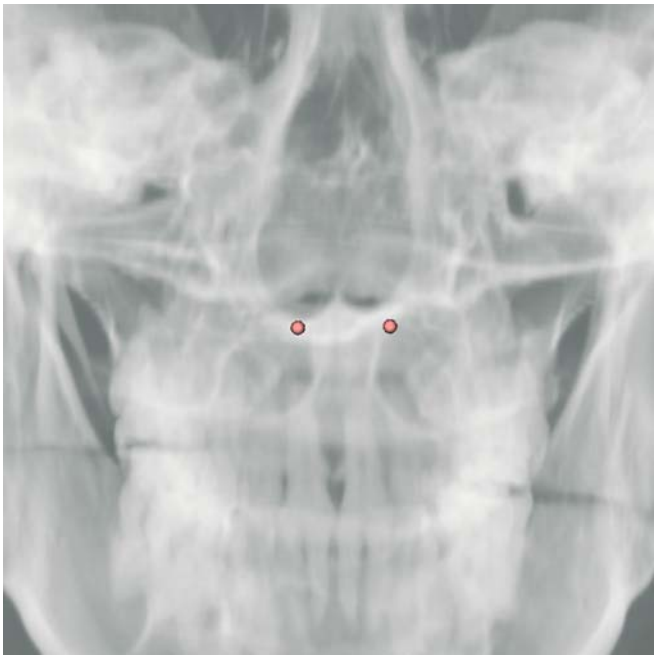

Fig. 4.29. Posterior Maxillary Point (PMP_r – PMP_l) landmarks. Virtual frontal cephalogram (3-D CT, patient K.C.)

Upper Incisor: UI_r – UI_l

Definition of the Upper Incisor Landmarks

Upper Incisor (UI) is the most mesial point of the tip of the crown of each upper central incisor.

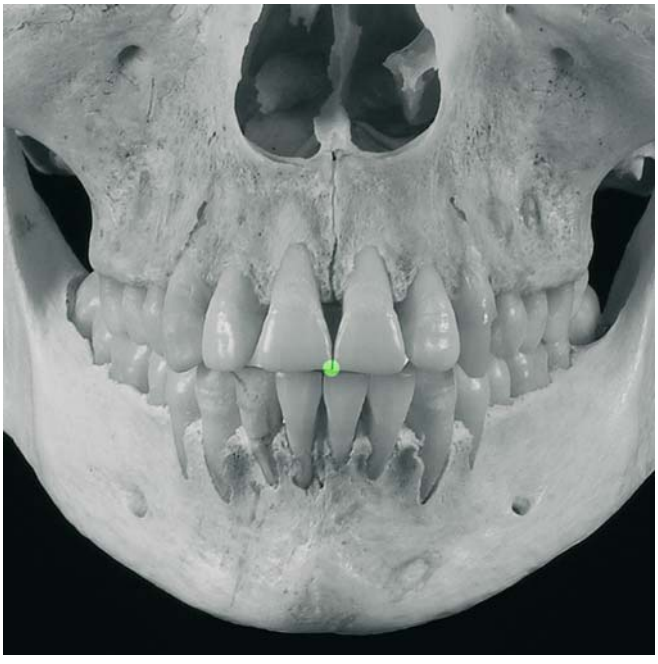

Fig. 4.30. Upper Incisor$_r$. Frontal view (cadaver skull)

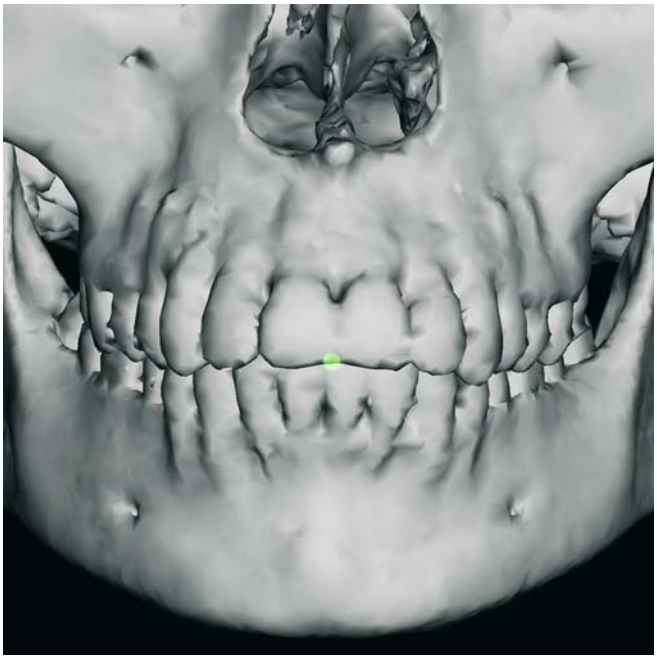

Fig. 4.31. Upper Incisor$_r$. Frontal view (3-D CT, cadaver skull)

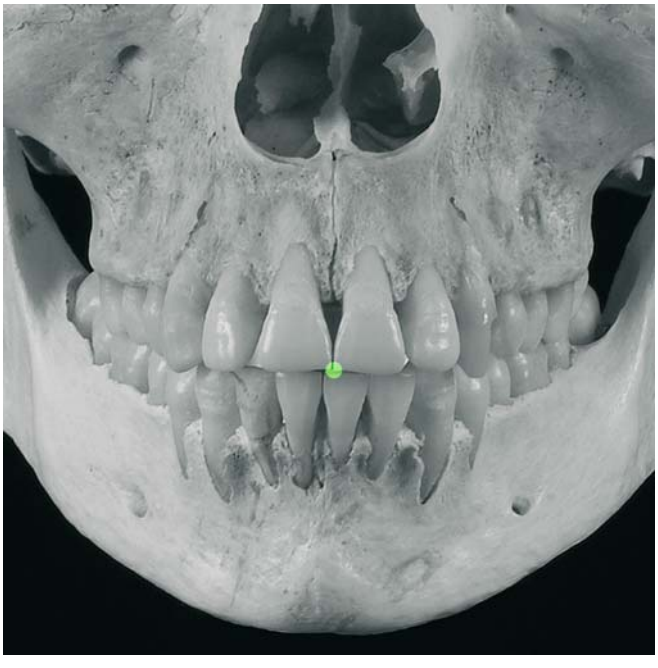

Fig. 4.32. Upper Incisor$_l$. Frontal view (cadaver skull)

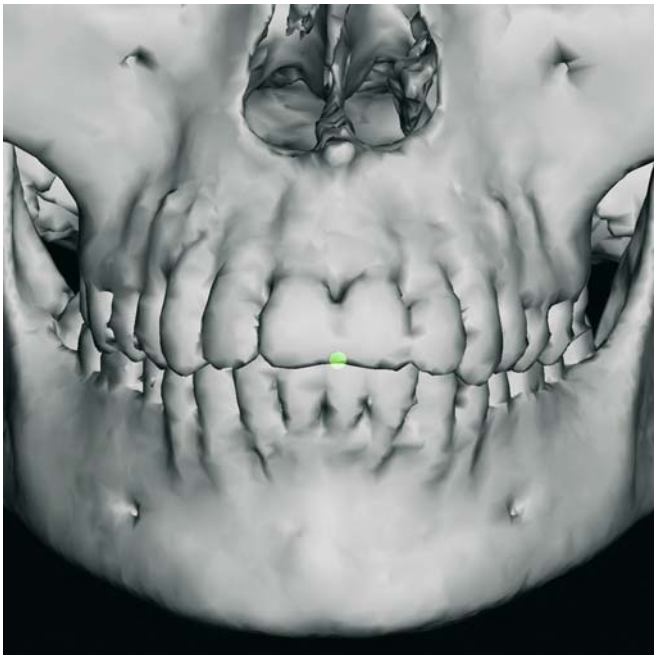

Fig. 4.33. Upper Incisor$_l$. Frontal view (3-D CT, cadaver skull)

Virtual Definition of the Upper Incisor Landmarks

Step 1: Define Upper Incisor$_r$ and Upper Incisor$_l$ on the frontal view of the 3-D hard tissue surface representation (Figs. 4.34–4.36).

Step 2: Verify the position of Upper Incisor$_r$ and Upper Incisor$_l$ on the virtual lateral (Figs. 4.37, 4.38) and frontal (Fig. 4.39) cephalograms which are linked to the 3-D hard tissue surface representation.

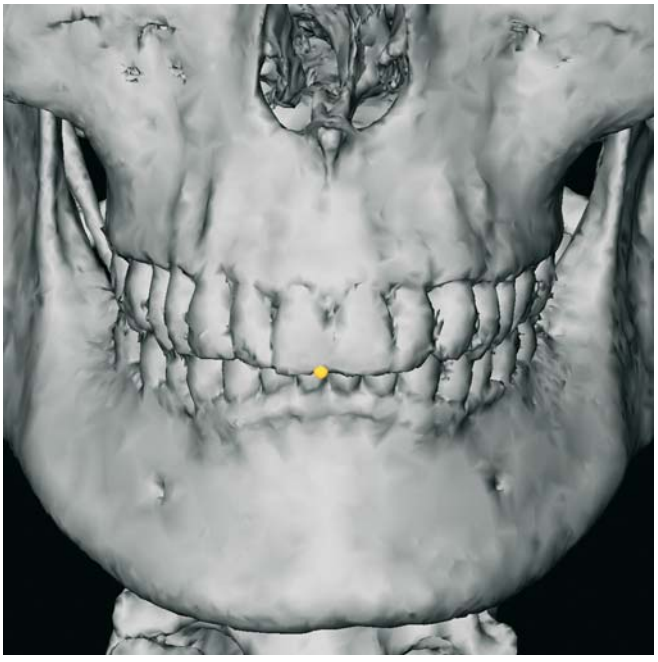

Fig. 4.34. Upper Incisor$_r$. Frontal view (3-D CT, patient K.C.)

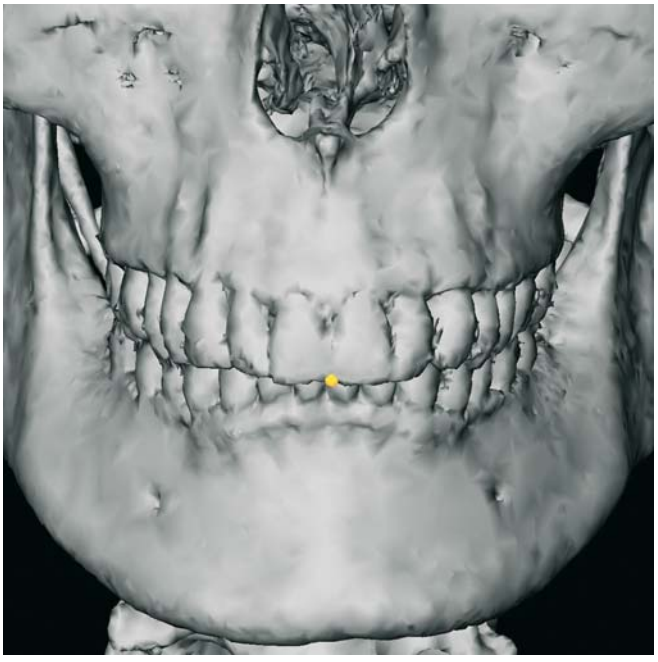

Fig. 4.35. Upper Incisor$_l$. Frontal view (3-D CT, patient K.C.)

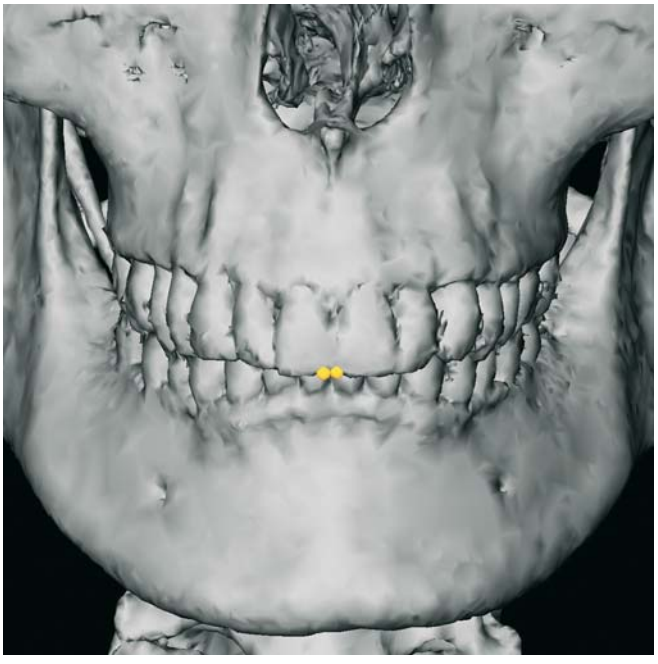

Fig. 4.36. Upper Incisor$_r$. and Upper Incisor$_l$. Frontal view (3-D CT, patient K.C.)

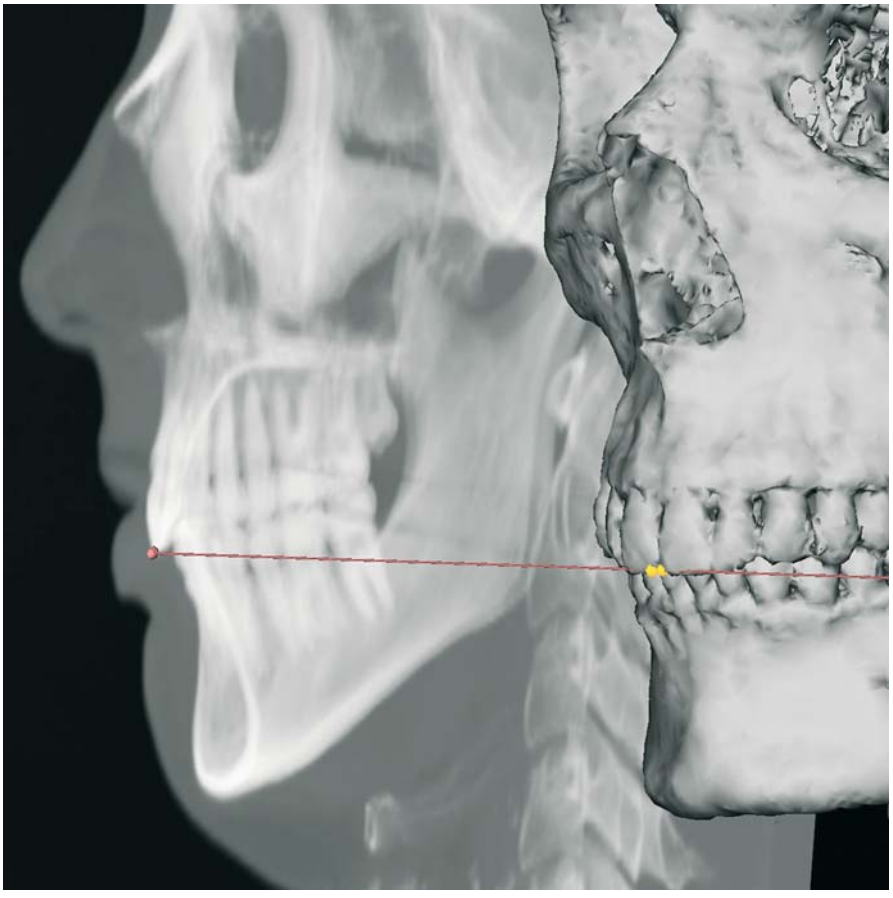

Fig. 4.37. Upper Incisor (UI_r – UI_l) landmarks. Virtual lateral cephalogram linked to the 3-D hard tissue surface representation (3-D CT, patient K.C.)

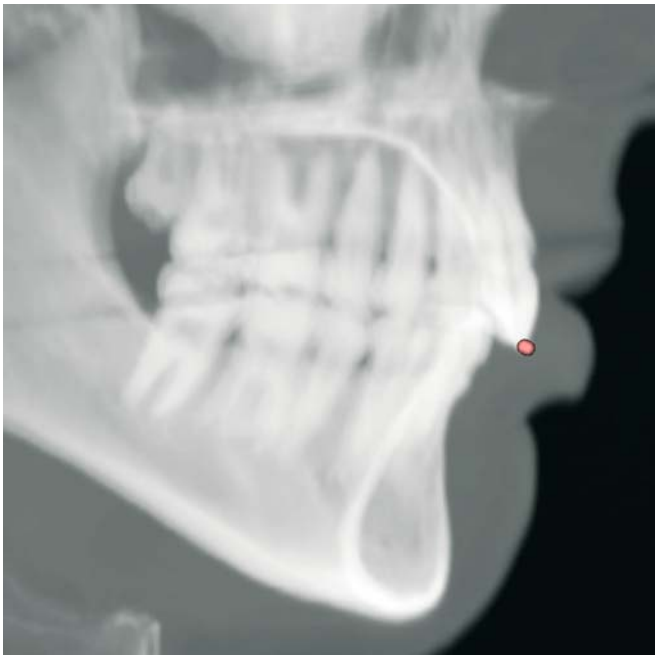

Fig. 4.38. Upper Incisor (UI_r – UI_l) landmarks. Virtual lateral cephalogram (3-D CT, patient K.C.)

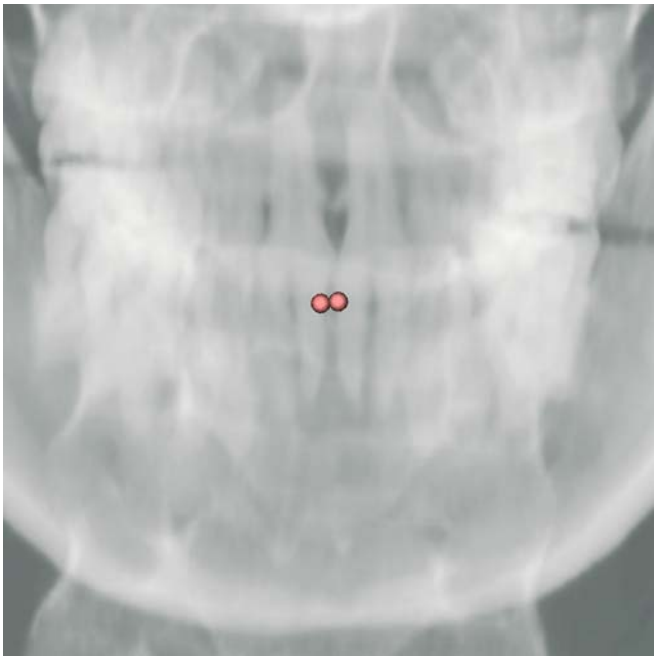

Fig. 4.39. Upper Incisor (UI_r – UI_l) landmarks. Virtual frontal cephalogram (3-D CT, patient K.C.)

Lower Incisor: LI_r – LI_l

Definition of the Lower Incisor Landmarks

Lower Incisor (LI) is the most mesial point of the tip of the crown of each lower central incisor.

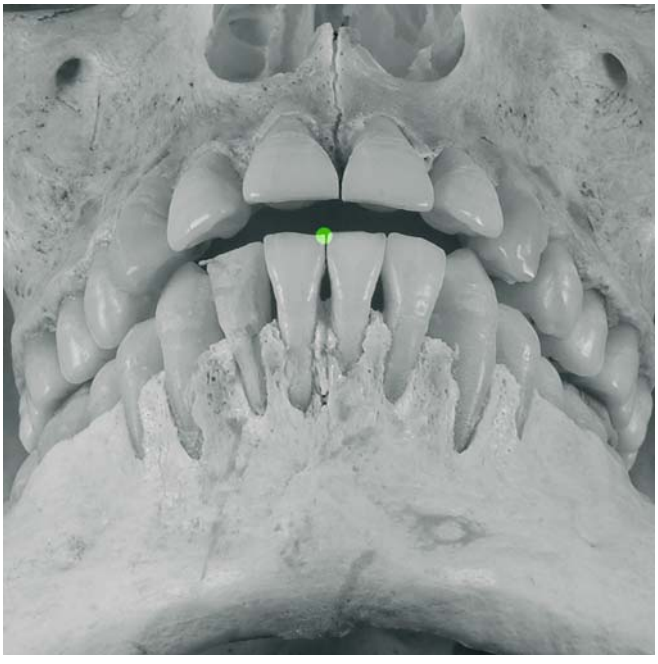

Fig. 4.40. Lower Incisor$_r$. Submental view (cadaver skull)

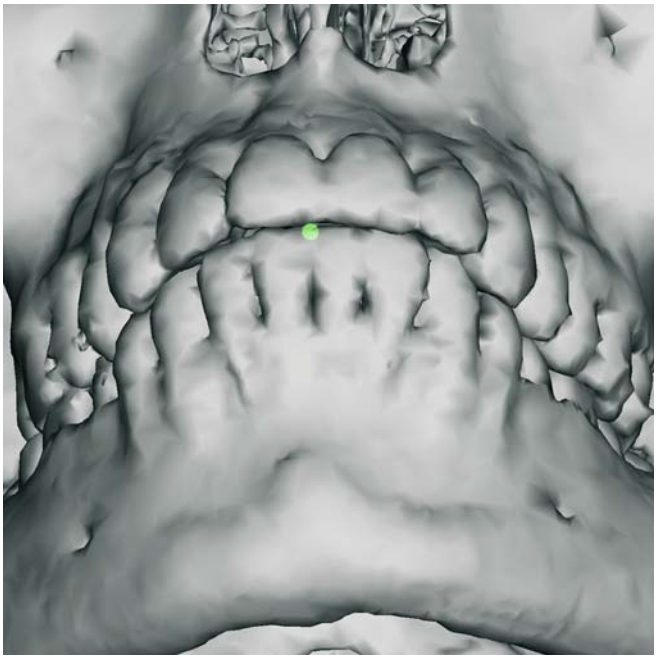

Fig. 4.41. Lower Incisor$_r$. Submental view (3-D CT, cadaver skull)

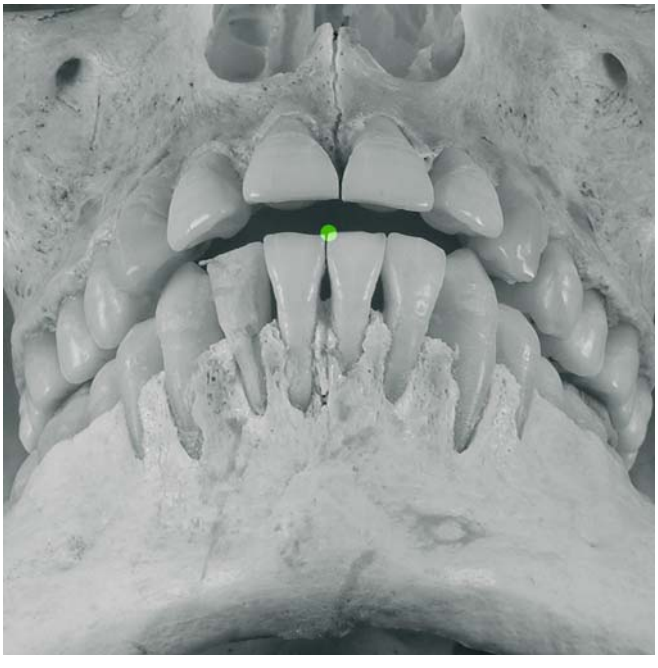

Fig. 4.42. Lower Incisor$_l$. Submental view (cadaver skull)

Fig. 4.43. Lower Incisor$_l$. Submental view (3-D CT, cadaver skull)

Virtual Definition of the Lower Incisor Landmarks

Step 1: Define Lower Incisor$_r$ and Lower Incisor$_l$ on the submental view of the 3-D hard tissue surface representation (Figs. 4.44–4.46)

Step 2: Verify the position of Lower Incisor$_r$ and Lower Incisor$_l$ on the virtual lateral (Figs. 4.47, 4.48) and frontal (Fig. 4.49) cephalograms which are linked to the 3-D hard tissue surface representation.

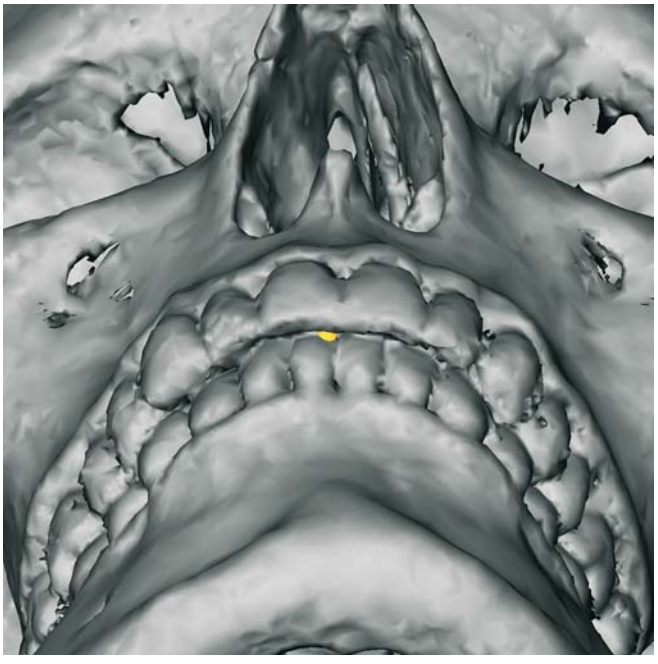

Fig. 4.44. Lower Incisor$_r$. Submental view (3-D CT, patient K.C.)

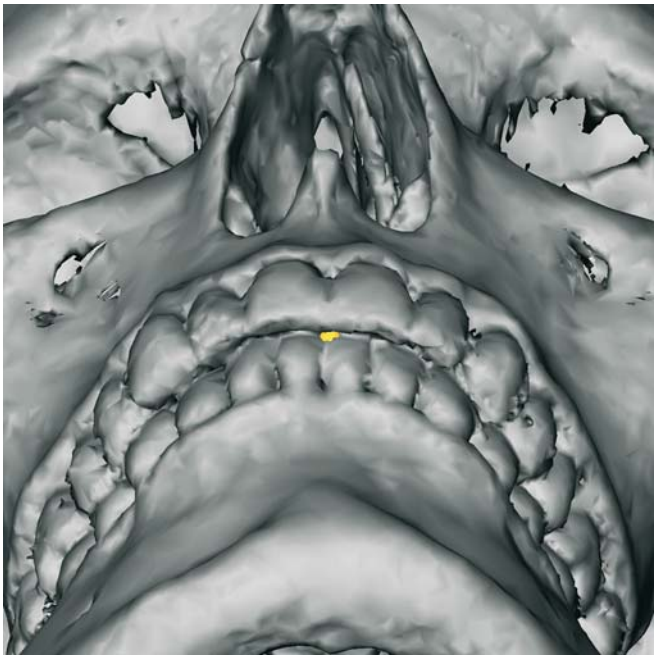

Fig. 4.45. Lower Incisor$_l$. Submental view (3-D CT, patient K.C.)

Fig. 4.46. Lower Incisor$_r$. and Lower Incisor$_l$ landmarks. Submental view (3-D CT, patient K.C.)

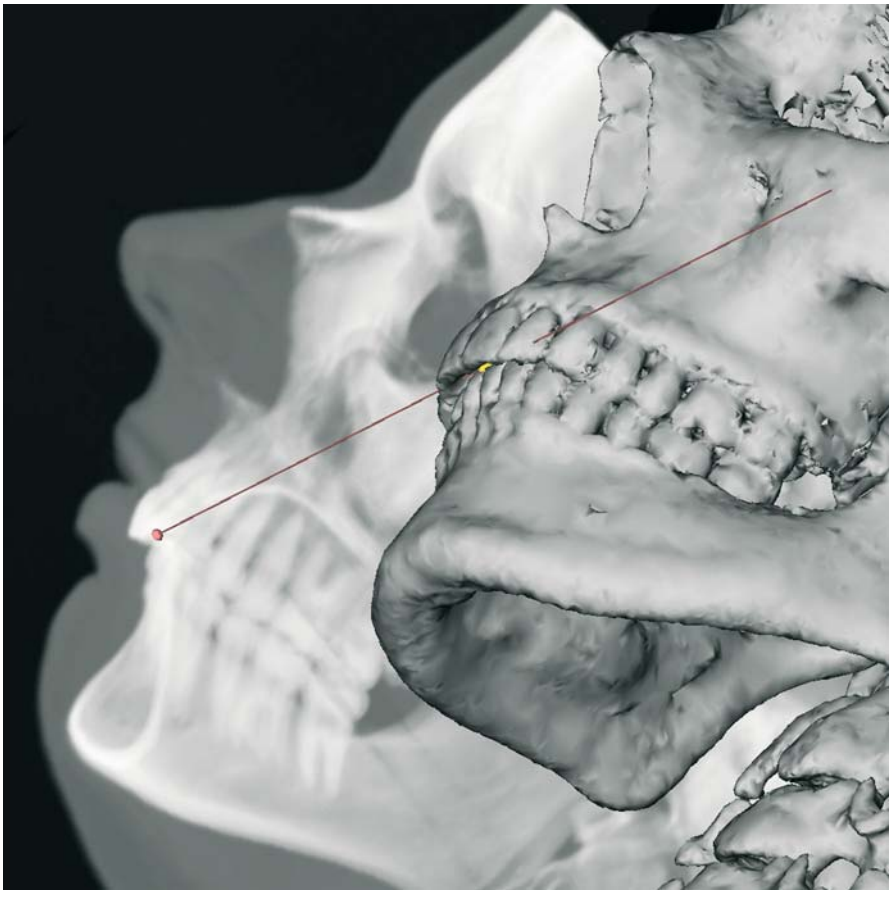

Fig. 4.47. Lower Incisor (LI_r – LI_l) landmarks. Virtual lateral cephalogram linked to the 3-D hard tissue surface representation (3-D CT, patient K.C.)

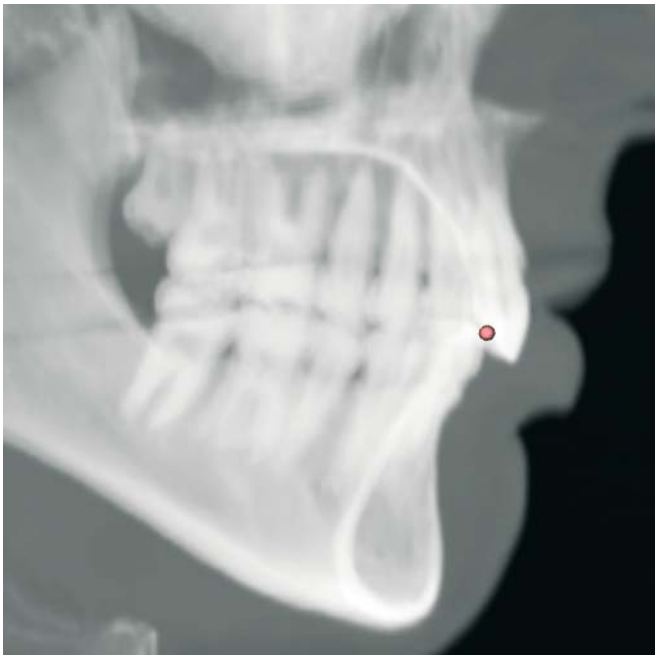

Fig. 4.48. Lower Incisor (LI_r – LI_l) landmarks. Virtual lateral cephalogram (3-D CT, patient K.C.)

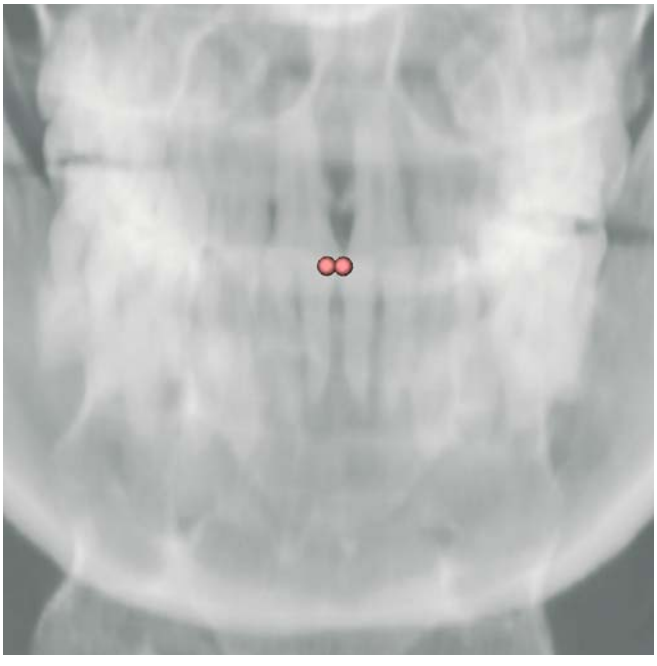

Fig. 4.49. Lower Incisor (LI_r – LI_l) landmarks. Virtual frontal cephalogram (3-D CT, patient K.C.)

Upper Molar Cusp: $UMcusp_r$ – $UMcusp_l$

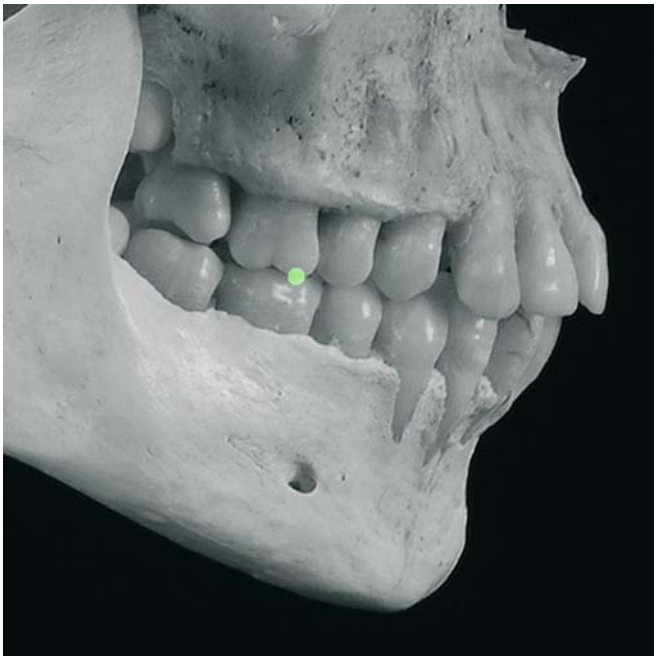

Fig. 4.50. Upper Molar $Cusp_r$. Profile view right (cadaver skull)

Fig. 4.51. Upper Molar $Cusp_r$. Profile view right (3-D CT, cadaver skull)

Definition of the Upper Molar Cusp Landmarks

Upper Molar cusp (UMcusp) is the most inferior point of the mesial cusp of the crown of each first upper molar in the profile plane.

Virtual Definition of the Upper Molar Cusp Landmarks

Step 1: Define Upper Molar $Cusp_r$ and Upper Molar $Cusp_l$ on the profile views of the 3-D hard tissue surface representation (Fig. 4.52, 4.53).

Step 2: Verify the position of Upper Molar $Cusp_r$ and Upper Molar $Cusp_l$ on the virtual lateral (Fig. 4.54) cephalogram linked to the 3-D hard tissue surface representation.

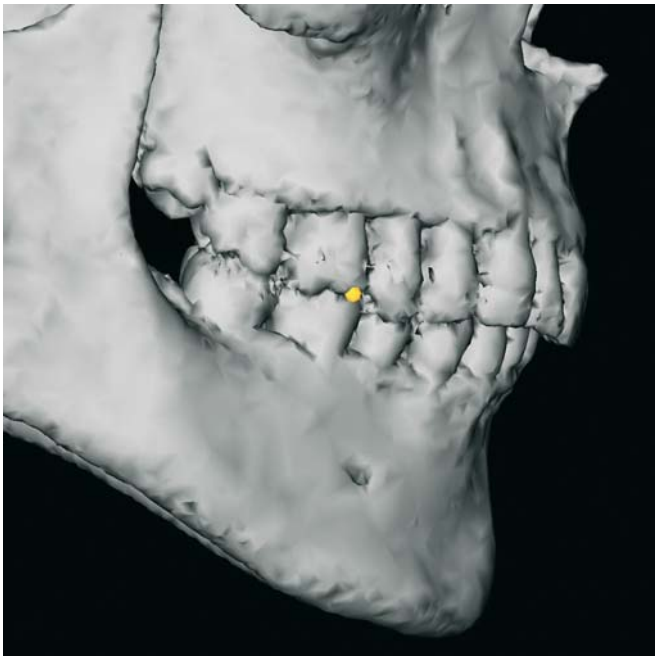

Fig. 4.52. Upper Molar Cusp$_r$. Profile view right (3-D CT, patient K.C)

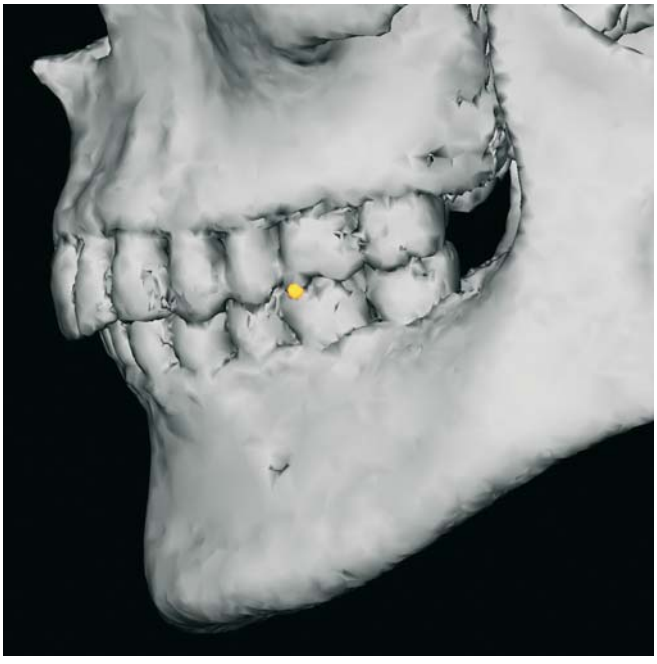

Fig. 4.53. Upper Molar Cusp$_l$. Profile view left (3-D CT, patient K.C.)

Fig. 4.54. Upper Molar Cusp$_r$. and Upper Molar Cusp$_l$. Virtual lateral cephalogram linked to the 3-D hard tissue surface representation (3-D CT, patient K.C.)

Lower Molar Cusp: $LMcusp_r$ – $LMcusp_l$

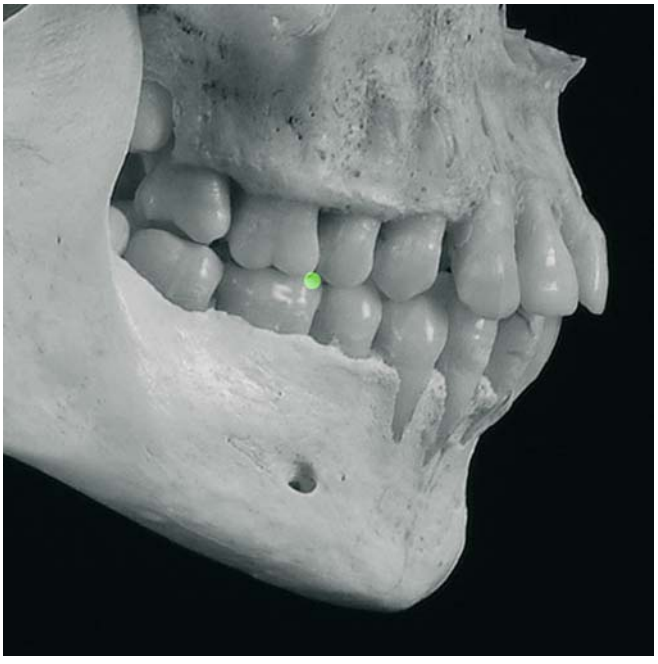

Fig. 4.55. Lower Molar $Cusp_r$. Profile view right (cadaver skull)

Fig. 4.56. Lower Molar $Cusp_r$. Profile view right (3-D CT, cadaver skull)

Definition of the Lower Molar Cusp Landmarks

Lower Molar Cusp (LMcusp) is the most superior point of the mesial cusp of the crown of each first lower molar in the profile plane.

Virtual Definition of the Lower Molar Cusp Landmarks

Step 1: Define Lower Molar $Cusp_r$ and Lower Molar $Cusp_l$ on the profile views of the 3-D hard tissue surface representation (Figs. 4.57, 4.58).

Step 2: Verify and correct the position of Lower Molar $Cusp_r$ and Lower Molar $Cusp_l$ on the virtual lateral (Fig. 4.59) cephalogram linked to the 3-D hard tissue surface representation.

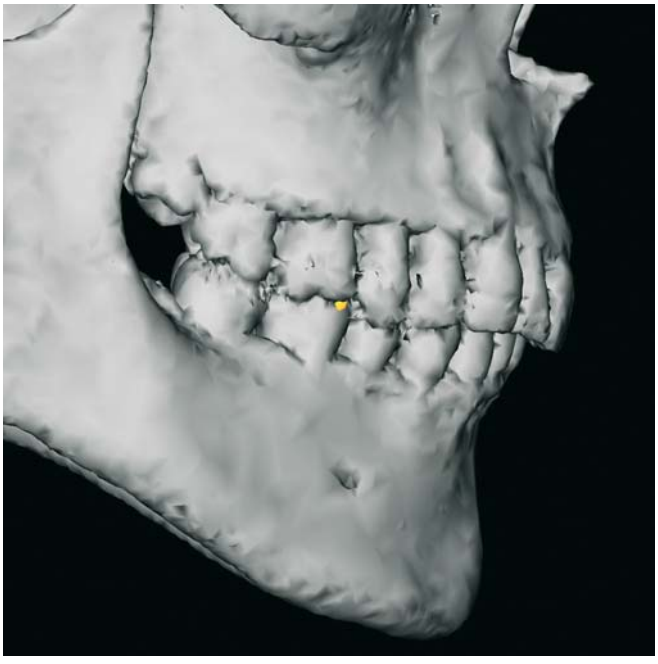

Fig. 4.57. Lower Molar Cusp$_r$. Profile view right (3-D CT, patient K.C.)

Fig. 4.58. Lower Molar Cusp$_l$. Profile view left (3-D CT, patient K.C.)

Fig. 4.59. Lower Molar Cusp$_r$. and Lower Molar Cusp$_l$. Virtual lateral cephalogram linked to the 3-D hard tissue surface representation (3-D CT, patient K.C.)

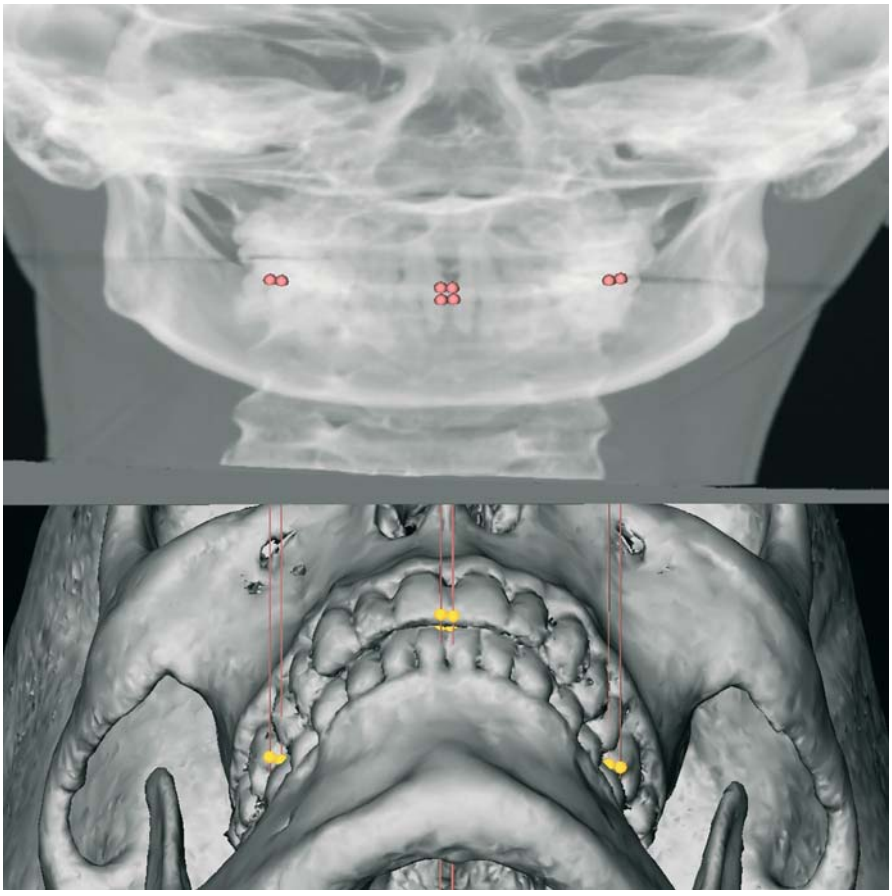

Fig. 4.60. Virtual frontal cephalogram linked to the 3-D hard tissue surface representation shows an overview of dental landmarks (3-D CT, patient K.C.)

Menton: Men

Definition of the Menton Landmark

Menton is the most inferior midpoint of the chin on the outline of the mandibular symphysis.

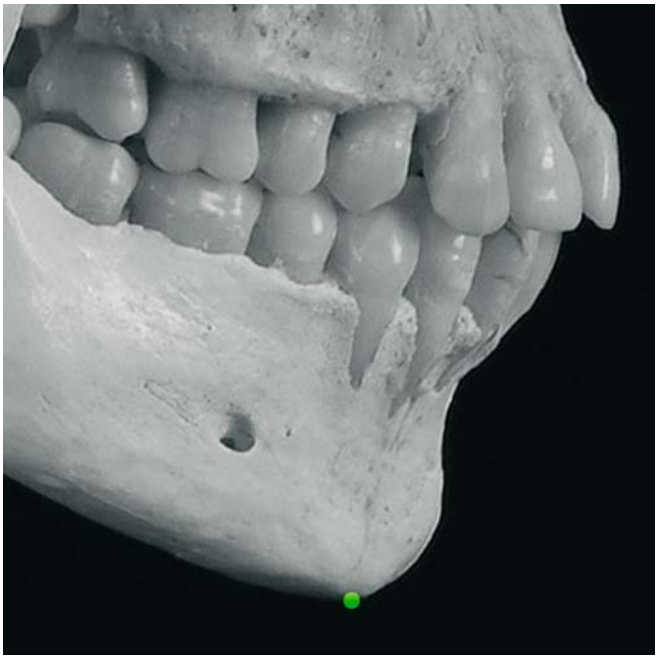

Fig. 4.61. Menton. Profile view right (cadaver skull)

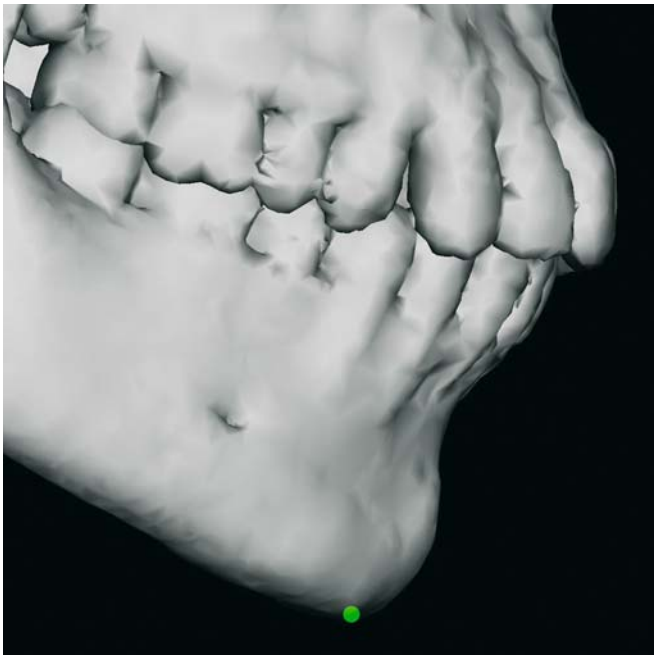

Fig. 4.62. Menton. Profile view right (3-D CT, cadaver skull)

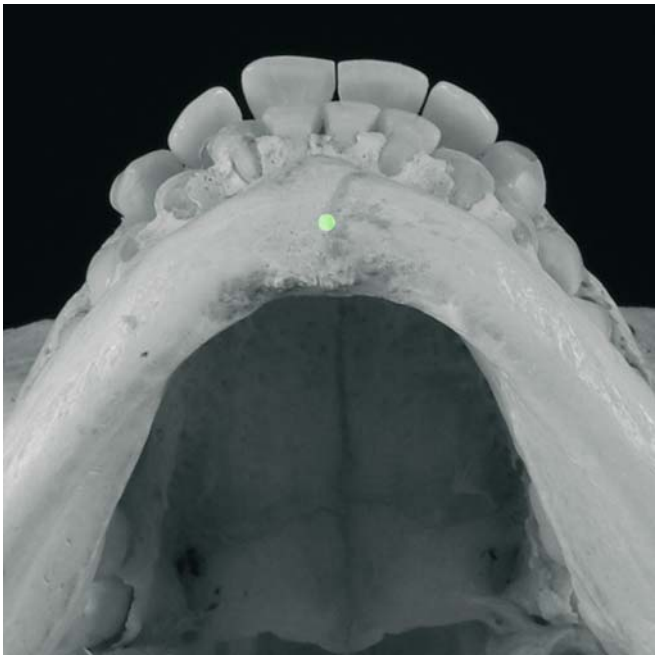

Fig. 4.63. Menton. Base view (cadaver skull)

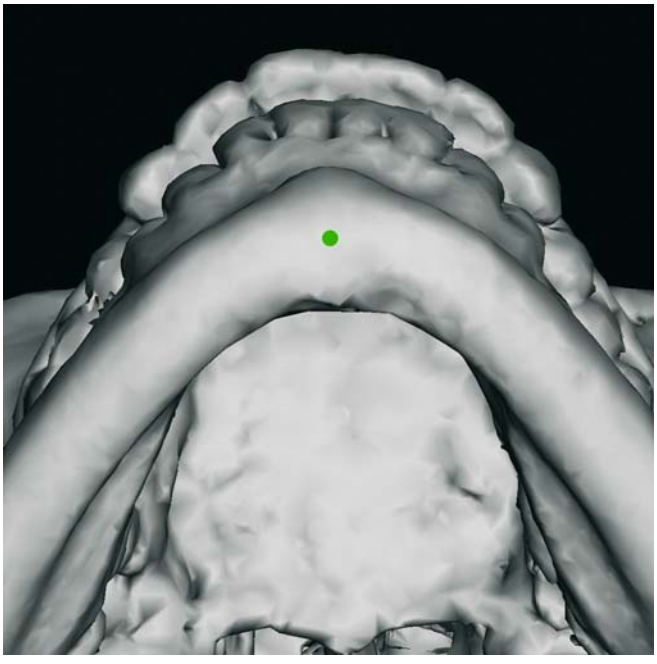

Fig. 4.64. Menton. Base view (3-D CT, cadaver skull)

Virtual Definition of the Menton Landmark

Step 1: Define Menton on the virtual lateral cephalogram (Figs. 4.65, 4.66).

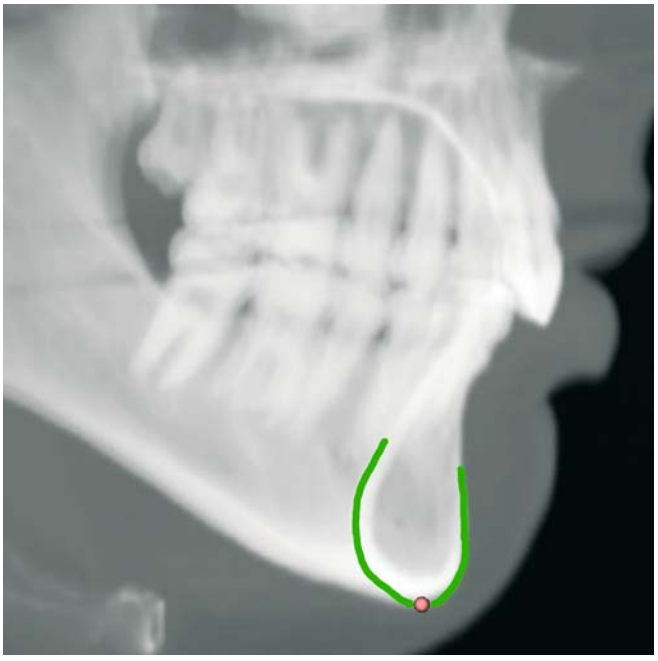

Fig. 4.65. Menton. Virtual lateral cephalogram (patient K.C.)

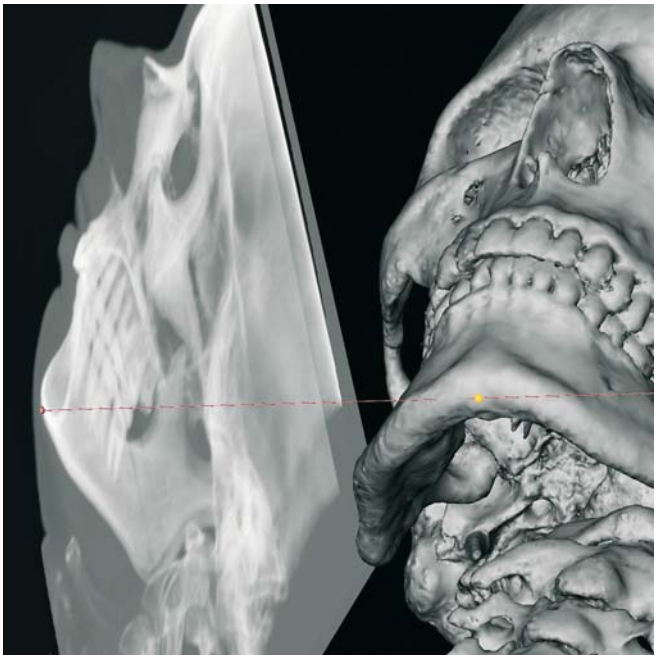

Fig. 4.66. Menton. Virtual lateral cephalogram linked to the 3-D hard tissue surface representation (patient K.C.)

Fig. 4.67. Menton. Profile view right (3-D CT, patient K.C.)

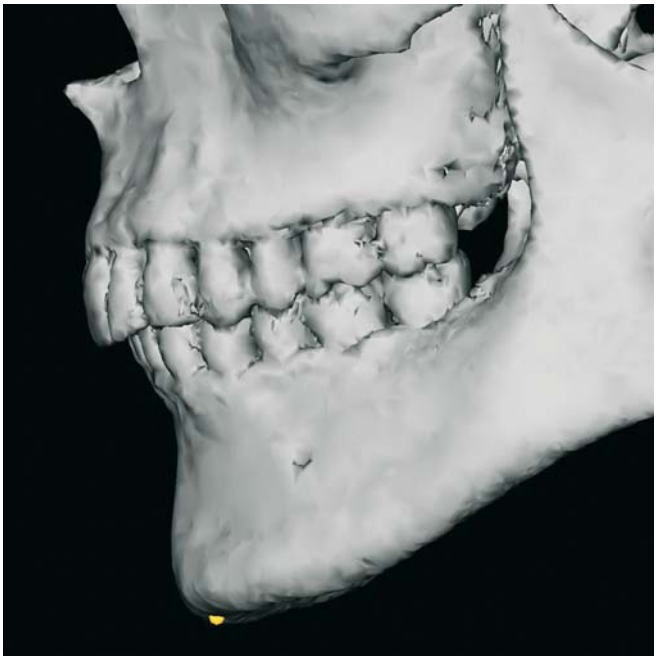

Fig. 4.68. Menton. Profile view left (3-D CT, patient K.C.)

Step 2: The position of Menton is verified on the right (Fig. 4.67) and left (Fig. 4.68) profile views of the 3-D hard tissue surface representations.

Step 3: Verify the midline position of Menton on the base view of the 3-D hard tissue surface representation (Fig. 4.69). Note that Menton is the skeletal midline point of the chin and can therefore be out of the midplane.

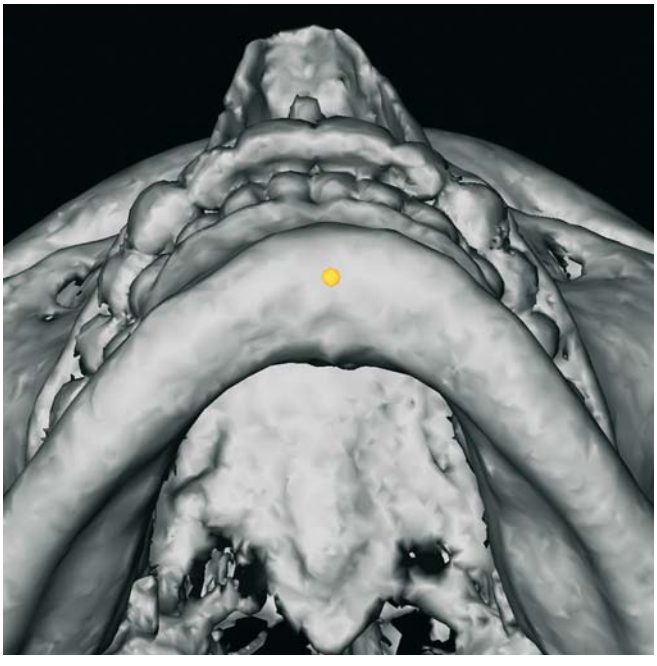

Fig. 4.69. Menton. Base view (3-D CT, patient K.C.)

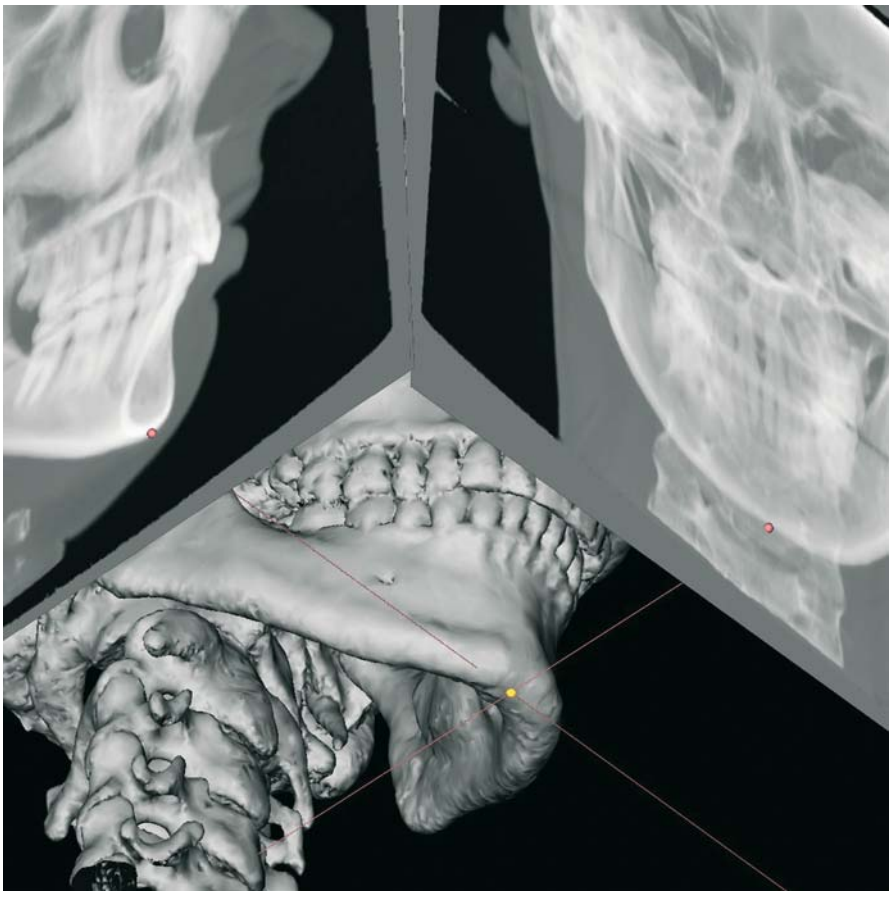

Fig. 4.70. Menton. Virtual lateral and frontal cephalograms linked to the 3-D hard tissue surface representation (3-D CT, patient K.C.)

Gonion: Go_r – Go_l

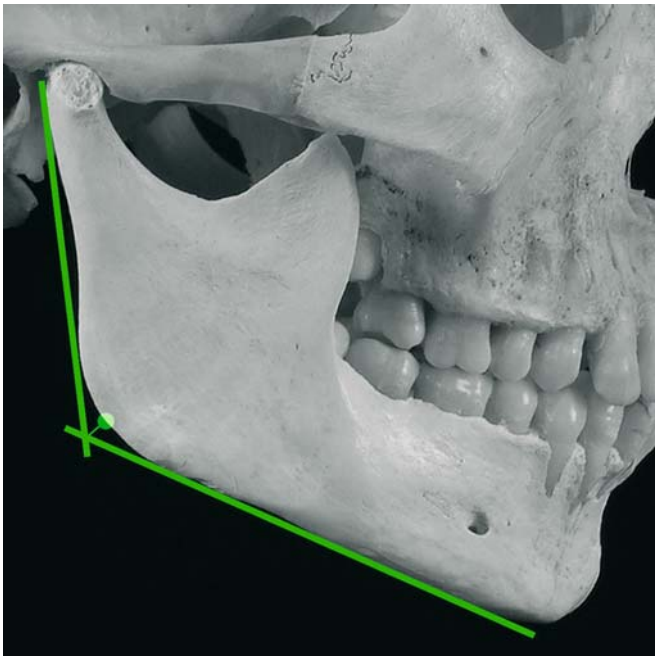

Fig. 4.71. $Gonion_r$. Profile view right (cadaver skull)

Fig. 4.72. $Gonion_r$. Profile view right (3-D CT, cadaver skull)

Definition of the Gonion Landmarks

Gonion (Go) is the point at each mandibular angle that is defined by dropping a perpendicular from the intersection point of the tangent lines to the posterior margin of the mandibular vertical ramus and inferior margin of the mandibular body or horizontal ramus.

Virtual Definition of the Gonion Landmarks

Step 1: Define $Gonion_r$ and $Gonion_l$ on the right (Fig. 4.73) and left (Fig. 4.74) profile views of the 3-D hard tissue surface representation.

Step 2: Verify the correct transversal position of $Gonion_r$ and $Gonion_l$ on the base view (Fig. 4.75) of the 3-D hard tissue surface representation.

Fig. 4.73. Gonion$_r$. Profile view right (3-D CT, patient K.C.)

Fig. 4.74. Gonion$_l$. Profile view left (3-D CT, patient K.C.)

Fig. 4.75. Gonion$_r$ and Gonion$_l$. Caudal view (3-D CT, patient K.C.)

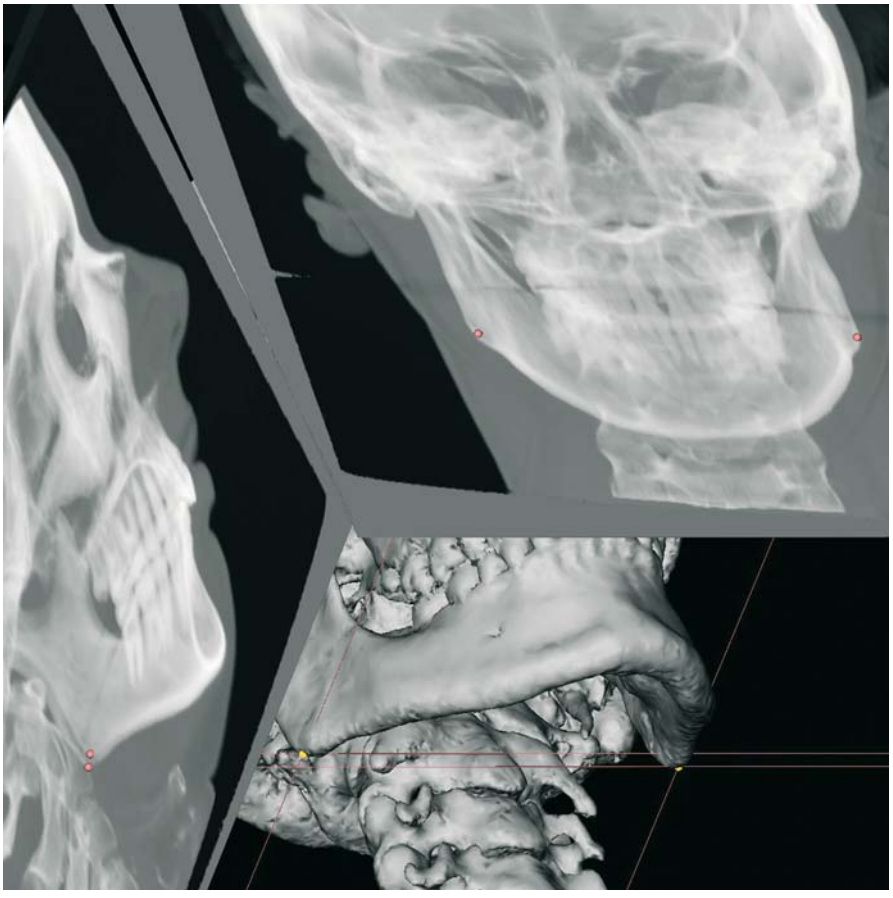

Fig. 4.76. $Gonion_r$ and $Gonion_l$. Virtual lateral and frontal cephalograms linked to the 3-D hard tissue surface representation (3-D CT, patient K.C.)

Frontozygomatic Point: Fz_r – Fz_l

Fig. 4.77. Frontozygomatic$_r$ and Frontozygomatic$_l$. Frontal view (cadaver skull)

Fig. 4.78. Frontozygomatic$_r$ and Frontozygomatic$_l$. Frontal view (3-D CT, cadaver skull)

Definition of the Frontozygomatic Landmarks

Frontozygomatic (Fz) is the most medial and anterior point of each frontozygomatic suture at the level of the lateral orbital rim

Virtual Definition of the Frontozygomatic Landmarks

Fig. 4.79. Frontozygomatic$_r$ and Frontozygomatic$_l$. Frontal view (3-D CT, patient K.C.)

Fig. 4.80. Frontozygomatic$_r$ and Frontozygomatic$_l$. Virtual frontal cephalogram (3-D CT, patient K.C.)

Step 1: Define Frontozygomatic$_r$ and Frontozygomatic$_l$ on the frontal view (Fig. 4.79) of the 3-D hard tissue surface representation.

Step 2: Verify the sagittal position of Frontozygomatic$_r$ and Frontozygomatic$_l$ on the virtual lateral cephalogram linked to the 3-D hard tissue surface representation (Fig. 4.81)

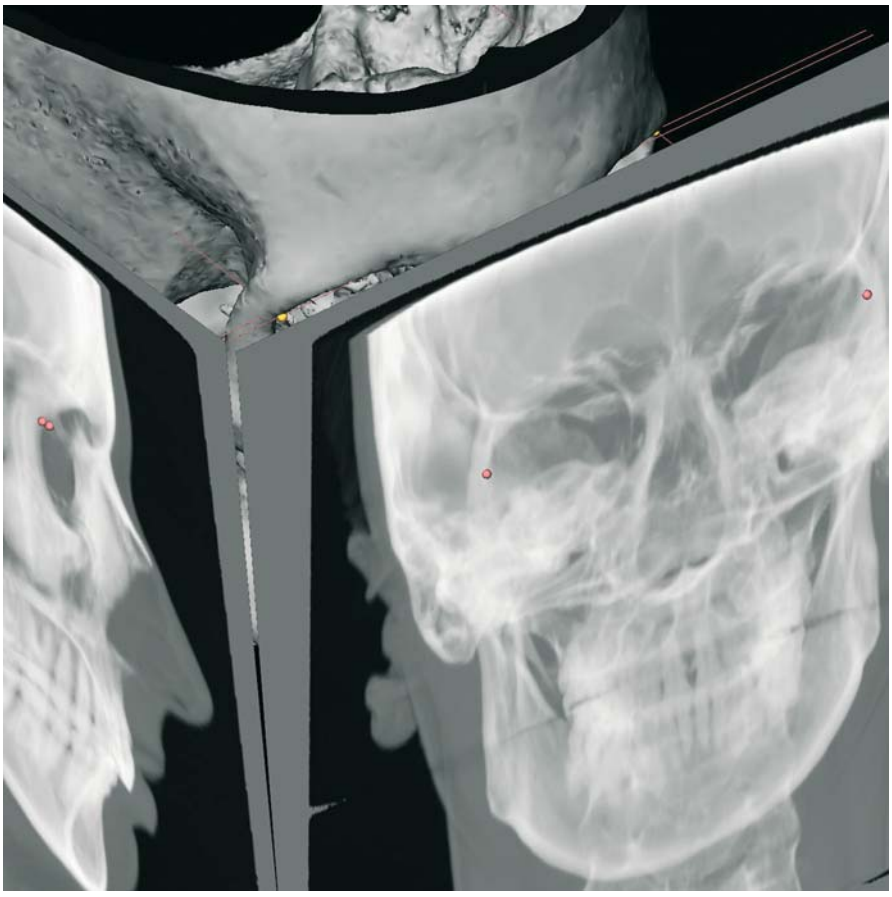

Fig. 4.81. Frontozygomatic$_r$ and Frontozygomatic$_l$. Virtual lateral and frontal cephalograms linked to the 3-D hard tissue representation (3-D CT, patient K.C.)

Zygion: Zy_r – Zy_l

Definition of the Zygion Landmarks

Zygion (Zy) is the most lateral point on the outline of each zygomatic arch.

Fig. 4.82. $Zygion_r$ and $Zygion_l$. Exocranial skull base view (cadaver skull)

Fig. 4.83. $Zygion_r$ and $Zygion_l$. Exocranial skull base view (3-D CT, cadaver skull)

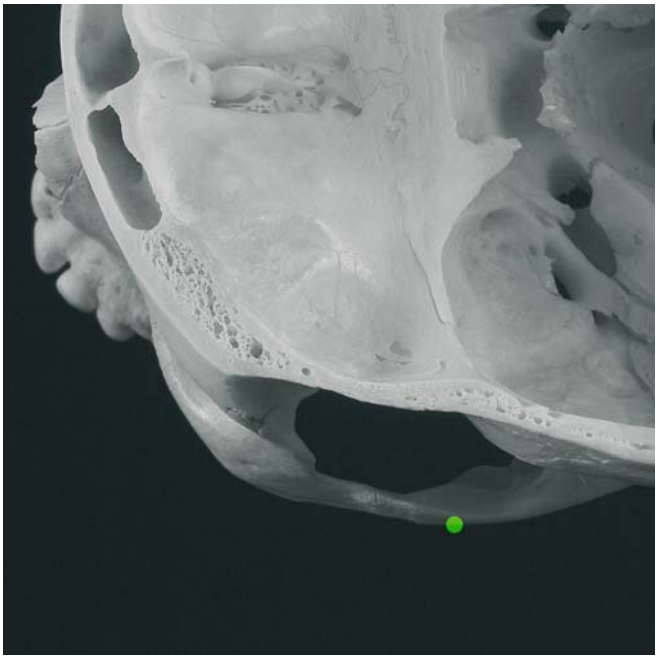

Fig. 4.84. $Zygion_l$. Close-up zygomatic arch, endocranial skull base view (cadaver skull)

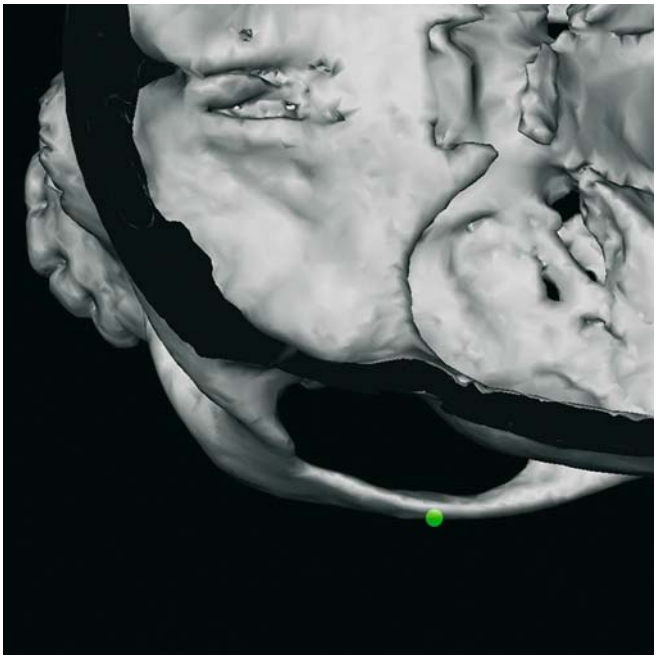

Fig. 4.85. $Zygion_l$. Close-up zygomatic arch, endocranial skull base view (3-D CT, cadaver skull)

Virtual Definition of the Zygion Landmarks

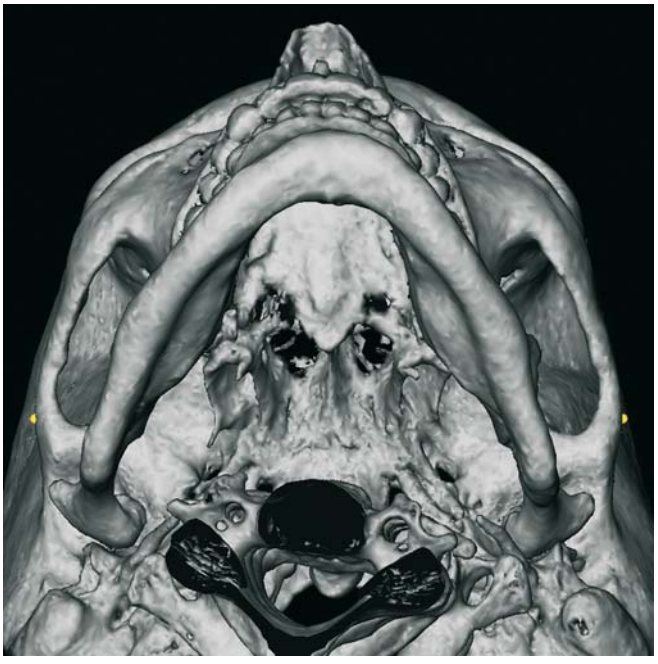

Fig. 4.86. $Zygion_r$ and $Zygion_l$. Exocranial skull base view (3-D CT, patient K.C.)

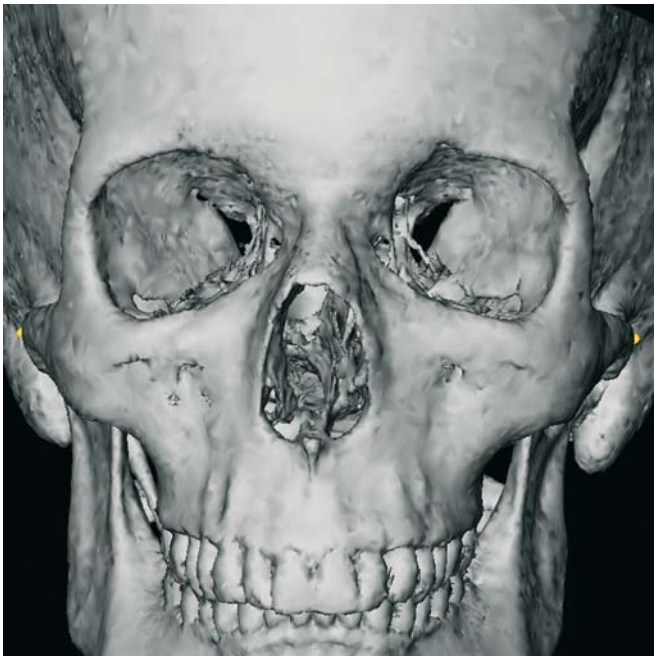

Fig. 4.87. $Zygion_r$ and $Zygion_l$. Frontal view (3-D CT, patient K.C.)

Step 1: Define $Zygion_r$ and $Zygion_l$ on the exocranial skull base view (Fig. 4.86) of the 3-D hard tissue surface representation. If marked amalgam artefacts are present (Fig. 4.90), Zygion can be defined on the endocranial skull base view by inclining medially until the complete zygomatic arch is visualized (Figs. 4.91, 4.92).

Step 2: Verify the vertical position of $Zygion_r$ and $Zygion_l$ on the frontal (Figs. 4.87, 4.93) and/or profile (Figs. 4.88, 4.89, 4.94, 4.95) views of the 3-D hard tissue surface representation.

Fig. 4.88. Zygion$_r$. Profile view right (3-D CT, patient K.C.)

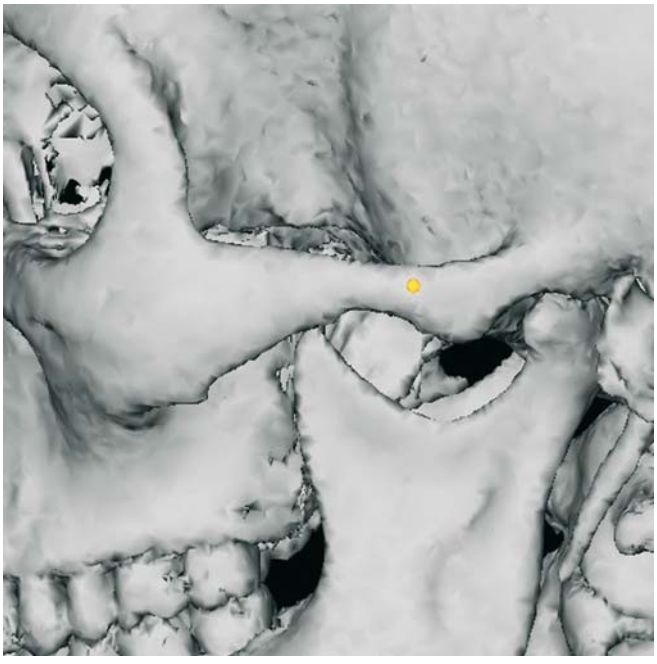

Fig. 4.89. Zygion$_l$. Profile view left (3-D CT, patient K.C.)

Fig. 4.90. Due to amalgam artefacts, definition of Zygion$_r$ and Zygion$_l$ landmarks is not possible on the exocranial skull base view (3-D CT, patient A.G.)

Fig. 4.91. $Zygion_r$. Close-up zygomatic arch, endocranial skull base view (3-D CT, patient A.G.)

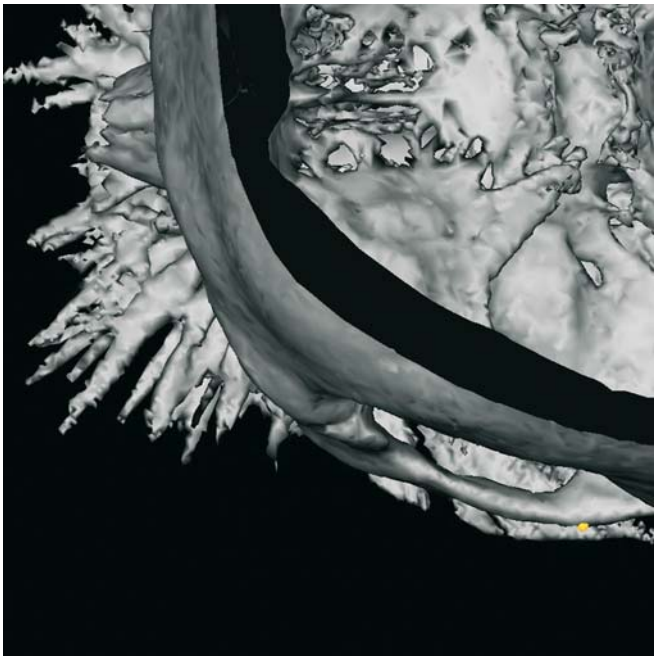

Fig. 4.92. $Zygion_l$. Close-up zygomatic arch, endocranial skull base view (3-D CT, patient A.G.)

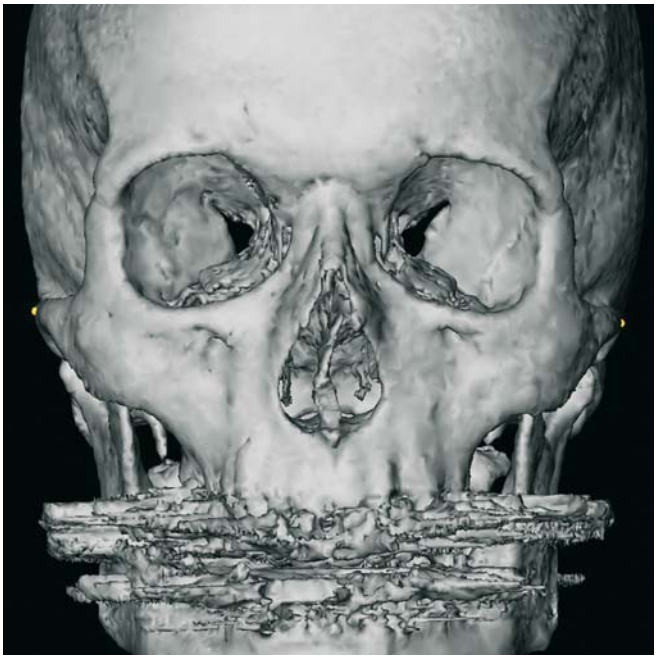

Fig. 4.93. $Zygion_r$ and $Zygion_l$. Frontal view (3-D CT, patient A.G.)

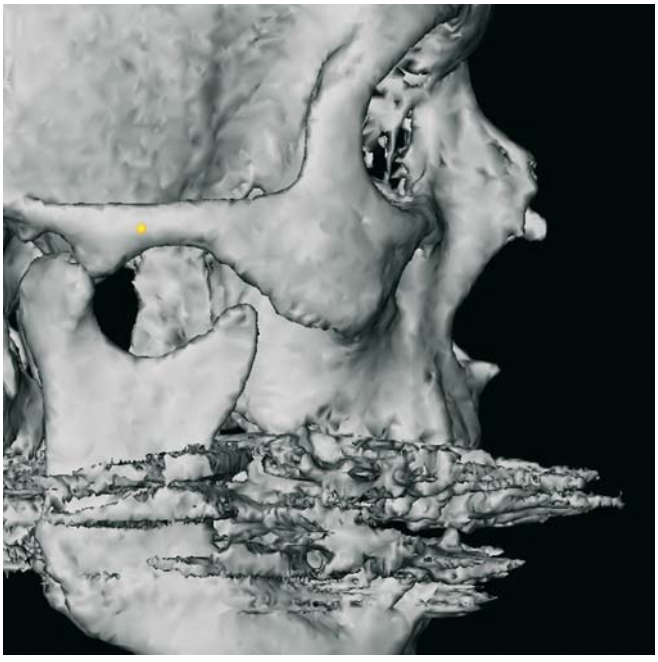

Fig. 4.94. $Zygion_r$. Profile view right (3-D CT, patient A.G.)

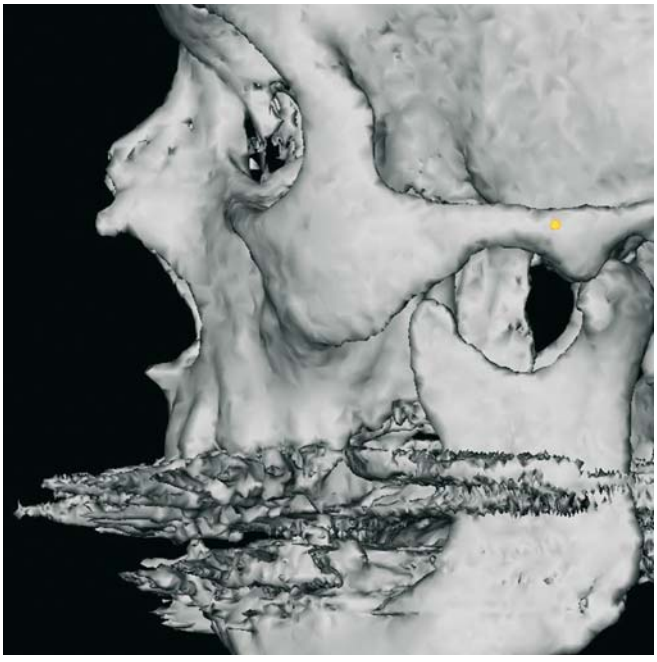

Fig. 4.95. $Zygion_l$. Profile view left (3-D CT, patient A.G.)

A-Point: A

Definition of the A-Point Landmark

A-Point is the point of maximum concavity in the midline of the alveolar process of the maxilla.

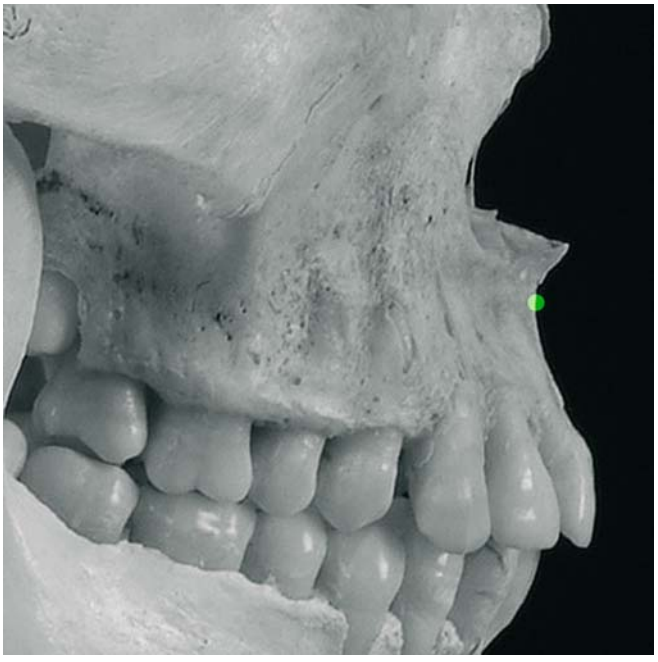

Fig. 4.96. A-Point. Profile view right (cadaver skull)

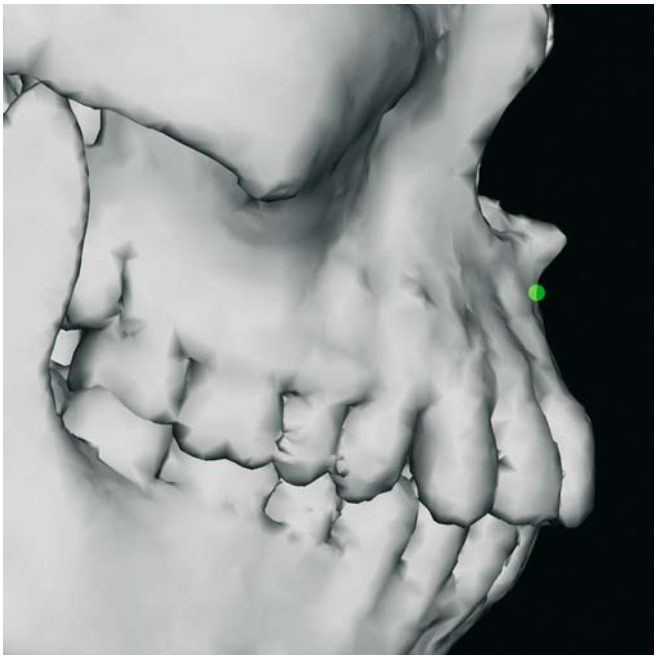

Fig. 4.97. A-Point. Profile view right. (3-D CT, cadaver skull)

Virtual definition of the A-Point Landmark

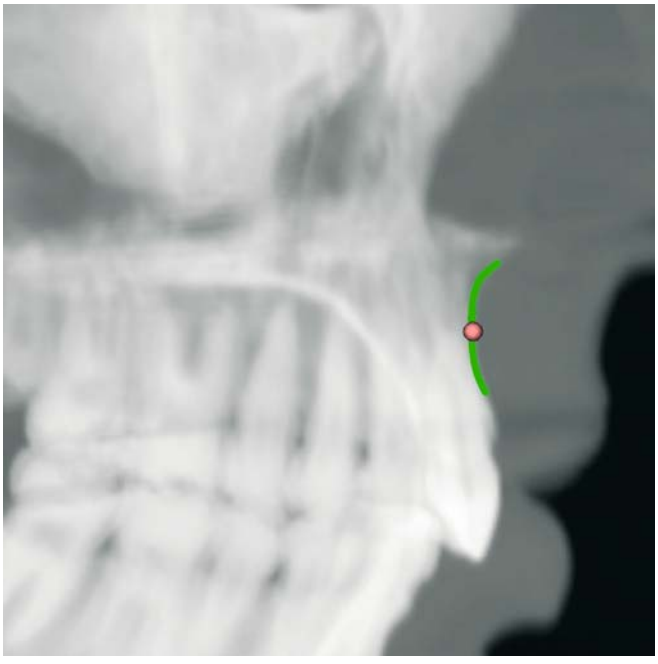

Fig. 4.98. A-Point. Virtual lateral cephalogram (patient K.C.)

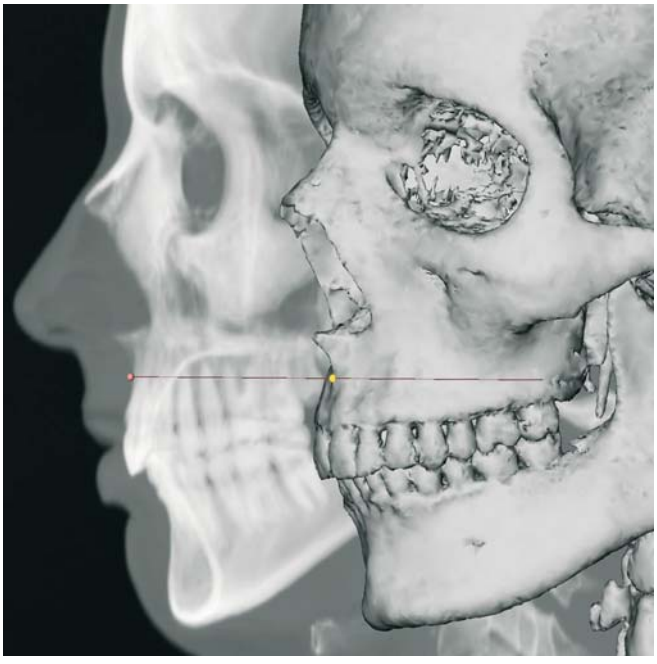

Fig. 4.99. A-Point. Virtual lateral cephalogram linked to the 3-D hard tissue surface representation (patient K.C.)

Step 1: Define A-Point on the virtual lateral cephalogram (Figs. 4.98, 4.99).

Step 2: The position of A-Point is verified on the right (Fig. 4.100) and left (Fig. 4.101) profile views of the 3-D hard tissue surface representations.

Step 3: Verify the midline position of A-Point on the maxillary dento-alveolar process on the frontal view of the 3-D hard tissue surface representation (Fig. 4.102). The virtual frontal cephalogram (Fig. 4.103, 4.104) is helpful to define the midline position of A-Point.

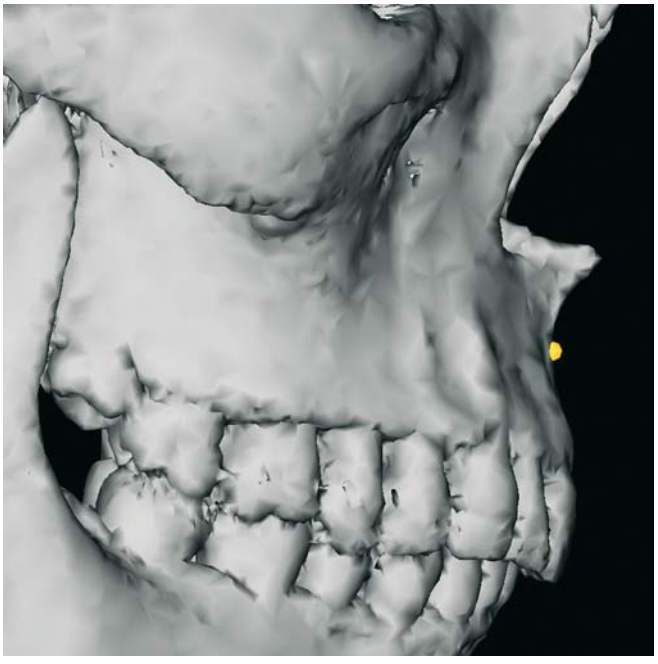

Fig. 4.100. A-Point. Profile view right (3-D CT, patient K.C.)

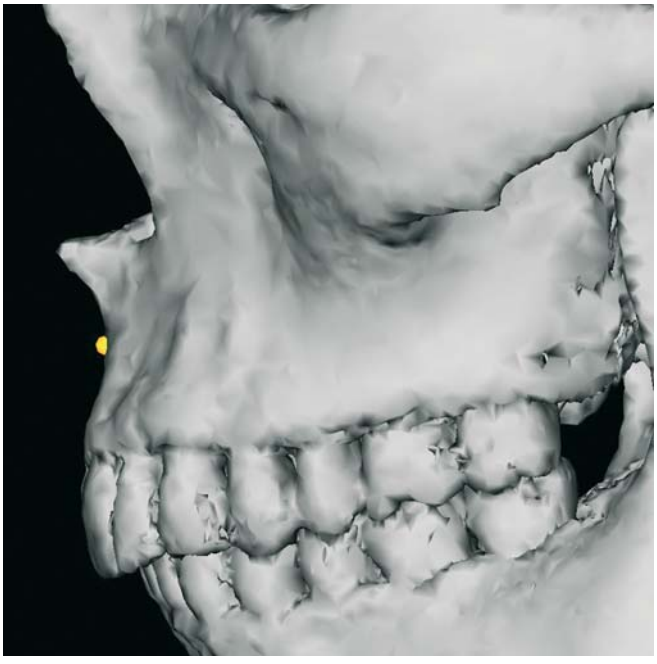

Fig. 4.101. A-Point. Profile view left (3-D CT, patient K.C.)

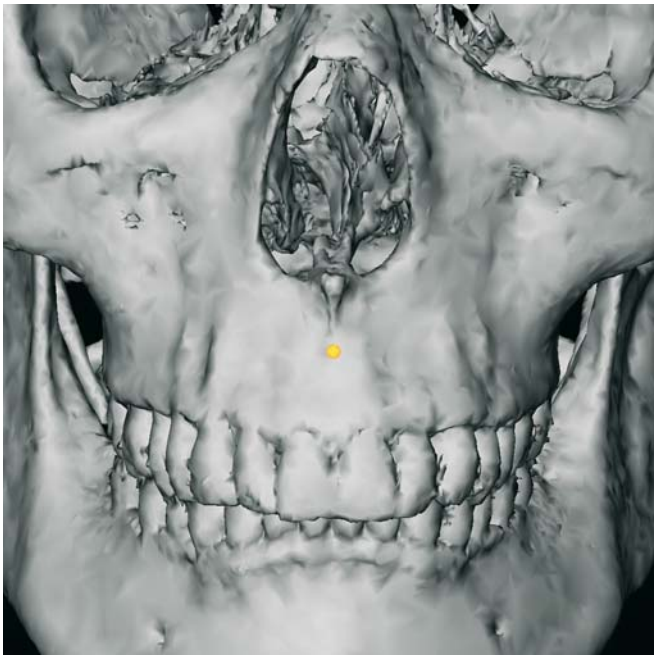

Fig. 4.102. A-Point. Frontal view (3-D CT, patient K.C.)

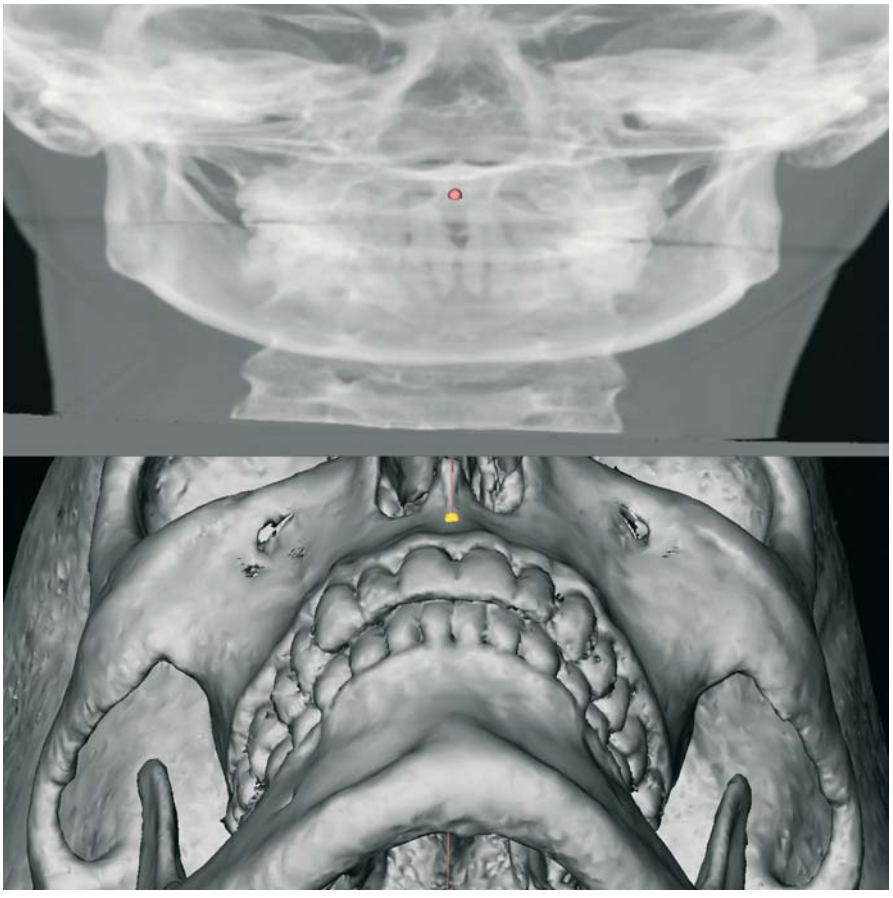

Fig. 4.103. A-Point. Virtual frontal cephalogram linked to the 3-D hard tissue surface representation (3-D CT, patient K.C.)

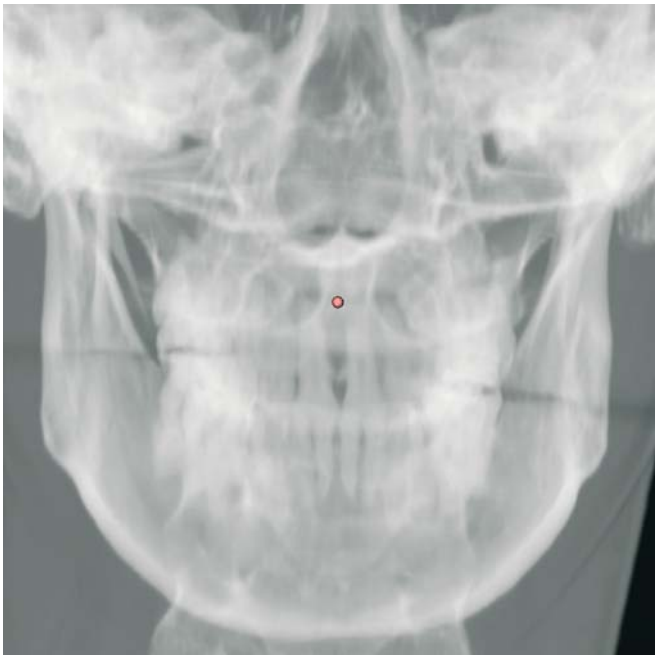

Fig. 4.104. A-Point. Virtual frontal cephalogram (patient K.C.)

B-Point: B

Definition of the B-Point Landmark

B-Point is the point of maximum concavity in the midline of the alveolar process of the mandible.

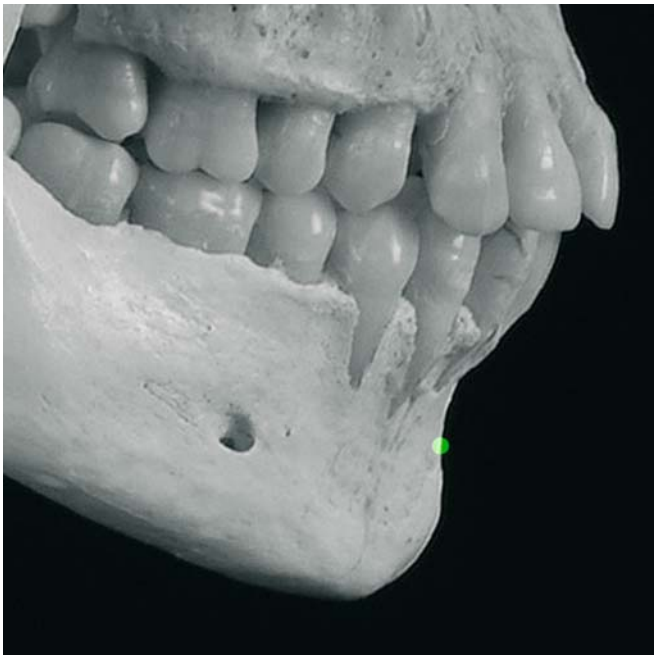

Fig. 4.105. B-Point. Profile view right (cadaver skull)

Fig. 4.106. B-Point. Profile view right. (3-D CT, cadaver skull)

Virtual Definition of the B-Point Landmark

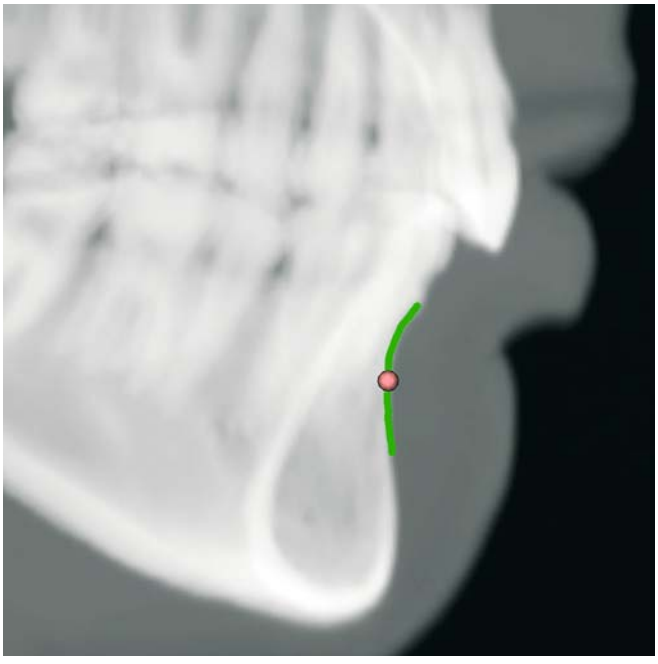

Fig. 4.107. B-Point. Virtual lateral cephalogram (patient K.C.)

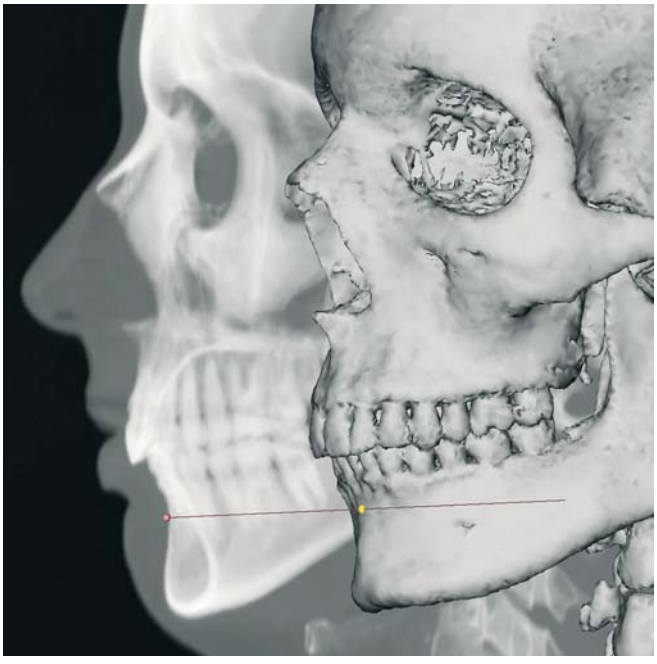

Fig. 4.108. B-Point. Virtual lateral cephalogram linked to the 3-D hard tissue surface representation (patient K.C.)

Step 1: Define B-Point on the virtual lateral cephalogram (Figs. 4.107, 4.108).

Step 2: The position of B-Point is verified on the right (Fig. 4.109) and left (Fig. 4.110) profile views of the 3-D hard tissue surface representations.

Step 3: Verify the midline position of B-Point on the mandibular dento-alveolar process on the frontal view of the 3-D hard tissue surface representation (Fig. 4.111). The virtual frontal cephalogram (Figs. 4.112, 4.113) is helpful to define the midline position of B-Point.

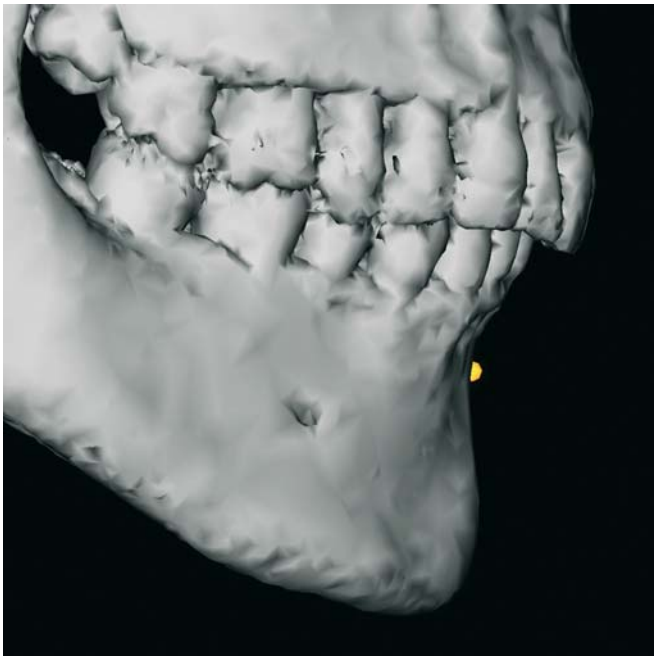

Fig. 4.109. B-Point. Profile view right (3-D CT, patient K.C.)

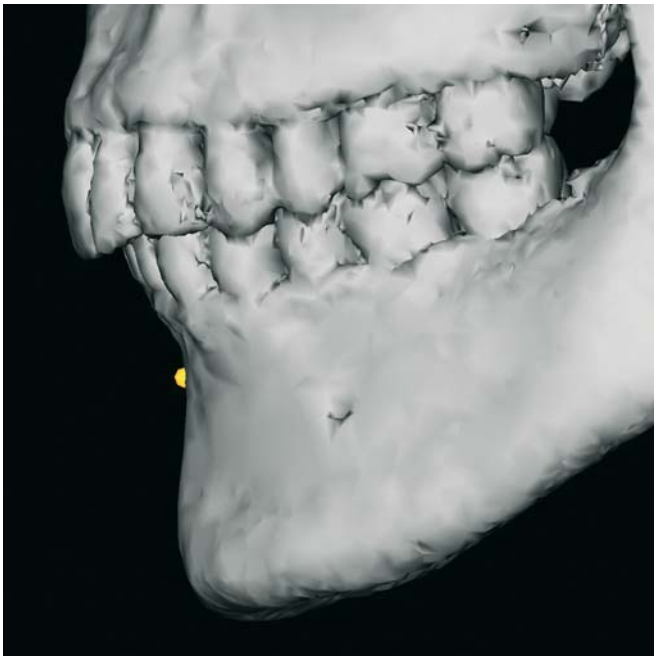

Fig. 4.110. B-Point. Profile view left (3-D CT, patient K.C)

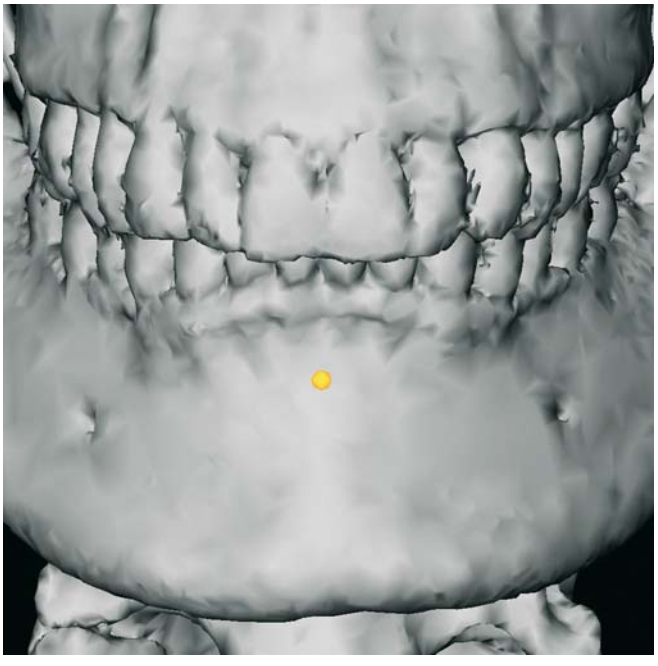

Fig. 4.111. B-Point. Frontal view (3-D CT, patient K.C.)

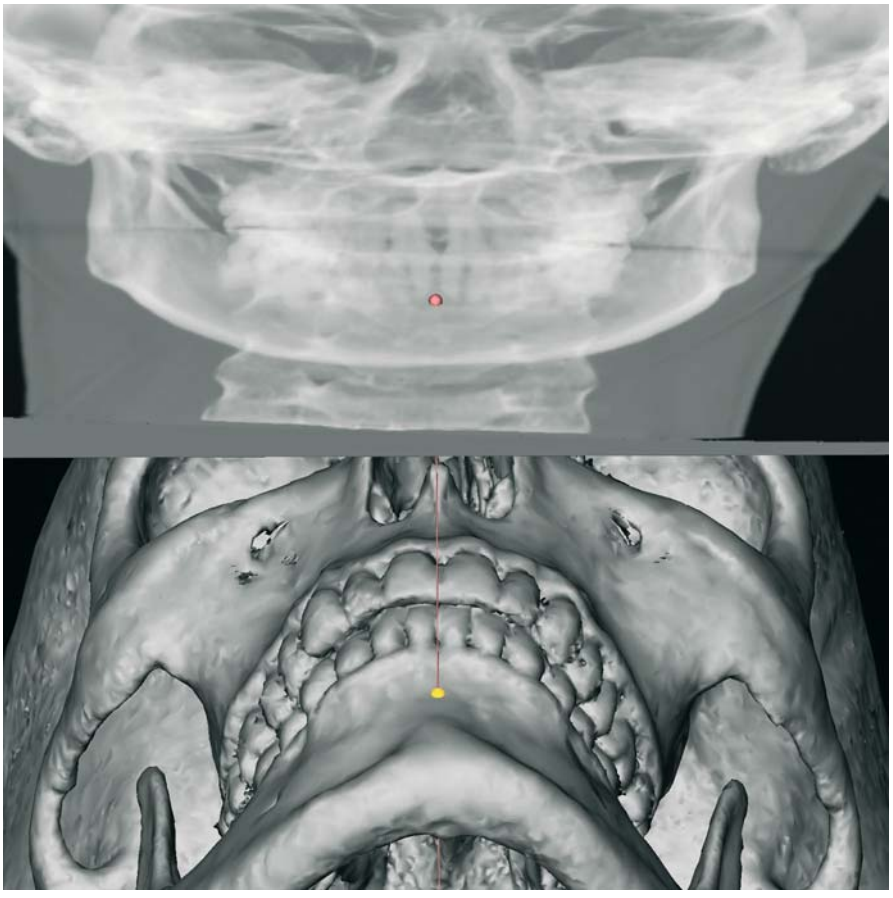

Fig. 4.112. B-Point. Virtual frontal cephalogram linked to the 3-D hard tissue surface representation (3-D CT, patient K.C.)

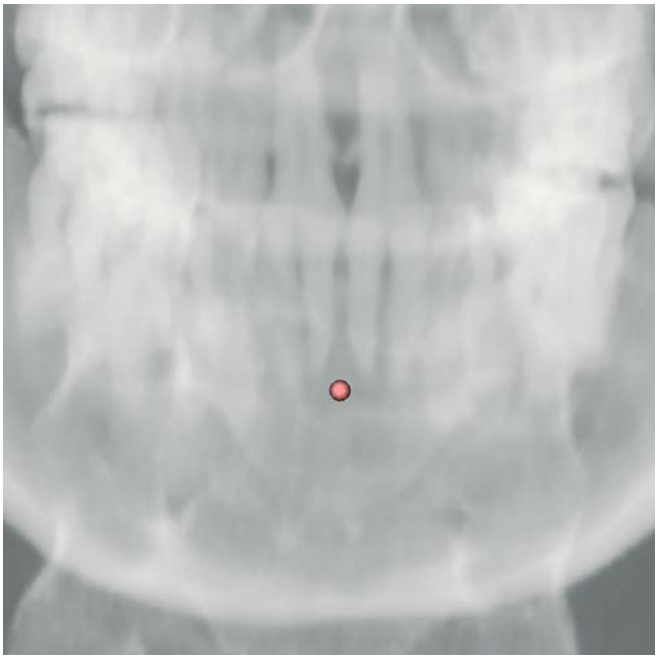

Fig. 4.113. B-Point. Virtual frontal cephalogram (patient K.C.)

Pogonion: Pog

Definition of the Pogonion Landmark

Pogonion is the most anterior midpoint of the chin on the outline of the mandibular symphysis.

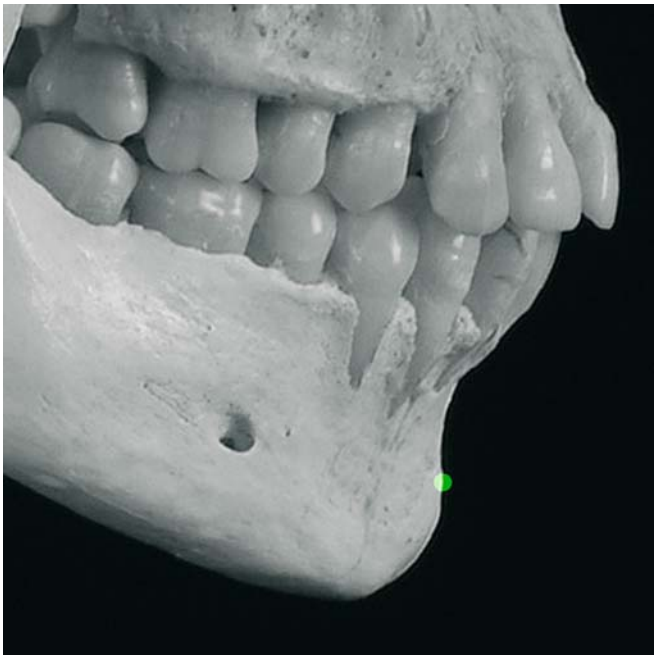

Fig. 4.114. Pogonion. Profile view right (cadaver skull)

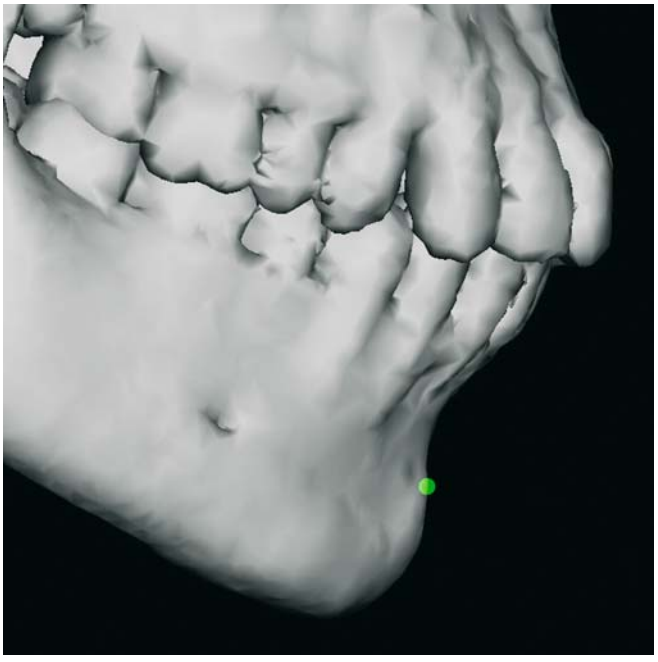

Fig. 4.115. Pogonion. Profile view right (3-D CT, cadaver skull)

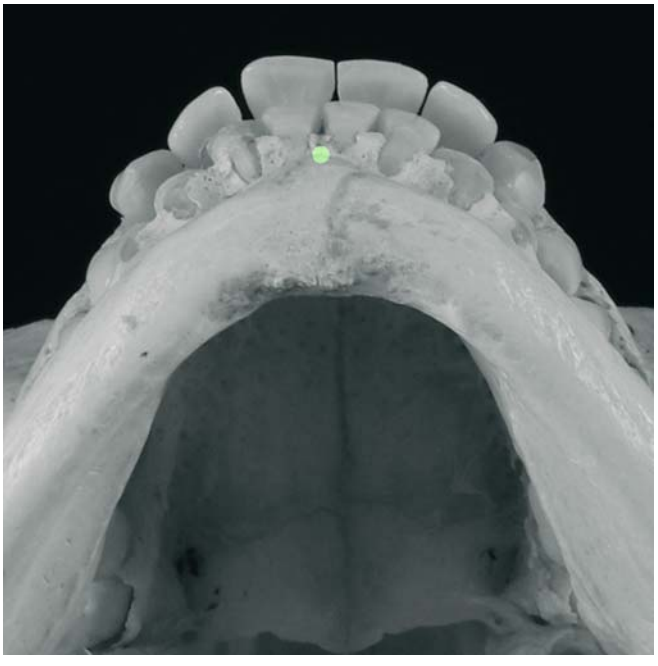

Fig. 4.116. Pogonion. Base view (cadaver skull)

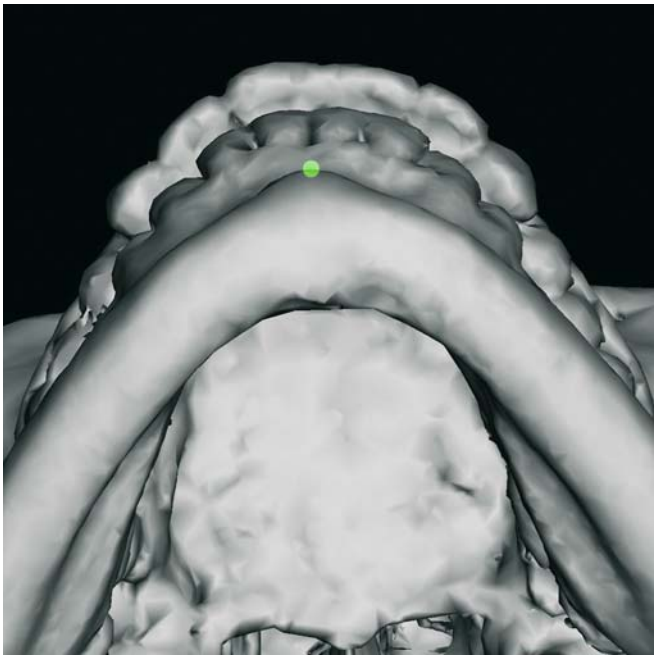

Fig. 4.117. Pogonion. Base view (3-D CT, cadaver skull)

Virtual Definition of the Pogonion Landmark

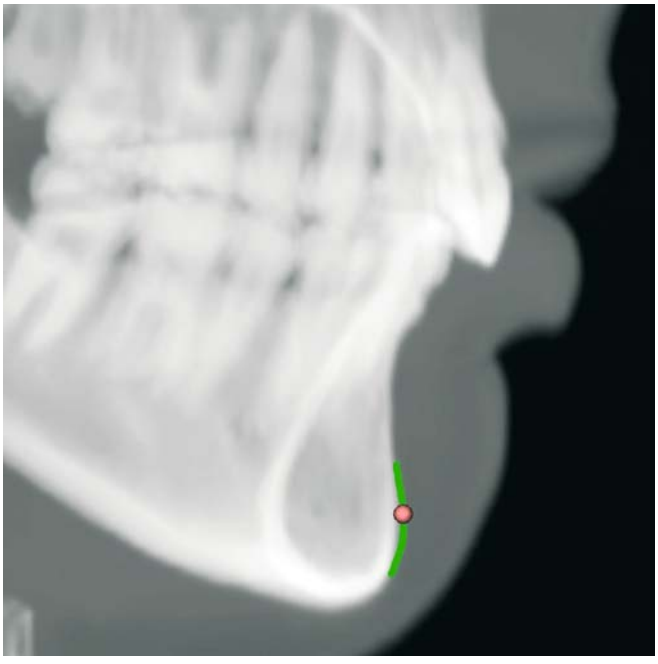

Fig. 4.118. Pogonion. Virtual lateral cephalogram (patient K.C.)

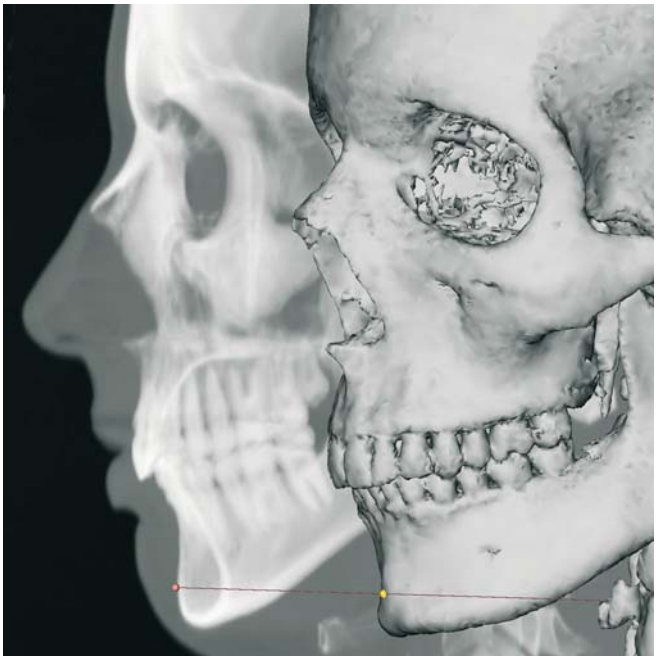

Fig. 4.119. Pogonion. Virtual lateral cephalogram linked to the 3-D hard tissue surface representation (patient K.C.)

Step 1: Define Pogonion on the virtual lateral cephalogram (Figs. 4.118, 4.119).

Step 2: The position of Pogonion is verified on the right (Fig. 4.120) and left (Fig. 4.121) profile views of the 3-D hard tissue surface representations.

Step 3: Verify the midline position of Pogonion on the base view of the 3-D hard tissue surface representation (Fig. 4.122). Note that Pogonion is the most anterior skeletal midline point of the chin and can therefore be out of the midplane.

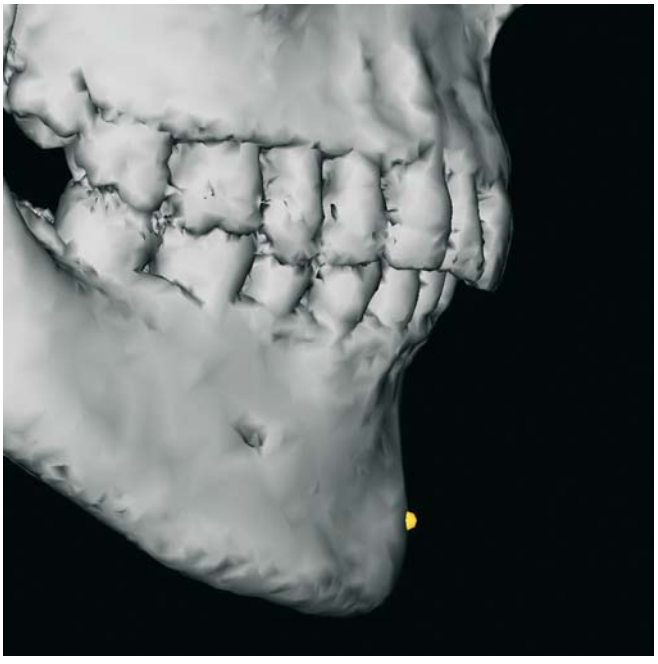

Fig. 4.120. Pogonion. Profile view right (3-D CT, patient K.C.)

Fig. 4.121. Pogonion. Profile view left (3-D CT, patient K.C.)

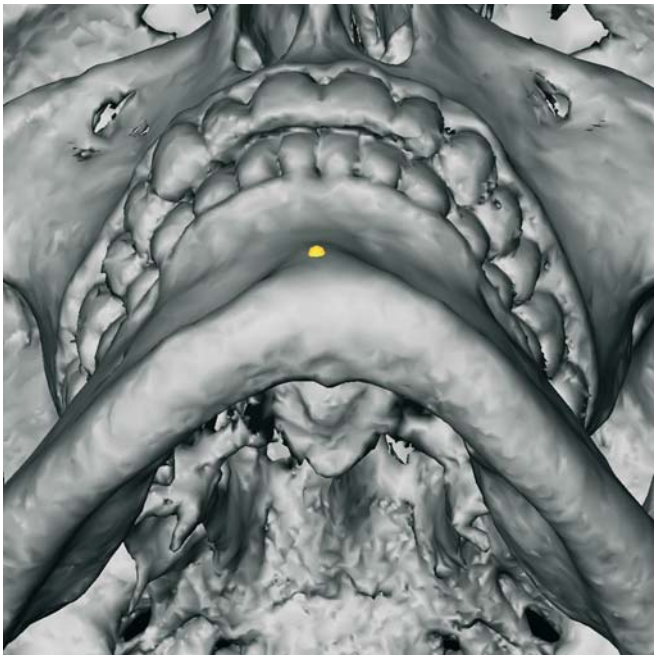

Fig. 4.122. Pogonion. Base view (3-D CT, patient K.C.)

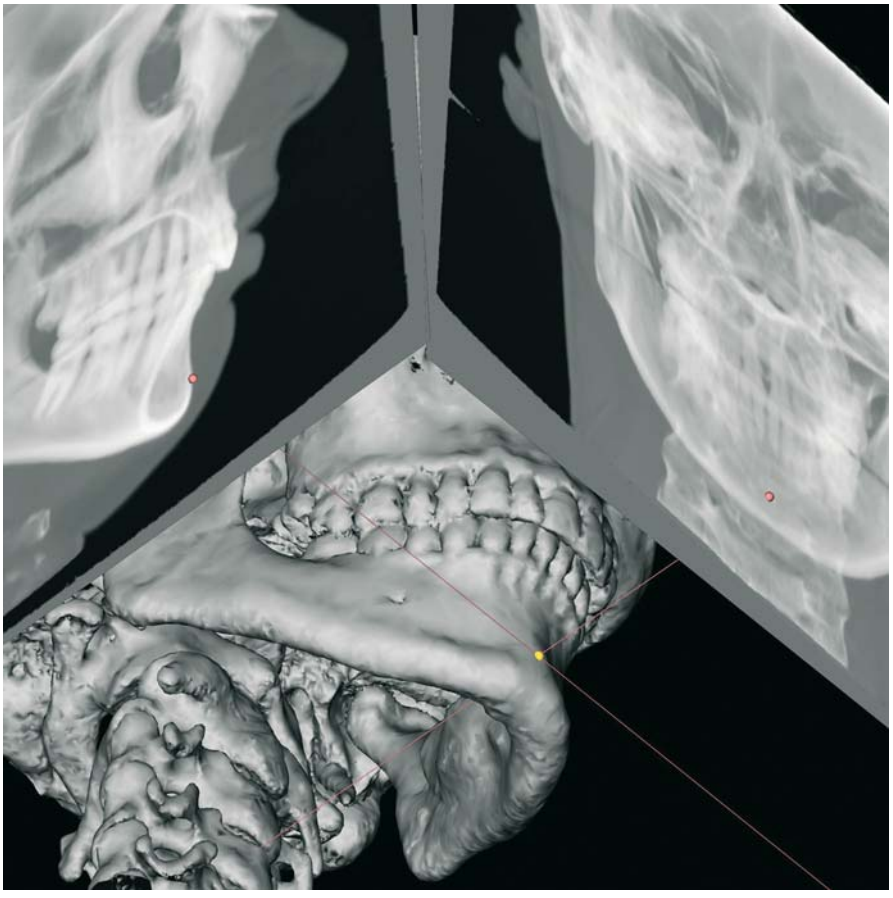

Fig. 4.123. Pogonion. Virtual lateral and frontal cephalograms linked to the 3-D hard tissue surface representation (3-D CT, patient K.C.)

Basion: Ba

Definition of the Basion Landmark

Basion is the most anterior point of the great foramen (foramen magnum)

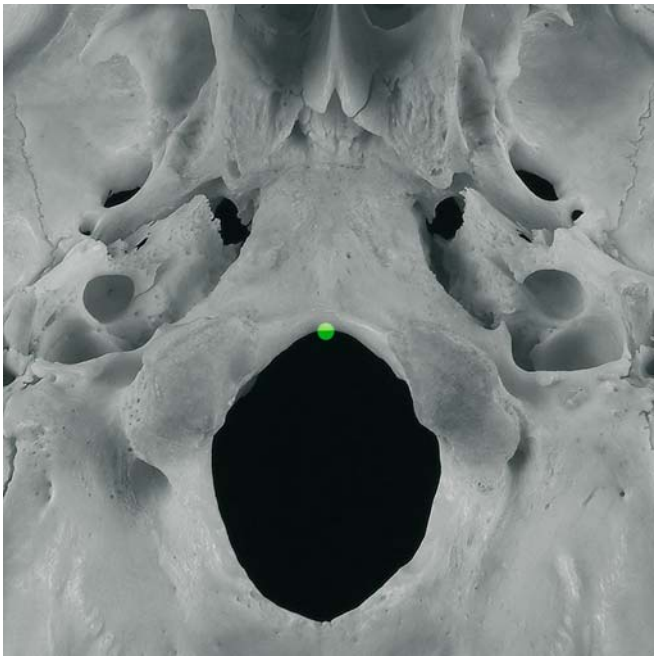

Fig. 4.124. Basion. Exocranial skull base view (3D-CT, cadaver skull)

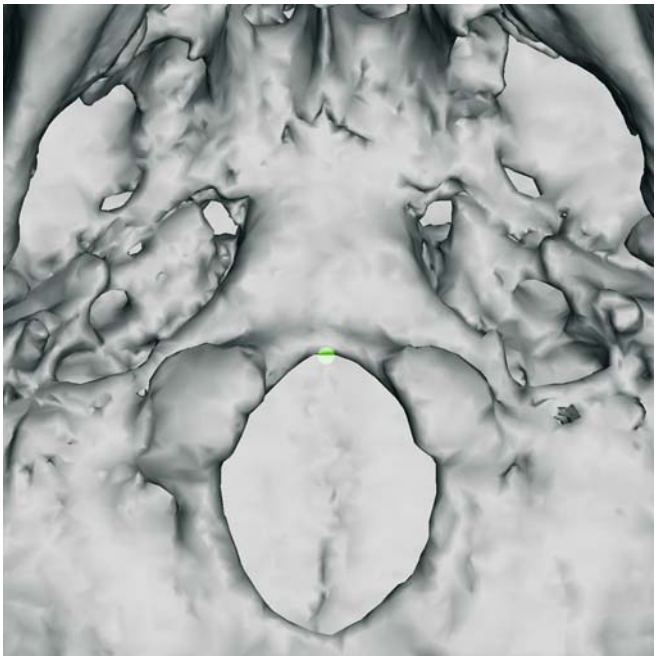

Fig. 4.125. Basion. Exocranial skull base view (3-D CT, cadaver skull)

Virtual Definition of the Basion Landmark

Step 1: Define Basion on the exocranial skull base view (Fig. 4.126) of the 3-D hard tissue surface representation.

Step 2: Verify the vertical position of Basion on the virtual lateral cephalogram linked to the 3-D hard tissue surface representation (Figs. 4.127, 4.128).

Fig. 4.126. Basion. Exocranial skull base view (3-D CT, patient K.C.)

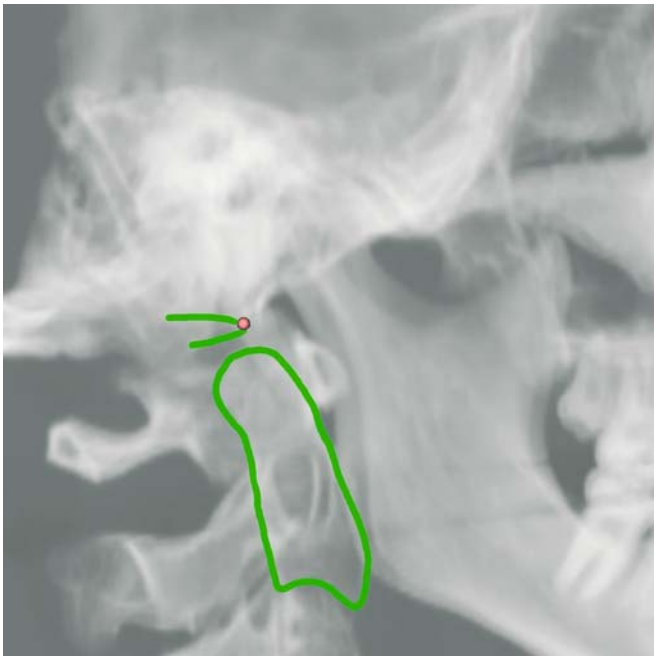

Fig. 4.127. Basion. Virtual lateral cephalogram (3-D CT, patient K.C.)

Fig. 4.128. Basion. Virtual lateral cephalogram linked to the 3-D hard tissue surface representation (3-D CT, patient K.C.)

Condylion: Co_r – Co_l

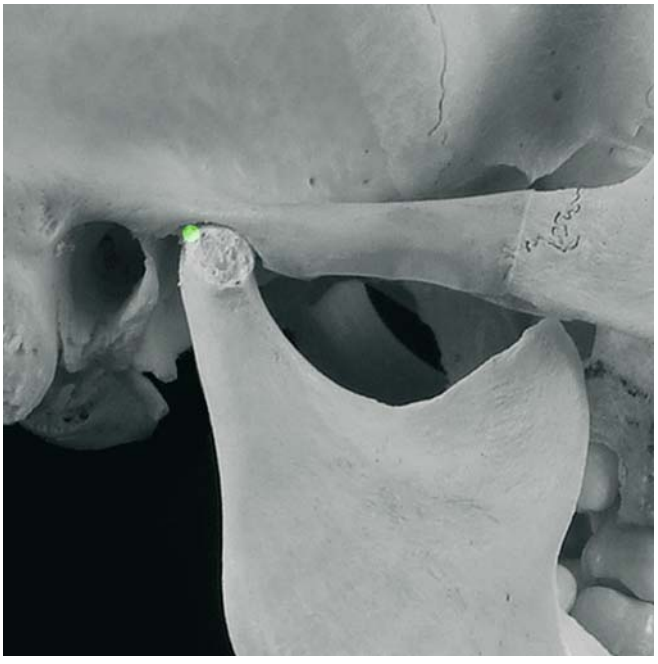

Fig. 4.129. $Condylion_r$. Profile view right (cadaver skull)

Fig. 4.130. $Condylion_r$. Profile view right (3-D CT, cadaver skull)

Definition of the Condylion Landmarks

Condylion (Co) is the most postero-superior point of each mandibular condyle in the sagittal plane.

Virtual Definition of the Condylion Landmarks

Step 1: Define $Condylion_r$ and $Condylion_l$ on the right (Fig. 4.131) and left (Fig. 4.132) profile views of the 3-D hard tissue surface representations.

Step 2: Verify the transverse position of $Condylion_r$ and $Condylion_l$ on the linked virtual frontal cephalogram (Fig. 4.134).

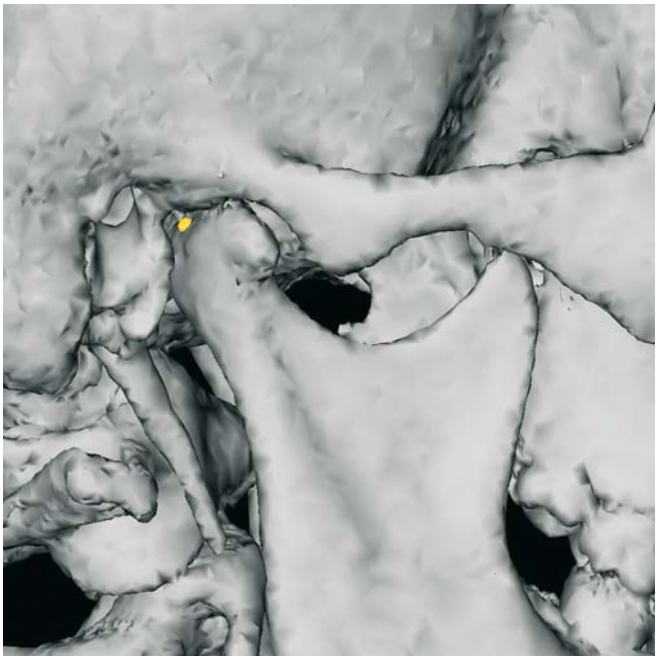

Fig. 4.131. Condylion$_r$. Profile view right (3-D CT, patient K.C.)

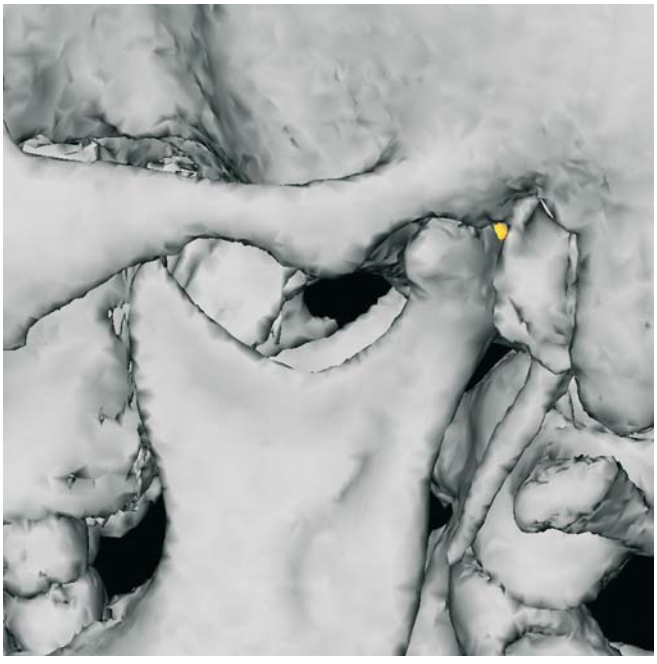

Fig. 4.132. Condylion$_l$. Profile view left (3-D CT, patient K.C.)

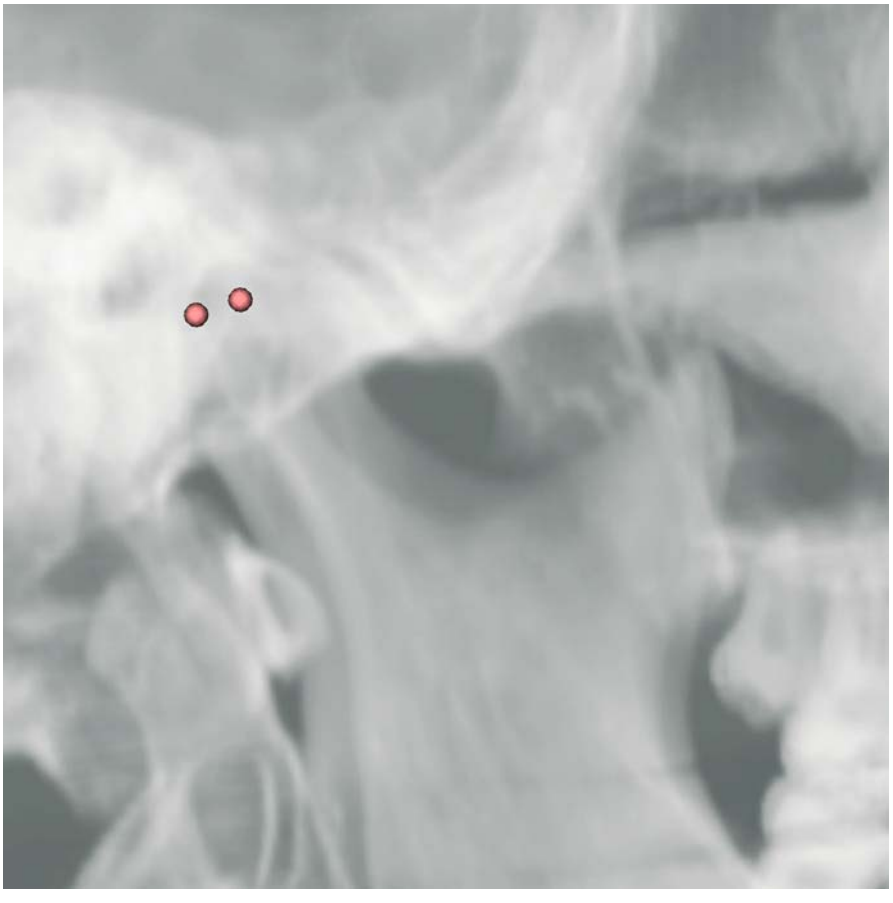

Fig. 4.133. Condylion$_r$ and Condylion$_l$. Virtual lateral cephalogram (3-D CT, patient K.C.)

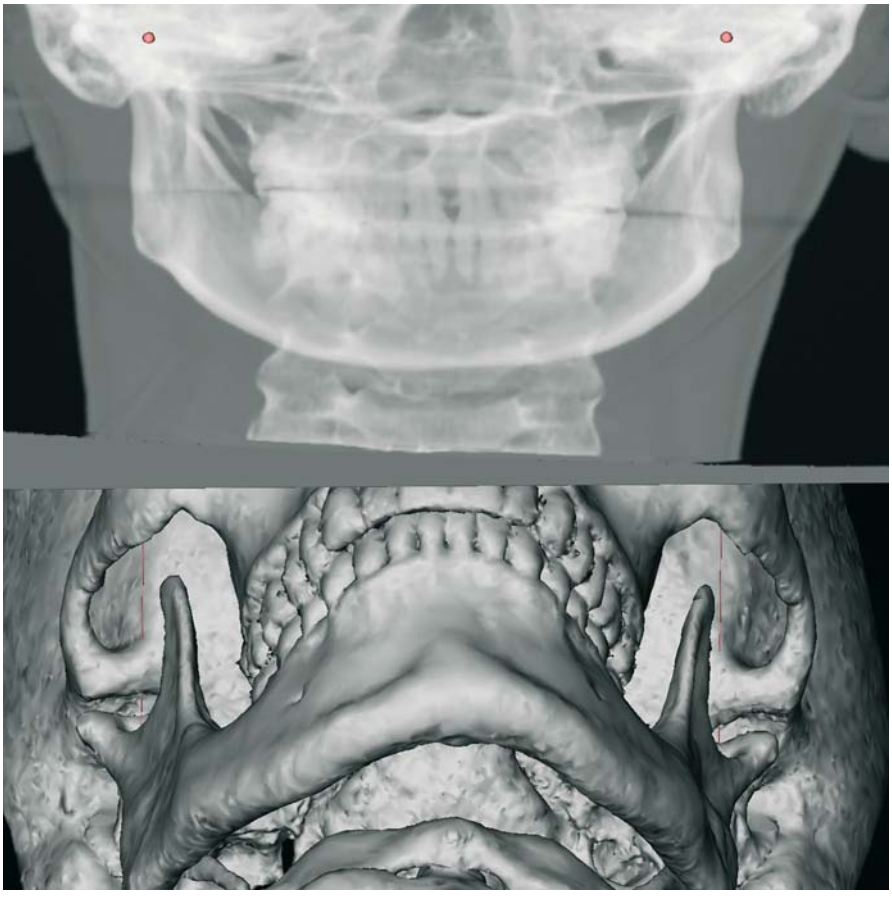

Fig. 4.134. Condylion$_r$ and Condylion$_l$. Virtual frontal cephalogram linked to the 3-D hard tissue surface representation (3-D CT, patient K.C.) allows verification of the transverse position of the Condylion landmarks

4.2 Set-up of 3-D Cephalometric Hard Tissue Landmarks

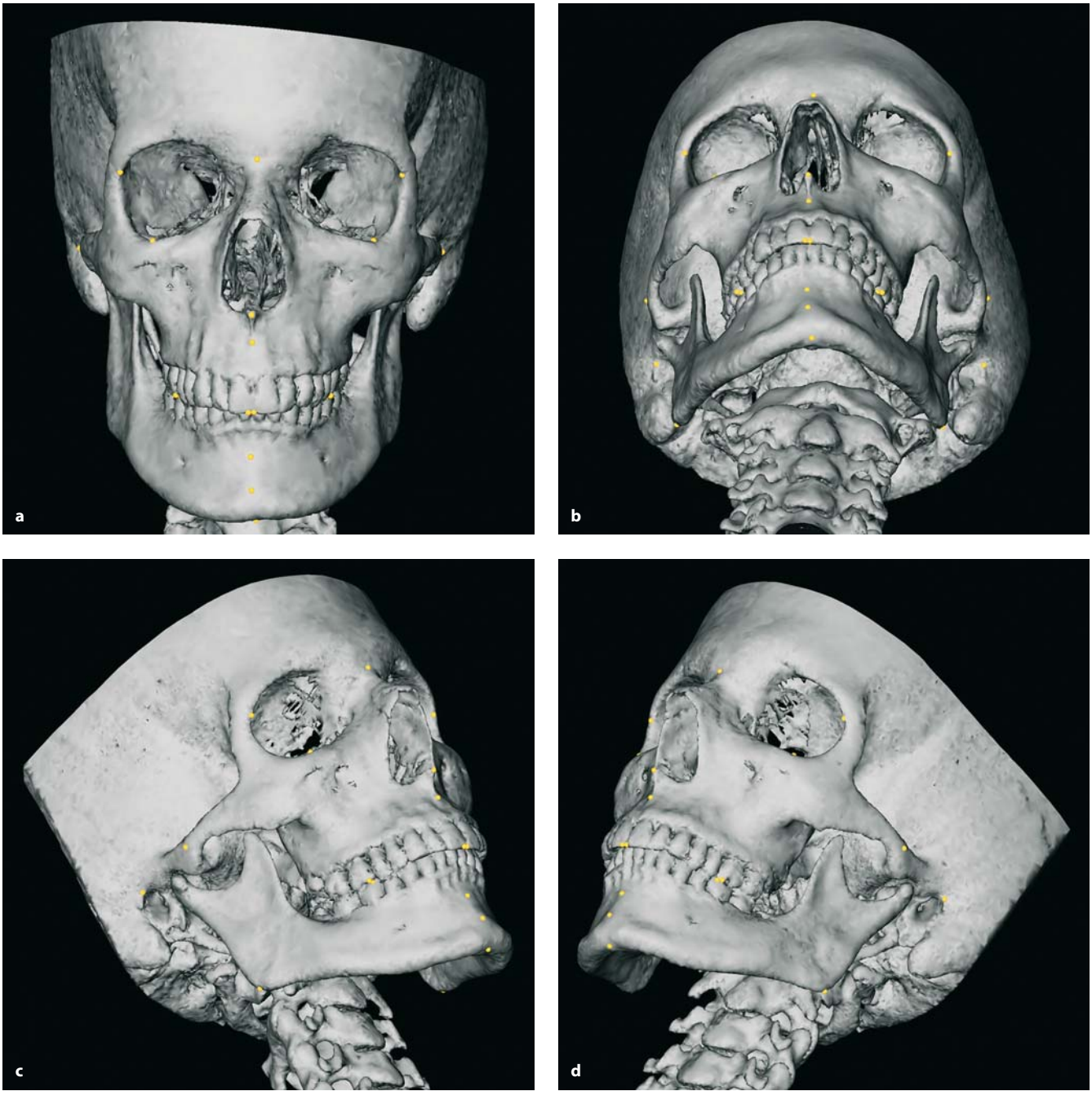

Fig. 4.135 a–d. Set-up of 3-D cephalometric hard tissue landmarks. (3-D CT, patient K.C.)

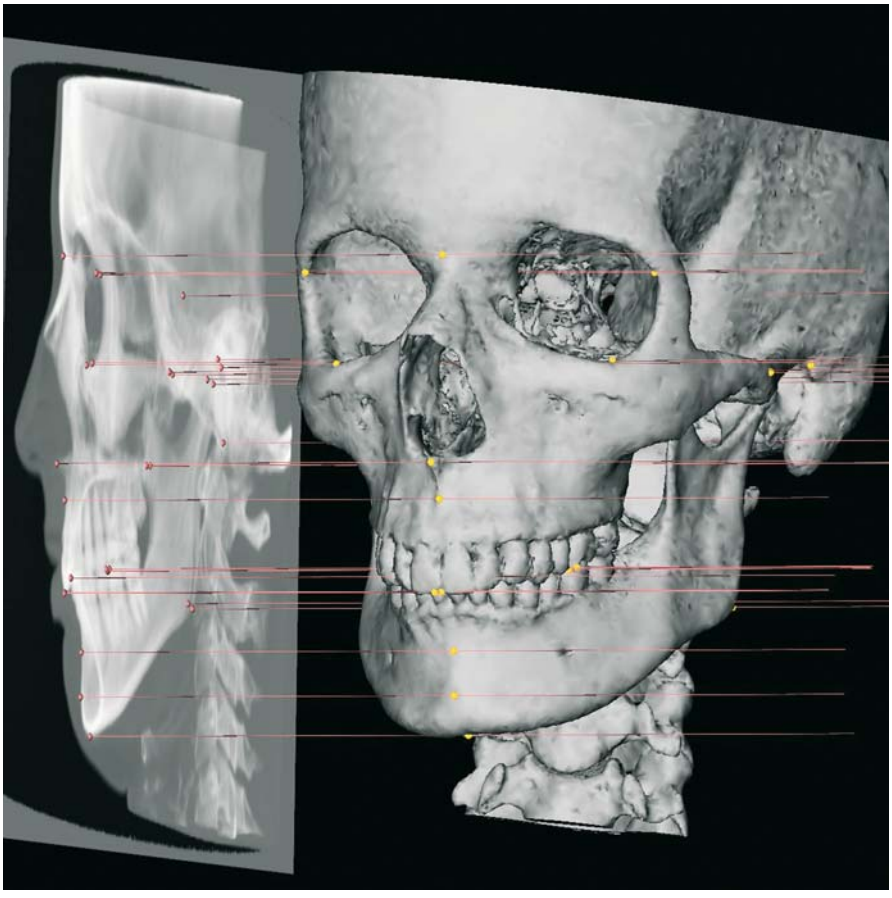

Fig. 4.136. Set-up of 3-D cephalometric hard tissue landmarks. Virtual lateral cephalogram linked to the 3-D hard tissue surface representation (3-D CT, patient K.C.)

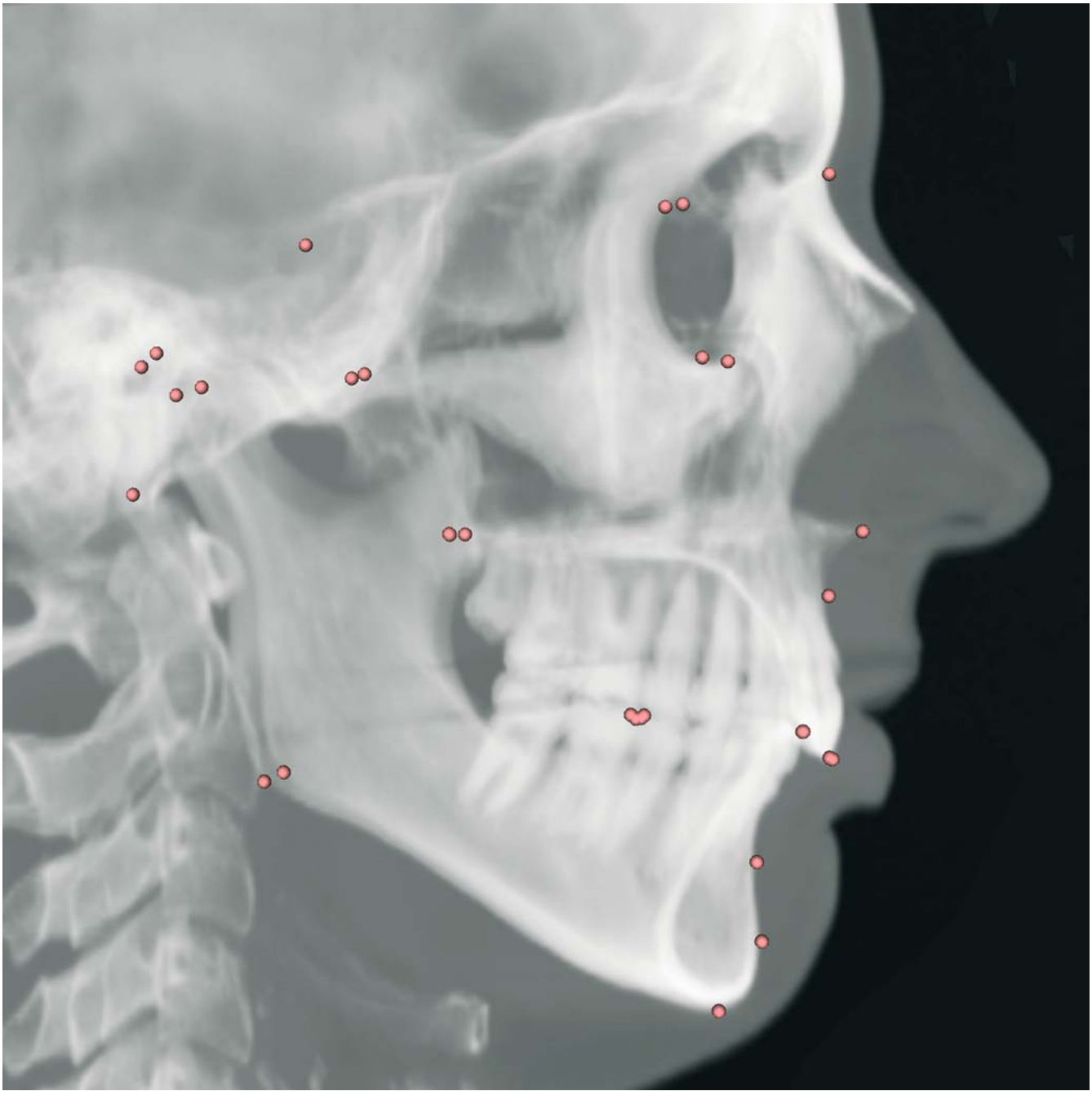

Fig. 4.137. Set-up of 3-D cephalometric hard tissue landmarks. Virtual lateral cephalogram (3-D CT, patient K.C.)

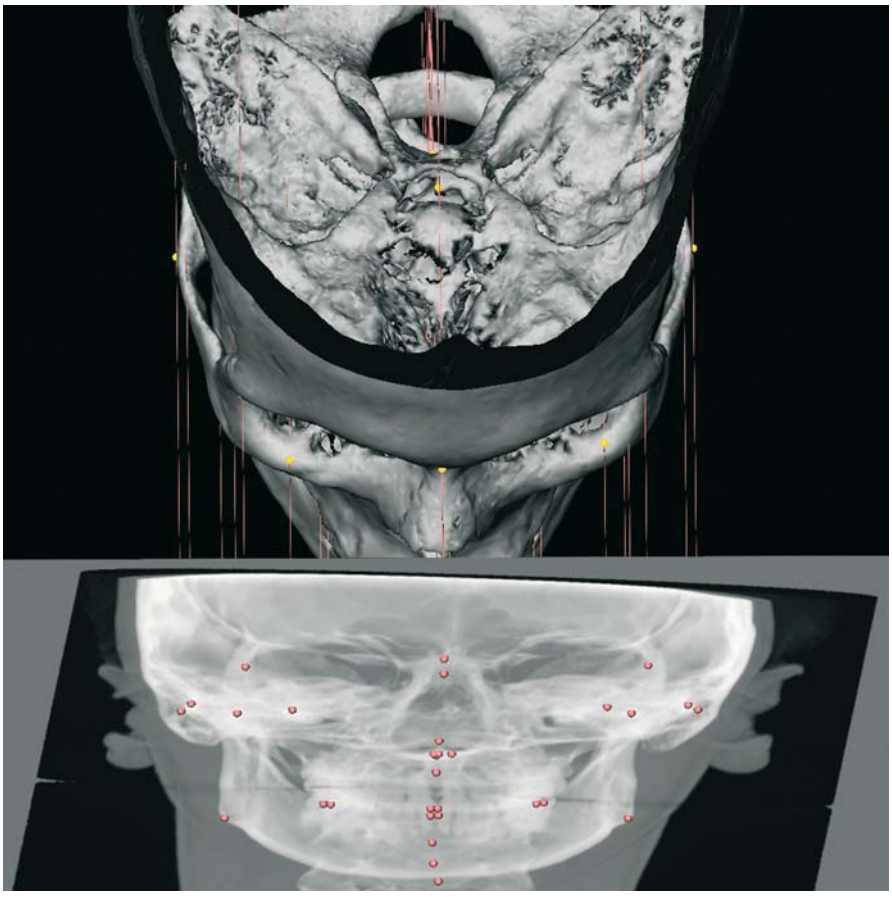

Fig. 4.138. Set-up of 3-D cephalometric hard tissue landmarks. Virtual frontal cephalogram linked to the 3-D hard tissue surface representation (3-D CT, patient K.C.)

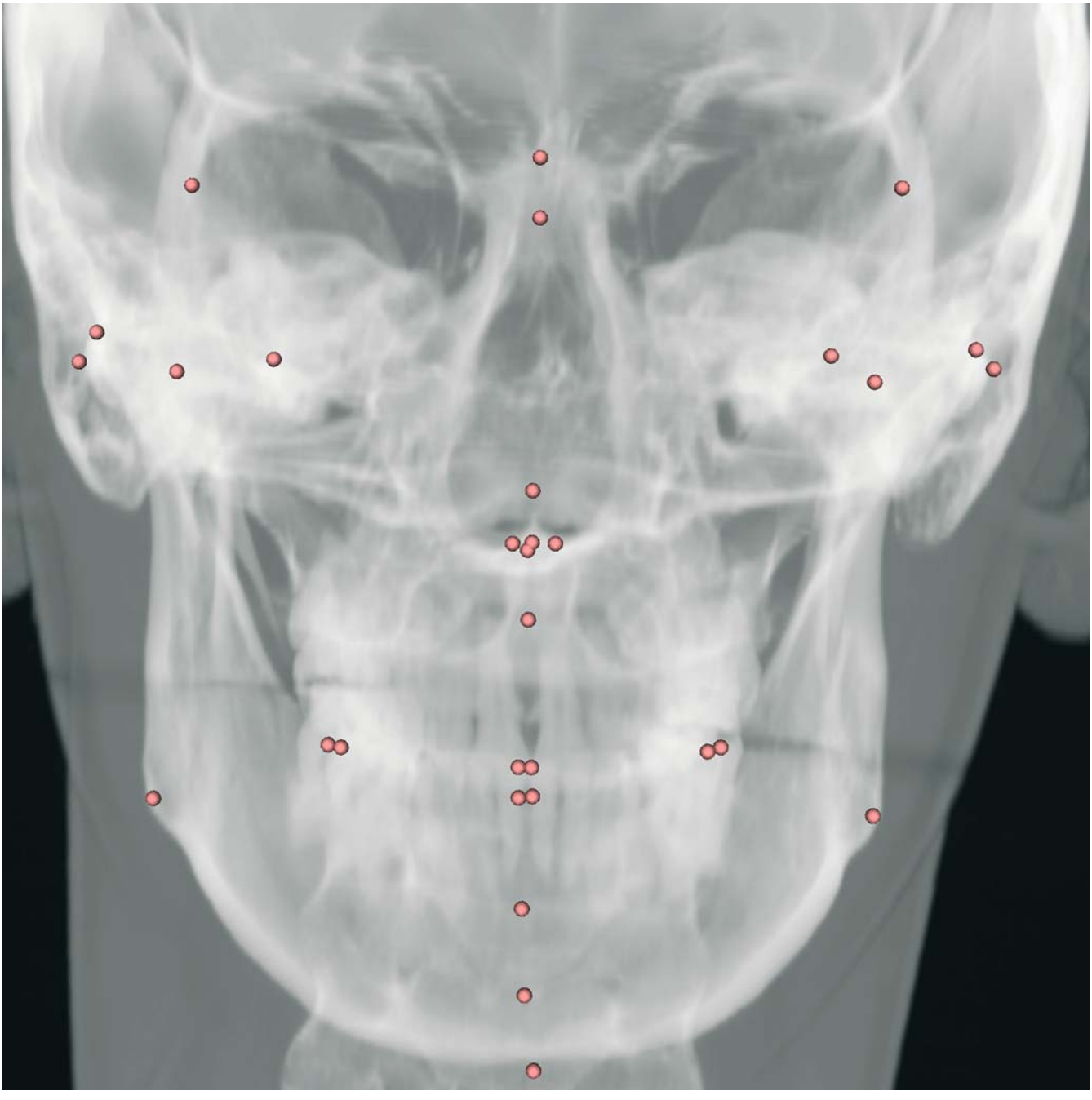

Fig. 4.139. Set-up of 3-D cephalometric hard tissue landmarks. Virtual frontal cephalogram (3-D CT, patient K.C.)

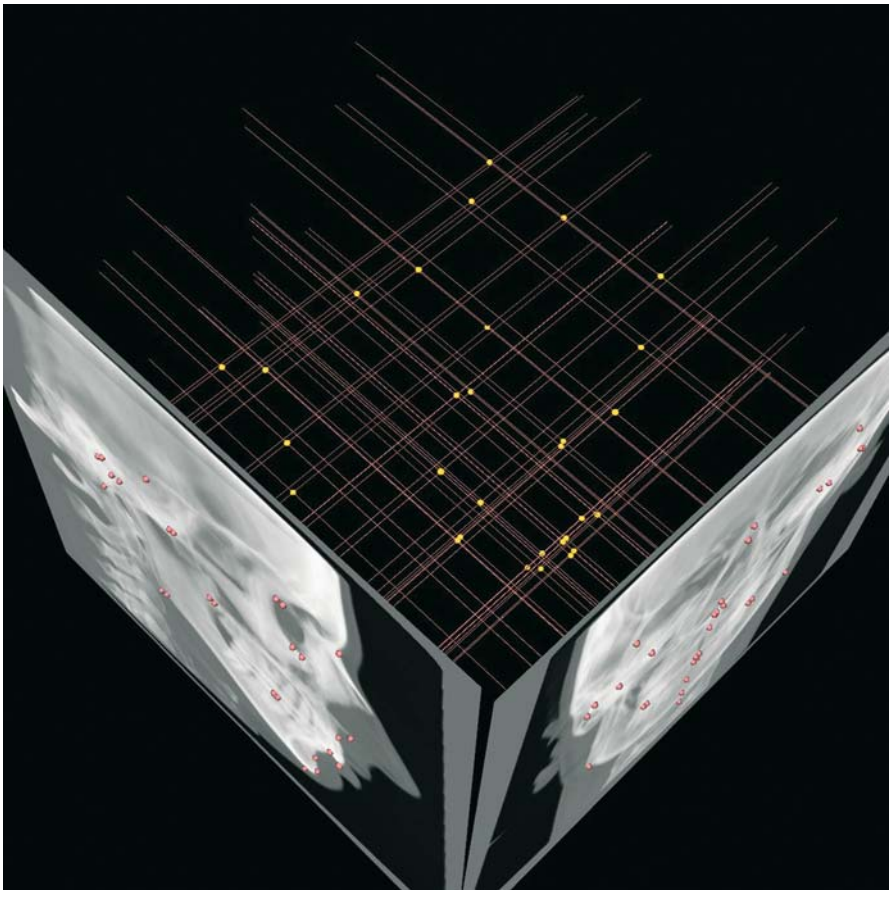

Fig. 4.140. Set-up of 3-D cephalometric hard tissue landmarks. Linked virtual lateral and frontal cephalograms (3-D CT, patient K.C.)

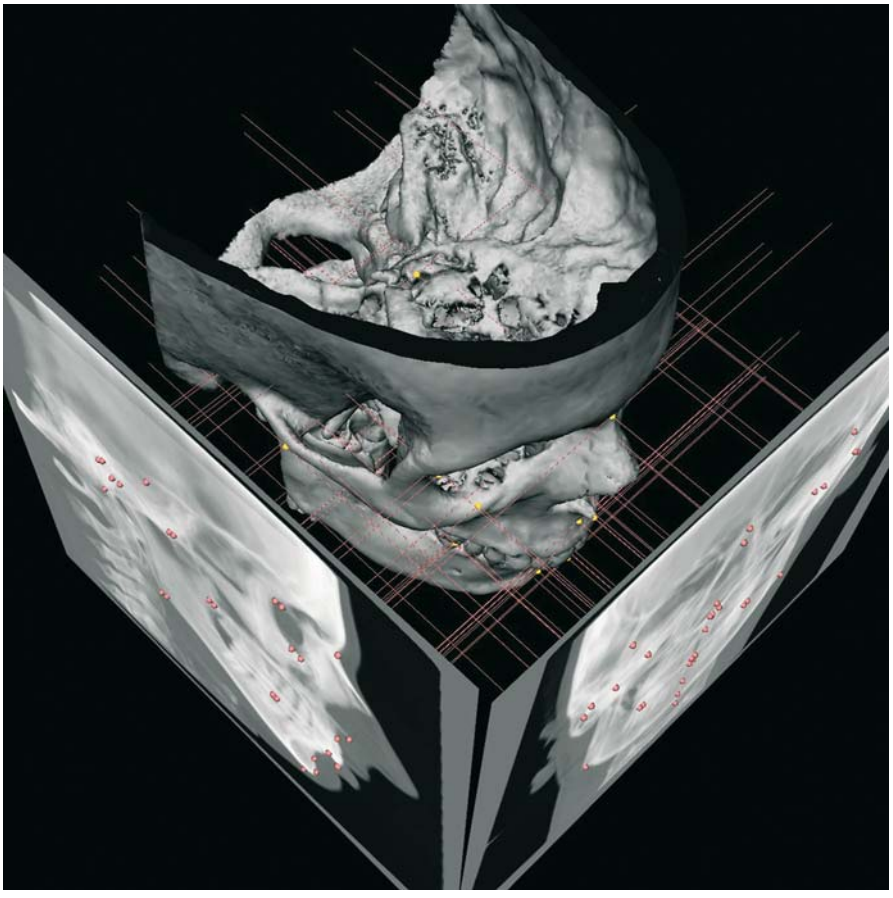

Fig. 4.141. Set-up of 3-D cephalometric hard tissue landmarks. Virtual lateral and frontal cephalograms linked to the 3-D hard tissue surface representation (3-D CT, patient K.C.)

4.3 Additional 3-D Cephalometric Hard Tissue Landmarks

The following list shows some other conventional cephalometric landmarks described in the literature that could be used in 3-D cephalometry.

- *Antegonion*: The highest point of the notch or concavity of the lower border of the vertical mandibular ramus where it joins the body of the mandible
- *Articulare according to Bjork:* The intersection of the posterior border of the vertical mandibular ramus and the outer margin of the cranial base
- *Articulare according to Bolton:* The intersection of the posterior border of the condyle of the mandible with the Bolton plane (a line joining the Bolton point and the Nasion landmark on the lateral cephalogram)
- *Bolton point:* A point in space about the centre of the foramen magnum that is located on the lateral cephalogram by the highest point in the profile image of the postcondylar notches of the occipital bone
- *Bregma:* The crossing of the coronal and sagittal sutures on top of the skull
- *Coronoid process:* The most superior point of the coronoid process
- *Dacryon*: Point on the inner wall of the orbit at the junction of the nasal process of the frontal bone, the frontal process of the maxilla and the lacrimal bone
- *Frontomaxillary nasal suture*: The junction of the frontal, maxillary and nasal bones
- *Frontotemporale*: Point near the root of the zygomatic process of the frontal bone at the most anterior point along the curvature of the temporal line
- *Glabella*: The most anterior point of the frontal bone
- *Gnathion*: The most anterior and inferior point on the contour of the mandibular symphysis
- *Infradentale*: The anterior superior point on the mandible at its labial contact between the mandibular central incisors
- *Inferior zygoma*: The lowest point of the outline of each zygoma
- *O-Point*: The centre for convergence area of horizontal planes used in Sassouni's analysis
- *Opisthion*: The posterior midsagittal point on the posterior margin of the foramen magnum
- *Prosthion*: The lowest, most anterior point on the alveolar portion of the premaxilla, in the median plane, between the upper central incisors
- *Sellion according to A.M. Schwarz:* The midpoint of the entrance of the sella turcica
- *Sphenoethmoidal suture:* The most superior point of the sphenoethmoidal suture
- *Spheno-occipital synchondrosis:* The most superior point of the junction between the sphenoid and occipital bones
- *Staphylion:* Point in the medial line (interpalatal suture) of the posterior part of the hard palate where it is crossed by a line drawn tangent to the curves of the posterior margins of the palate
- *Supradentale*: The anterior inferior point on the maxilla at its labial contact between the lower central incisors
- *Supraorbitale:* The most superior point of the superior orbital rim
- *Temporale:* Point at the intersection of the shadows of the ethmoid and the anterior wall of the infratemporal fossa
- *Vertex:* The most superior point on the cranial vault
- *Zygion:* Point on the zygoma on either side at the extremity of the bizygomatic diameter

CHAPTER 5 3-D Cephalometric Soft Tissue Landmarks

Gwen R. J. Swennen

According to the ancient Greeks, facial beauty derives from harmony and balance of the proportions of the individual components of the face. In daily clinical practice, orthodontists and maxillofacial and plastic surgeons often decide on what is beautiful and balanced based on anthroscopy (from the Greek "*anthropos*", human and "*copein*", examine) or visual assessment. Because the examiner's judgement is inherently influenced by his or her aesthetic perception and personal experience, anthroscopy remains highly subjective. Anthropometry ("*metron*", measure), in contrast, is the biological science of studying and measuring human physical dimensions. Anthropometry of the head and face was pioneered by Aleš Hrdlička (1869–1943) but extensively developed and popularized by Leslie G. Farkas, whose clinical and scientific work on direct and indirect (photogrammetry) anthropometry has made a major contribution on today's clinical assessment of the head and face. Potential sources of error in anthropometry are incorrect landmark definition, improper use of measuring equipment and/or an inadequate measuring method. The major shortcoming of direct anthropometry is that it necessitates a wide range of measurement tools (sliding and spreading callipers, soft measuring tape, etc.), demands great experience on the part of the investigator and is very time-consuming. The disadvantages of indirect anthropometry or photogrammetry are difficulties in standardization of photographs, inaccuracy in definition of bone-related soft tissue landmarks (e.g. soft tissue orbitale, soft tissue gonion and zygion) and its two-dimensional character.

Advances in both computer hardware and software technology led to 3-D anthropometric methods such as laser surface scanning, stereo photogrammetry, CT and MRI (Chap. 10). Recently a new innovative voxel-based method of 3-D cephalometry was developed by our research group. CT based 3-D cephalometry of soft tissues has the advantage that bone-related landmarks can be defined in a more accurate and reliable way because the 3-D virtual scene approach allows visualization of the underlying hard tissues. Therefore, no surface analogues of bony landmarks are necessary. Moreover, analysis bias caused by improper use of measuring equipment or inadequate measurement technique is decreased because of standardized virtual positioning of the skull with the set-up of a 3-D cephalometric reference system (Chap. 3) and the automatic generation of measurements (Chap. 7). The important disadvantages of spiral-CT based 3-D cephalometry are the radiation dose (Chap. 1) and the horizontal position of the head during scanning, which has an impact on the facial soft tissue mask due to gravity. These problems will be resolved in the near future with the application of cone-beam CT in clinical routine because of its low radiation dose and its ability to scan the patient in the vertical rest position (Chap. 1). Cone-beam-CT-based 3-D cephalometry will allow the generation of 3-D cephalometric reference data including hard and soft tissue data and bone–soft tissue movement ratios.

As already mentioned in Chap. 4, landmarks situated on the skin are referred to as 3-D cephalometric soft tissue landmarks and their abbreviations (symbols) are marked in lower-case letters as in anthropometry and conventional soft tissue cephalometry. This chapter offers "step-by-step" guidelines for precise definition of such landmarks. Sometimes the anthropometric definitions had to be modified. A total of 28 landmarks with regard to the facial soft tissue units (forehead, nasal, periorbital, midface and mandible) are described in detail. Additionally, ear- and head-related landmarks are listed at the end of the chapter because they have not yet been validated. An important shortcoming of CT-based 3-D cephalometry of soft tissues remains improper or impossible identification of soft tissue landmarks that are related to the hair (trichion, superciliare, frontotemporale) or eye-lids (palpebrale superius, palpebrale inferius). Registration of the natural texture of the face by means of 3-D photographic techniques could be a solution and is therefore an interesting topic for future research (Chap. 10).

5.1 Definition of 3-D Cephalometric Soft Tissue Landmarks

Glabella: g

Definition of the glabella Landmark

Glabella (g) is the most anterior midpoint on the fronto-orbital soft tissue contour. In 3-D cephalometry, this is a well-defined soft tissue landmark and is therefore not the same as the anthropometric glabella landmark according to L.G. Farkas, which is identical to the bony Glabella landmark on the frontal bone.

Virtual Definition of the glabella Landmark

Step 1: Define glabella on the right profile view of the 3-D soft tissue surface representation (Fig. 5.1) and verify its position on the left profile view (Fig. 5.2). The position of the glabella landmark can also be verified on the virtual lateral cephalogram (Figs. 5.76, 5.77).

Step 2: Verify the midline position of the glabella landmark on the frontal view of the 3-D soft tissue surface representation (Fig. 5.4).

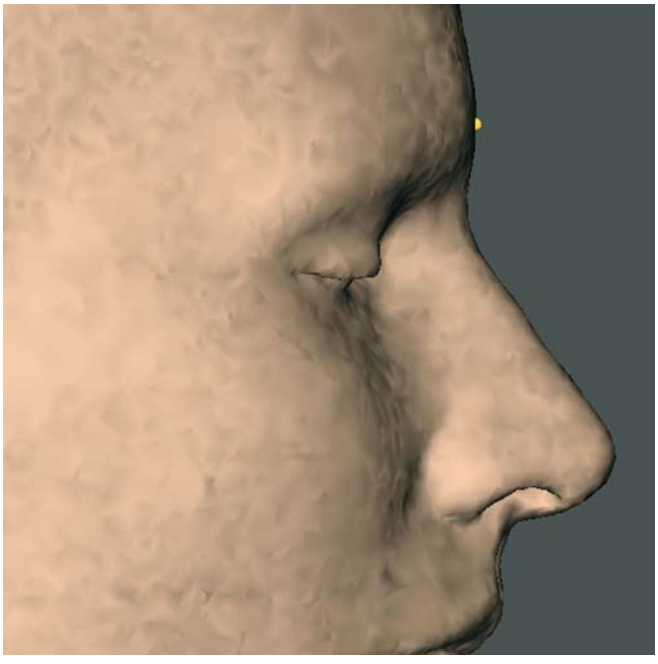

Fig. 5.1. Glabella. Profile view right (3-D CT, patient K.C.)

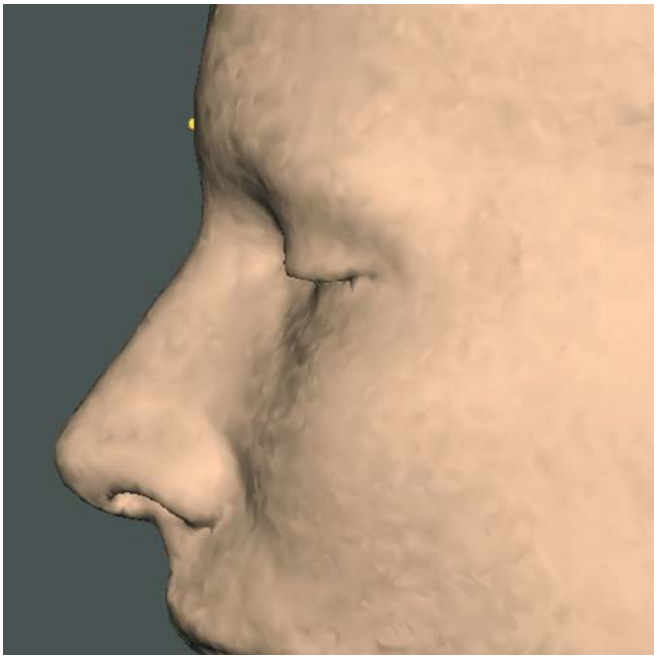

Fig. 5.2. Glabella. Profile view left (3-D CT, patient K.C.)

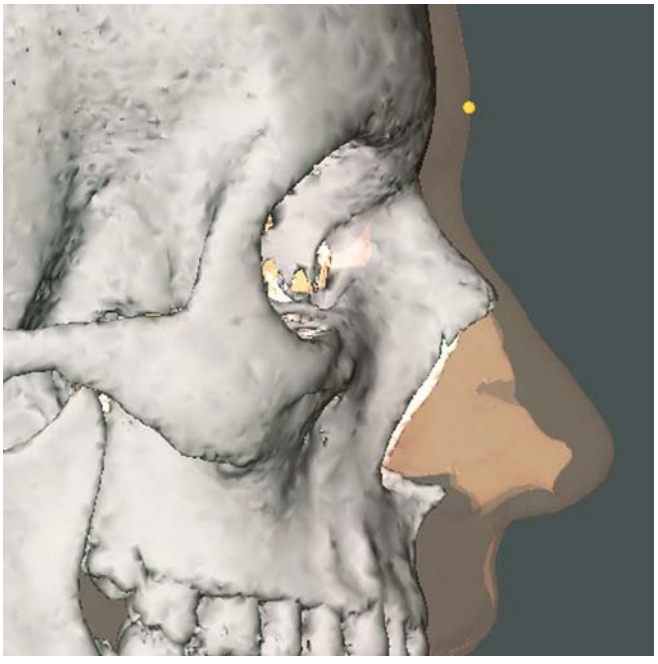

Fig. 5.3. Glabella. Profile view right. Note that the 3-D soft tissue cephalometric glabella landmark is located on the soft tissues and is therefore not identical to the anthropometric glabella landmark, which is the same as the bony Glabella landmark. (3-D CT, transparent soft tissues, patient K.C.)

Fig. 5.4. Glabella. Frontal view (3-D CT, patient K.C.)

Soft tissue nasion: n

Definition of the soft tissue nasion Landmark

Soft tissue nasion (n) is the midpoint on the soft tissue contour of the base of the nasal root at the level of the frontonasal suture. In 3-D cephalometry, this is a well-defined soft tissue landmark and is therefore not the same as the anthropometric soft nasion landmark according to L.G. Farkas, which is identical to the bony Nasion.

Virtual Definition of the soft tissue nasion Landmark

Step 1: Define soft tissue nasion on the right profile view of the 3-D transparent soft tissue surface representation (Fig. 5.5).

Step 2: Visualize the position of the soft tissue nasion on the right (Fig. 5.6) and left (Fig. 5.7) profile view of the 3-D soft tissue surface representation. The position of the soft tissue nasion landmark can also be verified on the virtual lateral cephalogram (Figs. 5.76, 5.77).

Step 3: Verify the midline position of the soft tissue nasion landmark on the frontal view of the 3-D soft tissue surface representation (Fig. 5.8).

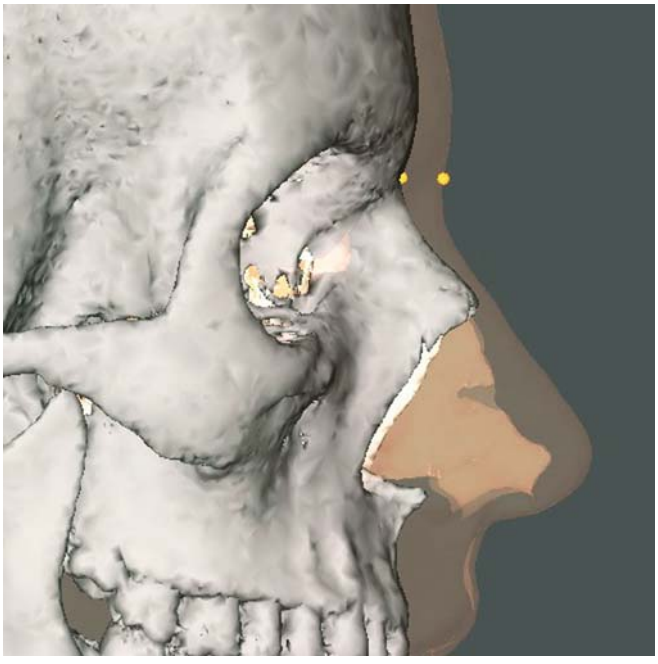

Fig. 5.5. Soft tissue nasion. Note that the 3-D cephalometric soft tissue nasion landmark is located on the soft tissues and is therefore not identical to the anthropometric soft nasion landmark, which is the same as the bony Nasion landmark. (3-D CT, transparent soft tissues, patient K.C.)

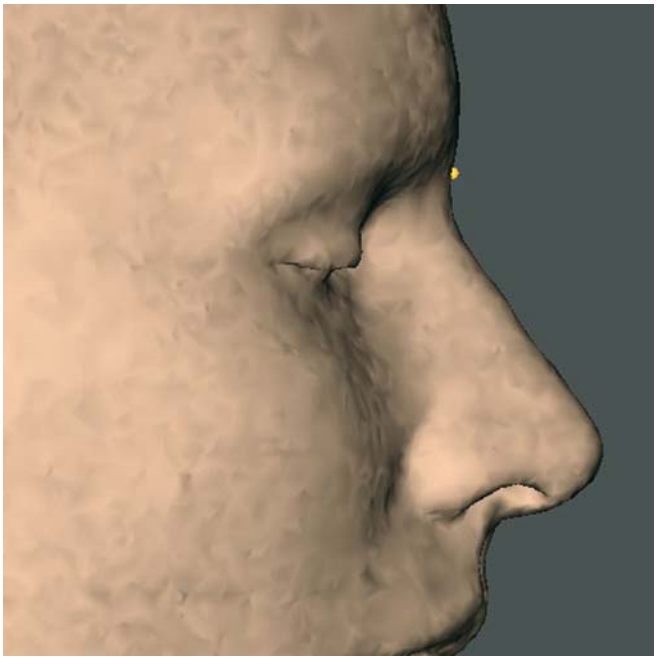

Fig. 5.6. Soft tissue nasion. Profile view right (3-D CT, patient K.C.)

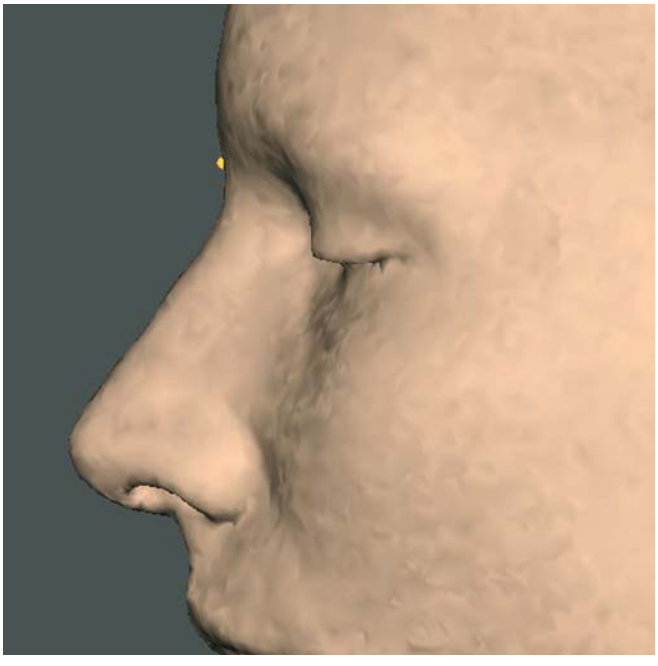

Fig. 5.7. Soft tissue nasion. Profile view left (3-D CT, patient K.C.)

Fig. 5.8. Soft tissue nasion. Frontal view (3-D CT, patient K.C.)

Sellion (subnasion): se

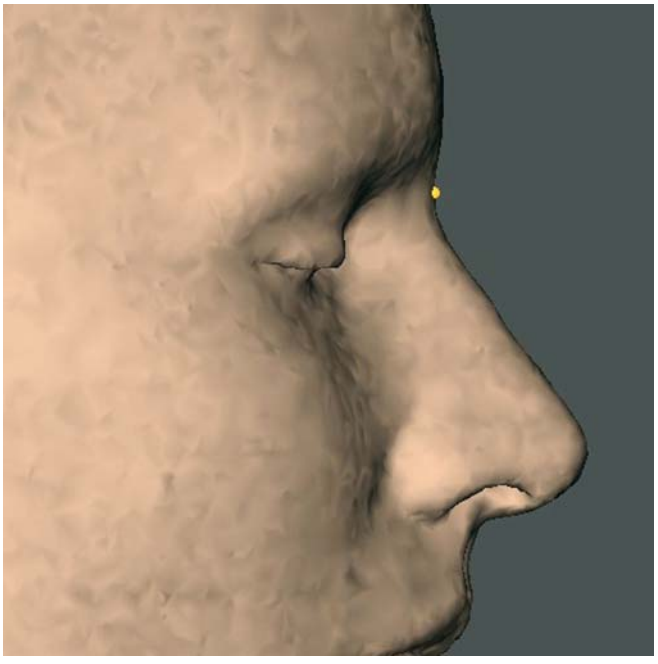

Fig. 5.9. Sellion. Profile view right (3-D CT, patient K.C.)

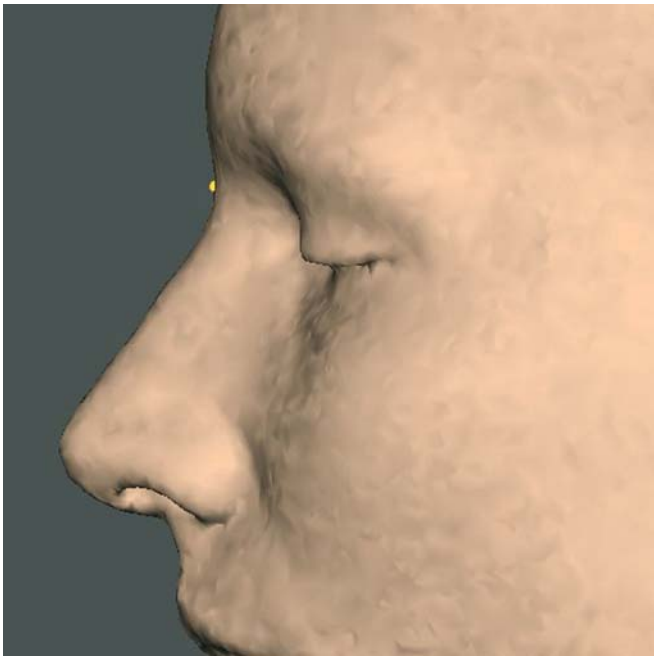

Fig. 5.10. Sellion. Profile view left (3-D CT, patient K.C.)

Definition of the sellion Landmark

Sellion (se) is the most posterior point of the frontonasal soft tissue contour in the midline of the base of the nasal root.

Virtual Definition of the sellion Landmark

Step 1: Define sellion on the right profile view of the 3-D soft tissue surface representation (Fig. 5.9) and verify its position on the left profile view (Fig. 5.10). The position of the sellion landmark can also be verified on the virtual lateral cephalogram (Figs. 5.76, 5.77).

Step 2: Verify the midline position of the sellion landmark on the frontal view of the 3-D soft tissue surface representation (Fig. 5.12).

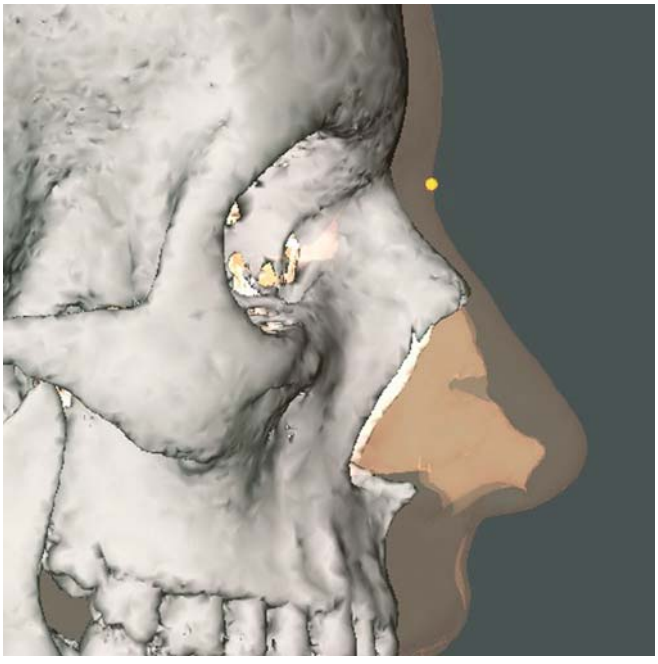

Fig. 5.11. Sellion. Profile view right. Note that sellion is usually situated more inferiorly than soft tissue nasion (3-D CT, transparent soft tissues, patient K.C.)

Fig. 5.12. Sellion. Frontal view (3-D CT, patient K.C.)

Endocanthion: en_r, en_l

Fig. 5.13. Endocanthion$_r$ and endocanthion$_l$. Frontal view (3-D CT, patient K.C.)

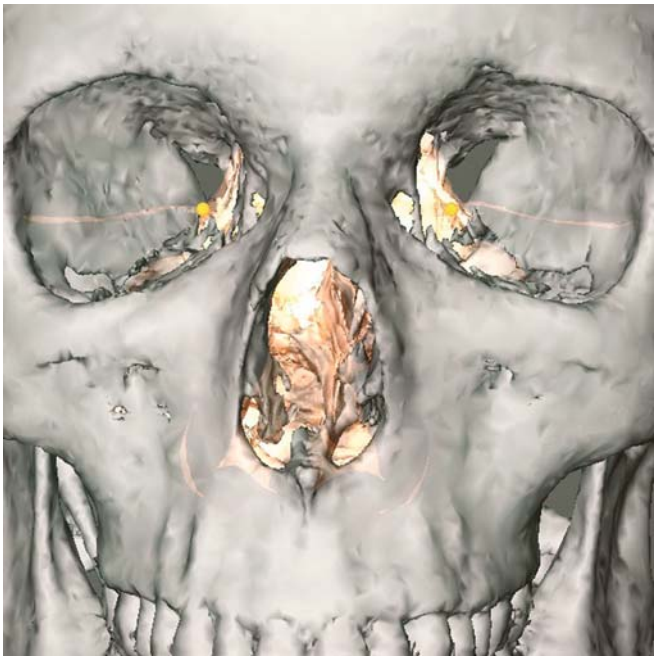

Fig. 5.14. Endocanthion$_r$ and endocanthion$_l$. Note that the endocanthion landmarks are located laterally from the medial orbital wall. Frontal view (3-D CT, transparent soft tissues, patient K.C.)

Definition of the endocanthion Landmarks

Endocanthion (en) is the soft tissue point located at the inner commissure of each eye fissure.

Virtual Definition of the endocanthion Landmarks

Define endocanthion$_r$ and endocanthion$_l$ on the frontal view of the 3-D soft tissue surface representation (Fig. 5.13).

Exocanthion: ex_r, ex_l

Fig. 5.15. Exocanthion$_r$ and exocanthion$_l$. Frontal view (3-D CT, patient K.C.)

Fig. 5.16. Exocanthion$_r$ and exocanthion$_l$. Note that although the exocanthion landmarks are mostly located slightly medially from the lateral orbital rim, they can be projected onto the lateral orbital rim, especially if scanning was done with closed eyes. Frontal view (3-D CT, transparent soft tissues, patient K.C.)

Definition of the exocanthion Landmarks

Exocanthion (ex) is the soft tissue point located at the outer commissure of each eye fissure.

Virtual Definition of the exocanthion Landmarks

Define exocanthion$_r$ and exocanthion$_l$ on the frontal view of the 3-D soft tissue surface representation (Fig. 5.15).

Maxillofrontale: mf_r, mf_l

Fig. 5.17. Maxillofrontale$_r$ and maxillofrontale$_l$. Frontal view (3-D CT, patient K.C.)

Definition of the maxillofrontale Landmarks

Maxillofrontale (mf) is the soft tissue point located at each lateral margin of the base of the nasal root at the level of the endocanthion.

Virtual Definition of the maxillofrontale Landmarks

Step 1: Define maxillofrontale$_r$ and maxillofrontale$_l$ on the frontal view of the 3-D soft tissue surface representation (Fig. 5.17).

Soft tissue orbitale: or_r - or_l

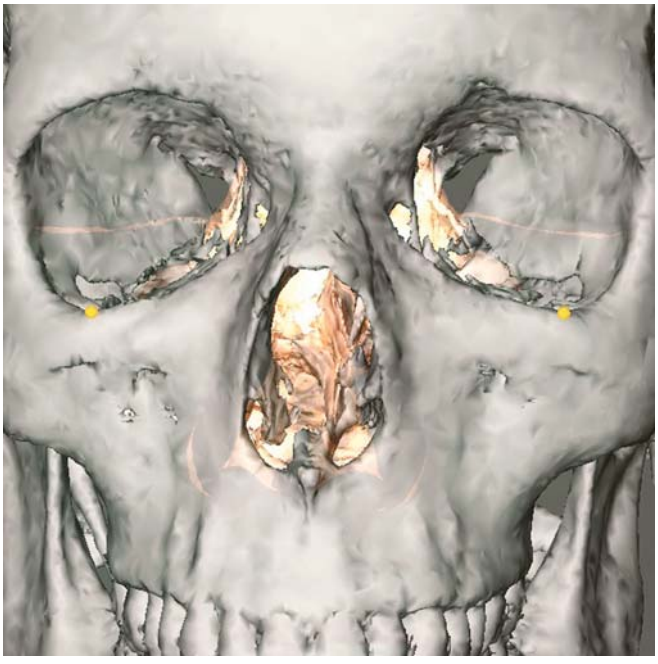

Fig. 5.18. Soft tissue $orbitale_r$ and soft tissue $orbitale_l$. Frontal view. The transparent soft tissue representation visualizes the underlying bony structures and allows accurate definition of the soft tissue orbitale landmarks (3-D CT, transparent soft tissues, patient K.C.)

Fig. 5.19. Soft tissue $orbitale_r$ and soft tissue $orbitale_l$. Frontal view (3-D CT, patient K.C.)

Definition of the soft tissue orbitale Landmarks

Soft tissue orbitale (or) is the soft tissue point located at the most inferior level of each infraorbital rim, located at the level of the 3-D hard tissue cephalometric Orbitale landmark (Chap. 4). In 3-D cephalometry, this is a well-defined soft tissue landmark and is therefore not the same as the anthropometric orbitale landmark according to L.G. Farkas, which is identical to the bony Orbitale.

Virtual Definition of the soft tissue orbitale Landmarks

Step 1: Define soft tissue $orbitale_r$ and soft tissue $orbitale_l$ on the frontal view of the 3-D transparent soft tissue surface representation (Fig. 5.18).

Step 2: Visualize both soft tissue orbitale landmarks on the frontal view of the 3-D soft tissue surface representation (Fig. 5.19).

Orbitale superius: os_r, os_l

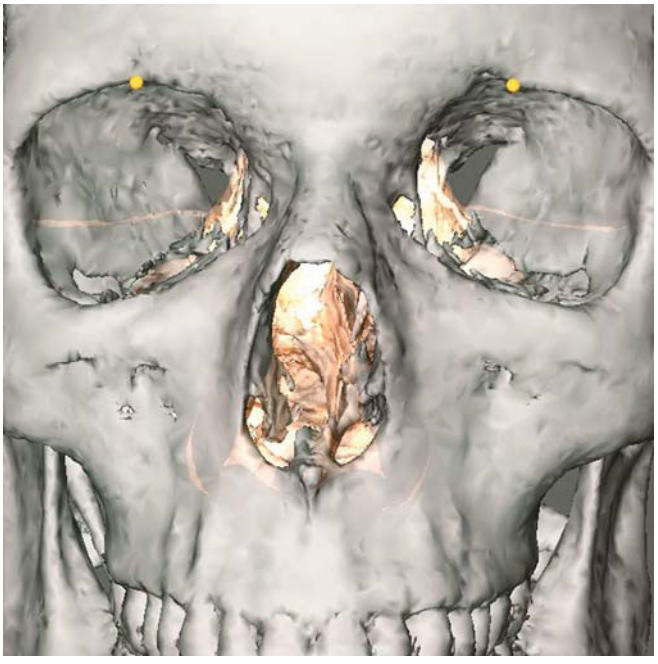

Fig. 5.20. Orbitale superius$_r$ and orbitale superius$_l$. Frontal view. The transparent soft tissue representation visualizes the underlying bony structures and allows accurate definition of the soft tissue orbitale landmarks (3-D CT, transparent soft tissues, patient K.C.)

Fig. 5.21. Orbitale superius$_r$ and orbitale superius$_l$. Frontal view (3-D CT, patient K.C.)

Definition of the orbitale superius Landmarks

Orbitale superius (os) is the soft tissue point located at the most superior level of each supraorbital rim. This landmark is close to the anthropometric orbitale landmark according to L.G. Farkas, which is defined as the highest point on the lower border of the eyebrow.

Virtual Definition of the orbitale superius Landmarks

Step 1: Define orbitale superius$_r$ and orbitale superius$_l$ on the frontal view of the 3-D transparent soft tissue surface representation (Fig. 5.20).

Step 2: Visualize both orbitale superius landmarks on the frontal view of the 3-D soft tissue surface representation (Fig. 5.21).

Zygion: zy_r, zy_l

Fig. 5.22. $Zygion_r$. Right profile view. The transparent soft tissue representation visualizes the underlying bony structures and allows accurate definition of the zygion landmarks (3-D CT, transparent soft tissues, patient K.C.)

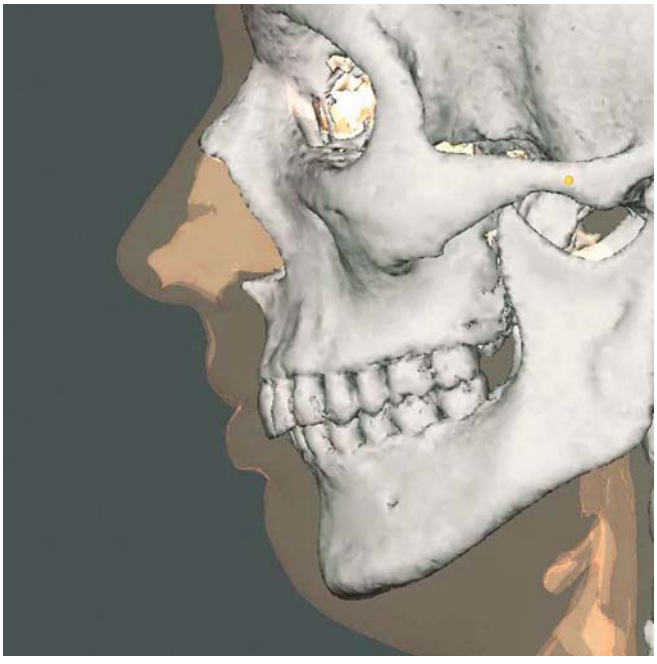

Fig. 5.23. $Zygion_l$. Left profile view (3-D CT, transparent soft tissues, patient K.C.)

Definition of the zygion Landmarks

Zygion (zy) is the most lateral point on the soft tissue contour of each zygomatic arch, located at the level of the 3-D hard tissue cephalometric Zygion landmark (Chap. 4). In 3-D cephalometry, zygion is a well-defined soft tissue landmark and is therefore not the same as the anthropometric zygion landmark according to L.G. Farkas, which is identical to the bony Zygion.

Virtual Definition of the zygion Landmarks

Step 1: Define $zygion_r$ and $zygion_l$ on the right (Fig. 5.22) and left (Fig. 5.23) profile views of the 3-D transparent soft tissue surface representation at the level of the 3-D hard tissue cephalometric Zygion landmarks.

Step 2: Verify the position of both zygion landmarks on the frontal view of the 3-D soft tissue surface representation (Fig. 5.24, Fig. 5.25).

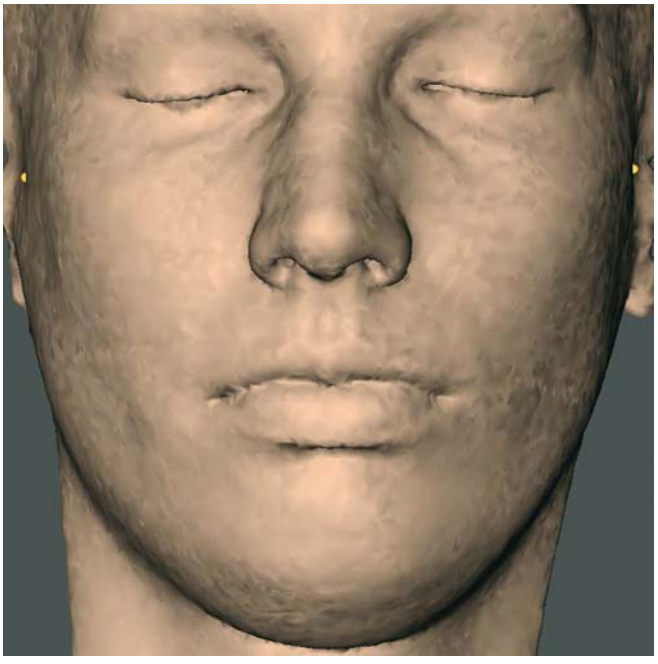

Fig. 5.24. Zygion$_r$ and zygion$_l$. Frontal view (3-D CT, patient K.C.)

Fig. 5.25. Zygion$_r$ and zygion$_l$. Proclined frontal view (3-D CT, transparent soft tissues, patient K.C.)

Tragion: t_r, t_l

Fig. 5.26. Tragion$_r$. Right profile view (3-D CT, transparent soft tissues, patient K.C.)

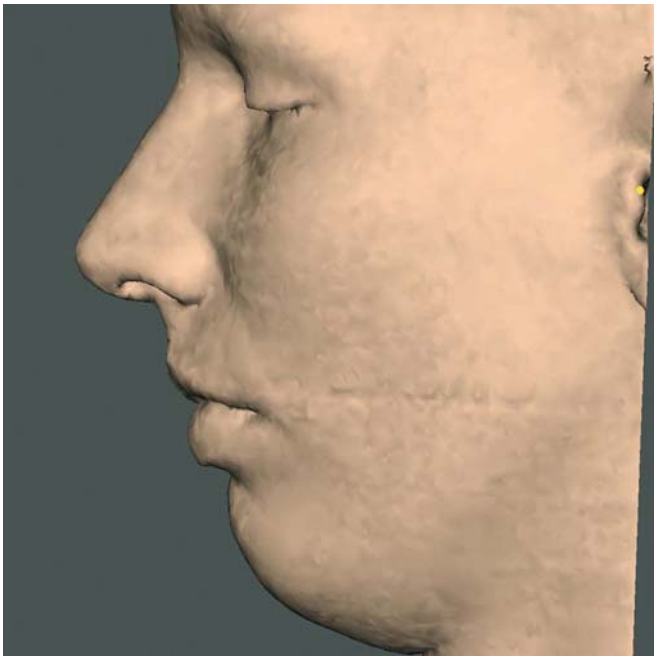

Fig. 5.27. Tragion$_l$. Left profile view (3-D CT, transparent soft tissues, patient K.C.)

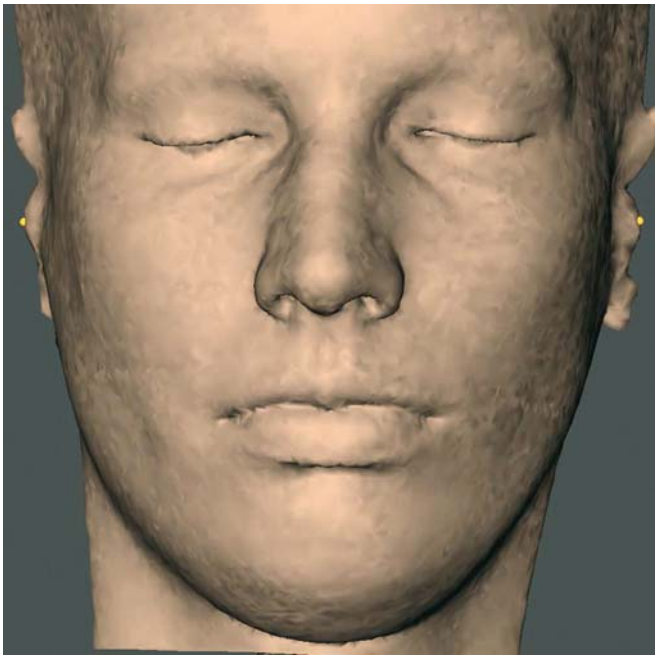

Fig. 5.28. Tragion$_r$ and tragion$_l$. Frontal view (3-D CT, transparent soft tissues, patient K.C.)

Definition of the tragion Landmarks

Tragion (t) is the point located at the upper margin of each tragus.

Virtual Definition of the tragion Landmarks

Step 1: Define tragion$_r$ and tragion$_l$ on the right (Fig. 5.26) and left (Fig. 5.27) profile views of the 3-D soft tissue surface representation.

Step 2: Verify the position of both tragion landmarks on the frontal view of the 3-D soft tissue surface representation (Fig. 5.28).

Pronasale: prn

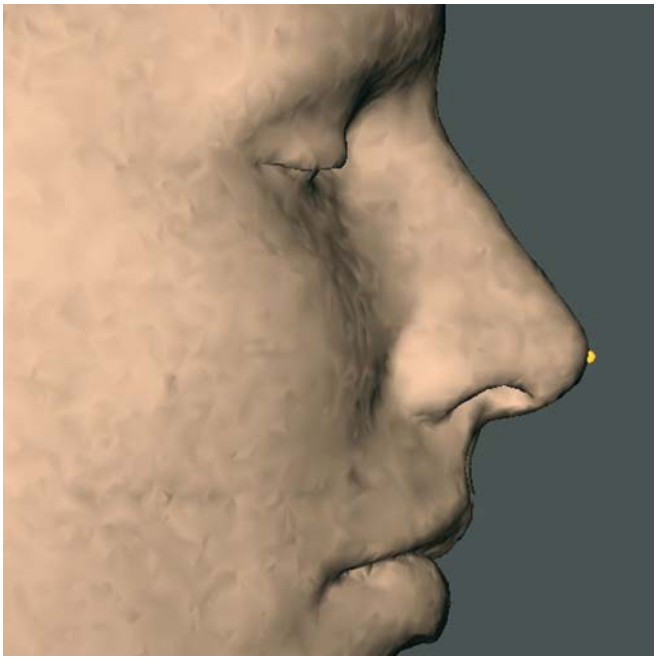

Fig. 5.29. Pronasale. Profile view right (3-D CT, patient K.C.)

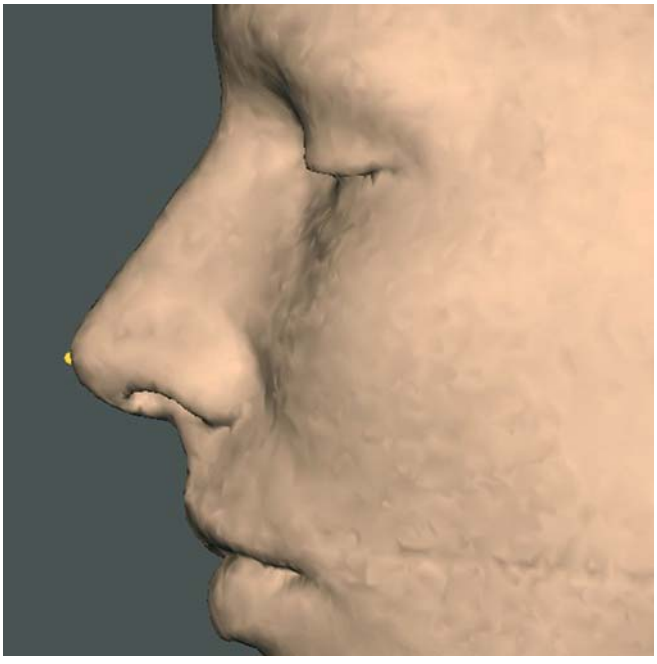

Fig. 5.30. Pronasale. Profile view left (3-D CT, patient K.C.)

Definition of the pronasale Landmark

Pronasale (prn) is the most anterior midpoint of the nasal tip. If a bifid nose is present, the more protruding tip is chosen to determine pronasale as proposed by L.G. Farkas.

Virtual Definition of the pronasale Landmark

Step 1: Define pronasale on the right profile view of the 3-D soft tissue surface representation (Fig. 5.29) and verify its position on the left profile view (Fig. 5.30). The position of the pronasale landmark can also be verified on the virtual lateral cephalogram (Figs. 5.76, 5.77).

Step 2: Verify the midline position of the pronasale landmark on the base view of the 3-D soft tissue surface representation (Fig. 5.31).

Subnasale: sn

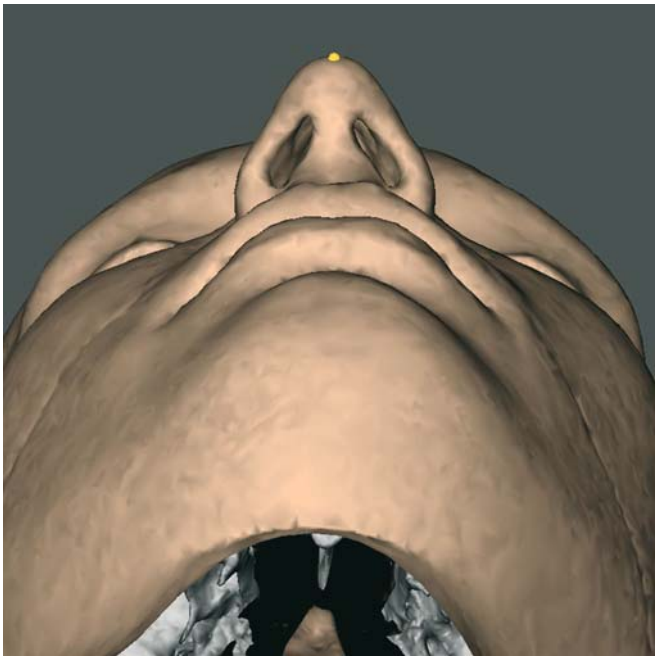

Fig. 5.31. Pronasale. Base view (3-D CT, patient K.C.)

Definition of the subnasale Landmark

Subnasale (sn) is the midpoint on the nasolabial soft tissue contour between the columella crest and the upper lip.

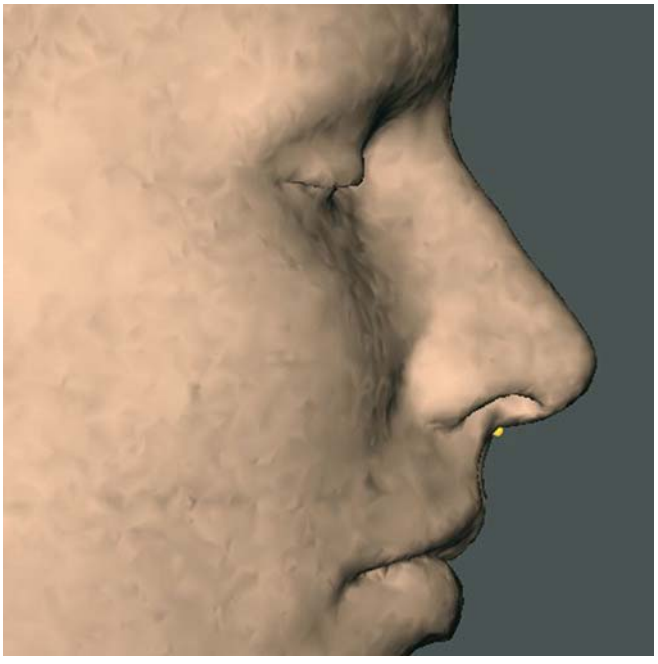

Fig. 5.32. Subnasale. Profile view right (3-D CT, patient K.C.)

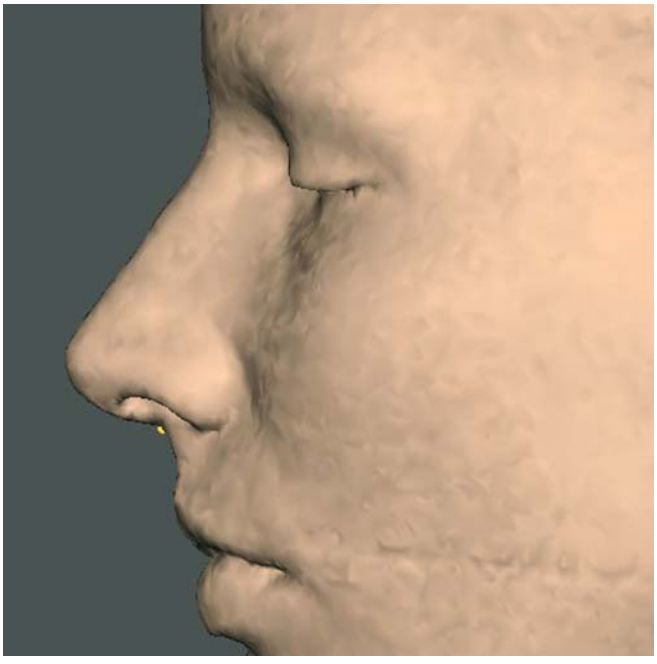

Fig. 5.33. Subnasale. Profile view left (3-D CT, patient K.C.)

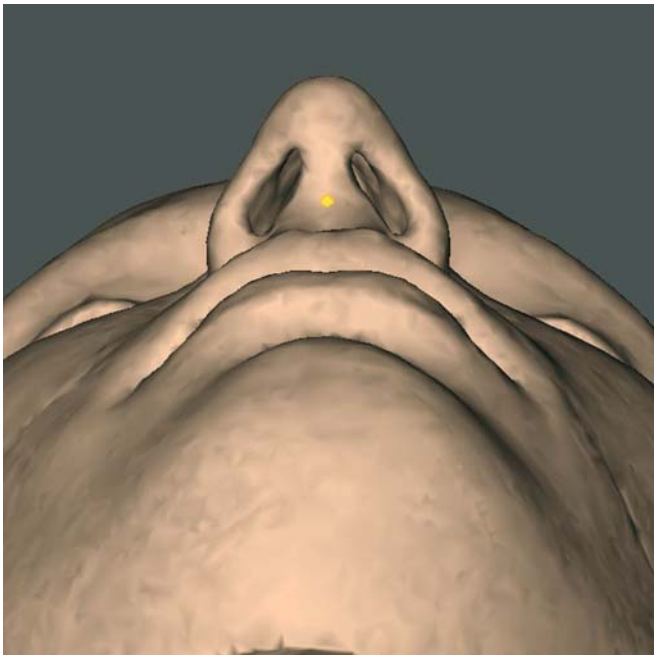

Fig. 5.34. Subnasale. Base view (3-D CT, patient K.C.)

Virtual Definition of the subnasale Landmark

Step 1: Define subnasale on the right profile view of the 3-D soft tissue surface representation (Fig. 5.32) and verify its position on the left profile view (Fig. 5.33). The position of the subnasale landmark can also be verified on the virtual lateral cephalogram (Figs. 5.76, 5.77).

Step 2: Verify the midline position of the subnasale landmark on the base view of the 3-D soft tissue surface representation (Fig. 5.34)

Subnasale': sn_r', sn_l'

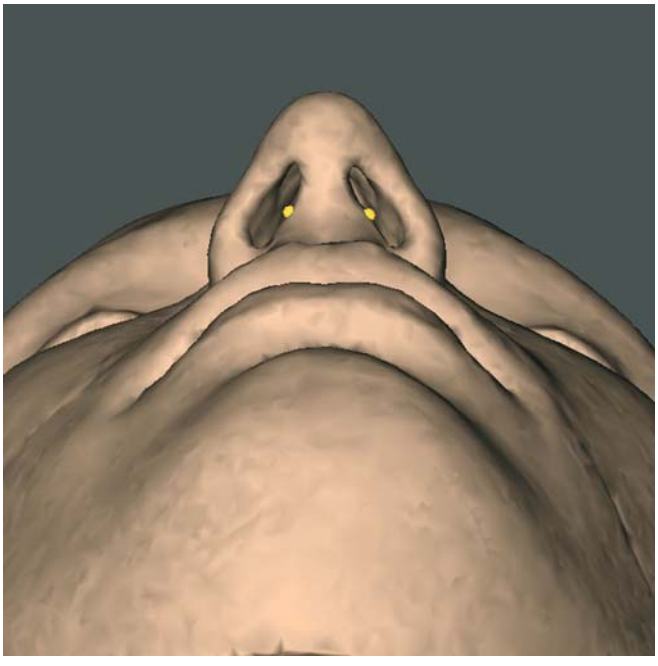

Fig. 5.35. Subnasale'$_r$ and subnasale'$_l$. Base view (3-D CT, patient K.C.)

Definition of the subnasale' Landmarks

Subnasale' (sn') is the point at each margin of the mid-portion of the columella crest.

Virtual Definition of the subnasale' Landmarks

Define subnasale'$_r$ and subnasale'$_l$ on the base view of the 3-D soft tissue surface representation (Fig. 5.35)

Alare: al_r, al_l

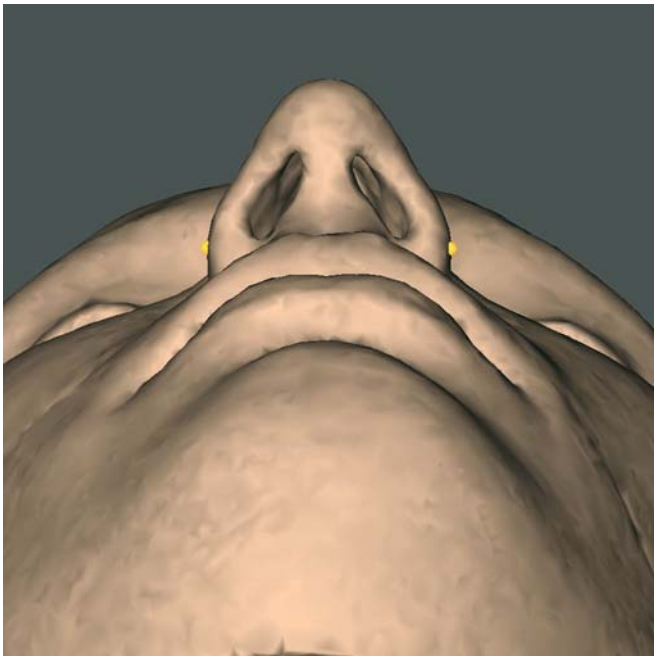

Fig. 5.36. $Alare_r$ and $alare_l$. Base view (3-D CT, patient K.C.)

Definition of the alare Landmarks

Alare (al) is the most lateral point on each alar contour.

Virtual Definition of the alare Landmarks

Define $alare_r$ and $alare_l$ on the base view of the 3-D soft tissue surface representation (Fig. 5.36).

Alar curvature point: ac_r, ac_l

Fig. 5.37. Alar curvature point$_r$ and alar curvature point$_l$. Submental view (3-D CT, patient K.C.)

Definition of the alar curvature point Landmarks

Alar curvature point (ac) is the point located at the facial insertion of each alar base.

Virtual Definition of the alar curvature point Landmarks

Define alar curvature point$_r$ and alar curvature point$_l$ on the submental view of the 3-D soft tissue surface representation (Fig. 5.37).

Nostril top point: nt_r, nt_l

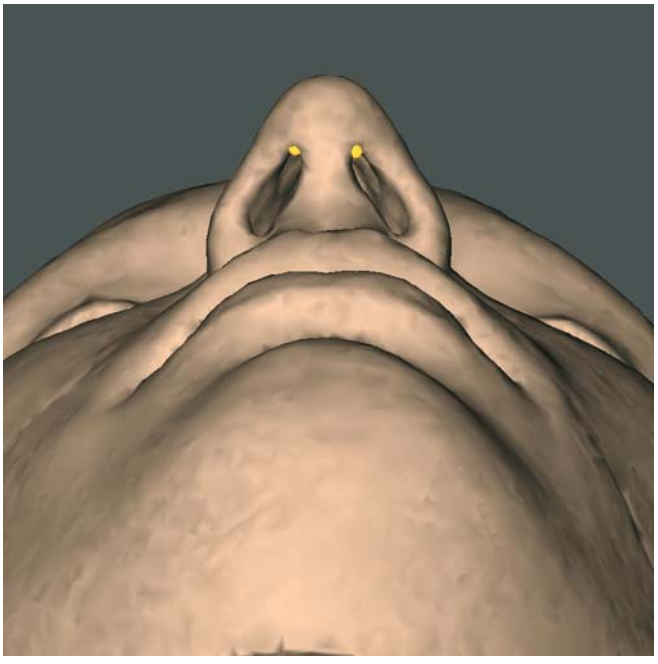

Fig. 5.38. Nostril top point$_r$ and nostril top point$_l$. Base view (3-D CT, patient K.C.)

Definition of the nostril top point Landmarks

Nostril top point (nt) is the highest point of each nostril or the superior terminal point of each nostril axis. This landmark is close to the columella breakpoint (c') of Daniel.

Virtual Definition of the nostril top point Landmarks

Define nostril top point$_r$ and nostril top point$_l$ on the base view of the 3-D soft tissue surface representation (Fig. 5.38).

Columella constructed point: c″

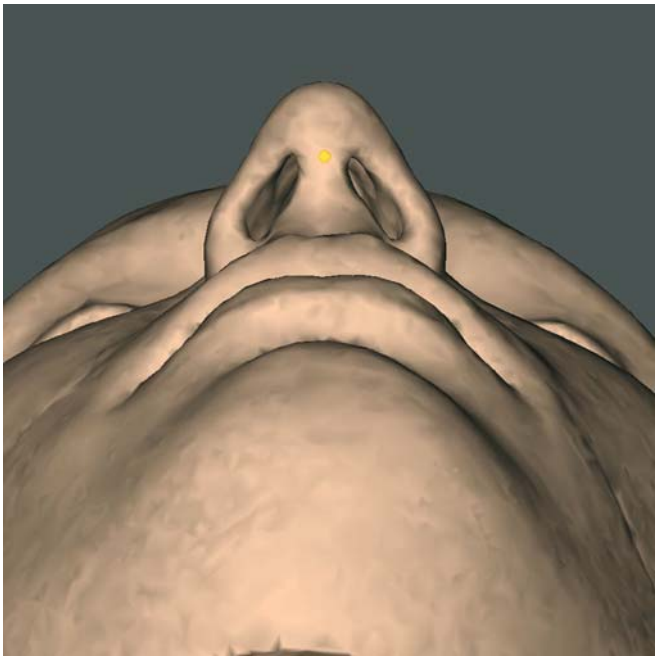

Fig. 5.39. Columella constructed point. Base view (3-D CT, patient K.C.)

Definition of the columella constructed point Landmark

Columella constructed point (c'') is the midpoint of the columella crest at the level of the nostril top points.

Virtual Definition of the columella constructed point Landmark

Define columella constructed point on the base view of the 3-D soft tissue surface representation (Fig. 5.39).

Nostril base point: nb_r, nb_l

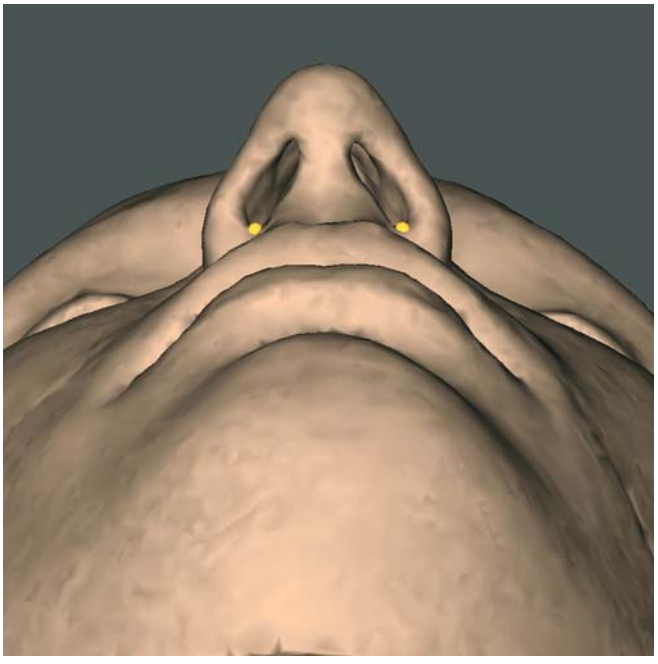

Fig. 5.40. Nostril base point$_r$ and nostril base point$_l$. Base view (3-D CT, patient K.C.)

Definition of the nostril base point Landmarks

Nostril base point (nb) is the lowest point of each nostril or the inferior terminal point of each nostril axis.

Virtual Definition of the nostril base point Landmarks

Define nostril base point$_r$ and nostril base point$_l$ on the base view of the 3-D soft tissue surface representation (Fig. 5.40).

Subspinale: ss

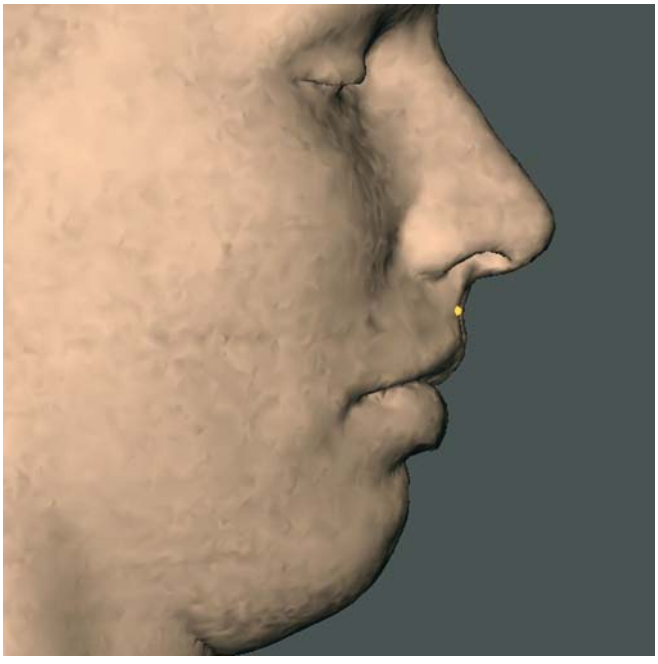

Fig. 5.41. Subspinale. Profile view right (3-D CT, patient K.C.)

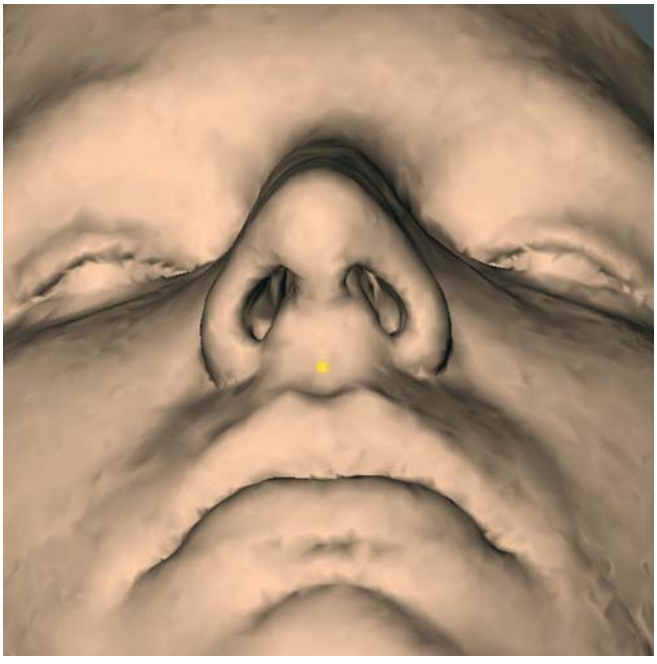

Fig. 5.42. Subspinale. Submental view (3-D CT, patient K.C.)

Definition of the subspinale Landmark

Subspinale (ss) is the most posterior midpoint of the philtrum.

Virtual Definition of the subspinale Landmark

Step 1: Define subspinale on the right or left profile view of the 3-D soft tissue surface representation (Fig. 5.41).

Step 2: Correct the midline position of the subspinale landmark on the submental view of the 3-D soft tissue surface representation (Fig. 5.42). In most cases the landmark is now no longer visible on the right and left profile views of the 3-D soft tissue surface representation (Fig. 5.43). However, it is still visible on the profile 3-D transparent soft tissue surface representation (Fig. 5.44) and on the virtual lateral cephalogram (Figs. 5.76, 5.77).

Step 3: Verify the position of the subspinale landmark on the right (Fig. 5.45) and left (Fig. 5.46) three-quarter views of the 3-D soft tissue surface representation.

Fig. 5.43. Subspinale. Profile view right (3-D CT, patient K.C.)

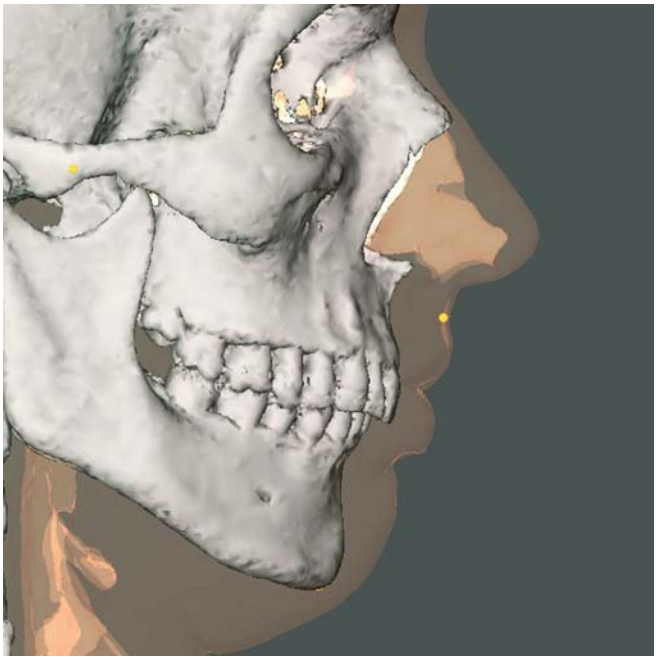

Fig. 5.44. Subspinale. Profile view left (3-D CT, transparent soft tissues, patient K.C.)

Fig. 5.45. Subspinale. Three-quarter view right (3-D CT, patient K.C.)

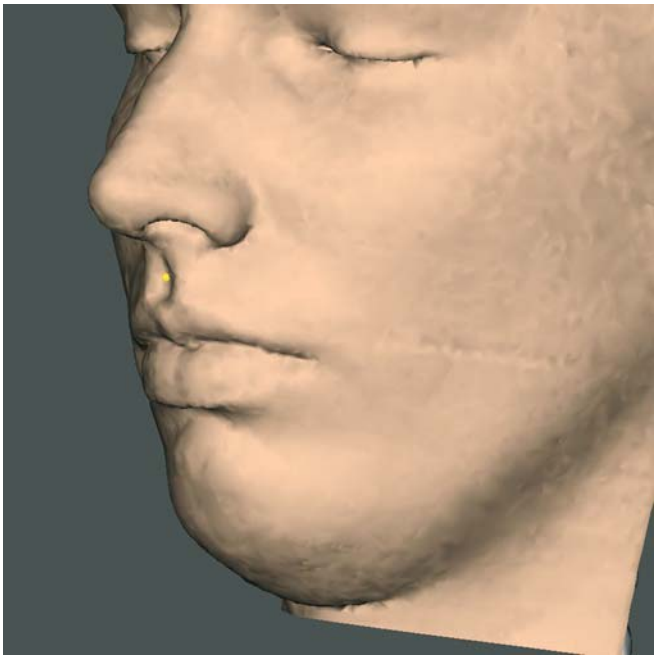

Fig. 5.46. Subspinale. Three-quarter view left (3-D CT, patient K.C.)

Labiale (or labrale) superius: ls

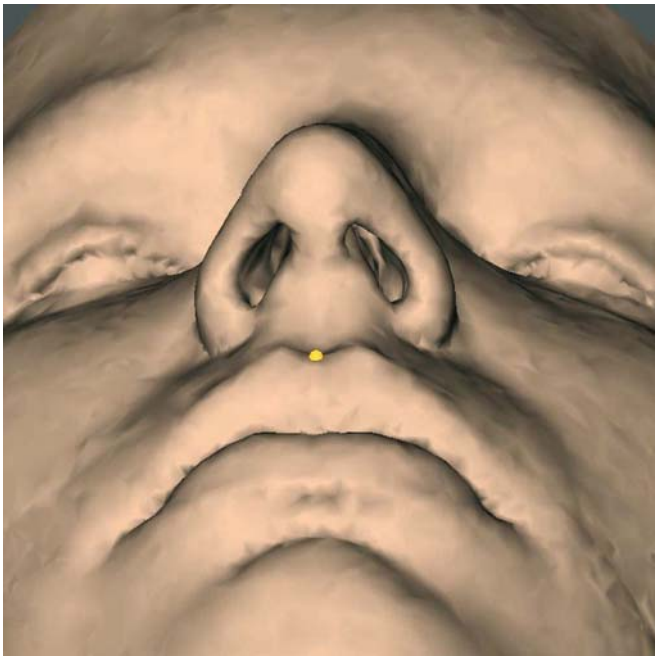

Fig. 5.47. Labiale superius. Submental view (3-D CT, patient K.C.)

Definition of the labiale superius Landmark

Labiale superius (ls) is the midpoint of the vermilion line of the upper lip.

Virtual Definition of the labiale superius Landmark

Step 1: Define labiale superius on the submental view of the 3-D soft tissue surface representation (Fig. 5.47).

Step 2: Verify the position of the labiale superius landmark on the right (Fig. 5.48) and left (Fig. 5.49) three-quarter views of the 3-D soft tissue surface representation. The position of the subspinale (ss) landmark can also be verified on the virtual lateral cephalogram (Figs. 5.76, 5.77).

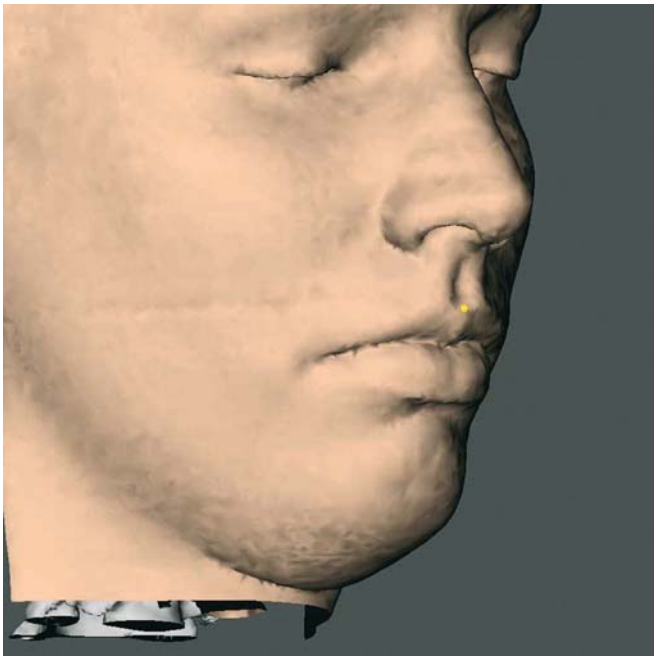

Fig. 5.48. Labiale superius. Three-quarter view right (3-D CT, patient K.C.)

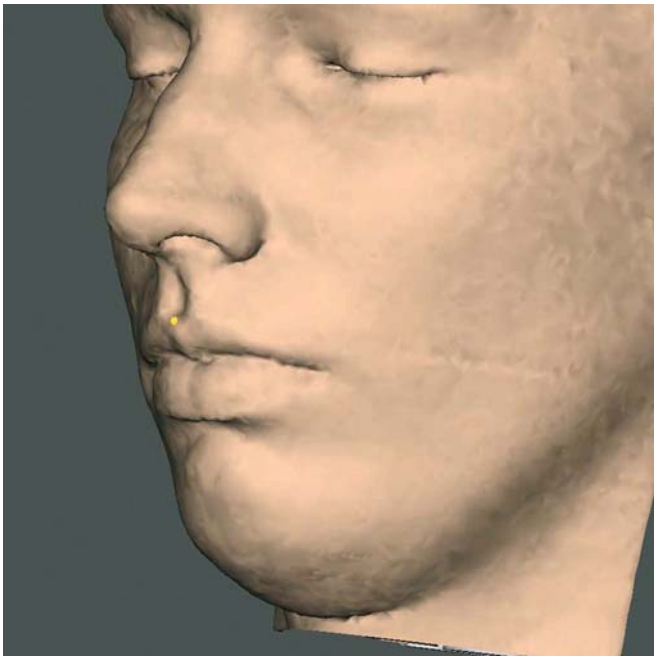

Fig. 5.49. Labiale superius. Three-quarter view left (3-D CT, patient K.C.)

Crista philtri: cph_r, cph_l

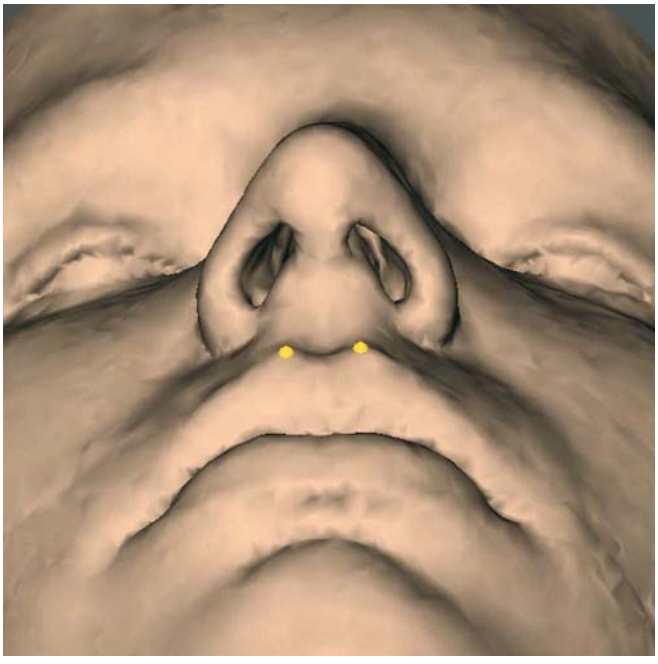

Fig. 5.50. Crista philtri$_r$ and crista philtri$_l$. Submental view (3-D CT, patient K.C.)

Definition of the crista philtri Landmarks

Crista philtri (cph) is the point at each crossing of the vermilion line and the elevated margin of the philtrum.

Virtual Definition of the crista philtri Landmarks

Step 1: Define crista philtri$_r$ and crista philtri$_l$ on the submental view of the 3-D soft tissue surface representation (Fig. 5.50).

Step 2: Verify the position of the crista philtri landmarks on the right (Fig. 5.51) and left (Fig. 5.52) three-quarter views of the 3-D soft tissue surface representation.

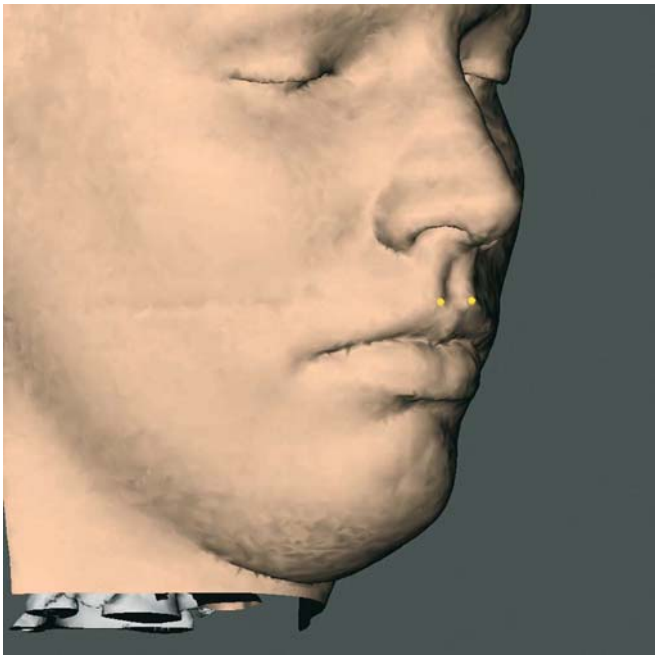

Fig. 5.51. Crista philtri$_r$ and crista philtri$_l$. Three-quarter view right (3-D CT, patient K.C.)

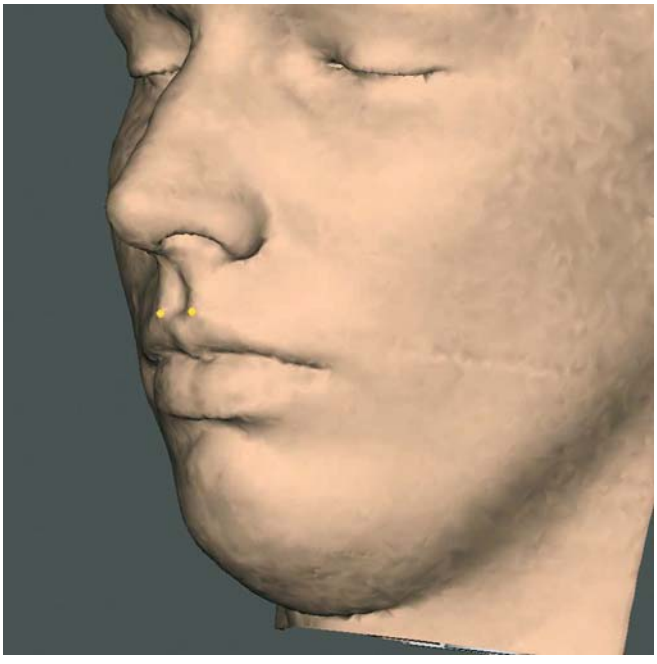

Fig. 5.52. Crista philtri$_r$ and crista philtri$_l$. Three-quarter view left (3-D CT, patient K.C.)

Stomion: sto

Definition of the stomion Landmark

Stomion (sto) is the midpoint of the horizontal labial fissure. When the lips are not closed in the rest position, stomion is a constructed point defined as the midpoint of the interlabial gap. In this case, additional landmarks stomion$_u$ (sto$_u$; midpoint of the lower border of the upper lip) and stomion$_i$ (sto$_i$; midpoint of the upper border of the lower lip) are defined to construct stomion.

Virtual Definition of the stomion Landmark

Step 1: Define stomion on the right profile view of the 3-D soft tissue surface representation (Fig. 5.53) and verify its position on the left profile view (Fig. 5.54). The position of the stomion landmark can also be verified on the virtual lateral cephalogram (Figs. 5.76, 5.77).

Step 2: Verify the midline position of the stomion landmark on the frontal view of the 3-D soft tissue surface representation (Fig. 5.55).

Fig. 5.53. Stomion. Profile view right (3-D CT, patient K.C.)

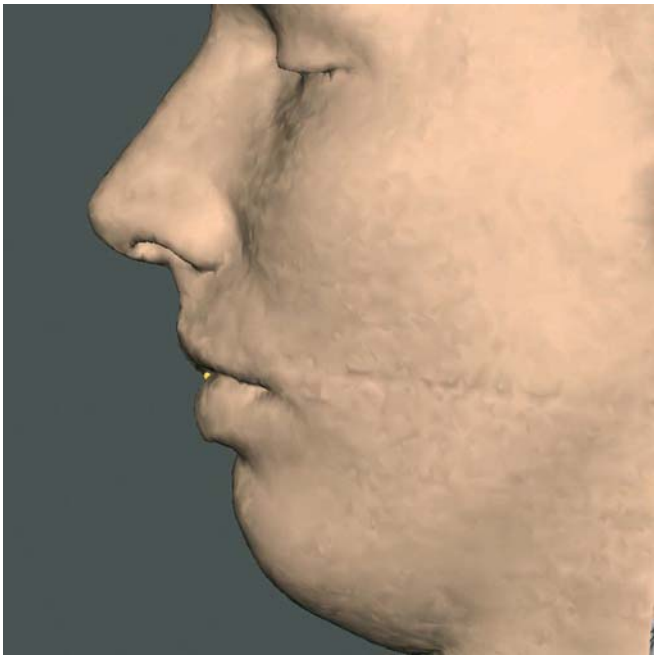

Fig. 5.54. Stomion. Profile view left (3-D CT, patient K.C.)

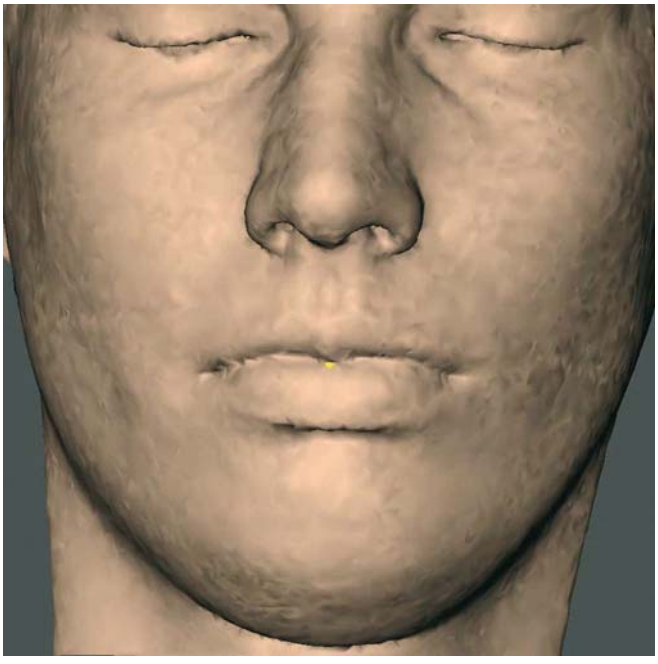

Fig. 5.55. Stomion. Frontal view (3-D CT, patient K.C.)

Cheilion: ch_r, ch_l

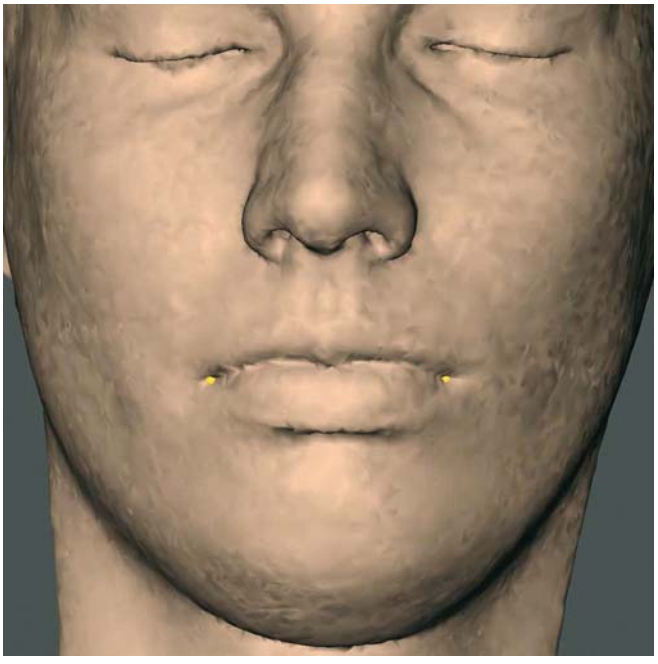

Fig. 5.56. Cheilion$_r$ and cheilion$_l$. Frontal view (3-D CT, patient K.C.)

Definition of the cheilion Landmarks

Cheilion (ch) is the point located at each labial commissure.

Virtual Definition of the cheilion Landmarks

Step 1: Define the cheilion$_r$ and cheilion$_l$ landmarks on the frontal view of the 3-D soft tissue surface representation (Fig. 5.56).

Labiale (or labrale) inferius: li

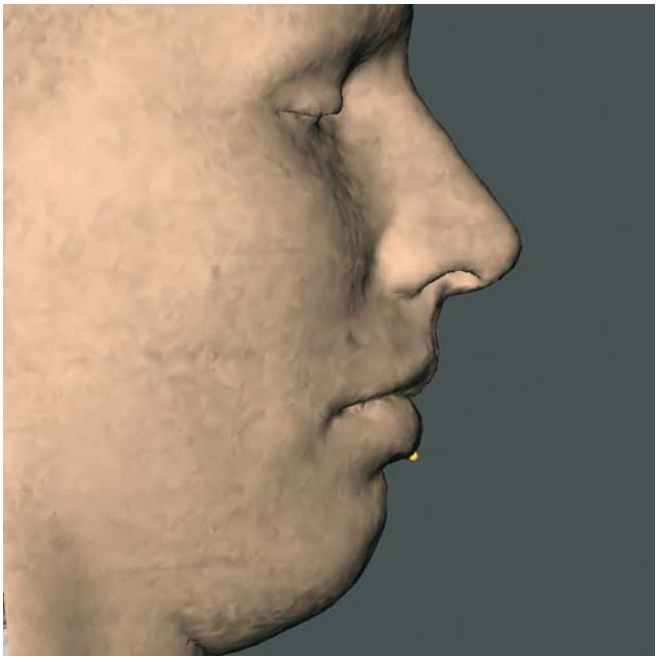

Fig. 5.57. Labiale inferius. Profile view right (3-D CT, patient K.C.)

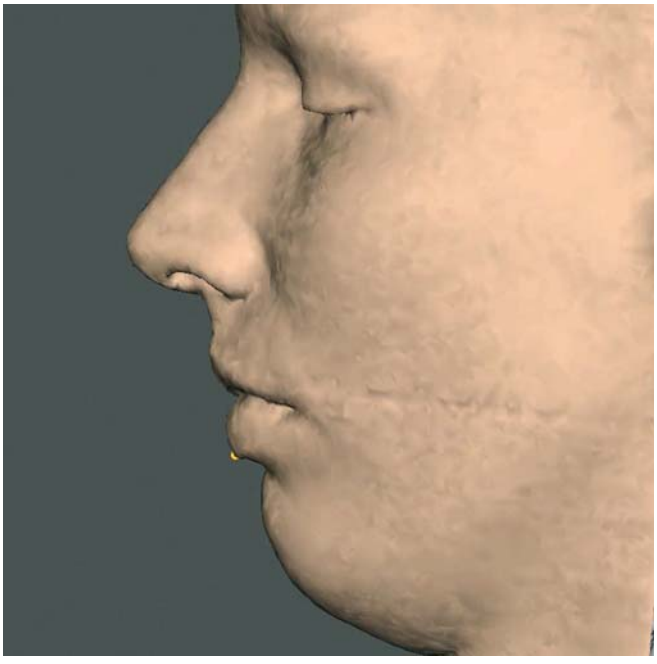

Fig. 5.58. Labiale inferius. Profile view left (3-D CT, patient K.C.)

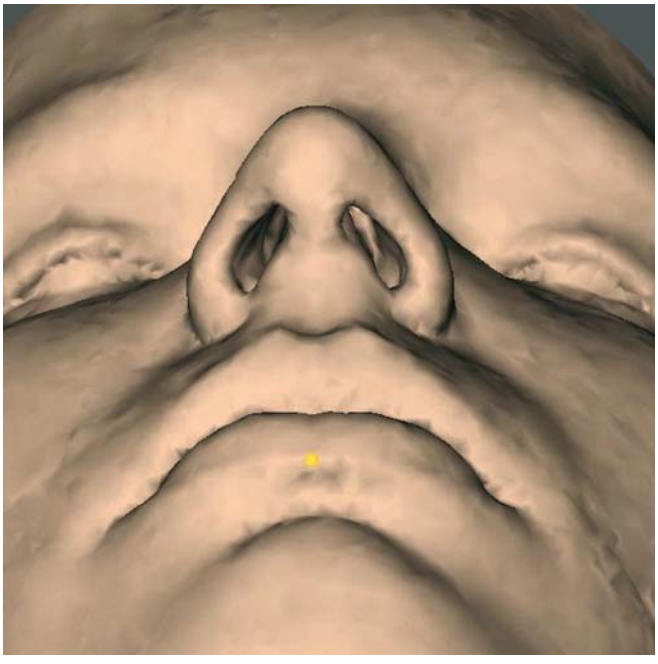

Fig. 5.59. Labiale inferius. Submental view (3-D CT, patient K.C.)

Definition of the labiale inferius Landmark

Labiale inferius (li) is the midpoint of the vermilion line of the lower lip.

Virtual Definition of the labiale inferius Landmark

Step 1: Define labiale inferius on the right profile view of the 3-D soft tissue surface representation (Fig. 5.57) and verify its position on the left profile view (Fig. 5.58). The position of the labiale inferius landmark can also be verified on the virtual lateral cephalogram (Figs. 5.76, 5.77).

Step 2: Verify the midline position of the labiale inferius landmark on the submental view of the 3-D soft tissue surface representation (Fig. 5.59).

Soft tissue gonion: go_r, go_l

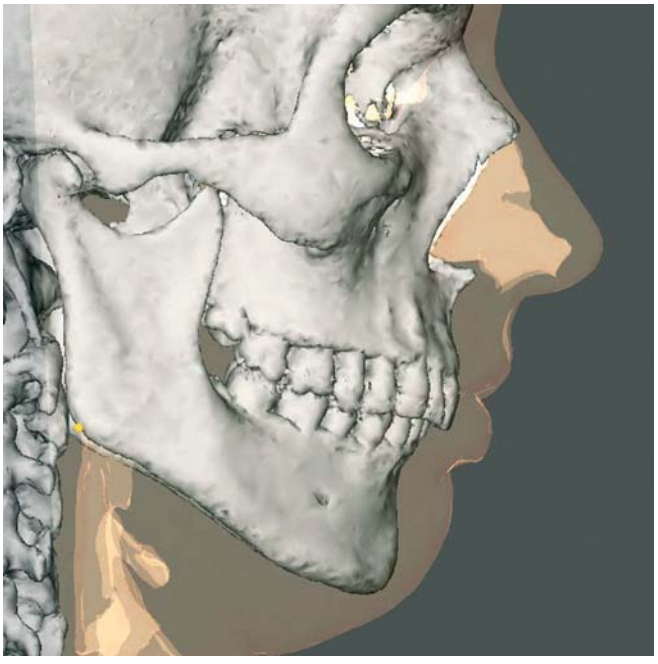

Fig. 5.60. Soft tissue $gonion_r$. Profile view right (3-D CT, transparent soft tissues, patient K.C.)

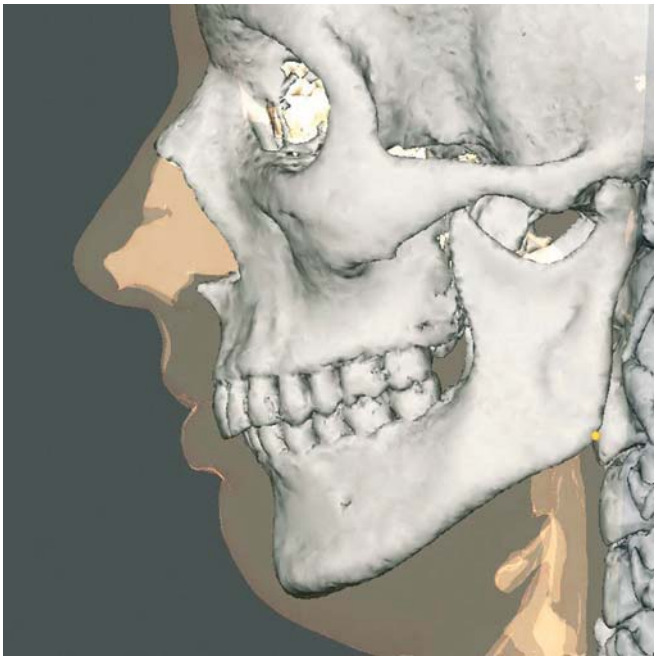

Fig. 5.61. Soft tissue $gonion_l$. Profile view left (3-D CT, transparent soft tissues, patient K.C.)

Definition of the soft tissue gonion Landmarks

Soft tissue gonion (go) is the most lateral point on the soft tissue contour of each mandibular angle, located at the same level as the 3-D hard tissue cephalometric Gonion landmark (Chap. 4).

Virtual Definition of the soft tissue gonion Landmarks

Step 1: Define soft tissue $gonion_r$ and soft tissue $gonion_l$ on the right (Fig. 5.60) and left (Fig. 5.61) profile views of the 3-D transparent soft tissue surface representation.

Step 2: Verify the position of both soft tissue gonion landmarks on the frontal view of the 3-D transparent soft tissue surface representation (Fig. 5.62).

Step 3: Visualize both soft tissue gonion landmarks on the frontal view of the 3-D soft tissue surface representation (Fig. 5.63).

Fig. 5.62. Soft tissue gonion$_r$ and soft tissue gonion$_l$. Frontal view. The transparent soft tissue representation visualizes the underlying bony structures and allows accurate definition of the soft tissue gonion landmarks (3-D CT, transparent soft tissues, patient K.C.)

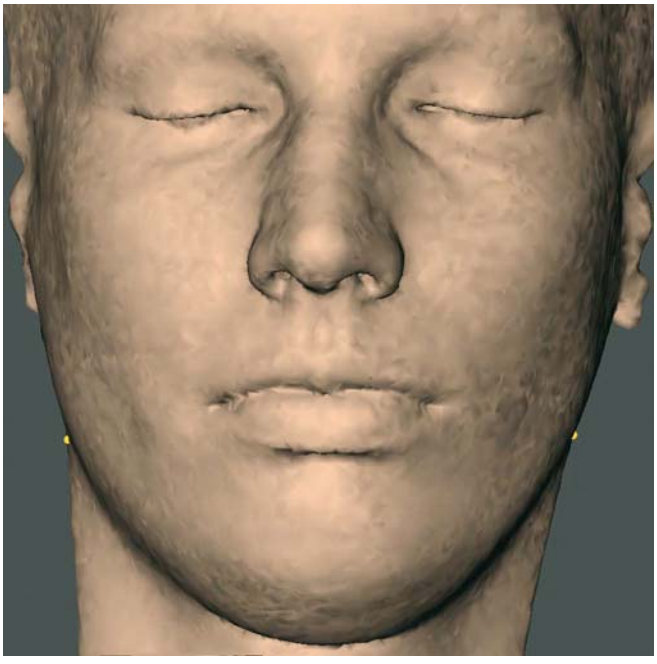

Fig. 5.63. Soft tissue gonion$_r$ and soft tissue gonion$_l$. Frontal view (3-D CT, patient K.C.)

Sublabiale: sl

Fig. 5.64. Sublabiale. Profile view right (3-D CT, patient K.C.)

Fig. 5.65. Sublabiale. Profile view left (3-D CT, patient K.C.)

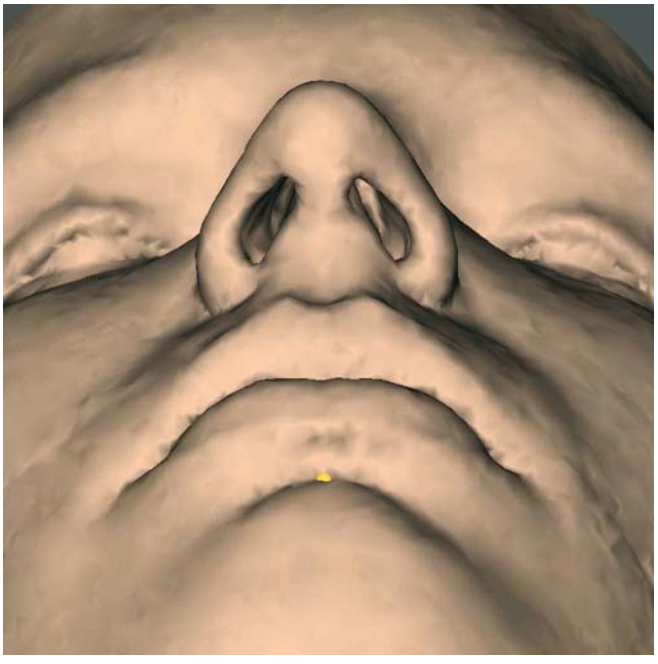

Fig. 5.66. Sublabiale. Submental view (3-D CT, patient K.C.)

Definition of the sublabiale Landmark

Sublabiale (sl) is the most posterior midpoint on the labiomental soft tissue contour that defines the border between the lower lip and the chin.

Virtual Definition of the sublabiale Landmark

Step 1: Define sublabiale on the right profile view of the 3-D soft tissue surface representation (Fig. 5.64) and verify its position on the left profile view (Fig. 5.65). The position of the sublabiale landmark can also be verified on the virtual lateral cephalogram (Figs. 5.76, 5.77).

Step 2: Verify the midline position of the sublabiale landmark on the submental view of the 3-D soft tissue surface representation (Fig. 5.66).

Soft tissue pogonion: pg

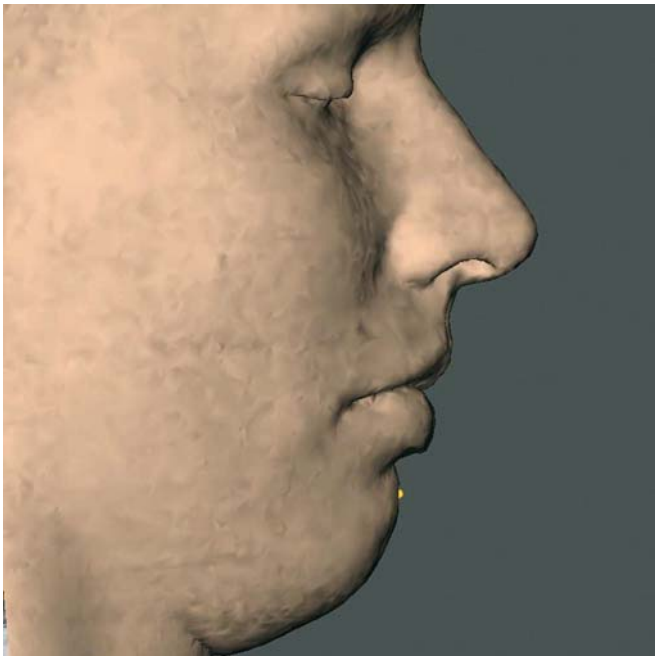

Fig. 5.67. Soft tissue pogonion. Profile view right (3-D CT, patient K.C.)

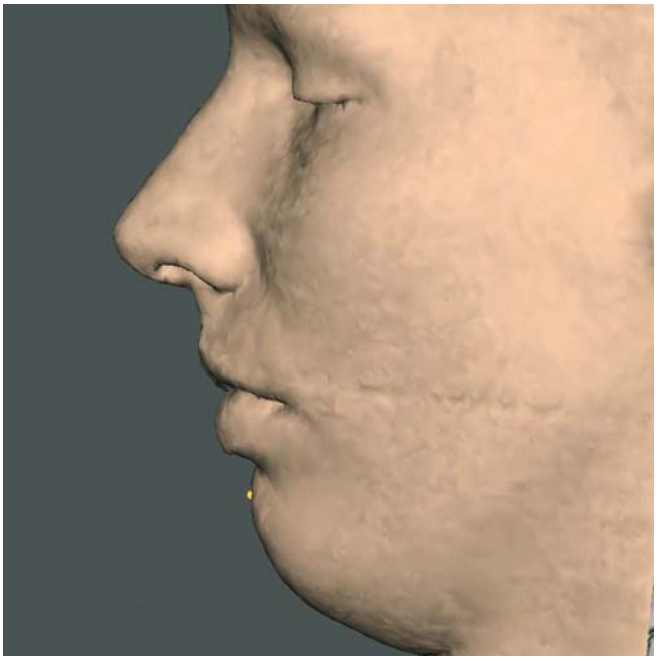

Fig. 5.68. Soft tissue pogonion. Profile view left (3-D CT, patient K.C.)

Definition of the soft tissue pogonion Landmark

Soft tissue pogonion (pg) is the most anterior midpoint of the chin.

Virtual Definition of the soft tissue pogonion Landmark

Step 1: Define soft tissue pogonion on the right profile view of the 3-D soft tissue surface representation (Fig. 5.67) and verify its position on the left profile view (Fig. 5.68). The position of the soft tissue pogonion landmark can also be verified on the virtual lateral cephalogram (Figs. 5.76, 5.77).

Step 2: Verify the midline position of the soft tissue pogonion landmark on the submental view of the 3-D soft tissue surface representation (Figs. 5.69, 5.70).

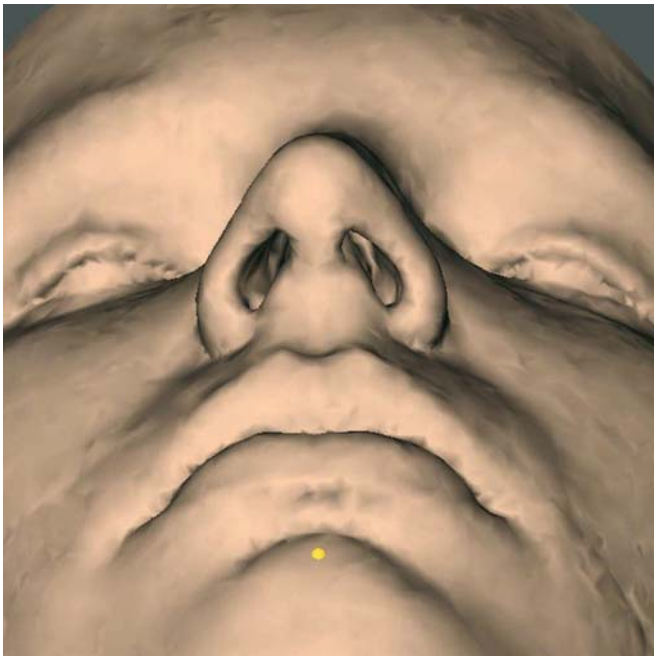

Fig. 5.69. Soft tissue pogonion. Submental view left (3-D CT, patient K.C.)

Fig. 5.70. Soft tissue pogonion. Profile view right. Note that the soft tissue pogonion landmark is usually more superiorly located than the bony Pogonion landmark (3-D CT, transparent soft tissues, patient K.C.)

Soft tissue gnathion (or menton): gn

Fig. 5.71. Soft tissue gnathion. Profile view right (3-D CT, transparent soft tissues, patient K.C.)

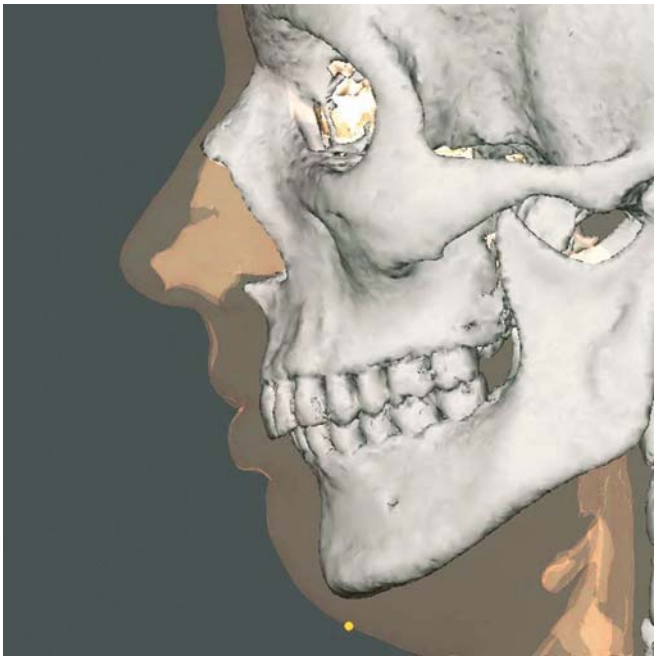

Fig. 5.72. Soft tissue gnathion. Profile view left (3-D CT, transparent soft tissues, patient K.C.)

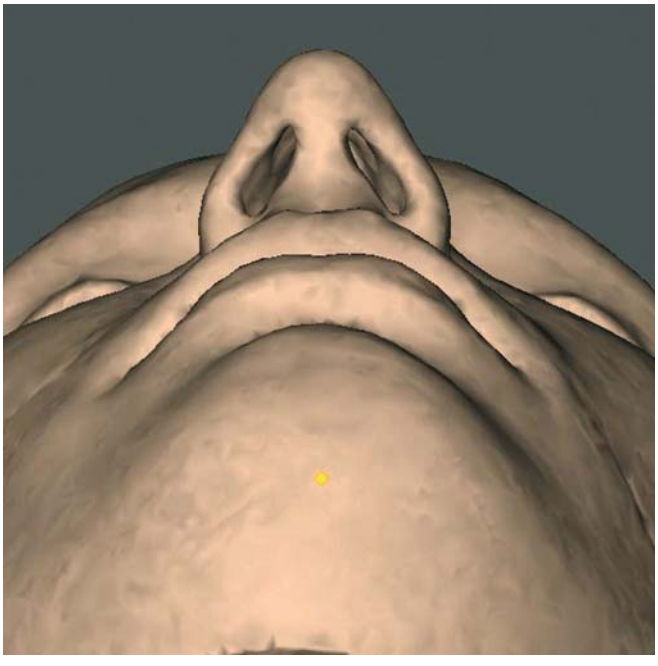

Fig. 5.73. Soft tissue gnathion. Base view (3-D CT, patient K.C.)

Definition of the soft tissue gnathion Landmark

Soft tissue gnathion (gn) is the most inferior midpoint on the soft tissue contour of the chin located at the level of the 3-D cephalometric hard tissue Menton landmark (Chap. 4). In 3-D cephalometry, soft tissue gnathion is a well-defined soft tissue landmark and is therefore not the same as the anthropometric gnathion landmark according to L.G. Farkas, which is identical to the bony Gnathion.

Virtual Definition of the soft tissue gnathion Landmark

Step 1: Define soft tissue gnathion on the right profile view of the transparent 3-D soft tissue surface representation (Fig. 5.71) and verify its position on the left profile view of the transparent 3-D soft tissue surface representation (Fig. 5.72). The position of the soft tissue gnathion landmark can also be verified on the virtual lateral cephalogram (Figs. 5.76, 5.77).

Step 2: Verify the midline position of the soft tissue gnathion landmark on the base view of the 3-D soft tissue surface representation (Fig. 5.73).

5.2
Set-up of 3-D Cephalometric Soft Tissue Landmarks

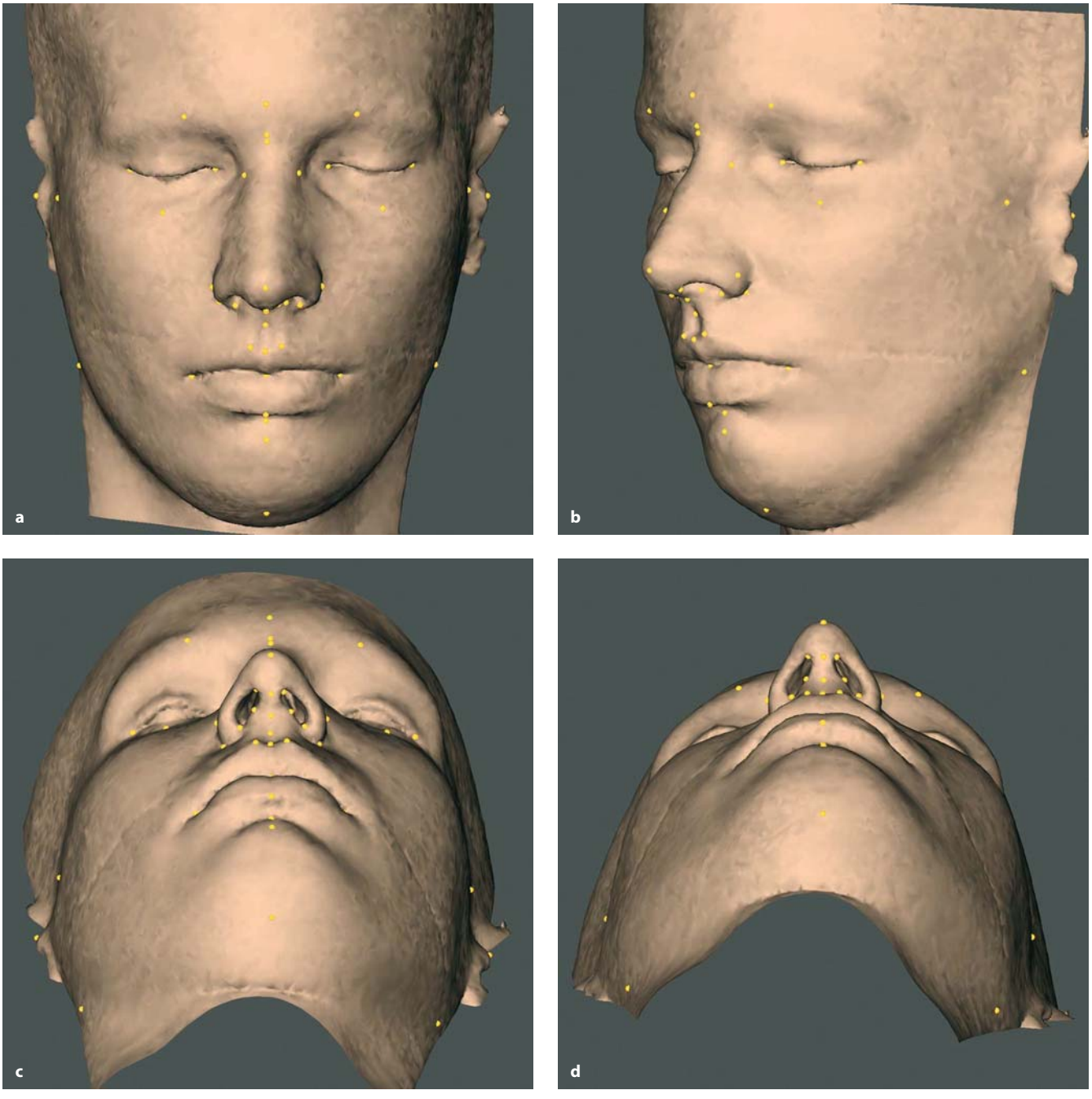

Fig. 5.74 a–d. Set-up of 3-D cephalometric soft tissue landmarks. (3-D CT, patient K.C.)

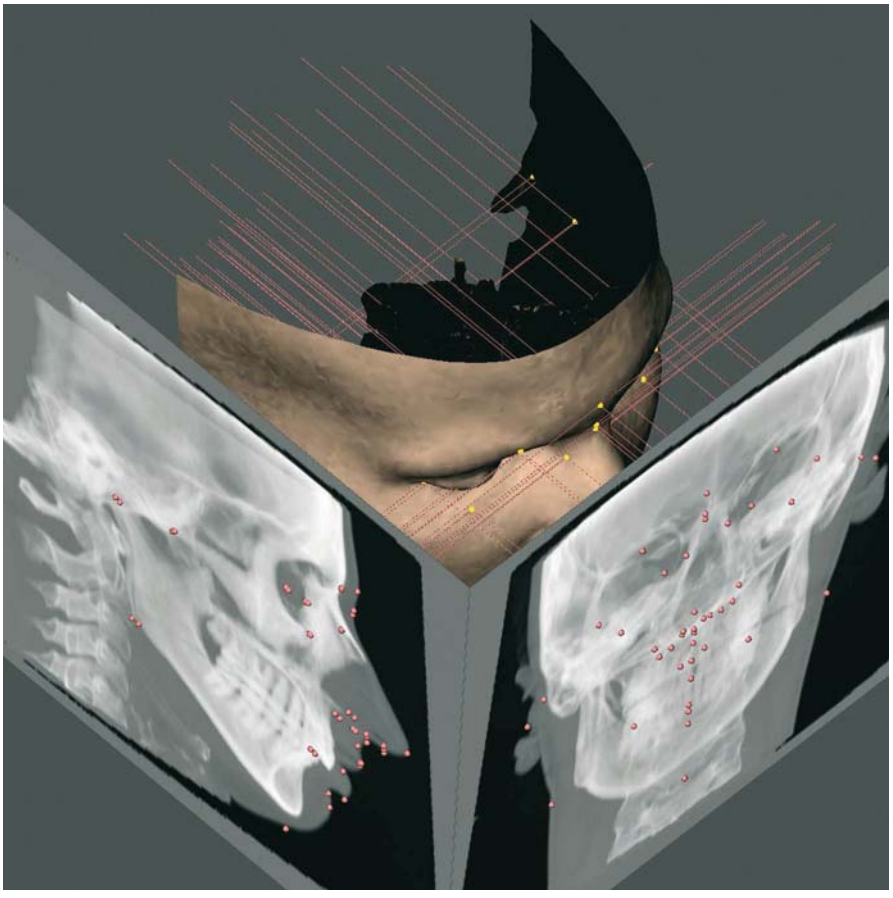

Fig. 5.75. Set-up of 3-D cephalometric soft tissue landmarks. Virtual lateral and frontal cephalograms linked to the 3-D soft tissue surface representation (3-D CT, patient K.C.)

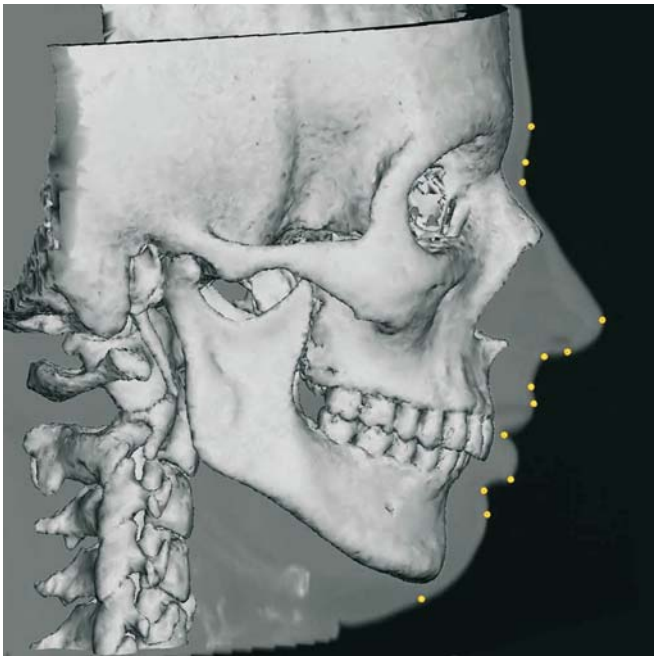

Fig. 5.76. Virtual lateral cephalogram linked to the 3-D hard tissue surface representation, illustrating 3-D soft tissue cephalometric landmarks located in the midplane (3-D CT, patient K.C.)

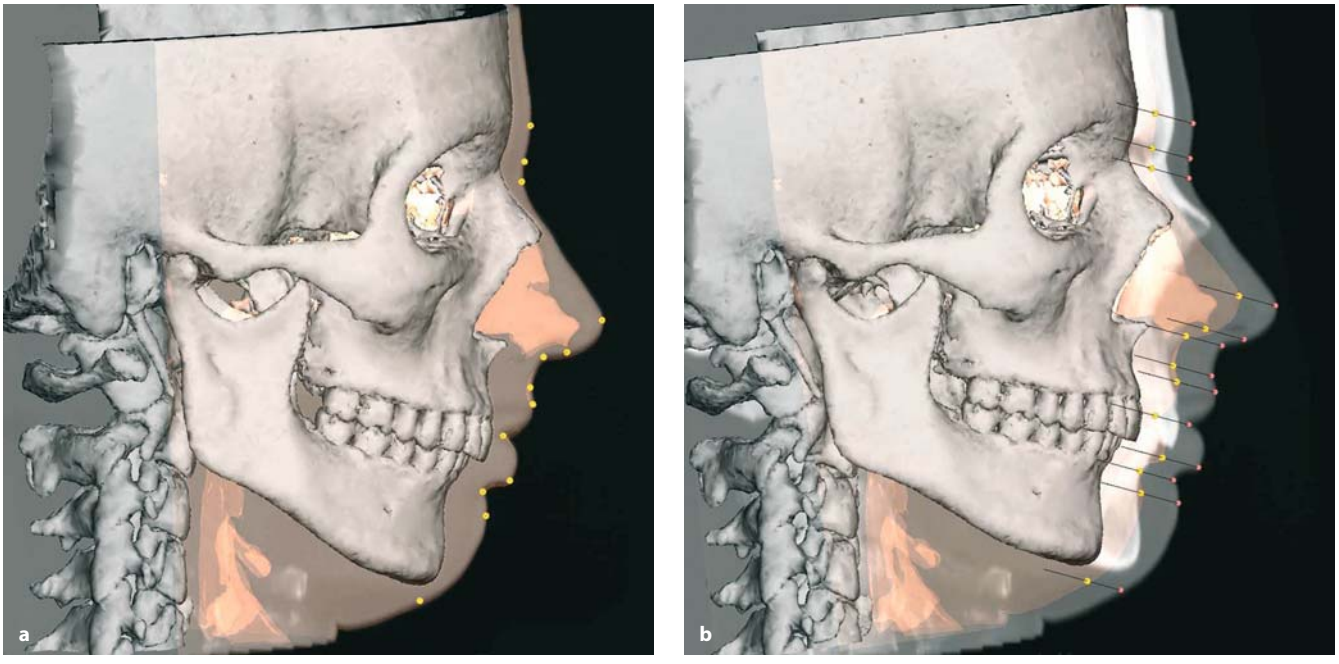

Fig. 5.77 a,b. Virtual lateral cephalograms linked to the 3-D hard and transparent soft tissue surface representations, illustrating 3-D soft tissue cephalometric landmarks located in the midplane (3-D CT, patient K.C.)

5.3 Additional 3-D Cephalometric Soft Tissue Landmarks

The following list shows some additional anthropometric landmarks described by L.G. Farkas that can be used in 3-D cephalometry, once these are validated.

- *Eurion:* Landmark defined as the most lateral point of the parieto-temporal region of the skull
- *Opisthocranion:* Landmark defined as the most posterior point of the occipital region of the head and the most distant from glabella
- *Otobasion inferius:* Landmark defined as the point of attachment of the ear lobe to the cheek, which determines the lower border of the ear insertion
- *Otobasion superius:* Landmark defined as the point of attachment of the helix in the temporal region, which determines the upper border of the ear insertion
- *Porion (soft):* Landmark defined as the highest point on the upper margin of the cutaneous auditory meatus
- *Postaurale:* Landmark defined as the most posterior point on the free margin of the ear
- *Preaurale:* Landmark defined as the most anterior point of the ear, located at the level of the helix attachment to the head
- *Subaurale:* Landmark defined as the lowest point on the free margin of the ear lobe
- *Superaurale:* Landmark defined as the highest point on the free margin of the auricle
- *Vertex:* Landmark defined as the highest point of the head when the head is oriented to the Frankfort horizontal

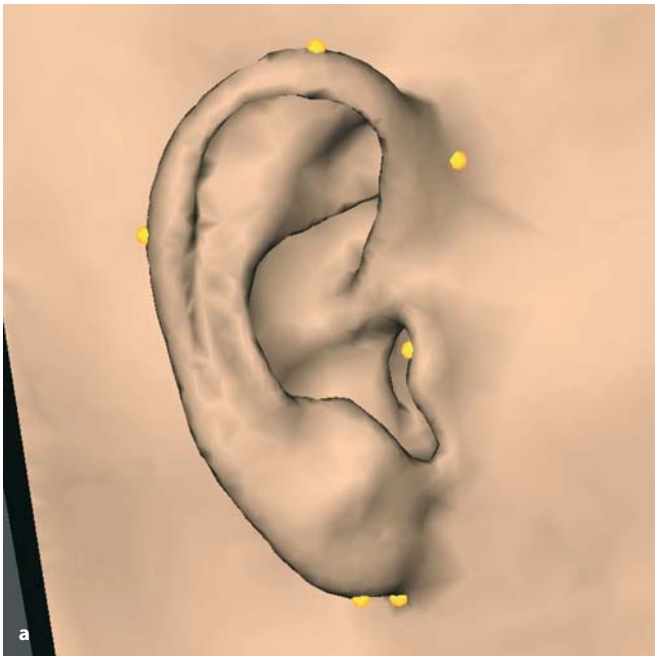

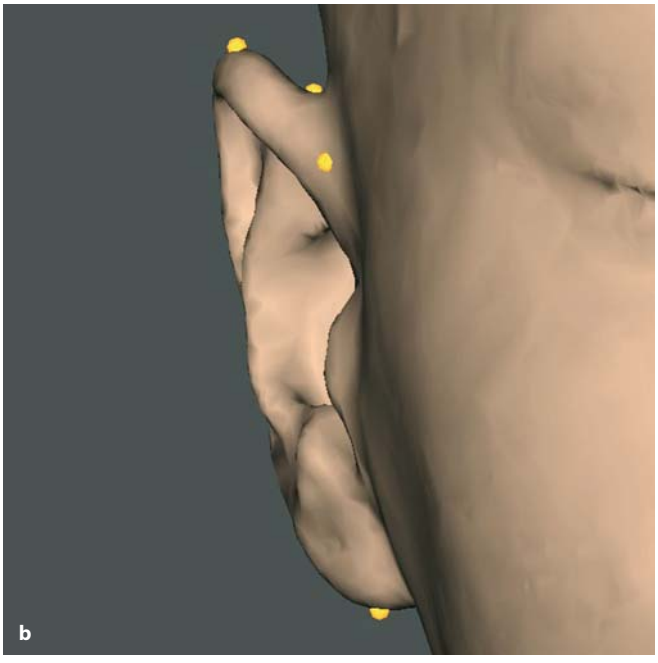

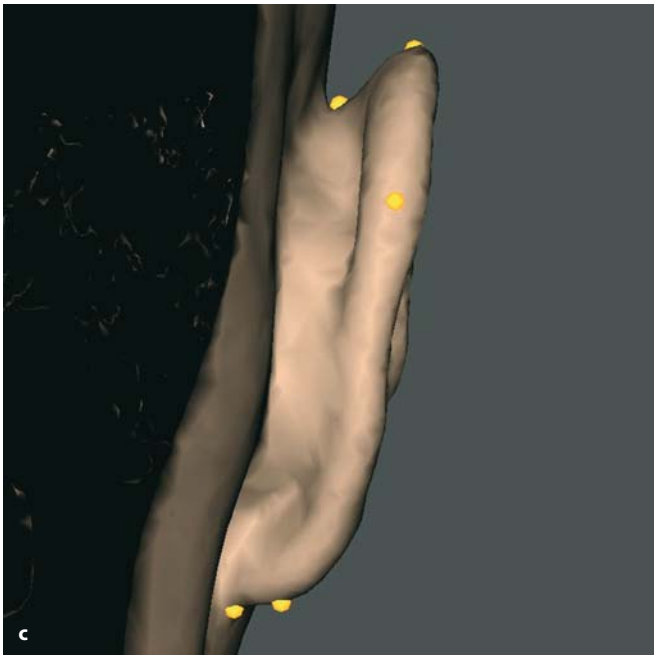

Fig. 5.78 a–c. Ear related 3-D cephalometric soft tissue landmarks. Right profile (**a**), frontal (**b**), dorsal (**c**) view (3-D CT, patient K.C.)

CHAPTER 6 3-D Cephalometric Planes

Gwen R. J. Swennen

Once virtual definition of the 3-D cephalometric hard and soft tissue landmarks has been accomplished, 3-D cephalometric planes can be automatically computed. 3-D cephalometric hard and soft tissue planes can be used for both qualitative and quantitative assessment of craniofacial morphology.

The 3-D virtual scene approach allows the generation of several types of 3-D cephalometric planes that are automatically computed based on one or more 3-D cephalometric hard tissue (Chap. 4) or soft tissue (Chap. 5) landmarks, with regard to the virtual cephalograms or the 3-D cephalometric reference planes (Chap. 3):

- A 3-D cephalometric plane computed from *one* 3-D cephalometric landmark is defined by a plane that passes one landmark and that is parallel to one of the 3-D cephalometric reference planes
- A 3-D cephalometric plane computed from *two* 3-D cephalometric landmarks is defined by a plane that passes two landmarks and that is perpendicular to one of the 3-D cephalometric reference planes
- A 3-D cephalometric plane computed from *three* 3-D cephalometric landmarks is defined by a plane that passes three landmarks (e.g. maxillary plane, mandibular plane, facial midplane)
- A 3-D cephalometric plane computed from *four* 3-D cephalometric landmarks is defined by a plane that passes two landmarks and the mean of two other landmarks (e.g. Frankfort horizontal plane)
- A 3-D cephalometric plane computed from *more than four* 3-D cephalometric landmarks is defined by a plane that passes the means of different pairs of landmarks (e.g. occlusal plane)

In this chapter important craniofacial 3-D cephalometric planes are described whose accuracy and reliability has been tested (Chap. 7). Other 3-D cephalometric hard and soft tissue planes can easily be computed depending on the clinical or research purpose.

6.1 3-D Cephalometric Planes

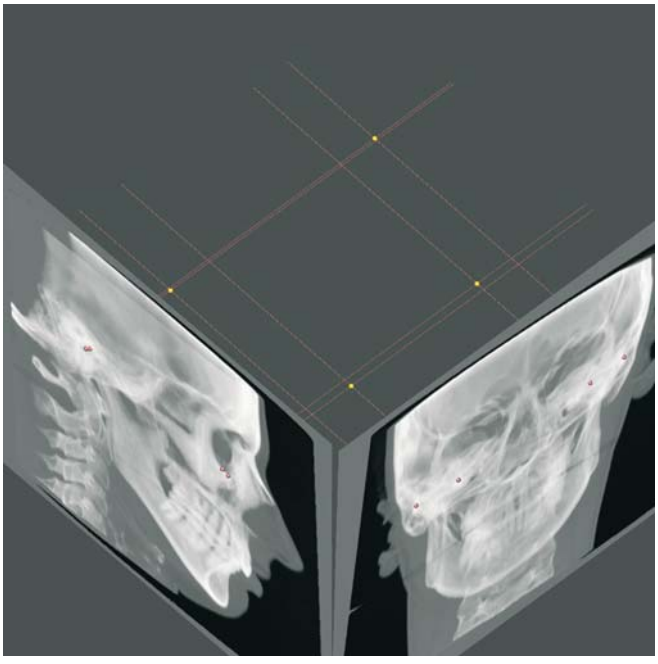

Fig. 6.1. $Orbita_r$,$Orbita_l$ and the mean of $Porion_r$ and $Porion_l$ define the Frankfort horizontal plane (linked virtual lateral and frontal cephalograms, patient K.C.)

Frankfort horizontal Plane: FH-Pl

Virtual Definition of the Frankfort horizontal Plane

The Frankfort horizontal plane is defined by a plane that passes both Orbita ($Orbita_r$ and $Orbita_l$) landmarks and the mean of the two Porion ($Porion_r$ and $Porion_l$) landmarks.

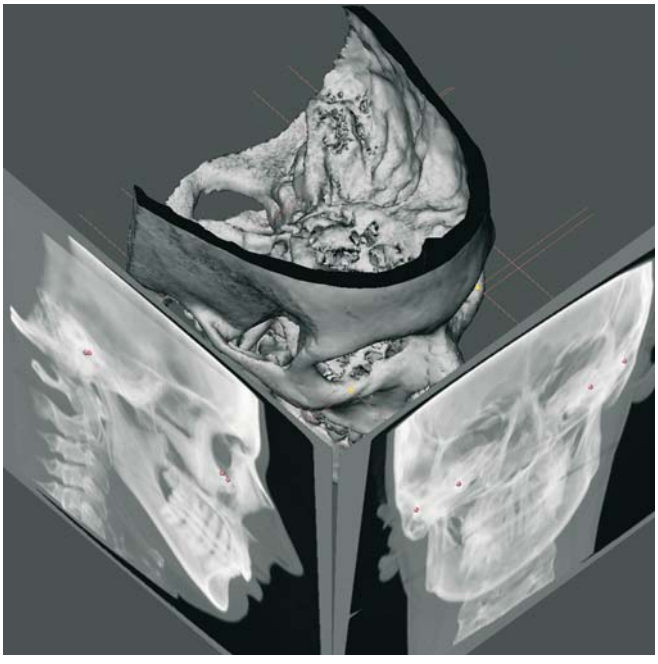

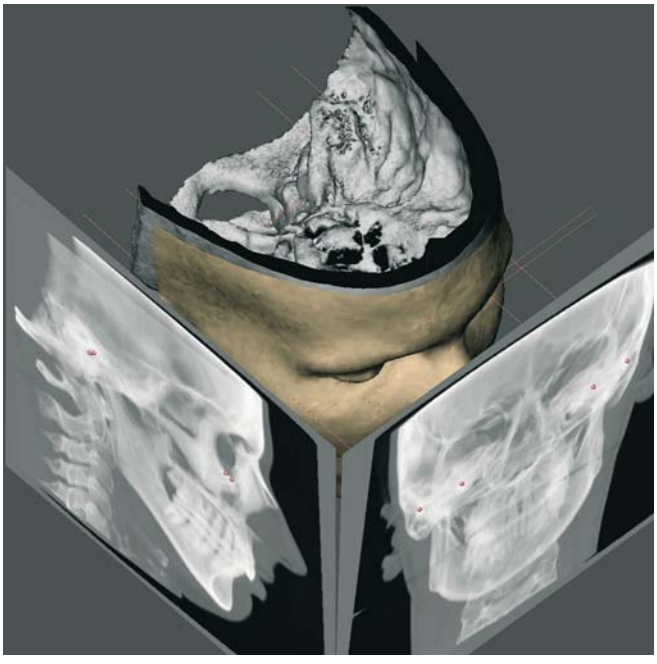

Figs. 6.2, 6.3. $Orbita_r$,$Orbita_l$ and the mean of $Porion_r$ and $Porion_l$ define the Frankfort horizontal plane [linked virtual lateral and frontal cephalograms to 3-D hard (**6.2**) and soft (**6.3**) tissue representations, patient K.C.]

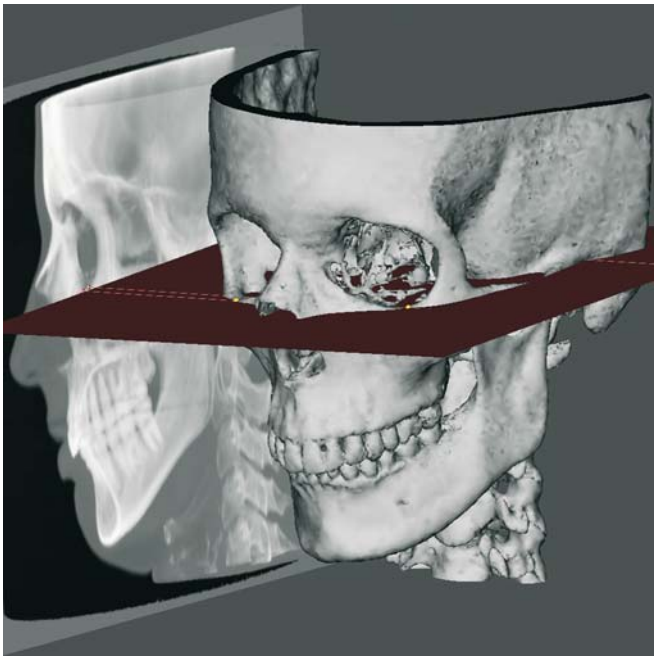

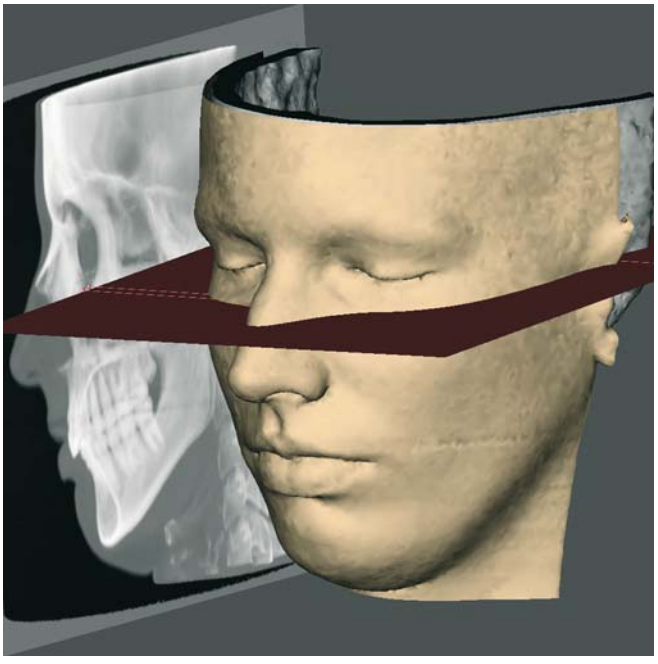

Figs. 6.4, 6.5. Frankfort horizontal plane [linked virtual lateral cephalogram to 3-D hard (**6.4**) and soft (**6.5**) tissue representations, patient K.C.]

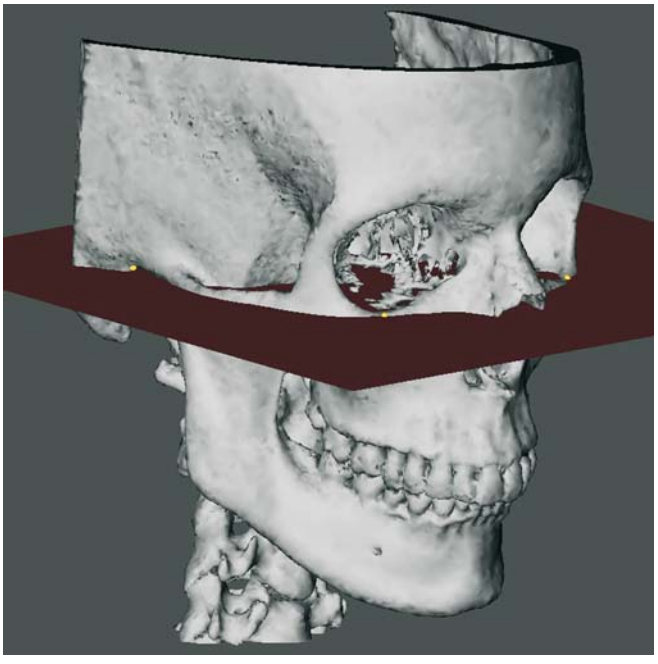

Fig. 6.6. Frankfort horizontal plane (3-D hard tissue representation, patient K.C.)

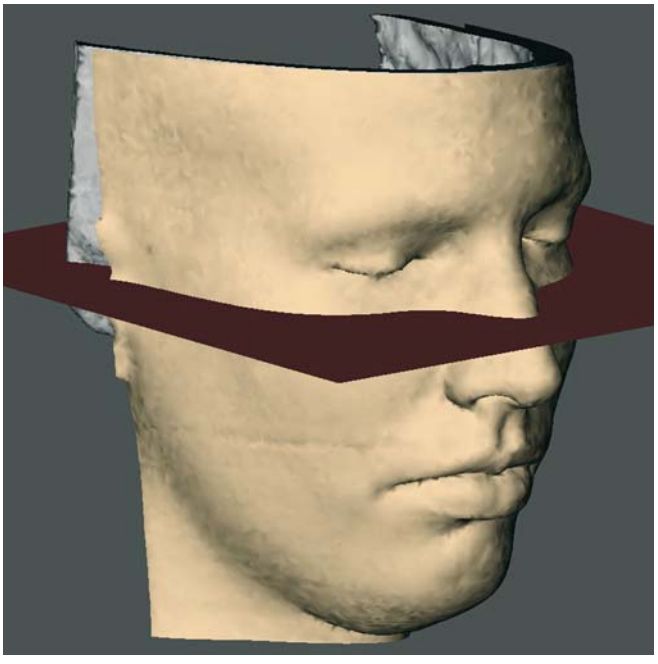

Fig. 6.7. Frankfort horizontal plane (3-D soft tissue representation, patient K.C.)

Maxillary Plane: Mx-Pl

Virtual Definition of the Maxillary Plane

The maxillary plane is defined by a plane that passes the Anterior Nasal Spine and both Posterior Maxillary Point (PMP_r – PMP_l) landmarks.

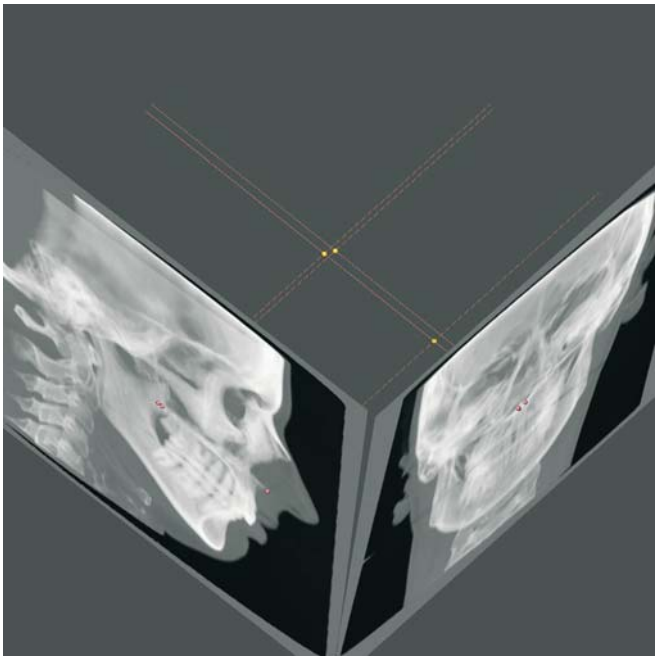

Fig. 6.8. Anterior Nasal Spine and both Posterior Maxillary Point (PMP_r – PMP_l) landmarks define the maxillary plane (linked virtual lateral and frontal cephalograms, patient K.C.)

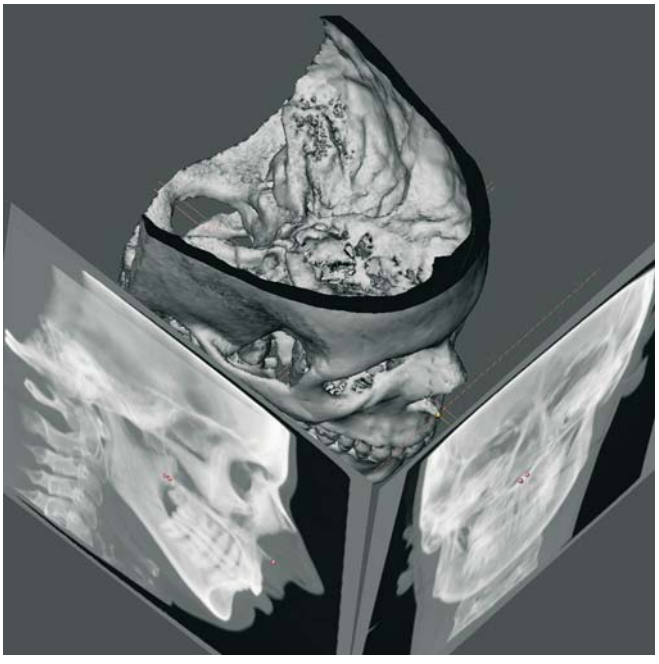

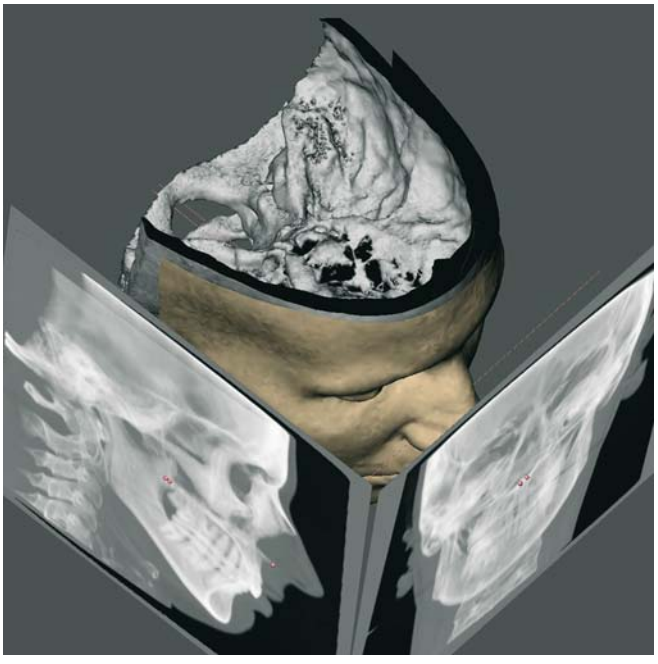

Figs. 6.9, 6.10. Anterior Nasal Spine and both Posterior Maxillary Point (PMP_r-PMP_l) landmarks define the maxillary plane [linked virtual lateral and frontal cephalograms to 3-D hard (**6.9**) and soft (**6.10**) tissue representations, patient K.C.]

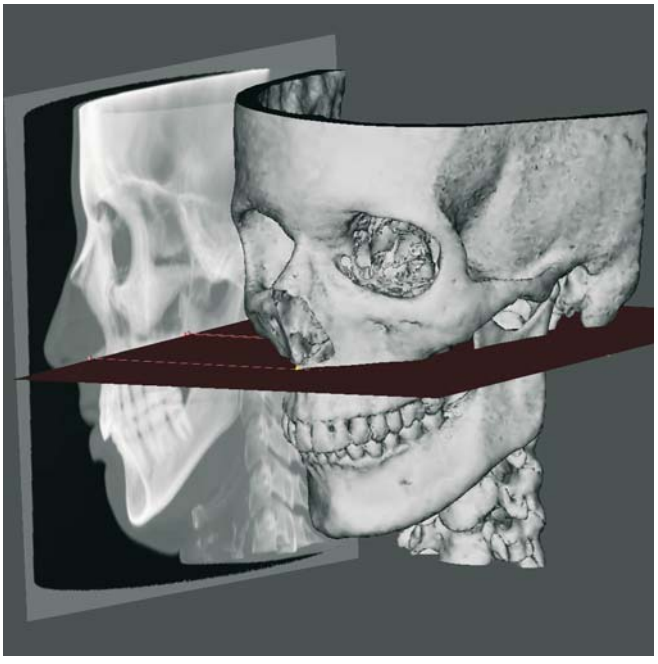

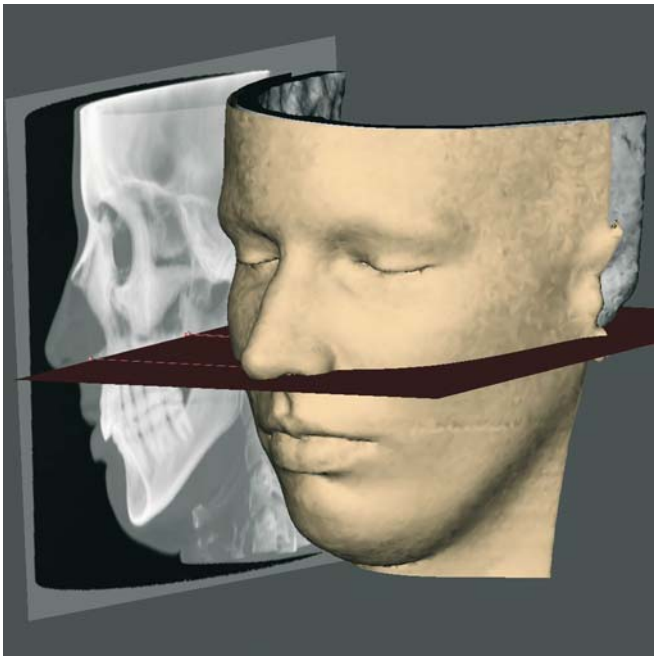

Figs. 6.11, 6.12. Maxillary plane [linked virtual lateral cephalogram to 3-D hard (**6.11**) and soft (**6.12**) tissue representations, patient K.C.]

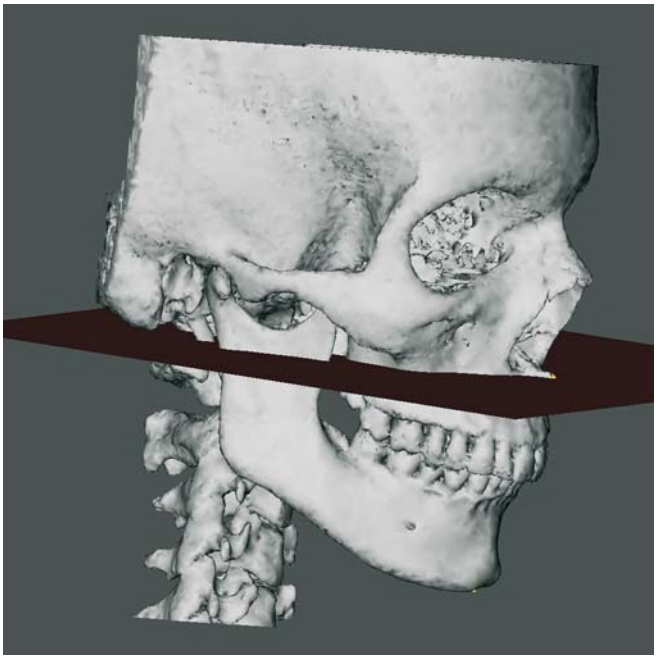

Fig. 6.13. Maxillary plane (3-D hard tissue representation, patient K.C.)

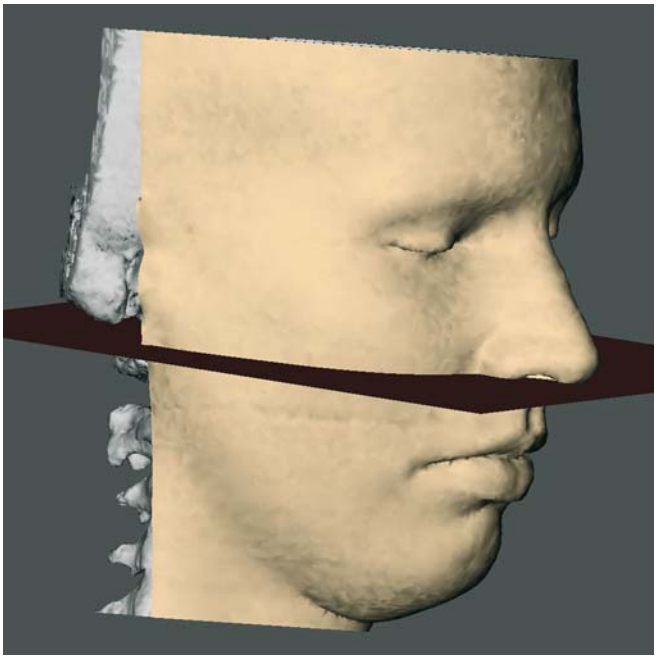

Fig. 6.14. Maxillary plane (3-D soft tissue representation, patient K.C.)

Occlusal Plane: Occ-Pl

Virtual Definition of the Occlusal Plane

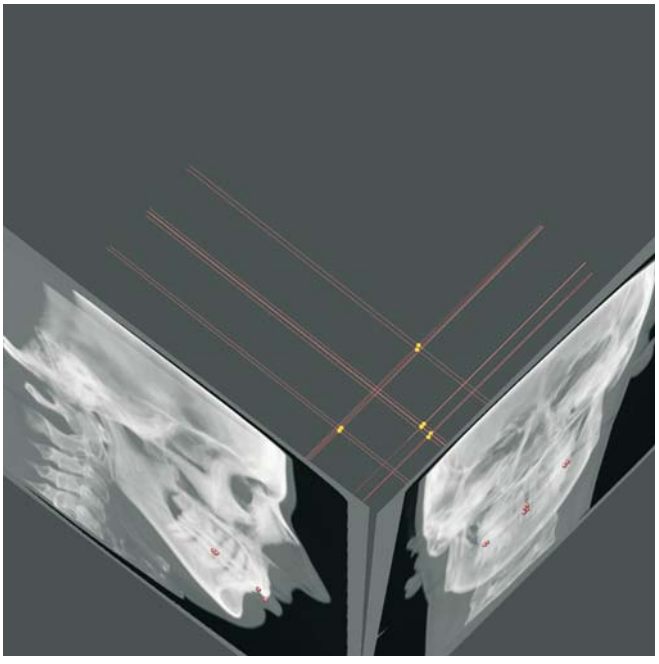

The occlusal plane is defined by a plane that passes (1) the mean of Upper Incisor$_r$ – Upper Incisor$_l$ and Lower Incisor$_l$ – Lower Incisor$_l$ landmarks, (2) the mean of Upper Molar Cusp$_r$ and Lower Molar Cusp$_r$ landmarks and (3) the mean of Upper Molar Cusp$_r$ and Lower Molar Cusp$_r$ landmarks.

Fig. 6.15. Tooth-related landmarks that define the occlusal plane (linked virtual lateral and frontal cephalograms, patient K.C.)

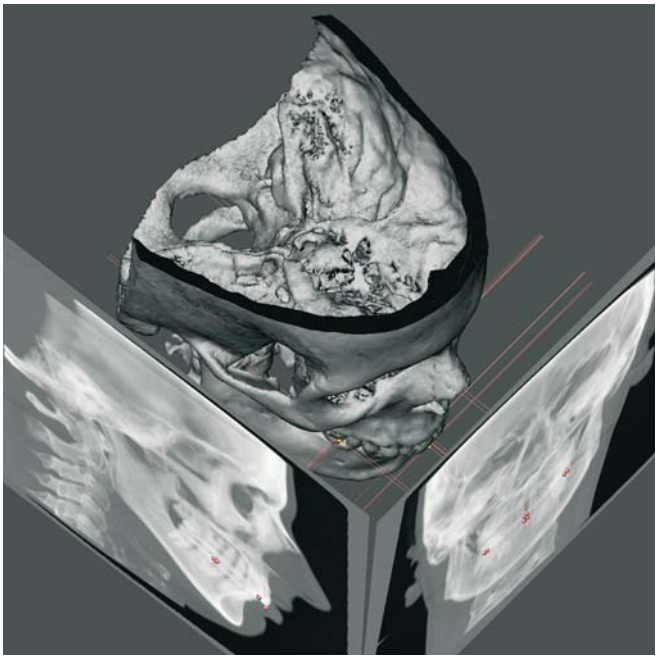

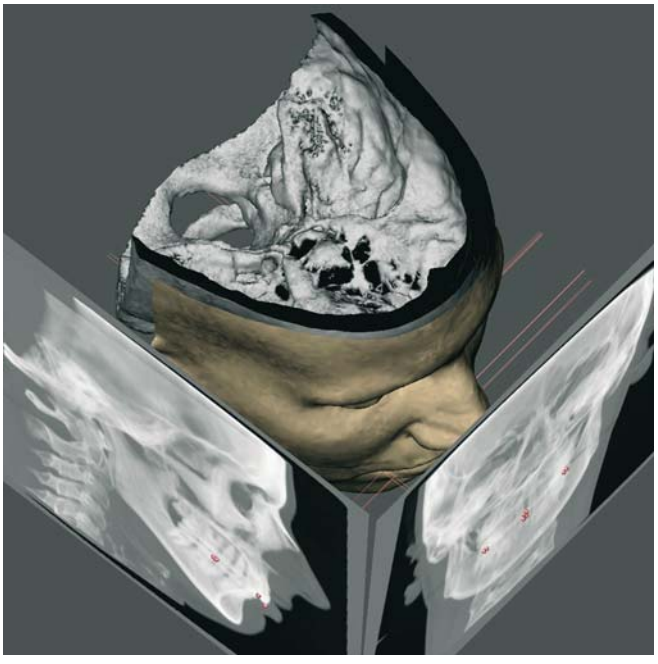

Figs. 6.16, 6.17. Tooth-related landmarks that define the occlusal plane [linked virtual lateral and frontal cephalograms to 3-D hard (**6.16**) and soft (**6.17**) tissue representations, patient K.C.]

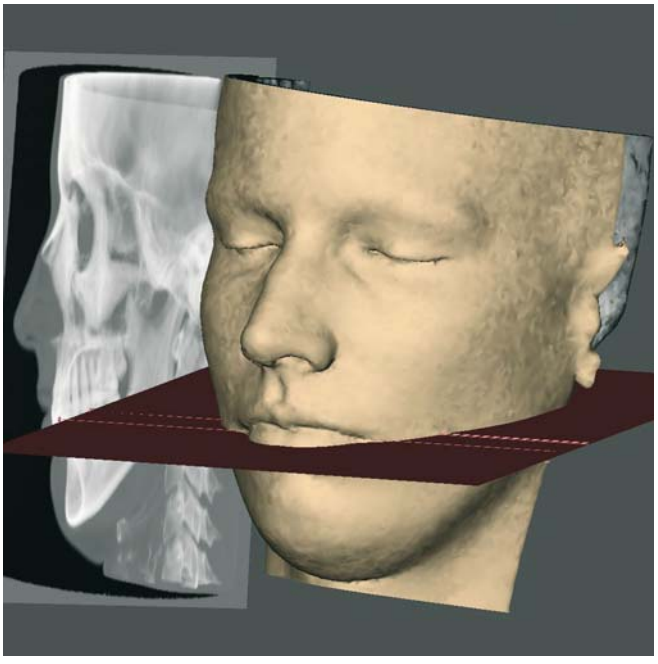

Figs. 6.18, 6.19. Occlusal plane [linked virtual lateral cephalogram to 3-D hard (**6.18**) and soft (**6.19**) tissue representations, patient K.C.]

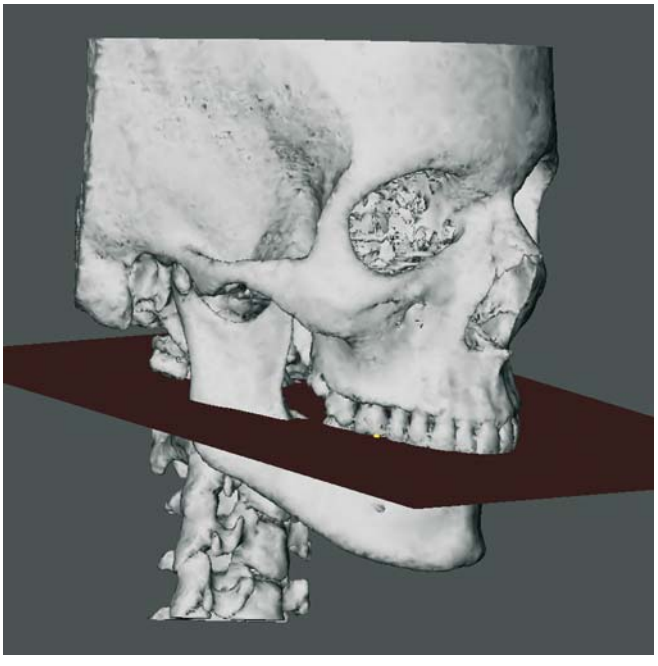

Fig. 6.20. Occlusal plane (3-D hard tissue representation, patient K.C.)

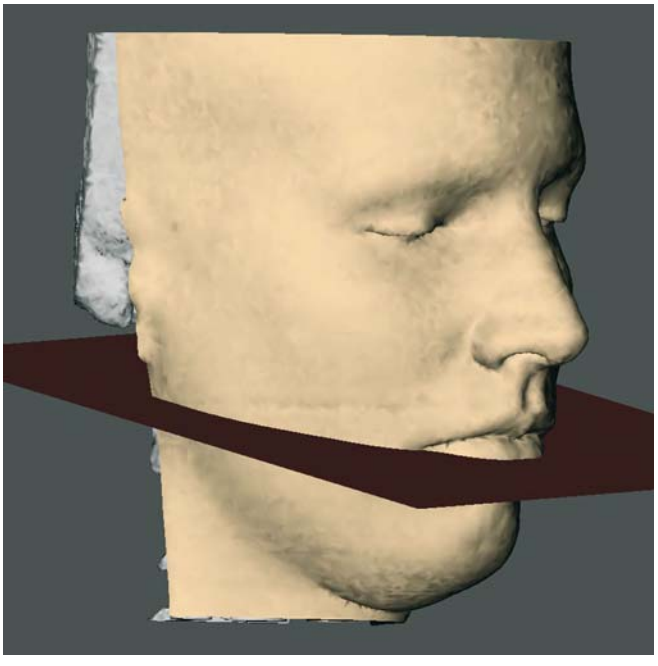

Fig. 6.21. Occlusal plane (3-D soft tissue representation, patient K.C.)

Mandibular Plane: Md-Pl

Virtual Definition of the Mandibular Plane

The mandibular plane is defined by a plane that passes the Menton and both Gonion (Go_r – Go_l) landmarks.

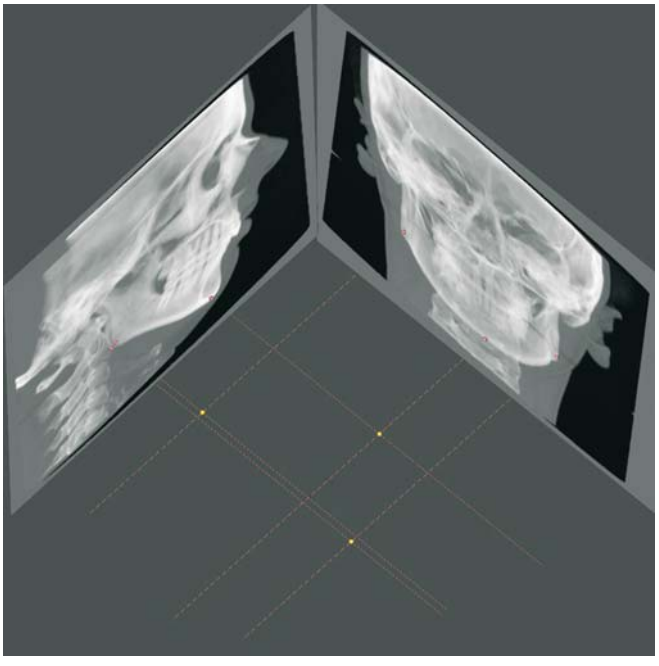

Fig. 6.22. Menton and both Gonion (Go_r – Go_l) landmarks define the mandibular plane (linked virtual lateral and frontal cephalograms, patient K.C.)

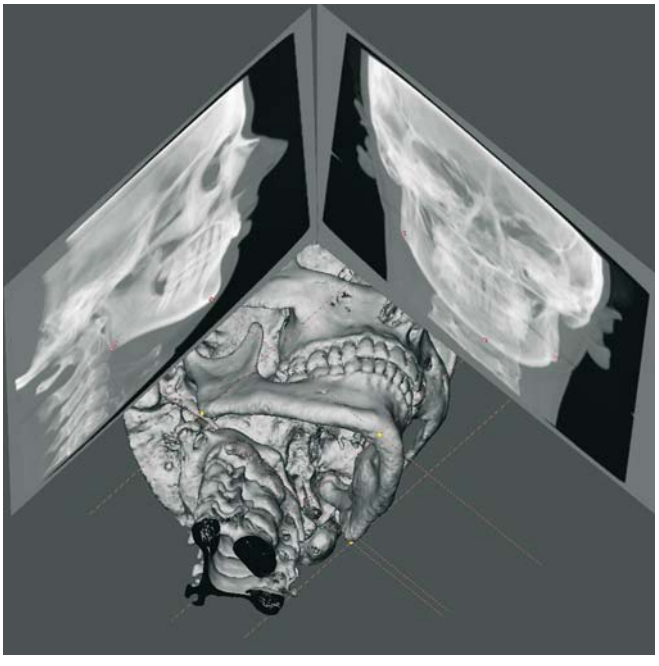

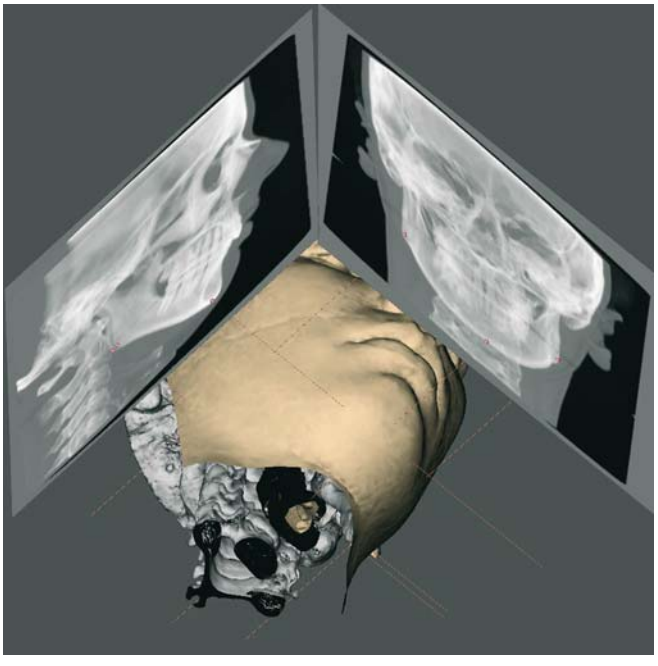

Figs. 6.23, 6.24. Menton and both Gonion (Go_r – Go_l) landmarks define the mandibular plane [linked virtual lateral and frontal cephalograms to 3-D hard (**6.23**) and soft (**6.24**) tissue representations, patient K.C.]

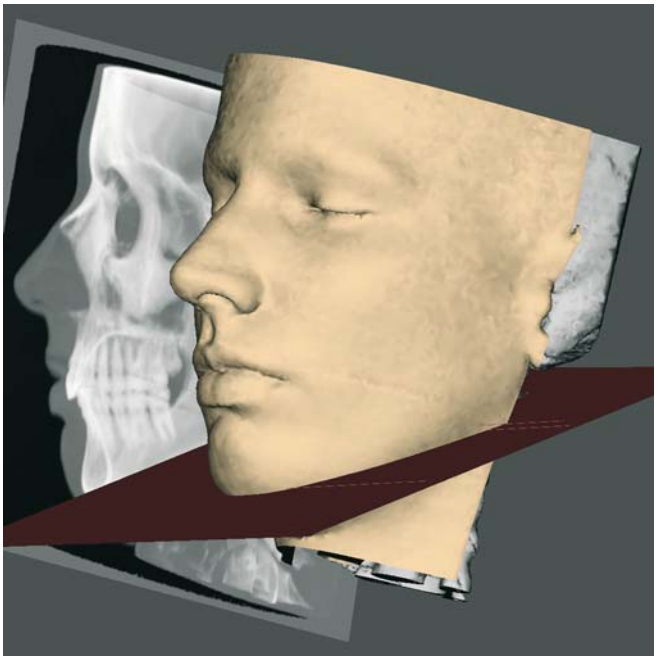

Figs. 6.25, 6.26. Mandibular plane [linked virtual lateral cephalogram to 3-D hard (**6.25**) and soft (**6.26**) tissue representations, patient K.C.]

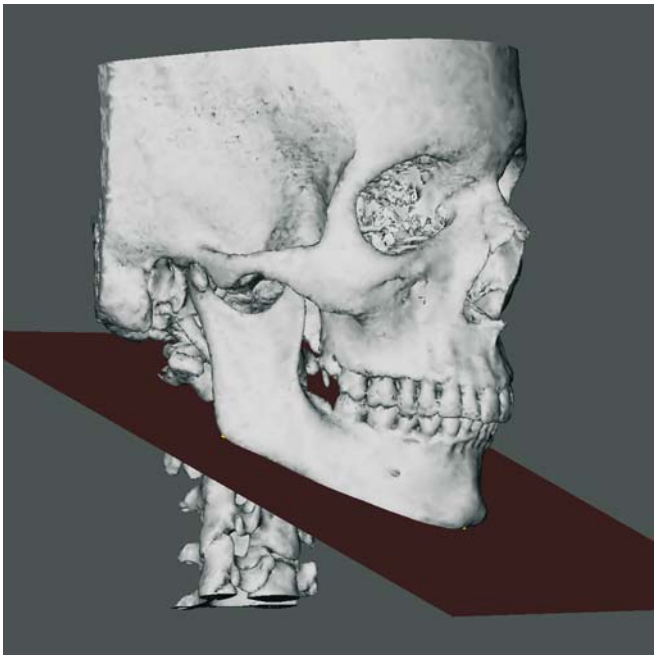

Fig. 6.27. Mandibular plane (3-D hard tissue representation, patient K.C.)

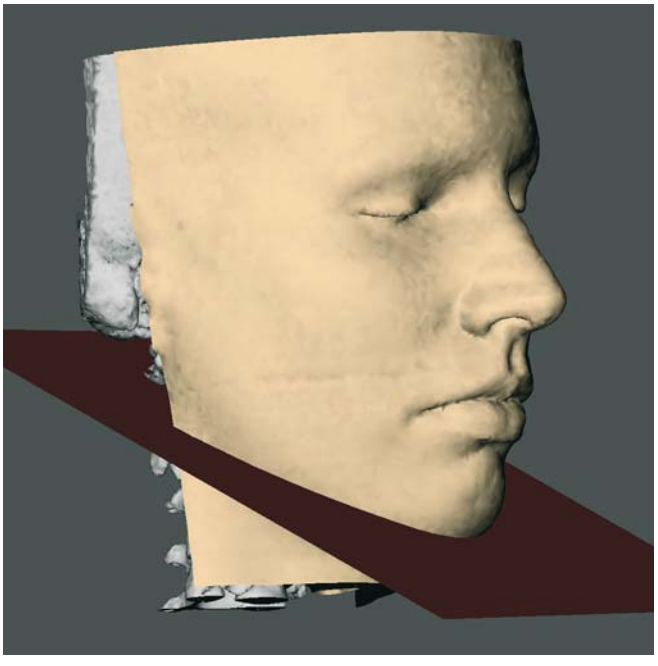

Fig. 6.28. Mandibular plane (3-D soft tissue representation, patient K.C.)

Facial Midplane

Virtual Definition of the Facial Midplane

The facial midplane is defined by a plane that passes the Sella, Nasion and Menton landmarks.

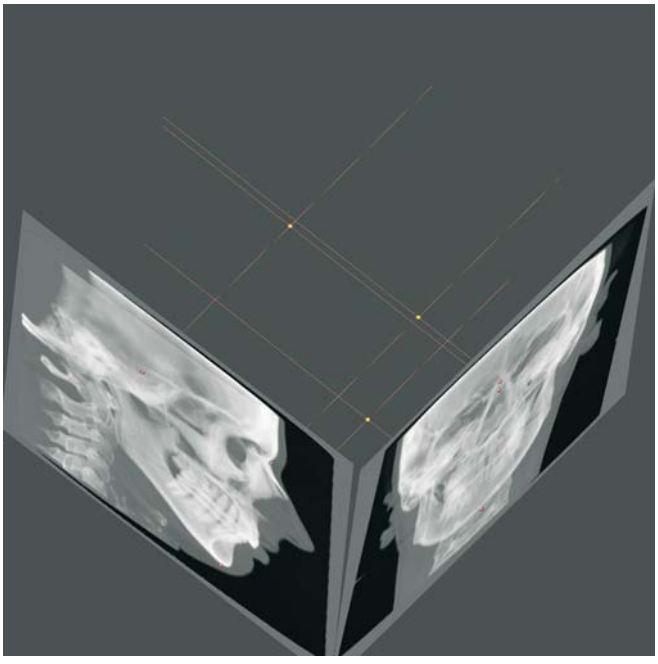

Fig. 6.29. Sella, Nasion and Menton landmarks define the facial midplane (linked virtual lateral and frontal cephalograms, patient K.C.)

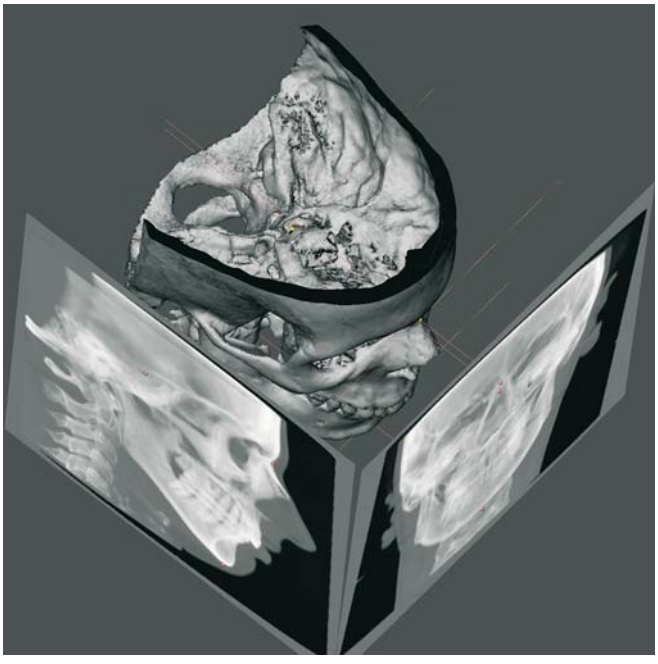

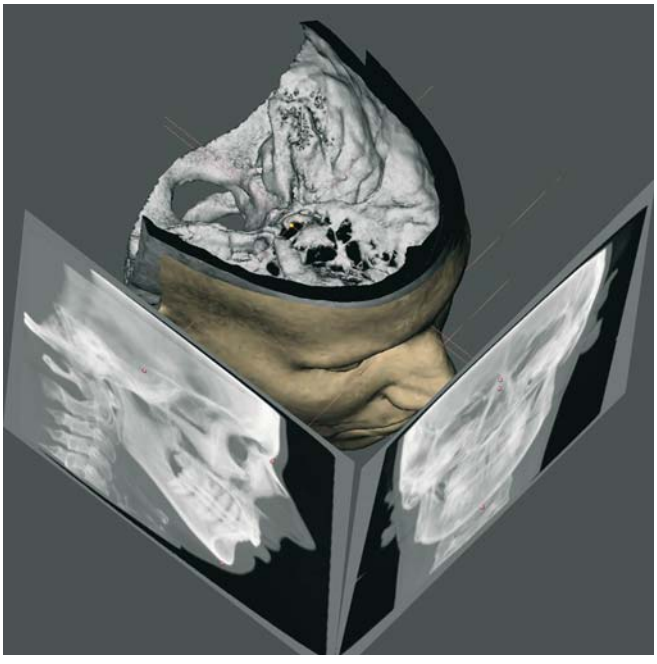

Figs. 6.30, 6.31. Sella, Nasion and Menton landmarks define the facial midplane [linked virtual lateral and frontal cephalograms to 3-D hard (**6.30**) and soft (**6.31**) tissue representations, patient K.C.]

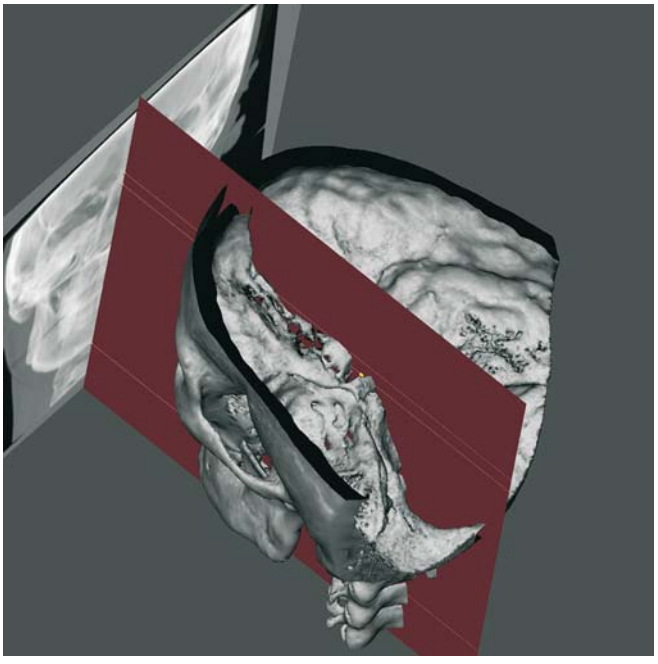

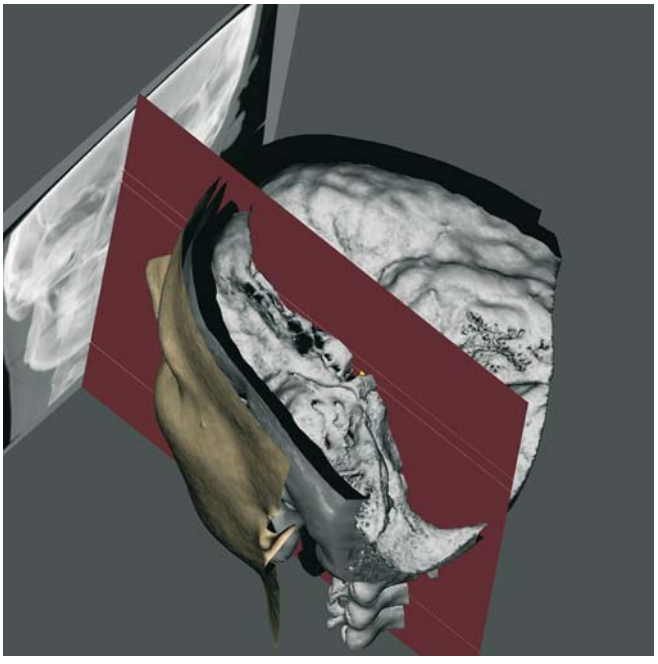

Figs. 6.32, 6.33. Facial midplane [linked virtual lateral cephalogram to 3-D hard (**6.32**) and soft (**6.33**) tissue representations, patient K.C.]

Fig. 6.34. Facial midplane (3-D hard tissue representation, patient K.C.)

Fig. 6.35. Facial midplane (3-D soft tissue representation, patient K.C.)

6.2 Set-up of 3-D Cephalometric Planes

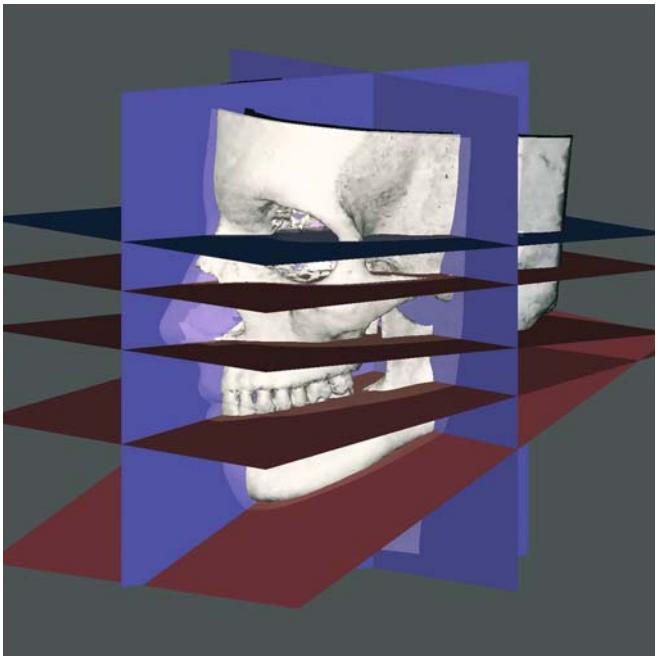

Fig. 6.36. Set-up of 3-D cephalometric reference system in conjunction with the Frankfort horizontal plane, maxillary plane, occlusal plane and mandibular plane (3-D hard tissue and transparent soft tissue surface representation, patient K.C.)

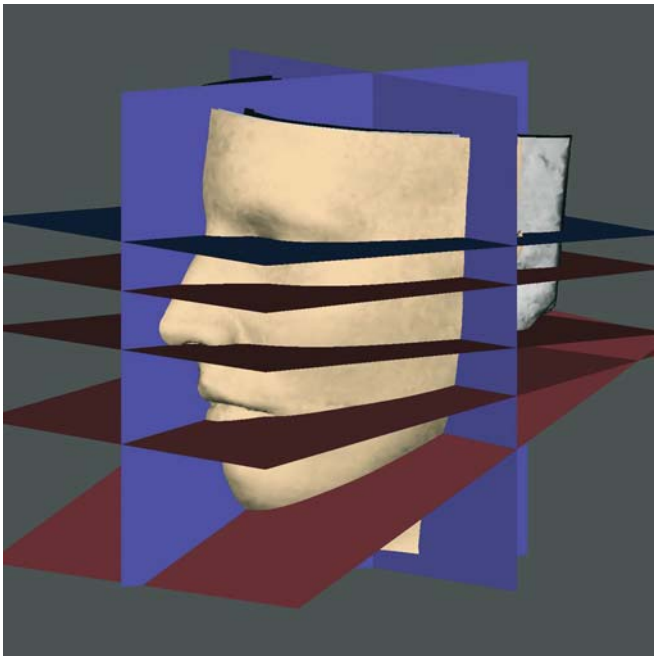

Fig. 6.37. Set-up of 3-D cephalometric reference system in conjunction with the Frankfort horizontal plane, maxillary plane, occlusal plane and mandibular plane (3-D soft tissue representation, patient K.C.)

CHAPTER 7 3-D Cephalometric Analysis

Gwen R. J. Swennen

Many different cephalometric and anthropometric analyses have been developed and are currently in use worldwide for assessment of the head and face in orthodontics, maxillofacial, plastic and craniofacial surgery, genetic dysmorphology and medical anthropology.

CT-based 3-D cephalometry is still in its early phase but has the potential to provide automatically a huge amount of accurate and reliable hard and soft tissue data without being time-consuming. The presented 3-D virtual scene approach allows generation of several types of 3-D cephalometric hard and soft tissue measurements for assessment of craniofacial morphology that can be used for both clinical and research purposes. Based on the 3-D cephalometric reference system (Chap. 3), the 3-D cephalometric hard (Chap. 4) and soft (Chap. 5) tissue landmarks and the 3-D cephalometric planes (Chap. 6), linear, angular, orthogonal and proportional measurements can automatically be computed.

- *Linear measurements*
  - *Linear projective measurements* are measurements between two 3-D cephalometric landmarks that are projected on one of the 3-D cephalometric reference planes and are expressed in millimetres.
    - Linear projective *width* measurements are horizontal measurements between two 3-D cephalometric landmarks projected parallel to the median (z) and horizontal (x) planes on the vertical (y) plane.
    - Linear projective *height* measurements are vertical measurements between two 3-D cephalometric landmarks projected parallel to the horizontal (x) and vertical (y) planes on the median (z) plane.
    - Linear projective *depth* measurements are sagittal projective measurements between two 3-D cephalometric landmarks projected parallel to the horizontal (x) and vertical (y) planes on the median (z) plane.
  - *3-D distances* are direct linear measurements between two 3-D cephalometric landmarks and are expressed in millimetres.
- *Angular measurements*
  - *Angular projective measurements (I)* are measurements between three or four 3-D cephalometric landmarks projected on one of the 3-D cephalometric reference planes and are expressed in degrees.
  - *Angular projective measurements (II)* are measurements between two 3-D cephalometric landmarks and a 3-D cephalometric reference plane projected on one of the 3-D cephalometric reference planes and are expressed in degrees.
  - *Angular projective measurements (III)* are measurements between two 3-D cephalometric planes projected on one of the 3-D cephalometric reference planes and are expressed in degrees.
- *Orthogonal measurements* are perpendicular measurements from the various 3-D cephalometric landmarks to each of the 3-D cephalometric reference planes and are expressed in millimetres.
- *Proportional correlation measurements* are ratios between two 3-D cephalometric measurements and are expressed as percentages.

This chapter gives an introduction to voxel-based 3-D cephalometric analysis of hard and soft tissues. Because many different conventional cephalometric and anthropometric analyses have been developed to answer different questions, it is simply not possible to implement all existing cephalometric analyses.

The 3-D cephalometric analyses presented here are based on a set of measurements that are useful for clinical routine and that were used for statistical validation. As far as 3-D cephalometric soft tissue analysis is concerned, an effort was made to implement the direct anthropometric measurements of the head and face described by L.G. Farkas. Direct anthropometric measurements consist of direct linear (projective or tangential) and angular measurements with the head in rest, Frankfort horizontal or recumbent position. In 3-D cephalometry, modifications were made because 3-D cephalometric projective linear and angular measurements are automatically computed with regard to the

3-D cephalometric reference system. Tangential linear measurements were not implemented; instead, 3-D distances were computed. The 3-D virtual scene approach presents several advantages. It allows automatic generation of a huge amount of real-size cephalometric data that are immediately available for clinical decision making or statistical evaluation without being time-consuming.

This chapter illustrates the different 3-D cephalometric hard and soft tissue measurements. Only statistically validated measurements are shown. For validation a total of 7,360 hard tissue and 20,560 soft tissue 3-D cephalometric measurements were performed. Statistical evaluation of 3-D cephalometric hard tissue measurements showed that the intra-observer measurement error was less than 0.85° for angular measurements and less than 0.78 mm, 0.88 mm, 0.76 mm and 0.84 mm for linear, horizontal, vertical and transverse orthogonal measurements, respectively. The inter-observer measurement error was less than 1.03° for angular measurements and less than 0.84 mm, 0.78 mm, 0.86 mm and 1.26 mm for linear, horizontal, vertical and transverse orthogonal measurements, respectively. Squared correlation coefficients showed high intra-observer and inter-observer reliability (Swennen et al. 2004). As far as validation of 3-D cephalometric soft tissue measurements is concerned, measurement error and reliability were found to be in the same range as the 3-D cephalometric hard tissue measurements (unpublished results). The presented 3-D cephalometric hard and soft tissue analyses proved to be accurate and reliable and therefore represent a valuable tool for objective evaluation of craniofacial morphology.

7.1 3-D Cephalometric Hard Tissue Analysis

7.1.1 Linear Hard Tissue Analysis

7.1.1.1 Linear Projective Hard Tissue Analysis

7.1.1.1.1 Hard Tissue Widths

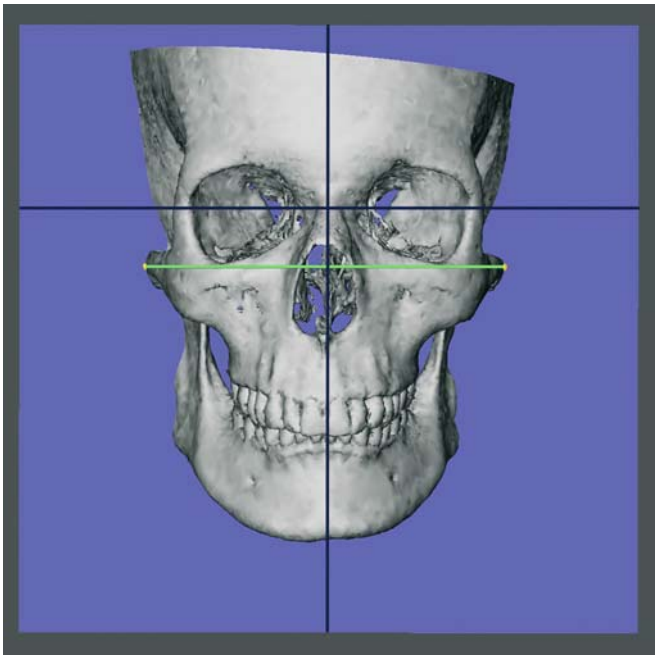

Fig. 7.1. Bizygomatic width, Zy_r-Zy_l (3-D CT, hard tissues, patient K.C.)

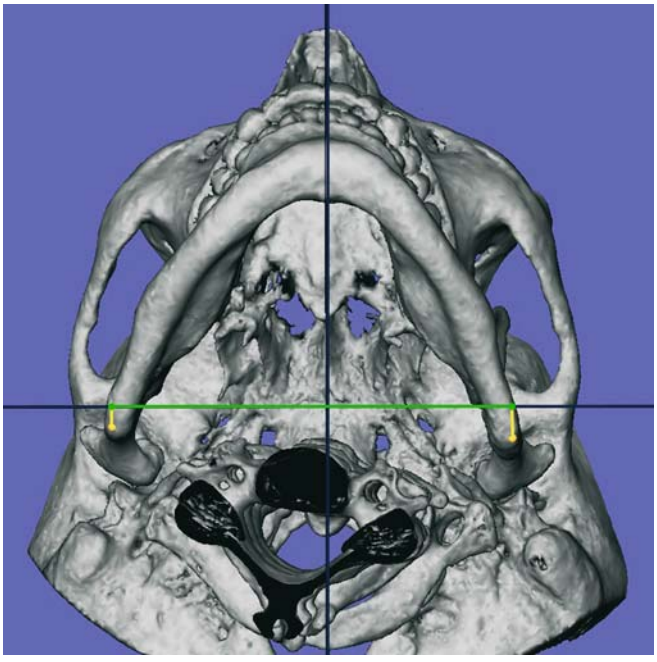

Fig. 7.2. Bigonial width, Go_r-Go_l (3-D CT, hard tissues, patient K.C.)

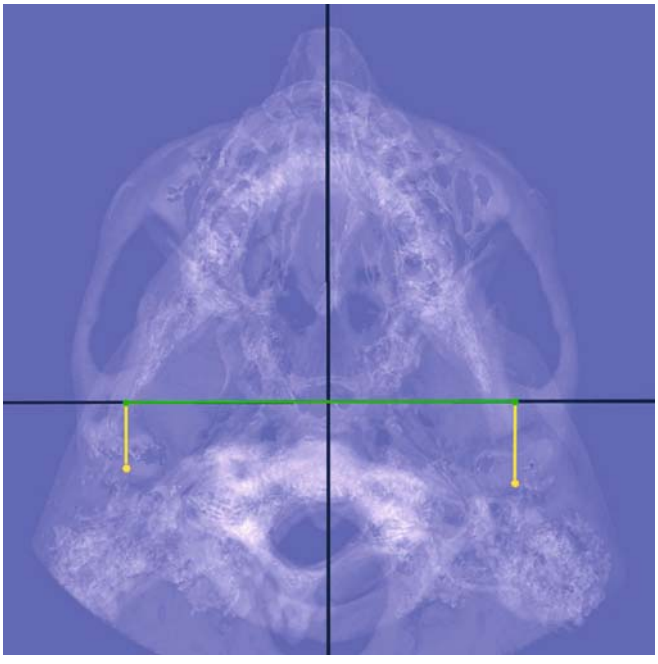

Fig. 7.3. Bicondylar width, Co_r-Co_l (3-D CT, transparent hard tissues, patient K.C.)

7.1.1.1.2
Hard Tissue Heights

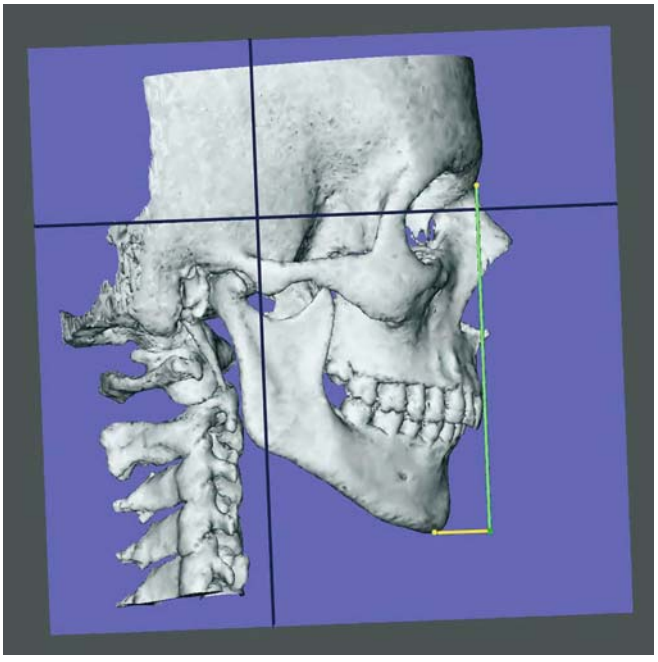

Fig. 7.4. Anterior total facial height, N-Men (3-D CT, hard tissues, patient K.C.)

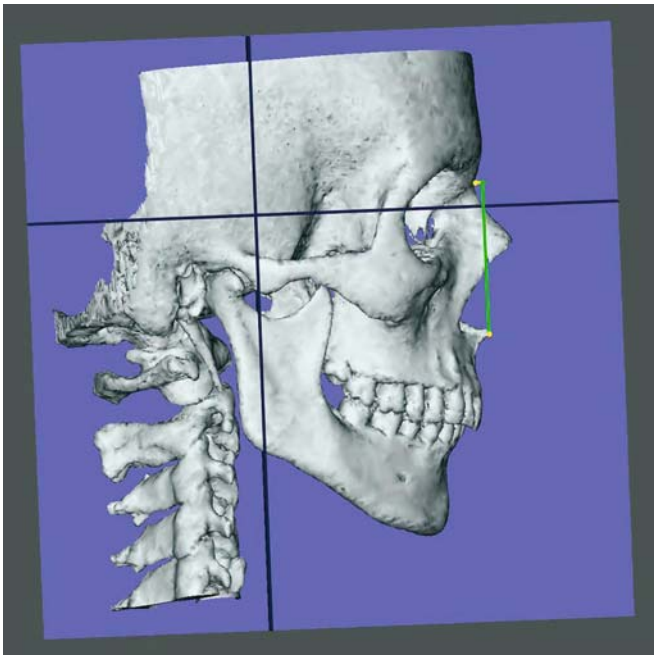

Fig. 7.5. Anterior midfacial height, N-ANS (3-D CT, hard tissues, patient K.C.)

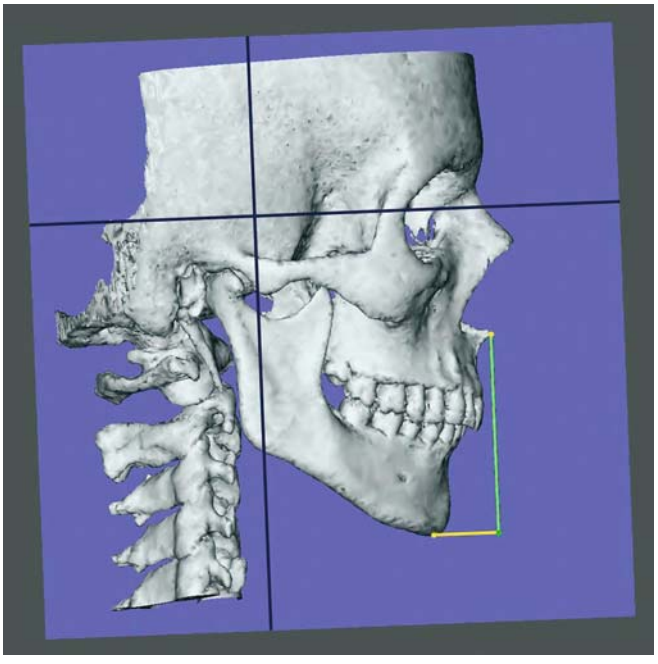

Fig. 7.6. Anterior lower facial height, ANS-Me (3-D CT, hard tissues, patient K.C.)

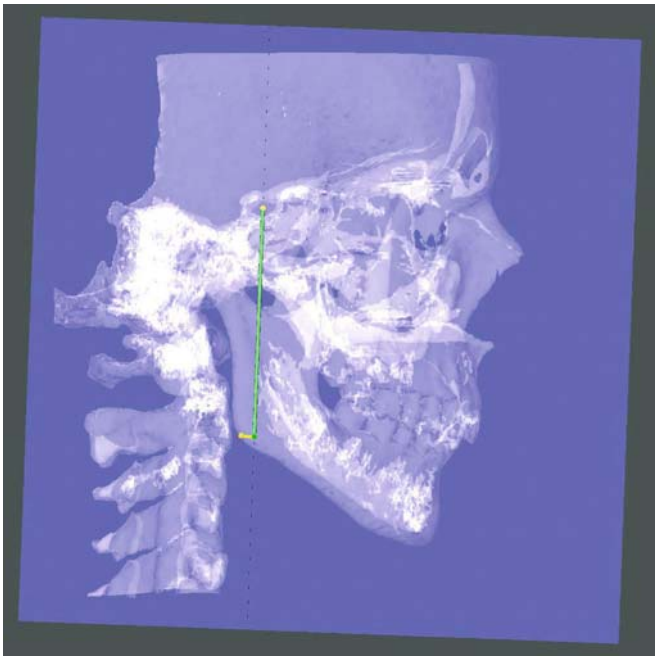

Fig. 7.7. Posterior total facial height right, S-Go_r (3-D CT, transparent hard tissues, patient K.C.)

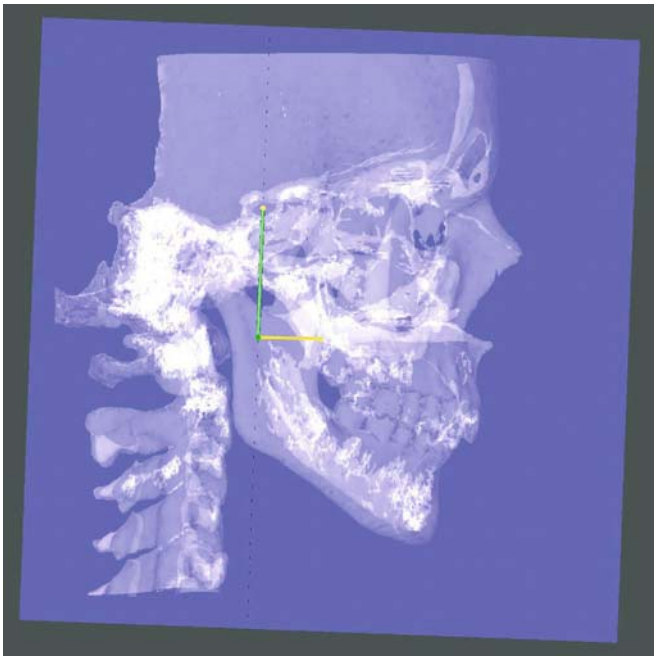

Fig. 7.8. Posterior midfacial height, S-PNS (3-D CT, transparent hard tissues, patient K.C.)

7.1.1.1.3
3-D Modified „Wit's" Measurement

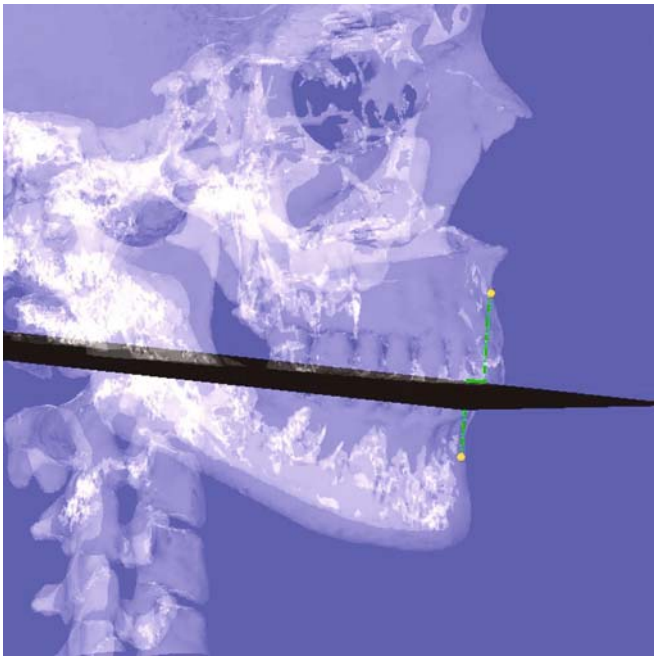

Fig. 7.9. The modified 3-D Wit's measurement is a projective linear measurement between the 3-D cephalometric hard tissue A and B landmarks that are projected perpendicular on the 3-D occlusal plane and the median (*z*) 3-D cephalometric reference plane (3-D CT, transparent hard tissues, patient K.C.)

7.1.1.2 3-D Hard Tissue Distances

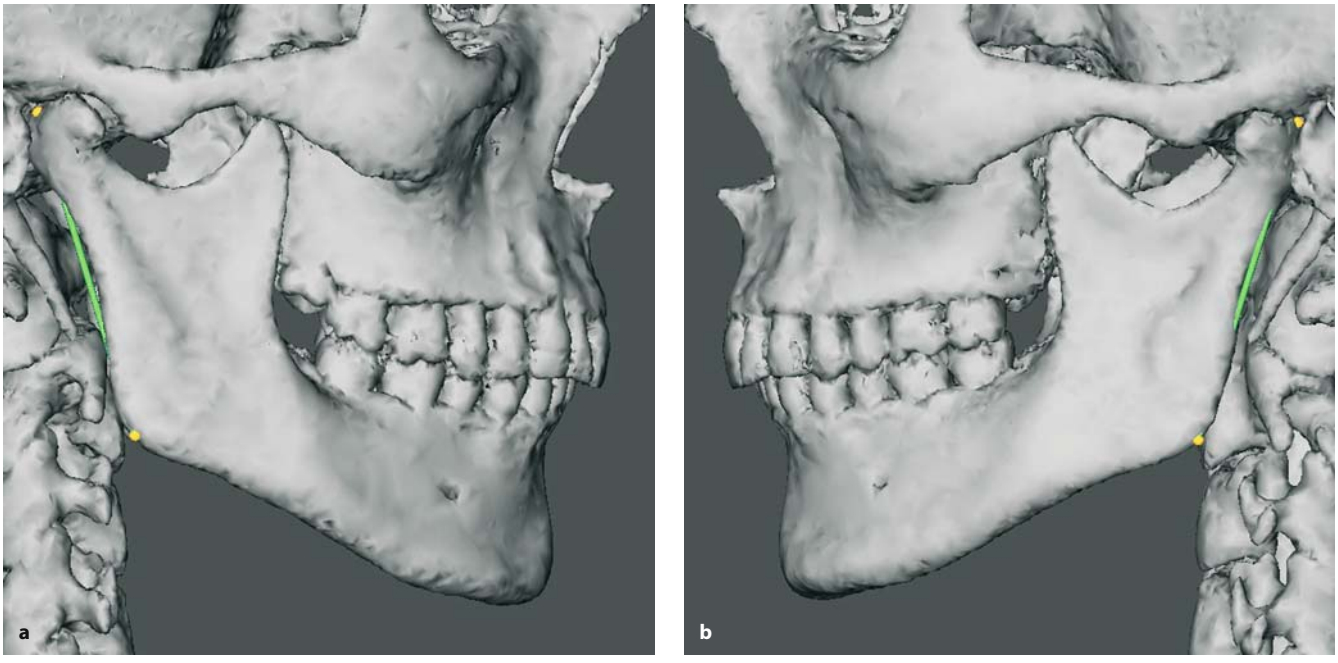

Fig. 7.10. Right (a) and left (b) mandibular vertical ramus length, Co_r-Go_r / Co_l-Go_l (3-D CT, hard tissues, patient K.C.)

Fig. 7.11. Mandibular horizontal ramus length, Go_r-Pog / Go_l-Pog (3-D CT, hard tissues, patient K.C.)

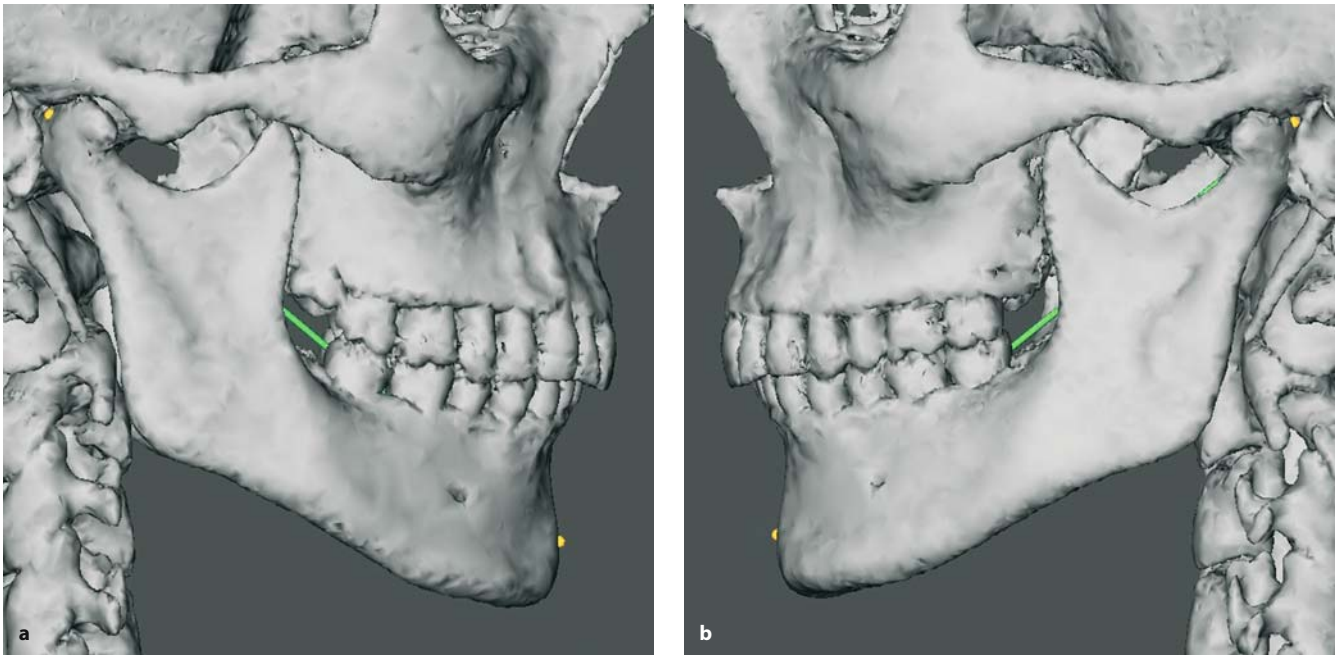

Fig. 7.12. Right (**a**) and left (**b**) total mandibular length, Co_r-Pog / Co_l-Pog (3-D CT, hard tissues, patient K.C.)

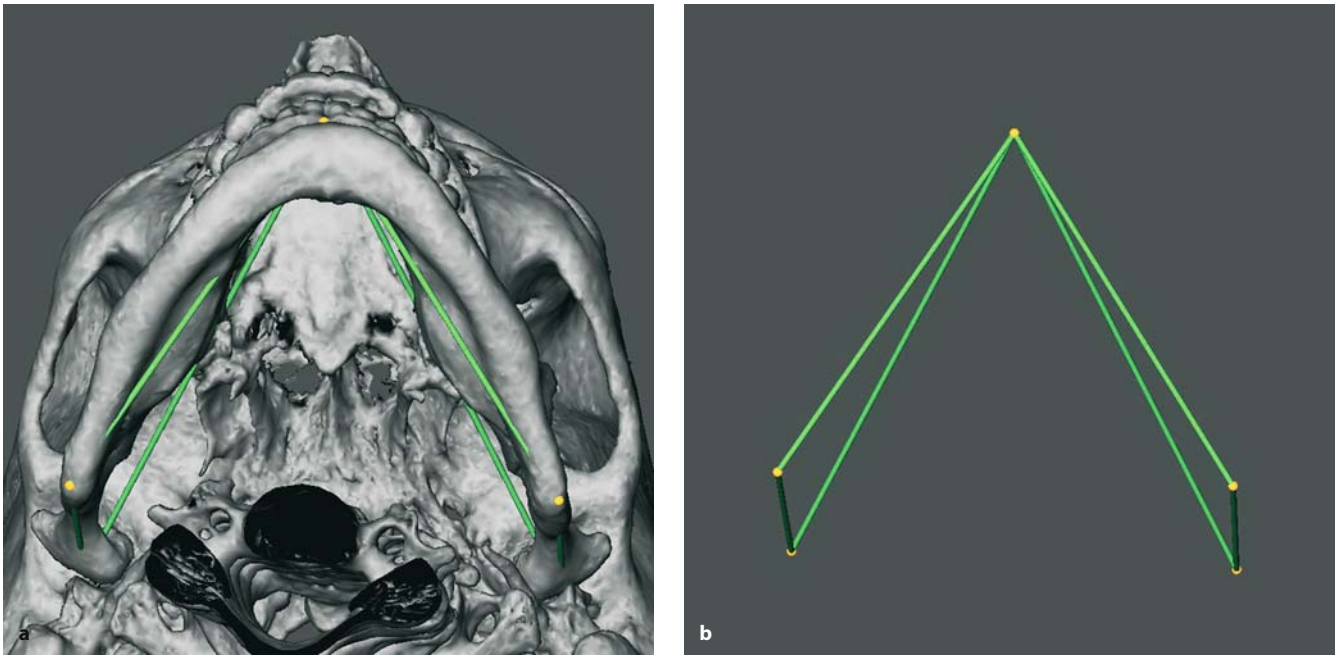

Fig. 7.13 a, b. Right and left mandibular vertical ramus, body and total mandibular length (3-D CT, hard tissues, patient K.C.)

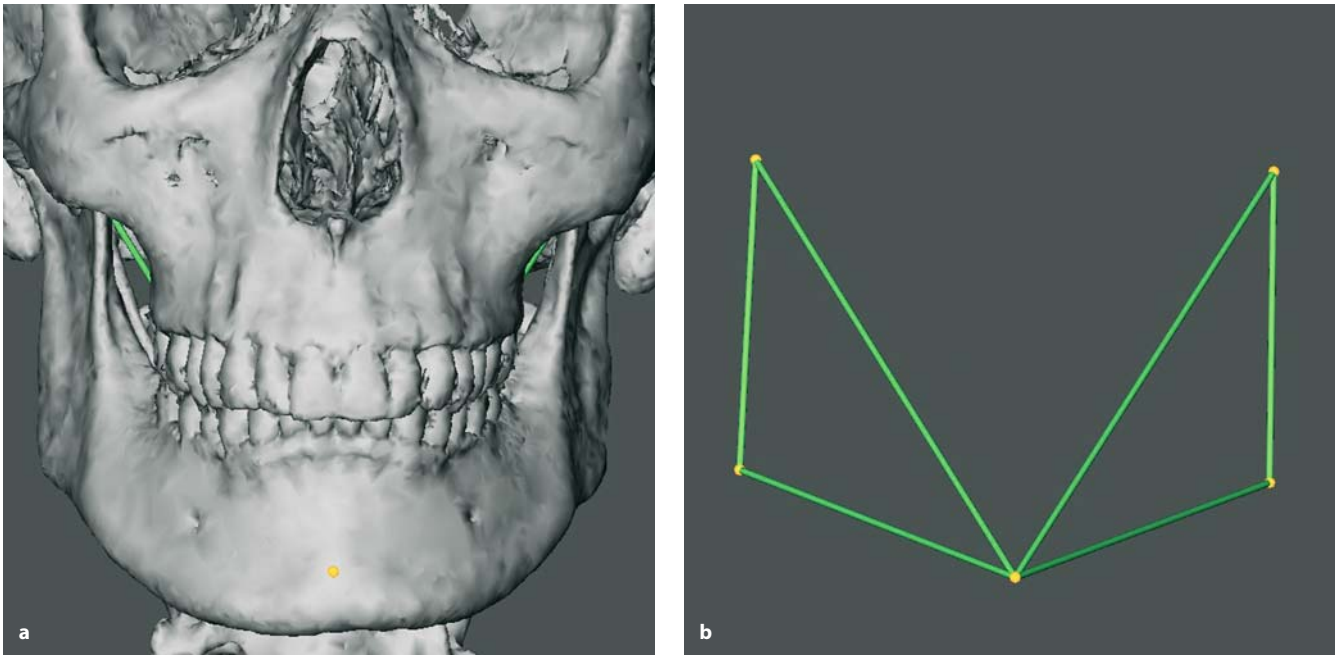

Fig. 7.14 a, b. Right and left mandibular vertical ramus, body and total mandibular length (3-D CT, hard tissues, patient K.C.)

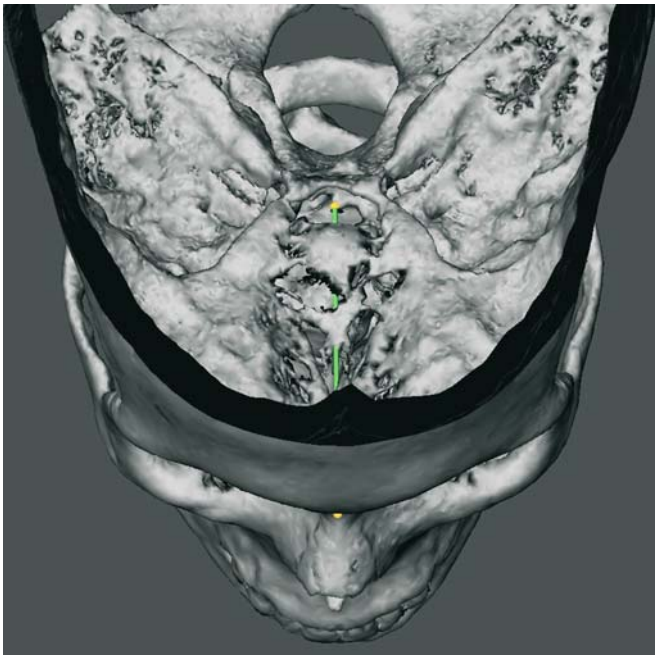

Fig. 7.15. Anterior cranial base length, S-N (3-D CT, hard tissues, patient K.C.)

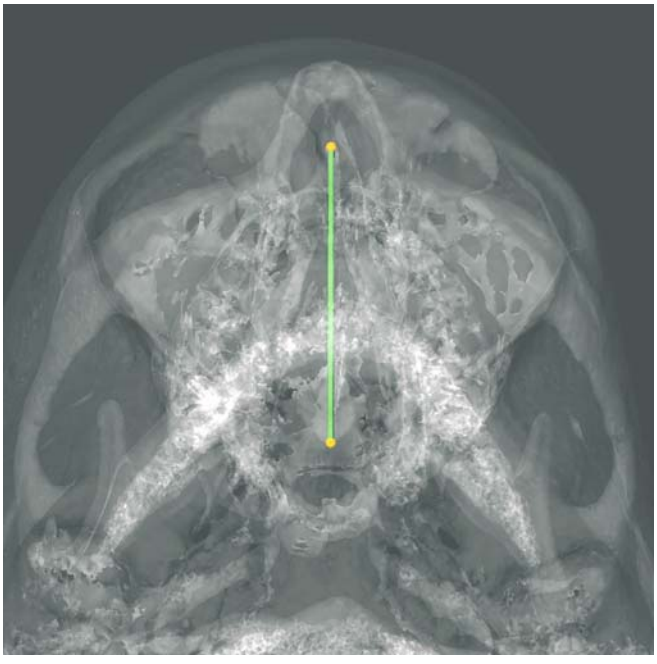

Fig. 7.16. Maxillary length, ANS-PNS (3-D CT, transparent hard tissues, patient K.C.)

7.1.2 Angular Hard Tissue Analysis

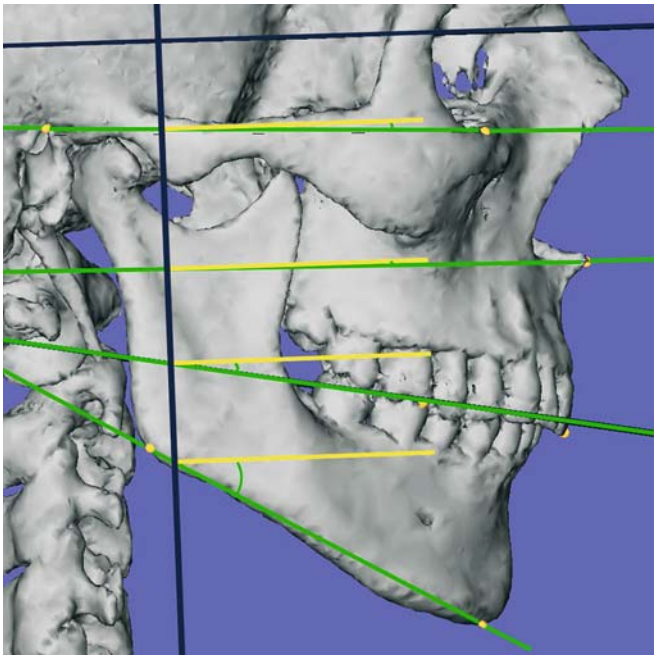

Fig. 7.17. The lateral inclinations of the Frankfort horizontal plane (FH-PI), the maxillary plane (Mx-PI), the occlusal plane (Occ-PI) and the mandibular plane (Md-PI) from the horizontal (*x*) 3-D cephalometric reference plane are projected angular measurements on the median (*z*) 3-D cephalometric reference plane (3-D CT, hard tissues, patient K.C.)

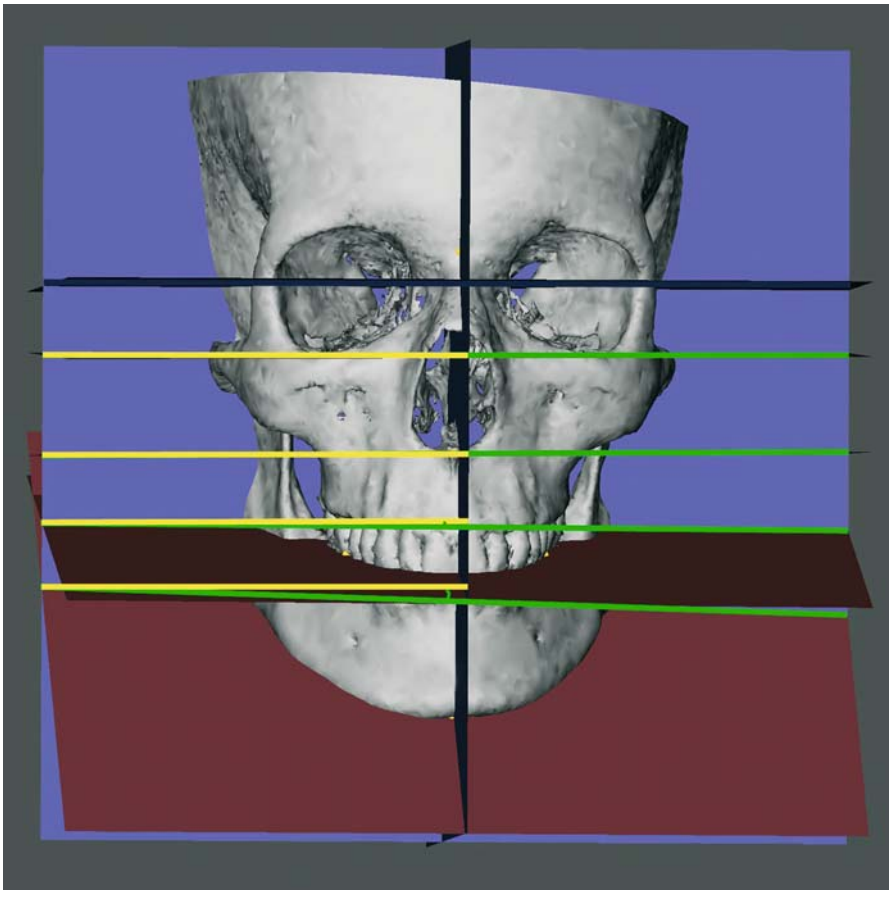

Fig. 7.18. The frontal inclinations of the Frankfort horizontal plane (FH-Pl), the maxillary plane (Mx-Pl), the occlusal plane (Occ-Pl) and the mandibular plane (Md-Pl) from the horizontal (*x*) 3-D cephalometric reference plane are projected angular measurements on the vertical (*y*) 3-D cephalometric reference plane (3-D CT, hard tissues, patient K.C.)

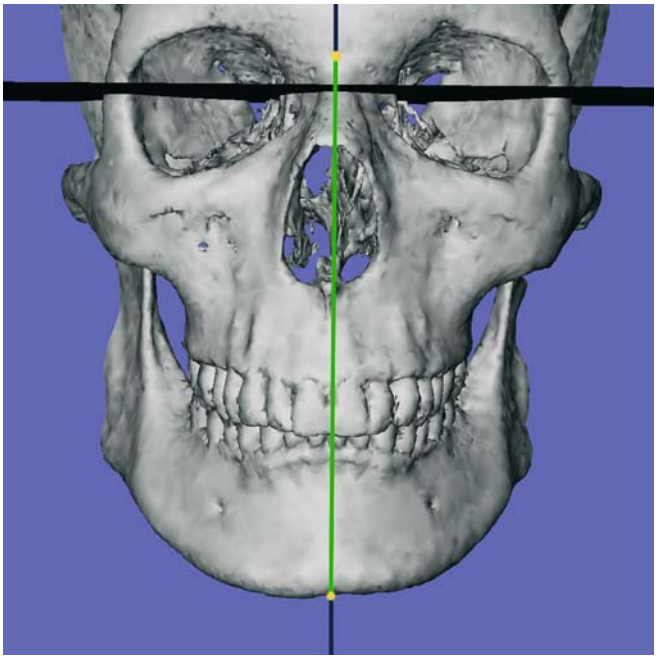

Fig. 7.19. The frontal inclination of the facial midplane from the median (*z*) 3-D cephalometric reference plane is a projected angular measurement on the vertical (*y*) 3-D cephalometric reference plane (3-D CT, hard tissues, patient K.C.)

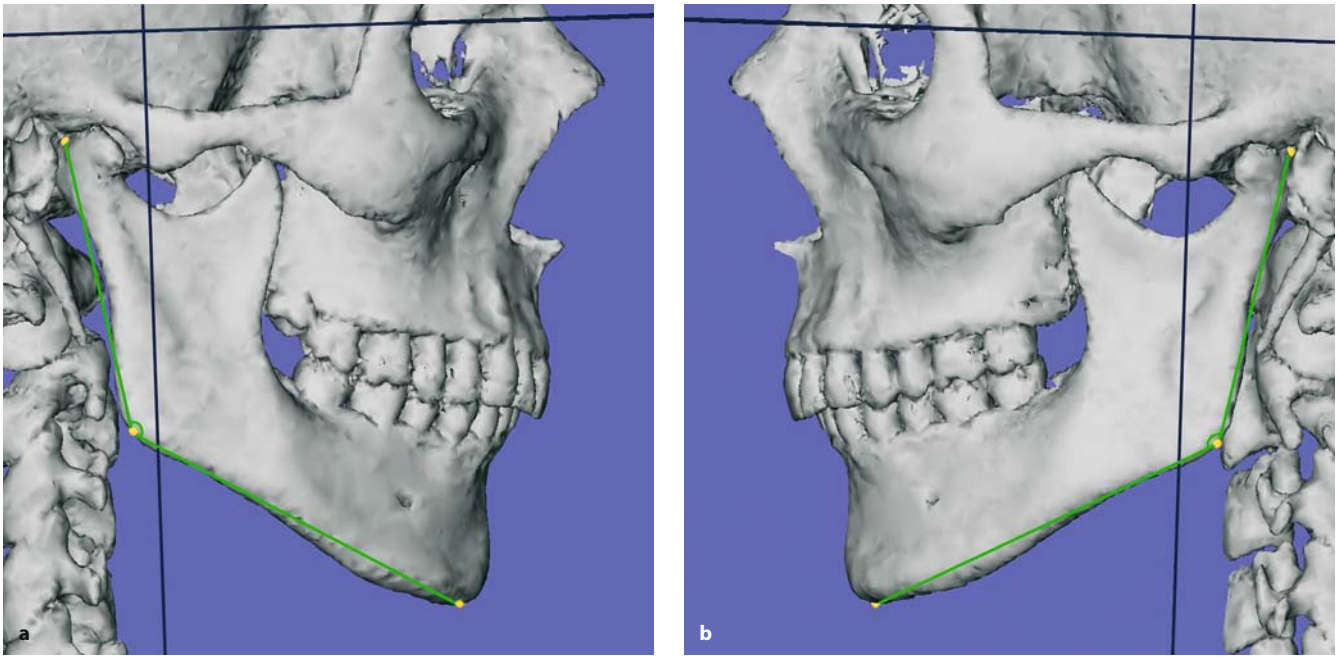

Fig. 7.20. The right (a) and left (b) gonial angles, Co_r-Go_r-Men / Co_l-Go_l-Men, are projected angular soft tissue measurements on the median (*z*) 3-D cephalometric reference plane (3-D CT, hard tissues, patient K.C.)

7.1.3 Orthogonal Arithmetical Hard Tissue Analysis

7.1.3.1 Orthogonal Analysis to the Horizontal (*x*) Plane

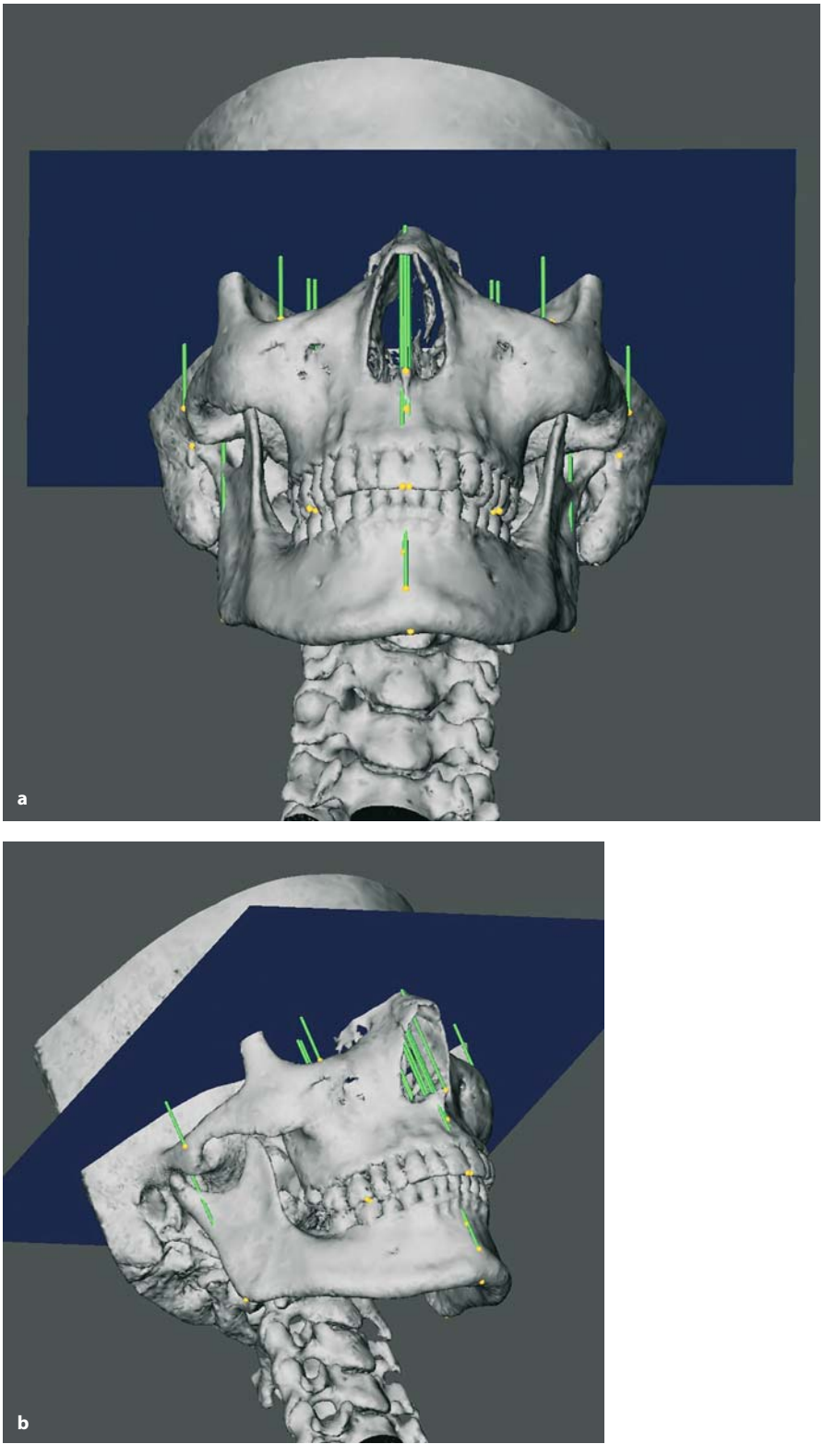

Fig. 7.21 a, b. Set-up of vertical orthogonal hard tissue measurements to the horizontal (*x*) plane (3-D CT, patient K.C.)

7.1.3.2 Orthogonal Analysis to the Vertical (*y*) Plane

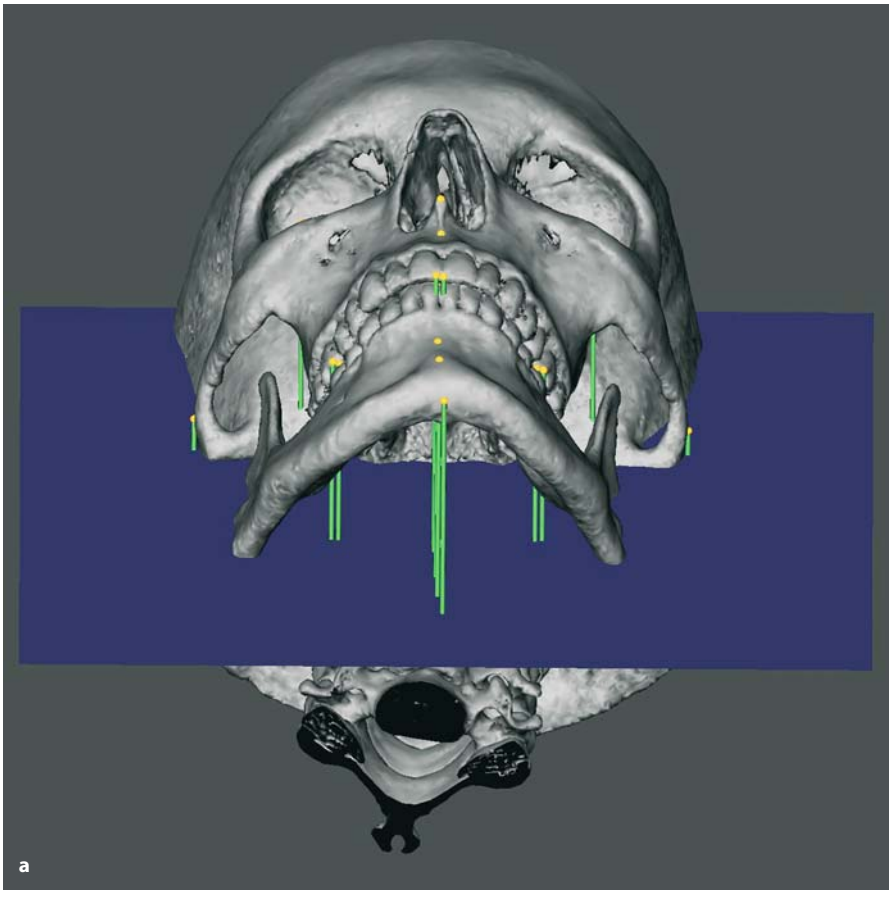

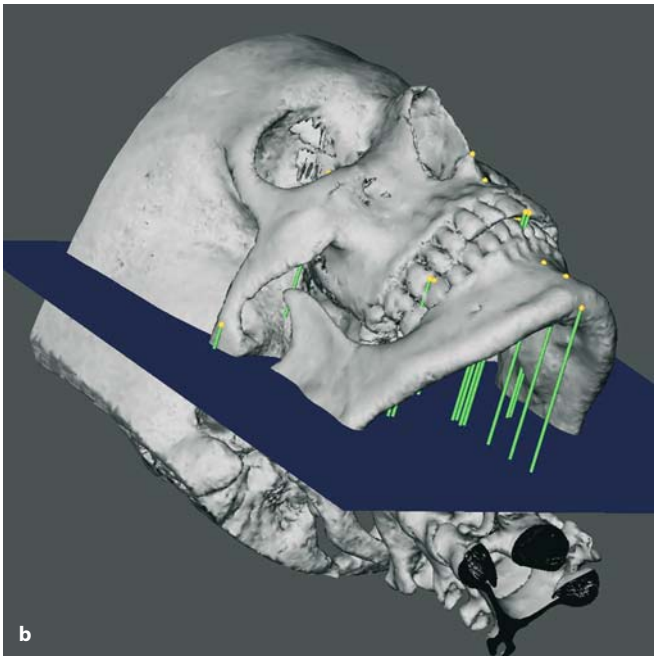

Fig. 7.22 a, b. Set-up of horizontal orthogonal hard tissue measurements to the vertical (*y*) plane (3-D CT, patient K.C.)

7.1.3.3 Orthogonal Analysis to the Median (*z*) Plane

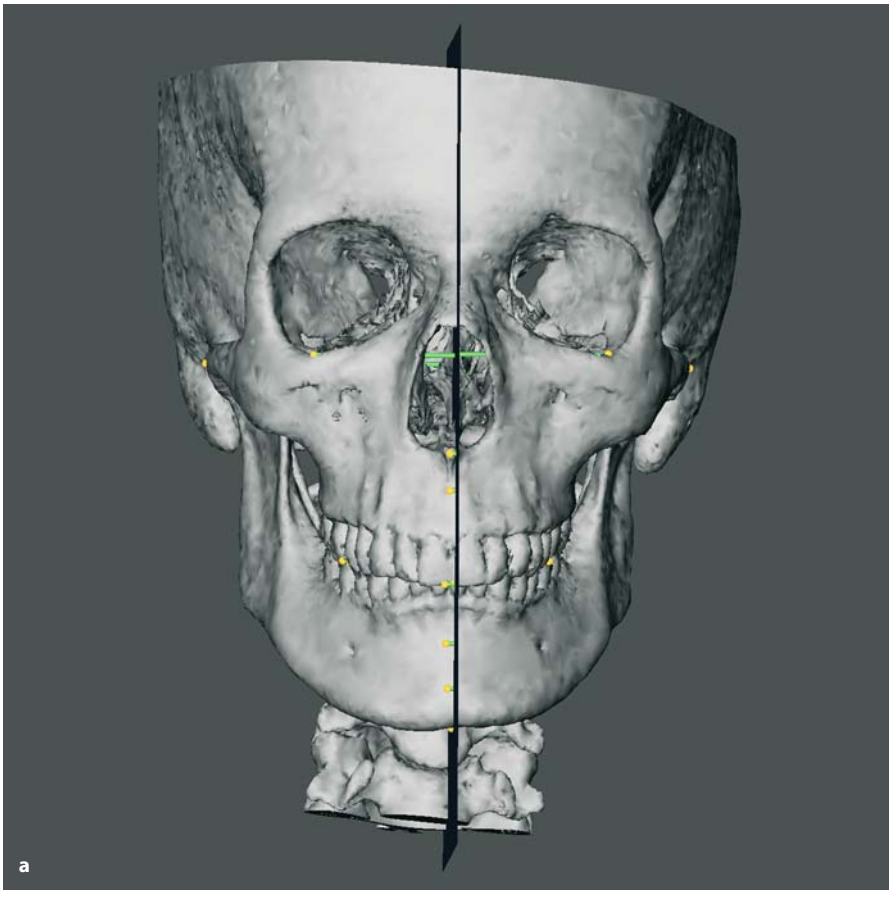

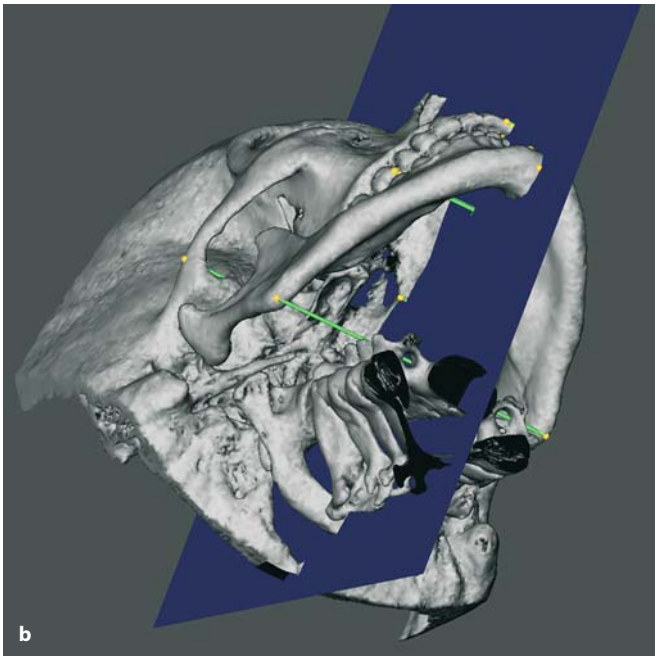

Fig. 7.23 a, b. Set-up of transverse orthogonal hard tissue measurements to the median (*z*) plane (3-D CT, patient K.C.)

7.2 3-D Cephalometric Soft Tissue Analysis

7.2.1 Linear Soft Tissue Analysis

7.2.1.1 Linear Projective Soft Tissue Analysis

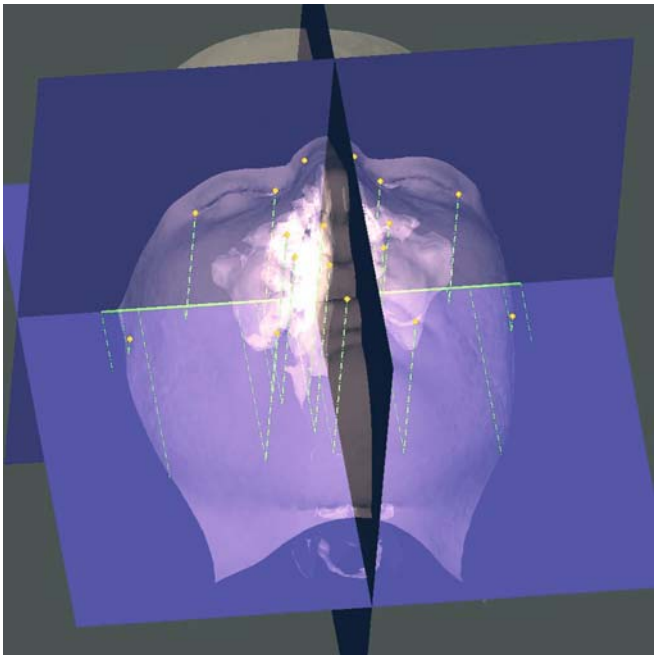

Fig. 7.24. 3-D cephalometric projective soft tissue width measurements (3-D CT, transparent soft tissues, patient K.C.)

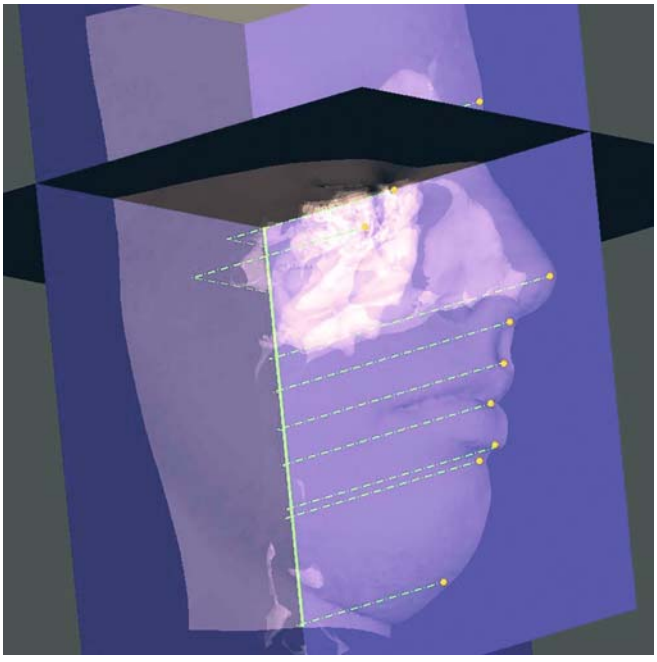

Fig. 7.25. 3-D cephalometric projective soft tissue height measurements (3-D CT, transparent soft tissues, patient K.C.)

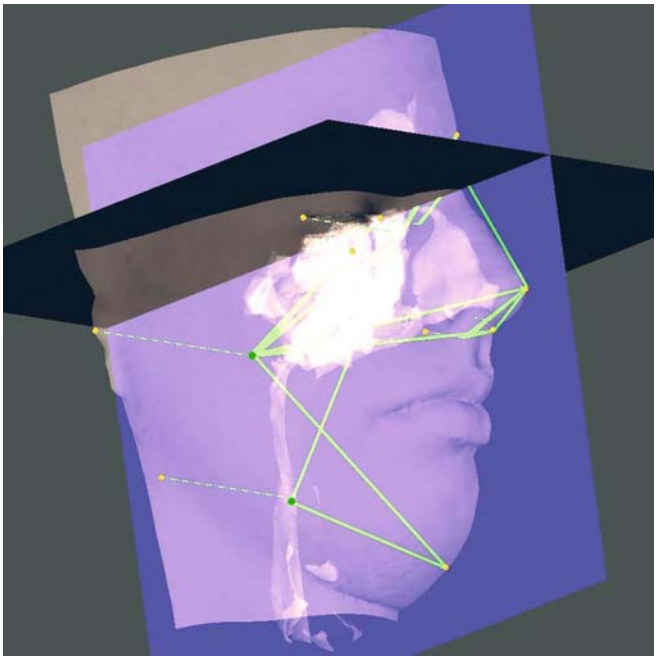

Fig. 7.26. 3-D cephalometric projective soft tissue depth measurements (3-D CT, transparent soft tissues, patient K.C.)

7.2.1.1.1 Soft Tissue Widths

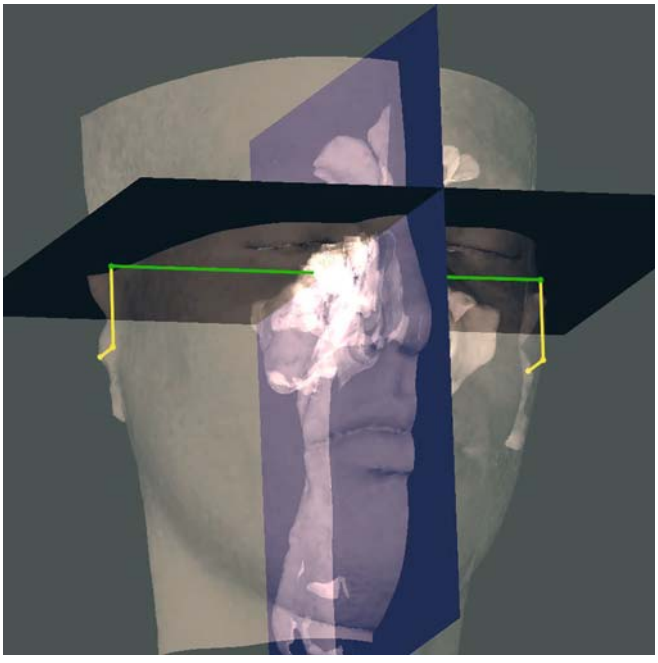

Fig. 7.27. Width of the skull base, t_r-t_l (3-D CT, transparent soft tissues, patient K.C.)

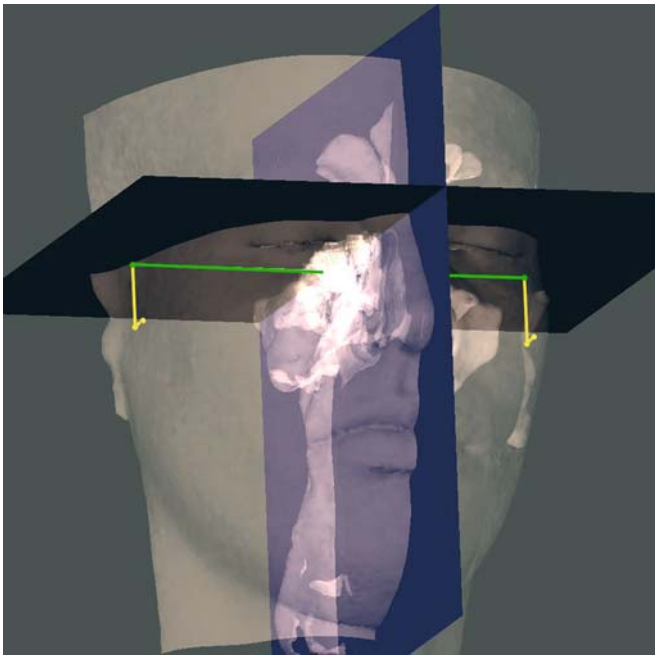

Fig. 7.28. Upper face width or bizygion diameter or width of the face, zy_r-zy_l (3-D CT, transparent soft tissues, patient K.C.)

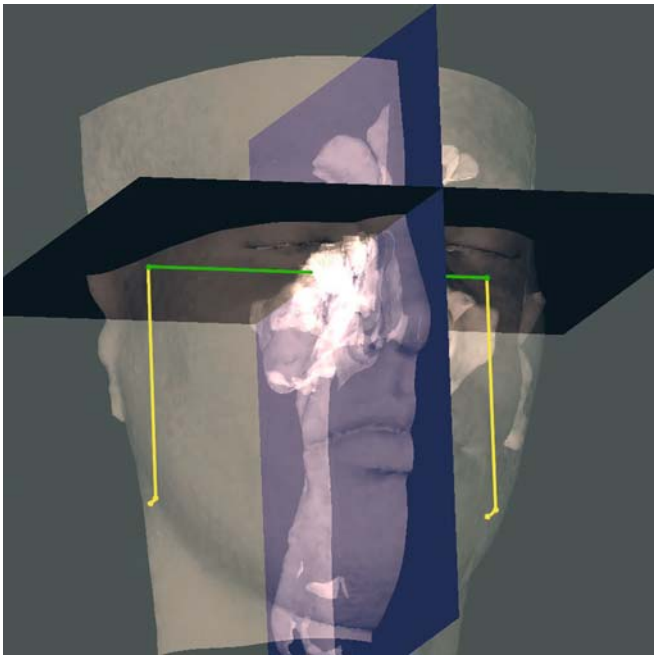

Fig. 7.29. Lower face width or bigonial diameter or mandibular width, go_r-go_l (3-D CT, transparent soft tissues, patient K.C.)

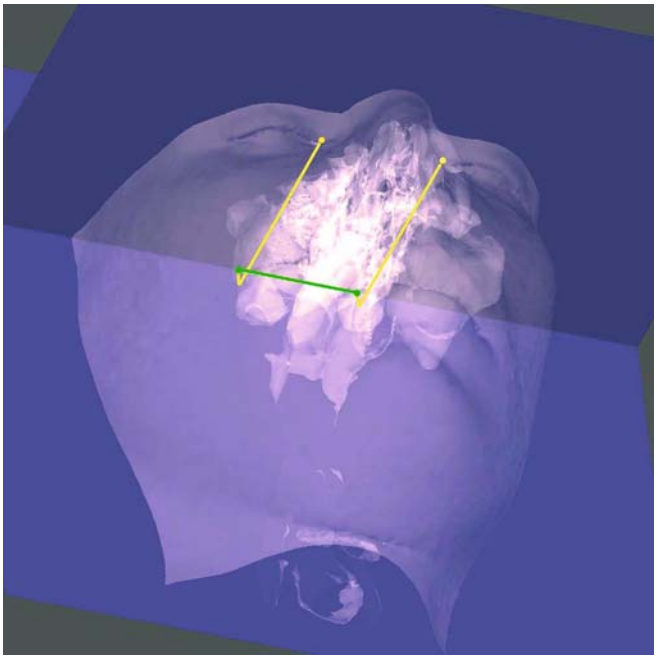

Fig. 7.30. Intercanthal width, en_r-en_l (3-D CT, transparent soft tissues, patient K.C.)

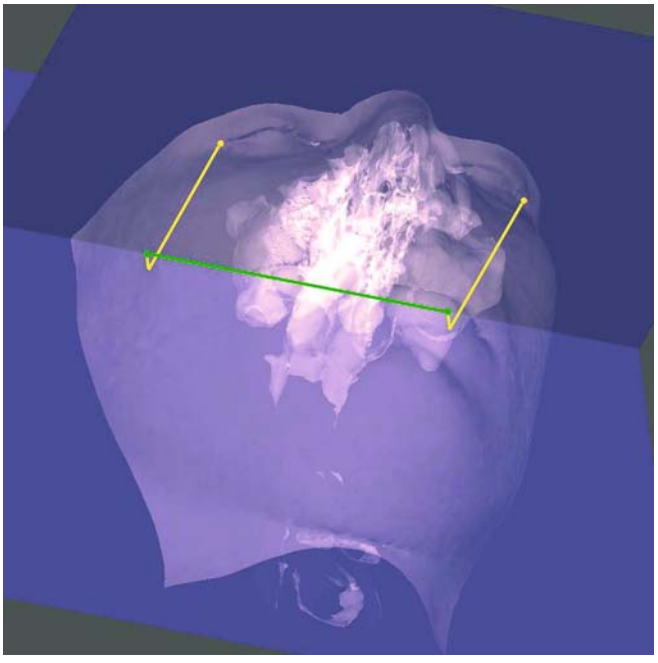

Fig. 7.31. Biocular width, ex_r-ex_l (3-D CT, transparent soft tissues, patient K.C.)

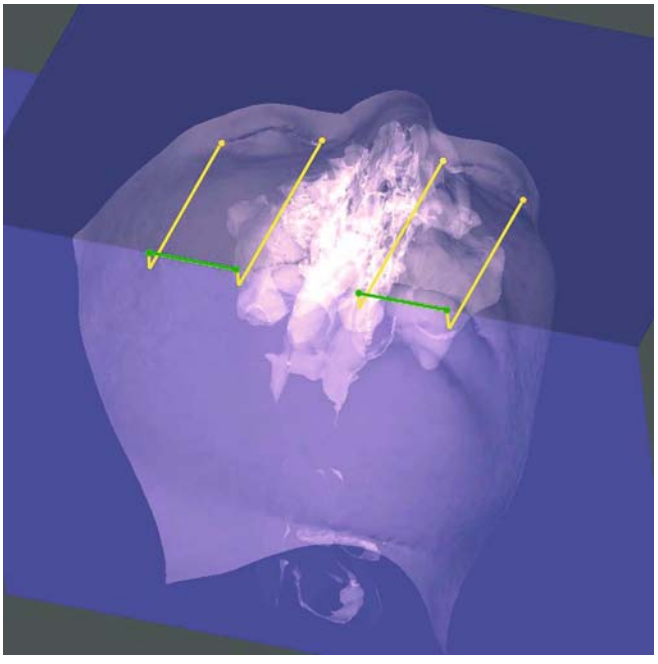

Fig. 7.32. Right and left eye fissure length, ex_r-en_r / ex_l-en_l (3-D CT, transparent soft tissues, patient K.C.)

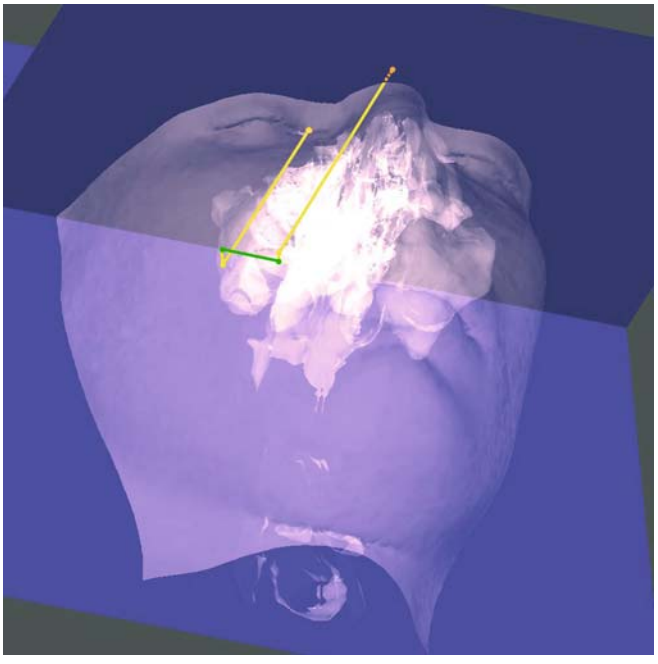

Fig. 7.33. Right endocanthion-facial midline, en_r-se (3-D CT, transparent soft tissues, patient K.C.)

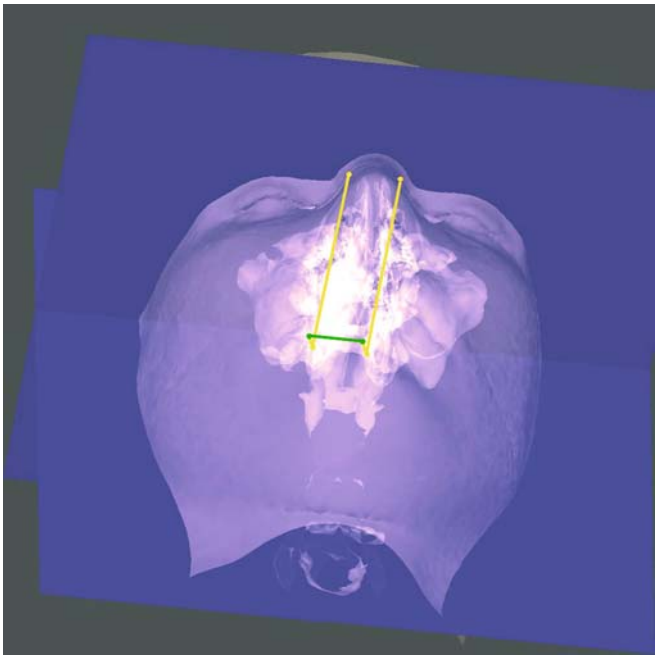

Fig. 7.34. Width of the nasal root, mf_r-mf_l (3-D CT, transparent soft tissues, patient K.C.)

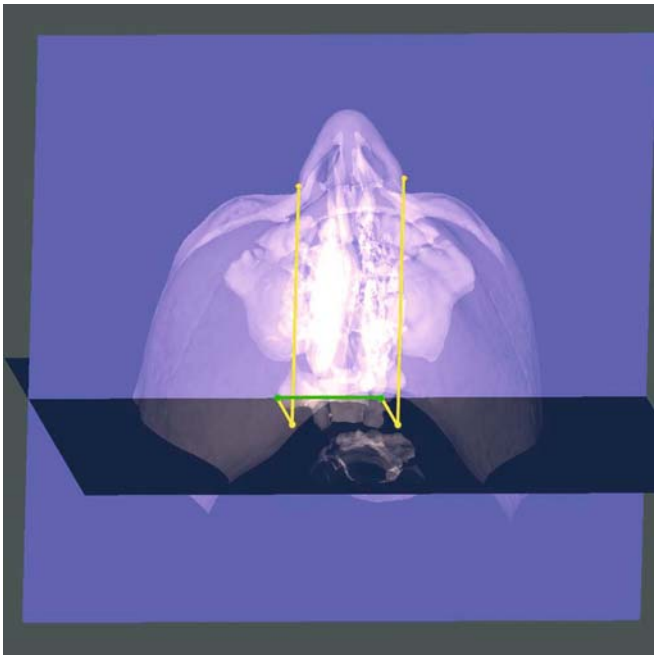

Fig. 7.35. Morphological width of the nose according to Farkas, al_r-al_l (3-D CT, transparent soft tissues, patient K.C.)

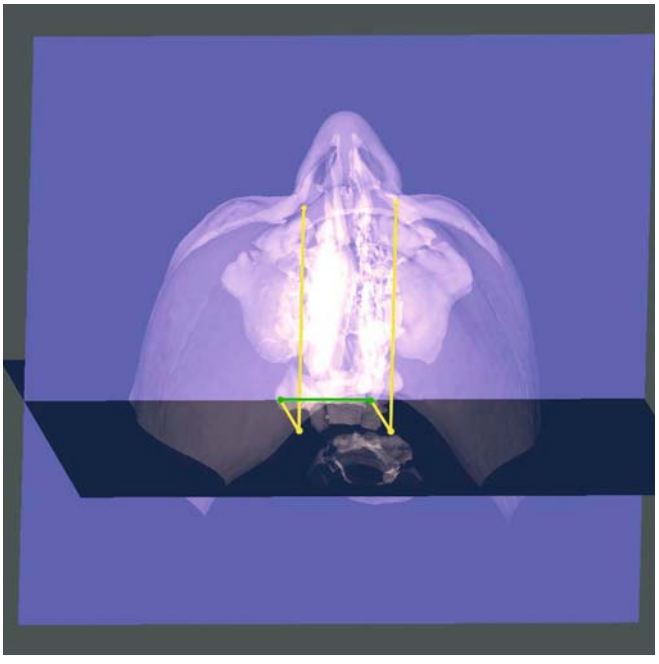

Fig. 7.36. Anatomical width of the nose according to Knussmann, ac_r-ac_l (3-D CT, transparent soft tissues, patient K.C.)

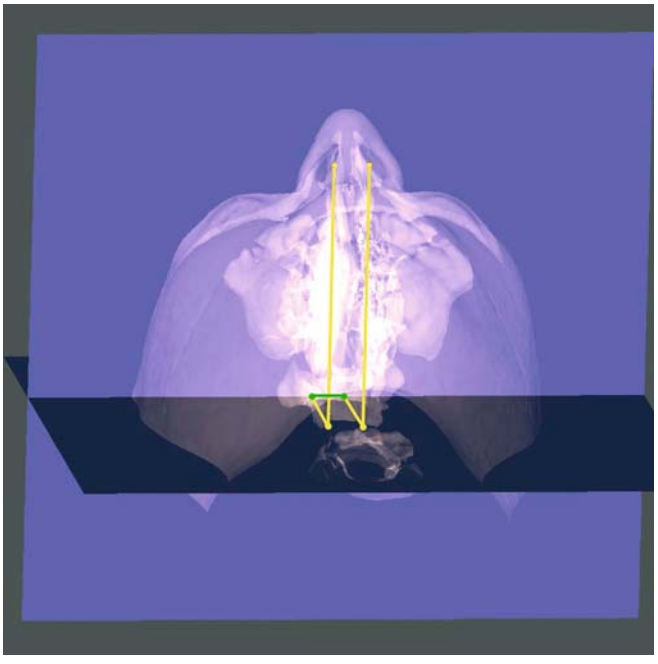

Fig. 7.37. Width of the columella according to Knussmann, sn_r'-sn_l' (3-D CT, transparent soft tissues, patient K.C.)

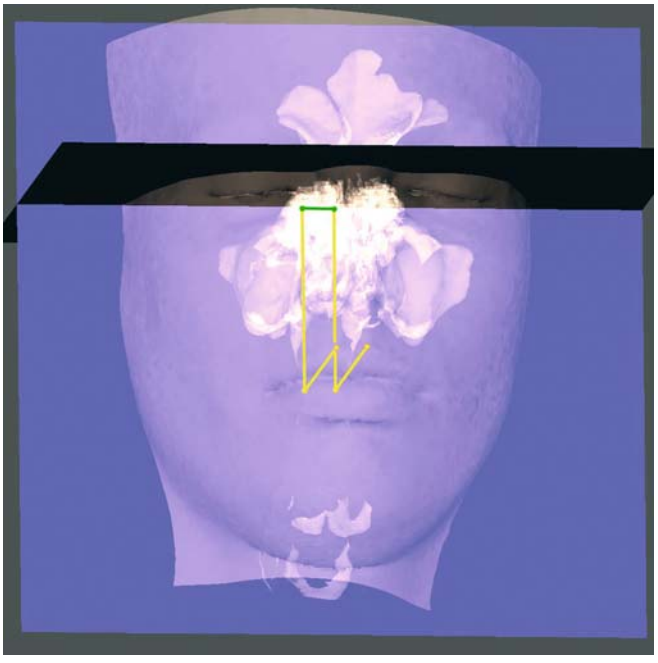

Fig. 7.38. Width of the philtrum, cph_r-cph_l (3-D CT, transparent soft tissues, patient K.C.)

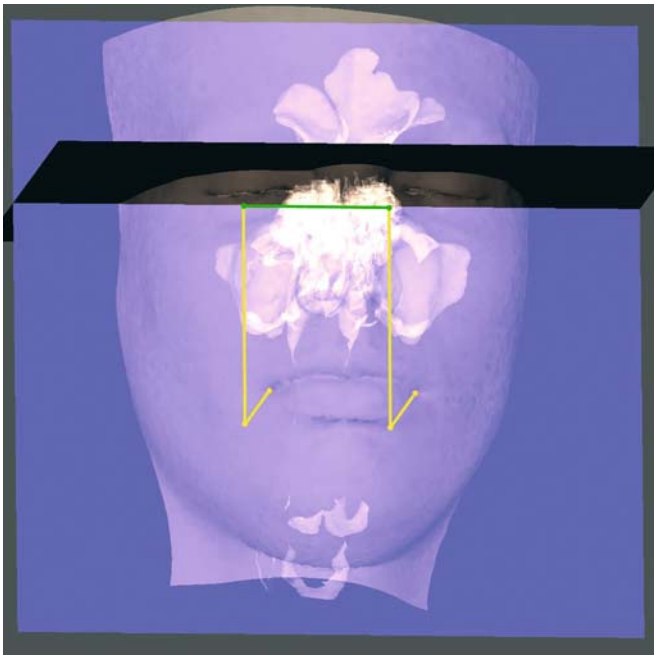

Fig .7.39. Width of the mouth, ch_r-ch_l (3-D CT, transparent soft tissues, patient K.C.)

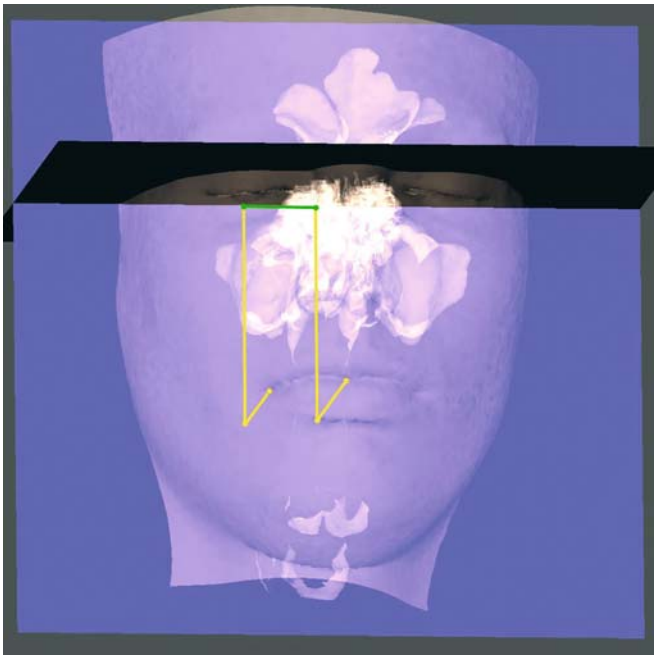

Fig. 7.40. Right half of the labial fissure length, ch_r-sto (3-D CT, transparent soft tissues, patient K.C.)

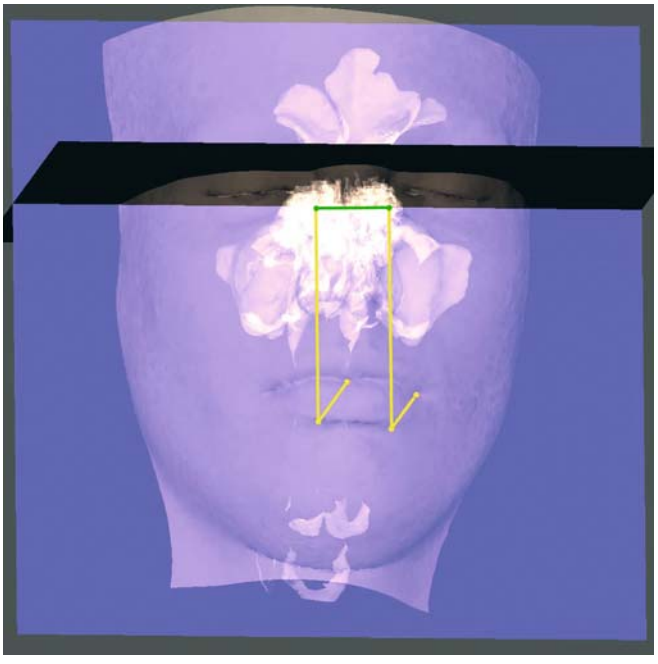

Fig. 7.41. Left half of the labial fissure length, ch_l-sto (3-D CT, transparent soft tissues, patient K.C.)

7.2.1.1.2
Soft Tissue Heights

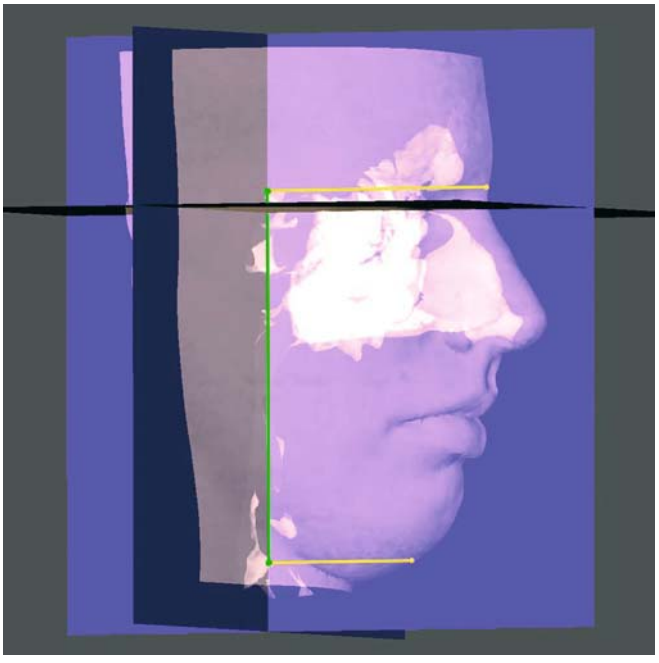

Fig. 7.42. Morphological height of the face, n-gn (3-D CT, transparent soft tissues, patient K.C.)

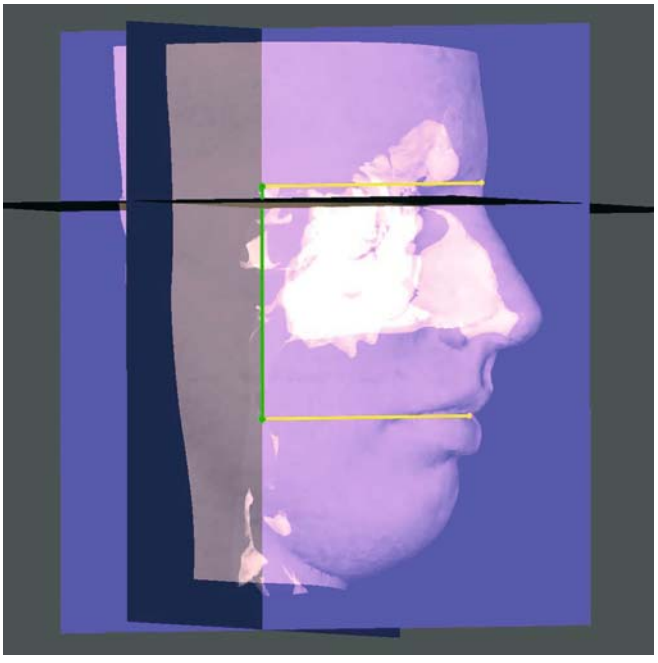

Fig. 7.43. Height of the upper face, n-sto (3-D CT, transparent soft tissues, patient K.C.)

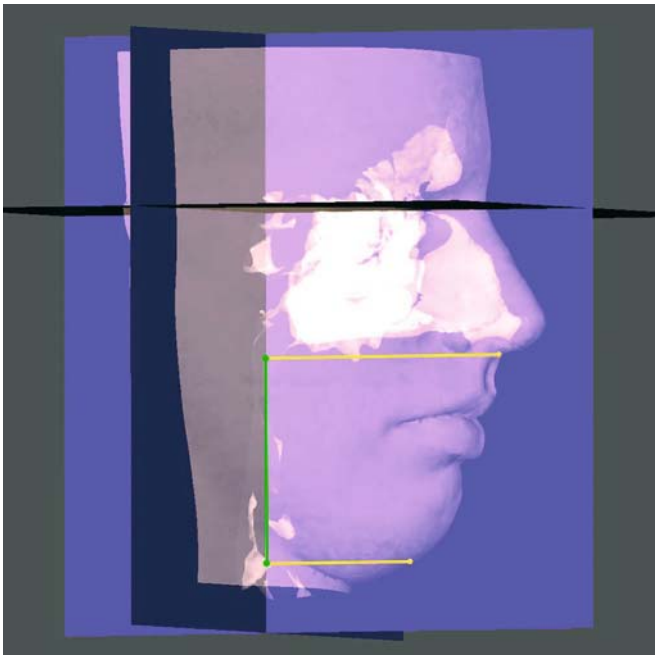

Fig. 7.44. Height of the lower face, sn-gn (3-D CT, transparent soft tissues, patient K.C.)

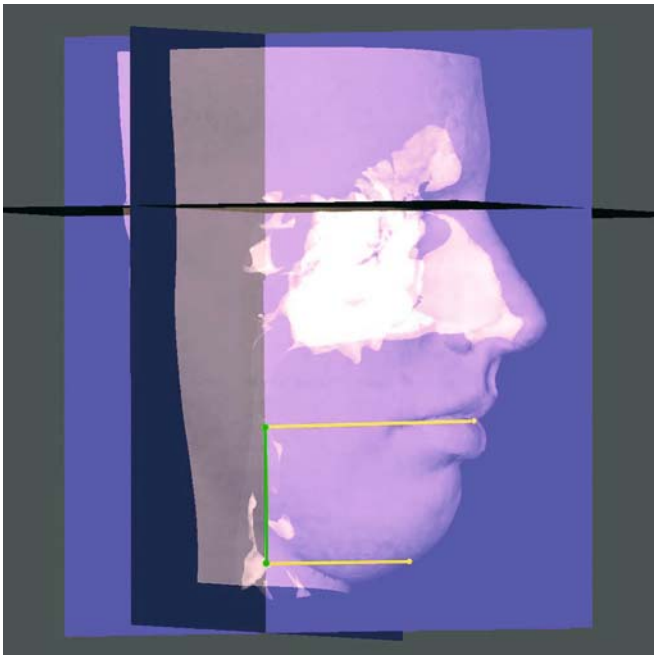

Fig. 7.45. Height of the mandible, sto-gn (3-D CT, transparent soft tissues, patient K.C.)

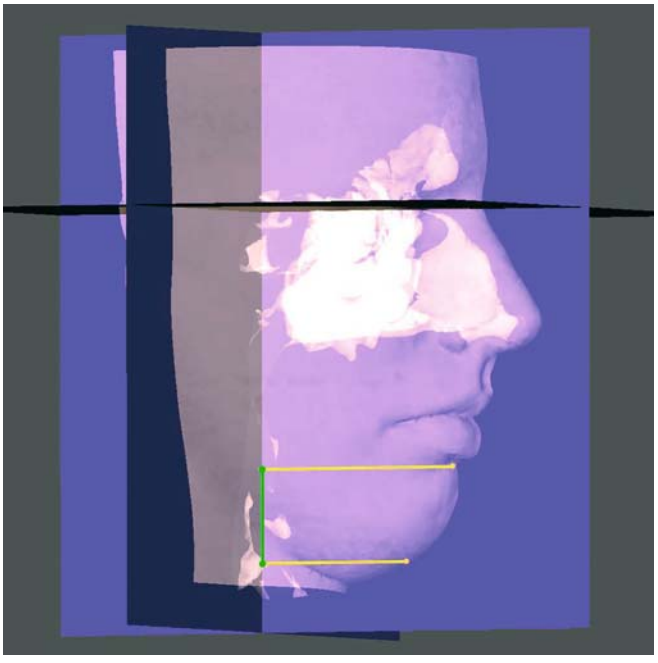

Fig. 7.46. Height of the chin, sl-gn (3-D CT, transparent soft tissues, patient K.C.)

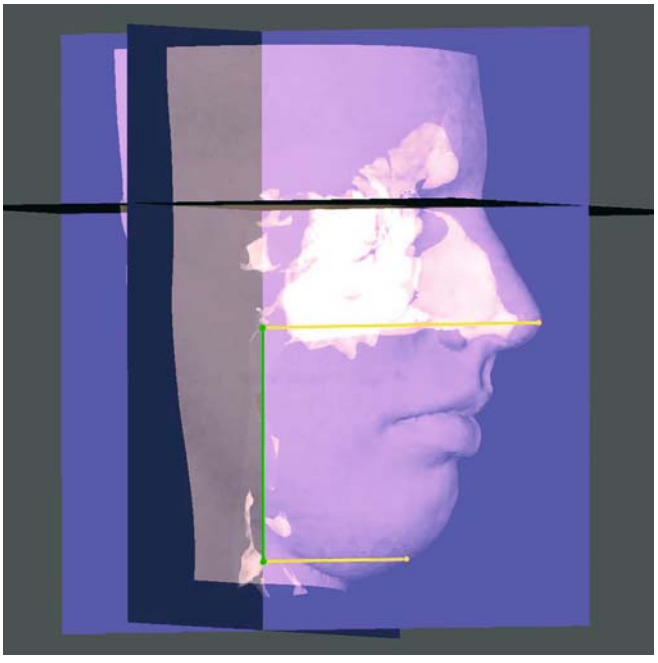

Fig. 7.47. Height of the lower profile, prn-gn (3-D CT, transparent soft tissues, patient K.C.)

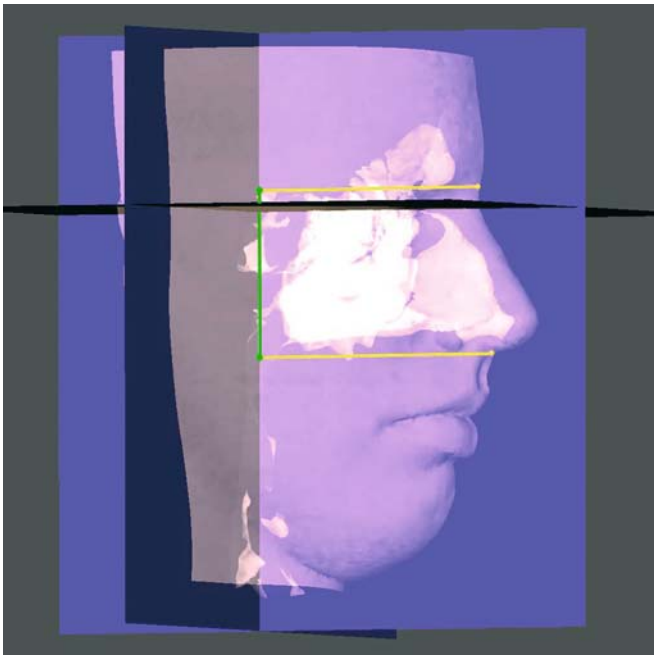

Fig. 7.48. Height of the nose, n-sn (3-D CT, transparent soft tissues, patient K.C.)

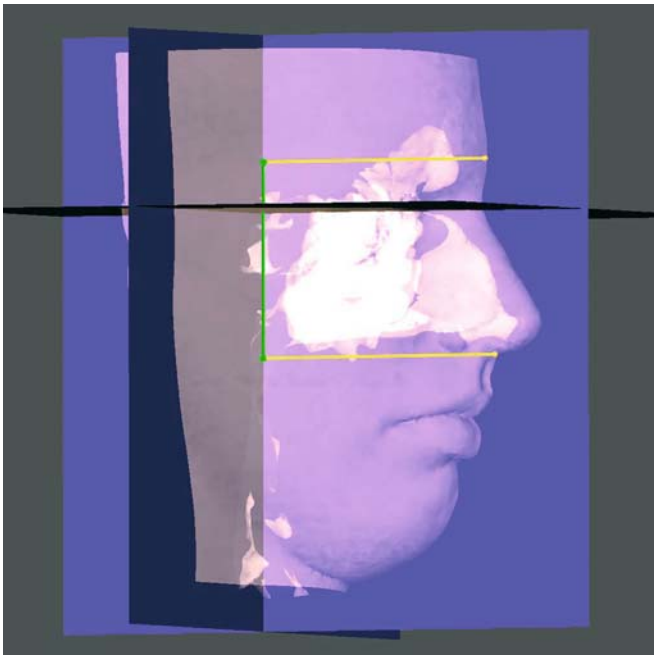

Fig. 7.49. glabella-subnasale height, g-sn (3-D CT, transparent soft tissues, patient K.C.)

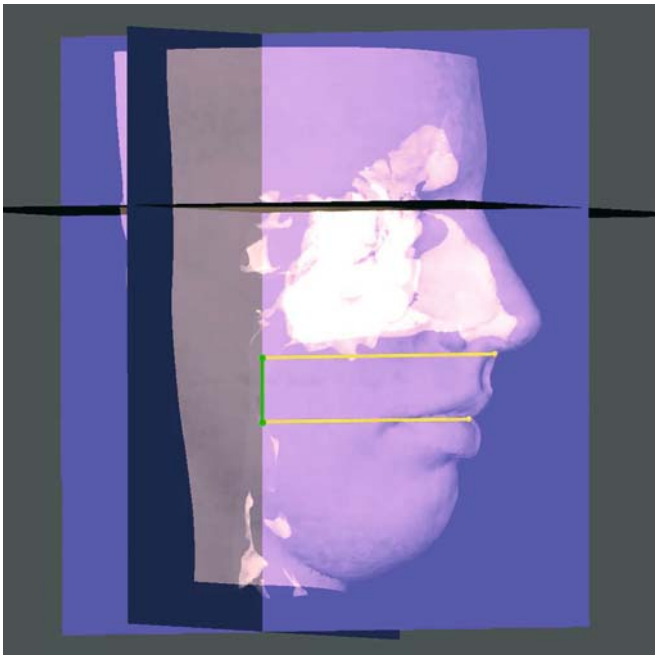

Fig. 7.50. Height of the upper lip, sn-sto (3-D CT, transparent soft tissues, patient K.C.)

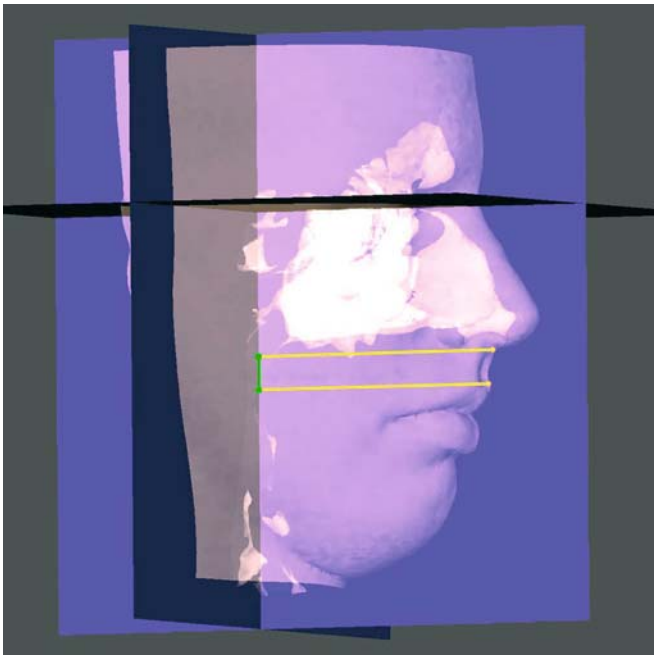

Fig. 7.51. Height of the skin portion of the upper lip, sn-ls (3-D CT, transparent soft tissues, patient K.C.)

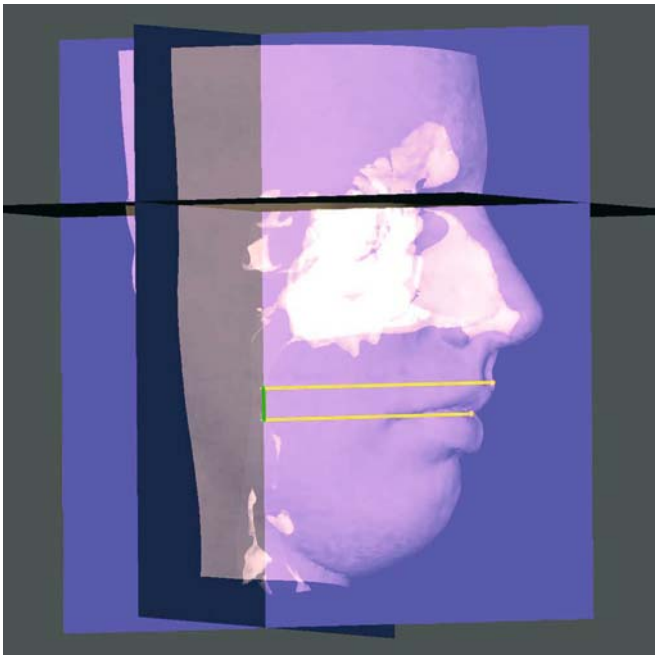

Fig. 7.52. Height of the vermilion of the upper lip, ls-sto (3-D CT, transparent soft tissues, patient K.C.)

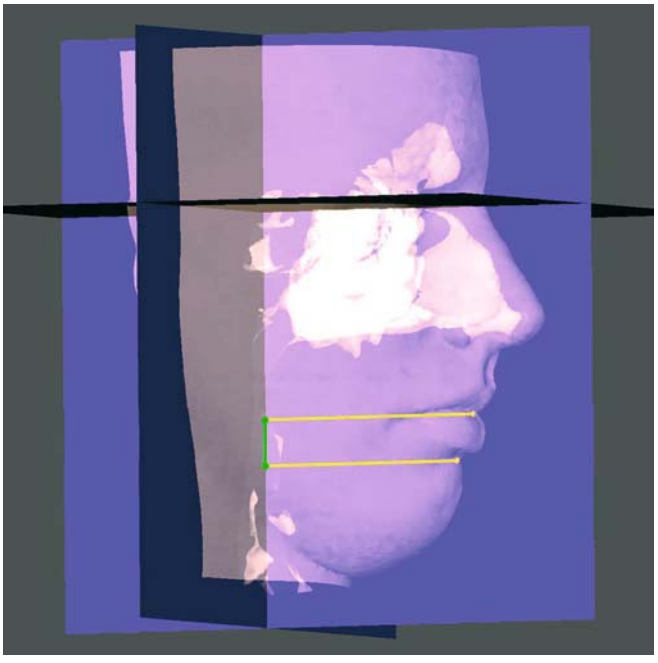

Fig. 7.53. Height of the lower lip, sto-sl (3-D CT, transparent soft tissues, patient K.C.)

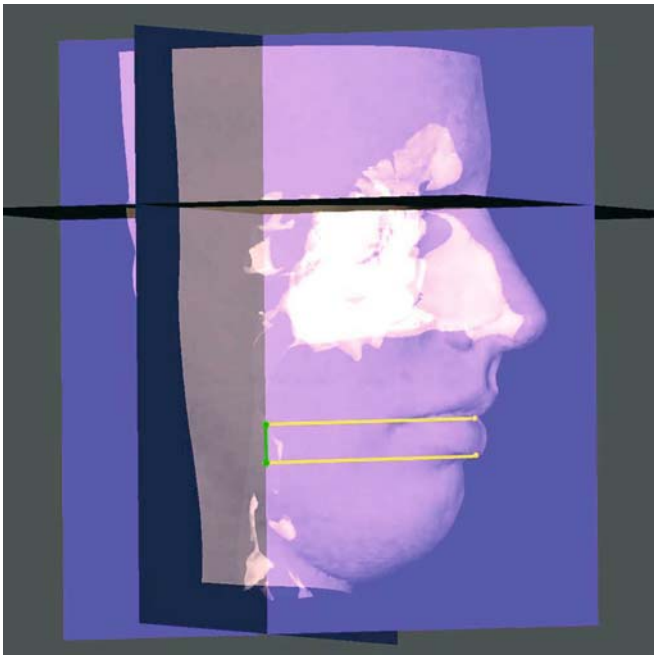

Fig. 7.54. Height of the vermilion of the lower lip, sto-li (3-D CT, transparent soft tissues, patient K.C.)

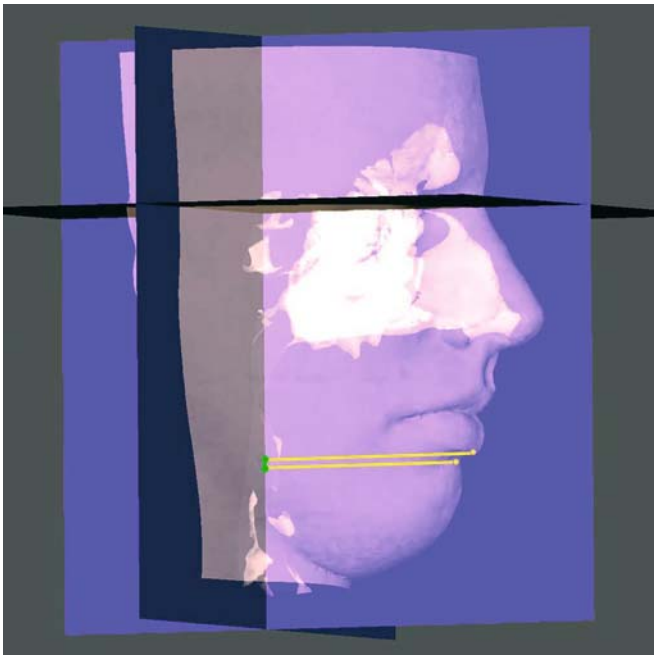

Fig. 7.55. Height of the skin portion of the lower lip, li-sl (3-D CT, transparent soft tissues, patient K.C.)

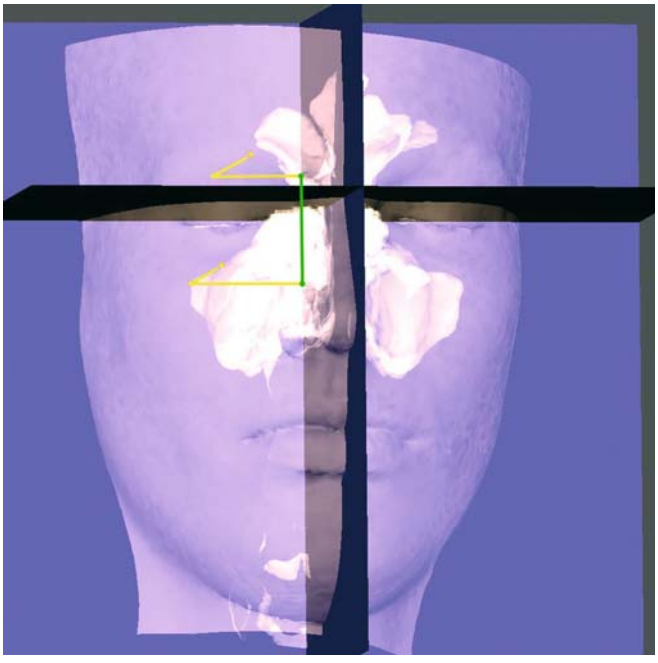

Fig. 7.56. Height of the right orbit according to Martin and Saller, or_r-os_r (3-D CT, transparent soft tissues, patient K.C.)

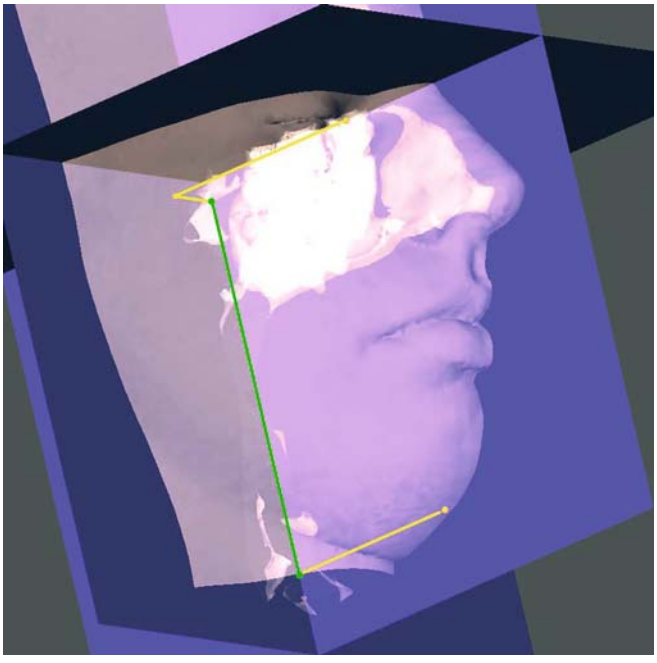

Fig. 7.57. Lower right half of the craniofacial height, en_r-gn (3-D CT, transparent soft tissues, patient K.C.)

7.2.1.1.3
Soft Tissue Depths

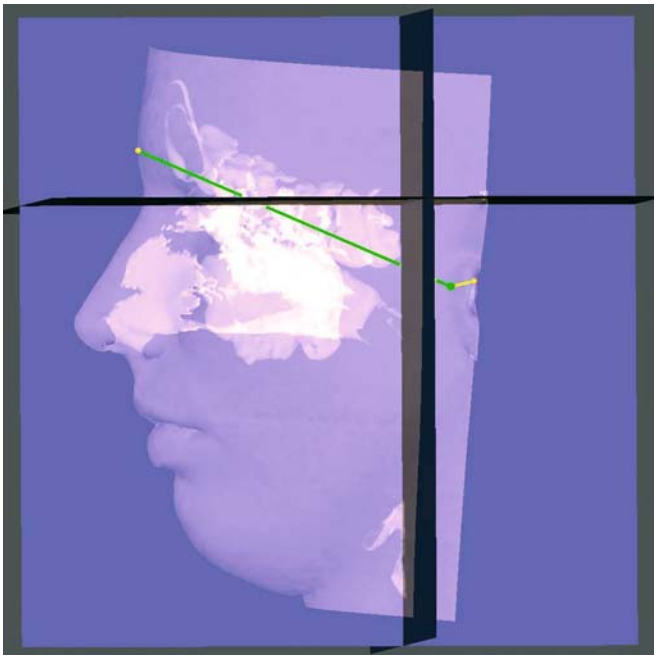

Fig. 7.58. Left depth of the upper third of the face measured between tragion and glabella or left tragion-glabellar depth, t_l-g (3-D CT, transparent soft tissues, patient K.C.)

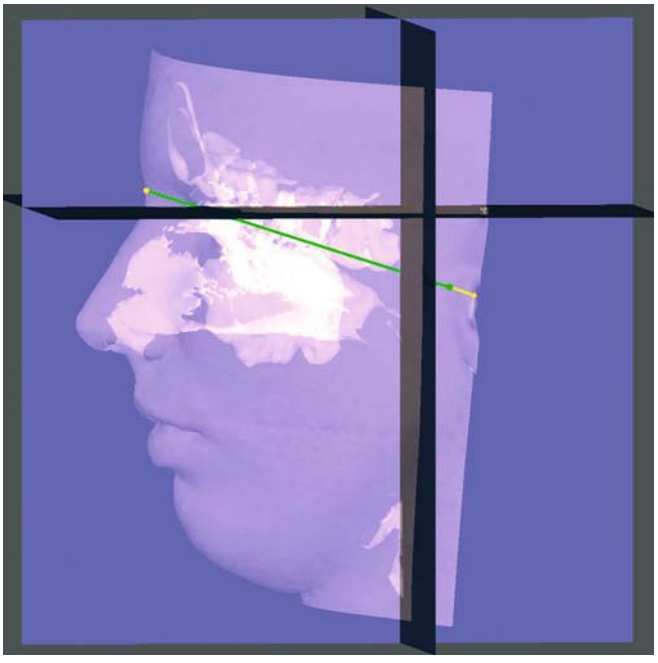

Fig. 7.59. Left depth of the upper third of the face measured between tragion and soft tissue nasion or left tragion-nasion depth, t_l-n (3-D CT, transparent soft tissues, patient K.C.)

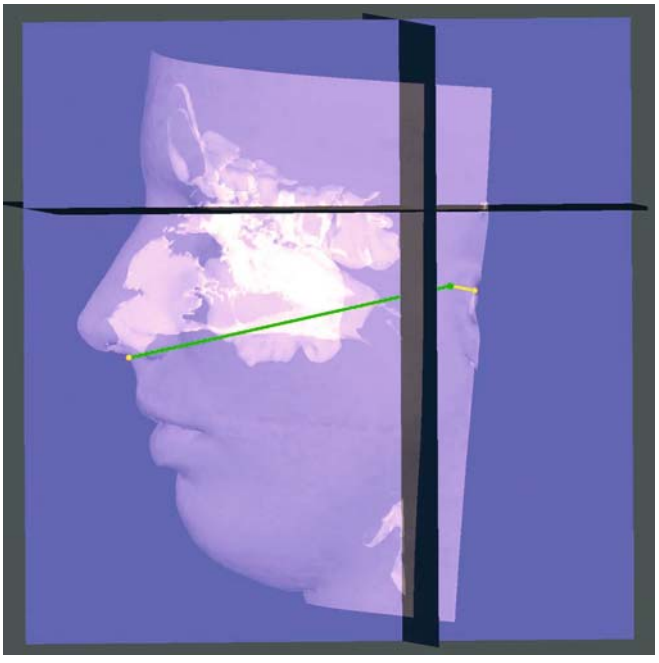

Fig. 7.60. Left depth of the middle third of the face, t_l-sn (3-D CT, transparent soft tissues, patient K.C.)

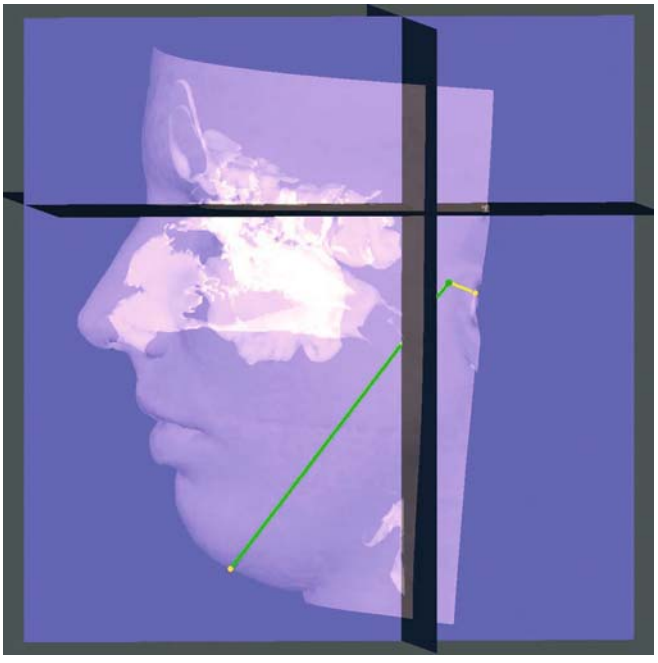

Fig. 7.61. Left depth of the lower third of the face, t_l-gn (3-D CT, transparent soft tissues, patient K.C.)

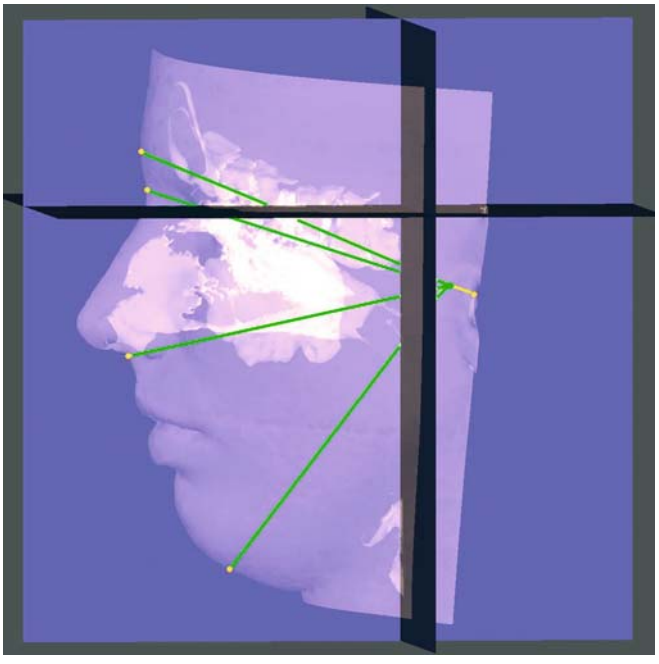

Fig. 7.62. Left depths of the upper, middle and lower thirds of the face (3-D CT, transparent soft tissues, patient K.C.)

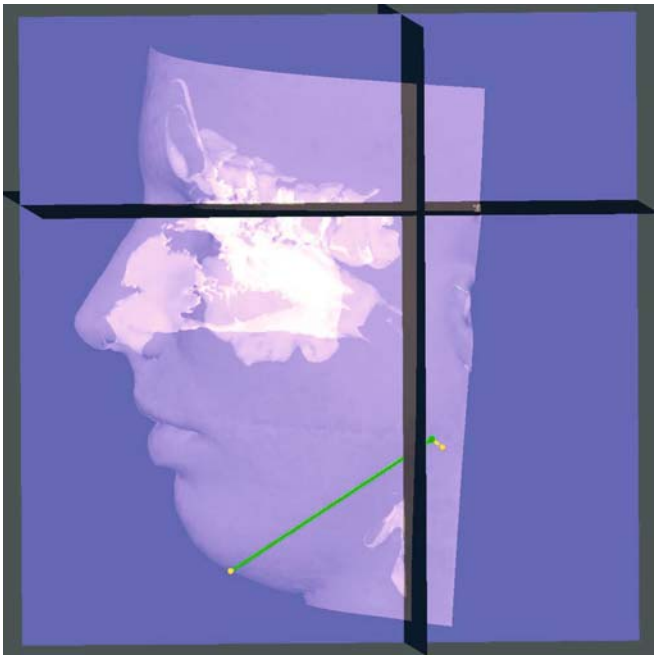

Fig. 7.63. Left depth of the mandible, go_l-gn (3-D CT, transparent soft tissues, patient K.C.)

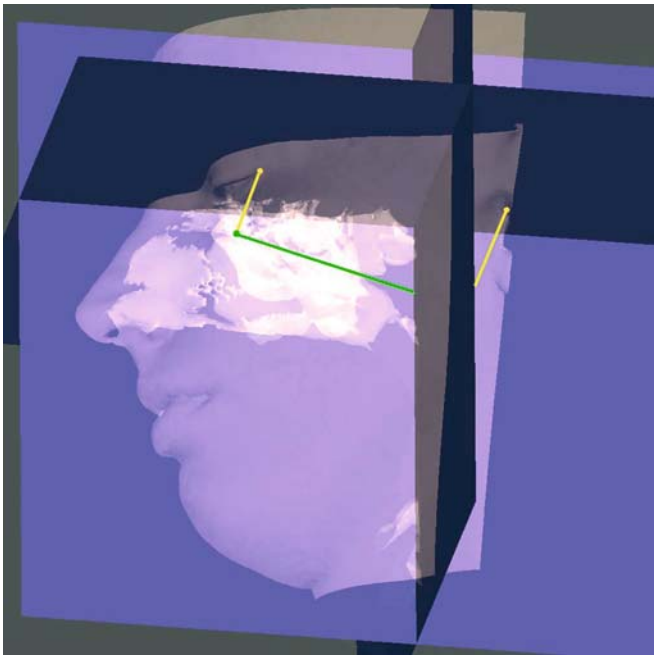

Fig. 7.64. Left orbito-tragion distance, ex_l-t_l (3-D CT, transparent soft tissues, patient K.C.)

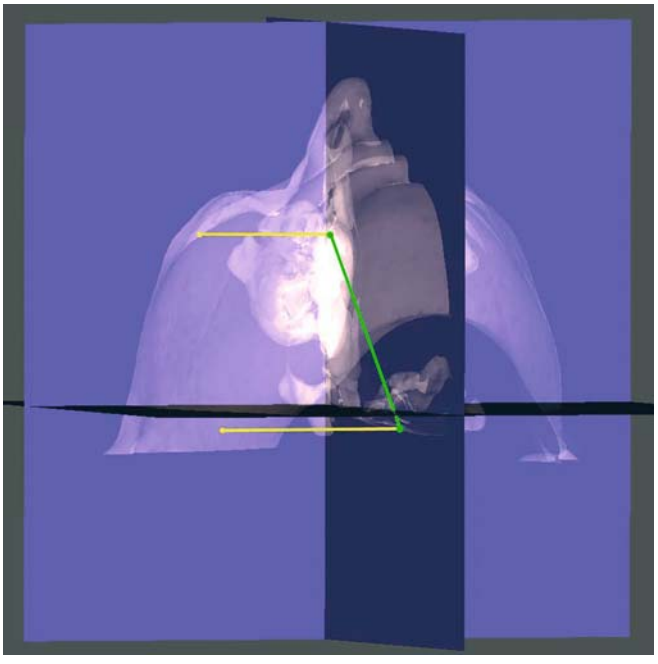

Fig. 7.65. Right orbito-gonial distance, ex_r-go_r (3-D CT, transparent soft tissues, patient K.C.)

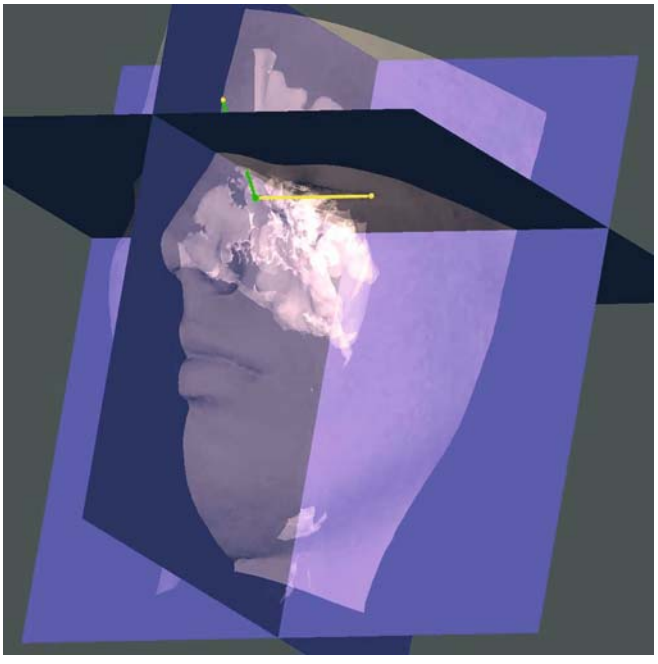

Fig. 7.66. Left orbito-glabellar distance, ex_l-g (3-D CT, transparent soft tissues, patient K.C.)

Fig. 7.67. Nasal tip protrusion, sn-prn (3-D CT, transparent soft tissues, patient K.C.)

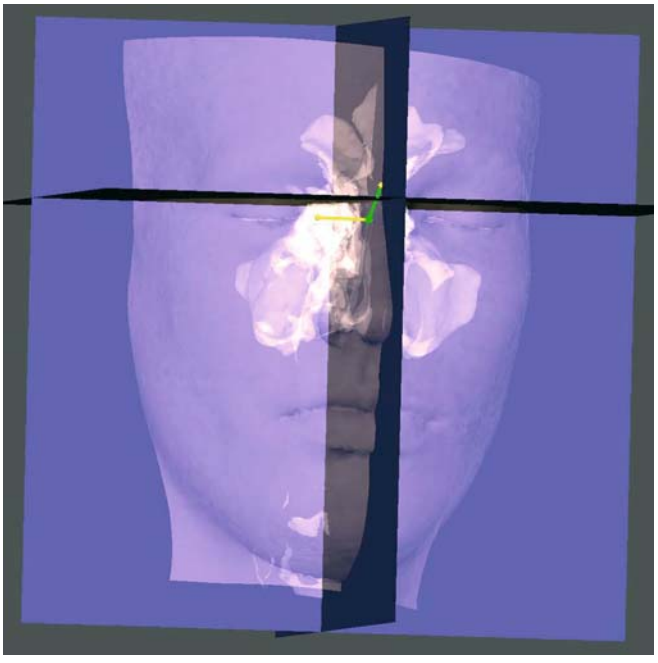

Fig. 7.68. Right nasal root protrusion, en_r-se (3-D CT, transparent soft tissues, patient K.C.)

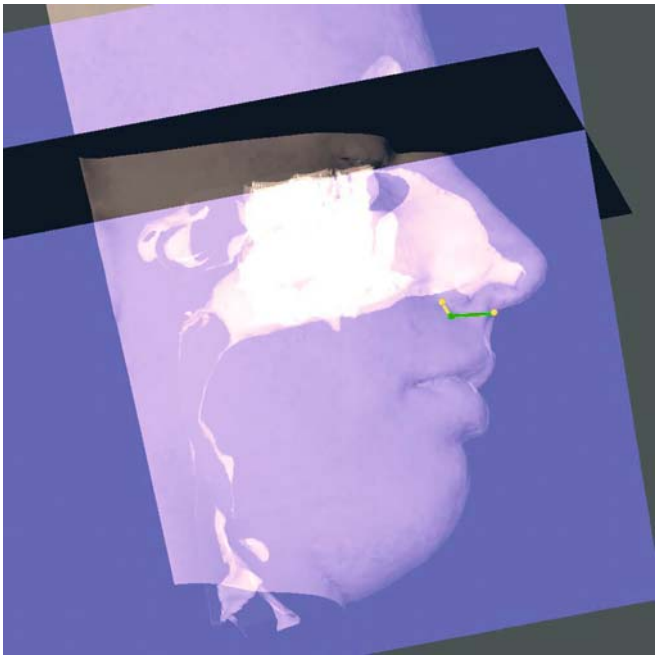

Fig. 7.69. Right columella base-facial insertion ala depth, ac_r-sn (3-D CT, transparent soft tissues, patient K.C.)

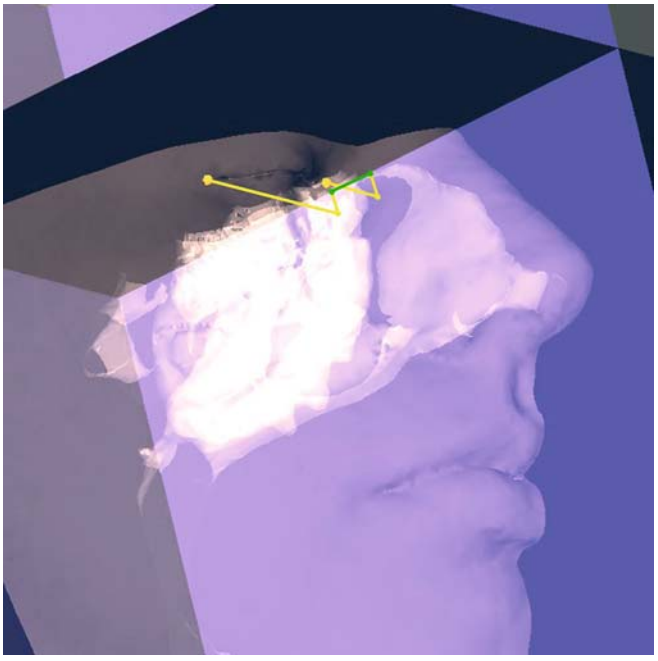

Fig. 7.70. Right endocanthion-exocanthion depth, en_r-ex_r (3-D CT, transparent soft tissues, patient K.C.)

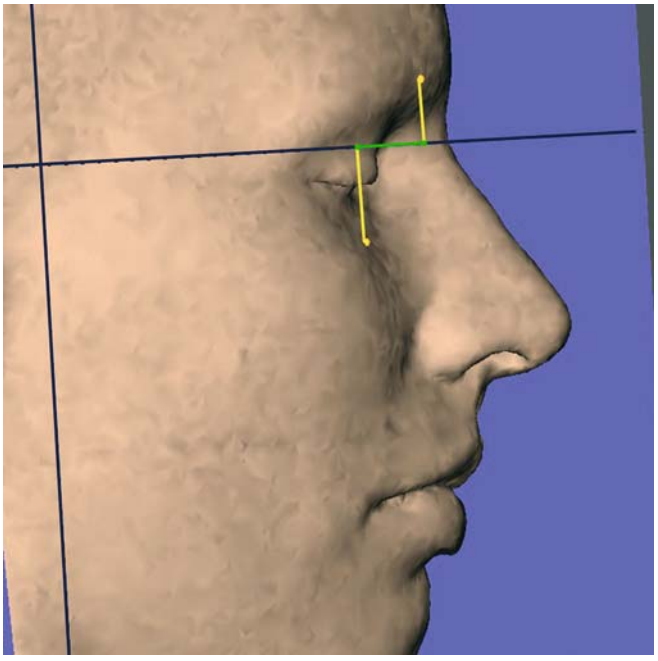

Fig. 7.71. Right upper-lower orbital rim depth, os_r-or_r (3-D CT, transparent soft tissues, patient K.C.)

7.2.1.2 3-D Soft Tissue Distances

Fig. 7.72. Right and left eye fissure length, ex_r-en_r / ex_l-en_l (3-D CT, patient K.C.)

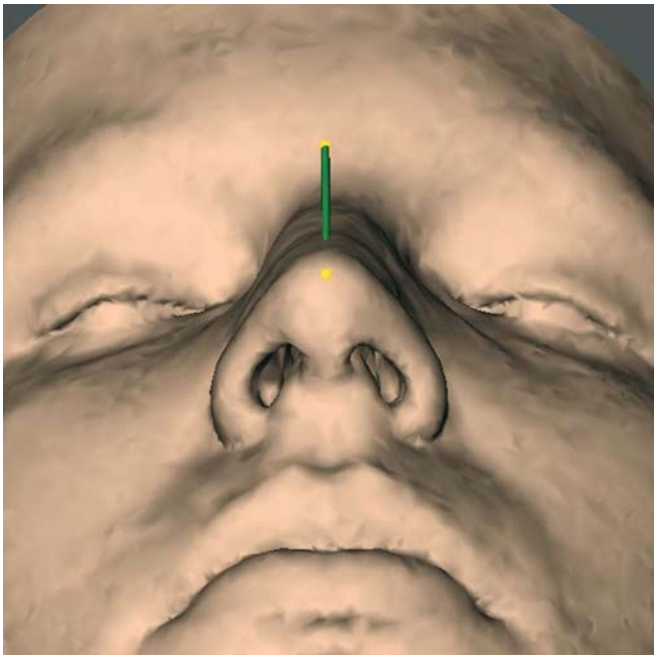

Fig. 7.73. Nasal bridge length, n-prn (3-D CT, patient K.C.)

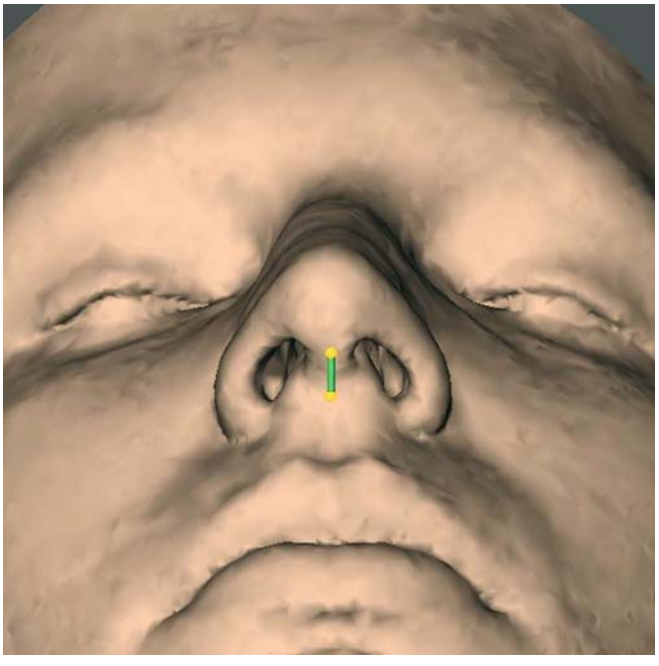

Fig. 7.74. Columella length, sn-c″ (3-D CT, patient K.C.)

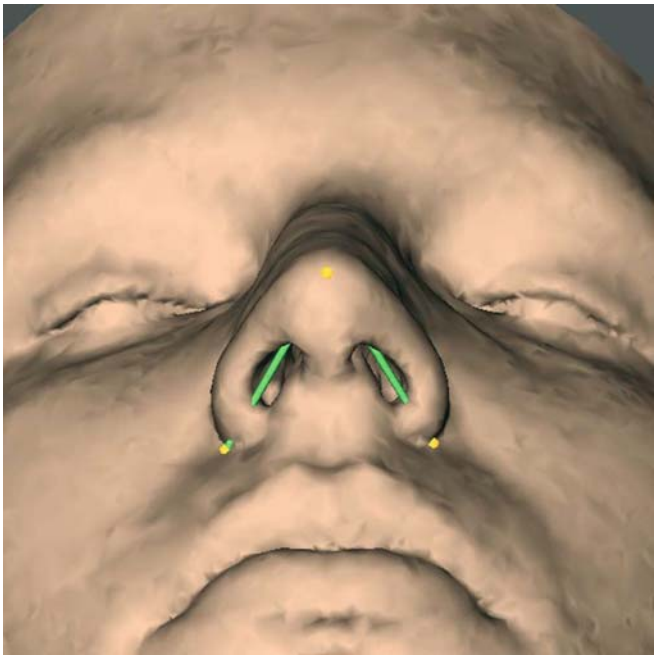

Fig. 7.75. Right and left ala length, ac_r-prn / ac_l-prn (3-D CT, patient K.C.)

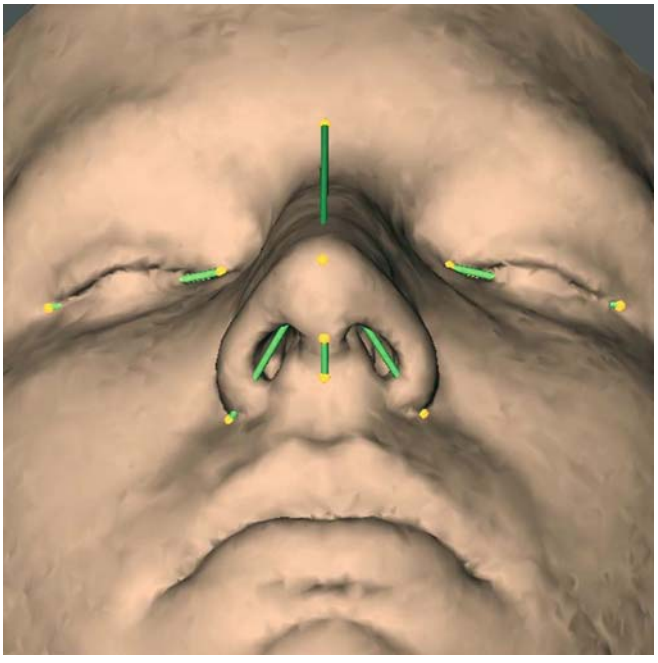

Fig. 7.76. Set-up of 3-D soft tissue distances (3-D CT, patient K.C.)

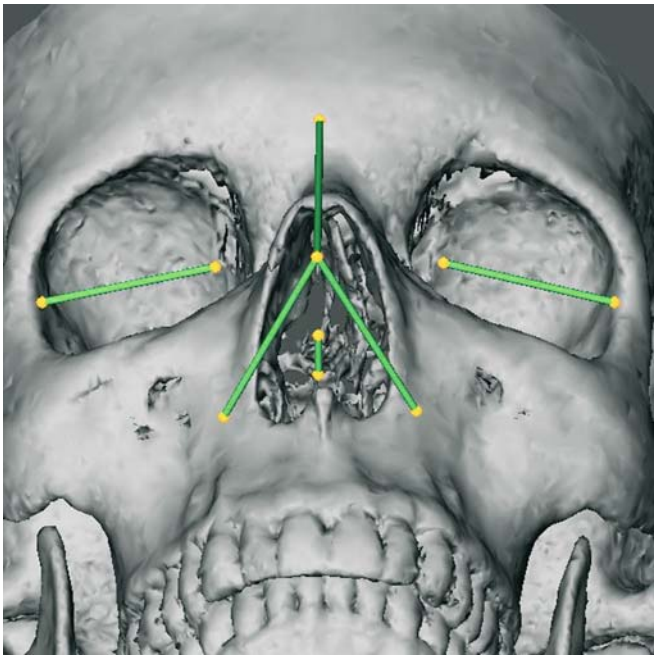

Fig. 7.77. Superimposition of 3-D soft tissue distances on the hard tissue surface representation (3-D CT, patient K.C.)

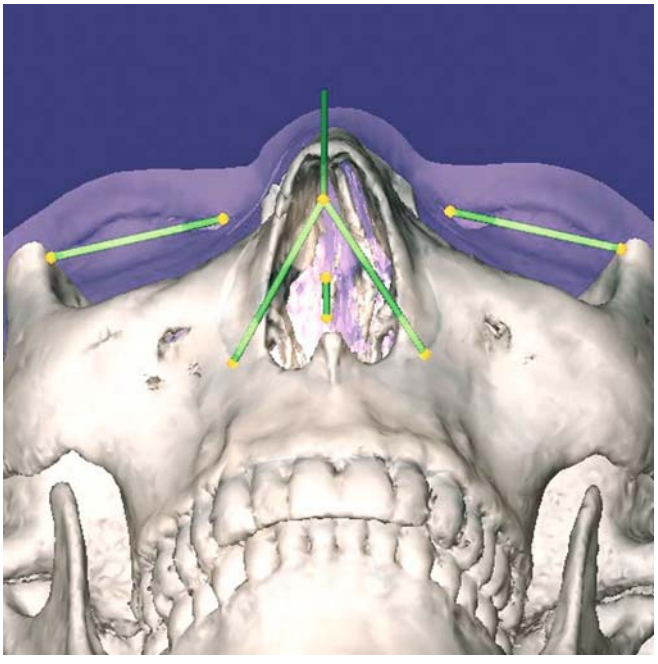

Fig. 7.78. Set-up of 3-D soft tissue distances (3-D CT, hard and transparent soft tissues, patient K.C.)

7.2.3 Angular Soft Tissue Analysis

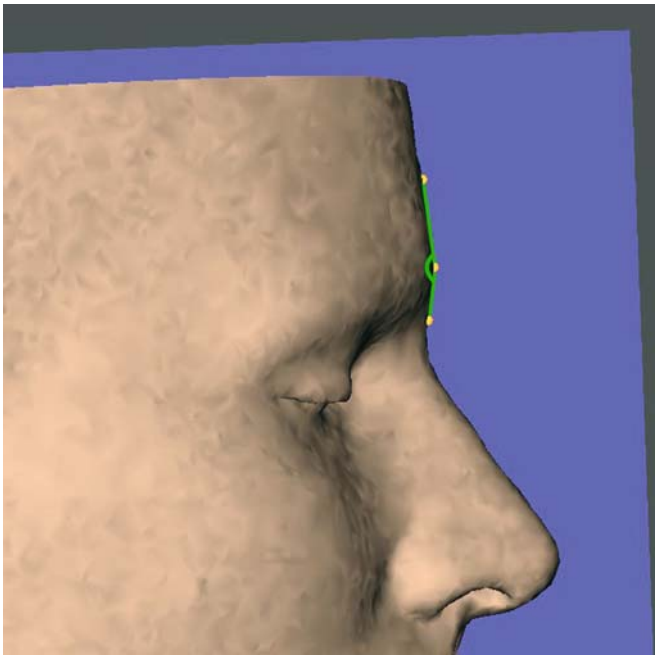

Fig. 7.79. The glabellonasal angle, g'-g-n, is a projected angular soft tissue measurement on the median (*z*) 3-D cephalometric reference plane. glabella' (g') localized on the midline tangent of the frontal contour cranial to glabella (g) is used to determine the glabellonasal angle (3-D CT, soft tissues, patient K.C.)

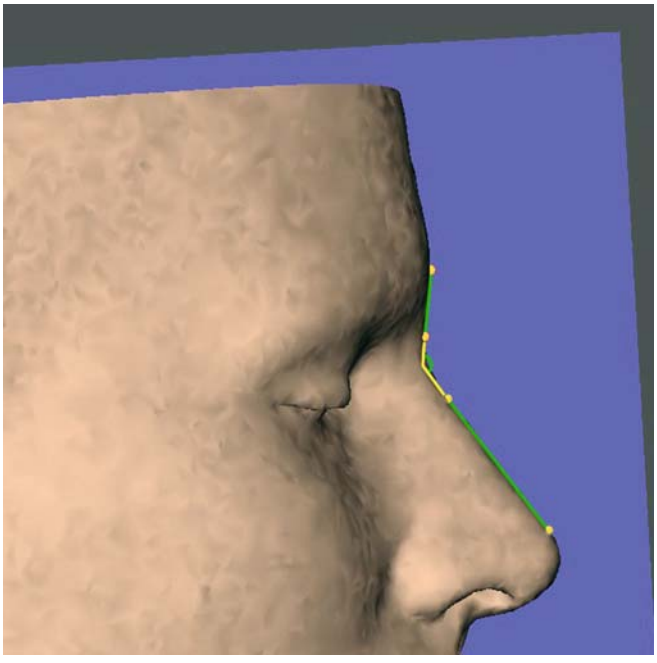

Fig. 7.80. The nasofrontal angle, g-se / nasal root tangent, is a projected angular soft tissue measurement on the median (*z*) 3-D cephalometric reference plane. The nasal root tangent is defined by a proximal and distal point on the midline of the nasal root (3-D CT, soft tissues, patient K.C.)

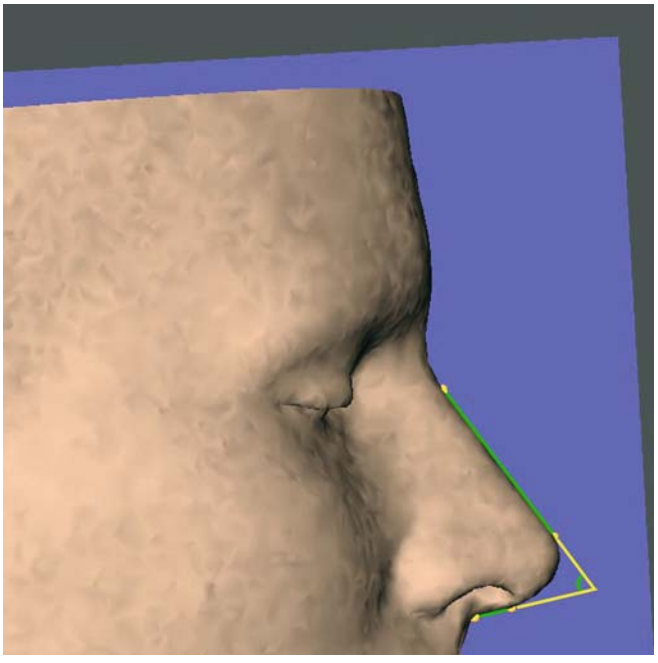

Fig. 7.81. The nasal tip angle or Joseph's septodorsal angle, nasal root tangent / c''-sn, is a projected angular soft tissue measurement on the median (*z*) 3-D cephalometric reference plane (3-D CT, soft tissues, patient K.C.)

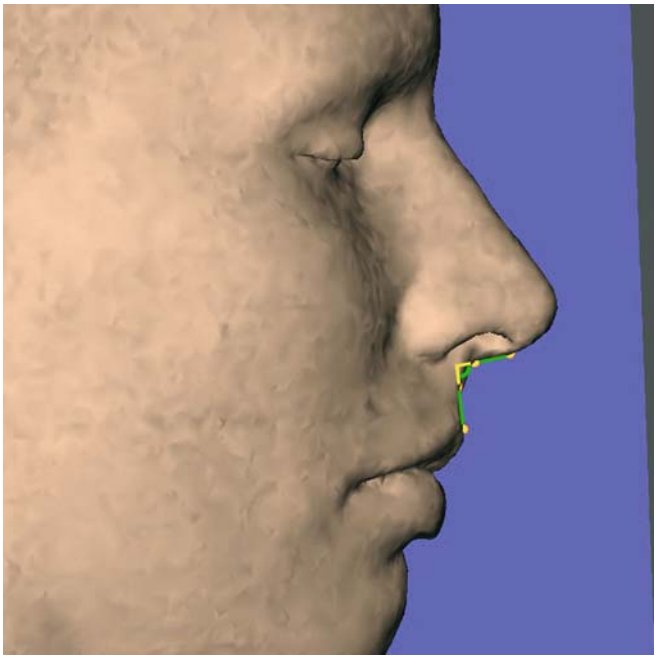

Fig. 7.82. The nasolabial angle, septolabial, columella-labial or labial-columellar angle, c''-sn-ss-ls, is a projected angular soft tissue measurement on the median (*z*) 3-D cephalometric reference plane (3-D CT, soft tissues, patient K.C.)

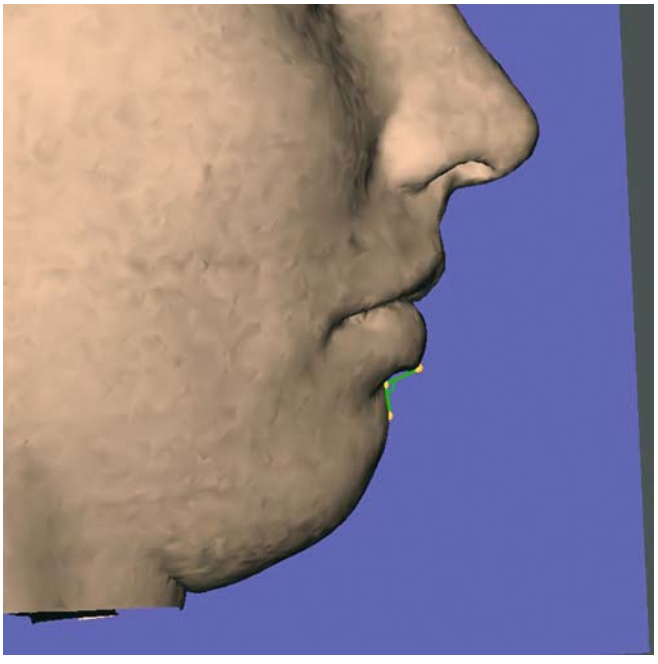

Fig. 7.83. The labiomental angle, li-sl-pg, is a projected angular soft tissue measurement on the median (*z*) 3-D cephalometric reference plane (3-D CT, soft tissues, patient K.C.)

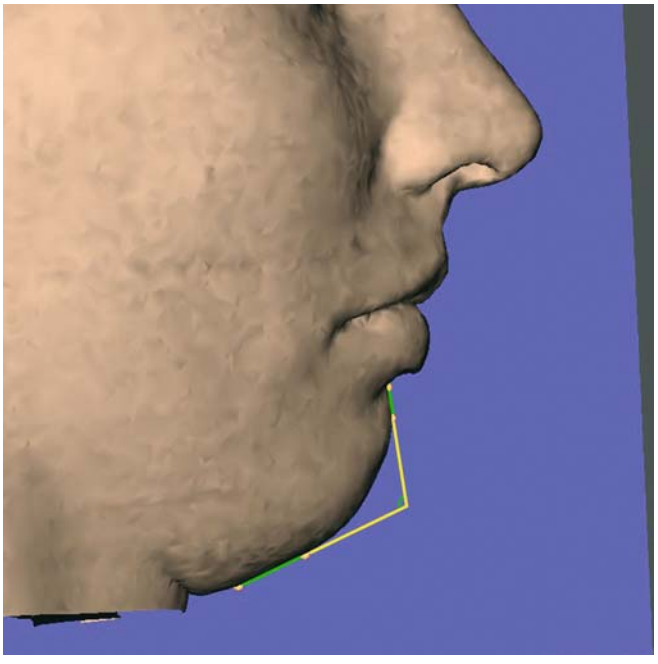

Fig. 7.84. The mentocervical angle, sl-pg / gn-gn', is a projected angular soft tissue measurement on the median (*z*) 3-D cephalometric reference plane. The landmark gnathion' (gn') localized on the midline tangent of the chin contour posterior to gnathion (gn), is used to determine the mentocervical angle (3-D CT, soft tissues, patient K.C.)

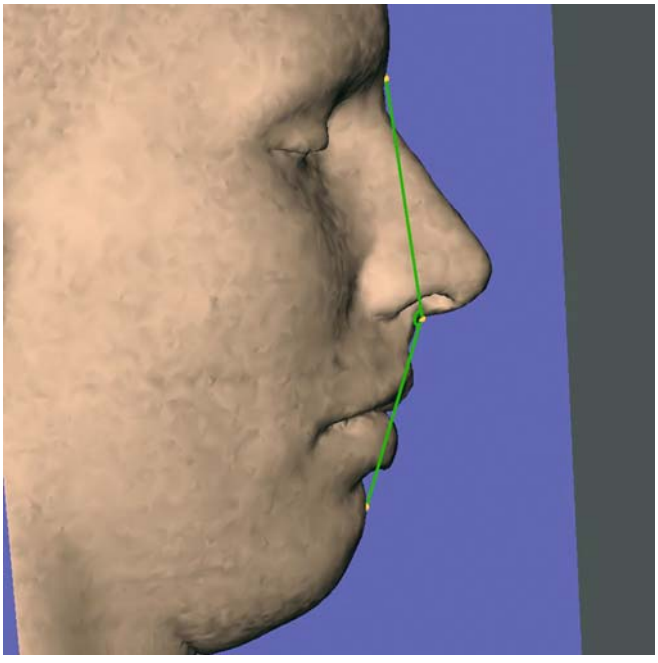

Fig. 7.85. The soft tissue convexity angle, n-sn-pg, is a projected angular soft tissue measurement on the median (*z*) 3-D cephalometric reference plane (3-D CT, soft tissues, patient K.C.)

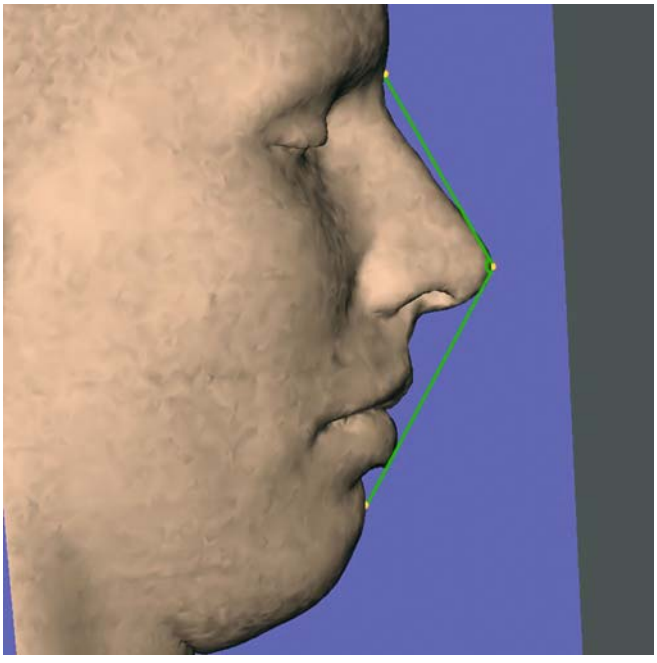

Fig. 7.86. The full soft tissue convexity angle, n-prn-pg, is a projected angular soft tissue measurement on the median (*z*) 3-D cephalometric reference plane (3-D CT, soft tissues, patient K.C.)

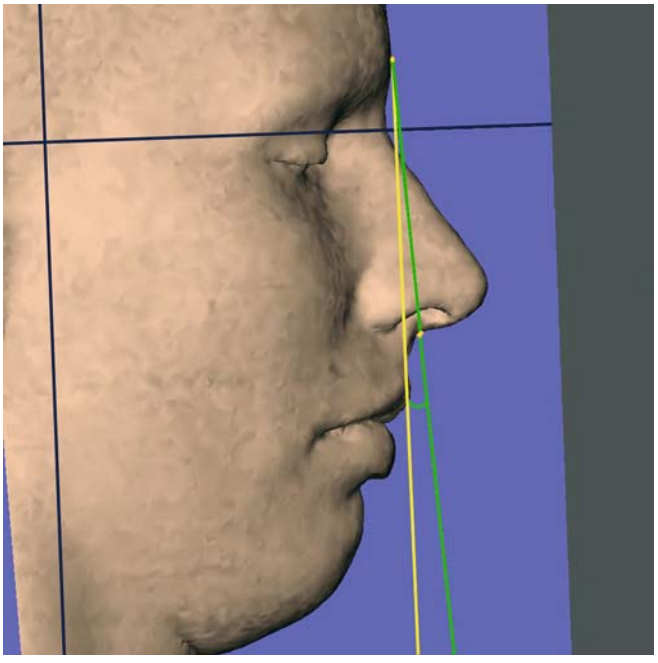

Fig. 7.87. The inclination of the upper face profile from the vertical plane, g-sn / *y*-plane, is a projected angular soft tissue measurement on the median (*z*) 3-D cephalometric reference plane (3-D CT, soft tissues, patient K.C.)

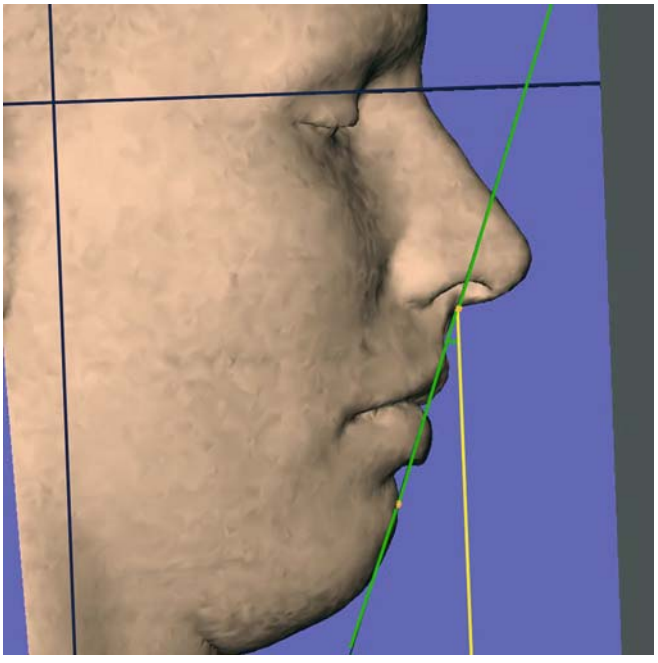

Fig. 7.88. The inclination of the lower face profile from the vertical plane, sn-pg / *y*-plane, is a projected angular soft tissue measurement on the median (*z*) 3-D cephalometric reference plane (3-D CT, soft tissues, patient K.C.)

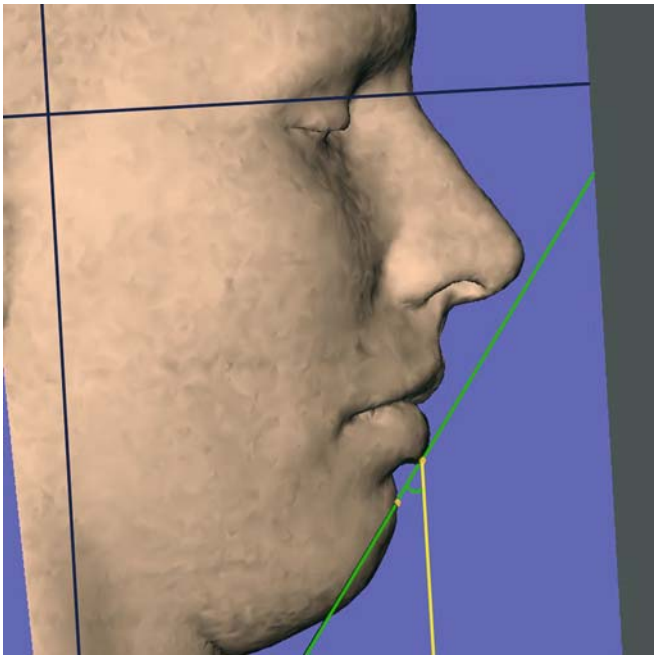

Fig. 7.89. The inclination of the mandible from the vertical plane, li-pg / *y*-plane, is a projected angular soft tissue measurement on the median (*z*) 3-D cephalometric reference plane (3-D CT, soft tissues, patient K.C.)

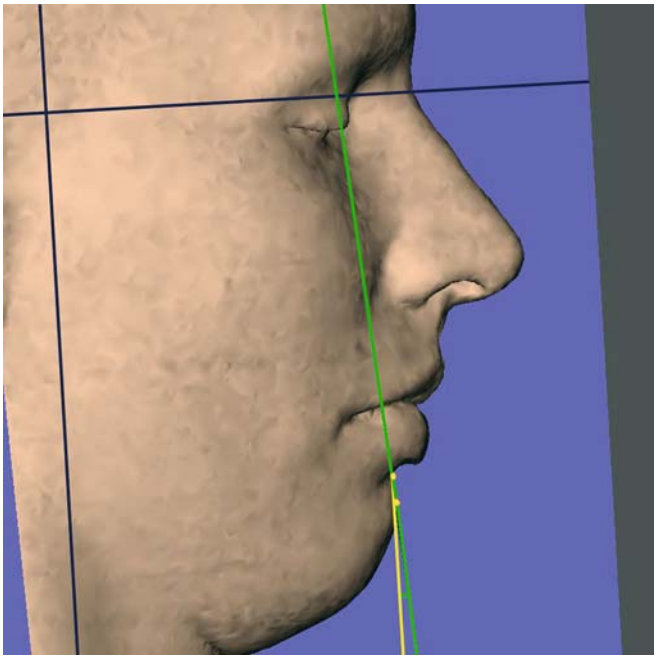

Fig. 7.90. The inclination of the chin from the vertical plane, sl-pg / *y*-plane, is a projected angular soft tissue measurement on the median (*z*) 3-D cephalometric reference plane (3-D CT, soft tissues, patient K.C.)

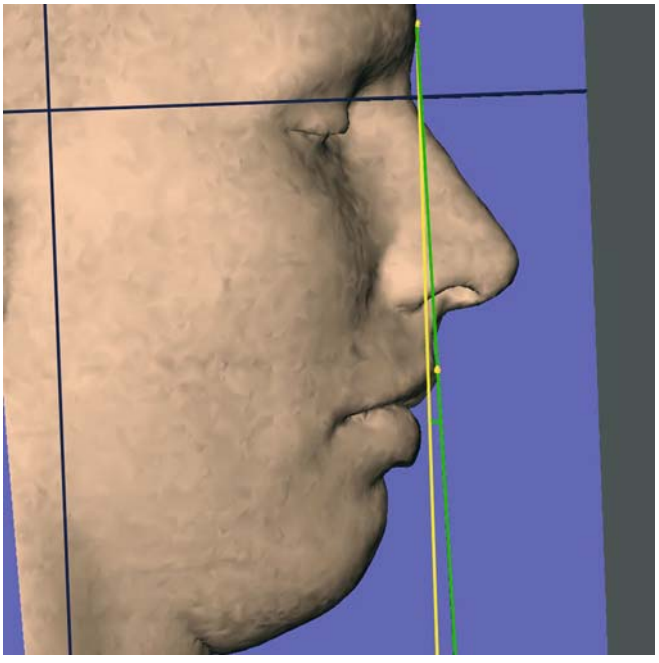

Fig. 7.91. The inclination of the Leiber line from the vertical plane, g-ls / *y*-plane, is a projected angular soft tissue measurement on the median (*z*) 3-D cephalometric reference plane (3-D CT, soft tissues, patient K.C.)

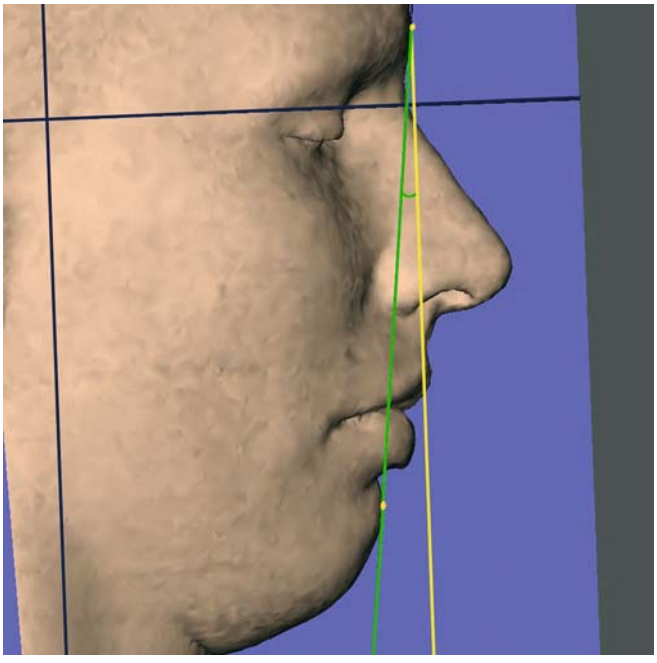

Fig. 7.92. The inclination of the general profile line from the vertical plane, g-pg / *y*-plane, is a projected angular soft tissue measurement on the median (*z*) 3-D cephalometric reference plane (3-D CT, soft tissues, patient K.C.)

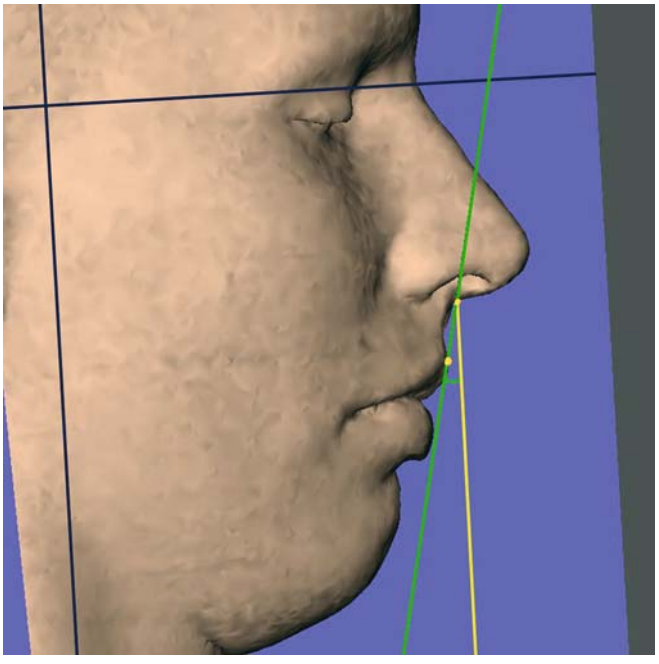

Fig. 7.93. The inclination of the upper lip from the vertical plane, sn-ls / *y*-plane, is a projected angular soft tissue measurement on the median (*z*) 3-D cephalometric reference plane (3-D CT, soft tissues, patient K.C.)

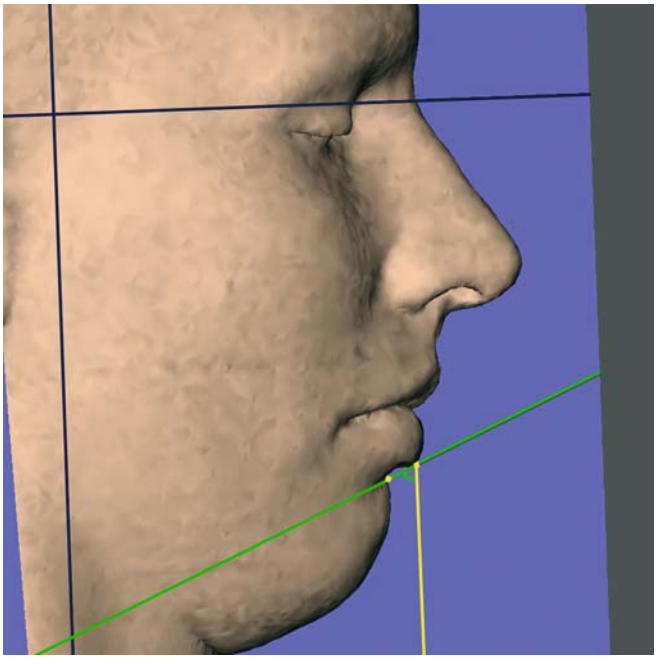

Fig. 7.94. The inclination of the lower lip from the vertical plane, li-sl / *y*-plane, is a projected angular soft tissue measurement on the median (*z*) 3-D cephalometric reference plane (3-D CT, soft tissues, patient K.C.)

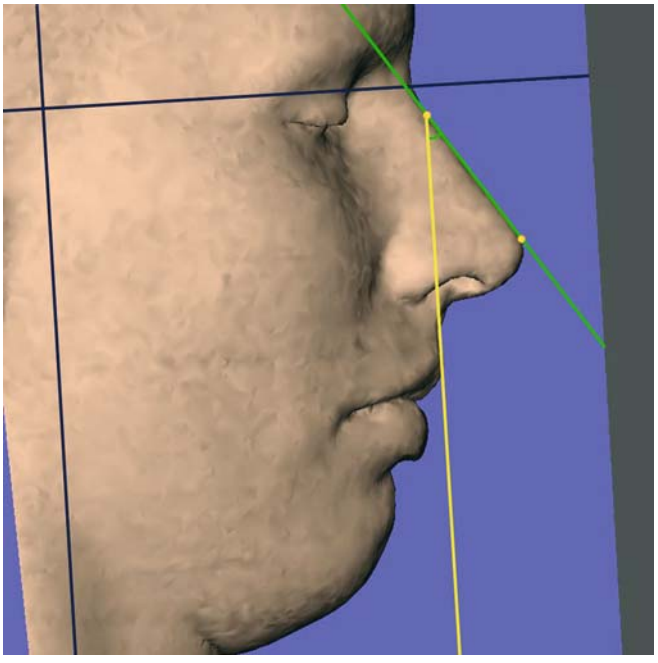

Fig. 7.95. The inclination of the nasal bridge from the vertical plane, nasal root tangent / *y*-plane, is a projected angular soft tissue measurement on the median (*z*) 3-D cephalometric reference plane (3-D CT, soft tissues, patient K.C.)

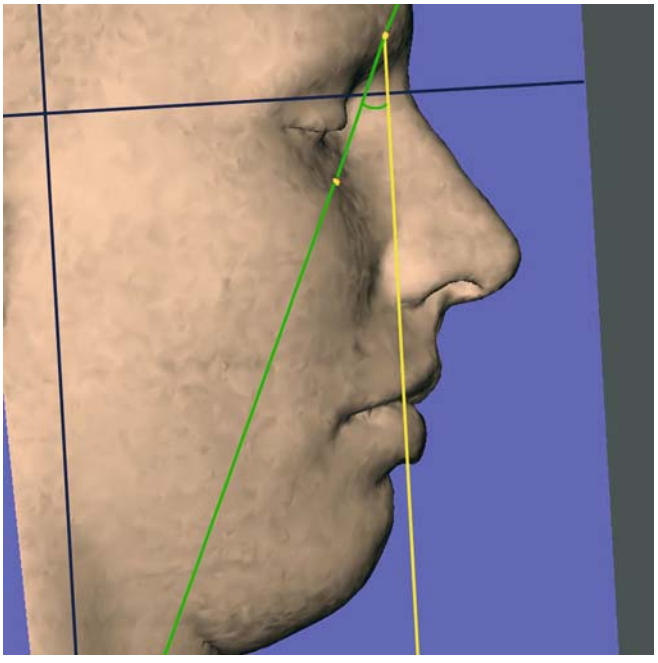

Fig. 7.96. The inclination of the right orbital rim line from the vertical plane, os_r-or_r / *y*-plane, is a projected angular soft tissue measurement on the median (*z*) 3-D cephalometric reference plane (3-D CT, soft tissues, patient K.C.)

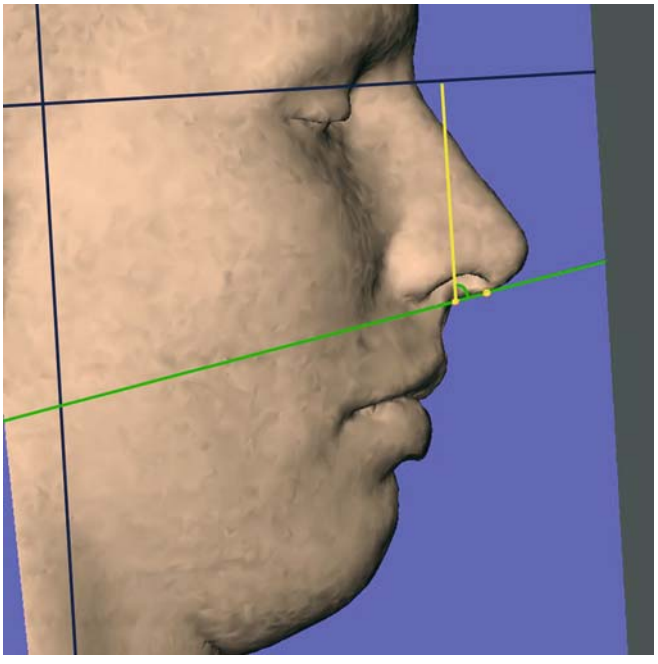

Fig. 7.97. The inclination of the columella from the vertical plane, sn-c" / *y*-plane, is a projected angular soft tissue measurement on the median (*z*) 3-D cephalometric reference plane (3-D CT, soft tissues, patient K.C.)

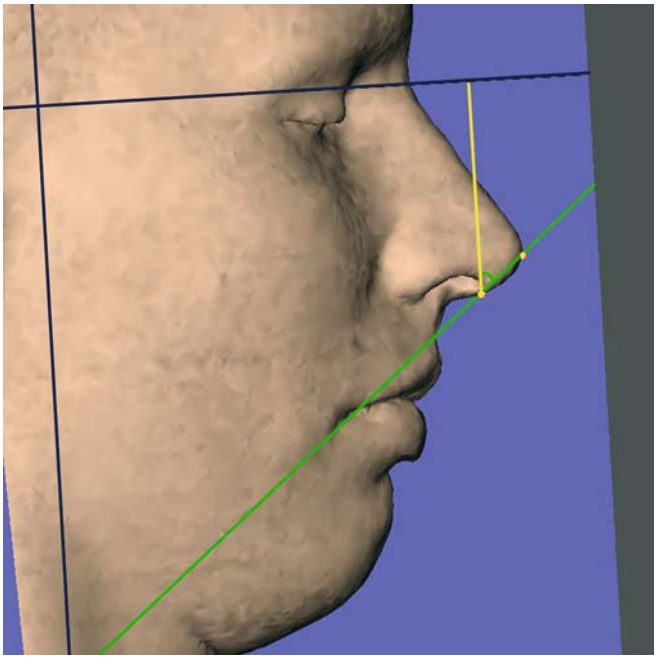

Fig. 7.98. The inclination of the nasal tip from the vertical plane, c"-prn / *y*-plane, is a projected angular soft tissue measurement on the median (*z*) 3-D cephalometric reference plane (3-D CT, soft tissues, patient K.C.)

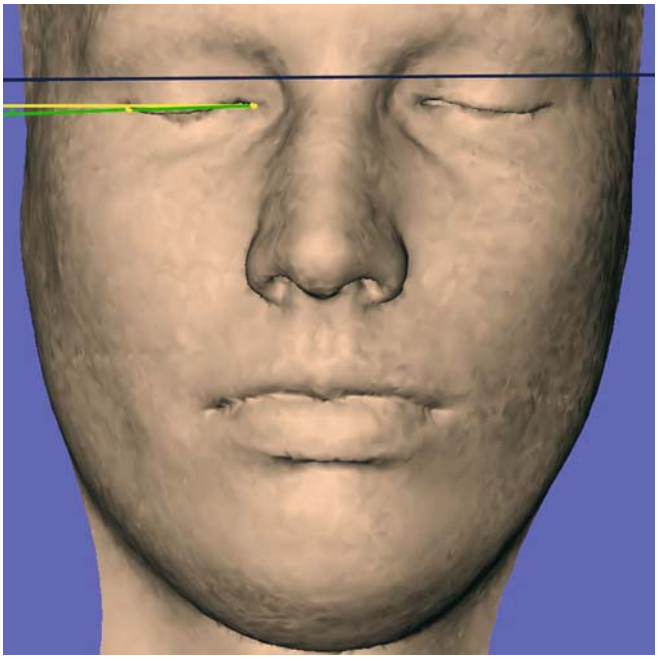

Fig. 7.99. The inclination of the right eye-fissure from the horizontal plane, ex_r-en_r / *x*-plane, is a projected angular soft tissue measurement on the vertical (*y*) 3-D cephalometric reference plane (3-D CT, soft tissues, patient K.C.)

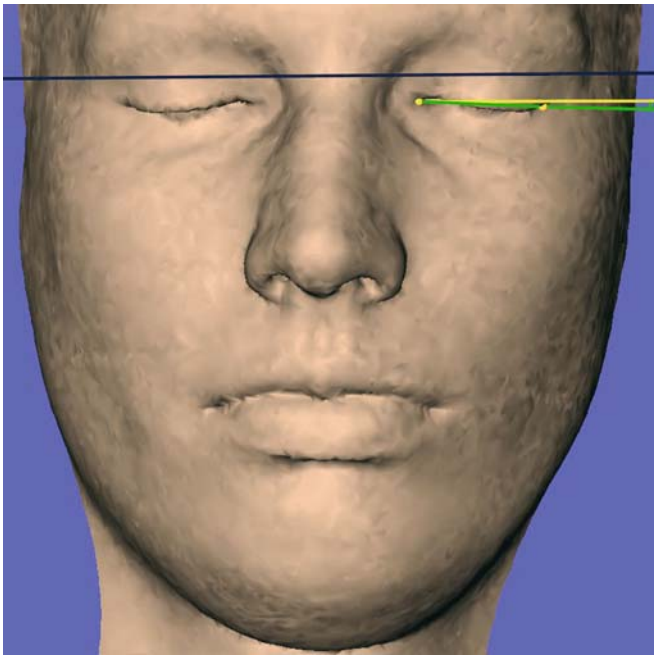

Fig. 7.100. The inclination of the left eye-fissure from the horizontal plane, ex_l-en_l / *x*-plane, is a projected angular soft tissue measurement on the vertical (*y*) 3-D cephalometric reference plane (3-D CT, soft tissues, patient K.C.)

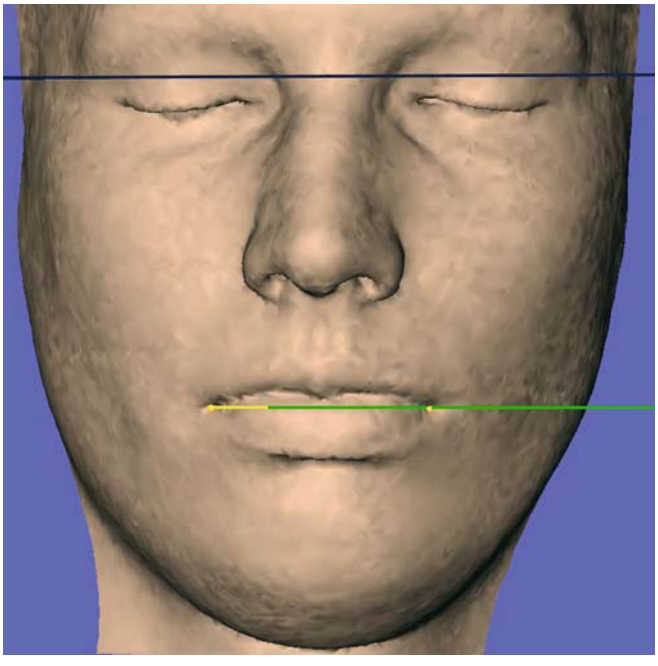

Fig. 7.101. The inclination of the labial fissure from the horizontal plane, ch_r-ch_l/ *x*-plane, is a projected angular soft tissue measurement on the vertical (*y*) 3-D cephalometric reference plane (3-D CT, soft tissues, patient K.C.). Note that in this particular case the inclination of the labial fissure from the horizontal plane is 0°

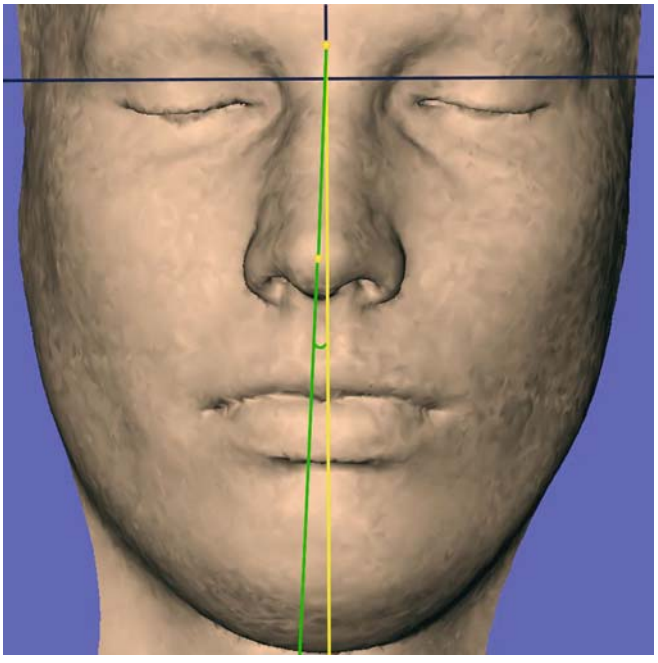

Fig. 7.102. The deviation of the nasal bridge from the median plane n-prn / *z*-plane, is a projected angular soft tissue measurement on the vertical (*y*) 3-D cephalometric reference plane (3-D CT, soft tissues, patient K.C.)

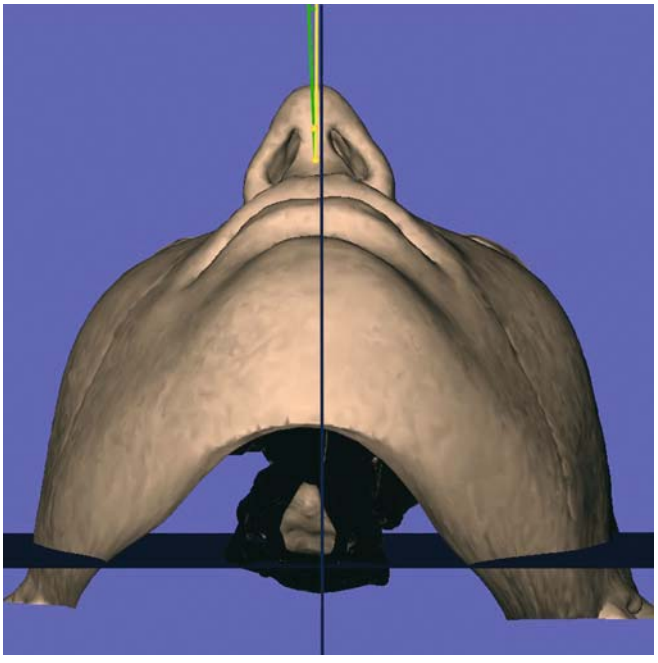

Fig. 7.103. The deviation of the columella from the median plane, sn-c″ / *z*-plane, is a projected angular soft tissue measurement on the horizontal (*x*) 3-D cephalometric reference plane (3-D CT, soft tissues, patient K.C.)

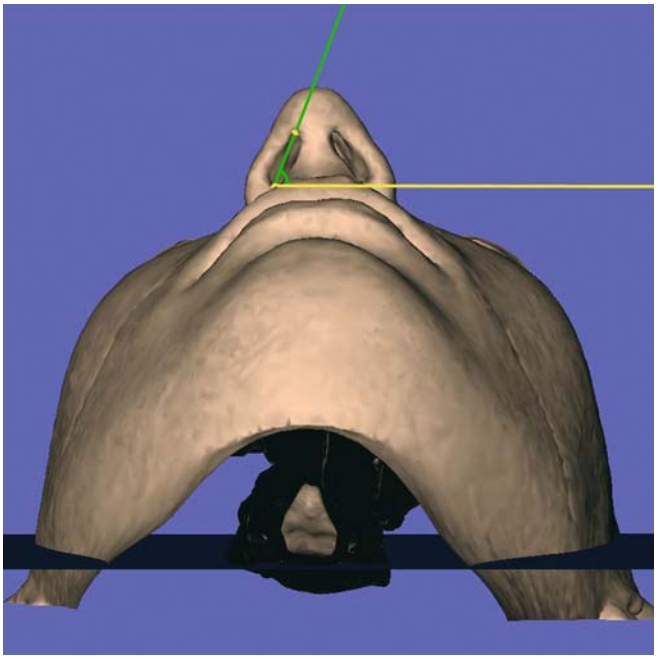

Fig. 7.104. The right nostril inclination nb_r-nt_r / *y*-plane, is a projected angular soft tissue measurement on the horizontal (*x*) 3-D cephalometric reference plane (3-D CT, soft tissues, patient K.C.)

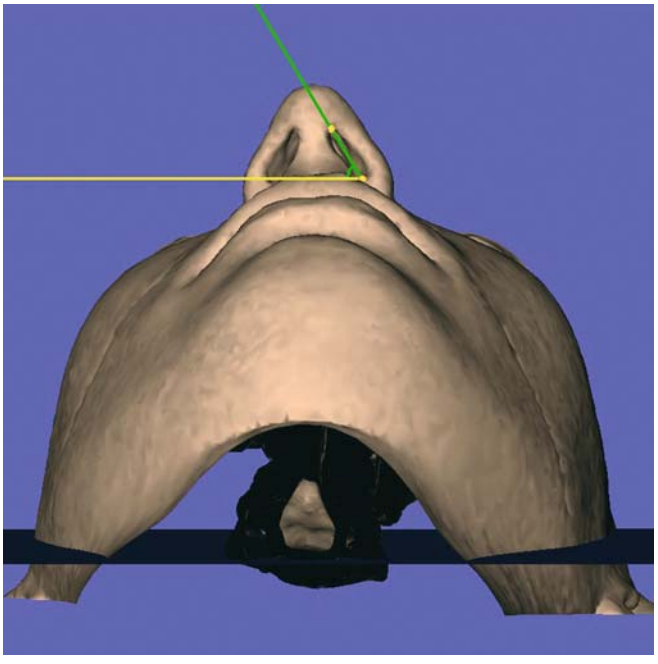

Fig. 7.105. The left nostril inclination nb_l-nt_l / *y*-plane, is a projected angular soft tissue measurement on the horizontal (*x*) 3-D cephalometric reference plane (3-D CT, soft tissues, patient K.C.)

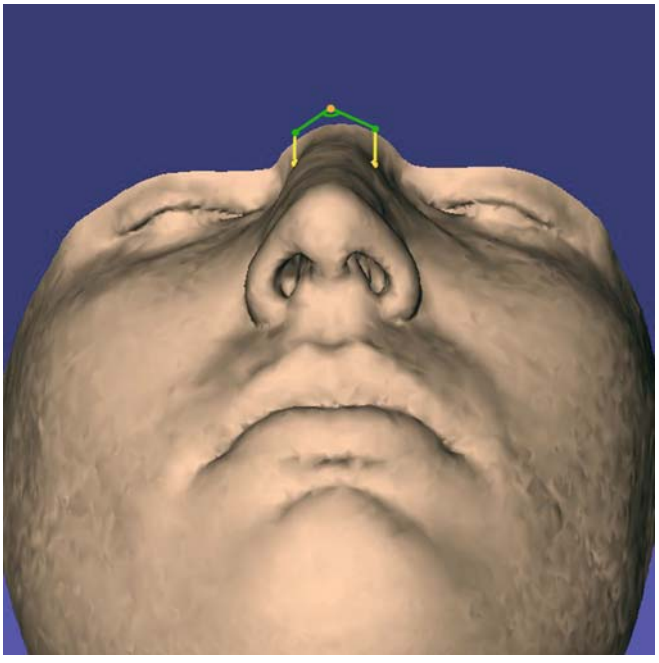

Fig. 7.106. The nasal root slope angle, mf_r-se-mf_l, is a projected angular soft tissue measurement on the horizontal (*x*) 3-D cephalometric reference plane (3-D CT, soft tissues, patient K.C.)

Fig. 7.107. The modified alar slope angle, al_r-prn-al_l, is a projected angular soft tissue measurement on the horizontal (*x*) 3-D cephalometric reference plane (3-D CT, soft tissues, patient K.C.). Note that the alar slope angle according to L.G. Farkas is the angle between the right and left alar slope tangents

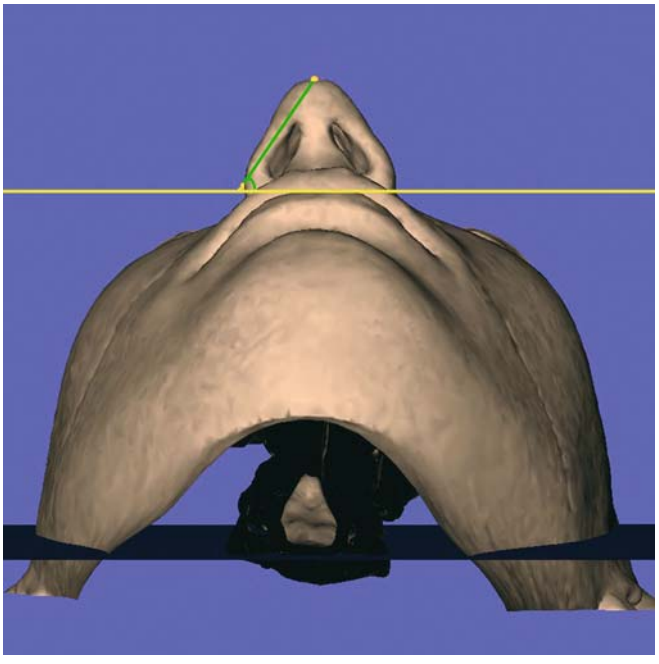

Fig. 7.108. The modified right alar slope inclination, al_r-prn / *y*-plane, is a projected angular soft tissue measurement on the horizontal (*x*) 3-D cephalometric reference plane (3-D CT, soft tissues, patient K.C.)

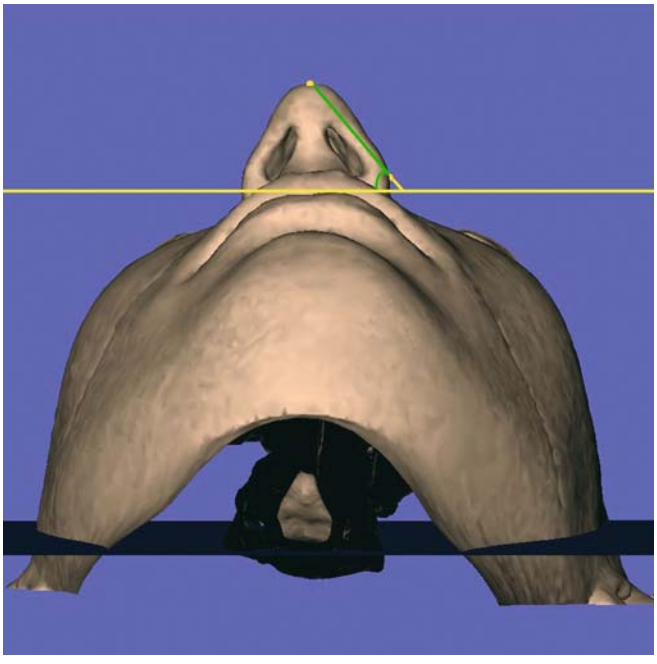

Fig. 7.109. The modified left alar slope inclination, al_l-prn / *y*-plane, is a projected angular soft tissue measurement on the horizontal (*x*) 3-D cephalometric reference plane (3-D CT, soft tissues, patient K.C.)

7.2.4 Orthogonal Arithmetical Soft Tissue Analysis

7.2.4.1 Orthogonal Analysis to the Horizontal (*x*) Plane

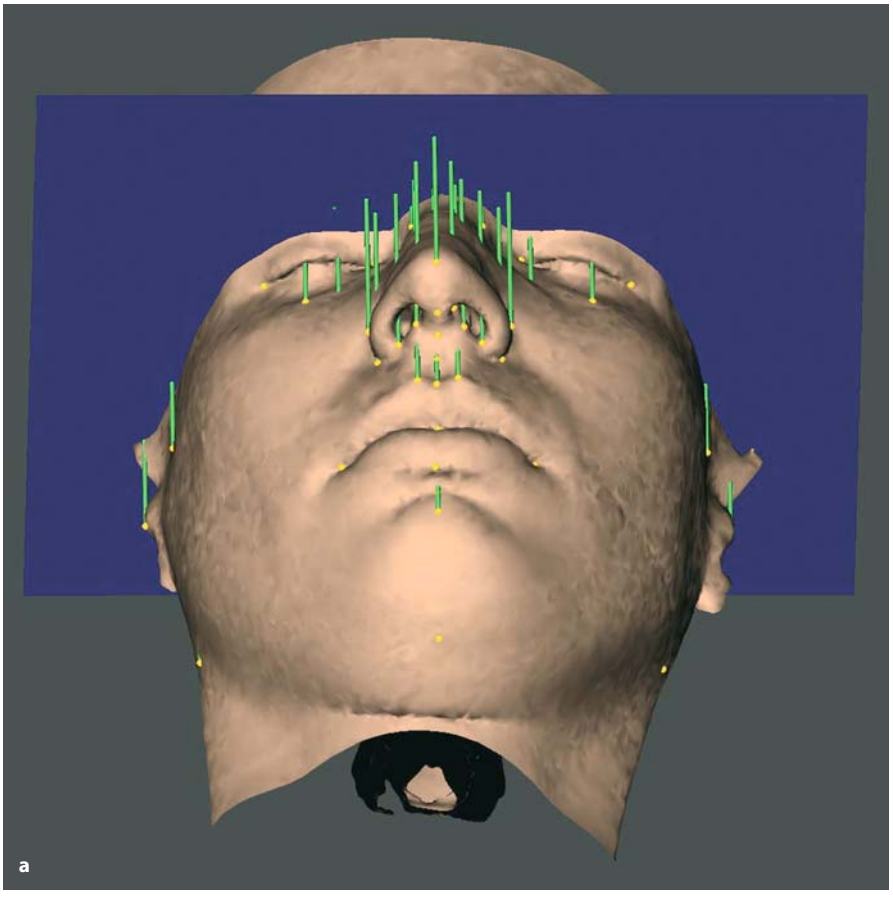

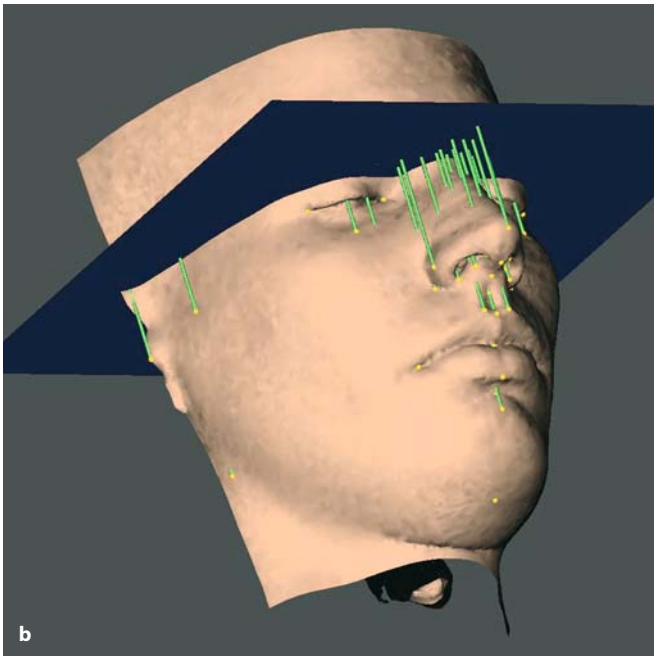

Fig. 110a, b. Set-up of vertical orthogonal soft tissue measurements to the *x*-plane (3-D CT, patient K.C.)

7.2.4.2 Orthogonal Analysis to the Vertical (*y*) Plane

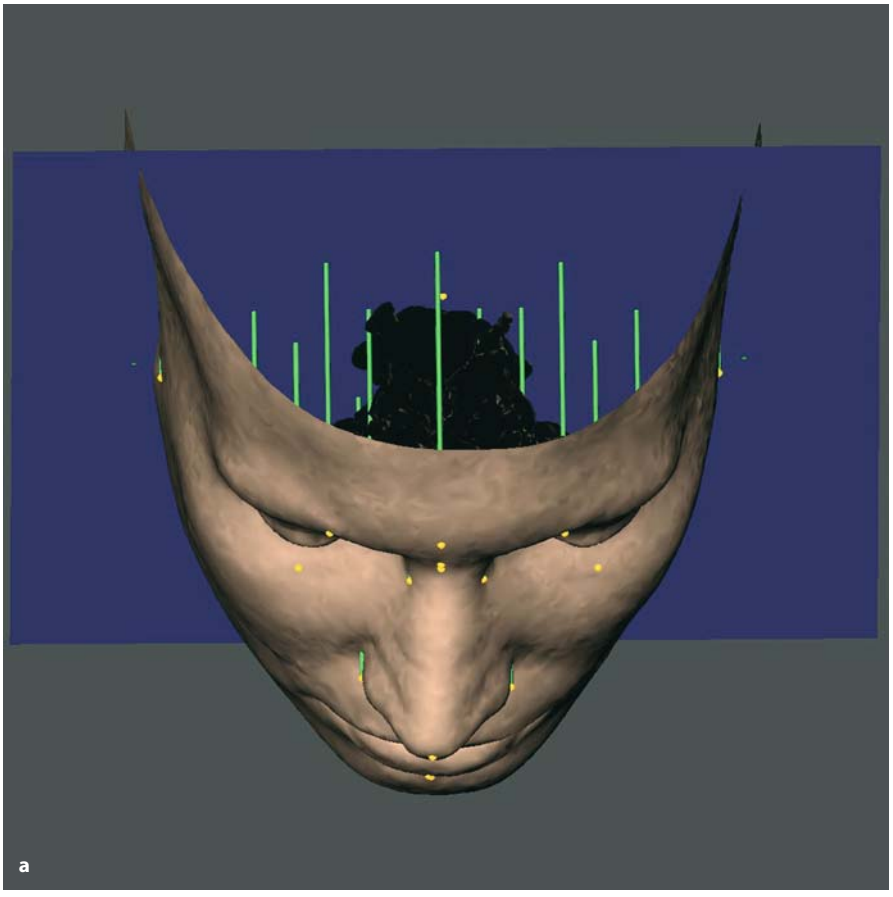

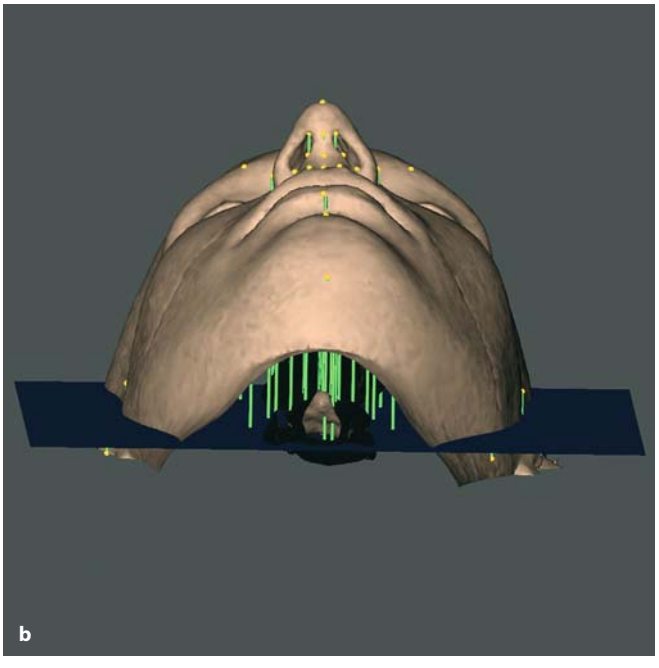

Fig. 7.111 a, b. Set-up of horizontal orthogonal soft tissue measurements to the *y*-plane (3-D CT, patient K.C.)

7.2.4.3 Orthogonal Analysis to the Median (*z*) Plane

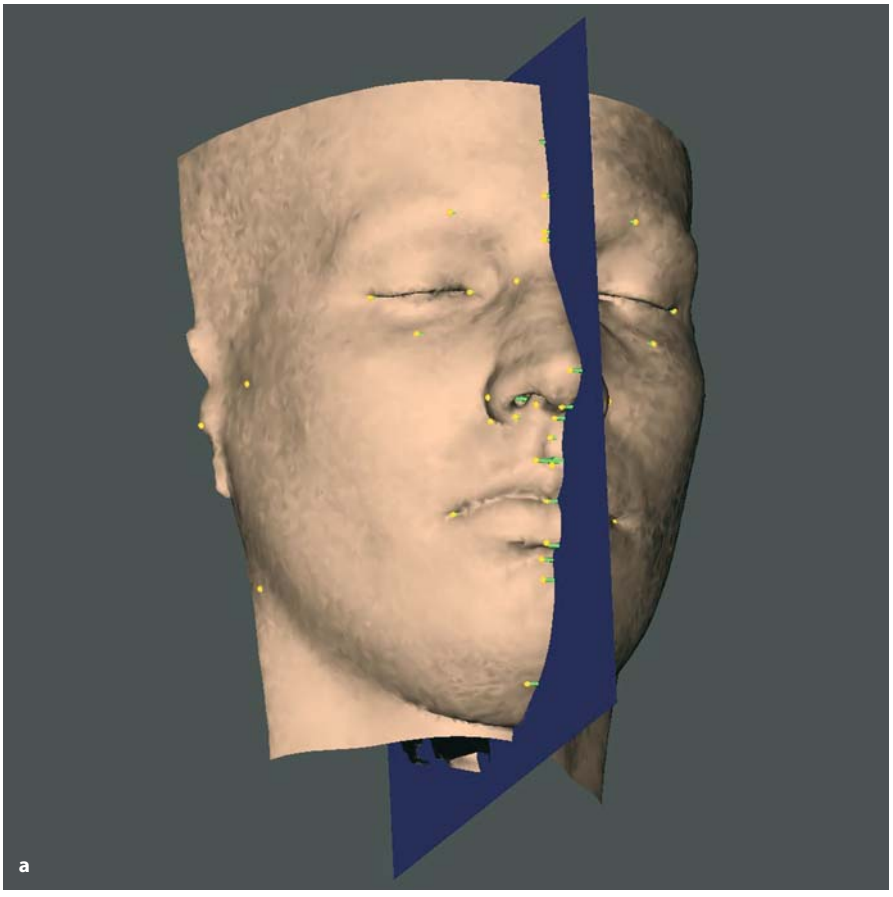

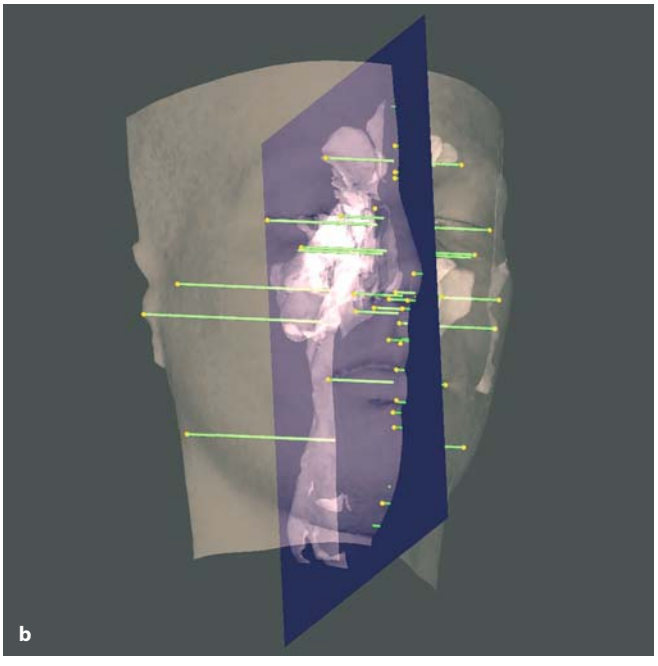

Fig. 7.112. a Set-up of transverse orthogonal soft tissue measurements to the *z*-plane (3-D CT, patient K.C.). **b** Set-up of transverse orthogonal soft tissue measurements to the *z*-plane (3-D CT, transparent soft tissues, patient K.C.)

7.2.5 Proportional Correlation Soft Tissue Analysis

$n\text{-}gn \times 100 / zy_r\text{-}zy_l$	Facial index
$sto\text{-}gn \times 100 / go_r\text{-}go_l$	Height of mandible / lower face width index
$n\text{-}sto \times 100 / n\text{-}gn$	Height of upper face / morphological height of face index
$sto\text{-}gn \times 100 / n\text{-}gn$	Height of mandible / morphological height of face index
$go_r\text{-}go_l \times 100 / zy_r\text{-}zy_l$	Lower face width / upper face width index
$t_r\text{-}sn \times 100 / t_r\text{-}gn$	Depth of middle / lower third of face (right) index
$t_l\text{-}sn \times 100 / t_l\text{-}gn$	Depth of middle / lower third of face (left) index
$en_r\text{-}en_l \times 100 / ex_r\text{-}ex_l$	Intercanthal index
$al_r\text{-}al_l \times 100 / n\text{-}sn$	Nasal index
$sn\text{-}prn \times 100 / al_r\text{-}al_l$	Nasal tip protrusion index
$n\text{-}sn \times 100 / n\text{-}gn$	Height of nose / morphological height of face index
$al_r\text{-}al_l \times 100 / zy_r\text{-}zy_l$	Width of nose / upper face width index
$sn\text{-}sto \times 100 / ch_r\text{-}ch_l$	Upper lip height / mouth width index
$sto\text{-}sl \times 100 / sn\text{-}sto$	Lower / upper lip height index
$sn\text{-}ls \times 100 / sn\text{-}sto$	Upper lip skin portion height / upper lip height index
$ls\text{-}sto \times 100 / sn\text{-}sto$	Upper vermilion height / upper lip height index
$ls\text{-}sto \times 100 / sn\text{-}ls$	Upper vermilion height / upper lip skin portion height index
$ch_r\text{-}ch_l \times 100 / zy_r\text{-}zy_l$	Width of mouth / upper face width index
$n\text{-}sto \times 100 / zy_r\text{-}zy_l$	Upper face index
$al_r\text{-}al_l \times 100 / ch_r\text{-}ch_l$	Width of nose / width of mouth index
$n\text{-}sn \times 100 / n\text{-}sto$	Height of nose / height of upper face index
$sn\text{-}gn \times 100 / n\text{-}gn$	Lower face height index
$sto\text{-}gn \times 100 / n\text{-}sto$	Height of mandible / height of upper face index
$sto\text{-}gn \times 100 / sn\text{-}gn$	Height of mandible / height of lower face index
$ls\text{-}sto \times 100 / sto\text{-}li$	Vermilion height index
$go_r\text{-}go_l \times 100 / n\text{-}gn$	Lower face width / morphological height of face index

7.2.6 Additional 3-D Cephalometric Soft Tissue Measurements

The following list shows some additional anthropometric measurements described by L.G. Farkas that can be used in 3-D soft tissue cephalometry, once the soft tissue landmarks that define these measurements have been validated.

Additional Soft Tissue Widths

eu_r-eu_l	Width of head
pra_r-pa_r	Width of right auricle
pra_l-pa_l	Width of left auricle

Additional Soft Tissue Heights

v-n	Anterior height of head
v-en	Special height of head
v-sn	Height of head and nose according to Knussmann
v-gn	Combined height of head and face
v-po_r	Right auricular height of head
v-po_l	Left auricular height of head
v-t_r	Right distance between vertex and tragion
v-t_l	Left distance between vertex and tragion
sa_r-sba_r	Length of right auricle
sa_l-sba_l	Length of left auricle

Additional Soft Tissue Depths

g-op	Length of head
ex_r-obs_r	Right orbito-aural distance
ex-$_lobs_l$	Left orbito-aural distance
n-obs_r	Right upper naso-aural distance
n-obs_l	Left upper naso-aural distance
n-obi_r	Right lower naso-aural distance
n-obi_l	Left lower naso-aural distance
sn-obs_r	Right upper subnasale-aural distance
sn-obs_l	Left upper subnasale-aural distance
sn-obi_r	Right lower subnasale-aural distance
sn-obi_l	Left lower subnasale-aural distance
gn-obs_r	Right upper gnathion-aural distance
gn-obs_l	Left upper gnathion-aural distance
gn-obi_r	Right lower gnathion-aural distance
gn-obi_l	Left lower gnathion-aural distance
op-po_r	Right occipito-aural distance
op-po_l	Left occipito-aural distance
obs_r-obi_r	Morphological width of right ear
obs_l-obi_l	Morphological width of left ear

Additional Soft Tissue Proportions

$pra_r\text{-}pa_r \times 100 / sa_r\text{-}sba_r$	Right ear index
$pra_l\text{-}pa_l \times 100 / sa_l\text{-}sba_l$	Left ear index
$sa_r\text{-}sba_r \times 100 / n\text{-}gn$	Right ear length / face height index
$sa_l\text{-}sba_l \times 100 / n\text{-}gn$	Left ear length / face height index
$eu_r\text{-}eu_l \times 100 / g\text{-}op$	Cephalic index
$v\text{-}po_r \times 100 / v\text{-}po_l$	Vertex / ear canal level index
$v\text{-}n \times 100 / v\text{-}gn$	Anterior height of head / combined height of head and face index

Other Soft Tissue Measurements

The following anthropometric measurements described by L.G. Farkas currently cannot be used in 3-D cephalometry of soft tissues. These measurements are based on soft tissue landmarks that are improper or impossible to identify in CT-based 3-D cephalometry of soft tissues. Methods registering the natural texture of the face with the 3-D CT skin surface could overcome this problem in the future (Chap. 10).

tr-g	Height of forehead I, according to Knussmann
tr-n	Height of forehead II, between trichion and nasion
ft-ft	Width of forehead
tr-gn	Physiognomic height of face
v-tr	Height of calvarium
tr-prn	Height of upper profile
p-se	Pupil-facial midline distance
ps-pi	Height of eye fissure
or-sci	Combined height of orbit and eyebrow
os-ps	Height of upper lid
p-os	Pupil-upper lid height
pi-or	Height of lower lid
p-or	Pupil-lower lid height
sbal-sn	Width of nostril floor
$sbal_r\text{-}sbal_l$	Width between labial insertions of alar base
tr-g / vertical	Inclination of anterior surface of forehead from vertical

CHAPTER 8 3-D Cephalometry and Craniofacial Growth

Gwen R. J. Swennen

Cephalometric radiography has yielded fundamental knowledge on craniofacial morphogenesis and led to the development of craniofacial growth concepts (e.g. Moss' functional matrix theory, Enlow's counterpart theory, Delaire's architectural craniofacial analysis). Huge amounts of cephalometric data have been collected, and cephalometric reference data have been developed by different research groups (e.g. Bolton standards of dentofacial developmental growth, cephalometric standards by Riolo and co-workers).

Craniofacial growth and development is a composite result of different fundamental growth processes that take place simultaneously in different regional developmental fields. Each of these has its proper amount and direction of growth which determine its growth vector. According to Enlow's counterpart theory, three principal craniofacial growing parts exist, each having its proper development timing although they are all interrelated: the neurocranium (brain) and basicranium (cranial base); the airway; and the oral region. The viscerocranium (the face) develops in phylogenetic association with the neurocranium, with the basicranium as a template in between.

Craniofacial growth and development of the viscerocranium and neurocranium are based on two different processes of skeletal movement that are interrelated and occur simultaneously: displacement and remodelling. *Primary displacement* involves a bony displacement away from the other skeletal parts triggered by the traction forces of the expanding functional soft tissue matrix (the so-called carry effect) in order to create space for enlargement and relocation of bones. During primary displacement the moving bone and other skeletal parts are growing simultaneously, while in *secondary displacement* the displacement of a bone is not directly related to its own enlargement. *Remodelling* is a different process that takes place through patterns of deposition and resorption, in an opposite direction to primary displacement. The amount of new bone regeneration by bony deposition is equal to the amount of primary bone displacement. During this complex process, developmental growth rotations and growth compensations (e.g. palatal, mandibular vertical ramus, dento-alveolar) take place as developmental adjustments in order to create balance during craniofacial development.

Although conventional cephalometry has made a huge contribution to the current concepts on craniofacial growth and development, it has the important limitation that it is two-dimensional. The separate effects of craniofacial growth by displacement or by deposition and resorption are not distinguishable. A conventional lateral cephalogram, for example, can show remodelling changes on the anterior and posterior surface of the vertical mandibular ramus but cannot visualize what is happening transversely. This chapter represents an introduction to the potential of 3-D cephalometry for further investigation of craniofacial growth patterns. It aims to illustrate some of the concepts of Enlow's counterpart theory of facial growth. Superimposition of 3-D hard tissue surface representations and serial 3-D cephalometric tracings of a newborn, a 6-year-old and an adult cadaver skull are used to illustrate the composite result of multi-directional growth changes relative to the 3-D cephalometric reference system based on the Sella and Nasion landmarks (Chap. 3). It is important to keep in mind that, according to Enlow, superimposition of cephalometric tracings is appropriate and valid, as long as one is aware that the cranial base also undergoes remodelling during craniofacial growth and that therefore cranial base-related landmarks such as Sella and Nasion are not absolutely fixed.

8.1 The Basicranium as a Template for Facial Growth

Human craniofacial growth and development is basically not different from that in other mammalian species. In mammals the neurocranium (brain) determines in a phylogenetic relationship the development and growth of the viscerocranium (face), with the basicranium (cranial base) as a template in between. The enormous expansion of the human brain led to expansion (Fig. 8.1) and bending (so-called basicranial flexure; Fig. 8.2) of the basicranium. This process resulted in an inferior and posterior rotation of the human face with forward rotation of the orbits. Therefore, the architectonic morphologic plan of the human face is wide and vertically flattened, in contrast to the narrow and long viscerocranium of phylogenetically lower mammalian species (e.g. sheep; Figs. 8.3, 8.4).

Fig. 8.1. Comparison of the human and sheep basicranium illustrates the enormous enlargement of the human anterior and middle cranial fossa due to expansion of the frontal and temporal cerebral lobes. Endocranial skull base view (3-D CT hard tissue surface representations of adult sheep and human cadaver skulls)

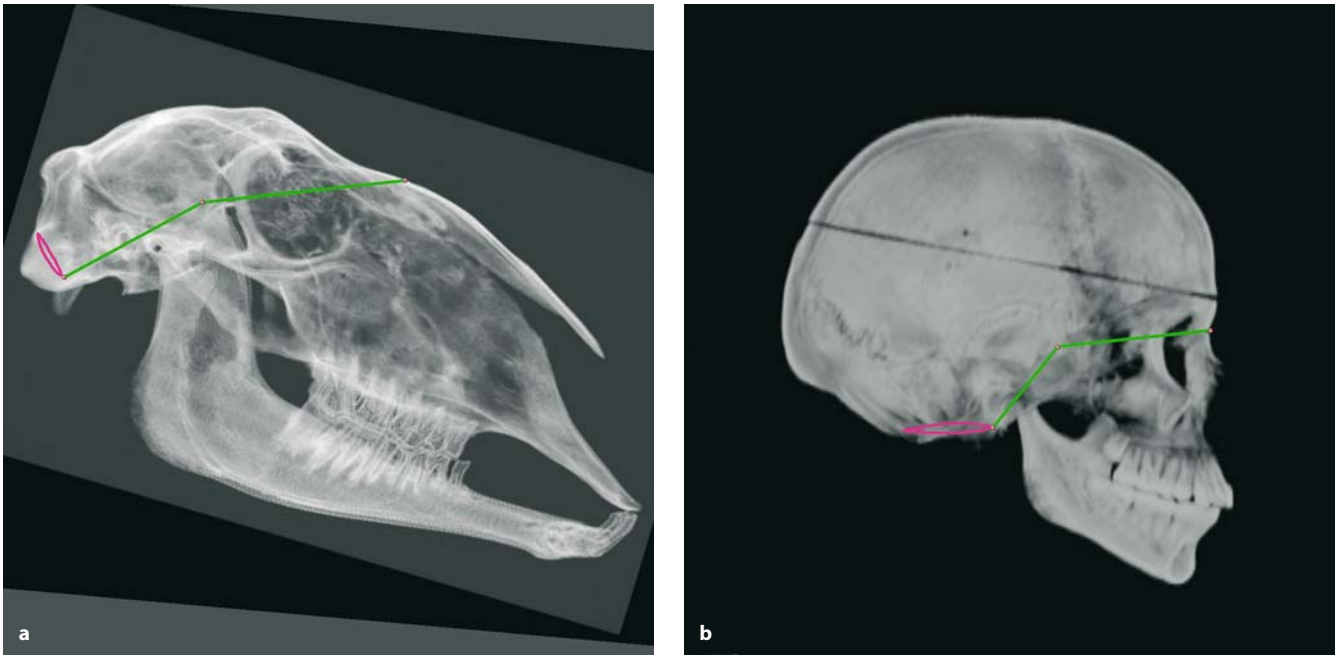

Fig. 8.2 a, b. Virtual lateral cephalograms with superimposed tracing of the cranial base (Basion–Sella–Nasion) show the typical flexure of the human basicranium with relocation of the foramen magnum in order to allow vertical passing of the spinal cord into the vertical directed vertebral column (**b**). In contrast, the basicranium of the sheep skull is flat with the foramen magnum located in the posterior region to allow horizontal passing of the spinal cord into the horizontally directed vertebral column (**a**). (adult sheep and human cadaver skulls)

Fig. 8.3. Comparison of frontal views of a sheep skull and a human skull illustrates the typical wide human face with squared zygomatic bones, a small nasal airway and the developmental horizontal and vertical rotation of the orbits to the midline due to frontal and temporal cerebral lobe expansion. In contrast the sheep has a narrow muzzle with a large nasal space, divergent orbital axes and a large intraorbital distance. (3-D CT hard tissue surface representations of adult sheep and human cadaver skulls)

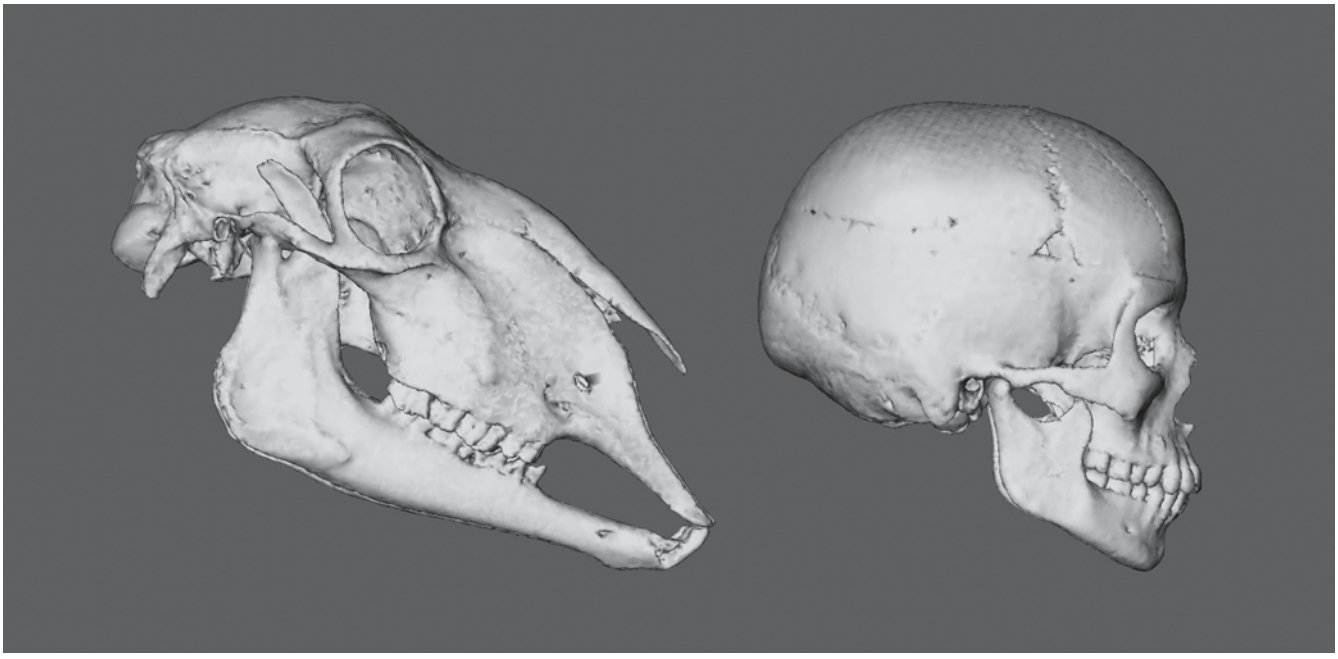

Fig. 8.4. Comparison of left profile views of a sheep skull and a human skull shows the forward remodelling rotation of the upper part of the human face and posterior rotation of the lower part due to the basicranial flexure. The human face is typically vertically flattened with an upright bulbous forehead and presents an anterior and inferior rotation of the orbits due to expansion of the frontal and temporal cerebral lobes. In contrast, the sheep displays a protruding muzzle and divergent orbits in front of the basicranium. (3-D CT hard tissue surface representations of adult sheep and human cadaver skulls)

The basicranium acts as a template for the growth fields in which the nasomaxillary complex, the zygomatic bones and the mandible develop. In infancy the human face appears wide and short due to the wide basicranium and the small mandible (Fig. 8.5). The increase in basicranial flexure (Fig. 8.6) and the expansion of the airway and oral region result in vertical changes, with lowering of the mandible by an increase in vertical mandibular ramus height. Ideally this results in a balanced face, which is proportionate in width and height. If the vertical changes are increased, this process leads to the dolichocephalic head form, with a narrower and longer face (so-called long-face). If, in contrast, the vertical changes are decreased, the result is the brachycephalic head form, with a wider and shorter face (so-called short-face).

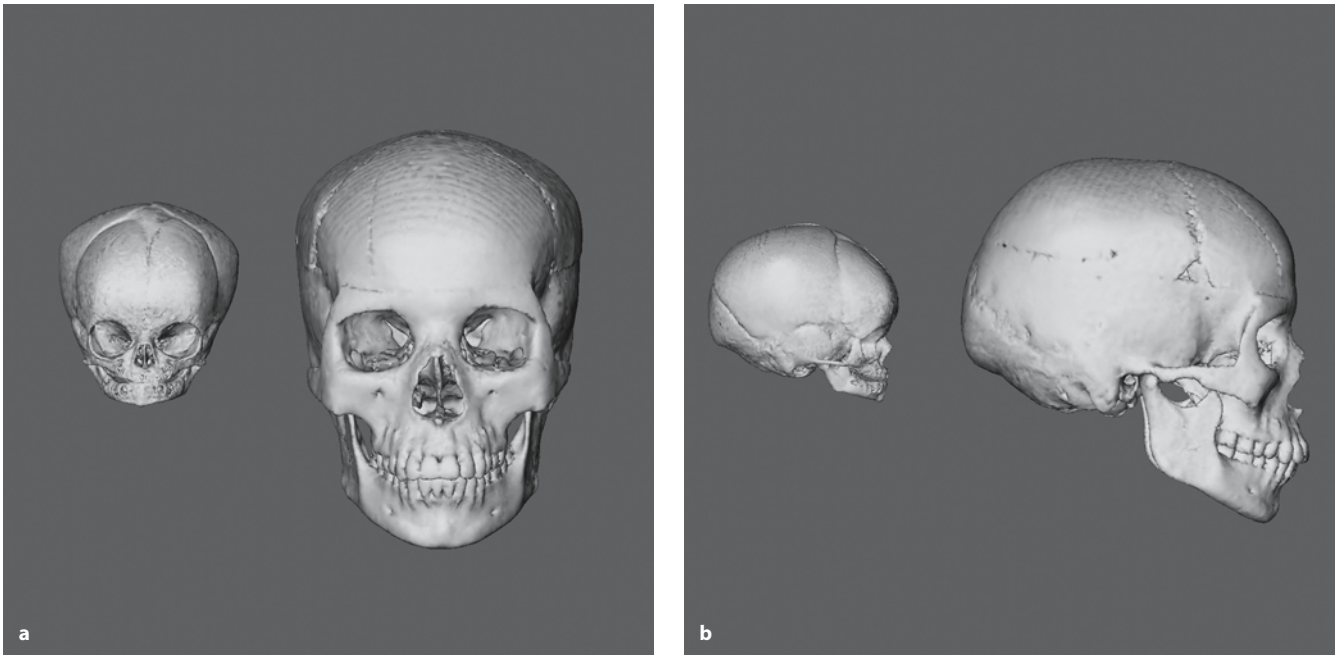

Fig. 8.5. Frontal (**a**) and left profile (**b**) views of a newborn and an adult skull illustrate the typical wide and short face in infancy in contrast to the adult face, which is more proportionate in width and height (3-D CT hard tissue surface representations of newborn and adult human cadaver skulls)

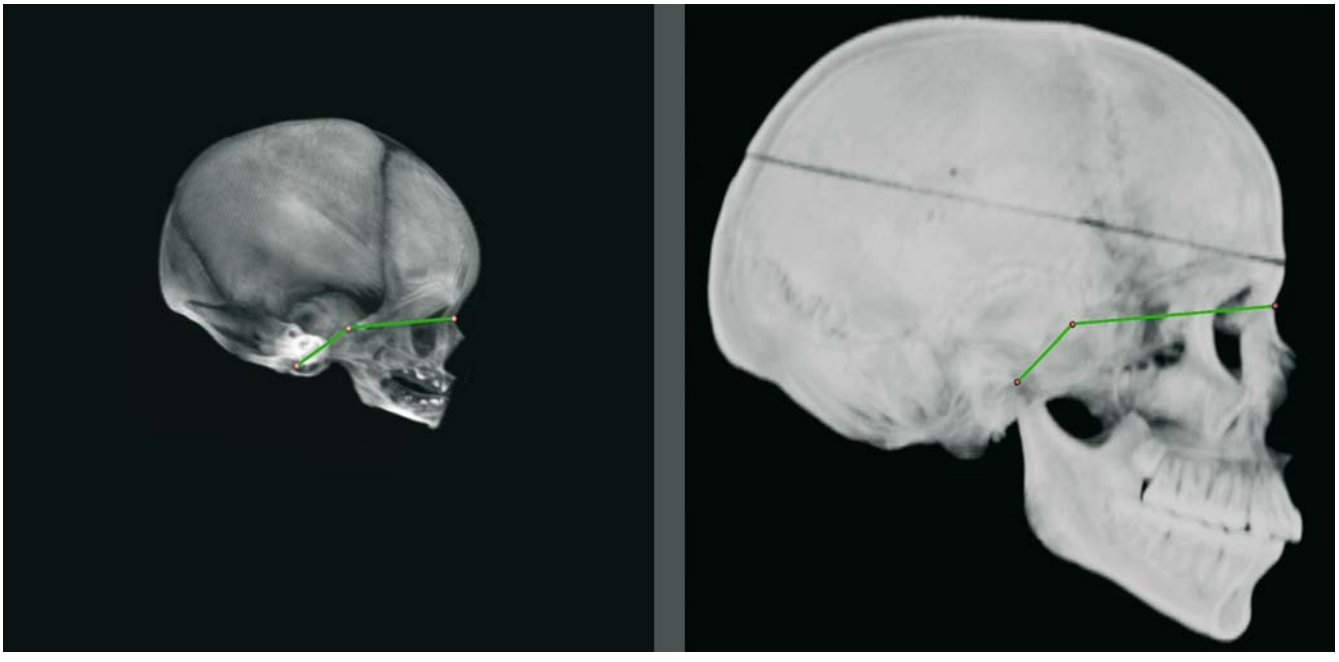

Fig. 8.6. Virtual lateral cephalograms of newborn and adult cadaver skulls with superimposed tracing of the cranial base (Basion–Sella–Nasion) show the increase in basicranial flexure

8.2 Superimposition of Serial 3-D Cephalometric Tracings

The 3-D virtual scene approach allows superimposition of serial 3-D cephalometric tracings and/or 3-D surface representations using the 3-D cephalometric reference system (Chap. 3) as a registration method (Figs. 8.7, 8.8).

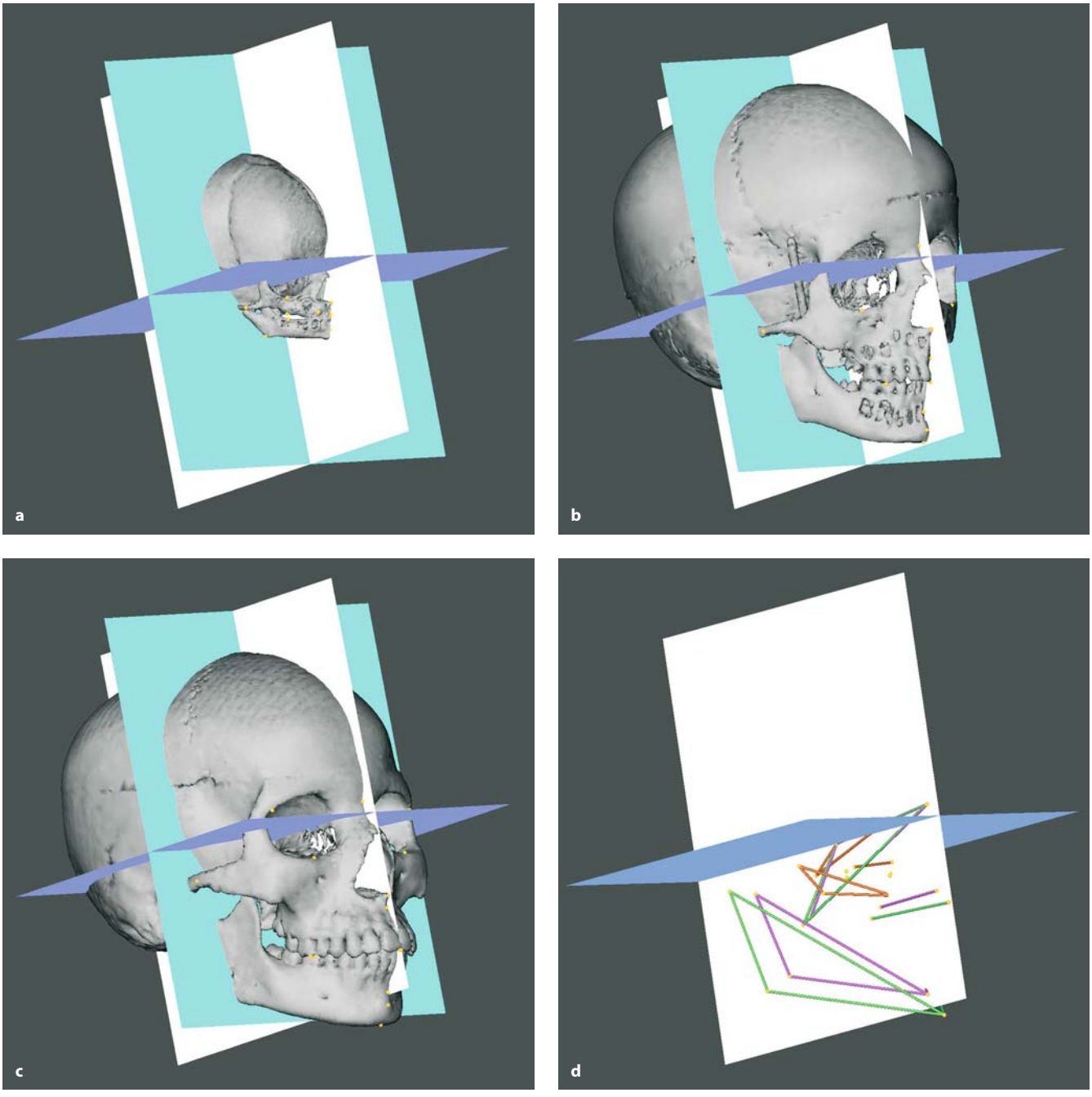

Fig. 8.7. a–c The cadaver skulls of a newborn (**a**), a 6-year-old child (**b**) and an adult (**c**) with overlay of the 3-D cephalometric reference system (*x*, *y*, *z*-plane) (3-D CT hard tissue surface representations). **d** Superimposition of 3-D cephalometric tracings of the newborn, the 6-year-old and the adult cadaver skull on the 3-D cephalometric reference system (the *y*-plane is blended out)

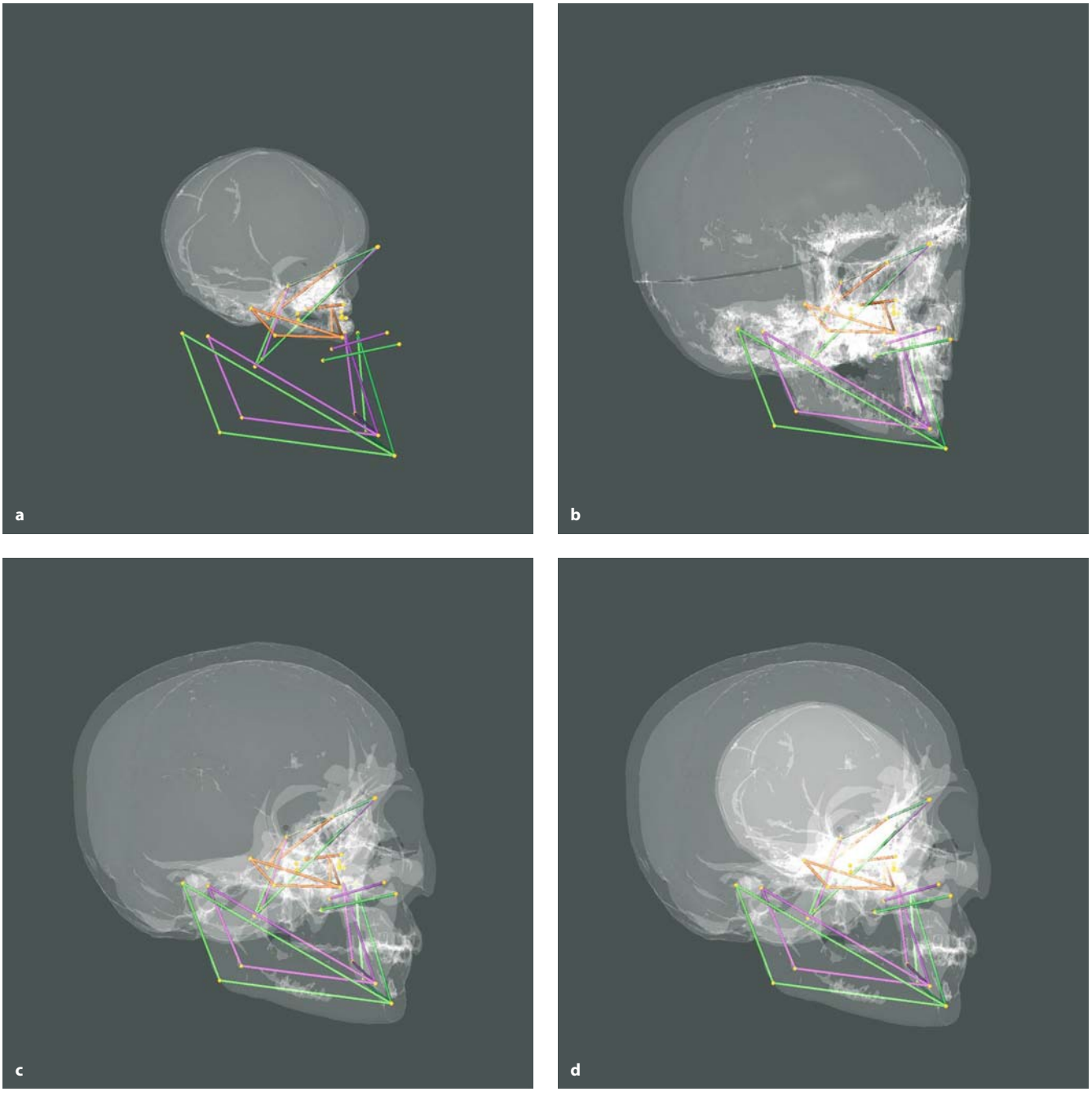

Fig. 8.8. a–c The cadaver skulls of a newborn (**a**), a 6-year-old child (**b**) and an adult (**c**) with superimposition of 3-D cephalometric tracings of the three skulls. **d** Overlay of the three skulls (transparent 3-D CT hard tissue surface representations; registration on the 3-D cephalometric reference system)

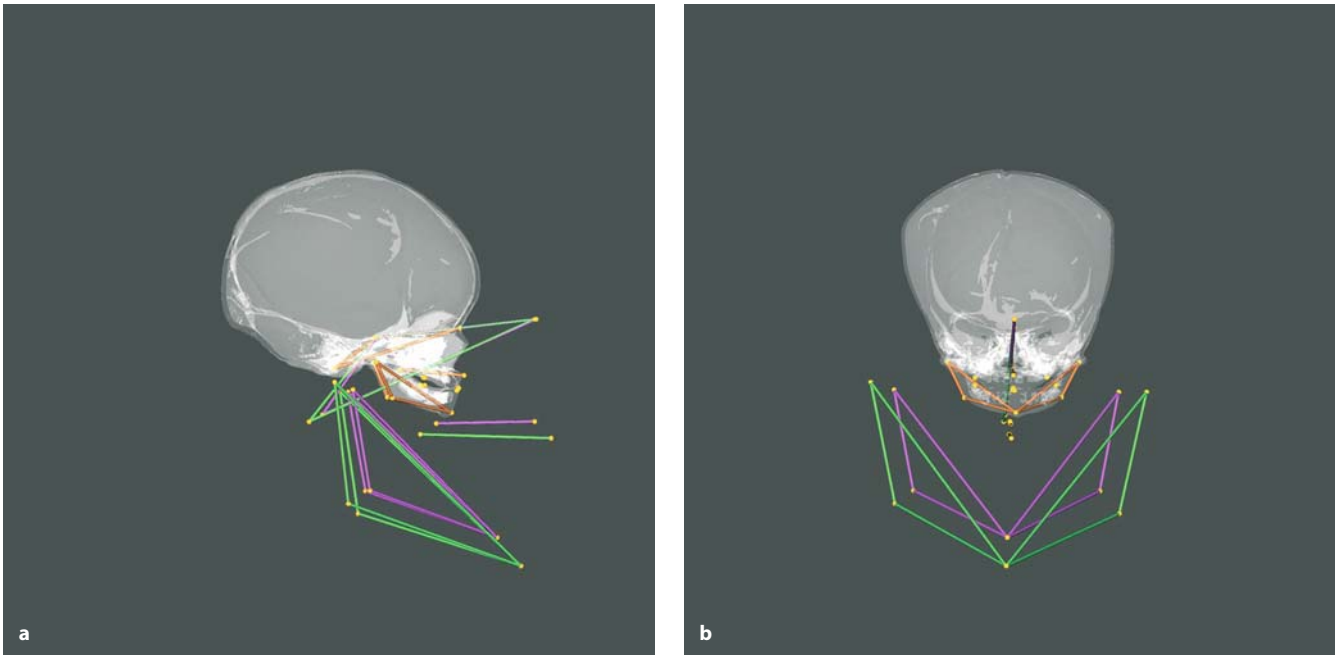

Fig. 8.9 a, b. Left profile (**a**) and frontal (**b**) views of the skull of a newborn with superimposition of 3-D cephalometric tracings of the cadaver skulls of the newborn, a 6-year-old child and an adult (transparent 3-D CT hard tissue surface representations; registration on the 3-D cephalometric reference system)

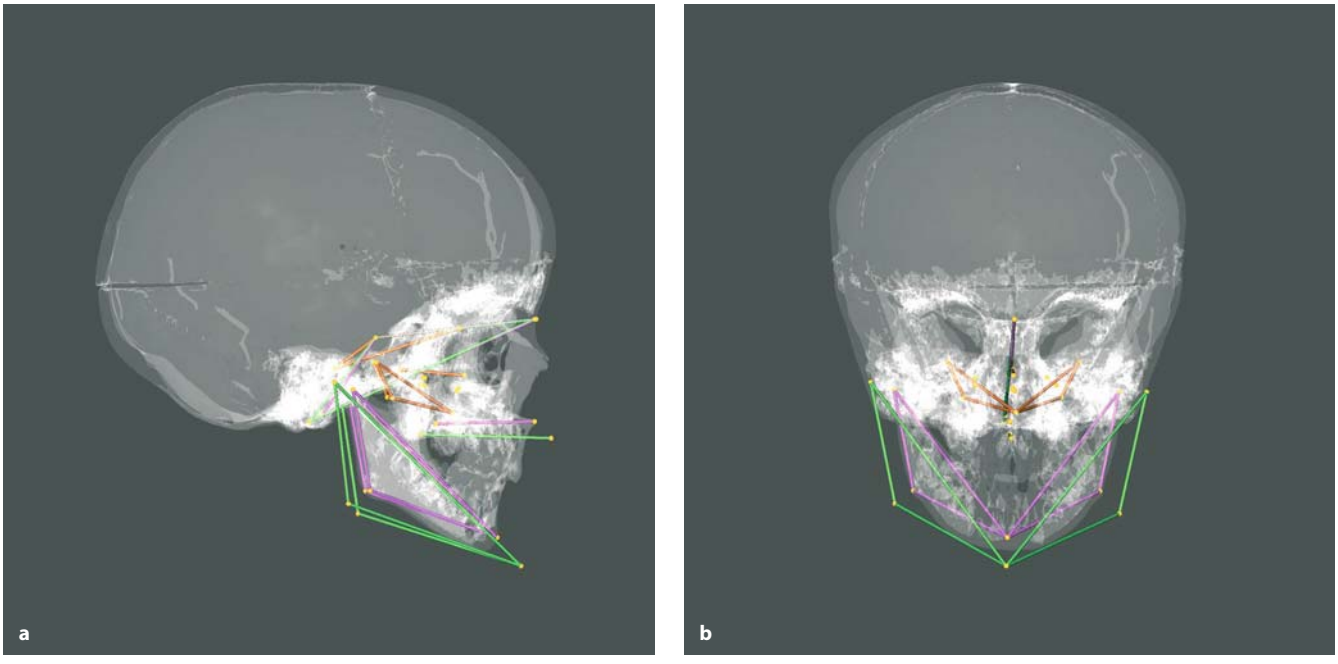

Fig. 8.10 a, b. Left profile (**a**) and frontal (**b**) views of the skull of a 6-year-old child with superimposition of 3-D cephalometric tracings of the cadaver skulls of a newborn, the 6-year-old child and an adult (transparent 3-D CT hard tissue surface representations; registration on the 3-D cephalometric reference system)

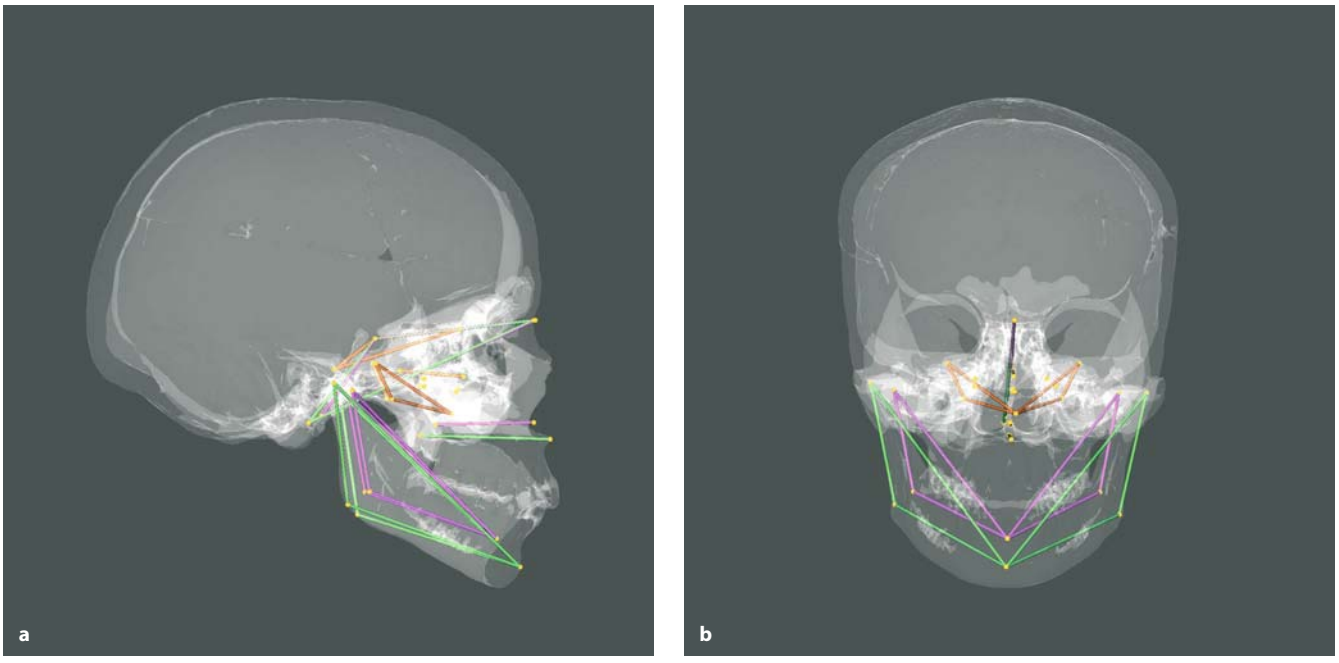

Fig. 8.11 a, b. Left profile (**a**) and frontal (**b**) views of an adult skull with superimposition of 3-D cephalometric tracings of the cadaver skulls of a newborn, a 6-year-old child and the adult (transparent 3-D CT hard tissue surface representations; registration on the 3-D cephalometric reference system)

8.3 Displacement – Remodelling – Relocation

The basicranium acts as a template for facial growth and development. Expansion of the functional soft tissue matrix triggers primary displacement of facial bones *(carry effect)* with simultaneous 3-D remodelling in the opposite direction resulting in relocation of bones.

Midface

During craniofacial growth and development the entire nasomaxillary complex is primary displaced from the basicranium in an antero-inferior direction (Figs. 8.9–8.11) with simultaneous remodelling in a postero-superior direction (Figs. 8.12, 8.13). The amount of bone deposition at the sutures is equal to the amount of primary displacement. The zygomatic bone and arch undergo antero-inferior displacement with the same growth vector (direction and amount) as the nasomaxillary complex. The maxillar and zygomatic bones relocate predominantly posteriorly while the zygomatic arch relocates predominantly laterally during enlargement.

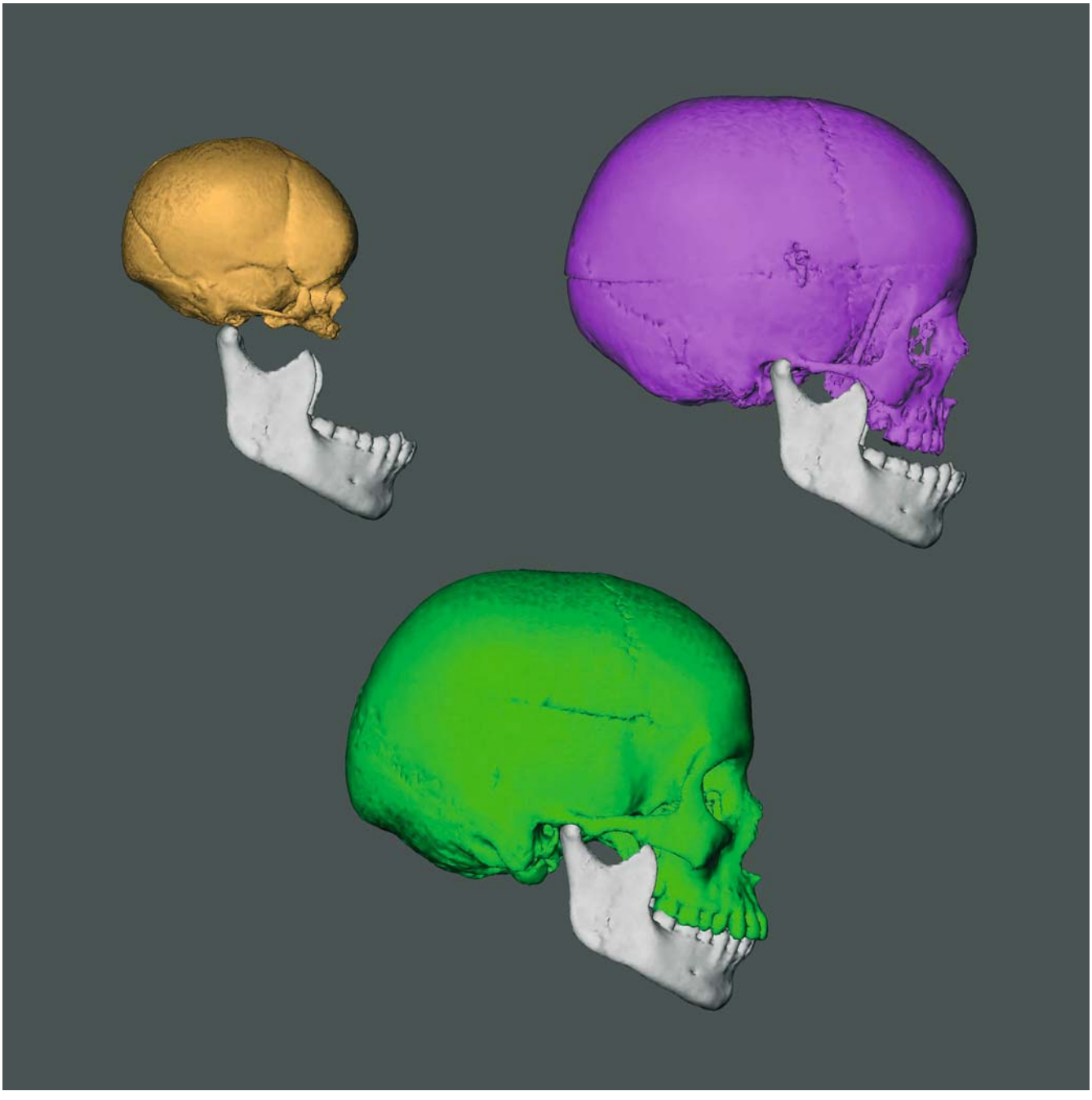

Fig. 8.12. Mandible of an adult cadaver skull with superimposition of the midfacial complex and cranium of the cadaver skulls of a newborn, a 6-year-old child and the adult illustrates extensive remodelling of the nasomaxillary complex during antero-inferior displacement (3-D CT hard tissue surface representations; registration on the 3-D cephalometric reference system)

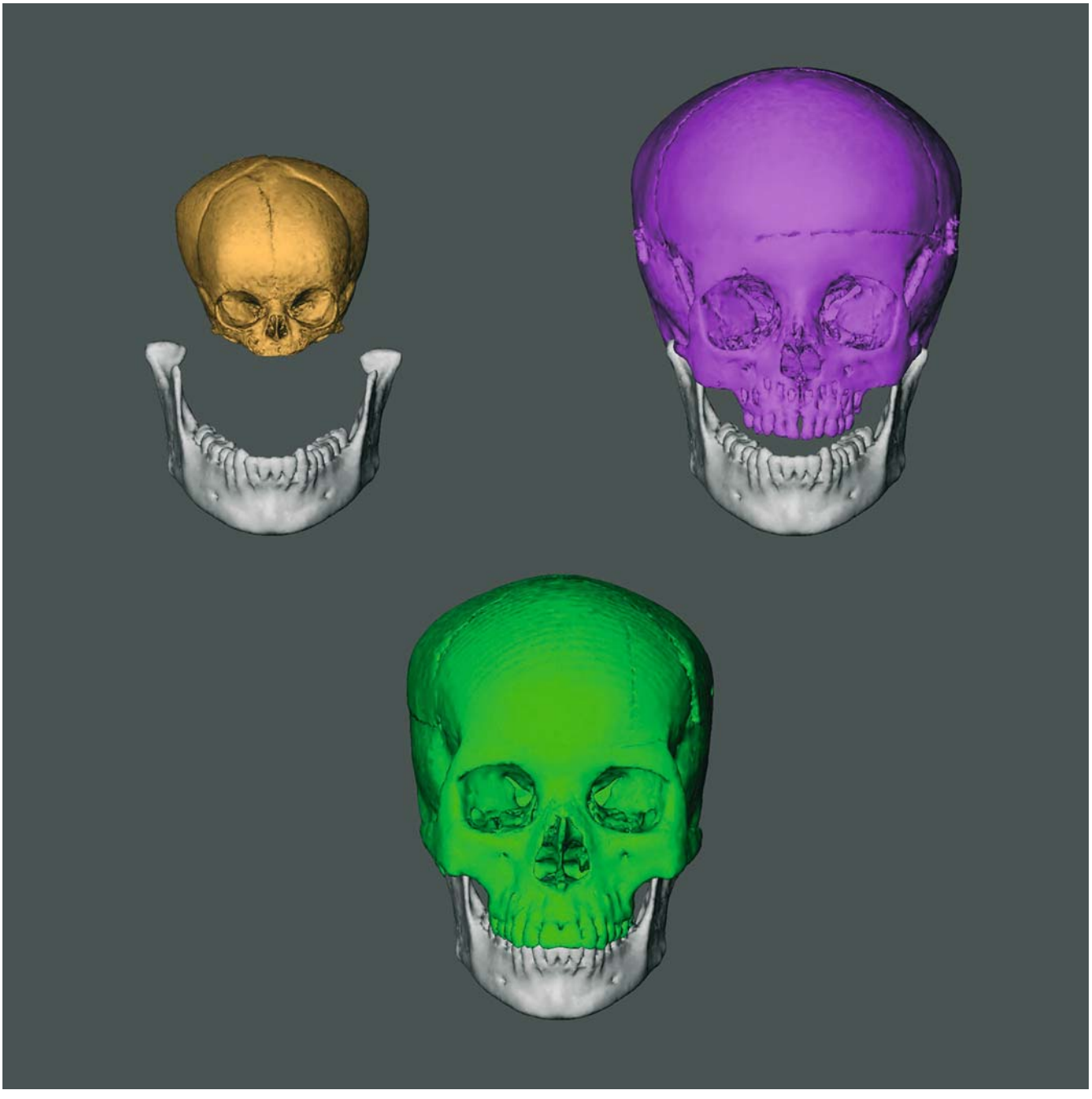

Fig. 8.13. Mandible of an adult cadaver skull with superimposition of the midfacial complex and cranium of a newborn, a 6-year-old child and an adult cadaver skull illustrates relocation of the zygomatic arch and lateral development of the midfacial complex (3-D CT hard tissue surface representations; registration on the 3-D cephalometric reference system)

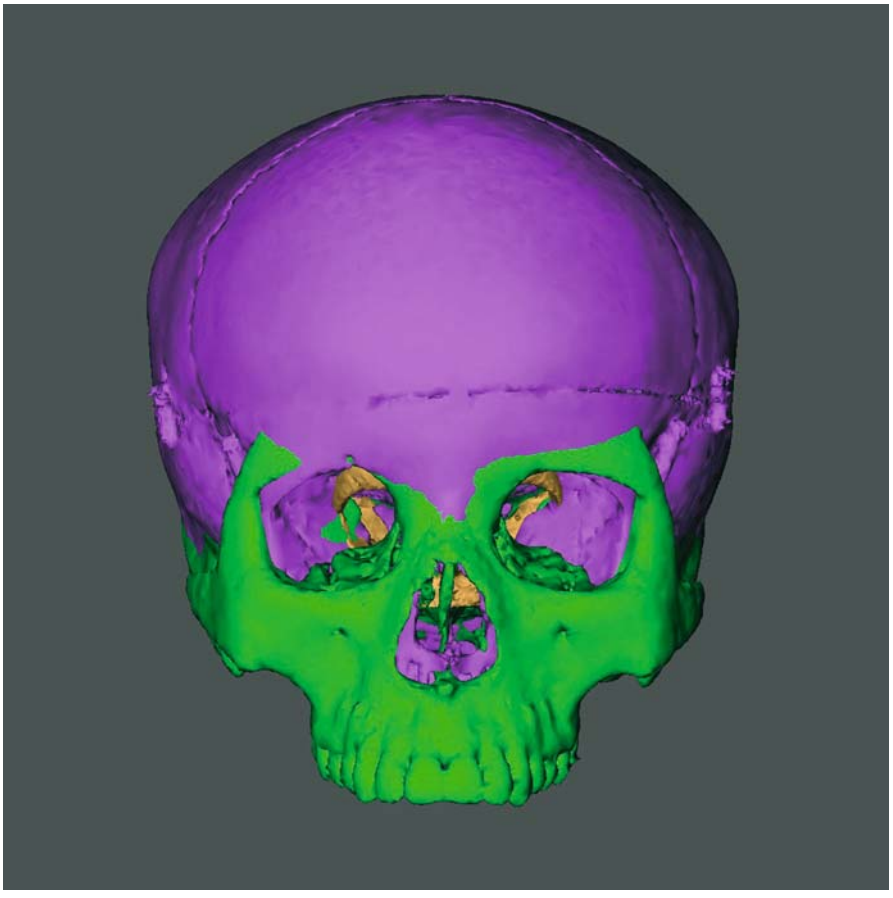

Fig. 8.14. Superimposition of the cadaver skulls of a newborn, a 6-year-old child and an adult with removed mandibles illustrates orbital relocation during craniofacial growth and development (3-D CT hard tissue surface representations; registration on the 3-D cephalometric reference system)

Mandible

The mandible displaces away from the mandibular fossa in an antero-inferior direction (Figs. 8.9–8.11) as it simultaneously remodels predominantly in the opposite postero-superior direction. The vertical mandibular ramus relocates postero-superiorly while the entire mandible displaces antero-inferiorly, which causes posterior lengthening of the horizontal mandibular ramus (Figs. 8.15, 8.16).

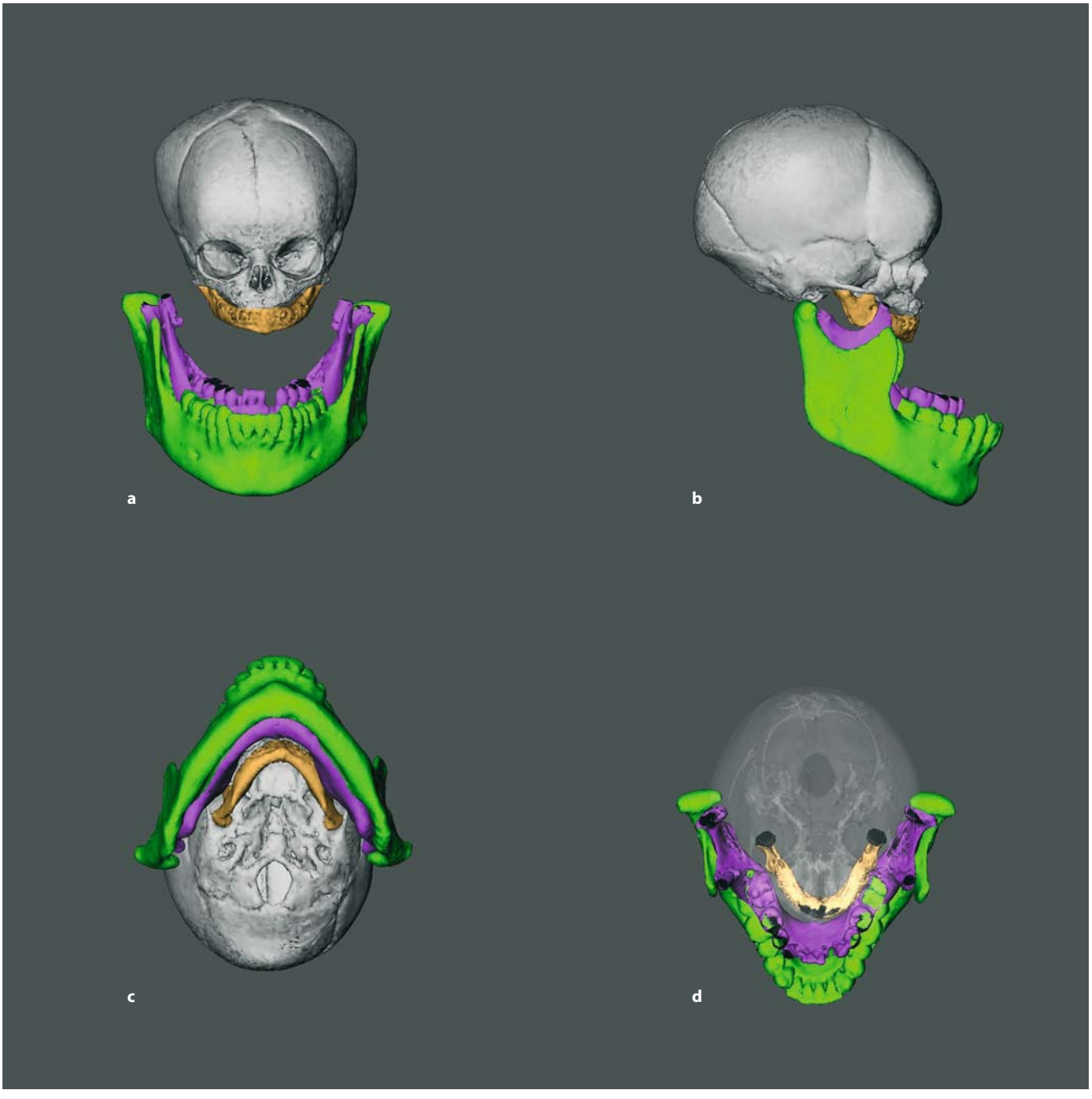

Fig. 8.15 a–d. Newborn cadaver skull with superimposition of the mandibles of the cadaver skulls of a 6-year-old child and an adult (transparent 3-D CT hard tissue surface representations; registration on the 3-D cephalometric reference system)

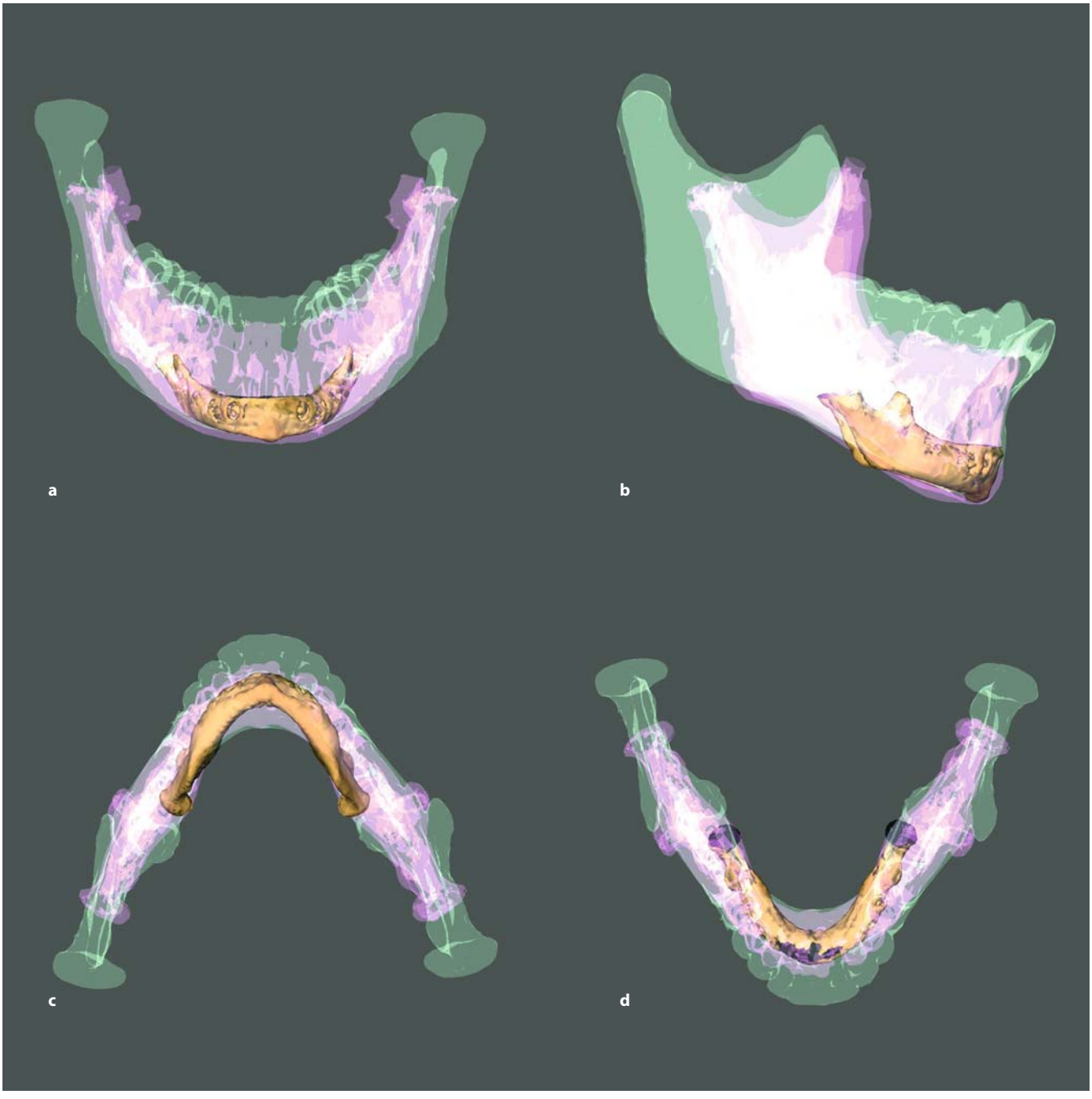

Fig. 8.16 a–d. Superimposition of the mandibles of the cadaver skulls of a newborn, a 6-year-old child and an adult on the mandibular symphysis shows that the principal vector of mandibular growth is postero-superior. This results in a superior and posterior relocation of the mandibular vertical ramus with lengthening of the mandibular horizontal ramus. Note also postero-medial growth and relocation of the lingual mandibular tuberosity. (transparent 3-D CT hard tissue surface representations)

8.4 Developmental Growth Rotations

During craniofacial growth and development two different types of growth rotations occur: *displacement* and *remodelling* rotations.

Remodelling Growth Rotation

Midfacial Complex

Due to the basicranial flexure, the upper part (upper facial region and midfacial complex) of the human face undergoes an anterior remodelling rotation. The combination of anterior remodelling of the superior orbital rim and nasal region and posterior remodelling of the zygomatic bones, inferior and lateral orbital rim results in the typical forward slant of the orbits in humans compared to other mammalian species (Figs. 8.2, 8.4).

Vertical Mandibular Ramus

The remodelling rotation of the vertical mandibular ramus plays a key role in facial growth and development. In order to position the mandibular horizontal ramus with its dento-alveolar process in a best-fit relationship to the nasomaxillary complex and middle cranial fossa, the vertical mandibular ramus becomes more upright with closing of the gonial angle (Fig. 8.17).

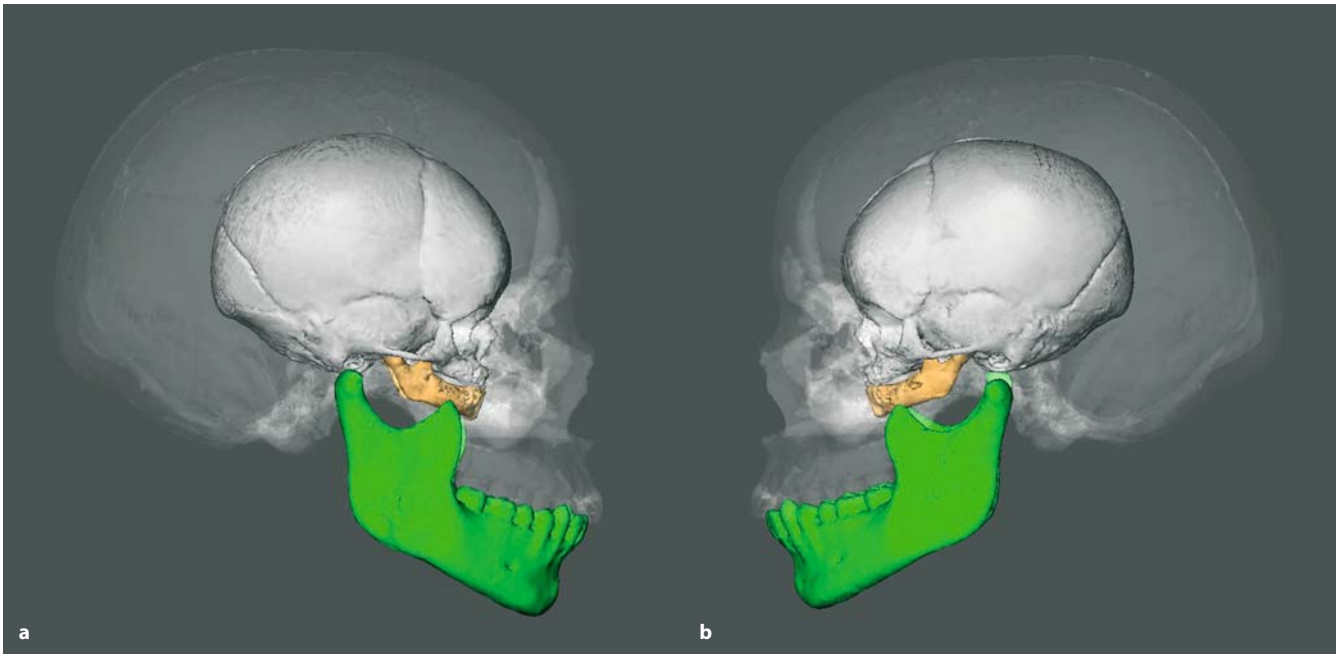

Fig. 8.17 a, b. Superimposition of the cadaver skulls of a newborn and an adult illustrates the remodelling rotation of the vertical ramus of the mandible with uprighting of the vertical ramus and closing of the gonial angle during facial growth and development (right and left profile 3-D CT hard tissue surface representations; registration on the 3-D cephalometric reference system)

Displacement Growth Rotation

Nasomaxillary Complex

During craniofacial growth and development displacement rotations of the nasomaxillary complex can occur, resulting in either a deep bite (clockwise) or open bite (counter-clockwise; Fig. 8.18) deformity depending on growth activities of the basicranium and midfacial sutural growth. In minor cases these can be intrinsically corrected by developmental adjustments („growth compensation mechanisms“) such as counter-directional palatal remodelling rotations or remodelling of the dento-alveolar curve of Spee. More important deformities, however, require orthodontic or combined orthodontic–surgical treatment.

Mandible

Displacement rotations of the mandible occur when mandibular growth and development does not accommodate to vertical nasomaxillary growth. The entire mandible (horizontal and vertical ramus) can rotate infero-posteriorly or supero-anteriorly (Fig. 8.19) to compensate increased or, more usually, decreased vertical height of the nasomaxillary complex, respectively.

Fig. 8.18. Counter-clockwise displacement rotation of the maxilla resulting in an open-bite deformity in a 5-year-old girl with plagiocephaly. (3-D CT hard tissue surface representation, patient G.P.)

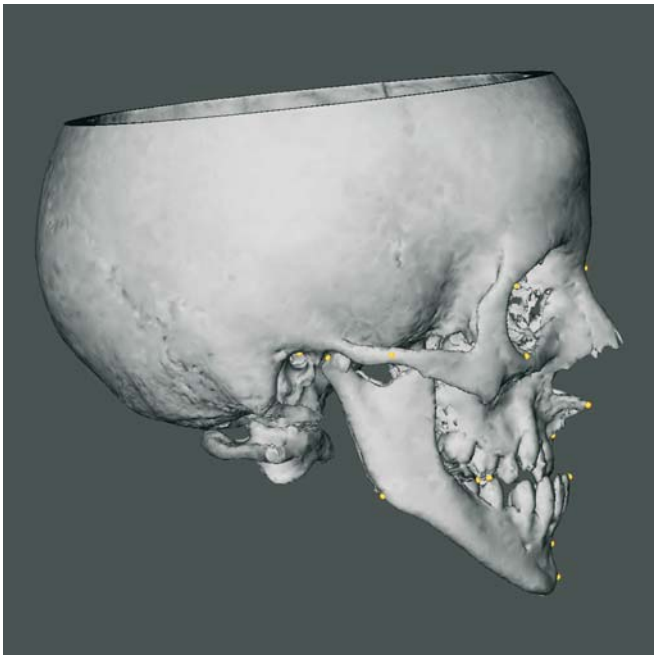

Fig. 8.19. Supero-anterior displacement rotation of the mandible in an adult cleft patient. The forward and upward rotation of the mandible to meet the short midface causes mandibular protrusion. (3-D CT hard tissue surface representation, patient B.V.)

CHAPTER 9 Clinical Applications

Gwen R. J. Swennen

Case 1

B.R. was a 9-year-old girl with mandibular asymmetry caused by loss of the right condylar process. In early infancy she had an episode of malignant external otitis (MEO) that resulted in temporomandibular joint involvement with bony destruction of the right condylar process. She had decreased length of the right vertical mandibular ramus with deviation of the chin to the right. Mouth opening was limited and painful due to trismus.

Reconstruction of the right condylar process by unilateral distraction osteogenesis (DO) was planned virtually and performed via an extra-oral submandibular approach using a modified McCormick technique. The 3-D virtual scene approach provided exact information on the position of the inferior alveolar nerve. A reverse-L osteotomy was created posterior to the path of the inferior alveolar nerve, to a position 15 mm below the mandibular notch (incisura mandibulae), 10 mm anterior and parallel to the posterior border of the right vertical mandibular ramus. Voxel-based virtual planning was transferred into the operation theatre through the use of a commercial caliper. An individual template was not necessary. Intraoperatively, the mobility of the proximal segment was verified. There was no bony ankylosis. A unidirectional internal distraction device was positioned parallel to the posterior border of the right vertical mandibular ramus. Because of trismus, right coronoidectomy was performed additionally. Distraction was initiated after a latency period of 5 days at a rate of 1.00 mm (2×0.5 mm) daily. A total of 12 mm of distraction was performed followed by a consolidation period of 8 weeks.

Five days after removal of the distraction device, spiral CT was carried out and voxel-based 3-D cephalometric hard and soft tissue analysis was performed. The length of the right vertical mandibular ramus was significantly increased. The deviation of the facial midplane was also partially corrected. Following distraction the patient was able to open her mouth wide and could masticate a regular diet. Note that 5 days after distractor removal, there was still significant soft tissue swelling. Therefore, one cannot make conclusions based on 3-D cephalometric soft tissue analysis. It is recommended to perform the post-operative spiral CT once soft tissue swelling has completely subsided (Figs. 9.1–9.22).

Fig. 9.1. Pre-operative clinical frontal view of a 9-year-old girl with a mandibular asymmetry due to loss of the right condylar process after a malignant external otitis (MEO) in early infancy. Note the deviation of the chin to the right (patient B.R.)

Fig. 9.2. Pre-operative 3-D CT soft tissue surface representation with set-up of 3-D cephalometric soft tissue landmarks. Frontal view. (3-D CT, patient B.R.)

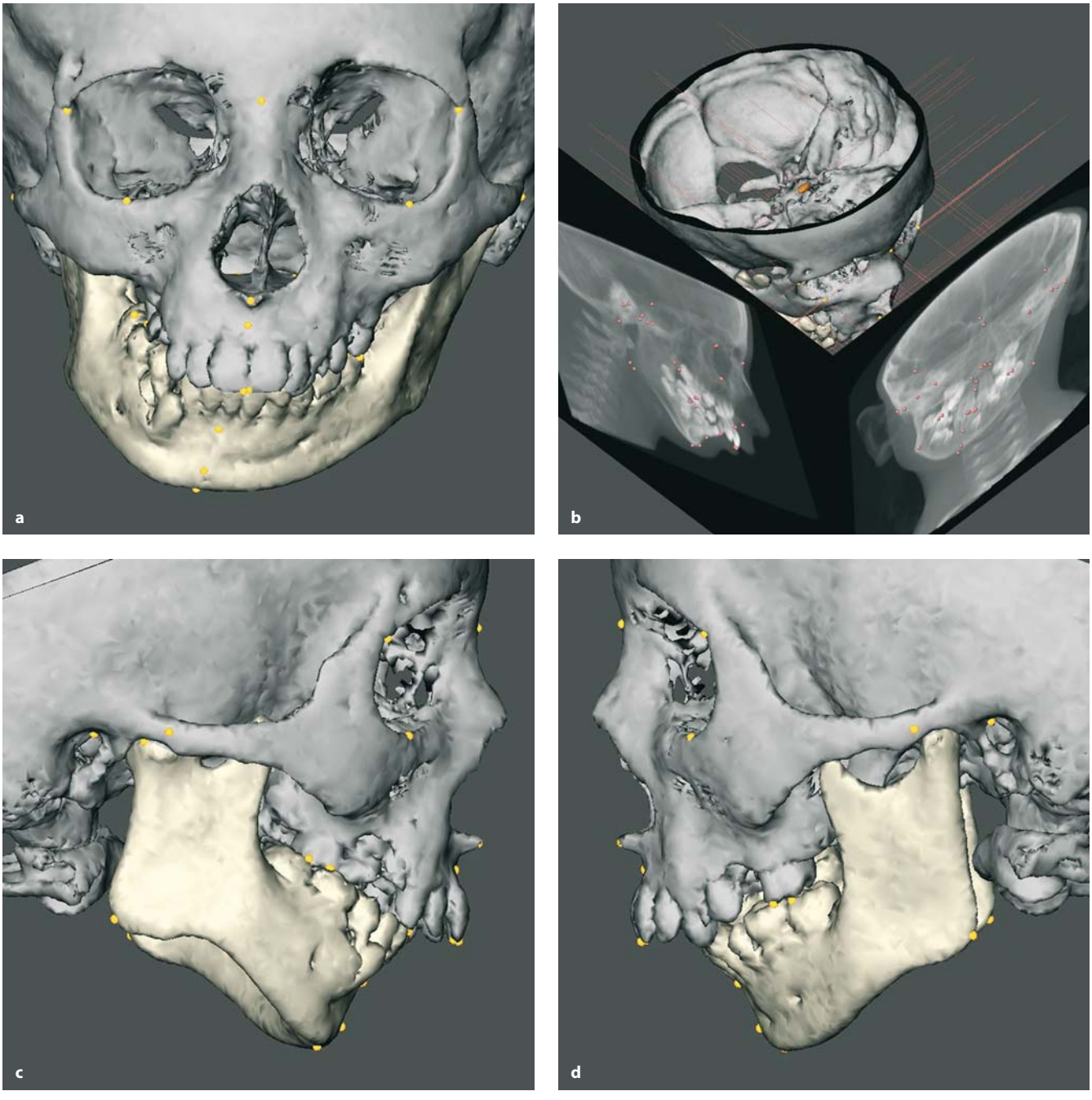

Fig. 9.3 a–d. Pre-operative 3-D CT hard tissue surface representations with set-up of 3-D cephalometric hard tissue landmarks. **a** Frontal view; **b** linked lateral and frontal virtual cephalograms; **c** profile view right; **d** profile view left. (3-D CT, patient B.R.)

Table 9.1. Results of pre-operative voxel-based 3-D cephalometric hard tissue analysis using the Maxilim version 1.3.0 software (Medicim NV, Sint-Niklaas, Belgium, http://www.medicim.com) (patient B.R.)

3-D Cephalometry Report (1)	
3-D Cephalometric Hard Tissue Analysis according to Swennen	
Patient name: B.R. **Physician name: S.G.**	
Angular analysis	
Lateral inclination to horizontal plane (deg)	
Frankfort plane	2.22
Maxillary plane	7.49
Occlusal plane	25.58
Mandibular plane	32.14
Frontal inclination to horizontal plane (deg)	
Frankfort plane	0.14
Maxillary plane	1.56
Occlusal plane	10.46
Mandibular plane	2.13
Frontal inclination to median plane (deg)	
Facial midplane	10.33
Further angular measurements (deg)	
Co_r-Go_r-Men $\perp$ *z*-plane (right gonial angle)	112.55
Co_l-Go_l-Men $\perp$ *z*-plane (left gonial angle)	114.06
Linear analysis	
3-D linear measurements (mm)	
Co_l-Go_l	47.64
Co_r-Go_r	39.80
Go_l-Pog	70.85
Go_r-Pog	60.80
Co_l-Pog	101.06
Co_r-Pog	83.61
S-N	63.00
PNS-ANS	48.07
Linear height measurements (mm)	
ANS-Men	43.42
S-PNS	31.23
N-ANS	37.81
S-Go	55.87
N-Men	89.68
Linear width measurements (mm)	
Zy_r-Zy_l	116.88
Co_r-Co_l	105.94
Go_r-Go_l	79.91
Further linear measurements (mm)	
Wit's	7.33

Table 9.1. (Continued)

3-D Cephalometry Report (2)			
3-D Cephalometric Hard Tissue Analysis according to Swennen			
Patient name: B.R. **Physician name: S.G.**			
Orthogonal analysis			
	To vertical plane (mm)	To horizontal plane (mm)	To median plane (mm)
Zy_l	–2.33	–14.50	56.85
Zy_r	–0.32	–16.01	–60.03
UI_l	57.33	–60.26	–2.40
UI_r	58.39	–60.61	–3.55
LI_l	47.84	–58.47	–7.50
LI_r	47.53	–57.96	–8.83
ANS	62.63	–39.68	–1.95
UM–$cusp_l$	29.03	–52.16	21.67
A	57.66	–45.37	–2.76
UM–$cusp_r$	32.21	–45.16	–27.22
PNS	15.33	–31.23	–0.81
LM–$cusp_l$	25.34	–51.46	18.39
B	38.06	–69.37	–10.29
LM–$cusp_r$	27.86	–43.11	–30.59
Pog	33.62	–78.91	–13.75
Men	28.55	–83.10	–15.71
Co_l	–8.95	–13.74	50.70
Co_r	–5.91	–18.02	–55.24
Go_l	–13.81	–58.35	34.70
Go_r	–13.03	–55.87	–45.21
Or_l	46.08	–16.93	33.59
Or_r	49.46	–16.90	–31.53

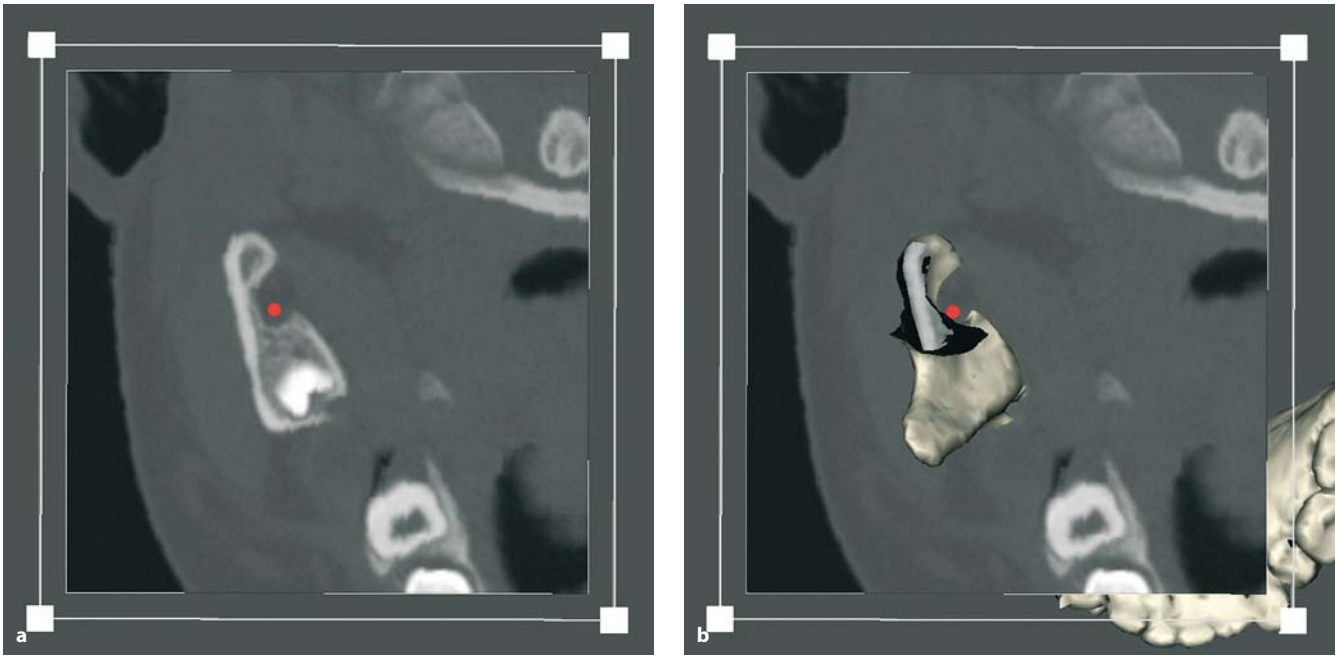

Fig. 9.4 a, b. Orbitomeatally oriented axial CT at the level of the lingula shows the entrance of the inferior alveolar nerve in the right vertical mandibular ramus. **a** Axial CT; **b** axial CT with overlay of 3-D hard tissue surface representation of the mandible (patient B.R.)

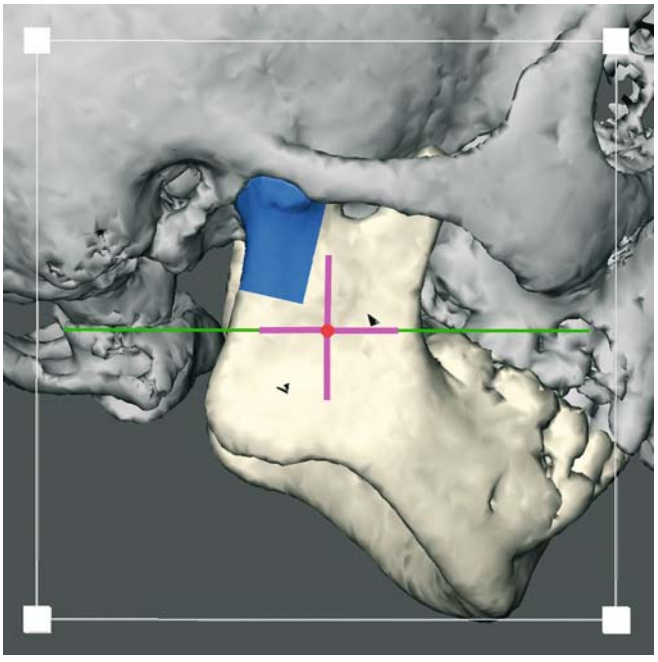

Fig. 9.5. Virtual planning of a reverse L-osteotomy of the right vertical mandibular ramus. The position of the lingula (15 mm anterior to the posterior border of the vertical mandibular ramus and 19 mm inferior to the mandibular notch) is marked on the buccal cortex of the right vertical mandibular ramus. The reverse-L osteotomy is planned 10 mm anterior and parallel to the posterior border of the vertical mandibular ramus and 15 mm inferior to the mandibular notch in order to avoid nerve lesion. Profile view right. (3-D CT hard tissue surface representation, patient B.R.)

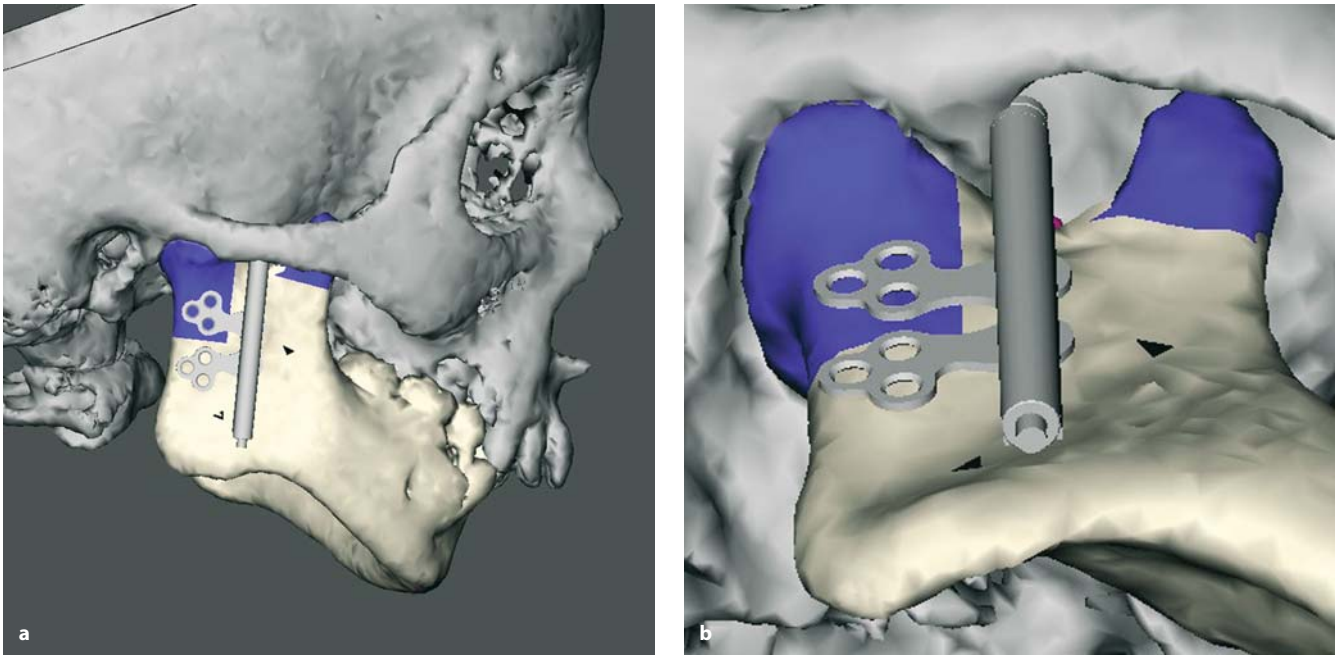

Fig. 9.6 a, b. Voxel-based virtual planning of a right reverse-L osteotomy for reconstruction of the right condylar process, positioning of a virtual internal unidirectional Zurich Pediatric Ramus Distractor (cloverleaf design) and osteotomy of the right mandibular coronoid process using the Maxilim version 1.3.0 software (Medicim NV, Sint-Niklaas, Belgium, http://www.medicim.com). **a** Profile view right; **b** close-up view. (3-D CT hard tissue surface representation, patient B.R.)

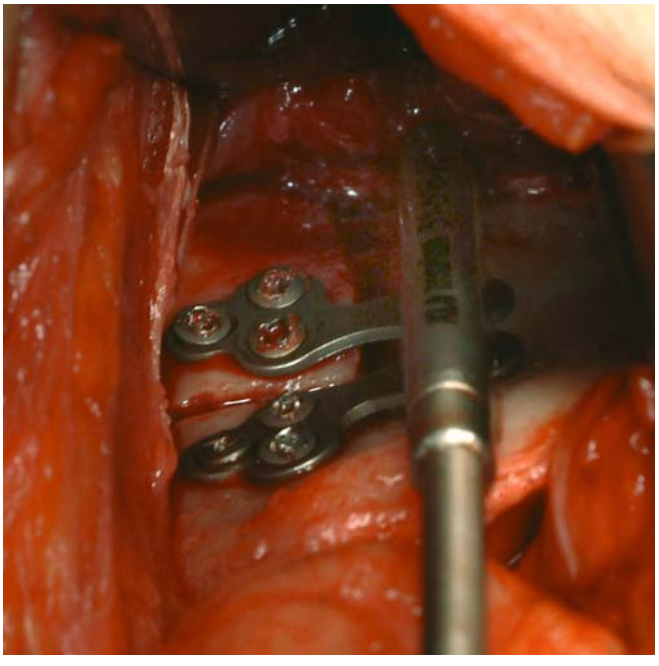

Fig. 9.7. Intra-operative view of the reverse-L osteotomy and positioning of the internal unidirectional Zurich Pediatric Ramus Distractor (cloverleaf design; KLS Martin, Tuttlingen, Germany, http://www.klsmartin.com) after a right submandibular approach. The voxel-based virtual surgical planning is clinically transferred to the patient using a commercial calliper (10 mm anterior and parallel to the posterior border of the vertical mandibular ramus and 15 mm inferior to the mandibular notch). Note that no lingual periosteal degloving is performed (patient B.R.)

Fig. 9.8. Post-operative clinical frontal view at 5 days shows the flexible activator of the distraction device which is passed extra-orally through a small incision (patient B.R.)

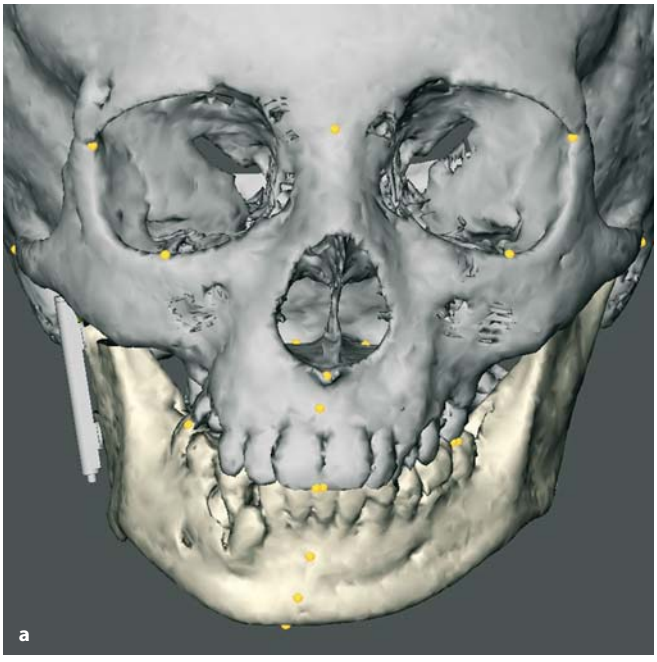

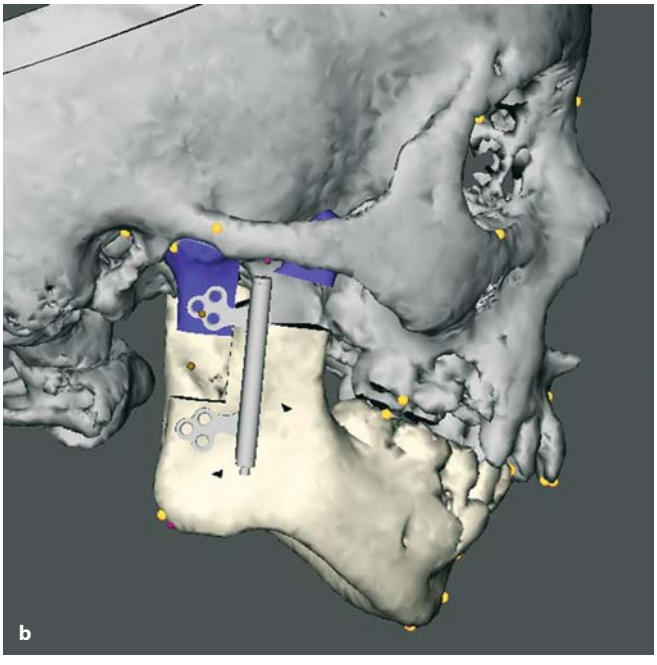

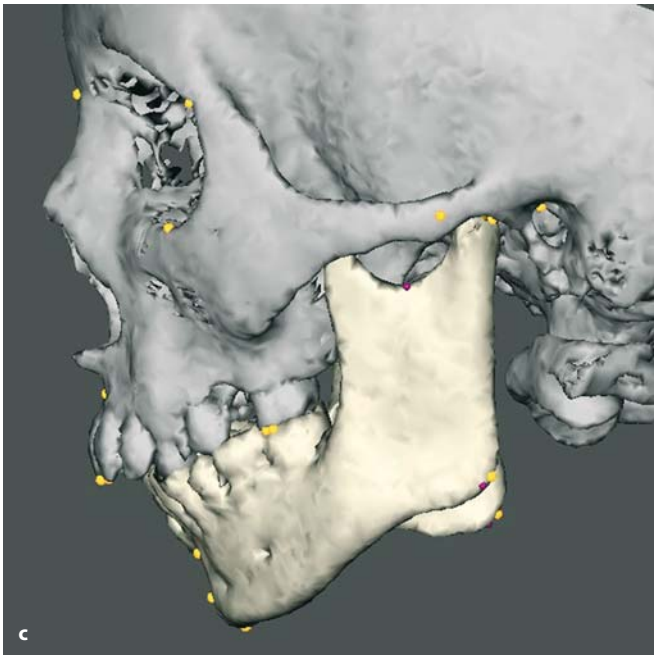

Fig. 9.9 a–c. Voxel-based virtual planning of 12 mm lengthening of the right vertical mandibular ramus by unidirectional distraction osteogenesis with the intra-oral Zurich Pediatric Ramus Distractor (Maxilim version 1.3.0). 3-D CT hard tissue surface representations with set-up of 3-D cephalometric hard tissue landmarks. **a** Frontal view; **b** profile view right; **c** profile view left. (3-D CT, patient B.R.)

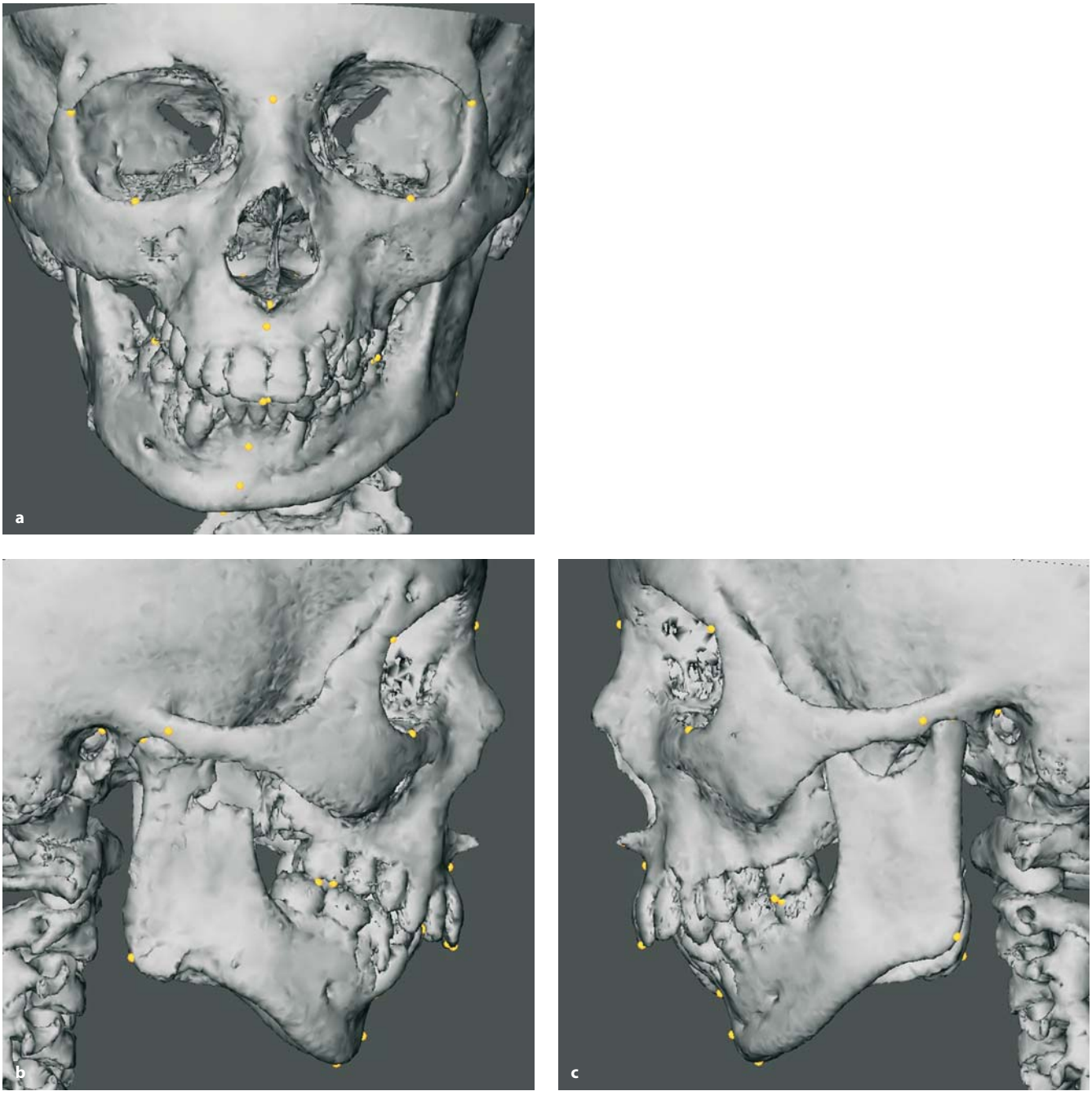

Fig. 9.10. Post-distraction 3-D CT hard tissue surface representations with set-up of 3-D cephalometric hard tissue landmarks show significant increase in length of the right vertical mandibular ramus. **a** Frontal view; **b** profile view right; **c** profile view left. (3-D CT, patient B.R.)

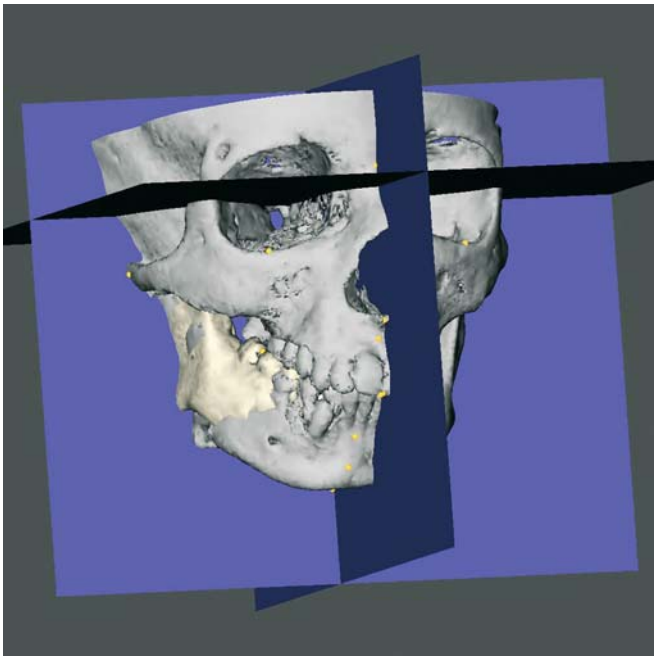

Fig. 9.11. Superimposition of pre-operative and post-distraction 3-D CT hard tissue surface representations using the 3-D cephalometric reference system (3-D CT, patient B.R.)

Table 9.2. The data of the voxel-based 3-D cephalometric hard tissue analysis showed that voxel-based virtual planning of increase of right vertical mandibular ramus length by unidirectional distraction osteogenesis was very precise. Anterior facial height and anterior lower facial height, however, were slightly overcorrected. The discrepancy in posterior facial height between the virtual planning and post-distraction result can be explained by the spontaneous closure of the right lateral open bite during the consolidation period with downward cant of the maxillary and occlusal plane (patient B.R.)

Parameter	Pre-operative	Virtual planning	Post-operative
Co_r-Go_r (mm)	39.80	*49.18*	*49.27*
Go_r-Pog (mm)	60.80	61.03	61.73
Co_r-Pog (mm)	83.61	91.11	92.30
Go_r-Go_l (mm)	79.91	79.77	81.61
N-Men (mm)	89.68	92.93	95.02
ANS-Men (mm)	43.42	46.61	47.98
S-PNS (mm)	31.23	31.81	34.86
S-Go (mm)	55.87	*66.70*	*66.70*
Gonial $angle_r$ (deg)	112.55	111.73	114.74
Facial midplane / *z* (deg)	10.33	6.08	7.72

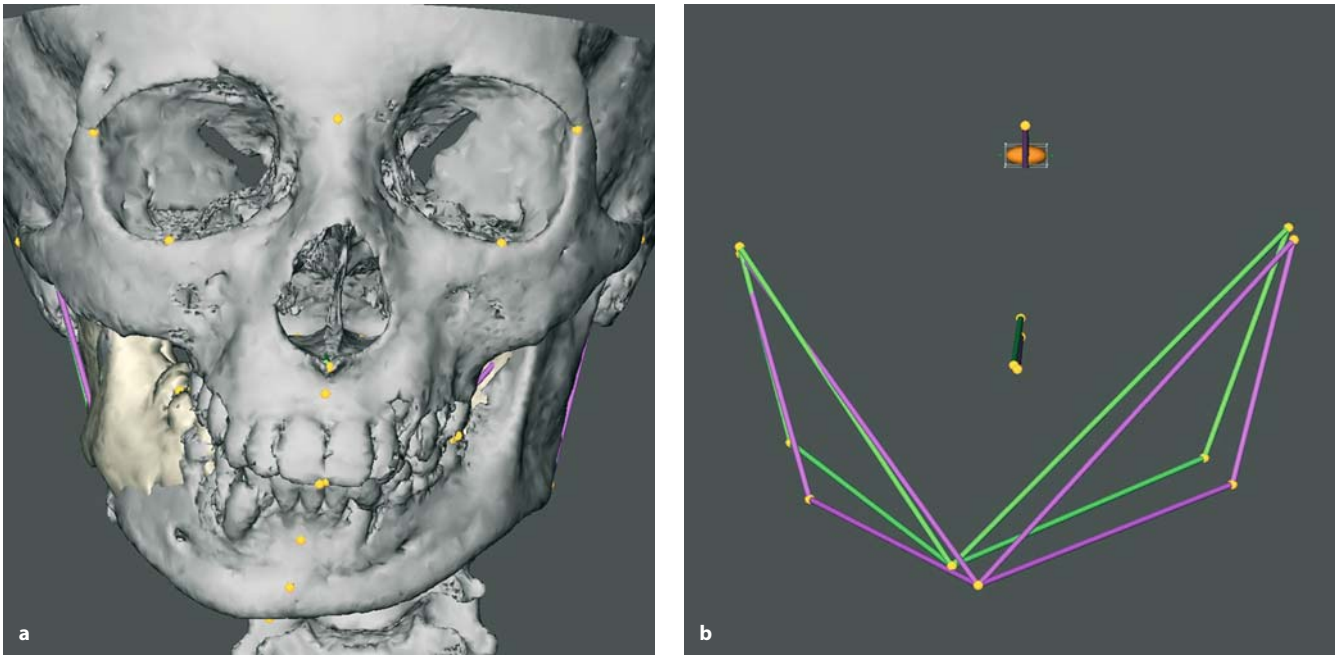

Fig. 9.12 a, b. Superimposition of pre-operative (*green*) and post-distraction (*purple*) 3-D CT hard tissue surface representations and 3-D cephalometric tracings using the 3-D cephalometric reference system. Note the lengthening of the right vertical mandibular ramus and improvement of chin position. Frontal view. (3-D CT, patient B.R.)

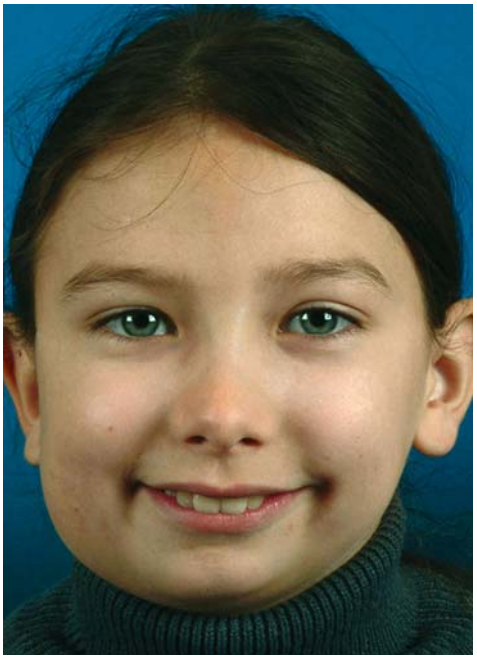

Fig. 9.13. Post-distraction clinical frontal view at 1 week after removal of the distraction device (patient B.R.)

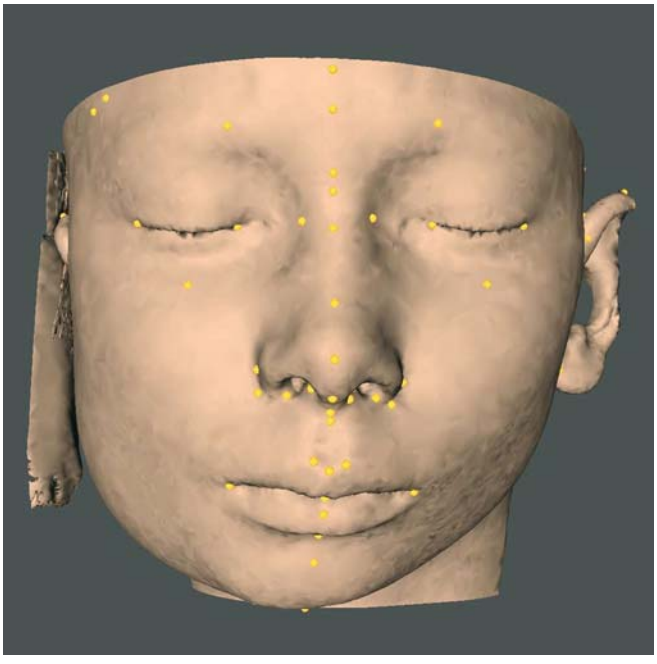

Fig. 9.14. Post-distraction 3-D CT soft tissue surface representation with set-up of 3-D cephalometric soft tissue landmarks. Frontal view. Note artefacts at the level of the right ear (3-D CT, patient B.R.)

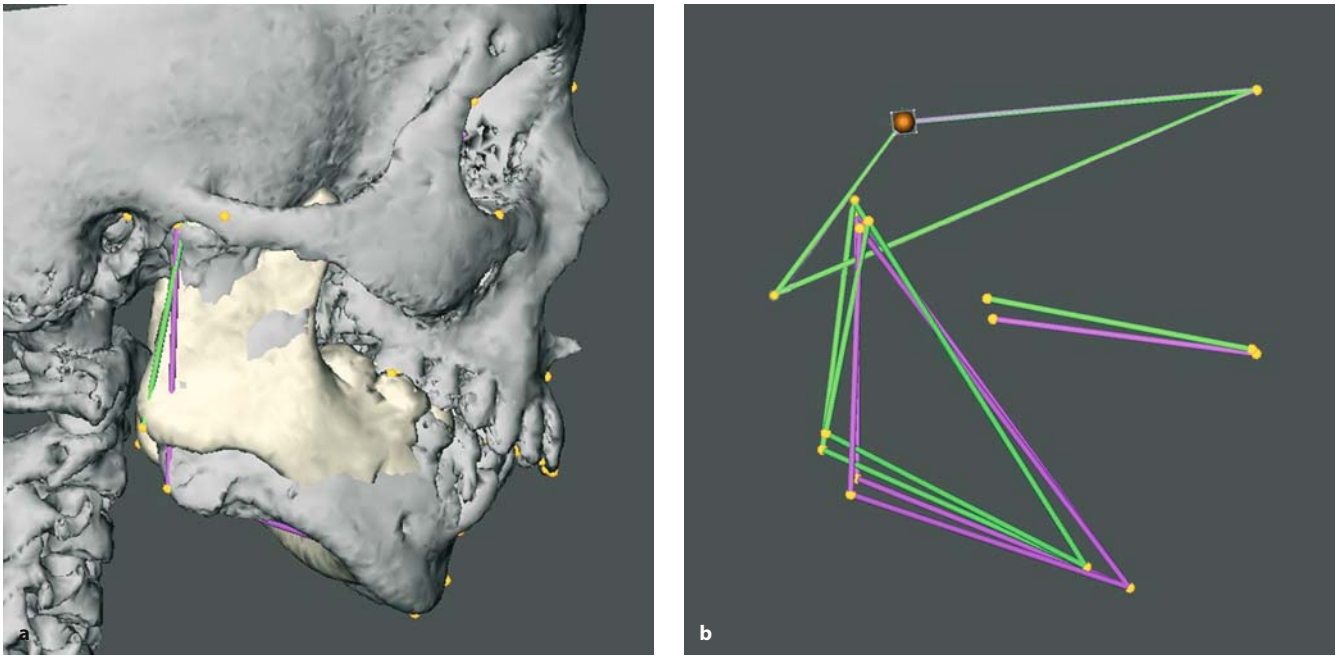

Fig. 9.15. Superimposition of pre-operative (*green*) and post-distraction (*purple*) 3-D CT hard tissue surface representations **(a)** and 3-D cephalometric tracings **(b)** using the 3-D cephalometric reference system. Note the lengthening of the right vertical mandibular ramus, improvement in chin projection and increase of anterior and posterior facial height. Profile view right. (3-D CT, patient B.R.)

Fig. 9.16. Pre-operative clinical right profile view (patient B.R.)

Fig. 9.17. Post-distraction clinical right profile view at 1 week after removal of the distraction device (patient B.R.)

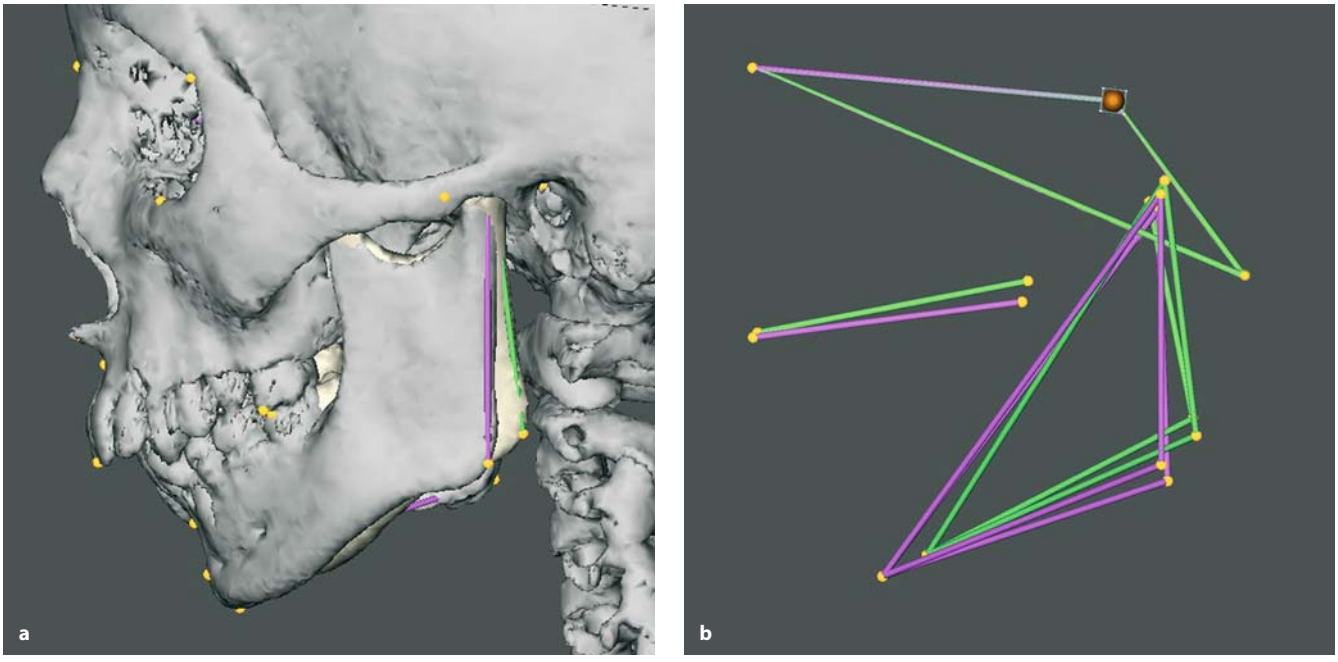

Fig. 9.18. Superimposition of pre-operative (*green*) and post-distraction (*purple*) 3-D CT hard tissue surface representations **(a)** and 3-D cephalometric tracings **(b)** using the 3-D cephalometric reference system. Note the improvement in chin projection and increase of anterior and posterior facial height. Profile view left. (3-D CT, patient B.R.)

Fig. 9.19. Pre-operative clinical left profile view (patient B.R.)

Fig. 9.20. Post-distraction clinical right profile view at 1 week after removal of the distraction device (patient B.R.)

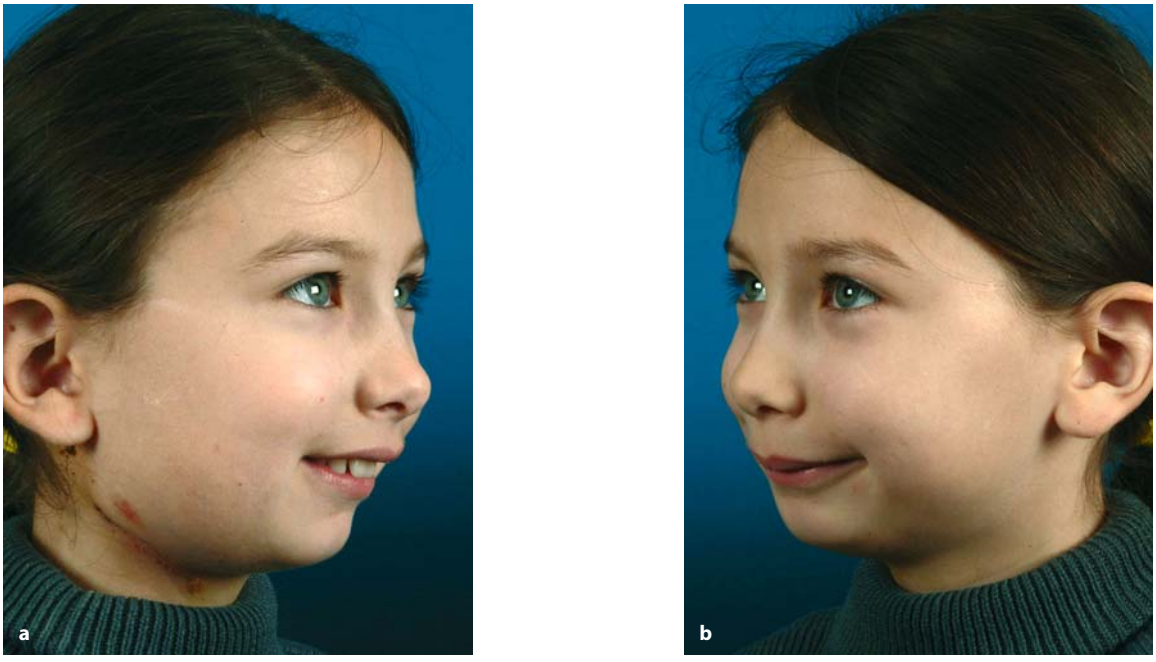

Fig. 9.21. Post-distraction clinical right **(a)** and left **(b)** three-quarter views at 1 week after removal of the distraction device (3-D CT, patient B.R.)

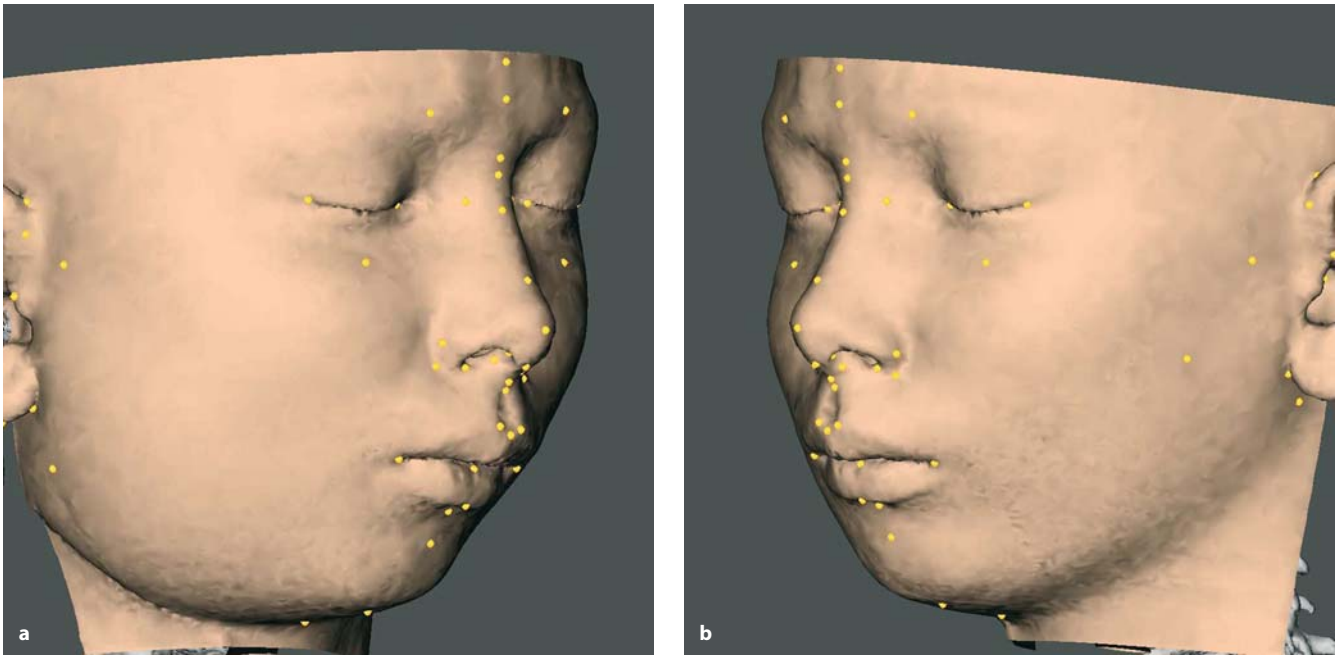

Fig. 9.22. Post-operative 3-D CT soft tissue surface representations with set-up of 3-D cephalometric soft tissue landmarks at 1 week after removal of the distraction device. Right **(a)** and left **(b)** three-quarter views. (3-D CT, patient B.R.)

Case 2

H.T. was a 5-year-old boy with left hemifacial microsomia (Goldenhar variant) (Pruzansky class IIb). He had a hypoplastic mandibular vertical ramus, a canted occlusal plane and labial fissure and a hypoplastic auricle. His left gonial angle was blunt and his chin was slightly deviated to the affected side.

Reconstruction of the left mandibular vertical ramus and gonial angle by unilateral DO was planned virtually and performed via an intra-oral approach. The 3-D virtual scene approach allowed definition of the ideal position and inclination of the osteotomy and distraction device. In order to transfer the voxel-based virtual surgical planning precisely into the operation theatre, a stereolithographic model was made of the mandible that incorporated the virtually planned osteotomy line and screw-holes of the distraction device. The use of two custom-made surgical guides allowed accurate and easy transfer of the position and inclination of both the osteotomy and the unidirectional distraction device into surgery. Distraction was initiated after a latency period of 5 days at a rate of 1.00 mm (2×0.5 mm) daily. A total of 12 mm of distraction was performed, followed by a consolidation period of 8 weeks.

One week after removal of the distraction device, spiral CT was carried out and voxel-based 3-D cephalometric analysis was performed. There was significant uprighting of the left mandibular vertical ramus with good restoration of the left gonial angle. The length of the left mandibular vertical ramus, however, was still undercorrected. The patient had good symmetry of the oral commissures and cheek contour (Figs. 9.23–9.41).

Fig. 9.23. Pre-operative clinical frontal view of a 5-year-old boy with Goldenhar syndrome (patient H.T.)

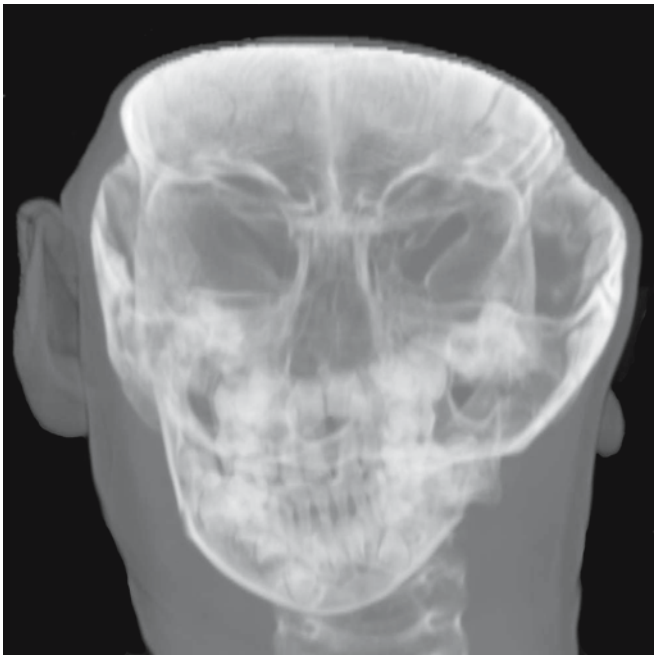

Fig. 9.24. Pre-operative virtual frontal cephalogram (patient H.T.)

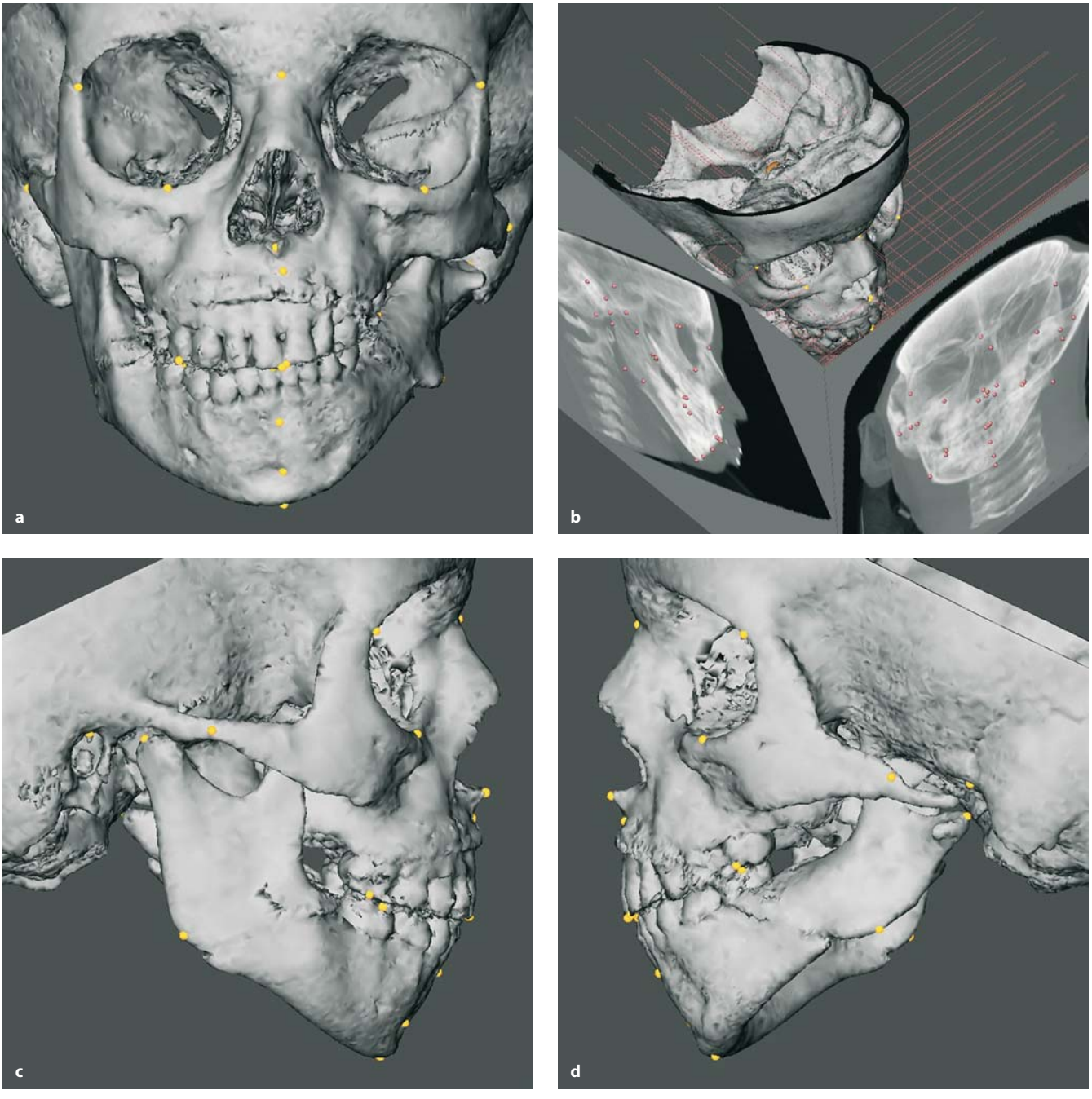

Fig. 9.25 a–d. Pre-operative 3-D CT hard tissue surface representations with set-up of 3-D cephalometric hard tissue landmarks. **a** Frontal view; **b** linked lateral and frontal virtual cephalograms; **c** profile view right; **d** profile view left. (3-D CT, patient H.T.)

Table 9.3. Results of pre-operative voxel-based 3-D cephalometric hard tissue analysis using the Maxilim™ version 1.3.0 software (Medicim NV, Sint-Niklaas, Belgium, http://www.medicim.com) (patient H.T.)

3-D Cephalometry Report (1)	
3-D Cephalometric Hard Tissue Analysis according to Swennen	
Patient name: H.T. **Physician name: S.G.**	
Angular analysis	
Lateral inclination to horizontal plane (deg)	
Frankfort plane	0.07
Maxillary plane	0.14
Occlusal plane	23.77
Mandibular plane	39.03
Frontal inclination to horizontal plane (deg)	
Frankfort plane	0.07
Maxillary plane	5.78
Occlusal plane	7.61
Mandibular plane	4.92
Frontal inclination to median plane (deg)	
Facial midplane	0.29
Further angular measurements (deg)	
Co_r-Go_r-Men ⊥ *z*-plane (right gonial angle)	132.86
Co_l-Go_l-Men ⊥ *z*-plane (left gonial angle)	165.65
Linear analysis	
3-D linear measurements (mm)	
Co_l-Go_l	30.81
Co_r-Go_r	42.08
Go_l-Pog	55.59
Go_r-Pog	63.73
Co_l-Pog	82.84
Co_r-Pog	92.15
S-N	63.56
PNS-ANS	44.30
Linear height measurements (mm)	
ANS-Men	53.38
S-PNS	29.31
N-ANS	35.94
S-Go	55.12
N-Men	89.98
Linear width measurements (mm)	
Zy_r-Zy_l	102.10
Co_r-Co_l	84.70
Go_r-Go_l	73.49
Further linear measurements (mm)	
Wit's	3.79

Table 9.3. (Continued)

3-D Cephalometry Report (2)			
3-D Cephalometric Hard Tissue Analysis according to Swennen			
Patient name: H.T. **Physician name: S.G.**			
Orthogonal analysis			
	To vertical plane (mm)	To horizontal plane (mm)	To median plane (mm)
Zy_l	7.44	–21.72	48.18
Zy_r	10.02	–13.61	–53.92
UI_l	60.29	–54.84	0.91
UI_r	60.90	–55.57	0.07
LI_l	58.39	–54.98	–0.49
LI_r	58.70	–55.31	–1.80
ANS	65.01	–30.34	–1.37
$UM–cusp_l$	38.84	–42.73	20.23
A	62.93	–35.16	0.33
$UM–cusp_r$	50.54	–53.37	–21.82
PNS	20.73	–29.31	–2.23
$LM–cusp_l$	37.57	–43.49	18.88
B	53.44	–66.70	–0.48
$LM–cusp_r$	47.07	–53.77	–20.29
Pog	45.82	–76.70	0.34
Men	40.29	–83.35	0.43
Co_l	–9.14	–28.88	39.78
Co_r	–3.91	–13.68	–44.91
Go_l	7.63	–54.02	33.76
Go_r	1.20	–55.12	–39.73
Or_l	47.77	–16.71	30.27
Or_r	52.82	–16.78	–24.29

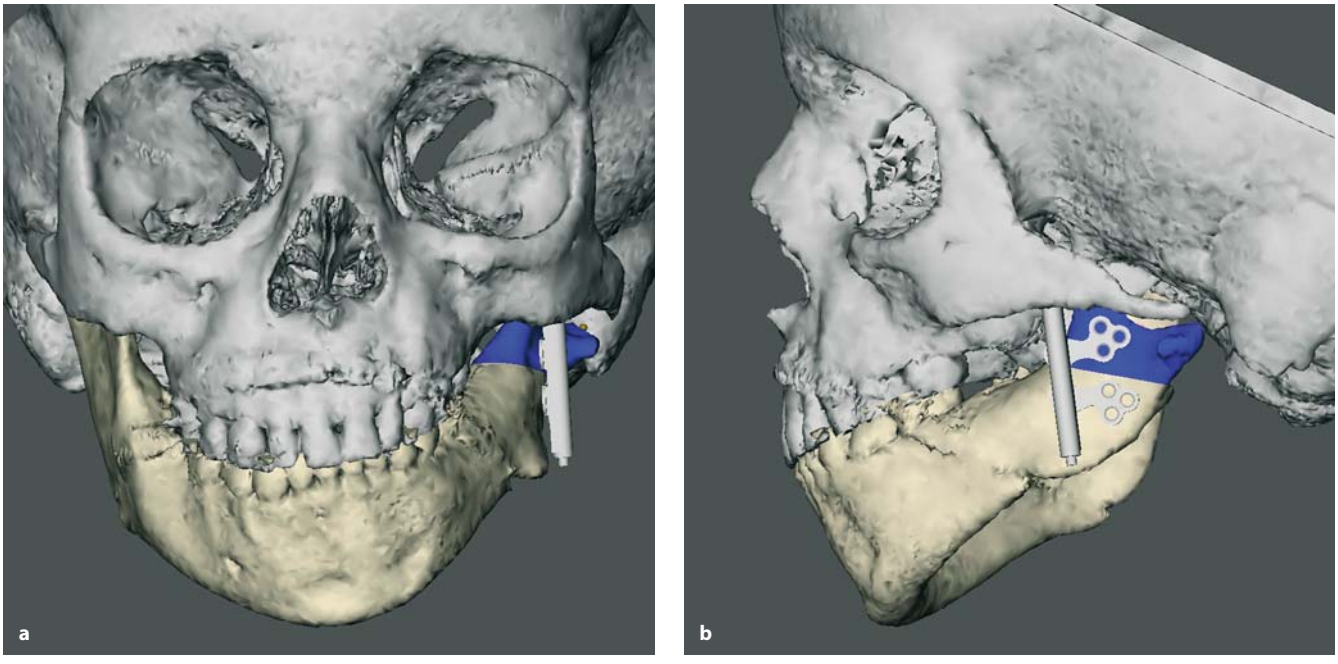

Fig. 9.26 a, b. Voxel-based virtual planning of a horizontal osteotomy of the left vertical ramus and positioning of a virtual internal unidirectional Zurich Pediatric Ramus Distractor (cloverleaf design, 15 mm) using the Maxilim version 1.3.0 software. Note that there was not enough space for a longer (20 or 25 mm) intra-oral distraction device. **a** Frontal view; **b** profile view left; (3-D CT hard tissue surface representation, patient H.T.)

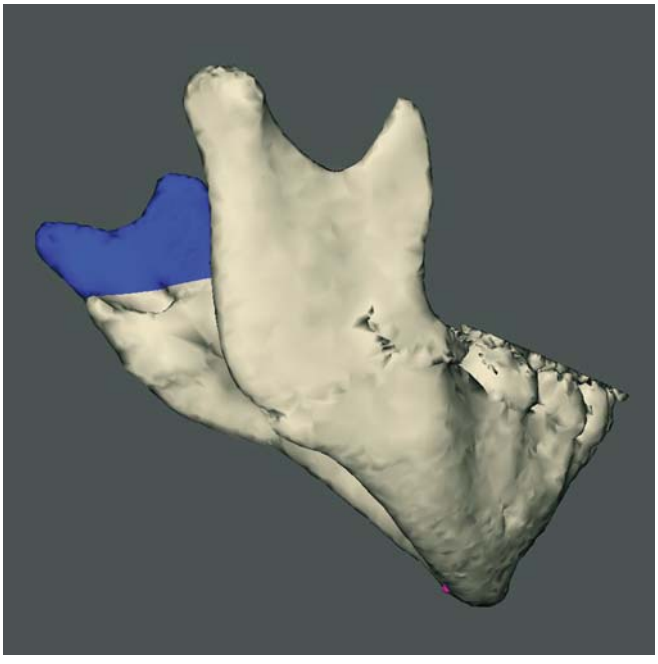

Fig. 9.27. Close-up view of the isolated mandible shows that the virtual horizontal osteotomy of the left vertical ramus is planned just above the entrance (lingula) of the inferior alveolar nerve in the mandible (3-D CT hard tissue surface representation, patient H.T.)

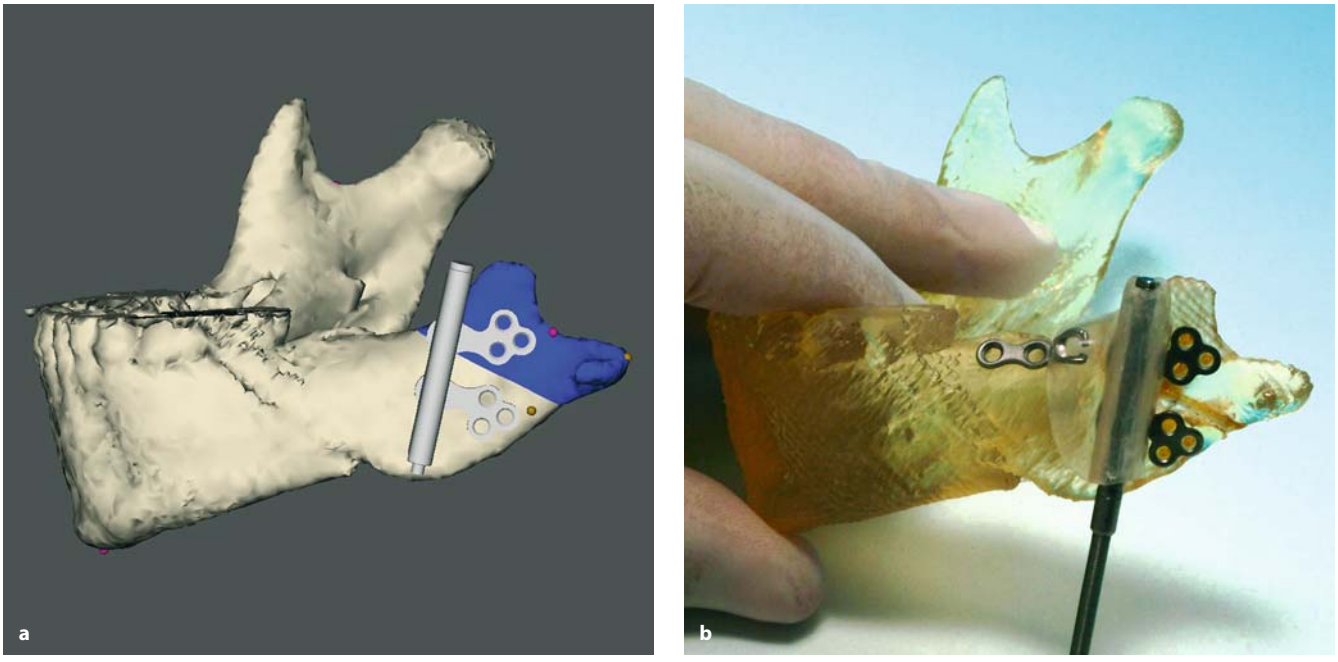

Fig. 9.28. For accurate transfer of **(a)** voxel-based virtual distraction planning into the operation theatre, **(b)** a stereolithographic model (KLS Martin) of the isolate mandible was manufactured. Both the osteotomy line and screw holes of the fixation plates of the distraction device were colour-marked in this model. Using two custom-made acrylic surgical guides, the position and inclination of both the osteotomy and the intra-oral unidirectional Zurich Pediatric Ramus Distractor (cloverleaf design) could be transferred precisely into the operation theatre after creation of a left intra-oral approach (patient H.T.)

Fig. 9.29. Custom-made acrylic surgical guide for precise transfer of the virtually planned osteotomy

Fig. 9.30. Post-operative clinical frontal view at 1 week shows the flexible activator of the distraction device, which is passed extra-orally through a small incision (patient H.T.)

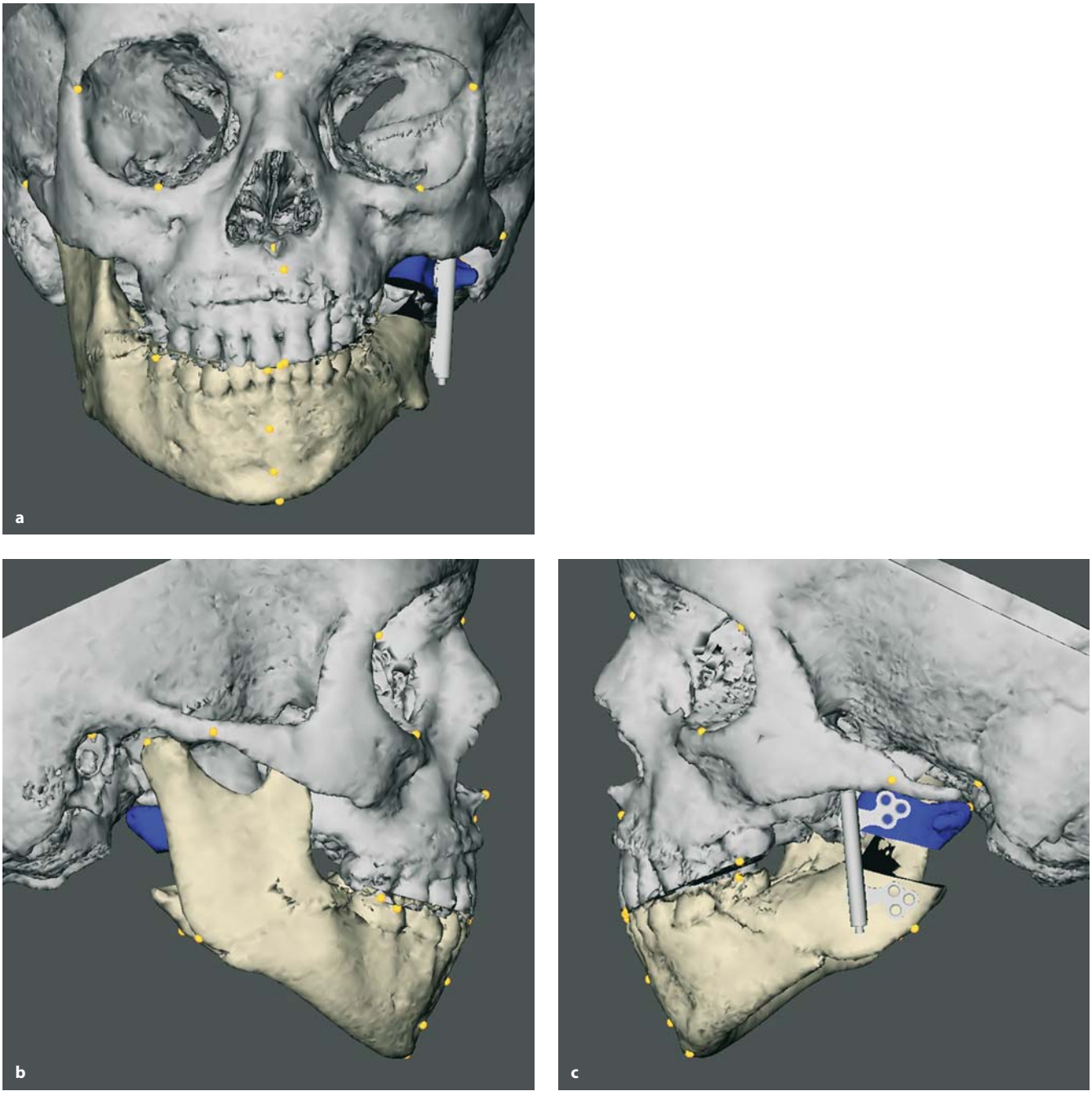

Fig. 9.31 a–c. Voxel-based virtual planning of 12 mm lengthening of the left vertical mandibular ramus by unidirectional distraction osteogenesis with the intra-oral Zurich Pediatric Ramus Distractor (Maxilim version 1.3.0. 3-D CT hard tissue surface representations with set-up of 3-D cephalometric hard tissue landmarks. **a** Frontal view; **b** profile view right; **c** profile view left. (3-D CT, patient H.T.)

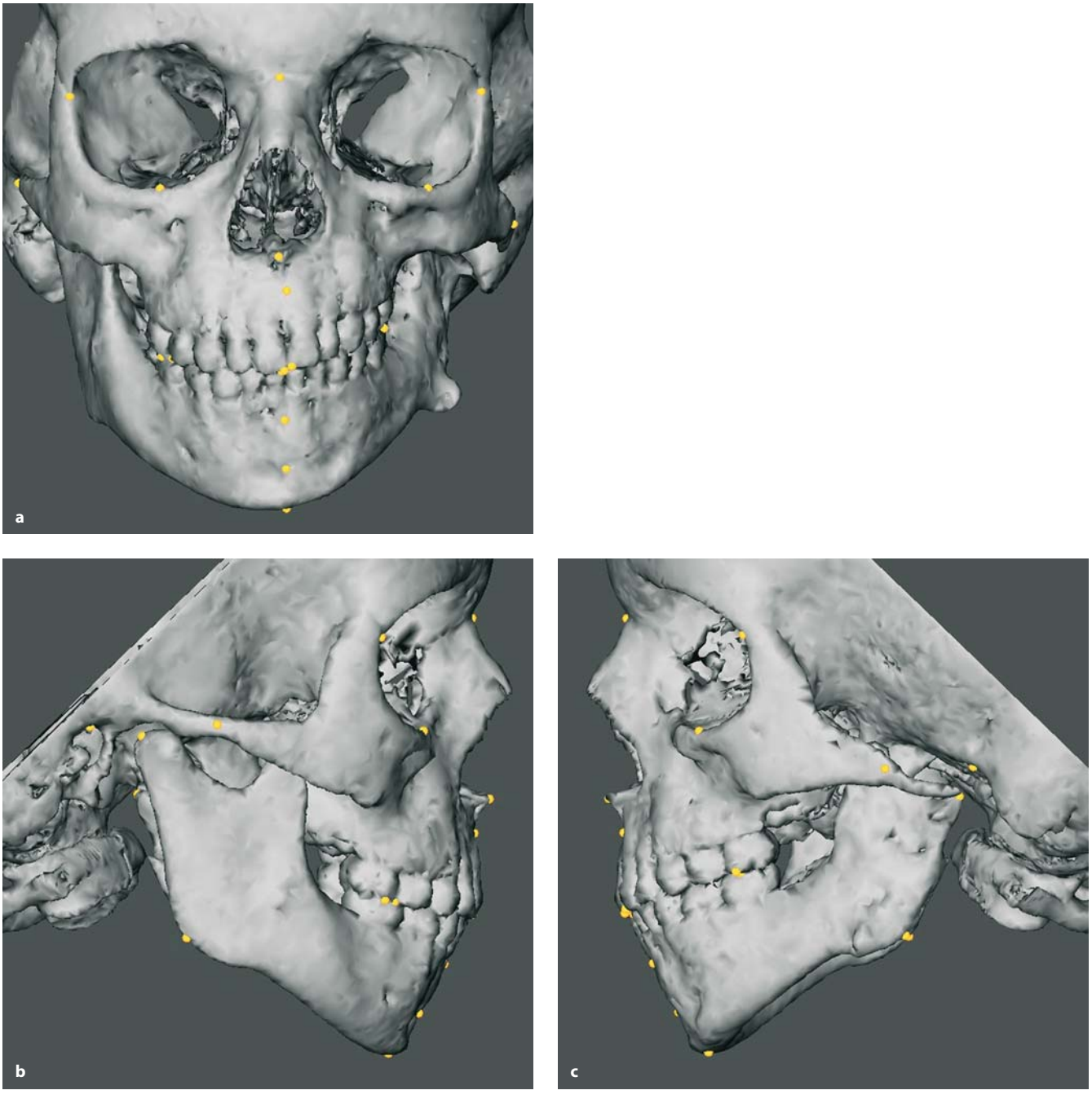

Fig. 9.32. Post-distraction 3-D CT hard tissue surface representations with set-up of 3-D cephalometric hard tissue landmarks. Note uprighting of the left mandibular vertical ramus with good morphology of the left gonial angle. **a** Frontal view; **b** profile view right; **c** profile view left. (3-D CT, patient H.T.)

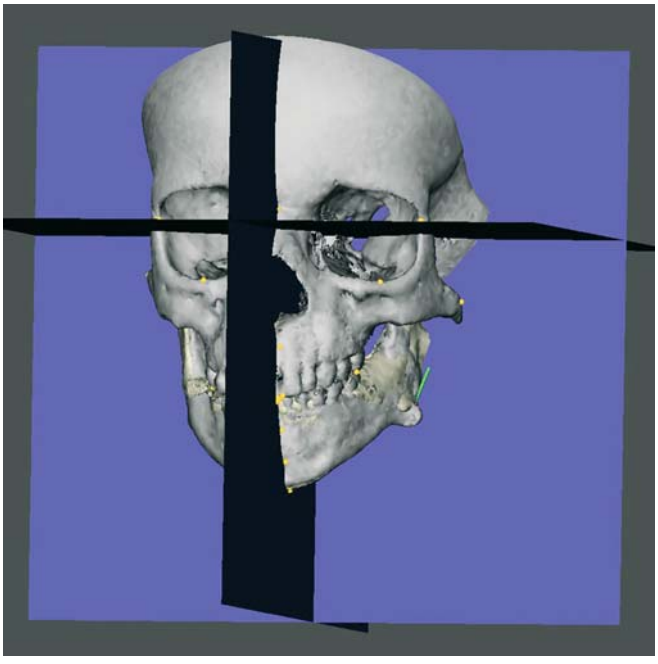

Fig. 9.33. Superimposition of pre-operative and post-distraction 3-D CT hard tissue surface representations using the 3-D cephalometric reference system (3-D CT, patient H.T.)

Table 9.4. The results of the voxel-based 3-D cephalometric hard tissue analysis showed a pleasing restoration of the left gonial angle. The uprighting of the left vertical ramus after DO also led to autorotation of the mandible with decrease in anterior lower facial height. The decrease in mandibular vertical ramus length in both the virtual planning and post-distraction results is misleading. Due to the uprighting of the left vertical ramus by DO, the position of the left Gonion landmark changed and moved posteriorly. The length of the mandibular vertical ramus remained, however, slightly undercorrected (patient H.T.)

Parameter	Pre-operative	Virtual planning	Post-operative
Co_l-Go_l (mm)	30.81	29.01	29.12
Go_l-Pog (mm)	55.59	61.97	59.95
Co_l-Pog (mm)	82.84	85.76	81.70
Go_r-Go_l (mm)	73.49	71.17	70.64
Co_r-Co_l (mm)	84.70	83.22	81.86
ANS-Men (mm)	53.38	53.26	51.65
S-Go (mm)	55.12	55.30	56.71
Occl-Pl frontal inclination (deg)	7.61	5.43	5.01
Md-Pl frontal inclination (deg)	4.92	0.36	1.54
Gonial $angle_l$ (deg)	165.65	*143.43*	*140.87*

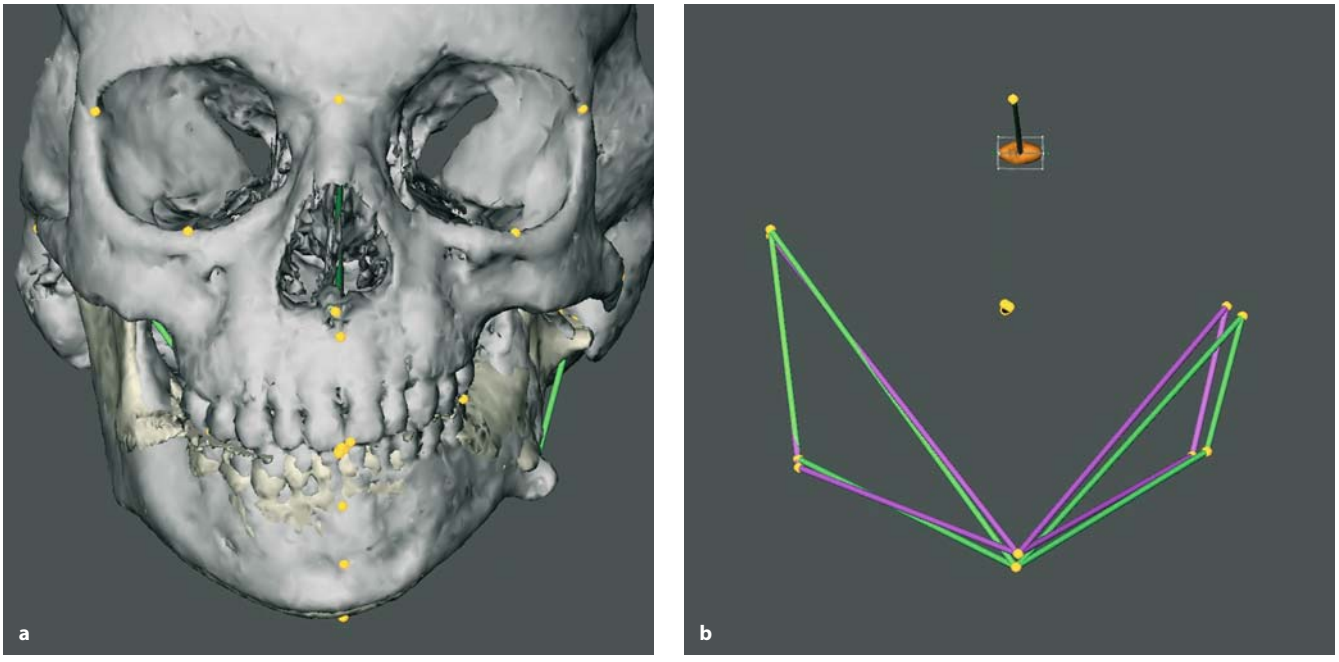

Fig. 9.34. Superimposition of pre-operative (*green*) and post-distraction (*purple*) 3-D CT hard tissue surface representations **(a)** and 3-D cephalometric tracings **(b)** using the 3-D cephalometric reference system. Frontal view. (3-D CT, patient H.T.)

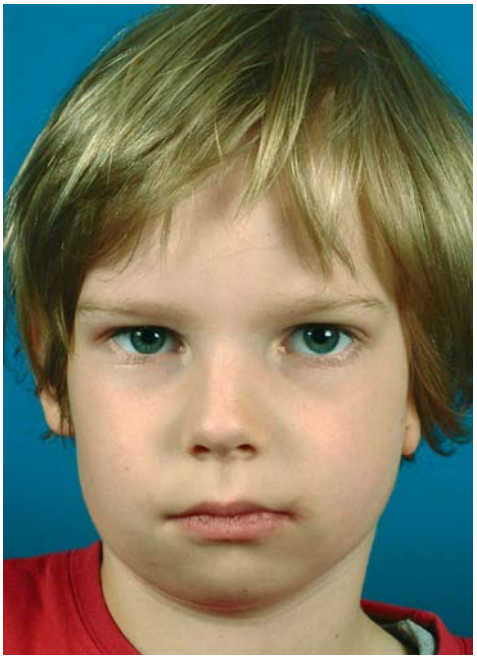

Fig. 9.35. Post-distraction clinical frontal view at 1 week after removal of the distraction device. Note good symmetry of the oral commissures and cheek contour. (patient H.T.)

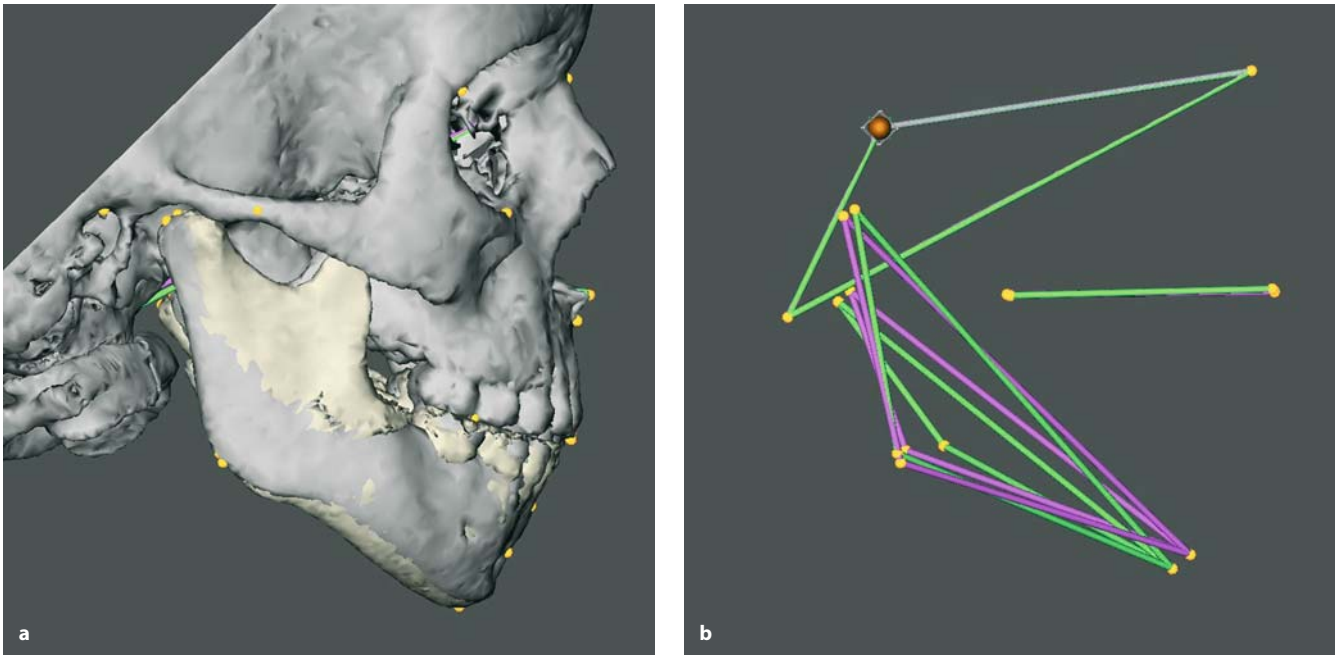

Fig. 9.36. Superimposition of pre-operative (*green*) and post-distraction (*purple*) 3-D CT hard tissue surface representations **(a)** and 3-D cephalometric tracings **(b)** using the 3-D cephalometric reference system. Profile view right. (3-D CT, patient H.T.)

Fig. 9.37. Pre-operative clinical right profile view (patient H.T.)

Fig. 9.38. Post-distraction clinical right profile view at 1 week after removal of the distraction device (patient H.T.)

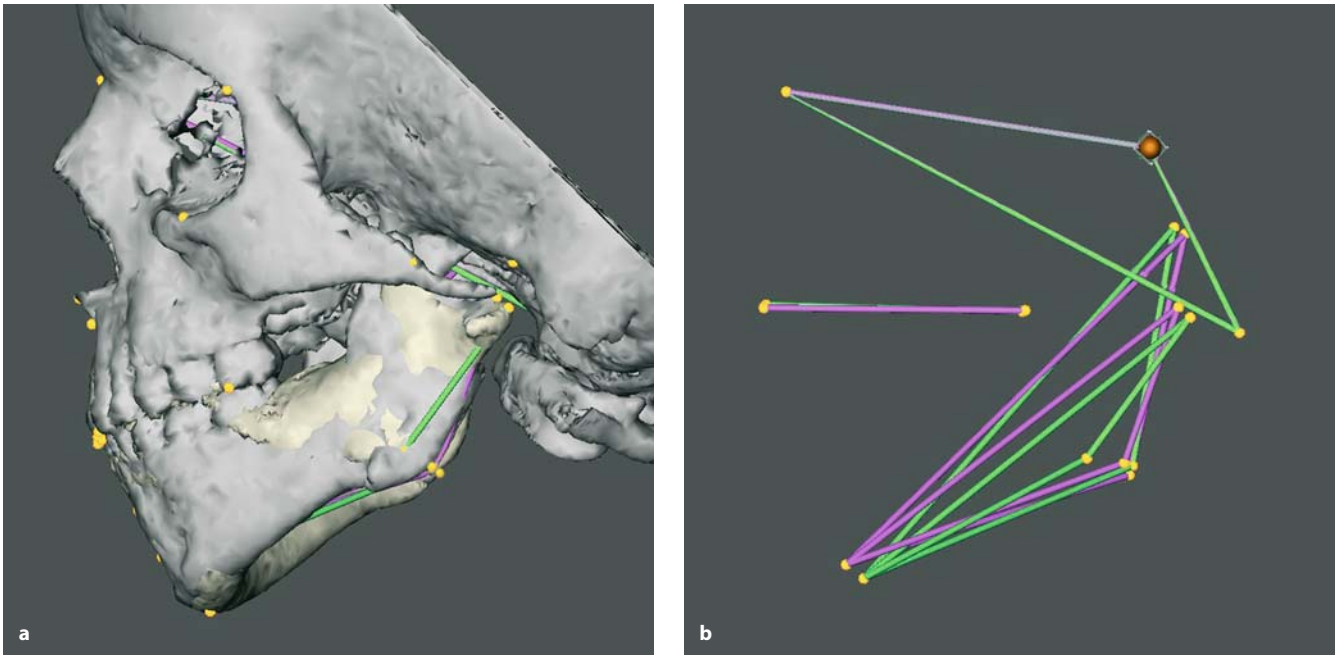

Fig. 9.39. Superimposition of pre-operative (*green*) and post-distraction (*purple*) 3-D CT hard tissue surface representations **(a)** and 3-D cephalometric tracings (**b**) using the 3-D cephalometric reference system. Note the uprighting of the left mandibular vertical ramus with closure of the left gonial angle. Profile view left. (3-D CT, patient H.T.)

Fig. 9.40. Pre-operative clinical left profile view (patient H.T.)

Fig. 9.41. Post-distraction clinical right profile view at 1 week after removal of the distraction device (patient H.T.)

Case 3

T.H. was a 56-year-old man with a recurrent carcinoma of the left mandible with infiltration of the buccal mucosa. The patient had undergone primary radiotherapy with a total radiation dose of 66 Gy for a squamous cell carcinoma of the tonsillar fossa several years before.

Panoramic X-ray and axial CT now showed extensive tumour infiltration of mandibular bone and soft tissues. Due to the extensive soft tissue infiltration, surgical planning included composite tumour resection of the left mandible and floor of the mouth and buccal mucosa with immediate primary micro-vascular reconstruction using a double-flap technique. For soft tissue reconstruction a radial forearm flap was selected. After thorough clinical and radiological investigation of the tumour, voxel-based virtual resection and reconstruction of the left mandible using a free fibula bone graft was planned. A modified voxel-based 3-D cephalometric hard tissue analysis allowed accurate planning of reconstruction of the left horizontal and vertical mandibular ramus as well as the left gonial angle. The ideal position and angulation of the osteotomies of the fibula bone graft could be calculated in the three planes (x, y, z) in order to create an ideal „best fit" of the neo-mandible into the resection site. To facilitate transfer of the voxel-based virtual planning into the operation theatre, an individual metal template was configured based on the 3-D cephalometric data. This approach allowed contouring of the fibula bone graft while it was still pedicled on the peroneal vessels, which significantly decreased the ischaemia time of the microsurgical bony transfer. The post-operative outcome was uneventful and no complications appeared.

After a 6-month follow-up period, no evidence of disease was found and the patient had almost undisturbed mandibular function. He showed a pleasing aesthetic reconstruction with good three-dimensional morphology and projection of the neo-mandible. 3-D cephalometric hard tissue analysis showed a nearly perfect reconstruction of the left gonial angle in the profile and base views. The frontal view, however, showed undercorrection of the left gonial angle (Figs. 9.42–9.52).

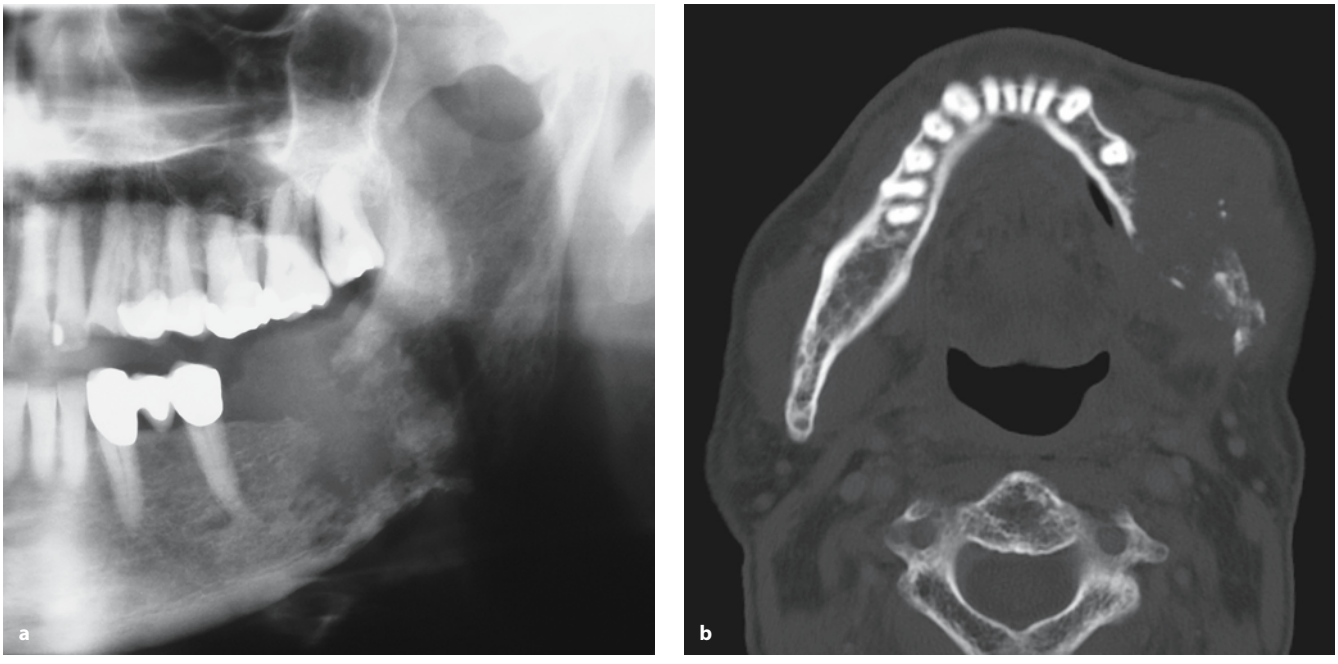

Fig. 9.42. A 56-year-old man diagnosed with a recurrent squamous cell carcinoma of the left mandible with infiltration of the buccal mucosa. Pre-operative panoramic X-ray **(a)** and axial CT **(b)** show the lesion. Note that application of an individual reconstruction template on the mandible is not possible due to extensive soft tissue infiltration (patient T.H.)

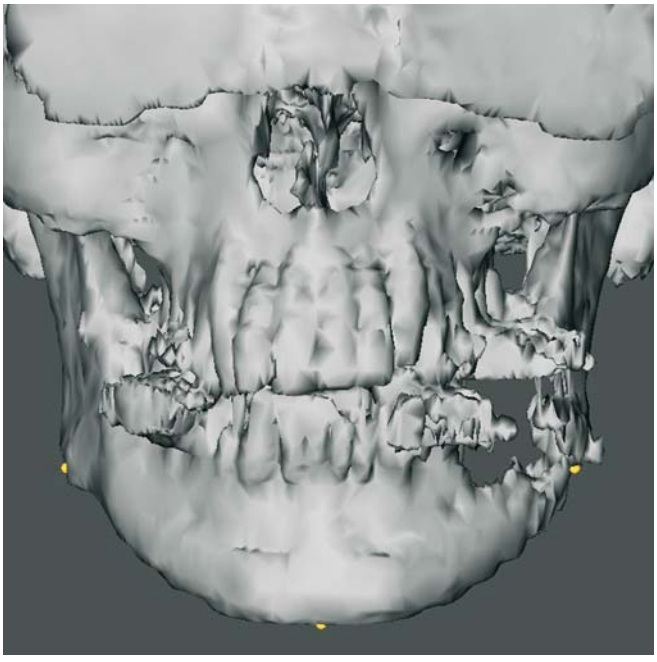

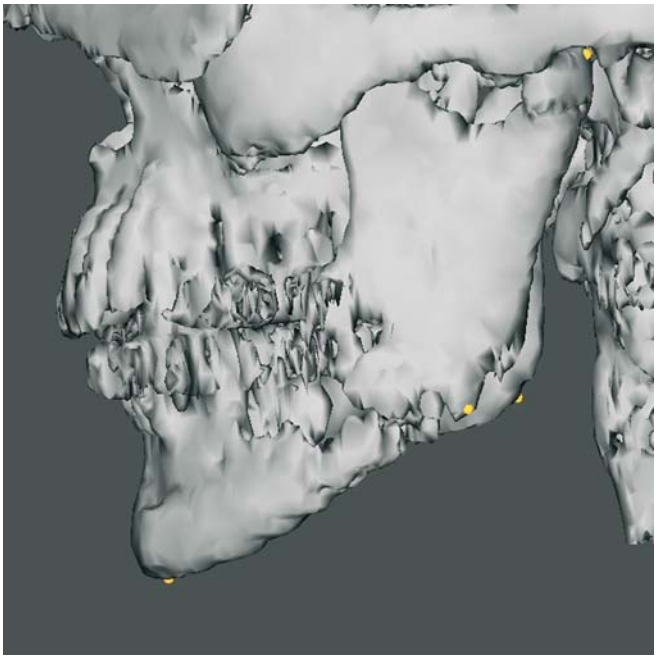

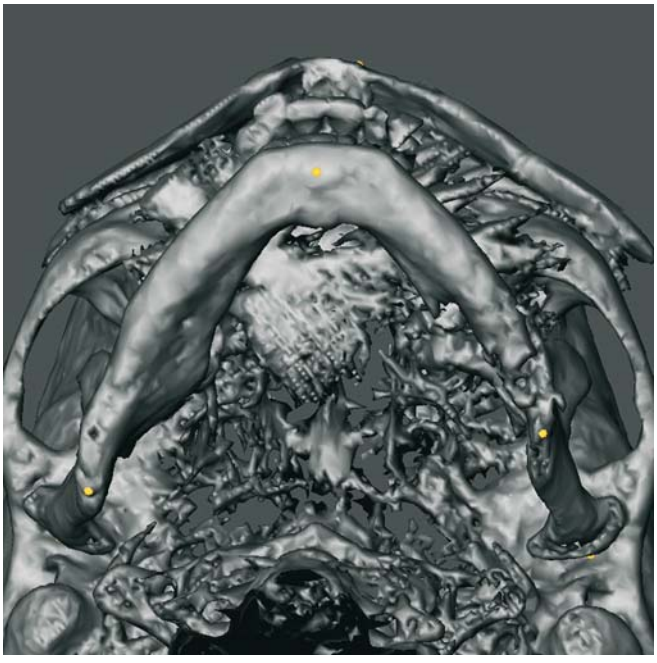

Fig. 9.43 a–c. Pre-operative 3-D CT hard tissue surface representations with set-up of 3-D cephalometric hard tissue landmarks. **a** Frontal view; **b** profile view left; **c** base view. Note that the quality of the 3-D CT hard tissue surface representations is less than ideal, because 3.75-mm axial slices from the spiral CT performed during pre-operative tumour staging were used. (3-D CT, patient T.H.)

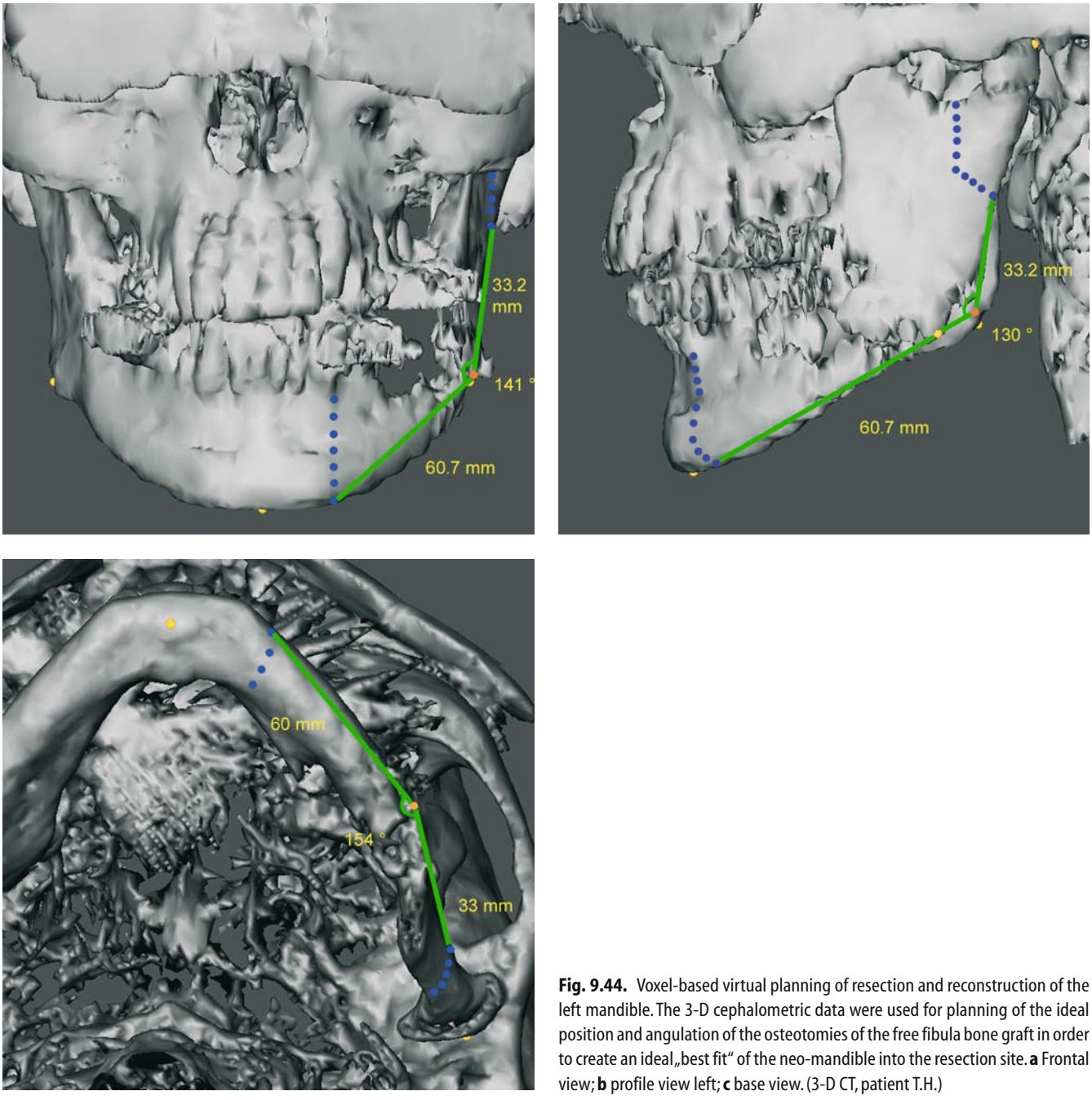

Fig. 9.44. Voxel-based virtual planning of resection and reconstruction of the left mandible. The 3-D cephalometric data were used for planning of the ideal position and angulation of the osteotomies of the free fibula bone graft in order to create an ideal „best fit" of the neo-mandible into the resection site. **a** Frontal view; **b** profile view left; **c** base view. (3-D CT, patient T.H.)

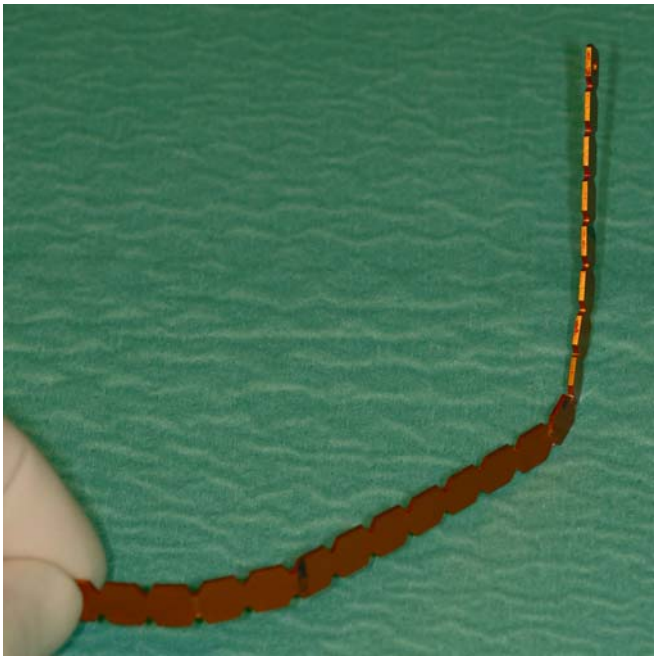

Fig. 9.45. A mandibular reconstruction template (Synthes, Bochum, Germany, http://www.synthes) was contoured using commercially available callipers based on the 3-D cephalometric data as an additional aid for optimal contouring of the free fibula bone graft

Fig. 9.46. Intra-operative clinical view shows contouring of the left fibula bone graft with titanium miniplates while is it still pedicled on the peroneal vessels to reduce ischaemia time. The ideal position and angulation of the osteotomies of the fibular bone graft were calculated using the 3-D cephalometric data and verified with the individual metal template (patient T.H.)

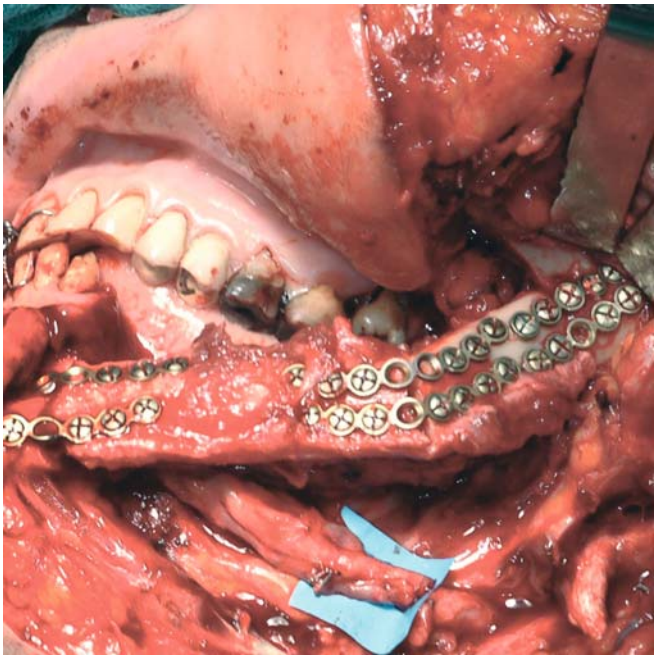

Fig. 9.47. Intra-operative clinical view shows osteosynthesis with miniplates of the contoured free fibula bone graft into the mandibular bony defect after tumour resection with micro-vascular anastomoses (patient T.H.)

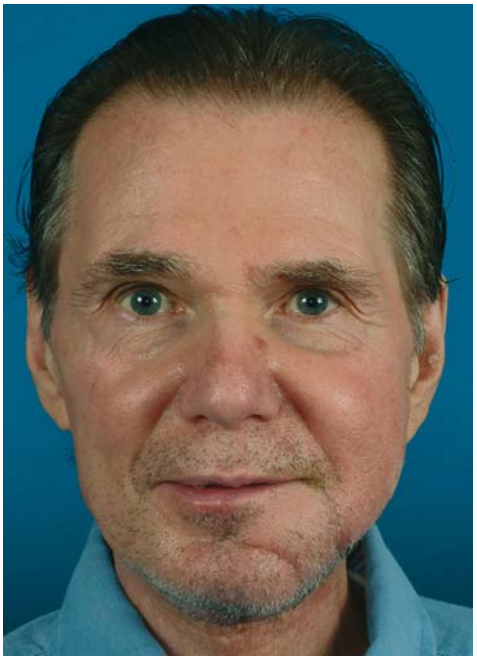

Fig. 9.48. Post-operative clinical frontal view at 1 month follow-up (patient T.H.)

Fig. 9.49. Post-operative clinical intra-oral view at 1 month follow-up shows good intra-oral soft tissue reconstruction with a free radial forearm flap (patient T.H.)

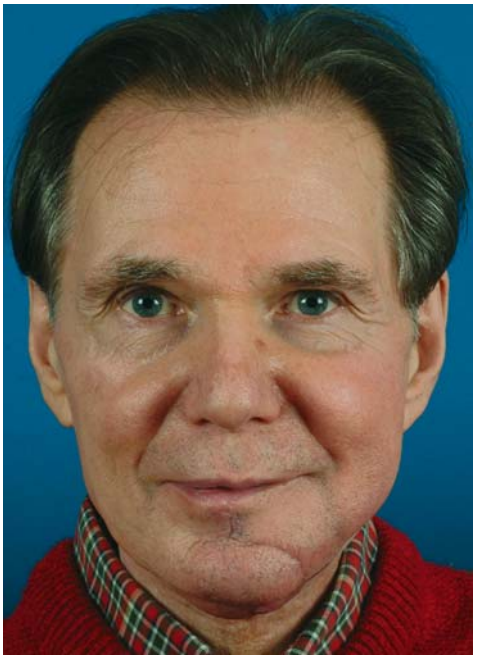

Fig. 9.50. Post-operative clinical frontal view at 6 months follow-up shows a pleasing aesthetic mandibular reconstruction (patient T.H.)

Fig. 9.51. Private clinical photograph of the same patient before his cancer disease (patient T.H.)

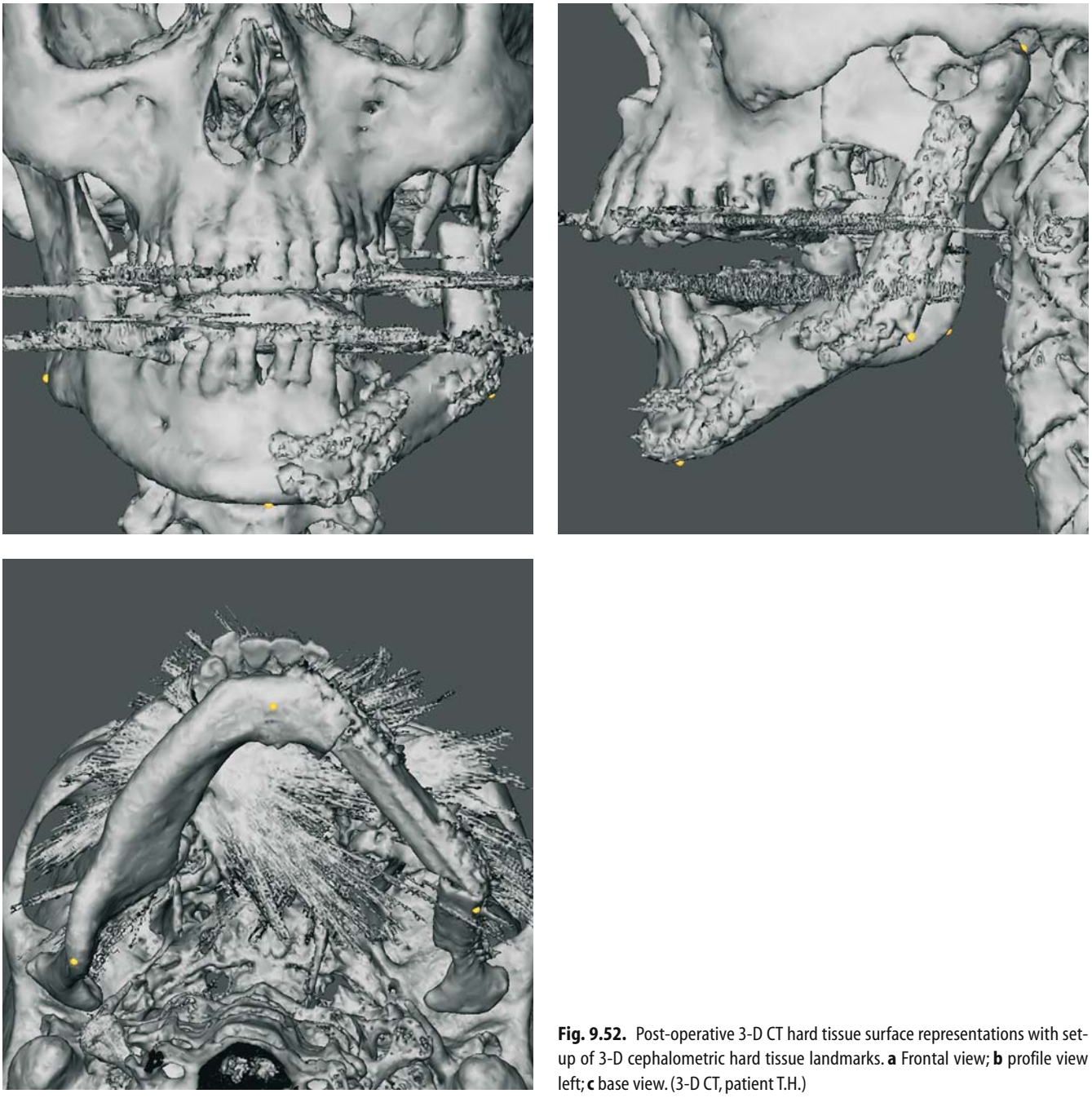

Fig. 9.52. Post-operative 3-D CT hard tissue surface representations with set-up of 3-D cephalometric hard tissue landmarks. **a** Frontal view; **b** profile view left; **c** base view. (3-D CT, patient T.H.)

Table 9.5. Results of a modified voxel-based 3-D cephalometric hard tissue analysis showed nearly perfect reconstruction of the left gonial angle in the profile and base views, while there was still some under-correction of the left gonial angle in the frontal view (patient T.H.)

	Pre-operative	Post-operative
Co_l-Go_l-Men $\perp$ *z*-plane (deg)	*138.79*	*141.08*
Co_l-Go_l-Men $\perp$ *x*-plane (deg)	*138.82*	*139.53*
Co_l-Go_l-Men $\perp$ *y*-plane (deg)	135.91	111.65

CHAPTER 10 Future Perspectives of 3-D Cephalometry

Gwen R. J. Swennen, Filip Schutyser

10.1 3-D Cephalometric Reference Data

Normative data on craniofacial morphology are essential for the assessment of the head and face. The literature provides a huge amount of conventional craniofacial data, mainly from cephalometric radiographs and anthropometric sources. However, age-, sex- and race-matched 3-D craniofacial normative datasets are not available yet. The necessity of collecting 3-D cross-sectional and longitudinal growth craniofacial reference data was pointed out by Hassfeld and co-workers. The effects of both growth and bone movements during surgery on the overlying soft tissue functional matrix also remain poorly understood.

3-D cephalometry of hard and soft tissues is a powerful measurement tool for the acquisition of 3-D craniofacial reference data because of its accuracy and reliability. Moreover, it has the advantage of providing both hard and soft tissue data and can therefore provide bone–soft tissue movement ratio data.

The challenge is to develop 3-D cephalometric reference data from birth to young adulthood, as has been done for conventional cephalometry and anthropometry. 3-D cephalometric reference data should be matched by age, sex and race and should ideally include:

- Normative hard and soft tissue craniofacial data
- Reference hard and soft tissue craniofacial data of congenital and developmental abnormalities
- Reference data on craniofacial bone–soft tissue movement ratios

These 3-D cephalometric reference data should be based on standardized CT protocols (see Chap. 1) and should include means and standard deviations. This will not be easy because from an ethical point of view, one cannot irradiate individuals just to obtain reference data. Hence, cooperation among craniofacial centres and intensive cooperation with radiological departments will be crucial to collect the necessary amount of reference data in the future.

Once available, reference 3-D cephalometric hard and soft tissue data will allow orthodontists, maxillofacial, craniofacial and plastic surgeons, medical anthropologists and genetic dysmorphologists to use these data for different clinical and research purposes, such as:

- Assessment of normal craniofacial morphology and dysmorphology (congenital and developmental)
- Assessment of craniofacial growth characteristics (e.g. rate of growth, changes of growth, prediction of growth)
- Assessment of treatment results
- Optimizing voxel-based surgical planning
- Optimizing surgical simulation of soft tissues
- Reconstruction of facial soft tissues (e.g. missing persons, ancient skulls)
- Optimizing manufacturing of custom-made craniofacial implants and epitheses

10.2 Registration of 3-D Cephalometric Data Sets with 3-D Photographs

An important shortcoming of CT-based 3-D cephalometry of soft tissues is improper or impossible identification of soft tissue landmarks that are related to hair (trichion, superciliare, frontotemporale) or eyelids (palpebrale superius, palpebrale inferius).

Registration of the natural texture of the face with the 3-D CT skin surface could be a solution. Several 3-D photographic techniques have been developed. With laser surface scanning, the skin surface is digitized by a laser scanner that consecutively senses the surface. Active systems project a pattern (e.g. a linear grid) on the patient's face. Based on the deformation of the grid on the photograph, 3-D depth information is obtained. Typically, several photos are combined to obtain a digitization of the complete face. Stereo imaging uses two or more cameras that acquire images simultaneously. Based on stereoscopic matching, 3-D depth information is computed. Another method to obtain a computerized surface model of the face is holographic imaging. After holographic acquisition, the hologram is digitized and a surface model is generated.

Although laser surface scanning permits very accurate measurements, this technique is quite slow, so that motion artefacts can impair the result. Active systems with multiple cameras (often a combination of active and stereoscopic methods) yield detailed face models with an acquisition time of a few milliseconds and are therefore very promising for the future. Holographic imaging has the potential for acquisition of a full face in a few nanoseconds but is still under development. Also the holographic digitization process needs further research.

De Groeve and co-workers have already shown that registration of 3-D photographs with spiral CT images provides an accurate match between the two surfaces. Our research group is currently testing the registration of 3-D CT data sets (Fig. 10.5) with commercially available 3-D photographic systems (Figs. 10.6–10.9.).

Acquisition of surface data using 3-D photographic techniques allows more detailed, textured rendering of facial surface structures (including hairline, eyebrows and eyelashes), which allows definition of the above-

Fig. 10.1. Soft tissue simulation of the patient (Chap. 9) who underwent right condylar reconstruction using intraoral unidirectional distraction osteogenesis (frontal view, 3-D CT soft tissue surface representation, patient B.R.). Soft tissue simulation is based on volumetric deformation algorithms including soft tissue properties such as elasticity and growth due to stress

Fig. 10.3. Soft tissue simulation of the same patient (right quarter view, 3-D CT soft tissue surface representation, patient B.R.)

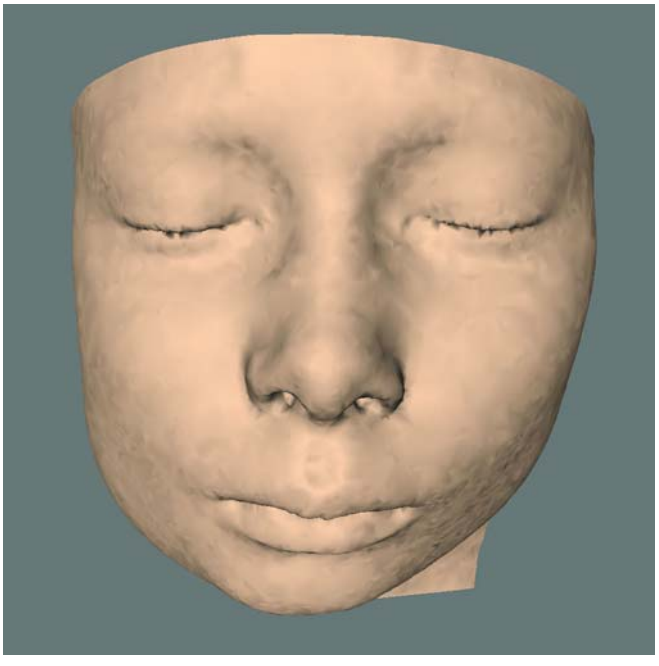

Fig. 10.2. Clinical post-operative result of the same patient (clinical frontal view, patient B.R.). Comparison of 3-D CT soft tissue simulation and the clinical outcome shows good similarity in chin position. An important discrepancy at the right mandibular angle is certainly partially due to post-operative swelling after distractor removal

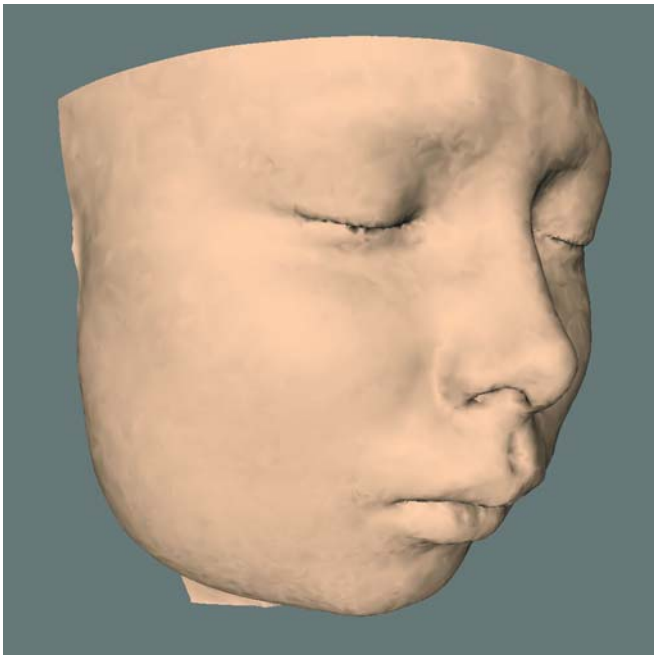

Fig. 10.4. Clinical post-operative result of the same patient (clinical right quarter view, patient B.R.). Comparison of 3-D CT soft tissue simulation and the clinical outcome illustrates the discrepancy at the right mandibular angle partially due to post-operative swelling after distractor removal

mentioned soft tissue landmarks. Moreover, acquisition of surface data using these systems involves no ionizing radiation and allows inexpensive serial soft-tissue data collection for long-term follow-up.

10.3 Visualization of 3-D Cephalometric Data with Stereoscopic Displays

Classically, the 3-D image content is rendered on a flat 2-D screen. Recent advances in computer hardware technology allow real-time, in-depth spatial viewing through the use of a new generation of so-called stereoscopic displays.

The key to in-depth spatial viewing of a 3-D image is presenting different views to the right and left eye. The difference between these two views is provided by a slightly different viewing position to mimic natural stereoscopic vision. The brain reconstructs the 3-D information and allows in-depth spatial viewing. Several techniques have been developed to realize in-depth spatial viewing. Currently, however, all systems have limited viewing angles.

An early attempt consisted of colour-coding the views. The user wears a special pair of glasses with one green and one red glass. In this way, reddish renderings are not visible for the eye with the red glass, and vice versa. The disadvantage of this method is that colour rendering is not possible.

Another technology is based on an alternative type of glasses, so-called shutter glasses. The computer screen renders first the image for the right eye and subsequently the image for the left eye. When the image for the right eye is rendered, the glass of the left eye is not transparent and vice versa. The computer screen and the glasses are synchronized. Typically the glasses consist of LCDs that switch between two states, "black" and "transparent".

More recently, auto-stereoscopic displays have been developed. Auto-stereoscopic 3-D displays incorporate a set of lenses, mounted on the computer screen. The lenses are manipulated in a way that the left eye sees one image, the right eye the other. Therefore, these displays track the position of the eyes. On the computer screen, every second vertical image line is viewed by one eye and the intervening lines by the other eye. The lenses ensure that the eyes see the appropriate images. A disadvantage is that the vertical resolution is divided by two because of the two images. Since the screen resolutions, however, are very large (e.g. 1600×1200 pixels) sufficient resolutions for detailed rendering are achieved.

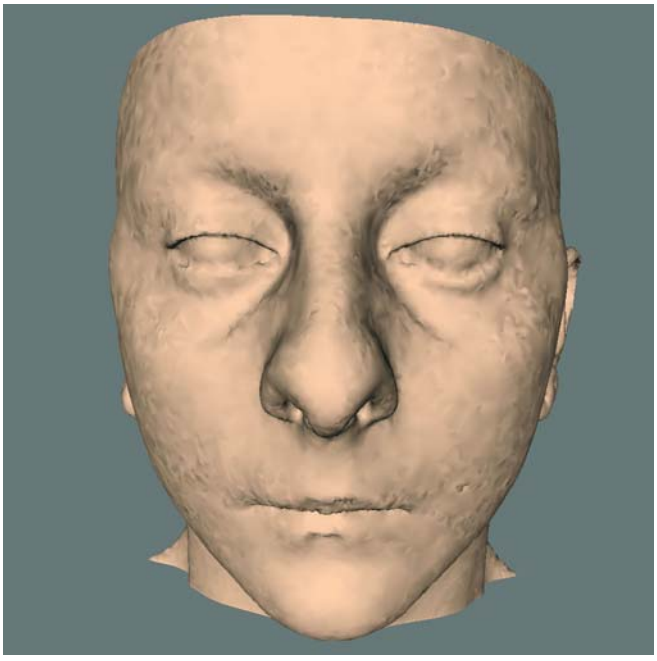

Fig. 10.5. 3-D CT soft tissue surface presentation (Maxilim, version 1.3, www.medicim.com) of a patient (patient F.L.)

Fig. 10.6. High-resolution full-face colour surface model of the same patient, acquired with a 3-D surface imaging system based on active stereo photogrammetry (Fig. 10.7.) (patient F.L.)

Fig. 10.7. Set-up of a commercial hardware system for 3-D surface imaging (3dMDface system, www.3dMD.com) based on active stereo photogrammetry

Stereoscopic viewing needs also in-depth spatial measurement tools. Our research group is currently testing different hardware tools (variants of the so-called space mouse) that allow in depth interaction for 3-D cephalometry. The accuracy and reliability, however, of in-depth spatial 3-D cephalometry has to be statistically validated.

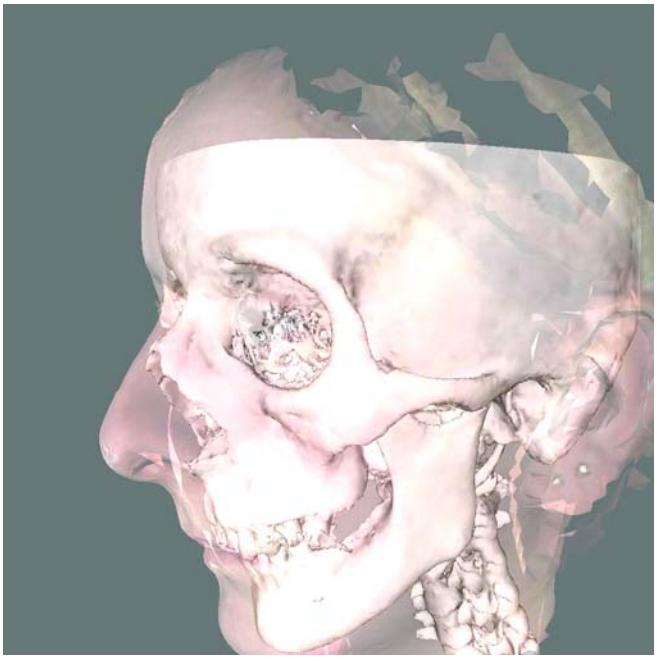

Figs. 10.8, 10.9. After registration of the 3-D photograph for 3-D CT, the texture map of the 3-D photograph is fitted onto the CT skin surface (Maxilim, version 1.3.0, www.medicim.com) (patient F.L.). In this way, all data remain related to the CT data. This technique allows identification of both bone- and hair-related soft tissue landmarks

Fig. 10.10. Workstation with a commercial auto-stereoscopic 3-D display (C-i display, www.seereal.com) for real time spatial in depth 3-D cephalometry

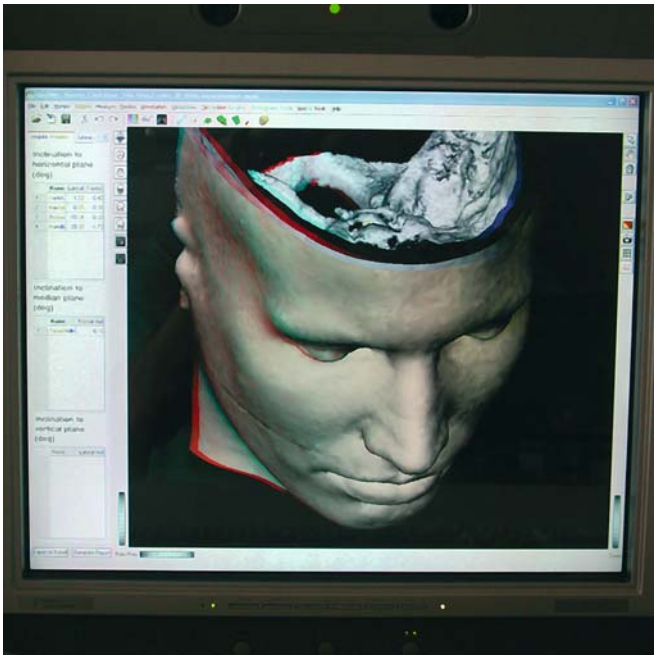

Fig. 10.11. Close-up view of auto-stereoscopic 3-D display (C-i display, www.seereal.com) (3-D CT hard and soft tissue surface presentation, patient K.C.)

References

Abbott AH, Netherway DJ, David DJ, Brown T. Craniofacial osseous landmark determination from stereo computer tomography reconstructions. Ann Acad Med Singapore. 1990; 19:595-604

Abbott AH, Netherway DJ, David DJ, Brown T. Application and comparison of techniques for three-dimensional analysis of craniofacial anomalies. J Craniofac. Surg. 1990; 1:119-134

Adams GL, Gansky SA, Miller AJ, Harrell WE, Jr., Hatcher DC. Comparison between traditional 2-dimensional cephalometry and a 3-dimensional approach on human dry skulls. Am J Orthod Dentofacial Orthop. 2004; 126:397-409

Akimoto M, Tamai J, Hyakusoku H, Fumiiri M. Three-dimensional CT system using a personal computer. Aesthetic Plast Surg. 1991; 15:181-185

Alcaniz M, Montserrat C, Grau V, Chinesta F, Ramon A, Albalat S. An advanced system for the simulation and planning of orthodontic treatment. Med Image Anal. 1998; 2:61-77

Altobelli DE, Kikinis R, Mulliken JB, Cline H, Lorensen W, Jolesz F. Computer-assisted three-dimensional planning in craniofacial surgery. Plast Reconstr Surg. 1993; 92:576-585

Arai Y, Tammisalo E, Iwai K, Hashimoto K, Shinoda K. Development of a compact computed tomographic apparatur for dental use. Dentomaxillofac Radiol. 1999; 28:245-248

Arridge SR, Moss JP, Linney AD. Three dimensional digitization of the face and skull. J Maxillofac Surg. 1985; 13:136-143

Athanasiou AE. Orthodontic cephalometry. London: Mosby-Wolfe; 1995

Aulsebrook WA, Iscan MY, Slabbert JH, Becker P. Superimposition and reconstruction in forensic facial identification: a survey. Forensic Sci Int. 1995; 75:101-120

Aung SC, Ngim RC, Lee ST. Evaluation of the laser scanner as a surface measuring tool and its accuracy compared with direct facial anthropometric measurements. Br J Plast Surg. 1995; 48:551-558

Aung SC. The role of laser surface imaging in the evaluation of craniomaxillofacial disorders: the Singapore General Hospital experience. Ann Acad Med Singapore. 1999; 28:714-720

Ayoub AF, Wray D, Moos KF, Siebert P, Jin J, Niblett TB, Urquhart C, Mowforth R. Three-dimensional modeling for modern diagnosis and planning in maxillofacial surgery. Int J Adult Orthodon Orthognath Surg. 1996; 11:225-233

Ayoub A, Garrahy A, Hood C, White J, Bock M, Siebert JP, Spencer R, Ray A. Validation of a vision-based, three-dimensional facial imaging system. Cleft Palate Craniofac J. 2003; 40:523-529

Bacher M, Goz G, Pham T, Bacher U, Werner O, Buchner P, Bacher A. Three-dimensional analysis of cleft palate topology in newborn infants with reference to the cranial skeleton. Cleft Palate Craniofac J. 1998; 35:379-395

Baumrind S, Peltzman P, Moffitt FH. New system for integrated three dimensional craniofacial mapping. J Dent Res. 1971; 50:1496-1497

Baumrind S, Moffitt FH, Curry S. The geometry of three-dimensional measurement from paired coplaner x-ray images. Am J Orthod. 1983; 84:313-322

Baumrind S, Carlson S, Beers A, Curry S, Norris K, Boyd RL. Using three-dimensional imaging to assess treatment outcomes in orthodontics: a progress report from the University of the Pacific. Orthod Craniofac Res. 2003; 6 Suppl 1:132-142

Beckmann G, Wingberg J, Hasund A. Computer-assisted cephalometry using the Bergen technic. Fortschr Kieferorthop. 1983; 44:359-369

Benateau H, Chevallier E, Hamon M, Edy E, Keswani R, Labbe D, Schmutz G, Compere JF. The three-dimensional spiral scanner and volume rendering technique: importance in craniofacial traumatology and reconstructive surgery. Rev Stomatol Chir Maxillofac. 2002; 103:233-238

Benfer RA. Morphometric analysis of Cartesian coordinates of the human skull. Am J Phys Anthropol. 1975; 42:371-382

Bernhard M, Schafer K, Seidler H. Numerical description of selected endo- and ectocranial dimensions in Homo sapiens and the three Homo heidelbergensis: Kabwe, Atapuerca and Petralona. Anthropol Anz. 2002; 60:321-332

Bettega G, Chenin M, Sadek H, Cinquin P, Lebeau J, Coulomb M, Raphael B. Three-dimensional fetal cephalometry. Cleft Palate Craniofac J. 1996; 33:463-467

Bettega G, Payan Y, Mollard B, Boyer A, Raphael B, Lavallee S. A simulator for maxillofacial surgery integrating 3D cephalometry and orthodontia. Comput Aided Surg. 2000; 5:156-165

Bhatia G, Vannier MW, Smith KE, Commean PK, Riolo J, Young VL. Quantification of facial surface change using a structured light scanner. Plast Reconstr Surg. 1994; 94:768-774

Bill JS, Reuther JF, Dittmann W, Kübler N, Meier JL, Pistner H, Wittenberg G. Stereolithography in oral and maxillofacial operation planning. Int J Oral Maxillofac Surg. 1995; 24:98-103

Bland J.M., Altman D. Statistical methods for assesing agreement between two methods of clinical measurement. Lancet. 1986; 8:307-310

Bland JM, Clinical measurement. In: Bland J.M. ed., An introduction to medical statistics. Third Edition. Oxford: Oxford University Press 2000; 15

Booth PA, Eppley B, Schmelzeisen R. Maxillofacial trauma and esthetic reconstruction. Edinburgh: Churchill Livingstone; 2003

Bou C, Pomar P, Pessey JJ, Rabino-Massa E. Three-dimensional facial reconstruction of computerized tomography images by computer-aided design: example of an anthropologic study. Rev Laryngol Otol Rhinol (Bord). 1998; 119:333-335

Brief J, Hassfeld S, Dauber S, Pernozzoli A, Munchenberg J, Redlich T, Walz M, Krempien R, Weisser H, Poeckler C, Raczkowsky J, Burgert O, Salb T, Kotrikova B, Rembold U, Worn H, Dillmann R, Muhling J. 3D norm data: the first step towards semiautomatic virtual craniofacial surgery. Comput Aided Surg. 2000; 5:353-358

Broadbent BH. A new technique and its application to orthodontics. Angle Orthodont. 1931; 1: 45

Broadbent BH. Bolton standards of dentofacial developmental growth. Saint Louis: C.V. Mosby; 1975

Bruce V, Burton M, Doyle T, Dench N. Further experiments on the perception of growth in three dimensions. Percept Pschophys. 1989; 46:528-536

Bruce V, Healey P, Burton M, Doyle T, Coombes A, Linney A. Recognising facial surfaces. Perception. 1991; 20:755-769

Budai M, Farkas LG, Tompson B, Katic M, Forrest CR. Relation between anthropometric and cephalometric measurements and proportions of the face of healthy young white adult men and women. J Craniofac Surg. 2003; 14:154-161

Buranarugsa M, Houghton P. Polynesian head form: an interpretation of a factor analysis of Cartesian co-ordinate data. J Anat. 1981; 133:333-350

Buschang PH, Tanguay R, Demirjian A. Cephalometric reliability. A full ANOVA model for the estimation of true and error variance. Angle Orthod. 1987; 57:168-175

Bush K, Antonyshyn O. Three-dimensional facial anthropometry using a laser surface scanner: validation of the technique. Plast Reconstr Surg. 1996; 98:226-235

Butow KW, van der Walt PJ. The use of triangle analysis for cephalometric analysis in three dimensions. J Maxillofac Surg. 1984; 12:62-70

Cakirer B, Dean D, Palomo JM, Hans MG. Orthognathic surgery outcome analysis: 3-dimensional landmark geometric morphometrics. Int J Adult Orthodon Orthognath Surg. 2002; 17:116-132

Caruso PA, Harris GJ, Padwa BL. CT imaging of craniofacial malformations. Neuroimaging Clin N Am. 2003; 13:541-572

Cavalcanti MGP, Vannier MW. Quantitative analysis of spiral computed tomography for craniofacial clinical applications. Dentomaxillofac Radiol. 1998; 27:344-350

Cavalcanti MG, Haller JW, Vannier MW. Three-dimensional computed tomography landmark measurement in craniofacial surgical planning: experimental validation in vitro. J Oral Maxillofac Surg. 1999; 57:690-694

Cavalcanti MG, Rocha SS, Vannier MW. Craniofacial measurements based on 3D-CT volume rendering: implications for clinical applications. Dentomaxillofac Radiol. 2004; 33:170-176

Cerovac S, Neil-Dwyer JG, Rich P, Jones BM, Hayward RD. Are routine preoperative CT scans necessary in the management of single suture craniosynostosis? Br J Neurosurg. 2002; 16:348-354

Chang PS, Parker TH, Patrick CW, Jr., Miller MJ. The accuracy of stereolithography in planning craniofacial bone replacement. J Craniofac Surg. 2003; 14:164-170

Chassagne JF, Corbel S, Gimenez F, Chassagne S, Gerard H. Rapid prototyping and bone reconstruction. Ann Chir Plast Esthet. 1999; 44:515-524

Cheah CM, Chua CK, Tan KH, Teo CK. Integration of laser surface digitizing with CAD/CAM techniques for developing facial prostheses. Part 1: Design and fabrication of prosthesis replicas. Int J Prosthodont. 2003; 16:435-441

Cheah CM, Chua CK, Tan KH. Integration of laser surface digitizing with CAD/CAM techniques for developing facial prostheses. Part 2: Development of molding techniques for casting prosthetic parts. Int J Prosthodont. 2003; 16:543-548

Chen LH, Tsutsumi S, Hyo Y, Iizuka T. A rapid three-dimensional measurement system for facial morphology by laser multi-slits. Int J Prosthodont. 1993; 6:573-578

Chen LH, Tsutsumi S, Iizuka T. A CAD/CAM technique for fabricating facial prostheses: a preliminary report. Int J Prosthodont. 1997; 10:467-472

Chen LH, Chen WH. Three-dimensional computer-assisted simulation combining facial skeleton with facial morphology for orthognathic surgery. Int J Adult Orthodon Orthognath Surg. 1999; 14:140-145

Cheung LK, Wong MC, Wong LL. Refinement of facial reconstructive surgery by stereo-model planning. Ann R Australas Coll Dent Surg. 2002; 16:129-132

Chidiac JJ, Shofer FS, Al-Kutoub A, Laster LL, Ghafari J. Comparison of CT scanograms and cephalometric radiographs in craniofacial imaging. Orthod Craniofac Res. 2002; 5:104-113

Choi JY, Choi JH, Kim NK, Lee JK, Kim MK, Lee JH, Kim MJ. Analysis of errors in medical rapid prototyping models. Int J Oral Maxillofac Surg. 2002; 31:23-32

Chu SA, Skultety KJ, Suvinen TI, Clement JG, Price C. Computerized three-dimensional magnetic resonance imaging reconstructions of temporomandibular joints for both a model and patients with temporomandibular pain dysfunction. Oral Surg Oral Med Oral Pathol Oral Radiol Endod. 1995; 80:604-611

Cohen SR. Three-dimensional imaging and computer-generated models. Plast Reconstr Surg. 1994; 94:211-218

Coombes AM, Moss JP, Linney AD, Richards R, James DR. A mathematical method for the comparison of three-dimensional changes in the facial surface. Eur J Orthod. 1991; 13:95-110

Coward TJ, Watson RM, Scott BJ. Laser scanning for the identification of repeatable landmarks of the ears and face. Br J Plast Surg. 1997; 50:308-314

Csaszar GR, Niederdellmann H. Reliability of bimaxillary surgical planning with the 3-D orthognathic surgery simulator. Int J Adult Orthodon Orthognath Surg. 2000; 15:51-58

Cutting C, Grayson B, Bookstein F, Fellingham L, McCarthy JG. Computer-aided planning and evaluation of facial and orthognathic surgery. Clin Plast Surg. 1986; 13:449-462

Cutting CB, McCarthy JG, Karron DB. Three-dimensional input of body surface data using a laser light scanner. Ann Plast Surg. 1988; 21:38-45

D'Urso PS, Barker TM, Earwaker WJ, Bruce LJ, Atkinson RL, Lanigan MW, Arvier JF, Effeney DJ. Stereolithographic biomodelling in cranio-maxillofacial surgery: a prospective trial. J Craniomaxillofac Surg. 1999; 27:30-37

Da Silveira AC, Daw JL, Jr., Kusnoto B, Evans C, Cohen M. Craniofacial applications of three-dimensional laser surface scanning. J Craniofac Surg. 2003; 14:449-456

Dahan J. Three-dimensional cephalometry in orthodontics. Rev Belge Med Dent. 1973; 28:329-340

Danforth RA, Dus I, Mah J. 3-D volume imaging for dentistry: a new dimension. J Calif Dent Assoc. 2003; 31:817-23

Danforth RA. Cone beam volume tomography: a new digital imaging option for dentistry. J Calif Dent Assoc. 2003; 31:814-815

Darwis WE, Messer LB, Thomas CD. Assessing growth and development of the facial profile. Pediatr Dent. 2003; 25:103-108

Deacon AT, Anthony AG, Bhatia SN, Muller JP. Evaluation of a CCD-based facial measurement system. Med Inform (Lond). 1991; 16:213-228

Dean D, Hans MG, Bookstein FL, Subramanyan K. Three-dimensional Bolton-Brush Growth Study landmark data: ontogeny and sexual dimorphism of the Bolton standards cohort. Cleft Palate Craniofac J. 2000; 37:145-156

De Groeve P, Schutyser F, Van Cleynenbreugel J, Suetens P. Registration of 3D photographs with spiral CT images for soft tissue simulation in maxillofacial surgery. Lecture notes in computer science. Springer-Verlag Berlin Heidelberg: 2001; 2208:991-996

Delaire J, Schendel SA, Tulasne JF. An architectural and structural craniofacial analysis: a new lateral cephalometric analysis. Oral Surg Oral Med Oral Pathol. 1981; 52:226-238

Delaire J. Pitfalls in the interpretation of cephalometric teleradiography. Rev Stomatol Chir Maxillofac. 1984; 85:176-185

Delaire J. Craniofacial architectural equilibrium in orthodontics and orthognathic surgery. Orthod Fr. 1985; 56:353-364

Douglas TS, Meintjes EM, Vaughan CL, Viljoen DL. Role of depth in eye distance measurements: comparison of single and stereo-photogrammetry. Am J Hum Biol. 2003; 15:573-578

Douglas TS. Image processing for craniofacial landmark identification and measurement: a review of photogrammetry and cephalometry. Comput Med Imaging Graph. 2004; 28:401-409

Douglas TS, Vaughan CL, Wynne SM. Three-dimensional point localisation in low-dose X-ray images using stereo-photogrammetry. Med Biol Eng Comput. 2004; 42:37-43

Duffy S, Noar JH, Evans RD, Sanders R. Three-dimensional analysis of the child cleft face. Cleft Palate Craniofac J. 2000; 37:137-144

Duterloo HS, Kragt G, Algra AM. Holographic and cephalometric study of the relationship between craniofacial morphology and the initial reactions to high-pull headgear traction. Am J Orthod. 1985; 88:297-302

Eckardt A, Swennen G. Virtual planning of composite mandibular reconstruction with free fibula bone graft. J Craniofac Surg. In press.

elBalso AM, Hall RE. Advances in maxillofacial imaging. Curr Probl Diagn Radiol. 1993; 22:91-142

Enciso R, Memon A, Mah J. Three-dimensional visualization of the craniofacial patient: volume segmentation, data integration and animation. Orthod Craniofac Res. 2003; 6 Suppl 1:66-71

Enciso R, Memon A, Fidaleo DA, Neumann U, Mah J. The virtual craniofacial patient: 3D jaw modeling and animation. Stud Health Technol Inform. 2003; 94:65-71

Enciso R, Lewis JP, Neumann U, Mah J. 3D tooth shape from radiographs using thin-plate splines. Stud Health Technol Inform. 2003; 94:62-64

Enlow DH, Hans MG. Essentials of facial growth. Philadelphia: W.B. Saunders; 1996

Eppley BL. Craniofacial reconstruction with computer-generated HTR patient-matched implants: use in primary bony tumor excision. J Craniofac Surg. 2002; 13:650-657

Erickson M, Caruso JM, Leggitt L. Newtom QR-DVT 9000 imaging used to confirm a clinical diagnosis of iatrogenic mandibular nerve paresthesia. J Calif Dent Assoc. 2003; 31:843-845

Eufinger H, Wehmoller M, Machtens E, Heuser L, Harders A, Kruse D. Reconstruction of craniofacial bone defects with individual alloplastic implants based on CAD/CAM-manipulated CT-data. J Craniomaxillofac Surg. 1995; 23:175-181

Eufinger H, Wehmoller M. Individual prefabricated titanium implants in reconstructive craniofacial surgery: clinical and technical aspects of the first 22 cases. Plast Reconstr Surg. 1998; 102:300-308

Eufinger H, Saylor B. Computer-assisted prefabrication of individual craniofacial implants. Aorn J. 2001; 74:648-654

Evenhouse R, Rasmussen M, Sadler L. Computer-aided forensic facial reconstruction. J Biocommun. 1992; 19:22-28

Falk A, Gielen S, Heuser. CT data acquisation as a basis for modern diagnosis and therapy in maxillofacial surgery. Int J Oral Maxillofac Surg. 1995; 24:69-75

Farkas LG, Lindsay WK. Morphology of the adult face following repair of bilateral cleft lip and palate in childhood. Plast Reconstr Surg. 1971; 47:25-32

Farkas LG, Lindsay WK. Morphology of the orbital region in adults following the cleft lip-palate repair in childhood. Am J Phys Anthropol. 1972; 37:65-73

Farkas LG, Lindsay WK. Morphology of adult face after repair of isolated cleft palate in childhood. Cleft Palate J. 1972; 9:132-142

Farkas LG, Lindsay WK. Morphology of the adult face following repair of unilateral cleft lip and palate in childhood. Plast Reconstr Surg. 1973; 52:652-655

Farkas LG, James JS. Anthropometry of the face in lateral facial dysplasia: the unilateral form. Cleft Palate J. 1977; 14:193-199

Farkas LG, Ross RB, James JS. Anthropometry of the face in lateral facial dysplasia: the bilateral form. Cleft Palate J. 1977; 14:41-51

Farkas LG. Anthropometry of normal and anomalous ears. Clin Plast Surg. 1978; 5:401-412

Farkas LG. Vertical location of the ear, assessed by the Leiber test, in healthy North American Caucasians 6–19 years of age. Arch Otorhinolaryngol. 1978; 220:9-13

Farkas LG. Ear morphology in Treacher Collins', Apert's, and Crouzon's syndromes. Arch Otorhinolaryngol. 1978; 220:153-157

Farkas LG, Cheung GC. Nostril asymmetry: microform of cleft lip palate? An anthropometrical study of healthy North American caucasians. Cleft Palate J. 1979; 16:351-357

Farkas LG, Cheung G. Orbital measurements in the presence of epicanthi in healthy North American Caucasians. Ophthalmologica. 1979; 179:309-315

Farkas LG, Bryson W, Klotz J. Is photogrammetry of the face reliable? Plast Reconstr Surg. 1980; 66:346-355

Farkas LG, Cheung G. Facial asymmetry in healthy North American Caucasians. An anthropometrical study. Angle Orthod. 1981; 51:70-77

Farkas LG, Deutsch CK. Two new instruments to identify the standard positions of the head and face during anthropometry. Plast Reconstr Surg. 1982; 69:879-880

Farkas LG, Hreczko TA, Deutsch CK. Objective assessment of standard nostril types – a morphometric study. Ann Plast Surg. 1983; 11:381-389

Farkas LG, Katic MJ, Hreczko TA, Deutsch C, Munro IR. Anthropometric proportions in the upper lip-lower lip-chin area of the lower face in young white adults. Am J Orthod. 1984; 86:52-60

Farkas LG, Katic MJ, Kolar J, Munro IR. The adult facial profile: relationships between the inclinations of its segments. Dtsch Z Mund Kiefer Gesichtschir. 1984; 8:182-186

Farkas LG, Deutsch CK, Hreczko TA. Asymmetries in nostrils and the surrounding tissues of the soft nose – a morphometric study. Ann Plast Surg. 1984; 12:10-15

Farkas LG, Kolar JC, Munro IR. Craniofacial disproportions in Apert's syndrome: an anthropometric study. Cleft Palate J. 1985; 22:253-265

Farkas LG, Sohm P, Kolar JC, Katic MJ, Munro IR. Inclinations of the facial profile: art versus reality. Plast Reconstr Surg. 1985; 75:509-519

Farkas LG, Hreczko TA, Kolar JC, Munro IR. Vertical and horizontal proportions of the face in young adult North American Caucasians: revision of neoclassical canons. Plast Reconstr Surg. 1985; 75:328-338

Farkas LG, Munro IR, Kolar JC. Abnormal measurements and disproportions in the face of Down's syndrome patients: preliminary report of an anthropometric study. Plast Reconstr Surg. 1985; 75:159-169

Farkas LG, Kolar JC, Munro IR. Geography of the nose: a morphometric study. Aesthetic Plast Surg. 1986; 10:191-223

Farkas LG, Kolar JC. Anthropometrics and art in the aesthetics of women's faces. Clin Plast Surg. 1987; 14:599-616

Farkas LG, Kolar JC. Anthropometric guidelines in cranio-orbital surgery. Clin Plast Surg. 1987; 14:1-16

Farkas LG, Ngim RC, Lee ST. The fourth dimension of the face: a preliminary report of growth potential in the face of the Chinese population of Singapore. Ann Acad Med Singapore. 1988; 17:319-327

Farkas LG, Posnick JC, Winemaker MJ. Orbital protrusion index in Treacher-Collins syndrome: a tool for determining the degree of soft-tissue damage. Dtsch Z Mund Kiefer Gesichtschir. 1989; 13:429-432

Farkas LG, Ross RB, Posnick JC, Indech GD. Orbital measurements in 63 hyperteloric patients. Differences between the anthropometric and cephalometric findings. J Craniomaxillofac Surg. 1989; 17:249-254

Farkas LG, Posnick JC. Detailed morphometry of the nose in patients with Treacher Collins syndrome. Ann Plast Surg. 1989; 22:211-219

Farkas LG. Anthropometry of the normal and defective ear. Clin Plast Surg. 1990; 17:213-221

Farkas LG, Posnick JC, Hreczko T. Anthropometry of the head and face in 95 Down syndrome patients. Prog Clin Biol Res. 1991; 373:53-97

Farkas LG, Posnick JC, Hreczko TM. Anthropometric growth study of the ear. Cleft Palate Craniofac J. 1992; 29:324-329
Farkas LG, Posnick JC, Hreczko TM, Pron GE. Growth patterns of the nasolabial region: a morphometric study. Cleft Palate Craniofac J. 1992; 29:318-324
Farkas LG, Posnick JC, Hreczko TM, Pron GE. Growth patterns in the orbital region: a morphometric study. Cleft Palate Craniofac J. 1992; 29:315-318
Farkas LG, Posnick JC, Hreczko TM. Growth patterns of the face: a morphometric study. Cleft Palate Craniofac J. 1992; 29:308-315
Farkas LG, Posnick JC, Hreczko TM. Anthropometric growth study of the head. Cleft Palate Craniofac J. 1992; 29:303-308
Farkas LG, Posnick JC. Growth and development of regional units in the head and face based on anthropometric measurements. Cleft Palate Craniofac J. 1992; 29:301-302
Farkas LG, Hajnis K, Posnick JC. Anthropometric and anthroposcopic findings of the nasal and facial region in cleft patients before and after primary lip and palate repair. Cleft Palate Craniofac J. 1993; 30:1-12
Farkas LG. Anthropometry of the head and face. New York: Raven Press; 1994
Farkas LG, Deutsch CK. Anthropometric determination of craniofacial morphology. Am J Med Genet. 1996; 65:1-4
Farkas LG. Accuracy of anthropometric measurements: past, present, and future. Cleft Palate Craniofac J. 1996; 33:10-18
Farkas LG. Clinical evaluation of facial morphology in cleft lip palate patients. Plast Reconstr Surg. 1997; 99:262-263
Farkas LG, Tompson B, Phillips JH, Katic MJ, Cornfoot ML. Comparison of anthropometric and cephalometric measurements of the adult face. J Craniofac Surg. 1999; 10:18-25
Farkas LG, Forrest CR, Phillips JH. Comparison of the morphology of the "cleft face" and the normal face: defining the anthropometric differences. J Craniofac Surg. 2000; 11:76-82
Farkas LG, Forrest CR, Litsas L. Revision of neoclassical facial canons in young adult Afro-Americans. Aesthetic Plast Surg. 2000; 24:179-184
Farkas LG, Katic MJ, Forrest CR. Surface anatomy of the face in Down's syndrome: anthropometric proportion indices in the craniofacial regions. J Craniofac Surg. 2001; 12:519-524
Farkas LG, Katic MJ, Forrest CR, Litsas L. Surface anatomy of the face in Down's syndrome: linear and angular measurements in the craniofacial regions. J Craniofac Surg. 2001; 12:373-379
Farkas LG, Katic MJ, Forrest CR. Age-related changes in anthropometric measurements in the craniofacial regions and in height in Down's syndrome. J Craniofac Surg. 2002; 13:614-622
Farkas LG, Katic MJ, Forrest CR. Surface anatomy of the face in Down's syndrome: age-related changes of anthropometric proportion indices in the craniofacial regions. J Craniofac Surg. 2002; 13:368-374
Farkas LG, Tompson BD, Katic MJ, Forrest CR. Differences between direct (anthropometric) and indirect (cephalometric) measurements of the skull. J Craniofac Surg. 2002; 13:105-108
Farkas LG, Hreczko TM, Katic MJ, Forrest CR. Proportion indices in the craniofacial regions of 284 healthy North American white children between 1 and 5 years of age. J Craniofac Surg. 2003; 14:13-28
Farkas LG, Eiben OG, Sivkov S, Tompson B, Katic MJ, Forrest CR. Anthropometric measurements of the facial framework in adulthood: age-related changes in eight age categories in 600 healthy white North Americans of European ancestry from 16 to 90 years of age. J Craniofac Surg. 2004; 15:288-298
Faure J, Treil J, Borianne P, Casteigt J, Baron P. 3-dimensional cephalometry in orthodontics. The current possibilities of Cepha 3DT software. Orthod Fr. 2002; 73:19-37
Ferrario VF, Sforza C, Poggio CE, Tartaglia G. Distance from symmetry: a three-dimensional evaluation of facial asymmetry. J Oral Maxillofac Surg. 1994; 52:1126-1132
Ferrario VF, Sforza C, Serrao G, Miani A, Jr. A computerized non-invasive method for the assessment of human facial volume. J Craniomaxillofac Surg. 1995; 23:280-286
Ferrario VF, Sforza C, Miani A, Jr., Serrao G. A three-dimensional evaluation of human facial asymmetry. J Anat. 1995; 186:103-110
Ferrario VF, Sforza C, Puleo A, Poggio CE, Schmitz JH. Three-dimensional facial morphometry and conventional cephalometrics: a correlation study. Int J Adult Orthodon Orthognath Surg. 1996; 11:329-338
Ferrario VF, Sforza C, Poggio CE, Serrao G. Facial three-dimensional morphometry. Am J Orthod Dentofacial Orthop. 1996; 109:86-93
Ferrario VF, Sforza C, Poggio CE, Schmitz JH. Three-dimensional study of growth and development of the nose. Cleft Palate Craniofac J. 1997; 34:309-317
Ferrario VF, Sforza C, Poggio CE, Schmitz JH, Colombo A. Soft tissue facial morphology related to headform: a three-dimensional quantitative analysis in childhood. J Craniofac Genet Dev Biol. 1997; 17:86-95
Ferrario VF, Sforza C, Schmitz JH, Miani A, Jr., Serrao G. A three-dimensional computerized mesh diagram analysis and its application in soft tissue facial morphometry. Am J Orthod Dentofacial Orthop. 1998; 114:404-413
Ferrario VF, Sforza C, Poggio CE, Schmitz JH. Facial volume changes during normal human growth and development. Anat Rec. 1998; 250:480-487
Ferrario VF, Sforza C, Poggio CE, Cova M, Tartaglia G. Preliminary evaluation of an electromagnetic three-dimensional digitizer in facial anthropometry. Cleft Palate Craniofac J. 1998; 35:9-15
Ferrario VF, Sforza C, Poggio CE, Schmitz JH. Craniofacial growth: a three-dimensional soft-tissue study from 6 years to adulthood. J Craniofac Genet Dev Biol. 1998; 18:138-149
Ferrario VF, Sforza C, Schmitz JH, Santoro F. Three-dimensional facial morphometric assessment of soft tissue changes after orthognathic surgery. Oral Surg Oral Med Oral Pathol Oral Radiol Endod. 1999; 88:549-556
Ferrario VF, Sforza C, Serrao G, Colombo A, Ciusa V. Soft tissue facial growth and development as assessed by the three-dimensional computerized mesh diagram analysis. Am J Orthod Dentofacial Orthop. 1999; 116:215-228
Ferrario VF, Sforza C, Poggio CE, Schmitz JH. Soft-tissue facial morphometry from 6 years to adulthood: a three-dimensional growth study using a new modeling. Plast Reconstr Surg. 1999; 103:768-778
Ferrario VF, Sforza C, Dellavia C, Tartaglia GM, Sozzi D, Caru A. A quantitative three-dimensional assessment of abnormal variations in facial soft tissues of adult patients with cleft lip and palate. Cleft Palate Craniofac J. 2003; 40:544-549
Figalova P, Farkas LG. Localisation of auricle by means of anthropometric methods. Acta Chir Plast. 1968; 10:7-14
Fortin T, Champleboux G, Bianchi S, Buatois H, Coudert JL. Precision of transfer of preoperative planning for oral implants based on cone-beam CT-scan imagesthrough a robotic drilling machine.Clin Oral Implants Res. 2002; 13:651-656
Fox LA, Vannier MW, West OC, Wilson AJ, Baran GA, Pilgram TK. Diagnostic performance of CT, MPR and 3D CT Imaging in maxillofacial trauma. Computerized Medical Imaging and Graphics 1995; 19:385-395
Fuhrmann RA, Frohberg U, Diedrich PR. Treatment prediction with three-dimensional computer tomographic skull models. Am J Orthod Dentofacial Orthop. 1994; 106:156-160
Fuhrmann R, Feifel H, Schnappauf A, Diedrich P. Integration of three-dimensional cephalometry and 3D-skull models in combined orthodontic/surgical treatment planning. J Orofac Orthop. 1996; 57:32-45
Gateno J, Teichgraeber JF, Aguilar E. Computer planning for distraction osteogenesis. Plast Reconstr Surg. 2000; 105:873-882

Gateno J, Allen ME, Teichgraeber JF, Messersmith ML. An in vitro study of the accuracy of a new protocol for planning distraction osteogenesis of the mandible. J Oral Maxillofac Surg. 2000; 58:985-990

Gateno J, Teichgraeber JF, Xia JJ. Three-dimensional surgical planning for maxillary and midface distraction osteogenesis. J Craniofac Surg. 2003; 14:833-839

Gateno J, Xia J, Teichgraeber JF, Rosen A. A new technique for the creation of a computerized composite skull model. J Oral Maxillofac Surg. 2003; 61:222-227

Gellrich NC, Schramm A, Hammer B, Rojas S, Cufi D, Lagreze W, Schmelzeisen R. Computer-assisted secondary reconstruction of unilateral posttraumatic orbital deformity. Plast Reconstr Surg. 2002; 110:1417-1429

Ghafari J, Engel FE. Laster LL. Cephalometric superimposition on the cranial base: a review and a comparison of four methods. Am J Orthod Dentofacial Orthop. 1987; 91:403-413

Gibbons AJ, Duncan C, Nishikawa H, Hockley AD, Dover MS. Stereolithographic modelling and radiation dosage. Br J Oral Maxillofac Surg. 2003; 41:416-422

Girod S, Keeve E, Girod B. Advances in interactive craniofacial surgery planning by 3D simulation and visualization. Int J Oral Maxillofac Surg. 1995; 24:120-125

Girod S, Teschner M, Schrell U, Kevekordes B, Girod B. Computer-aided 3-D simulation and prediction of craniofacial surgery: a new approach. J Craniomaxillofac Surg. 2001; 29:156-158

Grayson BH, McCarthy JG, Bookstein F. Analysis of craniofacial asymmetry by multiplane cephalometry. Am J Orthod. 1983; 84:217-224

Grayson BH, LaBatto FA, Kolber AB, McCarthy JG. Basilar multiplane cephalometric analysis. Am J Orthod. 1985; 88:503-516

Grayson BH, Cutting CB, Dufresne CR, Bookstein FL, McCarthy JG, Patnaik S. Three-dimensional computer simulation of craniofacial anatomy. N Y State Dent J. 1986; 52:29-31

Grayson B, Cutting C, Bookstein FL, Kim H, McCarthy JG. The three-dimensional cephalogram: theory, technique, and clinical application. Am J Orthod Dentofacial Orthop. 1988; 94:327-337

Grayson BH. Cephalometric analysis for the surgeon. Clin Plast Surg. 1989; 16:633-644

Grayson BH, Santiago PE. Treatment planning and biomechanics of distraction osteogenesis from an orthodontic perspective. Semin Orthod. 1999; 5:9-24

Gregory A, Lipczynski RT. The three dimensional reconstruction and monitoring of facial surfaces. Med Eng Phys. 1994; 16:249-252

Gross MM, Trotman CA, Moffatt KS. A comparison of three-dimensional and two-dimensional analyses of facial motion. Angle Orthod. 1996; 66:189-194

Haffner CL, Pessa JE, Zadoo VP, Garza JR. A technique for three-dimensional cephalometric analysis as an aid in evaluating changes in the craniofacial skeleton. Angle Orthod. 1999; 69:345-348

Hajeer MY, Ayoub AF, Millett DT, Bock M, Siebert JP. Three-dimensional imaging in orthognathic surgery: the clinical application of a new method. Int J Adult Orthodon Orthognath Surg. 2002; 17:318-330

Hajeer MY, Millett DT, Ayoub AF, Siebert JP. Applications of 3D imaging in orthodontics: part I. J Orthod. 2004; 31:62-70

Hajeer MY, Millett DT, Ayoub AF, Siebert JP. Applications of 3D imaging in orthodontics: part II. J Orthod. 2004; 31:154-162

Hajeer MY, Ayoub AF, Millett DT. Three-dimensional assessment of facial soft-tissue asymmetry before and after orthognathic surgery. Br J Oral Maxillofac Surg. 2004; 42:396-404

Hajeer MY, Mao Z, Millet DT, Ayoub AF, Siebert JP. A new three-dimensional method of assissing facial volumetric changes after orthognatic treatment. Cleft Palate Craniofac J. 2005; 42:113-120

Hajnis K, Farkas LG. Basic auricular characteristics in children with cleft anomalies as compared with the standard. Acta Chir Plast. 1968; 10:15-27

Hajnis K, Farkas LG. Anthropological record for congenital developmental defects of the face (especially clefts). Acta Chir Plast. 1969; 11:261-267

Halazonetis DJ. Acquisition of 3-dimensional shapes from images. Am J Orthod Dentofacial Orthop. 2001; 119:556-560

Hall RK. The role of CT, MRI and 3D imaging in the diagnosis of temporomandibular joint and other orofacial disorders in children. Aust Orthod J. 1994; 13:86-94

Hamada Y, Kondoh T, Noguchi K, Lino M, Isono H, Ishii H, Mishima A, Kobayashi K, Seto K. Application of limited cone beam computed tomography to clinical assessment of alveolar bone grafting: A preliminary report. Cleft Palate Craniofac J. 2005; 42:128-137

Hammond P, Hutton TJ, Allanson JE, Campbell LE, Hennekam RC, Holden S, Patton MA, Shaw A, Temple IK, Trotter M, Murphy KC, Winter RM. 3D analysis of facial morphology. Am J Med Genet. 2004; 126A:339-348

Haralabakis NB, Yiagtzis SC, Toutountzakis NM. Cephalometric characteristics of open bite in adults: a three-dimensional cephalometric evaluation. Int J Adult Orthodon Orthognath Surg. 1994; 9:223-231

Harrell WE, Jr., Hatcher DC, Bolt RL. In search of anatomic truth: 3-dimensional digital modeling and the future of orthodontics. Am J Orthod Dentofacial Orthop. 2002; 122:325-330

Hassfeld S, Brief J, Krempien R, Raczkowsky J, Munchenberg J, Giess H, Meinzer HP, Mende U, Worn H, Muhling J. Computer-assisted oral, maxillary and facial surgery. Radiologe. 2000; 40:218-226

Hasund A, Jenatschke F, Norderval K, Thunold K, Wisth PJ. Klinische Kephalometrie für die Bergen-Technik. Kieferorthopädische Abteilung des Zahnärztlichen Institutes der Universität Bergen, Norwegen 1973.

Hatcher DC, Dial C, Mayorga C. Cone beam CT for pre-surgical assessment of implant sites. J Calif Dent Assoc. 2003; 31:825-833

Hatcher DC, Aboudara CL. Diagnosis goes digital. Am J Orthod Dentofacial Orthop. 2004; 125:512-515

Hayashi K, Araki Y, Uechi J, Ohno H, Mizoguchi I. A novel method for the three-dimensional (3-D) analysis of orthodontic tooth movement-calculation of rotation about and translation along the finite helical axis. J Biomech. 2002; 35:45-51

Hayashi I. Morphological relationship between the cranial base and dentofacial complex obtained by reconstructive computer tomographic images. Eur J Orthod. 2003; 25:385-391

Heiland M, Schulze D, Adam G, Schmelzle R. 3D-imaging of the facial skeleton with an isocentric mobile C-arm system (Siremobil Iso-C3D). Dentomaxillofac Radiol. 2003; 32:21-25

Hennessy RJ, Moss JP. Facial growth: separating shape from size. Eur J Orthod. 2001; 23:275-285

Hennessy RJ, Kinsella A, Waddington JL. 3D laser surface scanning and geometric morphometric analysis of craniofacial shape as an index of cerebro-craniofacial morphogenesis: initial application to sexual dimorphism. Biol Psychiatry. 2002; 51:507-514

Hibi H, Sawaki Y, Ueda M. Three-dimensional model simulation in orthognathic surgery. Int J Adult Orthodon Orthognath Surg. 1997; 12:226-232

Hildebolt CF, Vannier MW. Three-dimensional measurement accuracy of skull surface landmarks. Am J Phys Anthropol. 1988; 76:497-503

Hildebolt CF, Vannier MW, Knapp RH. Validation study of skull three-dimensional computerized tomography measurements. Am J Phys Anthropol. 1990; 82:283-294

Hirschfelder U. The spiral CT imaging technic – the initial experience for orthodontic examinations. Fortschr Kieferorthop. 1992; 53:247-253

Hofrath H. Die Bedeutung von Röntgenfern- und Abstandsaufnahme für die Diagnostik von Kieferanomalien. Fortschr Orthodont. 1931; 1:232-236

Hollister SJ, Levy RA, Chu TM, Halloran JW, Feinberg SE. An image-based approach for designing and manufacturing craniofacial scaffolds. Int J Oral Maxillofac Surg. 2000; 29:67-71

Hood CA, Bock M, Hosey MT, Bowman A, Ayoub AF. Facial asymmetry–3D assessment of infants with cleft lip & palate. Int J Paediatr Dent. 2003; 13:404-410

Hood CA, Hosey MT, Bock M, White J, Ray A, Ayoub AF. Facial characterization of infants with cleft lip and palate using a three-dimensional capture technique. Cleft Palate Craniofac J. 2004; 41:27-35

Hounsfield GN. Computerized transverse axial scanning (tomography): Part I. Description of system. Br. J Radiol. 1973; 46:1016-1022

Huisinga-Fischer CE, Zonneveld FW, Vaandrager JM, Prahl-Andersen B. CT-based size and shape determination of the craniofacial skeleton: a new scoring system to assess bony deformities in hemifacial microsomia. J Craniofac Surg. 2001; 12:87-94

Huisinga-Fischer CE, Zonneveld FW, Vaandrager JM, Prahl-Andersen B. Relationship in hypoplasia between the masticatory muscles and the craniofacial skeleton in hemifacial microsomia, as determined by 3-D CT imaging. J Craniofac Surg. 2001; 12:31-40

Huisinga-Fischer CE, Vaandrager JM, Prahl-Andersen B. Longitudinal results of mandibular distraction osteogenesis in hemifacial microsomia. J Craniofac Surg. 2003; 14:924-933

ICRP International Commission on Radiological Protection. Recommendations of the International Commission on Radiological Protection. Pergamon Oxford. 1990(1991): Publication no. 60.

Ikai A, Sugisaki M, Young-Sung K, Tanabe H. Morphologic study of the mandibular fossa and the eminence of the temporomandibular joint in relation to the facial structures. Am J Orthod Dentofacial Orthop. 1997; 112:634-638

Ismail SF, Moss JP, Hennessy R. Three-dimensional assessment of the effects of extraction and nonextraction orthodontic treatment on the face. Am J Orthod Dentofacial Orthop. 2002; 121:244-256

Ismail SF, Moss JP. The three-dimensional effects of orthodontic treatment on the facial soft tissues – a preliminary study. Br Dent J. 2002; 192:104-108

Jackson IT, Bite U. Three-dimensional computed tomographic scanning and major surgical reconstruction of the head and neck. Mayo Clin Proc. 1986; 61:546-555

Jackson IT, Carls F, Bush K, Topf J, Xiao H, Gowda M, Audet B. Assessment and treatment of facial deformity resulting from radiation to the orbital area in childhood. Plast Reconstr Surg. 1996; 98:1169-1179

Jans G, Vander Sloten J, Gobin R, Van der Perre G, Van Audekercke R, Mommaerts M. Computer-aided craniofacial surgical planning implemented in CAD software. Comput Aided Surg. 1999; 4:117-128

Janson GR, Metaxas A, Woodside DG, de Freitas MR, Pinzan A. Three-dimensional evaluation of skeletal and dental asymmetries in Class II subdivision malocclusions. Am J Orthod Dentofacial Orthop. 2001; 119:406-418

Ji Y, Zhang F, Schwartz J, Stile F, Lineaweaver WC. Assessment of facial tissue expansion with three-dimensional digitizer scanning. J Craniofac Surg. 2002; 13:687-692

Kaban LB, Mulliken JB, Murray JE. Three-dimensional approach to analysis and treatment of hemifacial microsomia. Cleft Palate J. 1981; 18:90-99

Kakoschke D, Gabel H, Schettler D. 3-dimensional photogrammetry assessment of facial contours. Mund Kiefer Gesichtschir. 1997; 1:61-64

Kalender WA, Schmidt B, Zankl M, Schmidt M. A PC program for estimating organ dose and effective dose values in computed tomography. Eur Radiol. 1999; 9:555-562

Kau CH, Zhurov A, Scheer R, Bouwman S, Richmond S. The feasibility of measuring three-dimensional facial morphology in children. Orthod Craniofacial Res. 2004; 7:198-204

Kawai T, Natsume N, Shibata H, Yamamoto T. Three-dimensional analysis of facial morphology using moiré stripes. Part I. Method. Int. J. Oral Maxillofac Surg. 1990; 19:356-358

Kawai T, Natsume N, Shibata H, Yamamoto T. Three-dimensional analysis of facial morphology using moiré stripes. Part II. Analysis of normal adults. Int J Oral Maxillofac Surg. 1990; 19: 359-362

Kermer C, Lindner A, Friede I, Wagner A, Millesi W. Preoperative stereolithographic model planning for primary reconstruction in craniomaxillofacial trauma surgery. J Craniomaxillofac Surg. 1998; 26:136-139

Kessler P, Wiltfang J, Teschner M, Girod B, Neukam FW. Possibilities of computer graphics simulation in orthopedic surgery. Mund Kiefer Gesichtschir. 2000; 4:373-376

Khambay B, Nebel JC, Bowman J, Walker F, Hadley DM, Ayoub A. 3D stereophotogrammetric image superimposition onto 3D CT scan images: the future of orthognathic surgery. A pilot study. Int J Adult Orthodon Orthognath Surg. 2002; 17:331-341

Kim YH, Sato K, Mitani H, Shimizu Y, Kikuchi M. Asymmetry of the sphenoid bone and its suitability as a reference for analyzing craniofacial asymmetry. Am J Orthod Dentofacial Orthop. 2003; 124:656-662

Kitaura H, Yonetsu K, Kitamori H, Kobayashi K, Nakamura T. Standardization of 3-D CT measurements for length and angles by matrix transformation in the 3-D coordinate system. Cleft Palate Craniofac J. 2000; 37:349-356

Klein HM, Schneider W, Alzen G, Voy ED, Gunther RW. Pediatric craniofacial surgery: comparison of milling and stereolithography for 3D model manufacturing. Pediatr Radiol. 1992; 22:458-460

Kobayashi T, Ueda K, Honma K, Sasakura H, Hanada K, Nakajima T. Three-dimensional analysis of facial morphology before and after orthognathic surgery. J Craniomaxillofac Surg. 1990; 18:68-73

Kobayashi K, Shimoda S, Nakagawa Y, Yamamoto A. Accuracy in measurement of distance using limited cone-beam computerized tomography. Int J Oral Maxillofac Implants. 2004; 19:228-231

Kockro RA, Serra L, Tsai YT, Chan C, Sitoh YY, Chua GG, Hern N, Lee E, Hoe LY, Nowinski W. Planning of skull base surgery in the virtual workbench: clinical experiences. Stud Health Technol Inform. 1999; 62:187-188

Kolar JC, Farkas LG, Munro IR. Surface morphology in Treacher Collins syndrome: an anthropometric study. Cleft Palate J. 1985; 22:266-274

Kolar JC, Munro IR, Farkas LG. Anthropometric evaluation of dysmorphology in craniofacial anomalies: Treacher Collins syndrome. Am J Phys Anthropol. 1987; 74:441-451

Kolar JC, Munro IR, Farkas LG. Patterns of dysmorphology in Crouzon syndrome: an anthropometric study. Cleft Palate J. 1988; 25:235-244

Kopp S, Kuhmstedt P, Notni G, Geller R. G-scan-mobile multiview 3-D measuring system for the analysis of the face. Int J Comput Dent. 2003; 6:321-331

Kouame P, N'Dindin A, Savane S. Conventional and 3-D cephalometry: descriptive analysis. Odontostomatol Trop. 2003; 26:20-24

Kragskov J, Sindet-Pedersen S, Gyldensted C, Jensen KL. A Comparison of three-dimensional computed tomography scans and stereolithographic models for evaluation of craniofacial anomalies. J Oral Maxillofac Surg. 1996; 54:402-412

Kragskov J, Bosch C, Gyldensted C, Sindet-Pedersen S. Comparison of the reliability of craniofacial anatomic landmarks based on cephalometric radiographs and three-dimensional CT scans. Cleft Palate Craniofac J. 1997; 34:111-116

Krimmel M, Bacher M, Cornelius CP, Schubert S, Goz G, Reinert S. 3-dimensional image acquisition for analysis of primary, cleft-induced facial deformity with an optoelectronic surface scanner. Mund Kiefer Gesichtschir. 2002; 6:158-161

Krogman WM, Sassouni V. Syllabus in roentgenographic cephalometry. Philadelphia; Center for Research in Child Growth: 1957

Kusnoto B, Evans CA, BeGole EA, de Rijk W. Assessment of 3-dimensional computer-generated cephalometric measurements. Am J Orthod Dentofacial Orthop. 2002; 116:390-399

Kusnoto B, Figueroa AA, Polley JW. A longitudinal three-dimensional evaluation of the growth pattern in hemifacial microsomia treated by mandibular distraction osteogenesis: a preliminary report. J Craniofac Surg. 1999; 10:480-486

Kusnoto B, Evans CA. Reliability of a 3D surface laser scanner for orthodontic applications. Am J Orthod Dentofacial Orthop. 2002; 122:342-348

Kwon TG, Mori Y, Minami K, Lee SH, Sakuda M. Stability of simultaneous maxillary and mandibular osteotomy for treatment of class III malocclusion: an analysis of three-dimensional cephalograms. J Cranio Maxillofac Surg. 2000; 28:272-277

Lambrecht JT, Brix F. Individual skull model fabrication for craniofacial surgery. Cleft Palate J. 1990; 27:382-385

Lambrecht JT, Hammer B, Jacob AL, Schiel H, Hunziker M, Kreusch T, Kliegis U. Individual model fabrication in maxillofacial radiology. Dentomaxillofac Radiol. 1995; 24:147-154

Landes CA, Bitsakis J, Diehl T, Bitter K. Introduction of a three-dimensional anthropometry of the viscerocranium. Part I: measurement of craniofacial development and establishment of standard values and growth functions. J Craniomaxillofac Surg. 2002; 30:18-24

Landes CA, Zachar R, Diehl T, Kovacs AF. Introduction of a three-dimensional anthropometry of the viscerocranium. Part II: evaluating osseous and soft tissue changes following orthognathic surgery. J Craniomaxillofac Surg. 2002; 30:25-34

Lascala CA, Panella J, Marques MM. Analysis of the accuracy of linear measurements obtained by cone beam computed tomography (CBCT-NewTom). Dentomaxillofac Radiol. 2004; 33:291-294

Le TT, Farkas LG, Ngim RC, Levin LS, Forrest CR. Proportionality in Asian and North American Caucasian faces using neoclassical facial canons as criteria. Aesthetic Plast Surg. 2002; 26:64-69

Lee TY, Sun YN, Lin YC, Lin L, Lee C. Three-dimensional facial model reconstruction and plastic surgery simulation. IEEE Trans Inf Technol Biomed. 1999; 3:214-220

Lee JY, Han Q, Trotman CA. Three-dimensional facial imaging: accuracy and considerations for clinical applications in orthodontics. Angle Orthod. 2004; 74:587-593

Leonard MS, Johnson GW, Starfield AM, Speidel TM. Computer graphics in facial morphology analysis. Int J Oral Surg. 1981; 10:273-275

Lievin M, Ritter L, Hanssen N, Jansen T, Keeve E. Interactive 3D segmentation and inspection of volumetric medial datasets. Biomed Tech (Berl). 2002; 47:1:75-78

Lill W, Solar P, Ulm C, Watzek G, Blahout R, Matejka M. Reproducibility of three-dimensional CT-assisted model production in the maxillofacial area. Br J Oral Maxillofac Surg. 1992; 30:233-236

Littlefield TR, Kelly KM, Cherney JC, Beals SP, Pomatto JK. Development of a new three-dimensional cranial imaging system. J Craniofac Surg. 2004; 15:175-181

Loubele M, Jacobs R, Maes F, Schutyser F, Debaveye D, Bogaerts R, Coudyzer W, Vandermeulen D, Van Cleynenbreugel J, Marchal G, Suetens P. Radiation dose versus image quality for low-dose CT protocols of the head for maxillofacial surgery and dental implant planning. In press.

Luka B, Brechtelsbauer D, Gellrich N-C, König M. 2D and 3D reconstruction of facial skeleton: an unnecessary option or a diagnostic pearl? Int J Oral Maxillofac Surg. 1995; 24:76-83

Mah J. 3D imaging in private practice. Am J Orthod Dentofacial Orthop. 2002; 121:14A

Mah J, Hatcher D. Current status and future needs in craniofacial imaging. Orthod Craniofac Res. 2003; 6:10-16

Mah J, Enciso R, Jorgensen M. Management of impacted cuspids using 3-D volumetric imaging. J Calif Dent Assoc. 2003; 31:835-841

Maki K, Inou N, Takanishi A, Miller AJ. Computer-assisted simulations in orthodontic diagnosis and the application of a new cone beam X-ray computed tomography. Orthod Craniofac Res. 2003; 6:95-101

Malevez C, Dujardin T, Glorieux V, Swennen G, Schutyser F, Van Cleynenbreugel J. Bone distraction osteogenesis. Rev Belge Med Dent. 2002; 57:137-149

Mannsbach M. Die Stereophotogrammetrie als Hilfsmittel der Orthodontie. Deutsche Zeitschrift für Zahnärztliche Orthopädie. 1922; 14:105-107

Marcel TJ. Three-dimensional on-screen virtual models. Am J Orthod Dentofacial Orthop. 2001; 119:666-668

Marmulla R, Wörtche R, Mühling J, Hassfeld S. Geometric accuracy of the NewTom 9000 Cone Beam CT. Dentomaxillofac Radiol. 2005; 34:28-31

Marsh JL, Vannier MW, Stevens WG, Warren JO, Gayou D, Dye DM. Computerized imaging for soft tissue and osseous reconstruction in the head and neck. Clin Plast Surg. 1985; 12:279-291

Marsh JL, Vannier MW. Cartographic mapping of the skull from computed tomography scans. J Craniofac Surg. 1994; 5:188-194

McCance AM, Moss JP, Fright WR, James DR, Linney AD. A three dimensional analysis of soft and hard tissue changes following bimaxillary orthognathic surgery in skeletal III patients. Br J Oral Maxillofac Surg. 1992; 30:305-312

McCance AM, Moss JP, Wright WR, Linney AD, James DR. A three-dimensional soft tissue analysis of 16 skeletal class III patients following bimaxillary surgery. Br J Oral Maxillofac Surg. 1992; 30:221-232

McCance AM, Moss JP, Fright WR, Linney AD, James DR. Three-dimensional analysis techniques – Part 1: Three-dimensional soft-tissue analysis of 24 adult cleft palate patients following Le Fort I maxillary advancement: a preliminary report. Cleft Palate Craniofac J. 1997; 34:36-45

McCance AM, Moss JP, Fright WR, Linney AD, James DR. Three-dimensional analysis techniques – Part 2: Laser scanning: a quantitative three-dimensional soft-tissue analysis using a color-coding system. Cleft Palate Craniofac J. 1997; 34:46-51

McCance AM, Moss JP, Fright WR, Linney AD. Three-dimensional analysis techniques – Part 3: Color-coded system for three-dimensional measurement of bone and ratio of soft tissue to bone: the analysis. Cleft Palate Craniofac J. 1997; 34:52-57

McCance AM, Moss JP, Fright WR, Linney AD, James DR, Coghlan K, Mars M. Three-dimensional analysis techniques – Part 4: Three-dimensional analysis of bone and soft tissue to bone ratio of movements in 24 cleft palate patients following Le Fort I osteotomy: a preliminary report. Cleft Palate Craniofac J. 1997; 34:58-62

McDonagh S, Moss JP, Goodwin P, Lee RT. A prospective optical surface scanning and cephalometric assessment of the effect of functional appliances on the soft tissues. Eur J Orthod. 2001; 23:115-126

McNamara JA, Jr., Peterson JE, Jr., Alexander RG. Three-dimensional diagnosis and management of Class II malocclusion in the mixed dentition. Semin Orthod. 1996; 2:114-137

Medina LS, Richardson RR, Crone K. Children with suspected craniosynostosis: a cost-effectiveness analysis of diagnostic strategies. AJR Am J Roentgenol. 2002; 179:215-221

Meehan M, Teschner M, Girod S. Three-dimensional simulation and prediction of craniofacial surgery. Orthod Craniofac Res. 2003; 6:102-107

Mehta BV, Rajani S, Sinha G. Comparision of image processing techniques (magnetic resonance imaging, computed tomography scan and ultrasound) for 3D-Modeling and analysis of the human bones. J Digit Imaging. 1997; 10:203-206

Metho JD. Some limitations of roentgenographic cephalometry. Ala J Med Sci. 1964; 1:163-170

Meintjes EM, Douglas TS, Martinez F, Vaughan CL, Adams LP, Stekhoven A, Viljoen D. A stereo-photogrammetric method to measure the facial dysmorphology of children in the diagnosis of fetal alcohol syndrome. Med Eng Phys. 2002; 24:683-689

Metes A, Hoffstein V, Direnfeld V, Chapnik JS, Zamel N. Three-dimensional CT reconstruction and volume measurements of the pharyngeal airway before and after maxillofacial surgery in obstructive sleep apnea. J Otolaryngol. 1993; 22:261-264

Meyer U, Stamm T, Meier N, Joos U. First experience with a public domain computer-aided surgical system. Br J Oral Maxillofac Surg. 2002; 40:96-104

Miethke R.R. Zur Lokalisationsgenauigkeit kephalometrischer Referenzpunkte. Prakt Kieferorthop. 1989; 3:107-122

Mishima K, Sugahara T, Mori Y, Sakuda M. Application of a new method for anthropometric analysis of the nose. Plast Reconstr Surg. 1996; 98:637-644

Mole C, Gerard H, Mallet JL, Chassagne JF, Miller N. A new three-dimensional treatment algorithm for complex surfaces: applications in surgery. J Oral Maxillofac Surg. 1995; 53:158-162

Mollemans W, Schutyser F, Van Cleynenbreugel J, Suetens P. Fast soft tissue deformation with tetrahedral mass spring model for maxillofacial surgery planning systems. Lecture notes in computer science. Springer-Verlag Berlin Heidelberg: 2004; 3217:371-379

Mommaerts MY, Jans G, Vander Sloten J, Staels PF, Van der Perre G, Gobin R. On the assets of CAD planning for craniosynostosis surgery. J Craniofac Surg. 2001; 12:547-554

Mommaerts MY. Reliability and validity of a backlighted digitizer when used for craniofacial measurements. J Craniofac Surg. 1997; 8:222-228

Moss JP, Coombes AM, Linney AD, Campos J. Methods of three dimensional analysis of patients with asymmetry of the face. Proc Finn Dent Soc. 1991; 87:139-149

Moss JP, Linney AD, Grindrod SR, Arridge SR, Clifton JS,'. Three dimensional visualization of the face and skull using computerized tomography and laser scanning techniques. Eur J Orthod. 1987; 9:247-253

Moss JP, Grindrod RS, Linney AD, Arridge SR, James D. A computer system for the interactive planning and prediction ofmaxillofacial surgery. Am J Orthod Dentofac Orthop. 1988; 94:469-475

Moss JP, Linney AD, Lowey MN. The use of three-dimensional techniques in facial esthetics. Semin Orthod. 1995; 1:94-104

Moss JP, Ismail SF, Hennessy RJ. Three-dimensional assessment of treatment outcomes on the face. Orthod Craniofac Res. 2003; 6:126-131

Motegi N, Tsutsumi S, Okumura H, Yokoe Y, Iizuka T. Morphologic changes in the perioral soft tissues in patients with mandibular hyperplasia using a laser system for three-dimensional surface measurement. Int J Oral Maxillofac Surg. 1999; 28:15-20

Motohashi N, Kuroda T. A 3D computer-aided design system applied to diagnosis and treatment planning in orthodontics and orthognathic surgery. Eur J Orthod. 1999; 21:263-274

Moyers RE, Bookstein FL. The inappropriateness of conventional cephalometrics. Am J Orthod. 1979; 75:599-617

Mozzo P, Procacci C, Tacconi A, Martini PT, Andreis IA. A new volumetric CT machine for dental imaging based on the cone-beam technique: preliminary results. Eur Radiol. 1998; 8:1558-1564

Mulliken JB, Burvin R, Farkas LG. Repair of bilateral complete cleft lip: intraoperative nasolabial anthropometry. Plast Reconstr Surg. 2001; 107:307-314

Naftel AJ, Trenouth MJ. Stereo-assisted landmark detection for the analysis of changes in 3-D facial shape. Med Inform Internet Med. 2004; 29:137-155

Nagasaka S, Fujimura T, Segoshi K. Development of a non-radiographic cephalometric system. Eur J Orthod. 2003; 25:77-85

Nagashima M, Inoue K, Sasaki T, Miyasaka K, Matsumura G, Kodama G. Three-dimensional imaging and osteometry of adult human skulls using helical computed tomography. Surg Radiol Anat. 1998; 20:291-297

Nakagawa Y, Kobayashi K, Ishii H, Mishima A, Ishii H, Asada K, Ishibashi K. Preoperative application of limited cone beam computerized tomography as an assessment tool before minor oral surgery. Int J Oral Maxillofac Surg. 2002; 31:322-326

Nanda RS, Ghosh J, Bazakidou E. Three-dimensional facial analysis using a video imaging system. Angle Orthod. 1996; 66:181-188

Nechala P, Mahoney J, Farkas LG. Maxillozygional anthropometric landmark: a new morphometric orientation point in the upper face. Ann Plast Surg. 1998; 41:402-409

Nkenke E, Langer A, Laboureux X, Benz M, Maier T, Kramer M, Hausler G, Kessler P, Wiltfang J, Neukam FW. Validation of in vivo assessment of facial soft-tissue volume changes and clinical application in midfacial distraction: a technical report. Plast Reconstr Surg. 2003; 112:367-380

Nkenke E, Zachow S, Benz M, Maier T, Veit K, Kramer M, Benz S, Hausler G, Neukam FW, Lell M. Fusion of computed tomography data and optical 3D images of the dentition for streak artefact correction in the simulation of orthognathic surgery. Dentomaxillofac Radiol. 2004; 33:226-232

Noguchi N, Goto M. Computer simulation system for orthognatic surgery. Orthod Craniofacial. 2003; 6:176-178

Nute SJ, Moss JP. Three-dimensional facial growth studied by optical surface scanning. J Orthod. 2000; 27:31-38

O'Grady KF, Antonyshyn OM. Facial asymmetry: three-dimensional analysis using laser surface scanning. Plast Reconstr Surg. 1999; 104:928-937

Ogawa T, Enciso R, Memon A, Mah JK, Clark GT. Evaluation of 3D airway imaging of obstructive sleep apnea with cone-beam computed tomographic systems. J Craniomaxillofac Surg. 2005; 111:365-368

O'Higgins P, Jones N. Facial growth in Cercocebus torquatus: an application of three-dimensional geometric morphometric techniques to the study of morphological variation. J Anat. 1998; 193:251-272

Okada E. Three-dimensional facial simulations and measurements: changes of facial contour and units associated with facial expression. J Craniofac Surg. 2001; 12:167-174

Okumura H, Chen LH, Tsutsumi S, Oka M. Three-dimensional virtual imaging of facial skeleton and dental morphologic condition for treatment planning in orthognathic surgery. Am J Orthod Dentofacial Orthop. 1999; 116:126-131

Olszewski R, Reychler H. Limitations of orthognathic model surgery: theoretical and practical implications. Rev Stomatol Chir Maxillofac. 2004; 105:165-169

Ongkosuwito EM, Katsaros C, van 't Hof MA, Bodegom JC, Kuijpers-Jagtman AM. The reproducibility of cephalometric measurements: a comparison of analogue and digital methods. Eur J Orthod. 24: 2002:655-665

Ono I, Ohura T, Narumi E, Kawashima K, Matsuno I, Nakamura S, Ohhata N, Uchiyama Y, Watanabe Y, Tanaka F, et al. Three-dimensional analysis of craniofacial bones using three-dimensional computer tomography. J Craniomaxillofac Surg. 1992; 20:49-60

Papadopoulos MA, Christou PK, Athanasiou AE, Boettcher P, Zeilhofer HF, Sader R, Papadopulos NA. Three-dimensional craniofacial reconstruction imaging. Oral Surg Oral Med Oral Pathol Oral Radiol Endod. 2002; 93:382-393

Pernozzoli A, Brief J, Hassfeld S, Raczkowsky J, Muhling J, Worn H. Texture mapping based visualisation methods for the manipulation of CT data: interaction and ergonomics. Stud Health Technol Inform. 2000; 70:256-258

Perry M, Banks P, Richards R, Friedman EP, Shaw P. The use of computer-generated three-dimensional models in orbital reconstruction. Br J Oral Maxillofac Surg. 1998; 36:275-284

Ploder O, Klug C, Backfrieder W, Voracek M, Czerny C, Tschabitscher M. 2D- and 3D-based measurements of orbital floor fractures from CT scans. J Craniomaxillofac Surg. 2002; 30:153-159

Polley JW, Cohen M. Three-dimensional imaging and computer-generated models in complex facial reconstructions. Plast Reconstr Surg. 1993; 92:1204-1206

Polley JW, Breckler GL, Ramasastry S, Figueroa AA, Cohen M. Simultaneous distraction osteogenesis and microsurgical reconstruction for facial asymmetry. J Craniofac Surg. 1996; 7:469-472

Polley JW, Figueroa AA, Liou EJ, Cohen M. Longitudinal analysis of mandibular asymmetry in hemifacial microsomia. Plast Reconstr Surg. 1997; 99:328-339

Por YC, Barcelo CR, Sng K, Genecov DB, Sayler KE. A novel method for measuring and monitoring monobloc distraction osteogenesis using three-dimensional computed tomography rendered images with the 'biporion-dorsum sellae' plane. Part I: precision and reproducibility. J Craniofac Surg. 2005; 16:430-435

Powers DB, Edgin WA, Tabatchnick L. Stereolithography: a historical review and indications for use in the management of trauma. J Craniomaxillofac Trauma. 1998; 4:16-23

Prahl-Andersen B, Fischer CE. Management of developmental asymmetrical facial growth. Semin Orthod. 1996; 2:64-83

Profitt WR, Ackerman JL. Orthodontic diagnosis, Contemporary orthodontics, ed. 2. St. Louis: Mosby; 1991

Profitt WR, Phillips C, Dann C, Turvey TA, Stability after surgical-orthodontic correction of skeletal Class III malocclusion. I. Mandibular setback. Int J Adult Orthodont Orthognath Surg. 1991; 6:7-18.

Quatrehomme G, Cotin S, Subsol G, Delingette H, Garidel Y, Grevin G, Fidrich M, Bailet P, Ollier A. A fully three-dimensional method for facial reconstruction based on deformable models. J Forensic Sci. 1997; 42:649-652

Quintero JC, Trosien A, Hatcher D, Kapila S. Craniofacial imaging in orthodontics: historical perspective, current status, and future developments. Angle Orthod. 1999; 69:491-506

Radlanski RJ, van der Linden FP, Ohnesorge I. 4D-computerized visualisation of human craniofacial skeletal growth and of the development of the dentition. Anat Anz. 1999; 181:3-8

Rakosi T. An atlas and manual of cephalometric radiography. Worcester: Wolfe Medical Publications Ltd; 1979

Ras F, Habets LL, van Ginkel FC, Prahl-Andersen B. Three-dimensional evaluation of facial asymmetry in cleft lip and palate. Cleft Palate Craniofac J. 1994; 31:116-121

Ras F, Habets LL, van Ginkel FC, Prahl-Andersen B. Longitudinal study on three-dimensional changes of facial asymmetry in children between 4 to 12 years of age with unilateral cleft lip and palate. Cleft Palate Craniofac J. 1995; 32:463-468

Ras F, Habets LL, van Ginkel FC, Prahl-Andersen B. Quantification of facial morphology using stereophotogrammetry – demonstration of a new concept. J Dent. 1996; 24:369-374

Richtsmeier JT, Grausz HM, Morris GR, Marsh JL, Vannier MW. Growth of the cranial base in craniosynostosis. Cleft Palate Craniofac J. 1991; 28:55-67

Richtsmeier JT, Paik CH, Elfert PC, Cole TM, 3rd, Dahlman HR. Precision, repeatability, and validation of the localization of cranial landmarks using computed tomography scans. Cleft Palate Craniofac J. 1995; 32:217-227

Ricketts RM. New perspectives on orientation and their benefits to clinical orthodontics – part II. Angle Orthod. 1976; 46:26-36

Riolo ML, Moyers RE, McNamara AJ, Hunter WS. An atlas of craniofacial growth. Ann Arbor: University of Michigan; 1979

Riolo ML. Some recent developments in the computerization of craniofacial growth data. Am J Orthod. 1972; 62:96-97

Rocha Sdos S, Ramos DL, Cavalcanti Mde G. Applicability of 3D-CT facial reconstruction for forensic individual identification. Pesqui Odontol Bras. 2003; 17:24-28

Rose EH, Norris MS, Rosen JM. Application of high-tech three-dimensional imaging and computer-generated models in complex facial reconstructions with vascularized bone grafts. Plast Reconstr Surg. 1993; 91:252-264

Rousset MM, Simonek F, Dubus JP. A method for correction of radiographic errors in serial three-dimensional cephalometry. Dentomaxillofac Radiol. 2003; 32:50-59

Sailer HF, Haers PE, Zollikofer CPE, Warnke T, Carls FR, Stucki P. The value of stereolithographic models for preoperative diagnosis of craniofacial deformities and planning of surgical corrections. Int J Oral Maxillofac Surg. 1998; 27:327-333.

Salagnac JM, Delaire J. Prediction of growth and dento-facial orthopedics. Importance and accuracy of superposition. Rev Stomatol Chir Maxillofac. 2002; 103:221-232

Sander FG, Tochtermann H. 3-dimensional computer-supported model and hologram evaluations. Fortschr Kieferorthop. 1991; 52:218-229

Schenk HJ. 3-Dimensional model analysis of normal and dysgnathic bites using a coordinate measurement technic. Fortschr Kieferorthop. 1989; 50:81-98

Schierle H, Schliephake H, Gellrich NC, Schmelzeisen R. Complex reconstruction of the area of the maxilla and mid-face after radical tumor surgery. Mund Kiefer Gesichtschir. 1999; 3:S87-89

Schliephake H, Schmelzeisen R, Husstedt H, Schmidt-Wondera LU. Comparison of the late results of mandibular reconstruction using nonvascularized or vascularized grafts and dental implants. J Oral Maxillofac Surg. 1999. 57:944-950

Schmelzeisen R, Schon R, Schramm A, Gellrich NC. Computer-aided procedures in implantology, distraction and cranio-maxillofacial surgery. Ann R Australas Coll Dent Surg. 2002; 16:46-49

Schmelzeisen R, Schramm A. Computer-assisted reconstruction of the facial skeleton. Arch Facial Plast Surg. 2003; 5:437

Schultes G, Gaggl A, Karcher H. Results of measurement of pre- and postoperative milling models of orthodontic-surgical treatment of dysgnathia patients. Mund Kiefer Gesichtschir. 1998; 2 Suppl 1:S139-144

Schulze D, Heiland M, Thurmann H, Adam G. Radiation exposure during midfacial imaging using 4- and 16- slice computed tomography, cone beam computed tomography systems and conventional radiography. Dentomaxillofac Radiol. 2004; 33:83-86.

Schulze D, Heiland M, Blake F, Rother U, Schmelzle R. Evaluation of quality of reformatted images from two cone-beam computed tomographic systems. J Cranio Maxillofac Surg. 2005; 33:19-23

Schutyser F, Van Cleynenbreugel J, Ferrant M, Schoenaers J, Suetens P. Image-based 3D planning of maxillofacial distraction procedures including soft tissue implications. Lecture notes in computer science. Springer-Verlag Berlin Heidelberg: 2000; 1935:999-1007

Schwarz AM. Die Röntgenostatik. Wien: Urban & Schwarzenberg; 1958

Selvik G, Alberius P, Fahlman M. Roentgen stereophotogrammetry for analysis of cranial growth. Am J Orthod. 1986; 89:315-325

Sohmura T, Wakabayashi K, Lowmunkong R, Hojo H, Kusumoto N, Okuda H, Kojima T, Nakamura T, Yatani H, Takahashi J. 3D shape measurement of dental casts using medical X-ray CT. Dent Mater J. 2004; 23:121-128

Soncul M, Bamber MA. The reproducibility of the head position for a laser scan using a novel morphometric analysis for orthognathic surgery. Int J Oral Maxillofac Surg. 2000; 29:86-90

Spencer R, Hathaway R, Speculand B. 3D computer data capture and imaging applied to the face and jaws. Br J Oral Maxillofac Surg. 1996; 34:118-123

Spolyar JL, Vasileff W, MacIntosh RB. Image corrected cephalometric analysis (ICCA): design and evaluation. Cleft Palate Craniofac J. 1993; 30:528-539

Stamm T, Meyer U, Meier N, Ehmer U, Joos U. Public domain computer-aided surgery (CAS) in orthodontic and maxillofacial surgery. J Orofac Orthop. 2002; 63: 62-75

Steiner CC. Importance of cephalometry in orthodontic treatment. Inf Orthod Kieferorthop. 1969; 1:3-12

Stoelinga PJ. Distraction from the ground rules? Int J Oral Maxillofac Surg. 1998; 27:414-415

Stucki-McCormick SU, Fox RM, Mizrahi R, Erikson M.Distraction osteogenesis for congenital mandibular deformities. Atlas Oral Maxillofac Surg Clin North Am. 1999; 7:85-109

Stucki-McCromick SU, Fox R, Mizrahi R. Transport distraction: mandibular reconstruction. Atlas Oral Maxillofac Surg Clin North Am. 1999; 7:65-83

Suetens P. Fundamentals of Medical Imaging. Cambridge University Press 2002, ISBN 0-521-80362-4

Sukovic P. Cone beam computed tomography in craniofacial imaging. Orthod Craniofacial Res. 2003; 6:31-36

Surwald C, Ward-Booth P. Initial experiences with digital 3-dimensional stereophotogrammetry imaging. Mund Kiefer Gesichtschir. 2000; 4:183-186

Swennen G, Schliephake H, Dempf R, Schierle H, Malevez C. Craniofacial distraction osteogenesis: a review of the literature. Part 1: Clinical Studies. Int J Oral Maxillofac Surg. 2001; 30:89-103

Swennen G, Berten JL, Schliephake H, Treutlein C, Dempf R, Malevez C, De Mey A. Midfacial morphology in unilateral cleft lip palate children treated by different surgical protocols. Int J Oral Maxillofac Surg. 2002; 31:13-22

Swennen G, Treutlein C, Brachvogel P, Berten JL, Schwestka-Polly R, Hausamen JE. Segmental unilateral transpalatal distraction in cleft patients. J Craniofac Surg. 2003; 14:786-790

Swennen G, Grimaldi H, Berten JL, Kramer FJ, Dempf R, Schwestka-Polly R, Hausamen JE. Reliability and validity of a modified lateral cephalometric analysis for evaluation of craniofacial morphology and growth in cleft patients. J Craniofac J. 2004; 15:399-412

Swennen G, Berten JL, Kramer FJ, Malevez C, De Mey A, Schwestka-Polly R, Hausamen JE. Mandibular morphology in complete unilateral cleft lip and palate. Cleft Palate Craniofac J. 2004; 41:403-409

Swennen G, Barth EL, Schutyser F, Degroeve P, Lemaitre A. Three-dimensional (3-D) Cephalometry. The basics for virtual planning. J Cranio Maxillofac Surg. 2004; 32:(S1)135

Syriopoulos K, Velders XL, van der Stelt PF, van Ginkel FC, Tsiklakis K. Mail survey of dental radiographic techniques and radiation doses in Greece. Dentomaxillofac Radiol. 1998; 27:321-328

Taha F, Testelin S, Deschepper B, Devauchelle B. Orthognathic surgery and stereolithographic models. A new technic of dental occlusion transfer. Rev Stomatol Chir Maxillofac. 2000; 101:65-71

Techalertpaisarn P, Kuroda T. Three-dimensional computer-graphic demonstration of facial soft tissue changes in mandibular prognathic patients after mandibular sagittal ramus osteotomy. Int J Adult Orthodon Orthognath Surg. 1998; 13:217-225

Terai H, Shimahara M, Sakinaka Y, Tajima S. Accuracy of integration of dental casts in three-dimensional models. J Oral Maxillofac Surg. 1999; 57:662-665

Teschner M, Girod S, Girod B. 3-D simulation of craniofacial surgical procedures. Stud Health Technol Inform. 2001; 81:502-508

Tharanon W, Sinn DP. Mandibular distraction osteogenesis with multidirectional extraoral distraction device in hemifacial microsomia patients: three-dimensional treatment planning, prediction tracings, and case outcomes. J Craniofac Surg. 1999; 10:202-213

Tiddeman B, Rabey G, Duffy N. Synthesis and transformation of three-dimensional facial images. IEEE Eng Med Biol Mag. 1999; 18:64-69

Tiddeman B, Duffy N, Rabey G. Construction and visualisation of three-dimensional facial statistics. Comput Methods Programs Biomed. 2000; 63:9-20

Thompson JL, Illerhaus B. A new reconstruction of the Le Moustier 1 skull and investigation of internal structures using 3-D-muCT data. J Hum Evol. 1998; 35:647-665

Togashi K, Kitaura H, Yonetsu K, Yoshida N, Nakamura T. Three-dimensional cephalometry using helical computer tomography. Angle Orthod. 2002; 72:513-520

Treil J, Casteigt J, Madrid C, Borianne P. A new 3-dimensional cephalometry model. A new 3-dimensional parameter analysis: the axis of inertia. A new idea: maxillofacial equilibrium. Orthod Fr. 1997; 68:171-181

Treutlein C, Berten JL, Swennen G, Brachvogel P. Comparative cephalometric study of 10-year-old patients with complete unilateral cleft lip and palate. A cross-sectional study of the Hanover concept. J Orofac Orthop. 2003; 64:27-39

Trotman CA, Gross MM, Moffatt K. Reliability of a three-dimensional method for measuring facial animation: a case report. Angle Orthod. 1996; 66:195-198

Trotman CA, Faraway JJ, Silvester KT, Greenlee GM, Johnston LE, Jr. Sensitivity of a method for the analysis of facial mobility. I. Vector of displacement. Cleft Palate Craniofac J. 1998; 35:132-141

Trotman CA, Faraway JJ, Essick GK. Three-dimensional nasolabial displacement during movement in repaired cleft lip and palate patients. Plast Reconstr Surg. 2000; 105:1273-1283

Troulis MJ, Everett P, Seldin EB, Kikinis R, Kaban LB. Development of a three-dimensional treatment planning system based on computed tomographic data. Int J Oral Maxillofac Surg. 2002; 31:349-357

Tsiklakis K, Syriopoulos K, Stamatakis HC. Radiographic examination of the temporomandibular joint using cone beam computed tomography. Dentomaxillofac Radiol. 2004; 33:196-201

Vanarsdall RL, White RP, Jr. Three-dimensional analysis for skeletal problems. Int J Adult Orthodon Orthognath Surg. 1994; 9:159

Vandewalle P, Schutyser F, Van Cleynenbreugel J, Suetens P. Modelling of facial soft tissue growth for maxillofacial surgery planning environments. Lecture notes in computer science. Springer-Verlag Berlin Heidelberg: 2003; 2673:27-37

Vanezi P, Vanezis M, McCombe G, Niblett T. Facial reconstruction using 3-D computer graphics. Forensic Sci Int. 2000; 108:81-95

Vannier MW, Marsh JL, Warren JO. Three dimensional CT reconstruction images for craniofacial surgical planning and evaluation. Radiology. 1984; 150:179-184

Vannier MW, Conroy GC, Marsh JL, Knapp RH. Three-dimensional cranial surface reconstructions using high-resolution computed tomography. Am J Phys Anthropol. 1985; 67:299-311

Vannier MW. Craniofacial computed tomography scanning: technology, applications and future trends. Orthod Craniofacial. 2003; 6:23-30

Venkatadri G, Farkas LG, Kooiman J. Multipurpose anthropometric facial anglemeter. Plast Reconstr Surg. 1992; 90:507-510

Wang D, Qian G, Zhang M, Farkas LG. Differences in horizontal, neoclassical facial canons in Chinese (Han) and North American Caucasian populations. Aesthetic Plast Surg. 1997; 21:265-269

Ward RE. Facial morphology as determined by anthropometry: keeping it simple. J Craniofac Genet Dev Biol. 1989; 9:45-60

Ward RE, Jamison PL, Farkas LG. Craniofacial variability index: a simple measure of normal and abnormal variation in the head and face. Am J Med Genet. 1998; 80:232-240

Watzinger F, Wanschitz F, Wagner A, Enislidis G, Millesi W, Baumann A, Ewers R. Computer-aided navigation in secondary reconstruction of post-traumatic deformities of the zygoma. J Craniomaxillofac Surg. 1997; 25:198-202

Wehmoller M, Eufinger H, Kruse D, Massberg W. CAD by processing of computed tomography data and CAM of individually designed prostheses. Int J Oral Maxillofac Surg. 1995; 24:90-97

Weingartner T, Hassfeld S, Dillmann R. Virtual jaw: a 3D simulation for computer assisted surgery and education. Stud Health Technol Inform. 1998; 50:329-335

Westermark A, Zachow S, Eppley BL. Three-dimensional osteotomy planning in maxillofacial surgery including soft tissue prediction. J Craniofac Surg. 2005; 16:100-104.

Whyte AM, Hourihan MD, Earley MJ, Sugar A. Radiological assessment of hemifacial microsomia by three-dimensional computed tomography. Dentomaxillofac Radiol. 1990; 19:119-125

Williams FL, Richtsmeier JT. Comparison of mandibular landmarks from computed tomography and 3D digitizer data. Clin Anat. 2003; 16:494-500

Xia J, Samman N, Yeung RW, Shen SG, Wang D, Ip HH, Tideman H. Three-dimensional virtual reality surgical planning and simulation workbench for orthognathic surgery. Int J Adult Orthodon Orthognath Surg. 2000; 15:265-282

Xia J, Samman N, Yeung RW, Wang D, Shen SG, Ip HH, Tideman H. Computer-assisted three-dimensional surgical planing and simulation. 3D soft tissue planning and prediction. Int J Oral Maxillofac Surg. 2000; 29:250-258

Xia J, Ip HH, Samman N, Wong HT, Gateno J, Wang D, Yeung RW, Kot CS, Tideman H. Three-dimensional virtual-reality surgical planning and soft-tissue prediction for orthognathic surgery. IEEE Trans Inf Technol Biomed. 2001; 5:97-107

Yamada T, Sugahara T, Mori Y, Sakuda M. Rapid three-dimensional measuring system for facial surface structure. Plast Reconstr Surg. 1998; 102:2108-2113

Yamada T, Mori Y, Minami K, Mishima K, Sugahara T, Sakuda M. Computer aided three-dimensional analysis of nostril forms: application in normal and operated cleft lip patients. J Craniomaxillofac Surg. 1999; 27:345-353

Yamamoto K, Toshimitsu A, Mikami T, Hayashi S, Harada R, Nakamura S. Optical measurement of dental cast profile and application to analysis of three-dimensional tooth movement in orthodontics. Front Med Biol Eng. 1989; 1:119-130

Yamamoto K, Ueno K, Seo K, Shinohara D. Development of dento-maxillofacial cone beam X-ray computed totography system. Orthod Craniofacial Res. 2003; 6:160-162

Yoo SK, Kim YO, Kim HJ, Kim NH, Jang YB, Kim KD, Lee HY. Alignment of CT images of skull dysmorphology using anatomy-based perpendicular axes. Phys Med Biol. 2003; 48:2681-2695

Young SC, Kolar JC, Farkas LG, Munro IR. Acrocephalosyndactyly: comparison of morphometric measurements in Pfeiffer, Saethre-Chotzen, Carpenter and Apert syndrome. Dtsch Z Mund Kiefer Gesichtschir. 1986; 10:436-443

Yu CC, Wong FH, Lo LJ, Chen YR. Craniofacial deformity in patients with uncorrected congenital muscular torticollis: an assessment from three-dimensional computed tomography imaging. Plast Reconstr Surg. 2004; 113:24-33

Z'Graggen M, Schiel HJ, Kunz C, Lambrecht JT. Three-dimensional cephalometry using individual skeletal laser technology models. Clin Anat. 2001; 14:258-268

Zemann W, Santler G, Karcher H. Analysis of midface asymmetry in patients with cleft lip, alveolus and palate at the age of 3 months using 3D-COSMOS measuring system. J Craniomaxillofac Surg. 2002; 30:148-152

Zentner A, Sergl HG, Filippidis G. A holographic study of variations in bone deformations resulting from different headgear forces in a macerated human skull. Angle Orthod. 1996; 66:463-472

Zilberman O, Huggare JA, Parikakis KA. Evaluation of the validity of tooth size and arch width measurements using conventional and three-dimensional virtual orthodontic models. Angle Orthod. 2003; 73:301-306

Zumpano MP. Size and shape changes during late fetal growth (137-157 gestational days) in the pigtailed macaque (Macaca nemestrina) craniofacial complex: an application using three-dimensional coordinate data and finite element scaling analysis. Anat Rec. 2002; 267:307-320

Zumpano MP, Richtsmeier JT. Growth-related shape changes in the fetal craniofacial complex of humans (Homo sapiens) and pigtailed macaques (Macaca nemestrina): a 3D-CT comparative analysis. Am J Phys Anthropol. 2003; 120:339-351

Subject Index

U

V

W

X

Z